

AD A104761

LEVEL

PROJECT MANAGER SMOKE/OBSCURANTS  
DRCPM-SMK-T  
ABERDEEN PROVING GROUND, MD. 21005

VOLUME II, UNCLASSIFIED SECTION

(6) of the  
PROCEEDINGS

of the

SMOKE/OBSCURANTS SYMPOSIUM V

held at

HARRY DIAMOND LABORATORIES,  
ADELPHI, MARYLAND 20783

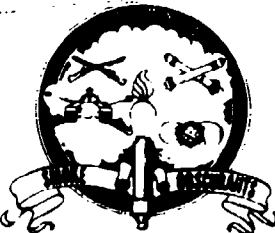
28, 29, & 30 APRIL, 1981.

Sponsored by the

OFFICE OF THE PROJECT MANAGER  
SMOKE/OBSCURANTS



(7) Spec. 1 report



(10) John E. Elkins  
R. H. Kohl

(11) J. 11 81

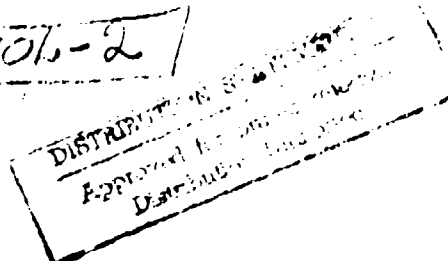
(12) 484

OPM SMOKE/OBSCURANTS

TECHNICAL REPORT

(13) DRCPM-SMK-T-801-81-VOL-2

(VOLUME II, pgs. 423-904)



DTIC FILE COPY

393645 D

81 9 29, 029

**UNCLASSIFIED**

(2)

# **PROCEEDINGS OF THE SMOKE/OBSCURANTS SYMPOSIUM V**

---

## **UNCLASSIFIED SECTION VOLUME II**

**Edited by:**

**Rush E. Elkins**

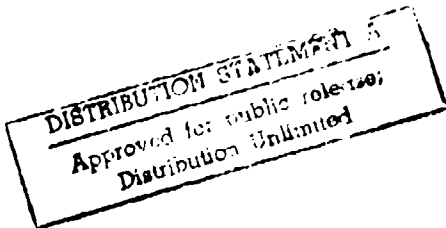
**R. H. Kohl**

**University of Tennessee Space Institute  
Tullahoma, Tennessee**

**OFFICE OF THE PROJECT MANAGER SMOKE/OBSCURANTS**

**1981**

**UNCLASSIFIED**



**UNCLASSIFIED**

SECURITY CLASSIFICATION OF THIS PAGE (When Data Entered)

REPORT DOCUMENTATION PAGE		READ INSTRUCTIONS BEFORE COMPLETING FORM
1. REPORT NUMBER <b>DRCPM-SMK-T-001-81</b>	2. GOVT ACCESSION NO. <b>AD-A104 761</b>	3. RECIPIENT'S CATALOG NUMBER
4. TITLE (and Subtitle) <b>Volumes I &amp; II of the UNCLASSIFIED SECTION, PROCEEDINGS OF THE SMOKE/OBSCURANTS SYMPOSIUM V, Held at HDL, 28, 29, &amp; 30, April 1981, Sponsored by PM Smoke/Obscurants</b>	5. TYPE OF REPORT & PERIOD COVERED <b>Special Report</b>	
6. AUTHOR(s) <b>Editors: Rush E. Elkins and R. H. Kohl of the University of Tennessee Space Institute</b>	7. PERFORMING ORG. REPORT NUMBER <b>A104760</b>	
8. PERFORMING ORGANIZATION NAME AND ADDRESS <b>Project Manager Smoke/Obscurants Aberdeen Proving Ground, MD 21005</b>	9. PROGRAM ELEMENT, PROJECT, TASK AREA & WORK UNIT NUMBERS	
10. CONTROLLING OFFICE NAME AND ADDRESS <b>PM Smoke/Obscurants Attn: DRCPM-SMK-T Aberdeen Proving Ground, MD 21005</b>	11. REPORT DATE <b>July, 1981</b>	
12. MONITORING AGENCY NAME & ADDRESS (if different from Controlling Office)	13. NUMBER OF PAGES <b>960 Vol. I, 460; Vol II, 500.</b>	
	14. SECURITY CLASS. (of this report) <b>UNCLASSIFIED</b>	
	15a. DECLASSIFICATION/DOWNGRADING SCHEDULE	
16. DISTRIBUTION STATEMENT (of this Report) <b>Unlimited</b>		
17. DISTRIBUTION STATEMENT (of the abstract entered in Block 20, if different from Report) <b>Unlimited</b>		
18. SUPPLEMENTARY NOTES		
19. KEY WORDS (Continue on reverse side if necessary and identify by block number) <b>Battlefield Environment, Screening, Smoke, Obscurant, Obscurants, Obscuration, Dust, Battlefield Obscurants, Smoke Obscuration, Dust Clouds, Smoke Clouds, Smoke Plumes, WP, RP, White Phosphorus, Red Phosphorus, Phosphorous Smoke, HC, Obscured Visibility Environment, DIRT I, DIRT II, DIRT III,</b>		
20. ABSTRACT (Continue on reverse side if necessary and identify by block number) <b>This report consists of sixty-seven papers in two volumes (I &amp; II) which, with the eight papers of DRCPM-SMK-T-002-81 and the eight papers of DRCPM-SMK-T - 003-81 (Limited Distribution) comprise the Proceedings of the Smoke/Obscurants Symposium V. Papers in this section fall into the following subject areas: A. Testing, Instrumentation and Methodology; B. Modeling; C. Smoke/Obscurants Technology and Hardware Development; D. Doctrine and Training, Concepts and System Evaluation and Analysis.</b>		

**UNCLASSIFIED**

SECURITY CLASSIFICATION OF THIS PAGE(When Data Entered)

**19. Key Words**

Smoke Week II, H<sup>3</sup>S, Proceedings, Symposium, Electro-optics, Electro-optics Countermeasure, Thermal Imaging, Lidar, Sensor, Tank Thermal Sight, TTS, Nightsight, Laser, Ultraviolet, Visible, Near IR, IR, Mid IR, Far IR, Infrared, Smoke Models, Dust Models, Obscuration Models, Smoke Deployment, Smoke Field Tests, Combat Obscuration, Smoke Test Data, Diffusion of Smoke, Gaussian Plumes, Smoke Test, Dust Test, Imaging Sensor, Crater, Cratering Parameters, Particle Sizing, Partical Size Measurement, Interferometric Particle Sizing, Millimeter Wave Propagation, Millitary Smokes, Backscatter Coefficient, Extinction Coefficient, Attenuation, Transmission, Laboratory Smoke, Field Smoke, Smoke Munitions, Screening Smokes, Obscurant Munitions, VEESS, Vehicle Exhaust Smoke, Smoke Projectile, Large Area Smoke Screening, Smoke Disseminators, Instant Smoke Disseminators, Common Military Smokes, Smoke Compositions, Condensational Growth, Relative Humidity Effects, Employment of Smoke, Night Vision, Tank, Concentration Length Product, Tactical Smoke, Spectral Transmittance, Transmittance, CL, CL Profiles, Inventory Smoke, Transmissometers, Smoke . Aerosol Working Group, Antitank, Laser Seeker, Obscurant Performance, Instantaneous Smoke Screening, Cold Environment, COPPERHEAD, Health Hazards, Obscurant Technology, Multispectral Screening, Smoke Toxicology, Gaming, Dirty Battlefield, Scenario, Scenario Analysis, Bi-modal Size Distribution, Propagation of CO<sub>2</sub> laser radiation, Phosphoric Acid, Stochastic Models, Obscurant Technology, High Wind Smoke Screening, SNOW-ONE, Optical Transmission, Millimeter Wave Transmission, IR Screening, Dusty Infrared Test Series, Dusty Infrared Test III, Smoke/Obscurants Measurements, Smoke/Obscurant Variability, Obscurant Field Data, Instrumentation Cluster, Obscurant Field Testing, Spectrophones, Fog Oil, Background Measurement Spectroradiometer, High Power Laser, CO<sub>2</sub> Laser, Laser Beam, Clearing by Laser Beam, Depolarization, Electro-Optical Test Facility, Smoke Munition Expenditure, BETS, Tailored Soils, Dust Observations, Tropics Dust, Soil Parameters, HE, Radiometer Measurements, Transmission Measurement, Cloud Geometry, Smoke Cloud Geometry, Dust Cloud Geometry, Two-Perspective Geometry, KWIK, KWIK Phase I, ACT II, BELOWSS, Laser Designator, Artillery Produced Dust, Dispersion of Obscurants, Error Bounds , Extinction by Smokes, Light Scattering, Irregular Particles, Smoke Persistency, Multicompnent Oil Smokes, Oil Smokes , SCREEN, EOSAEL 80, Target Acquisition Probability, Path Luminance, Background Luminance, Windblown Dust, Aerosol Materials, IR Obscuring Materials, Pyrotechnic Infrared Screening, Multistage Chaff Rocket, 2.75 Inch Rocket, Clutter Rejection, Laser Semi-Active Missile Systems, Felt Wedge, Diesel Fuel Obscurant, Inhalation Toxicology, Inhaled Aerosols, M18 Grenades, Colored Smoke, Nontoxic Smoke, Alkali Halide Smoke, XM49, XM49 Smoke Generator, Helicopter Smoke Grenade, Laser Induced Smoke, Multispectral Chaff, Training, Training Smoke, MILES, Small Unit Tactics, Operational Smoke Concept, SAWG, SAWG Concepts Study, Battlefield Environment Obscuration Handbook, Obscurant Countermeasure.

**UNCLASSIFIED**

SECURITY CLASSIFICATION OF THIS PAGE(When Data Entered)

## CONTENTS OF VOLUME II\*

### UNCLASSIFIED SECTION

TECHNICAL REPORT DRCPM-SMK-T-001-81  
(continued)

Contents of the Entire Proceedings .....	vii
Proceedings Papers by Author .....	xvii
Proceedings Papers by Organization .....	xix
<u>AREA B. MODELING</u> .....	423
B-1.* Temporal Characterization of Smoke and Dust Cloud Geometry by Processing of Two-Perspective Video Images .....	425
<i>G. R. Blackman (ASL) (presented by E. B. Sternmark)</i>	
B-2.* Munition Expenditure Model Verification KWIK Phase I .....	441
<i>R. Peña (ASL) (presented by Steve Cohn)</i>	
B-3.* Comparisons Between the Upgraded Model ACT II and Recent Smoke Week Tests .....	457
<i>R. A. Sutherland (ASL)</i>	
B-4.* Battlefield Environment Laser Designator Weapon System Simulation (BELOWSS) Test and Simulation Results .....	469
<i>R. E. Alongi, R. F. Yates (MICOM)</i>	
B-5. Withdrawn	
B-6. (Designation changed to C-26)	
B-7.* Sensitivity of Calculated Transmittances in Artillery Produced Dust Clouds to Variations in Model Inputs .....	481
<i>M. G. Heaps, D. W. Hock (ASL)</i>	
B-8.* Parameterization of the Dispersion of Battlefield Obscurants .....	517
<i>W. D. Ohmatede, E. B. Sternmark (ASL)</i>	
B-9.* Error Bounds for Smoke Obscuration Models .....	527
<i>M. D. Smith, J. R. Rowland, D. M. Anderson (CSU)</i>	
B-10.* MMTRN: Millimeter Wave Propagation Model for Rain, Fog and Snow Extinction and Gaseous Absorption .....	537
<i>D. R. Brown (ASL)</i>	
B-11.* Extinction by Smokes at Visible, Infrared and Millimeter Wavelengths .....	555
<i>J. F. Embury (CSL)</i>	

The Proceedings of the Smoke/Obscurants Symposium V are divided into the Unclassified Section, Volumes I and II (DRCPM-SMK-T-001-81), the Confidential Section (DRCFM-SMK-T-002-81) and the Restricted Addendum (DRCPM-SMK-T-003-81).

\*Indicates that paper was presented in the Symposium (presenter is underlined).

<sup>1</sup>Indicates a presented standby paper.

Contents of Volume II; Unclassified Section (continued)

B-12.* Some Aspects of Light Scattering from Clouds of Regularly and Irregularly Shaped Particles.....	557
<i>D. K. Anker (Logica)</i>	
B-13.* A Semiquantitative Model for the Prediction of the Persistency of Multicomponent Oil Smokes .....	573
<i>G. O. Rube (CSL)</i>	
B-14. Withdrawn	
B-15. SCREEN, an EOSAEL 80 Model for Smoke Munition Expenditure Based on Target Acquisition Probability.....	587
<i>D. W. Hoock (ASL)</i>	
B-16. Computed Path to Background Luminance Ratios for Obscuring Smoke Clouds .....	601
<i>D. W. Hoock, R. A. Sutherland (ASL)</i>	
B-17. Obscuring Effects of Windblown Dust.....	613
<i>H. A. Seagraves (ASL)</i>	
<b>AREA C. SMOKE/OBSCURANT TECHNOLOGY AND HARDWARE DEVELOPMENT.....</b>	<b>629</b>
C-1.* The Optical Properties of Phosphorus Smoke in the 7-14 $\mu\text{m}$ Infrared.....	631
<i>M. E. Milham, D. H. Anderson (CSL)</i>	
C-2.* Replacement of HC Smoke.....	659
<i>M. D. Smith (CSL)</i>	
C-3.* Smoke/Obscurants Health Effects Research .....	663
<i>CPT D. L. Johnson, J. C. Eaton (USAMRMC)</i>	
C-4.* An Investigation of Aerosol Materials that Obscure in the Middle-to-Far Infrared.....	667
<i>R. A. Kenley, S. L. Witham, K. M. Sancier (SRI)</i>	
C-9.* Pyrotechnic Infrared Screening Mechanisms .....	703
<i>J. A. Domanico (CSL)</i>	
C-10.* Feasibility Study of 2.75 Inch Multistage Chaff Warhead.....	709
<i>W. G. Rouse (CSL)</i>	
C-11.* Clutter Rejection Techniques for Laser Semi-Active Missile Systems.....	715
<i>H. F. Anderson (MICOM), R. J. Polge (UAH) (presented by G. Widerhofer)</i>	
C-12. <sup>P</sup> Copperhead Performance on the Modern Dirty Battlefield (abstract only) .....	735
<i>H. E. Weaver, G. D. Minto (Martin-Marietta)</i>	
C-14. Physical and Chemical Characterization of Smoke Produced from White Phosphorus/Felt Wedge (abstract only) .....	737
<i>W. Bock, R. Butler, S. Katz, N. Rajendaran and A. Snelack (ITT-RCA)</i>	
C-15. Chemical and Physical Characterization of a Diesel Fuel Obscurant for Inhalation Toxicology Studies.....	739
<i>R. A. Jenkins, R. W. Holmberg, J. H. Moneyham, and J. S. Wike (ORNL)</i>	
C-16. Acute Exposures of Rats to an Inhaled Aerosol of Diesel Fuel.....	759
<i>W. Miller, S. Bock, R. Holmberg, J. Moneyham, and M. Querido (ITT)</i>	

Contents of Volume II; Unclassified Section (continued)

C-17. Substitution of Nontoxic Dye in M18 Colored Smoke Grenades.....	773
<i>M. D. Smith (CSL)</i>	
C-18. Improvements and Proposed Development of Alkali Halide Smokes (abstract only).....	783
<i>L. A. Mathews, I. St. Armand (NWC)</i>	
C-19. A Laboratory Investigation of Aerosol and Extinction Characteristics of Obscurant Screens Produced from Alkali Halide Pyrotechnics .....	785
<i>J. T. Hanley, E. J. Mack (Calspan)</i>	
C-20. XM49 Mechanical Smoke Generator .....	807
<i>W. G. Rouse (CSL)</i>	
C-22. Helicopter Smoke Countermeasure Grenade--Phase II .....	815
<i>J. A. Domanico (CSL)</i>	
C-23. Laser-Induced Smoke Generation .....	819
<i>R. W. Lapple (ARRADCOM)</i>	
C-24. Not released	
C-25. Withdrawn	
C-27. Multispectral Absorption and Scattering Properties of an Experimental Chaff Cloud (abstract only).....	823
<i>J. R. Bassett et al. (Delco Electronics)</i>	
 <u>AREA D. DOCTRINE AND TRAINING, CONCEPTS AND SYSTEMS EVALUATION AND ANALYSIS</u> .....	825
D-1. * Training Smoke Generation (MILES System).....	827
<i>R. H. Trickey (CSL)</i>	
D-2. The Effect of Smoke in Small Unit Tactics .....	855
<i>B. W. Fowler (MICOM), CPT J. Price (MMUS)</i>	
D-3. * Smoke Employment: An Operational Concept .....	859
<i>J. W. Scully, MAJ P. B. Harrington (USACMDS)</i>	
D-4. The JTCA/ME SAWG Concepts Study.....	871
<i>C. K. Arpke (OSU), B. W. Fowler (MICOM)</i>	
D-6. * Development of the Battlefield Environment Obscuration Handbook .....	875
<i>R. F. Turner (SAI)</i>	
D-7. Obscurants as a Countermeasure to Modern Weapon Systems.....	891
<i>SFC J. P. Bulger (PM Smoke)</i>	

## CONTENTS OF THE PROCEEDINGS\*

### UNCLASSIFIED SECTION

#### TECHNICAL REPORT DRCPM-SMK-T-001-81

#### VOLUME I

Foreword.....	xiii
<u>COL Samuel L. Eure (PM Smoke/Obscurants)</u>	
Keynote Address*.....	xv
<u>MG Allen H. Light (Commander, ARRAADCOM)</u>	
Remarks at the Closing*.....	xxiii
<u>COL (Ret.) Henry R. Shelton (Systems Planning)</u>	
Closing Remarks*.....	xxv
<u>COL Samuel L. Eure (PM Smoke/Obscurants)</u>	
Agenda.....	xxvii
Attendance List.....	xxxi
Proceedings Papers by Author .....	xxxvii
Proceedings Papers by Organization .....	xxxix
AREA A. TESTING, INSTRUMENTATION AND METHODOLOGY.....	1
A-1.* High Wind Smoke Screening.....	3
<u>Stephen L. Cohn (ASL)</u>	
A-2.* A First Look at SNOW-ONE.....	15
<u>George W. Aitken (CREL)</u>	
A-3.* An Overview of Smoke Week III .....	45
<u>Gary Nelson (PM Smoke)</u>	
A-4.* UK Electro-Optic Equipment at the Smoke Week III Test - Performance, Results and Comments (in Confidential Section) <u>P. H. Davies, S. P. Braim, P. N. Griffith, K. F. Hulme, J. J. P. Payne</u> <u>and T. H. Richardson (Royal Signals and Radar Establishment, United</u> <u>Kingdom) (presented by W. A. Shand)</u>	
A-5. <sup>1</sup> Description of a System for the Measurement of Optical and Millimeter Wave Transmission through Battlefield Environments.....	47
<u>Robert J. Keyes (MIT-Lincoln Lab)</u>	

\* The Proceedings of the Smoke/Obscurants Symposium V are divided into the Unclassified Section, Volumes I and II (DRCPM-SMK-T-001-81), the Confidential Section (DRCPM-SMK-T-002-81) and the Restricted Addendum (DRCPM-SMK-T-003-81).

\* Indicates that paper was presented in the Symposium (presenter is underlined).

<sup>1</sup> Papers A-5 and A-6 were presented in a joint presentation

Contents of the Proceedings (continued)  
 Contents of the Unclassified Section (continued)

Contents of Volume I (continued)

A-6. <sup>1</sup>	Results of Simultaneous Transmission Measurements at MMW and Various Optical Frequencies in a Battlefield Environment.....	51
	<u>R. J. Sasiela (MIT-Lincoln Lab)</u>	
A-7.*	Characterization of 155 mm Smoke Projectile (Field Test) (in Confidential Section)	
	<u>S. Dayan (MOD/R&amp;D, Israel)</u>	
A-8.*	Canadian Program in Anti-IR Screening Aerosols	
	Abstract only .....	67
	(Entire Paper is in Restricted Addendum)	
	<u>P. E. Kluchert (DREV, Canada)</u>	
A-9.*	Dusty Infrared Test Series (Film) (abstract only).....	69
	<u>Bruce W. Kennedy (ASL) (Presented by Frank Niles)</u>	
A-10. <sup>2</sup>	Dusty Infrared Test III (DIRT-III)	
	Project Summary .....	71
	<u>Bruce W. Kennedy (ASL) (Presented by Frank Niles)</u>	
A-11. <sup>p</sup>	SAM Launch Cloud Interference with EO Surveillance (in Restricted Addendum)	
	<u>C. R. Sundiff and W. R. Price (OMEW), G. A. Buckle (Indian Head) and A. C. Victor (NWC)</u>	
A-12.*	Estimation of Precision of Smoke/Obscurant Measurements and Product Variability.....	89
	<u>James F. O'Bryan (AMSAA &amp; JICG/ME/SAWG)</u>	
A-13.*	A Data Reduction Technique for Field Data.....	97
	<u>Marvin D. Smith, Keith Jones and P. Kittikul (OSU)</u>	
A-14. <sup>3</sup>	The Instrumentation Cluster Concept in Obscurant Field Testing.....	127
	<u>W. M. Farmer (UTSI)</u>	
A-15.*	Data Obtained from the Smoke Week III Instrumentation Cluster.....	147
	<u>W. M. Farmer, F. A. Schwartz, R. D. Morris, M. A. Binkley and L. M. Boyd (UTSI)</u>	
A-16.*	Battlefield Smoke and Dust Parameters Measured in Situ Using Spectrophones .....	169
	<u>C. W. Bruce, Y. P. Yee, L. M. Moore (ASL), A. V. Jelinek (OptiMetrics) and N. Richardson (NMSU)</u>	
A-17.*	In Situ Measurements of Phosphorous Smokes During Smoke Week III.....	183
	<u>D. M. Garvey, G. Fernandes, C. W. Bruce, and R. G. Pinnick (ASL)</u>	
A-18.	Particle Size Analysis -Theory and Data on Bimodal Fog Oil Distribution.....	215
	<u>Robert W. Doherty and Robert H. Frickel (CSS)</u>	

<sup>2</sup> Due to the absence of the author, only a few viewgraphs from this paper were presented at the end of the presentation of paper A-9.

<sup>p</sup> On this and following papers "p" indicates the paper was presented in the Preliminary Session.

<sup>3</sup> Some aspects of this paper appeared in the presentation of the following paper.

Contents of the Proceedings (continued)  
Contents of the Unclassified Section (continued)

Contents of Volume I (continued)

- A-19. \* Particle Size and Infrared Absorption Measurements of IR Smokes During Smoke Week III (in Confidential Section)  
R. G. Pinnick, G. Fernandes, C. W. Bruce, D. M. Garvey  
and B. D. Hinds (ASL)
- A-20. \* Thermal Radiance of Smokes and Battlefield Fires  
(in Confidential Section)  
T. W. Cassidy and W. E. Stump (NV&EOL)
- A-21. The Infrared Characterization of Smokes and Obscurants Utilizing the Honeywell Background Measurement Spectroradiometer..... 241  
J. R. Bryson, M. J. Flanagan (Honeywell) and D. R. Snyder III  
(Eglin AFB)
- A-22. LIDAR Evaluation of Smoke and Dust Clouds (abstract only)..... 275  
Edward E. Uthe (SRI)
- A-23. \* Propagation of a High Power Pulsed CO<sub>2</sub> Laser Beam Through Battlefield Aerosols ..... 277  
Thomas G. Miller (MICOM)
- A-24. Evaporative Clearing for a CO<sub>2</sub> High Energy Laser Beam in White Phosphorous Smoke..... 293  
C. W. Bruce, Y. P. Yee and S. J. Duran (ASL)
- A-25. <sup>4</sup> Near-IR Extinction, Backscatter and Depolarization of Smoke Week III Aerosols ..... 313  
Z. G. Setanyay, D. McGuire, J. Griffin, W. Hattery,  
G. Martin and G. Wetzel (HDL)
- A-26. <sup>4</sup> IR Extinction Coefficients Determined from Smoke Week III  
(in Confidential Section)  
W. M. Farmer, F. A. Schwartz, R. D. Morris, M. A. Binkley,  
and E. M. Boyd (UTSI)
- A-27. <sup>4</sup> Degraded Visibility Testing at the Electro-Optical Test Facility ..... 341  
CPT William M. Decker IV (EPG)
- A-28. NV & EOL Smoke Week III Results  
(in Confidential Section)  
T. W. Cassidy, D. B. Newman and D. B. Simmons (NV&EOL)
- A-29. Plans for the Evaluation of Smoke Munition Expenditure Models ..... 351  
Bernard F. Engebos (ASL)
- A-30. Dust Observations in the Battlefield Environments with Tailored Soils (BETS) Series ..... 353  
James B. Mason, Katherine S. Long and Lewis E. Link (WES)
- A-31. Correlations Between Soil Parameters and Obscuration Features of Clouds Produced by Munitions in the Humid Tropics ..... 375  
Robert J. Fuchs and CPT Marie Martinucci (Tropic Test Center)

<sup>4</sup> Indicates a presented standby paper. Standby papers were not indicated on the Agenda.  
Paper A-27 was presented in the Preliminary Session.

Contents of the Proceedings (continued)  
Contents of the Unclassified Section (continued)

Contents of Volume I (continued)

- A-32. Withdrawn
- A-33. Withdrawn
- A-34.\* Infrared Measurements with the Midas III Radiometer during Smoke  
Week III Tests ..... 381  
A. G. Geiser (*Cincinnati Electronics*)
- A-35. Atmospheric Transmission Measurements of Smoke and Obscurants ..... 403  
Leonard V. Lucia, William E. Surrette, Jr. and  
Frederic M. Zweibaum (*Barnes*)

VOLUME II

- AREA B. MODELING ..... 423
- B-1.\* Temporal Characterization of Smoke and Dust Cloud Geometry by  
Processing of Two-Perspective Video Images ..... 425  
G. R. Blackman (*ASL*) (*presented by E. B. Stenmark*)
- B-2.\* Munition Expenditure Model Verification KWIK Phase I ..... 441  
R. Peña (*ASL*) (*presented by Steve Cohn*)
- B-3.\* Comparisons Between the Upgraded Model ACT II and Recent Smoke  
Week Tests ..... 457  
R. A. Sutherland (*ASL*)
- B-4.\* Battlefield Environment Laser Designator Weapon System Simulation  
(BELOWSS) Test and Simulation Results ..... 469  
R. E. Alorgi, R. F. Yates (*MICOM*)
- B-5. Withdrawn
- B-6. (Designation changed to C-26)
- B-7.\* Sensitivity of Calculated Transmittances in Artillery Produced Dust  
Clouds to Variations in Model Inputs ..... 481  
M. G. Heape, D. W. Hoak (*ASL*)
- B-8.\* Parameterization of the Dispersion of Battlefield Obscurants ..... 517  
W. D. Ohmetede, E. B. Stenmark (*ASL*)
- B-9.\* Error Bounds for Smoke Obscuration Models ..... 527  
M. D. Smith, J. R. Rowland, D. M. Anderson (*OSU*)
- B-10.\* MMTRN: Millimeter Wave Propagation Model for Rain, Fog and Snow  
Extinction and Gaseous Absorption ..... 537  
D. R. Brown (*ASL*)
- B-11.\* Extinction by Smokes at Visible, Infrared and Millimeter  
Wavelengths ..... 555  
J. F. Embury (*CSL*)

Contents of the Proceedings (continued)  
Contents of the Unclassified Section (continued)

Contents of Volume II (continued)

B-12.* Some Aspects of Light Scattering from Clouds of Regularly and Irregularly Shaped Particles.....	557
D. K. Anker (Logica)	
B-13.* A Semiquantitative Model for the Prediction of the Persistency of Multicomponent Oil Smokes .....	573
G. O. Rubel (CSL)	
B-14. Withdrawn	
B-15. SCREÉN, an EOSAEL 80 Model for Smoke Munition Expenditure Based on Target Acquisition Probability.....	587
D. W. Hock (ASL)	
B-16. Computed Path to Background Luminance Ratios for Obscuring Smoke Clouds .....	601
D. W. Hock, R. A. Sutherland (ASL)	
B-17. Obscuration Effects of Windblown Dust.....	613
M. A. Seagraves (ASL)	
<u>AREA C. SMOKE/OBSCURANT TECHNOLOGY AND HARDWARE DEVELOPMENT</u> .....	629
C-1.* The Optical Properties of Phosphorus Smoke in the 7-14 $\mu\text{m}$ Infrared.....	631
M. E. McIver, D. H. Anderson (CSL)	
C-2.* Replacement of HC Smoke.....	659
K. D. Smith (CSL)	
C-3.* Smoke/Obscurants Health Effects Research .....	663
CPT D. L. Johnson, J. C. Eaton (SAMPRU)	
C-4.* An Investigation of Aerosol Materials that Obscure in the Middle-to-Far Infrared.....	667
R. A. Kenley, C. S. Witham, K. M. Sancier (SRI)	
C-5. <sup>P</sup> Novel Multispectral Screening Materials (in Restricted Addendum) <u>Richard Kenley, Gerald August, Marie Soras and Zoila Reyes (SRI)</u>	
C-6. <sup>P</sup> Evaluation of Multispectral Screening Smoke Generators (in Restricted Addendum) <u>James J. Savage and Roy E. Shaffer (CSL)</u>	
C-7. <sup>P</sup> Characterization and Redispersal of Multispectral Obscuring Fibers (in Restricted Addendum) <u>Paul J. Buchman (Aerodyne)</u>	
C-8. <sup>P</sup> Infrared Screening Smoke Development (in Restricted Addendum) <u>D. R. Dillehay (Thiokol)</u>	
C-9.* Pyrotechnic Infrared Screening Mechanisms .....	703
J. A. Domarco (CSL)	

Contents of the Proceedings (continued)  
Contents of the Unclassified Section (continued)

Contents of Volume II (continued)

C-10.* Feasibility Study of 2.75 Inch Multistage Chaff Warhead.....	709
<u>H. G. Rouse (CSL)</u>	
C-11.* Clutter Rejection Techniques for Laser Semi-Active Missile Systems.....	715
<u>H. F. Anderson (MICOM), R. J. Polge (UAH)</u> <u>(presented by G. Widenhofer)</u>	
C-12.* Copperhead Performance on the Modern Dirty Battlefield (abstract only) .....	735
<u>H. E. Weaver, G. D. Minto (Martin-Marietta)</u>	
C-13.^ Copperhead/Hellfire Sematic Active Laser Seeker Performance in Battlefield Obscurants (in Restricted Addendum) <u>R. W. Schneider (MICOM)</u>	
C-14. Physical and Chemical Characterization of Smoke Produced from White Phosphorus/Felt Wedge (abstract only) .....	737
<u>W. Bock, R. Butler, S. Katz, N. Rajendran and A. Snelson (ITT-RI)</u>	
C-15. Chemical and Physical Characterization of a Diesel Fuel Obscurant for Inhalation Toxicology Studies.....	739
<u>R. A. Jenkins, R. W. Holmberg, J. H. Moneyhun, and J. S. Wike     (ORNL)</u>	
C-16. Acute Exposures of Rats to an Inhaled Aerosol of Diesel Fuel.....	759
<u>W. Dalbey, S. Lock, B. Holmberg, J. Moneyhun, and M. Guerin     (ORNL)</u>	
C-17. Substitution of Nontoxic Dye in M18 Colored Smoke Grenades.....	773
<u>M. D. Smith (CSL)</u>	
C-18. Improvements and Proposed Development of Alkali Halide Smokes (abstract only).....	783
<u>L. A. Mathews, P. St. Armand (NWC)</u>	
C-19. A Laboratory Investigation of Aerosol and Extinction Characteristics of Obscurant Screens Produced from Alkali Halide Pyrotechnics .....	785
<u>J. T. Hanley, E. J. Mack (Calspan)</u>	
C-20. XM49 Mechanical Smoke Generator .....	807
<u>W. G. Rouse (CSL)</u>	
C-21. Development of an Infrared Screening Grenade (in Confidential Section) <u>M. L. Erickson and W. W. Beyth (CSL), L. Lowe (AAI) and H. LaMuth     (Battelle Columbus)</u>	
C-22. Helicopter Smoke Countermeasure Grenade--Phase II .....	815
<u>J. A. Domenico (CSL)</u>	
C-23. Laser-Induced Smoke Generation .....	819
<u>E. W. Lappie (ARRADCOM)</u>	
C-24. Not released	
C-25. Withdrawn	

Contents of the Proceedings (continued)  
Contents of the Unclassified Section (continued)

Contents of Volume II (continued)

- C-26.\* Optimization Assessment of Chemically Non-Reactive Obscurants for Vehicle Self Protection (in Confidential Section)  
J. F. Ebercole and T. E. Spaulding (Aerodyne)
- C-27. Multispectral Absorption and Scattering Properties of an Experimental Chaff Cloud (abstract only) ..... 823  
J. R. Laskett et.al. (Delco Electronics)
- AREA D.. DOCTRINE AND TRAINING, CONCEPTS AND SYSTEMS EVALUATION AND ANALYSIS** ..... 825
- D-1.\* Training Smoke Consideration (MILES System) ..... 827  
R. H. Fricke (CSL)
- D-2. The Effect of Smoke in Small Unit Tactics ..... 855  
B. W. Fowler (MICOM), CPT J. Price (NMCS)
- D-3.\* Smoke Employment: An Operational Concept ..... 859  
J. W. Scully, MAJ P. B. Harrington (USACMIS)
- D-4. The JTCA/ME SAWG Concepts Study ..... 871  
C. K. Arpke (OSU), B. W. Fowler (MICOM)
- D-5.<sup>P</sup> Warsaw Pact Irritant Smokes -- A New Dimension in Combat  
(in Restricted Addendum)  
LTC John P. Bulger (PM Smoke) and Frank Poleski (Foreign Science and Technology Center)
- D-6.\* Development of the Battlefield Environment Obscuration Handbook ..... 875  
R. E. Turner (SAI)
- D-7. Obscurants as a Countermeasure to Modern Weapon Systems ..... 891  
LTC J. P. Bulger (PM Smoke)

Contents of the Proceedings (continued)

CONFIDENTIAL SECTION

TECHNICAL REPORT DRCPM-SMK-T-002-81

AREA A. TESTING, INSTRUMENTATION AND METHODOLOGY ..... 1  
(Confidential Papers)

A-4.* (U) UK Electro-Optic Equipment at Smoke Week III Test - Performance, Results and Comments (Confidential).....	3
<i>P. H. Davies, S. P. Braim, P. N. Griffith, K. F. Hulme, J. J. P. Payne, and T. H. Richardson (Royal Signals and Radar Establishment, United Kingdom) (presented by W. A. Shand)</i>	
A-7.* (U) Characterization of 155 mm HC Smoke Projectile (Field Test) (Confidential).....	25
<i>N. Duyar (MOD/R&amp;D, Israel)</i>	
A-19.* (U) Particle Size and Infrared Absorption Measurements of IR Smokes During Smoke Week III (Confidential).....	47
<i>J. G. Pinnick, G. Fernandes, C. W. Bruce, D. M. Garvey and B. D. Hines (ASL)</i>	
A-20.* (U) Thermal Radiance of Smokes and Battlefield Fires (Confidential) .....	59
<i>T. W. Cassidy and W. E. Stump (NV&amp;EOL)</i>	
A-26.* (U) IR Extinction Coefficients Determined from Smoke Week III (Confidential).....	73
<i>W. M. Farmer, F. A. Schwartz, R. D. Morris, M. A. Binkley and L. M. Boyd (UTSI)</i>	
A-28. (U) NV & EOL Smoke Week III Results (Confidential).....	85
<i>T. W. Cassidy, D. B. Newman and D. B. Simmons (NV&amp;EOL)</i>	

AREA C. SMOKE/OBSCURANT TECHNOLOGY AND HARDWARE DEVELOPMENT ..... 107  
(Confidential Papers)

C-21. (U) Development of an Infrared Screening Grenade (Confidential).....	109
<i>M. L. Erickson and W. W. Beyti (CSL), L. Lowe (AAI) and H. LaMuth (Battelle Columbus)</i>	
C-26.* (U) Optimization Assessment of Chemically Non-Reactive Obscurants for Vehicle Self Protection (Confidential).....	125
<i>J. F. Ebersole and T. E. Spaulding (Aerodyne)</i>	

Contents of the Proceedings (continued)

RESTRICTED ADDENDUM<sup>#</sup>

TECHNICAL REPORT DRCPM-SMK-T-003-81

<u>AREA A. TESTING, INSTRUMENTATION AND METHODOLOGY</u> (Restricted Papers)	1
A-8.* (U) Canadian Program in Anti-IR Screening Aerosols (Confidential) <u>R. E. Kluchert (DREV)</u>	3
A-11. <sup>P</sup> (U) SAM Launch Cloud Interference with EO Surveillance (Confidential). <u>C. R. Cundiff and W. R. Price (OMEW), C. A. Buckle (Indian Head)</u> <u>and A. C. Victor (NWC)</u>	25
<u>AREA C. SMOKE/OBSCURANT TECHNOLOGY AND HARDWARE DEVELOPMENT</u> (Restricted Papers)	43
C-5. <sup>P</sup> (U) Novel Multispectral Screening Materials (Confidential). <u>Richard Kenley, Gerald August, Marie Comas and Zoila Reiles (SRI)</u>	45
C-6. <sup>P</sup> (U) Evaluation of Multispectral Screening Smoke Generators (Confidential). <u>James J. Savage and Roy E. Shaffer (CSL)</u>	87
C-7. <sup>P</sup> (U) Characterization and Redispersion of Multispectral Obscuring Fibers (Confidential). <u>Paul L. Bachman (Aercdyn)</u>	123
C-8. <sup>P</sup> (U) Infrared Screening Smoke Development (Confidential). <u>D. R. Dillahay (Thiokol)</u>	151
C-13. <sup>P</sup> (U) Copperhead/Hellfire Semiactive Laser Seeker Performance in Battlefield Obscurants (Smoke Week III) (Confidential). <u>R. V. Schneider (MILCOM)</u>	167
<u>AREA D. DOCTRINE AND TRAINING, CONCEPTS AND SYSTEMS EVALUATION AND ANALYSIS</u> (Restricted Paper)	201
D-5. <sup>P</sup> (U) Warsaw Pact Irritant Smokes -- A New Dimension in Combat (Confidential). <u>LTC John P. Bulger (PM Smoke) and Frank Poleski (Foreign Sciences</u> <u>and Technology Center)</u>	203

<sup>#</sup> The Restricted Addendum is a Confidential document whose distribution is limited to U. S. Government Agencies. All other requests for the Addendum must be referred to PM Smoke/Obscurants, DRCPM-SMK-T, Aberdeen Proving Ground, MD 21005

## PROCEEDINGS PAPERS BY AUTHOR

Papers presented at the Symposium are indicated by an asterisk (\*).  
 Papers presented at the Preliminary Session of the Symposium are indicated by a superscript  
 Papers presented by the indicated author are underlined.

- |  |  |
|--|--|
| <p>Aitken, G. W. A-2*</p> <p>Alongi, R. E. <u>B-4*</u></p> <p>Anderson, D. H. C-1*</p> <p>Anderson, D. M. B-9*</p> <p>Anderson, H. F. C-11*</p> <p>Anker, D. K. <u>B-12*</u></p> <p>Arpke, C. K. <u>D-4</u></p> <p>August, G. C-5<sup>P</sup></p> <p>Bachman, P. L. <u>C-7<sup>P</sup></u></p> <p>Baskett, J. R. (<u>et.al.</u>) C-27</p> <p>Beyth, W. W. C-21</p> <p>Binkley, M. A. A-15*, A-26*</p> <p>Blackman, G. R. B-1*</p> <p>Bock, W. C-14</p> <p>Boyd, L. M. A-15*, A-26*</p> <p>Brain, S. P. A-4*</p> <p>Brown, D. R. B-10*</p> <p>Bruce, C. W. <u>A-16*</u>, A-17*, A-18*, A-24</p> <p>Bryson, J. R. <u>A-21</u></p> <p>Buckle, G. A. A-11<sup>P</sup></p> <p>Bulger, LTC J. P. <u>D-5<sup>P</sup></u>, D-7</p> <p>Butler, R. C-14</p> <p>Cassidy, T. W. A-20*, A-28</p> <p>Cohn, S. L. A-1*, (presenter of <u>B-2*</u>)</p> <p>Comas, M. C-5<sup>P</sup></p> <p>Cundiff, C. R. <u>A-11<sup>P</sup></u></p> <p>Dalbey, W. C-16</p> <p>Davlos, P. H. A-4*</p> <p>Dayan, N. A-7*</p> <p>Decker, CPT W. M., IV <u>A-27*</u></p> <p>Dilliehay, D. R. <u>C-8<sup>P</sup></u></p> <p>Doherty, R. W. A-18</p> <p>Domanico, J. A. C-9*, C-22</p> <p>Duran, S. J. A-24</p> <p>Eaton, J. C. C-3*</p> <p>Ebersole, J. F. C-26*</p> <p>Embry, J. F. <u>B-11*</u></p> <p>Engelbos, B. F. A-29</p> <p>Erickson, M. L. C-21</p> <p>Eure, COL S. L. Foreword, <u>Closing Remarks*</u></p> <p>Farmer, W. M. A-14, A-15*, A-26*</p> <p>Fernandez, G. A-17*, A-19*</p> <p>Flanagan, M. J. A-21</p> <p>Fowler, B. W. D-2, D-4</p> <p>Frickel, R. H. A-18, <u>D-1*</u></p> <p>Fuchs, R. J. A-31</p> <p>Garvey, D. M. A-17*, A-19*</p> <p>Geiser, A. G. A-34*</p> <p>Griffin, J. A-25*</p> <p>Griffith, P. M. A-4*</p> <p>Guerin, M. C-16</p> | <p>Hanley, J. T. C-19</p> <p>Harrington, MAJ P. B. D-3*</p> <p>Hattery, W. A-25*</p> <p>Heaps, M. G. B-7*</p> <p>Hinds, B. D. A-19*</p> <p>Holmberg, R. W. C-15, C-16</p> <p>Hoock, D. H. <u>B-7*</u>, B-15, B-16</p> <p>Hulme, K. F. <u>A-4*</u></p> <p>Jelinek, A. V. A-16*</p> <p>Jenkins, R. A. C-15</p> <p>Johnson, CPT D.L. C-3*</p> <p>Jones, K. A-13*</p> <p>Katz, S. C-14</p> <p>Kenley, R. A. <u>C-4*</u>, <u>C-5<sup>P</sup></u></p> <p>Kennedy, B. W. <u>A-9*</u>, <u>A-10*</u></p> <p>Keyes, R. J. A-5*</p> <p>Kittikul, P. A-13*</p> <p>Kluchert, R. E. <u>A-8*</u></p> <p>LaMuth, H. C-21</p> <p>Lapple, R. W. C-23</p> <p>Light, MG A. H. <u>Keynote Address*</u></p> <p>Link, L. E. A-30</p> <p>Lock, S. C-16</p> <p>Long, K. S. A-30</p> <p>Lowe, L. C-21</p> <p>Lucia, L. V. A-35</p> <p>Mack, E. J. C-19</p> <p>Martin, G. A-25*</p> <p>Martinucci, CPT M. A-31</p> <p>Mason, J. B. A-30</p> <p>Mathews, L. A. C-18</p> <p>McGuire, D. A-25*</p> <p>Milham, M. E. C-1*</p> <p>Miller, T. G. <u>A-23*</u></p> <p>Minto, G. D. C-12<sup>P</sup></p> <p>Moneyhun, J. G. C-15, C-16</p> <p>Moore, L. M. A-16*</p> <p>Morris, R. D. A-15*, A-26*</p> <p>Nelson, Gary A-3*</p> <p>Newman, D. B. A-<sup>~</sup>q</p> <p>Niles, F. (presenter of <u>A-9*</u> and <u>A-10*</u>)</p> <p>O'Bryon, J. F. A-12*</p> <p>Ohmstede, W. D. <u>B-8*</u></p> <p>Payne, J. J. P. A-4*</p> <p>Péña, R. B-2*</p> <p>Pinnick, R. G. A-17*, A-19*</p> <p>Price, CPT J. D-2</p> <p>Price, W. R. A-11<sup>P</sup></p> <p>Poleski, F. D-5<sup>P</sup></p> <p>Polge, R. J. C-11*</p> |
|--|--|

Proceedings Papers by Author (continued)

Rajendran, N. C-14  
Reyes, Z. C-5P  
Richardson, N. A-16\*  
Richardson, P. H. A-4\*  
Rouse, W. G. C-10\*, C-20  
Rowland, J. R. B-9\*  
Rubel, G. O. B-13\*

Sancier, K. M. C-4\*  
Sasiela, R. J. A-6\*  
Savage, J. J. C-6P  
Schneider, R. W. C-13P  
Schwartz, F. A. A-15\*, A-26\*  
Scully, J. W. D-3\*  
Seagraves, M.A. B-17  
Shaffer, Roy C-6P  
Shand, W. A. (presenter of A-4\*)  
Shelton, COL (Ret.) H. R. Remarks at Closing\*  
Simmons, D. B. A-28  
Smith, M. D. (CSL) C-2\*, C-17  
Smith, M. D. (OSU) A-13\*, B-9\*  
Snelson, A. C-14  
Snyder, D. R., III A-21  
Spaulding, T. E. C-26\*  
St. Armand, P. C-18  
Stenmark, E. B. (presenter of B-1\*), B-8\*  
Stump, W. E. A-20\*  
Surrette, W. E., Jr. A-35  
Sutherland, R.A. B-3\*, B-16  
Sztankay, Z. G., A-25\*  
Turner, R. E. D-6\*  
  
Uthe, E. E. A-22  
  
Victor, A. C. A-11P  
  
Weaver, H. E. C-12P  
Wetzel, G. A-25\*  
Widenhofer, G. (presenter of C-11\*)  
Wiike, J. S. C-15  
Witham, C. L. C-4\*  
  
Yates, R. E. B-4\*  
Yee, Y. P. A-16\*, A-24  
  
Zweibaum, F. M. A-35

PROCEEDINGS PAPERS BY ORGANIZATION

Papers presented at the Symposium are indicated by an asterisk (\*).

Papers presented at the Preliminary Session of the Symposium are indicated by a superscript "p".

Papers where the presenter was from the indicated organization are underlined.

Papers from a foreign country are listed under the country name also.

- AAI Corp. C-21  
Aerodyne Research, Inc. C-7<sup>p</sup>, C-26\*  
Air Force (US) A-21  
Armament Research and Development Command (ARRADCOM) Keynote Address\*, C-23  
Army Engineer Waterways Experiment Station A-30  
Army Materiel Systems Analysis Activity (AMSSAA) A-12\*  
Army Medical Bioengineering Research and Development Laboratory (AMBROL) C-3\*  
Atmospheric Sciences Laboratory (ASL) A-1\*, A-9\*, A-10\*, A-16\*, A-17\*, A-19\*, A-24, A-29, B-1\*,  
B-2\*, B-3\*, B-7\*, B-10\*, B-15, B-16, B-17.  
Barnes Engineering Co. A-35  
Battelle Columbus Laboratories C-21  
Calspan Corp. (Buffalo) C-19  
Canada A-8\*  
Chemical Systems Laboratory A-18, B-11\*, B-13\*, C-1\*, C-2\*, C-6<sup>p</sup>, C-7\*, C-10\*, C-17, C-20, C-21,  
C-22, D-1\*  
Cincinnati Electronics Corp. A-34\*  
Cold Regions Research and Engineering Laboratory A-2\*  
Defense Research Establishment Valcartier A-8\*  
Delco Electronics C-27  
Eglin Air Force Base A-21  
Electronic Proving Grounds A-27<sup>p</sup>  
Electronics Research and Development Command (ERADCOM) A-25\*  
Foreign Science and Technology Center D-5<sup>p</sup>  
Harry Diamond Laboratories (HDL) A-25\*  
Honeywell Tactical Support Operations A-21  
Illinois Institute of Technology Research Institute (ITT-RI) C-14  
Israel A-7\*  
Lincoln Laboratory (of MIT) A-5\*, A-6\*  
Logica Ltd. B-12\*  
Martin-Marietta Corp. C-12<sup>p</sup>  
Massachusetts Institute of Technology (MIT) Lincoln Laboratory A-5\*, A-6\*  
Missile and Munitions Center and School D-2  
Missile Command (MICOM) A-23\*, B-4\*, C-11\*, C-13<sup>p</sup>, D-2, D-4  
MOD/R&D A-7\*  
Naval Ordnance Station (Indian Head) A-11<sup>p</sup>  
Naval Weapons Center A-11<sup>p</sup>, C-18  
New Mexico State University (NMSU) Physical Science Laboratory A-16\*  
Night Vision and Electro-Optics Laboratory A-20\*, A-28  
Oak Ridge National Laboratory (ORNL) C-15, C-16  
Office of Missile Electronic Warfare A-11<sup>p</sup>  
Oklahoma State University (OSU) Division of Engineering, Technology and Architecture A-13\*, B-9\*  
Oklahoma State University (OSU) Engineering Research Field Office D-4  
OptiMetrics A-16\*  
Project Manager, Smoke/Obscurants Foreword, Closing Remarks\*, A-3\*, D-5<sup>p</sup>, D-7

Royal Signals and Radar Establishment A-4\*

Science Applications, Inc. D-6\*  
Smoke Aerosol Working Group (JTCG/ME/SAWG) A-12\*  
SRI International (SRI) A-22, C-4\*, C-5P  
Systems Planning Corp. Remarks at the Closing\*

Thinkol Corp. C-8P  
Tropic Test Center A-31

United Kingdom A-4\*, C-12\*  
University of Alabama, Huntsville C-11\*  
University of Tennessee Space Institute (UTSI) A-14, A-15\*, A-26\*  
US Army Chemical School (USACMLS) D-3\*

Waterways Experiment Station (WES) A-30

**UNCLASSIFIED**

AREA B

MODELING

**UNCLASSIFIED**

# UNCLASSIFIED

B-1

## TEMPORAL CHARACTERIZATION OF SMOKE AND DUST CLOUD GEOMETRY BY PROCESSING OF TWO-PERSPECTIVE VIDEO IMAGES

George R. Blackman  
Atmospheric Sciences Laboratory  
White Sands Missile Range, New Mexico

### ABSTRACT

This paper describes the algorithms and digital processing techniques that were developed for the purpose of temporal and three-dimensional measurement of typical battlefield smokes and dusts. The image data essential to the development and testing of these algorithms was acquired during near-realistic field experiments conducted by the Atmospheric Sciences Laboratory (DIRT series) and the Project Manager Smoke Office (SMOKE WEEK series). These controlled expenditures of a variety of munitions were observed at two widely separated stations each containing video-rate sensors that recorded in the four wavelengths most common to currently operational electro-optical battlefield designator and surveillance systems. The analysis techniques application results in information regarding size, shape, and the direction and transport rate of the cloud. Additionally, the length of the optical path vector (within the cloud), the location of the apparent center of mass, and a statistical estimate of the volume. The computational output is presented in temporal listing format and, graphically, as a sequence of ellipsoids viewed from three perspectives.

### 1. INTRODUCTION

A priority in current Army research is the development of models that will predict the effects of an unlimited range of types and concentrations of obscuration on the performance of battlefield surveillance and target designation devices. As in most research, empirical validation is essential prior to the reliable application of the theory. This paper discusses the progress in the development of one aspect of this validation process: the derivation of temporal dimensions for typical smokes and dusts from field-test video imagery.

### 2. DATA DESCRIPTION AND ACQUISITION

The fielded data acquisition equipment configuration consisted of two sensor observation sites positioned within a range of 500 meters to 2500 meters from the smoke or dust event and with an angular pointing separation of 45° to 90°. With the available systems the ideal observation setup, dictated by the optical fields-of-view and detector responsivity of the sensors, is at approximately 1500 meters and separated by approximately 75°. The localities selected for the field tests seldom allowed these conditions due to the presence of obstructions in the fields-of-view and positioning conflicts with other instrumentation. Each of the two sites was comprised of a bank of four boresighted sensors that recorded video images simultaneously in spectral bandpasses of 0.5 - 0.7 μm, 1.06 μm ± 0.2, 3.0 - 5.0 μm, and 8.0 - 14.0 μm. Over 200 individual smoke and HE events have been observed and recorded during the following field tests:

DIRT I. White Sands Missile Range, September 1978, sponsored by the US Army Atmospheric Sciences Laboratory, 32 events, HE.

SMOKE WEEK II. Eglin AFB, October 1978, sponsored by the PM Smoke Office, 30 events, smokes of all types.

UNCLASSIFIED

**UNCLASSIFIED**

DIRT II. White Sands Missile Range, August 1979, sponsored by the Atmospheric Sciences Laboratory, 40 events, HE - 105mm, 155mm, and C-4.

DIRT III. Fort Polk, Louisiana, April and May 1980, co-sponsored by the Atmospheric Sciences Laboratory and the US Army Corps of Engineers, 70 events, HE - 105mm, 155mm, and C-4.

SMOKE WEEK III. Eglin AFB, August 1980, sponsored by the PM Smoke Office, 44 events, smokes of all types and vehicular dust.

The raster-image output from each of the sensors was recorded on video tape at a rate of sixty-per-second and then later digitized onto nine-track computer tape in eight-bit gray-level picture element arrays of 250 by 300. The time increment selected for digitization varied through the course of the event. An increment of 0.1 second for the first second of the event and 0.5 seconds from 1.0 to 10.0 seconds achieved a comprehensive history of the effects of the initial blast phase. The externally apparent physical changes that occurred during the buoyant and transport phases were in most cases suitably described with a 2.0 second increment from 10.0 seconds into the event until dissipation.

### 3. TWO-DIMENSIONAL ANALYSIS

The technique for calculating the smoke or dust cloud geometry from digital images acquired from a single perspective (observation site) is fundamental only to the primary consideration, that of providing temporal geometry measurements of the solid feature in three-dimension space. The quality of the three-dimensional analysis, is to be discussed later, is dependent upon the precision achieved in the mathematical treatment of the separate raw data sets acquired from two widely-spaced observation perspectives. Of initial importance in the two-dimensional data reduction is the selection of a suitable scheme to be used for isolating the cloud feature from the surrounding scene: the delineation of the cloud perimeter. In the method used, this is achieved by the differencing (subtraction) of the gray level values of the array of picture elements (pixels) of a scene recorded immediately prior to the ignition of the event from those positionally correspondent pixels in scenes that follow in time and contain the cloud feature. The result of this operation then is a new image array in which those pixels that are positionally outside of the feature perimeter now have the value of zero (0) in the eight-bit range of gray and the pixels inside of the feature perimeter have values other than zero. Next, all values within the perimeter are automatically assigned to gray level value of

**UNCLASSIFIED**

## UNCLASSIFIED

one (1). The product of this new array, or mask, and the original raw data scene then results in a pixel array that accurately depicts only the cloud feature and a reconstitution of its radiance in terms of gray level gradient. This closed feature outline within the array, described by those pixels positioned adjacent to and just inside of the mask, becomes the extremity, or endpoints, for all vector-distance dimension calculations made of the cloud. For example, the dimensions for the height and width of the cloud are the products of the maximum pixel spatial distances in the vertical and horizontal, respectively, and the object-plane spatial dimension of a pixel (resolution). The area computation is simply the sum of all pixels within this perimeter (Figure 1).

After much experimentation it was concluded that an ellipsoid fitting to these perimeter pixels would best typify the form of most smoke or dust clouds for the purpose of temporal evaluation of size and shape. Also, for feature tracking, the centroid of this ellipse provides the best estimate of the position of the center-of-mass in two-dimensional space from the perspective of the sensor (Figure 2). Another important reason for this approach is that it permits an expeditious and simplistic method for the automatic handling of the large volume of data inherent in digital imagery. The parameters that describe the ellipse were computed by first deriving the eigenvalues and eigenvectors of the scatter matrix of the perimeter pixel positions (Appendix 1). A coordinate system origin (centroid) was established by a least-squares juncture of these vectors and then, the transformed perimeter pixel locations fitted to an ellipse in standard position. This results in provision of values for the lengths of the major and minor axes, inclination of the major axis, and the coordinates of the centroid.

Up to this step in the process all operations have related to the static condition of the feature, the analysis of the geometry for a given instant in time. Now, with knowledge of the location of the apparent center-of-mass (centroid), calculations can be generated that relate to the dynamics of the feature: the temporal relationships for growth and dissipation, relative shape changes, and transport distances and rates. The procedures discussed above are then applied to time-coincident digital data sets of the event scenes from both sensor observation sites. The geometric projection of these pairs of two-dimension data sets into a common three-dimensional object-space coordinate system permits the calculation of new parameters that describe the dynamics of the solid feature and the geographic relationships.

## UNCLASSIFIED

**UNCLASSIFIED**

## 4. THREE-DIMENSIONAL ANALYSIS

The construction of an ellipsoid, as representative of the external form of the cloud, provides a logical means of estimating the actual form of the side of the feature opposite the perspective of the sensors. A reasonable assumption is that the feature surface geometry of the far side resembles that of the front. Generally, in excess of 65% of the surface was in view of the sensors since the angular separation of the stations in most prior field tests was within the range of  $60^{\circ}$  to  $90^{\circ}$ . Of course, the inclusion of a third sensor perspective would improve the geometric solution immeasurably, and this will likely become the configuration in field tests in the near future.

In the algorithm, the point in object-space where the smoke or dust event initiation occurs is designated to be the point of normal juncture of three planes of projection - the origin of the three-dimensional coordinate system (Figure 2). The location of this point in the image data is established to be at the intersection of the two vectors projected from the respective centroids calculated for the very first evidence of a cloud in the scene as simultaneously observed from the two stations. The xz and yz planes of projection are aligned parallel to the x and y axes specified in the field survey grid system. This permits positional correlation of the computed feature geometry with the results from other measurements systems (i.e., alignments of transmissometer paths, etc.). The respective centroid vector distances from each pair of sensors to their point of intersection in space provide coefficients of scale; therefore, the product of this value (relative to a given sensor) and a number of pixels in the image array will be an object-scale dimension. The assumption is that all pixels have the same spatial dimension, within the facility to make this measure, when treating the sensor focal plane as the parallel projection of the object-plane. The object-plane is a plane of cross-section of the cloud that is normal to the optical axis of the sensor. This operation is valid when the sensor and the object are separated by a distance adequate to reduce the effect of perspective foreshortening to within the minimum spatial resolution of the system, a factor taken into account during setup for each field experiment.

The calculations of the five ellipse parameters ( $x, y, a, b, \theta$ ) for each of the two common wavelength perspectives are projected via their centroid vectors into the two vertical planes of normal juncture in the three-dimensional system. Next, the parameters of a "first estimate" ellipsoid are computed, representing the initial attempt at the fitting of the ellipse parameters of the separated data sets. The centroid of this ellipsoid is common in space with the intersection of the projected

**UNCLASSIFIED**

**UNCLASSIFIED**

centroid; the lengths of its major and minor axes result from the least-squares average of the lengths projected from the two data sets, and the inclination is a least-square of the respective angles. The construction of this rudimentary feature simply provides a generalization of shape, size, and direction of motion - an efficient initialization of the statistical process for arriving at the optimum configuration. Ellipse parameters that result from the cross-sectioning of this "initial" ellipsoid, parallel to each of the two ellipse planes described above, are superimposed on these planes and centered at their centroid locations. An "objective function" is computed from the measures of parameter deviation between the estimated ellipsoid cross-sections and the separate ellipses computed from the sensor data (Appendix 2). Iteration of this process, the ultimate minimization of the objective function, will produce the parameters of a best statistical representation of the "true" object-spaced feature and its centroid location in space. This procedure is repeated for each pair of parameter projections that were calculated from the images for the entire time-history of the smoke or dust event. This provides a time-history of dimensional change and movement of the feature.

Specific information that is presently being derived by this technique is as follows: incremental measures of height, width, area, distance transported, the direction and rate of transportation, volume and the optical path length within the cloud. The optical path is a vector representing a selected perspective of the feature, generally from the vantage of one of the principle transmissometers associated with the field test. A plane of cross-section of the ellipsoid is easily obtainable normal to any viewpoint in space. In the examples shown in Figures 3 and 4, Smoke Week III - trial 16, the perspective was translated to a point at the 800 meter instrumentation site and viewing along the L3 line-of-sight. In Figure 5 the viewpoint is along L2. The Dirt III - event A-2, Figure 6, has the perspective from the NRL transmissometer located at the principle instrumentation site. The top and side view graphics in Figures 3, 5 and 6 are cross-section depictions of the features from the viewpoints stated above. All measurements are metric and the values associated with the ellipsoids are seconds from the ignition time ( $T = 0.0$  sec.). The data columns in Figures 3, 5 and 6 are partial listings of those data available, for the purpose of brevity in this paper. The six columns of information that follow the time-increment columns relate to measurements of the ellipse in the cross-section. Clarification of these measurements are as follows:

Height - Vertical distance from top of the ellipse cross-section to a horizontal plane that contains the detonation location.

**UNCLASSIFIED**

**UNCLASSIFIED**

Horizontal Extent - The width of the ellipse at the two most widely spaced lateral points on the ellipse perimeter.

Vertical Extent - The distance between the greatest vertical separation of points on the ellipse perimeter.

Area - Square measure within the ellipse perimeter.

Lateral Offset - Distance measured in the horizontal plane of the track of the ellipsoid centroid.

Path Length - The vector segment distance of the optical path from entry to exit points on the ellipsoid surface.

The measurements listed in the last four columns are independent of perspective:

Volume - Cubic measure of the ellipsoid.

Centroid Height - The vertical distance of the centroid from the horizontal plane that contains the detonation point.

Transport Direction - The geographic azimuth of the ground track of the ellipsoid centroid.

Transport Rate - The speed between centroid points on the ground track (meters/second),

The summary graphic shown in Figure 4 is a generalization of the dimensional time-progression of four of the more important measurements: Height, width, rate of transport, and height of the apparent center-of-mass above the terrain.

##### 5. SUMMARY AND CONCLUSIONS

In this initial phase of our research, as reflected in the results shown in Figures 3 through 6, we believe that most difficulties have been resolved to within the limitations of our hardware. On occasion, a new problem will surface due to the unique circumstances associated with a given smoke or dust event and, consequently, the effort to diversify the algorithms continues in convergence toward a purely operational method. As for the raw data quality, the acquisition procedures and computer enhancement routines have improved progressively, now to the point that only the quality of the sensors has become the limiting factor.

As mentioned earlier, the inclusion of a third observation station would permit further clarification of the geometry and the dynamics of the cloud. This would not only increase the accuracy of the ellipsoid algorithm but also allow for a more comprehensive evaluation of the finer detail of the feature's surface.

**UNCLASSIFIED**

**UNCLASSIFIED**

A number of interpretive investigations are ongoing and utilizing the results of the dimensioning analyses. The means for deriving wind direction and speed in the object-space is completed; note the last two columns in Figures 3, 5, and 6. This technique provides the only direct method for these derivations at the cloud location since meteorological instrumentation can not be positioned near the ignition point of HE rounds or in most cases in the vicinity of corrosive smokes. We are proceeding in the investigation for calibrating the cloud surface radiance gradient. At present we are only able to generate a relative gradient contour map for each time-increment during the event (Figure 1). During the next field test calibration sources will be imaged simultaneously with the cloud observation, which will possibly result in a means for quantifying the radiance gradient. Statistical schemes are being applied to measurements derived from the earlier data sets of an event as a means for detecting trends for the purpose of cloud type identification, and growth and motion prediction.

Refinement in the combination of image array processing techniques and statistical interpretation brings to within reach the solutions for a number of problems that exist in battlefield smoke and dust characterization.

## 6. REFERENCES

1. Wilks, S. S., Mathematical Statistics, 1962, New York, John Wiley and Sons.
2. Hotelling, H., 1933, "Analysis of a Complex of Statistical Variables Into Principle Components", "J. Educ. Psyc.", 24:417-441.
3. Blackman, G. R., 1980, "Multispectral Digital Image Analysis of Smoke/Dust Aerosols", Smoke/Obscurants (DRCPM-SMK-T), Adelphi, MD.
4. Marvin, J. W., Telephone conversation, formerly of University of New Mexico State.
5. Blackman, G. R., and Marvin, J. W., August 1979, "Automatic Temporal Analysis of Smoke/Dust Clouds"; Image Understanding Systems II, SPIE Proceedings, San Diego, CA.

**UNCLASSIFIED**

## UNCLASSIFIED

## APPENDIX 1.

## COMPUTATION OF ELLIPTICAL PARAMETERS

The directions along which a set of points  $p_i$ ;  $i = 1, n$  have greatest spread are given by the eigenvectors of their "internal scatter matrix,"  $W = [w_{ij}]$ , which, in two dimensions is formed from the mean values

$$\bar{x} = \frac{1}{n} \sum_{i=1}^n x_i, \quad \bar{y} = \frac{1}{n} \sum_{i=1}^n y_i$$

and the second order statistics

$$w_{11} = \sum_{i=1}^n (x_i - \bar{x})^2, \quad w_{22} = \sum_{i=1}^n (y_i - \bar{y})^2, \quad w_{12} = w_{21} = \sum_{i=1}^n (x_i - \bar{x})(y_i - \bar{y})$$

Let the eigenvalues of  $W$  be denoted  $\lambda_1$  and  $\lambda_2$  with corresponding eigenvectors  $\{E_1, E_2\}$  i.e.:

$$WE_1 = \lambda_1 E_1, \quad i = 1, 2$$

and order the  $\lambda_i$  so that

$$\lambda_1 \geq \lambda_2$$

The result quoted above also states that  $E_1$  is the direction of maximum spread and that  $E_1$  and  $E_2$  are perpendicular. Thus, if the points  $p_i$ ,  $i = 1, n$  constitute a sample from an elliptical distribution of points, then  $E_1$  and  $E_2$  are "good" estimates of the directions of the major and minor axes, respectively, of the ellipse.

We then make a change of coordinates by rotating to the system defined by  $E_1, E_2$  and translating the origin from  $(0, 0)$  to  $(\bar{x}, \bar{y})$ , the mean point of the data points. Calling the resulting coordinates  $(u, v)$ , we now have data points  $p_i = (u_i, v_i)$ ,  $i = 1, n$  to which we wish to fit an ellipse in standard position;

$$\frac{u^2}{a^2} + \frac{v^2}{b^2} = 1$$

To derive a least-squares solution to this problem, let  $A = 1/a^2$  and  $B = 1/b^2$ ; then the problem is to minimize the objective function:

UNCLASSIFIED

**UNCLASSIFIED**

$$R(A, B) = \sum_{i=1}^n (Au_i^2 + Bv_i^2 - 1)^2,$$

which yields the (linear) normal equations:

$$\left\{ \begin{array}{l} A \sum u_i^4 + B \sum u_i^2 v_i^2 - \sum u_i^2 \\ A \sum u_i^2 v_i^2 + B \sum v_i^4 - \sum v_i^2 \end{array} \right\}$$

This procedure requires a second pass through the data to calculate the coefficients of these normal equations, but the alternative would be to solve a five-dimensional linear program with constraints (i.e., fit a general polynomial of the second degree in two-variables whose discriminant is constrained to the elliptical case). The algorithm used here has proved to be quite efficient on a minicomputer and it outputs, in a natural way, the desired parameters: major and minor axes, inclination of the major axis, and the center. Note also that the eigenvalue problem to be solved is two-dimensional so that the solution can be written down directly.

**UNCLASSIFIED**

**UNCLASSIFIED**

## APPENDIX 2.

## COMPUTATION OF ELLIPSOID PARAMETERS

An initial estimate is computed for the ellipsoid parameters by establishing the centroid and the direction of the major axis as least-squares fits to the corresponding parameters of the two ellipses. Assuming that it is an ellipsoid of revolution, the remaining two axes can be found by orthogonality, leaving only two parameters to be determined; the lengths  $a$  and  $b$  of the semi-major and semi-minor axes. The method of steepest descent is used to minimize the objective function;

$$\begin{aligned} F(a,b) = & (P_1(a)-a_1)^2 + (P_1(b)-b_1)^2 \\ & + (P_2(a)-a_2)^2 + (P_2(b)-b_2)^2 \end{aligned}$$

where

$a$  and  $b$  are the ellipsoidal semi-axes as defined above,

$a_1$  and  $b_1$  are the lengths of the semi-major and minor axes of the ellipse given in the focal plane of the first sensor,

$a_2$  and  $b_2$  the analogous quantities for the ellipse in the second sensor focal plane,

$P_1(a)$  and  $P_1(b)$  the semi-major and minor axes of an ellipse obtained by projecting the ellipsoid into focal plane 1,

$P_2(a)$  and  $P_2(b)$  the corresponding results of projection of the ellipsoid into focal plane 2.

The procedure converges with reasonable rapidity.

**UNCLASSIFIED**

UNCLASSIFIED

DIRT II	EVENT # AB7		
1857 Z	07-18-79	STATION #1	SENSOR 0.5-0.7 MICRON
		T+36.0	



HEIGHT (ABOVE DETONATION PT.) = 18 M  
 WIDTH(MAX. HORIZONTAL EXTENT) = 57 M  
 VERTICAL EXTENT = 15 M  
 AREA = 471 SQM

HEIGHT OF CENTROID = 9 M  
 LATERAL OFFSET = 123 M  
 AXES = 57, 16 M  
 INCLINATION = -3.7 DEG

CENTROID OF BOUYANT PORTION OF CLOUD:  
 HEIGHT=10 M      OFFSET=134 M  
 HORIZONTAL EXTENT AT 7 METERS ABOVE SURFACE = 51 M  
 HOR. EXTENT OF LINE CONTAINING PT. OF MAX. OFFSET OF LEADING EDGE=46 M  
 SHEAR(HOR. DISTANCE BETWEEN PT. OF MAX OFFSET AND PT. AT 7 METERS) = .3 M

- \* \* = DETONATION POINT
- + = CENTROID OF PRIMARY ELLIPSE
- \* = CENTROID OF BOUYANT PORTION OF CLOUD

UNCLASSIFIED

FIGURE 1. (1)  
MEASUREMENTS AND GRAPHICS TYPICAL OF TWO-DIMENSION/SINGLE-STATION ANALYSIS.

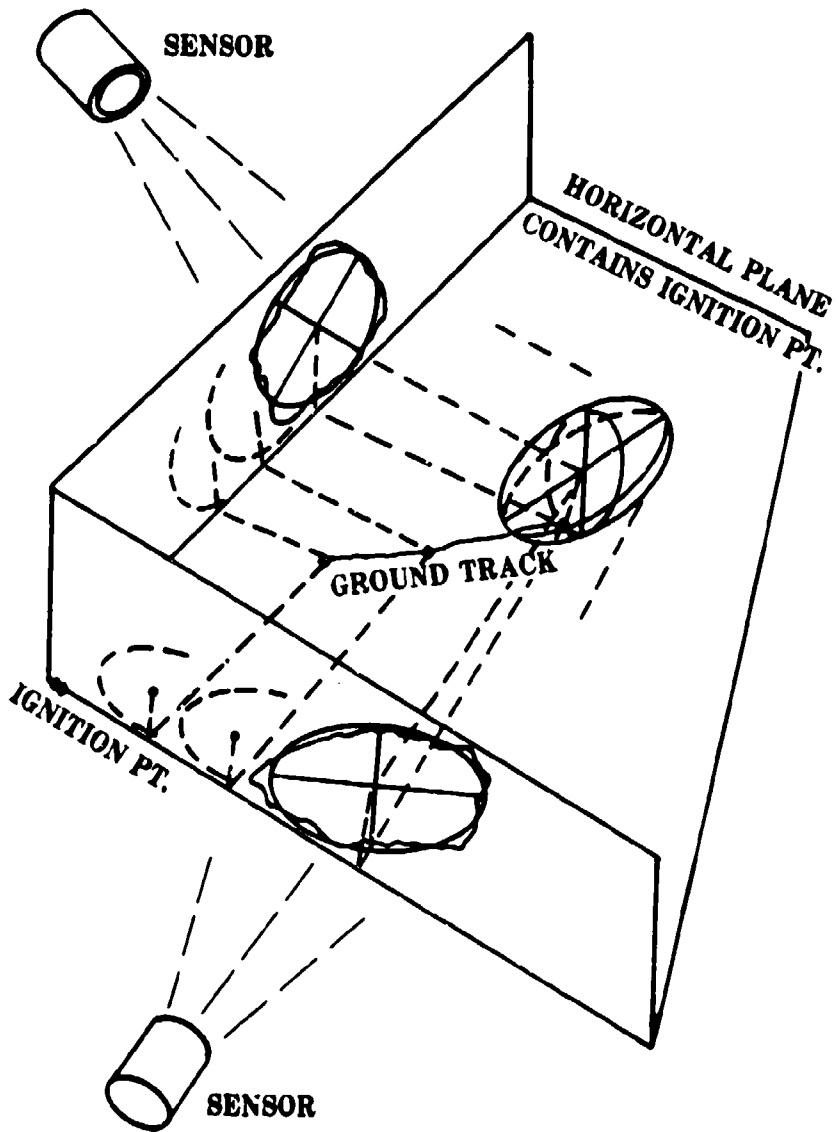
**UNCLASSIFIED**

FIGURE 2. (U)  
GRAPHICAL REPRESENTATION  
OF THREE-DIMENSIONAL ANALYSIS ALGORITHM.

**UNCLASSIFIED**

**UNCLASSIFIED**

B-1

TIME (SEC)	DIMENSIONS OF OBJECT CROSSECTION NORMAL TO OPTICAL PATH (METERS)			DIMENSIONS INDEPENDENT OF PERSPECTIVE			
	HEIGHT (REF DET PT)	HORIZONTAL AREA	VERTICAL EXTENT	(SQ. METERS)	PATH LENGTH	CENTROID VOLUME (CUBIC METERS)	TRANSPORT RATE
0.0	8.0	9.8	8.1	62.2	-0.1	1930.3	3.9
1.0	9.5	10.7	10.0	83.6	-1.8	0.0	0.0
2.0	11.0	12.0	11.9	111.4	-3.5	0.0	26.9
3.0	12.6	13.6	13.8	147.8	-5.3	0.0	27.1
4.0	14.1	15.4	15.6	167.6	-7.1	0.0	27.2
5.0	15.5	17.4	17.5	236.3	-8.9	6022.2	6.2
6.0	17.0	19.3	19.3	292.5	-10.8	7593.9	6.8
7.0	18.5	21.3	21.2	332.1	-12.7	938.3	7.4
8.0	19.9	23.2	22.9	414.2	-14.6	11262.4	7.9
9.0	21.3	25.1	24.6	481.3	-16.6	13270.8	8.5
10.0	22.7	27.0	26.3	551.4	-18.6	15483.9	9.0
11.0	24.1	28.8	27.7	623.0	-20.4	17808.0	9.6
12.0	25.4	30.6	29.5	696.7	-22.7	20209.2	10.1
13.0	26.7	32.4	31.1	773.1	-24.8	22269.2	10.6
14.0	28.0	34.1	32.6	849.2	-26.9	25284.1	11.2
15.0	29.2	35.9	34.0	927.4	-29.1	27849.5	11.7
16.0	30.4	37.6	35.4	1003.9	-31.3	304F.8	12.2
17.0	31.6	39.3	36.7	1083.9	-33.5	33083.1	12.7
18.0	32.7	41.0	38.0	1162.5	-35.8	36591.4	13.2
19.0	33.9	42.8	39.3	1242.4	-38.1	38163.8	13.7
20.0	35.0	44.6	40.5	1320.5	-40.4	40657.1	14.2

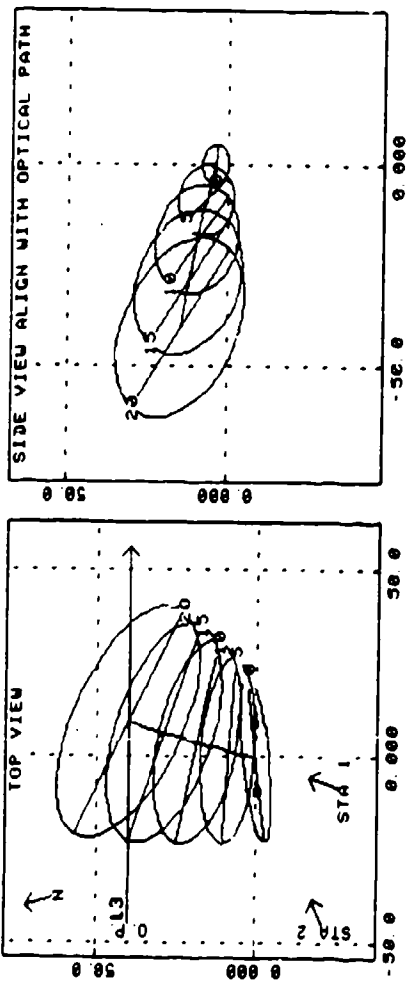


FIGURE 3. (II)  
MEASUREMENTS AND GRAPHICS TYPICAL OF THREE-DIMENSION/MULTI-STATION ANALYSIS.  
Multi-round smoke - explosive.

**UNCLASSIFIED**

437

**UNCLASSIFIED**

SMOKE III EQLIN AFB, FLA.  
EVENT 16 TIME 1841Z DATE 081580  
XM825 WP TWIN CHARGES SENSOR 0.5-0.7

PERSPECTIVE FROM PRIMARY INSTRUMENTATION SITE

## SUMMARY GRAPHIC

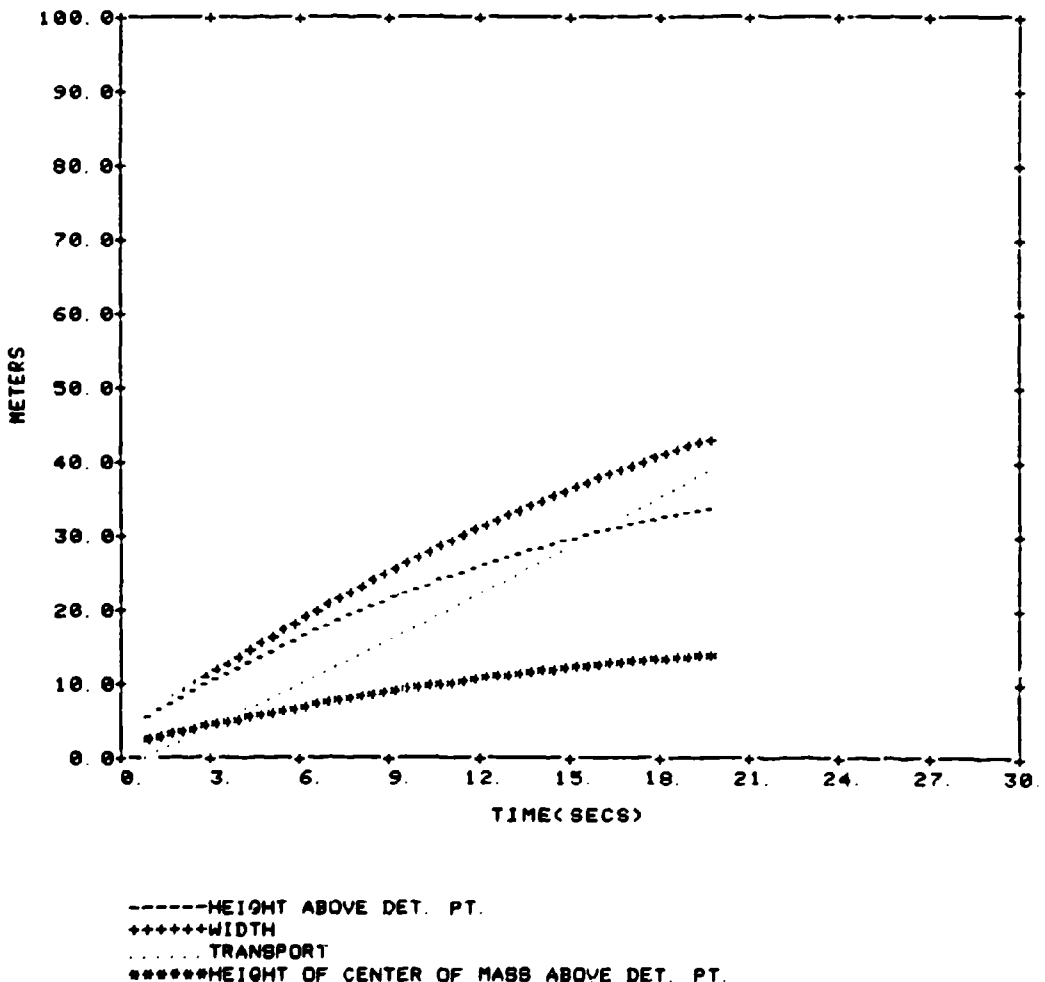


FIGURE 4. (U)

SUMMARY GRAPHIC OF TRENDS OF  
SELECTED ANALYSIS RESULTS**UNCLASSIFIED**

**UNCLASSIFIED**

B-1

EVENT 05 SMOKE 111 EG LIN AFB, FLA  
XMAS GENERATOR TIME 2149Z DATE 081180  
SENSOR 0 9-0 7

TIME (SEC)	DIMENSIONS OF OBJECT CROSSECTION NORMAL TO OPTICAL PATH(METERS)			DIMENSIONS INDEPENDENT OF PERSPECTIVE TRANSPORT		
	HEIGHT (REF DET PT)	HORIZONTAL AREA EXTENT (SQ METERS)	LATERAL OFFSET	PATH LENGTH	VOLUME (CUBIC METERS)	CENTROID HEIGHT
20.0	8.9	16.0	11.7	145.3	-7.1	0.0
23.0	9.9	18.0	13.1	182.8	-8.8	0.0
26.0	11.0	19.9	14.4	222.6	-10.7	0.0
29.0	12.1	21.7	15.7	265.1	-12.8	0.0
32.0	13.3	23.4	16.9	308.7	-15.2	0.0
35.0	14.4	25.0	18.1	352.8	-17.8	0.0
38.0	15.6	26.6	19.2	396.2	-20.6	0.0
41.0	16.8	28.3	20.3	443.0	-23.6	0.0
44.0	18.1	29.4	21.4	489.5	-26.8	0.0
47.0	19.4	30.6	22.3	532.7	-30.3	0.0
50.0	20.7	31.7	23.3	575.9	-34.0	0.0
53.0	22.0	32.7	24.2	617.4	-36.0	0.0
56.0	23.4	33.6	25.0	658.7	-42.1	0.0
59.0	24.8	34.4	25.8	694.5	-46.5	0.0
62.0	26.2	35.1	26.6	728.6	-51.1	0.0
65.0	27.7	35.7	27.3	760.9	-56.0	0.0
68.0	29.1	36.1	28.0	782.6	-61.0	5.5
71.0	30.7	36.4	28.6	815.1	-66.3	7.8
74.0	32.2	36.6	29.3	836.6	-71.4	0.0
77.0	33.6	36.6	29.8	854.1	-77.6	0.0
80.0	35.0	36.0	31.1	869.1	-83.6	0.0
83.0	37.5	35.8	31.8	881.4	-89.8	0.0
86.0	39.3	35.5	32.3	890.4	-96.2	0.0
89.0	41.1	35.0	32.9	895.5	-102.9	0.0
92.0	42.9	34.6	33.4	901.5	-104.7	0.0
95.0	44.8	34.2	33.9	905.6	-116.9	0.0
98.0	46.7	33.8	34.5	911.9	-124.2	0.0
101.0	48.8	33.9	35.2	935.5	-131.7	0.0
104.0	50.8	34.1	35.6	953.1	-139.5	0.0

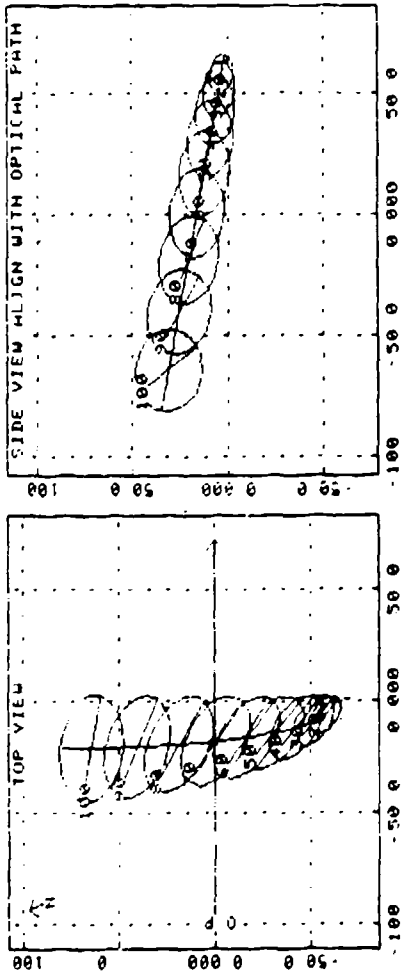


FIGURE 5. (II)  
MEASUREMENTS AND GRAPHICS TYPICAL OF THREE-DIMENSION/MULTI-STATION ANALYSIS.  
Continuous-source smoke.

**UNCLASSIFIED**

439

UNCLASSIFIED

DIRT IIIA FORT POLK, LA.  
EVENT A-2 TIME 1938Z  
150MM SURFACE TANGENT  
DATE 011490  
SENSOR 0.5 - 0.7

DIMENSIONS OF OBJECT CROSSTSECTION NORMAL TO OPTICAL PATH (METERS)							DIMENSIONS INDEPENDENT OF PERSPECTIVE			
TIME (SEC)	HEIGHT (OFP DEP PT)	HORIZONTAL EXTENT	VERTICAL EXTENT	AREA (SQ. METERS)	LATERAL OFFSET	PATH LENGTH	VOLUME (CUBIC METERS)	CENTROID HEIGHT	TRANSPORT DIRECTION	TRANSPORT RATE
0.0	12.1	16.0	13.0	160.1	6.7	6.0	3662.4	5.6	71.7	0.0
1.0	15.9	23.7	17.0	313.3	12.0	6.0	4672.1	7.4	78.9	3.3
2.0	13.5	30.6	20.0	480.3	17.3	16.9	5662.9	9.1	84.6	3.3
3.0	22.8	36.9	24.3	704.3	22.4	26.9	14651.9	16.7	87.3	3.2
4.0	25.9	42.5	27.5	917.3	27.5	22.6	21301.5	12.2	88.7	4.1
5.0	28.0	47.3	30.4	1130.1	32.5	22.4	28767.7	13.6	88.3	3.9
6.0	31.5	51.4	32.3	1333.9	37.4	20.7	36607.2	14.9	88.4	3.9
7.0	34.1	54.6	35.9	1536.9	42.2	16.9	47798.9	16.1	88.1	3.9
8.0	36.5	57.3	38.4	1694.3	47.0	6.3	52519.4	17.3	88.7	4.3
9.0	38.7	59.2	40.6	1841.6	51.6	6.0	58582.7	18.3	88.1	4.3
10.0	40.6	60.7	42.6	1952.6	56.2	6.0	65617.7	19.3	87.5	4.7
11.0	42.2	61.7	44.1	2065.0	60.6	6.0	70566.7	20.2	86.9	4.7
12.0	43.7	62.2	45.4	2122.0	65.0	6.0	73678.0	20.9	86.4	4.7
13.0	44.8	62.4	46.3	2157.9	69.3	6.0	75392.3	21.6	86.1	4.7
14.0	45.7	62.2	46.9	2163.7	73.5	6.0	75291.3	22.2	85.9	4.7
15.0	46.2	61.7	47.9	2161.3	77.6	6.0	73702.4	22.7	85.8	4.6
16.0	46.5	60.9	46.7	2065.0	81.6	6.0	70578.0	23.1	85.9	4.7
17.0	46.5	59.4	46.1	2004.7	85.6	6.0	65632.5	23.5	85.9	4.7
18.0	46.2	57.7	45.1	1867.6	89.4	6.0	59731.0	23.7	86.1	4.7
19.0	45.7	55.5	43.6	1768.7	93.2	6.0	53021.8	23.8	86.1	4.7
20.0	44.8	52.7	41.7	1532.0	96.9	6.0	45425.6	23.9	85.9	4.7

UNCLASSIFIED

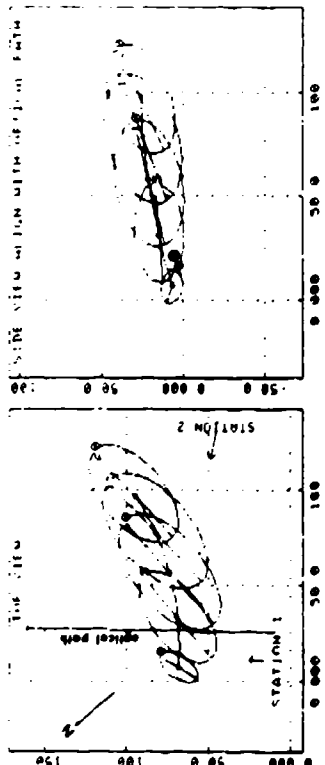


FIGURE 6. (II)  
MEASUREMENTS AND GRAPHICS TYPICAL OF THREE-DIMENSION/MULTI-STATION ANALYSIS.  
High-explosive munitions - dust.

**UNCLASSIFIED**  
MUNITION EXPENDITURE MODEL  
VERIFICATION KWIK PHASE I

8-2

Ricardo Peña  
Atmospheric Sciences Laboratory  
White Sands Missile Range, New Mexico

**ABSTRACT**

The US Army Atmospheric Sciences Laboratory (ASL) at White Sands Missile Range (WSMR), New Mexico (NM), has developed a diffusion model called KWIK (crosswind integrated concentration). The model uses micrometeorology, atmospheric optics, and diffusion theory for determining smoke munition expenditures for field army applications and can be run on several desktop computers, including one in use by US Army artillery units. Use of the model may reduce the number of munitions currently expended to achieve a given screening or obscuration objective.

Phase I of the KWIK Munition Expenditure Model verification tests was conducted during the summer of 1980 at Dugway Proving Ground (DPG), Utah, for visible wavelengths using static hexachloroethane (HC) smoke sources. Results are presented showing observer assessment data as compared with photographic documentation. Also, munition expenditure assessment is made by comparing KWIK calculations with current Army Field Manual.

**1. INTRODUCTION**

The threat imposed by the Soviet bloc tank forces requires that the subject of obscuration at ground level, for both offensive and defensive planning, receive the most thorough research and developmental efforts. Economic considerations for munition expenditures further dictate pursuit of more efficient mechanisms for obtaining obscuration objectives.

The development of munition expenditure algorithms require micrometeorology, atmospheric optics, turbulence and diffusion in the surface boundary layer of the atmosphere. Primary criteria for a workable prototype system require that: (1) the algorithm function reliably in the near, mid, and far infrared as well as in the visible wavelengths of the electromagnetic spectrum; (2) the model output include munition expenditure estimates; (3) the predicted smoke concentration obscure the optical path to a predetermined attenuation level; and (4) input parameters are at a minimum and readily obtainable.

Other criteria of significant importance, include: (1) relative humidity effects upon the hygroscopic characteristics of the smoke aerosols; (2) the impact separation of projectiles from an adjustment point to establish and maintain a smoke screen; (3) the rate of fire necessary to maintain a smoke screen; (4) the meteorological limits for practical applications of screening/obscuration on a battlefield; and (5) the relationships between transmittance through the smoke versus concentration over the pathlength as a function of wavelength.

The above criteria were considered in developing the US Army Atmospheric Sciences Laboratory (ASL) KWIK (mnemonic for crosswind integrated concentration) smoke algorithm [1]. KWIK is a hybrid model which produces munition expenditures based on atmospheric optics and turbulent diffusion theory as a function of battlefield meteorological observations.

**UNCLASSIFIED**

# UNCLASSIFIED

B-2

A large data base from previous experiments exists in the literature, covering chemically-generated military smokes. These data have been used to verify and/or evaluate several different approaches to atmospheric diffusion including the Gaussian formulae. These previous tests have verified the predictability of relatively long average downwind concentrations of some diffusing materials in the atmosphere; however, a deficiency exists in the case of military smokes for which the actual obscuration has not been reliably predicted or verified, especially over short time intervals. It is fundamentally important to ascertain the categorical performance of a concept before proceeding with extensive proposals for developmental effort or modifications to systems or processes.

In order to verify the munition expenditure predictions of the KWIK model, an evaluation plan was devised by ASL, consisting of three phases. This report deals only with Phase I, an effectiveness evaluation test for visible wavelengths. This test was conducted, using hexachloroethane (HC) smoke sources, at Dugway Proving Grounds (DPG) during the summer of 1980.

## 2. DESCRIPTION OF MODEL

The KWIK model consists of a blending of meteorological and site parameters, atmospheric optics, and turbulent diffusion theory. Each of these are briefly discussed below.

Meteorological and Site Parameters. Meteorological data requirements for the KWIK algorithm are based upon observations that would hypothetically be available on a modern battlefield, that is hourly airway or synoptic data obtained from the United States Air Force Air Weather Service via the USAF Global Weather Central, or information furnished by the US Army Field Artillery Meteorological sections.

Observational requirements for the microscale diffusion, atmospheric optics, ambient stability, and wind direction effects upon the obscuring screen were investigated; the determination being that eight standard parameters plus one terrain characterization index would be sufficient. Meteorologically, the KWIK algorithm requires data inputs consisting of:

- ceiling height in feet
- cloud cover in percent
- visibility in miles
- precipitation, yes or no
- temperature in degrees F
- dewpoint temperature in degrees F

# UNCLASSIFIED

B-2

wind direction in degrees

wind speed in knots

The terrain index is in terms of the average height in centimeters of the surface roughness elements, i.e., trees, bushes, grasses, buildings, etc., relative humidities which are required for extrapolating yield factors for the smoke munitions are calculated from the temperatures and dewpoints.

The stability category scheme used is a composite version developed from the published results of Pasquill [2], Turner [3], and Smith [4]. The composite approach uses Turner's radiation index, ceiling and cloud modifications to the index, plus Smith's wind speeds associated with each Pasquill Category.

Other inputs related to the calculation of insolation for the determination of the atmospheric stability category, are:

latitude in degrees

direction from equator (north or south)

longitude in degrees

direction from Greenwich (east or west)

altitude above MSL in kilometers

julian date in three digits

Greenwich civil time in hours

Atmospheric Optics. The optics portion of KWIK is adapted from an approach to atmospheric transmission suggested by Downs [5]. Transmittance of light at various wavelengths through a path is determined by calculating the attenuation due to absorption by water vapor, scattering by haze or fog, and precipitation. When the attenuation due to atmospheric conditions is known, the attenuation due to smoke that is required to lower transmittance to a threshold contrast for a particular wavelength can be computed. By use of the transmittance and empirically derived relationships between transmittance and concentration for various smokes, the crosswind integrated concentration for a particular smoke can then be computed.

The approach used to determine the line of sight integrated concentration, CL, of the obscuring smoke screen necessary to attenuate an optical path to a threshold level that denies target acquisition is based upon the transmittance due to attenuation by Smoke, Ts, as a function of CL, as stated in the following relationship:

# UNCLASSIFIED

443

# UNCLASSIFIED

B-2

$$CL = \frac{\ln Ts}{-\alpha} \quad (1)$$

where CL is the minimum integrated smoke concentration necessary to obscure an optical path. Equation (1) is applicable to both visible and infrared wavelengths if values of  $\alpha$ , the extinction coefficient, are known.

Microscale Diffusion. Smoke screening may be considered microscale since screen lengths and time fall within the definition of micrometeorological processes, i.e., a few meters to a few kilometers and on the order of an hour or less. In the case of battlefield obscuration, the integrated concentrations from projectile smoke sources generally fall below acceptable levels of obscuration over downwind travel distances of 50 to 200 meters.

For a semi-continuous plume, such as the HC smoke source used in the KWIK Phase I trials, a Gaussian distribution is assumed to diffuse independently in three coordinates directions (X, Y, Z). The crosswind integrated concentration (CWIC) equation used is based on the Gaussian distribution function described by Pasquill [2] and Gifford [6]. Integrating the Gaussian function used to calculate the CWIC results in the following expression

$$x_{CWIC} = \left( \frac{2}{\pi} \right)^{1/2} \frac{Q}{\delta \sigma_z} \exp \left\{ - \frac{1}{2} \left( \frac{z-h}{\sigma_z} \right)^2 \right\} \quad (2)$$

After applying the Pasquill [2] power law,  $\sigma_z = cx^d$ , rearranging terms and evaluating the exponential expression, we find that equation (2) solved for the downwind distance x, becomes

$$x = \delta^{-1} \left( \frac{0.731 \lambda \eta Q}{c \bar{V} x_{CWIC}} \right)^{d^{-1}} \quad (3)$$

where the source strength Q is modified by the munition efficiency factor  $\lambda$  and the relative humidity dependent yield factor  $\eta$ .  $\bar{V}$  is the mean wind speed,  $\delta$  is a wind correction factor and c and d are stability and surface roughness dependent coefficients.

Equation (3) is used to obtain the smoke projectile impact separation distance required to screen a given length.

# UNCLASSIFIED

# UNCLASSIFIED

B-2

## 3. DESCRIPTION OF TRIALS

Thirty trials were conducted at DPG during July and September of 1980. Groups of three M1 and one M2 HC smoke canisters, each group arranged to simulate a dynamically fired 155mm M116BE projectile (Figure 2), were utilized.

Test Objectives. The objectives of the KWIK Phase I evaluation test were:

- a. To provide an evaluation of the KWIK smoke model by correlating model predictions of obscuration effectiveness with empirical (observer) data.
- b. To collect meteorological, photographic and observer data in order to characterize the meteorological, environmental and smoke plume behavior for each trial.
- c. To compare and evaluate smoke munition expenditure calculations of the KWIK model with those obtained by the current method used by the field army [7, 8, 9].

Meteorological limitations. No limitations were placed on cloud cover, ambient temperature and relative humidity. Wind directions were limited to  $135^\circ \pm 45^\circ$  or  $315^\circ \pm 45^\circ$  (SE or NW winds). Desired wind speed range was set at 5-17 knots, however, during last day of the trials winds greater than 17 knots were encountered. After reviewing initial results it was decided to continue screening under these high wind conditions (see report by Cohn [10]). Atmospheric stability categories desired for the trials were B, C, D, and E.

Data Requirements. The main data requirements consisted of meteorological, photographic and visual observational data.

Meteorological data were measured at the test site from three different towers (Figure 1). Two 10-meter towers were located at the southeast and northwest ends of the grid, respectively, and a 32-meter tower was located on the northeast side of the grid next to the observation post. Wind speed and direction were measured on all three towers at 2, 10, 16, and 32 meters. Temperature was measured at all four levels of the 32-meter tower and at the 2-meter level of the 10-meter towers. Dew point temperature was measured only at the 2-meter level on all meteorological towers.

# UNCLASSIFIED

445

# UNCLASSIFIED

B-2

The photographic coverage provided during the trials consisted of three 16mm color motion picture cameras located as shown on Figure 1. The two side cameras were zoomed in on the target area during all trials and the center camera covered the width of the screening area, including smoke sources and target area, for all trials for the duration of the cloud passage.

Color still photographs were taken every 30 seconds during each trial with a 35mm camera located near the area of the observation post. Also, television coverage of the targets (taken from behind the target area) for all trials, and for the duration of the cloud passage, was recorded on video tape.

Visible smoke obscuration assessments were made from the observation post. Each observer (with binoculars) was situated in a booth and had unrestricted view of the target area. Separate booths prevented communication between the observers. Each of three observers was assigned one of the three targets; the fourth observer was assigned three targets. The first three observers activated a recording device when their assigned target was visible. The fourth observer activated a recording device when one or more targets were visible. The signals from each observer were recorded on magnetic tape.

Smoke Impact Area. This area included the screening area plus 30m to the southeast and to the northwest of the screening area for a total of 560m (Figure 1). The required HC smoke canisters for each test were placed on lines a, b, and c (Figure 2) along the 115-meter length. The munitions along each selected "a" line were ignited simultaneously while the ignition of the "b" and "c" lines occurred respectively after an interval of 2 minutes. Each line contained one M2 and three M1 smoke canisters placed lengthwise in a southwest - northeast direction. This arrangement was used to simulate the dispersion pattern of dynamically fired 155mm HC rounds.

KWIK Calculations. An HP9825 desktop calculator, located at the command post, was used to perform the KWIK smoke model munition expenditure calculations. Using the meteorological and site data from the test grid prior to each trial as input to the model, we obtained outputs as illustrated by Figure 3 (sample calculations from Trial No. 12).

The munition spacing was approximated to the nearest 35 meters in relation to the HC canister array described above. The initial volley was then detonated from the selected "a" lines and the sustaining volleys from the selected "b" and "c" lines according to the KWIK calculations.

# UNCLASSIFIED

B-2

## 4. EVALUATION OF RESULTS

The evaluation of the data was performed in two parts. The first was the obscuration assessment based on the target observation data, and the second part the munition expenditure assessment comparing the results of the KWIK calculations with those obtained utilizing the current Field Manual (FM 6-40-5) and references [7, 8]. Both of these assessments were divided into three groups according to wind speed regimes. Group 1 contained trials conducted under 2.3-2.8 m/s winds, Group 2, 3.3 - 5.8 m/s and Group 3, 6.0 - 6.8 m/s winds.

Obscuration Assessment. Photographic data from each trial were used to verify the target observer assessment data. The latter was plotted as a function of time as shown in Figure 4, which is an assessment of Trial 12. These data were then tabulated, as shown in Table 1, for Group 1, 2, and 3. In Figure 4, for example, the smoke screen buildup time for the tank target was recorded as 18 seconds, but for the jeep and the moving targets this time could not be determined precisely because these targets were not scheduled to be in the line of sight at  $T_0$ . Table 1 also shows the total time each target was observed as compared to the time the target was scheduled to be in the field of view. In the case of the fourth observer (labeled "All"), the table shows the total time he viewed any of the targets as compared to the maximum time any target was scheduled to be visible. From this assessment, the percentage of obscuration was obtained.

Munition Expenditure Assessment. For each wind regime or group, Table 2 shows the number of rounds KWIK predicted would obscure the entire 500 meters for six minutes. The corresponding number of munitions obtained from the current Field Manual method are also shown for each trial. The percentage gain or loss for each trial in munition expenditures by the KWIK model are shown as well as the wind direction in relation to the line of sight. For each group, the net gain or loss is also indicated. In the case of Trial No. 12 (Figure 4) both the KWIK model and the Field Manual predicted a total of 18 munitions to obscure the optical path during quartering/head wind conditions.

For the purpose of this paper, only eighteen trials were evaluated. Of these, Trials 14 and 16 are not included in group 1 of the munition expenditure assessments because the wind speeds were below 2 m/s and could not be evaluated with the Field Manual method. The first four trials of KWIK Phase I, which were conducted during July, are also excluded due to light and variable wind conditions and lack of observation assessment data. Evaluation of Trials 23 through 30 are included in the paper by S. L. Cohn [10].

# UNCLASSIFIED

# UNCLASSIFIED

B-2

## 5. CONCLUSIONS

The munition expenditure assessment (Table 2) for Group 1 (unstable cases) shows the KWIK predictions with a net loss in munition expenditures of 9.3%. In Trials 11 and 18, KWIK predicted the same number of munitions as the Field Manual but in Trial 13 KWIK predicted 15 rounds while the FM called for only 12. Taking a close look at the wind data for Trials 13 and 17 we find that the wind speed and direction were quite variable. During Trial 13, for example, wind direction for the test grid varied between 130 and 335 degrees and wind speed ranged between 0.5 and 6.0 m/s. Another factor to be considered is the manner in which the atmospheric stability is determined by the Field Manual. It includes all stabilities into three categories: ideal (inversion), favorable (neutral) and marginal (lapse) [7, 8, 9]. These categories are based only on wind speed, sky cover and time of day. KWIK utilizes a more precise method [1] of calculating solar radiation. Using the FM method, Trial 13 is considered "neutral", where the KWIK calculations determined it to be "slightly unstable" or "C" category.

The obscuration assessment for Group 1 shows a mean obscuration of 64% for six trials under unstable to neutral stability conditions. Two of these trials were under 14% but four were over 80% obscuration. Because of the marginal wind conditions under which these trials were conducted, the KWIK obscuration assessments of Group 1 are considered good.

For Group 2 (Table 2), the munition expenditure assessments for six trials under neutral conditions show a net gain, or savings, in munition expenditures, over the FM of 4.5%. On three cases, KWIK calculated less munitions than the FM, another two produced the same number and one trial calculated one round more than the Field Manual. The obscuration assessment data for this group (Table 1) indicate KWIK predicted obscuration 95% of the time during six trials. These assessments ranged from 76 to 100%. Trials 5 through 8 demonstrate the consistency of KWIK munition expenditures under very similar meteorological conditions, as shown in Table 2. In the case of interpreting the FM tables for these same trials, a variety of expenditure values is obtained due to interpolations for wind speed and direction.

Group 3 represents neutral to stable conditions where smoke screening is considered near ideal. In this stability regime, the KWIK model predicted a 10.2% savings in munition expenditure over the current Field Manual method. The obscuration assessment resulted in 99.8% successful screening. The difference, in part, between KWIK and the Field Manual results for Trial 19 is that KWIK calculated an E, or stable, category as compared to a neutral regime determined by using the FM tables.

# UNCLASSIFIED

B-2

In summary, the KWIK Phase I evaluation test had an overall 86% success in providing effective smoke screens. Also, comparisons with the Field Manual method showed KWIK obtained a net savings in munitions of 3.2% (only for 18 trials considered here) over the current method. It is also pointed out that the current Field Manual method does not take into account certain factors such as relative humidity. The FM also assumes a 100% munition efficiency for HC smoke where KWIK uses 40% based on reference [11].

The success of KWIK Phase I is of great encouragement, but further evaluation will be pursued in Phase II and III.

## REFERENCES

1. Umstead, R.K., R. Peña, and F. V. Hansen [1979] "KWIK: An Algorithm for Calculating Munition Expenditures for Smoke Screening/Obscuration in Tactical Situations" ASL-TR-0030, USAERADCOM, Atmospheric Sciences Laboratory, White Sands Missile Range, N.M.
2. Pasquill, F. [1974] Atmospheric Diffusion 2nd Ed. Halsted Press, div. of John Wiley & Sons, New York, N.Y. 429 pp.
3. Turner, D. B., 1964, "A Diffusion Model for an Urban Area," J Appl Meteorol, 3:83.
4. F. B. Smith, 1973, "A Scheme for Estimating the Vertical Dispersion of a Plume from a Source Near Ground-Level" (unpublished Meteorological Office note)
5. Downs, A. R., 1976, "A Review of Atmospheric Transmission Information in the Optical and Microwave Spectral Regions," Ballistics Research Laboratories Report 2710.
6. Gifford, F. A. [1968] "An Outline of Theories of Diffusion in the Lower Layers of the Atmosphere" Meteorology and Atomic Energy (D. Slade, ed.) US Atomic Energy Commission, Washington, DC.
7. JTCG/ME, "Summary Tables of Estimated Ammunition Expenditures to Establish and Maintain Smoke Screens", (Unpublished manuscript).
8. TC 6-20-5, 1975, "Field Artillery Smoke".
9. FM 6-40-5, 1976, "Modern Battlefield Cannon Gunnery", Headquarters, Department of the Army.
10. Cohn, S. L. [1981] "High Wind Smoke Screening", Atmospheric Sciences Laboratory, White Sands Missile Range, N.M.
11. Cullumbine, H. [1957] "The Toxicity of Screening Smokes" J. R. Army Medical Corps 103, 119.

# UNCLASSIFIED

449

# UNCLASSIFIED

B-2

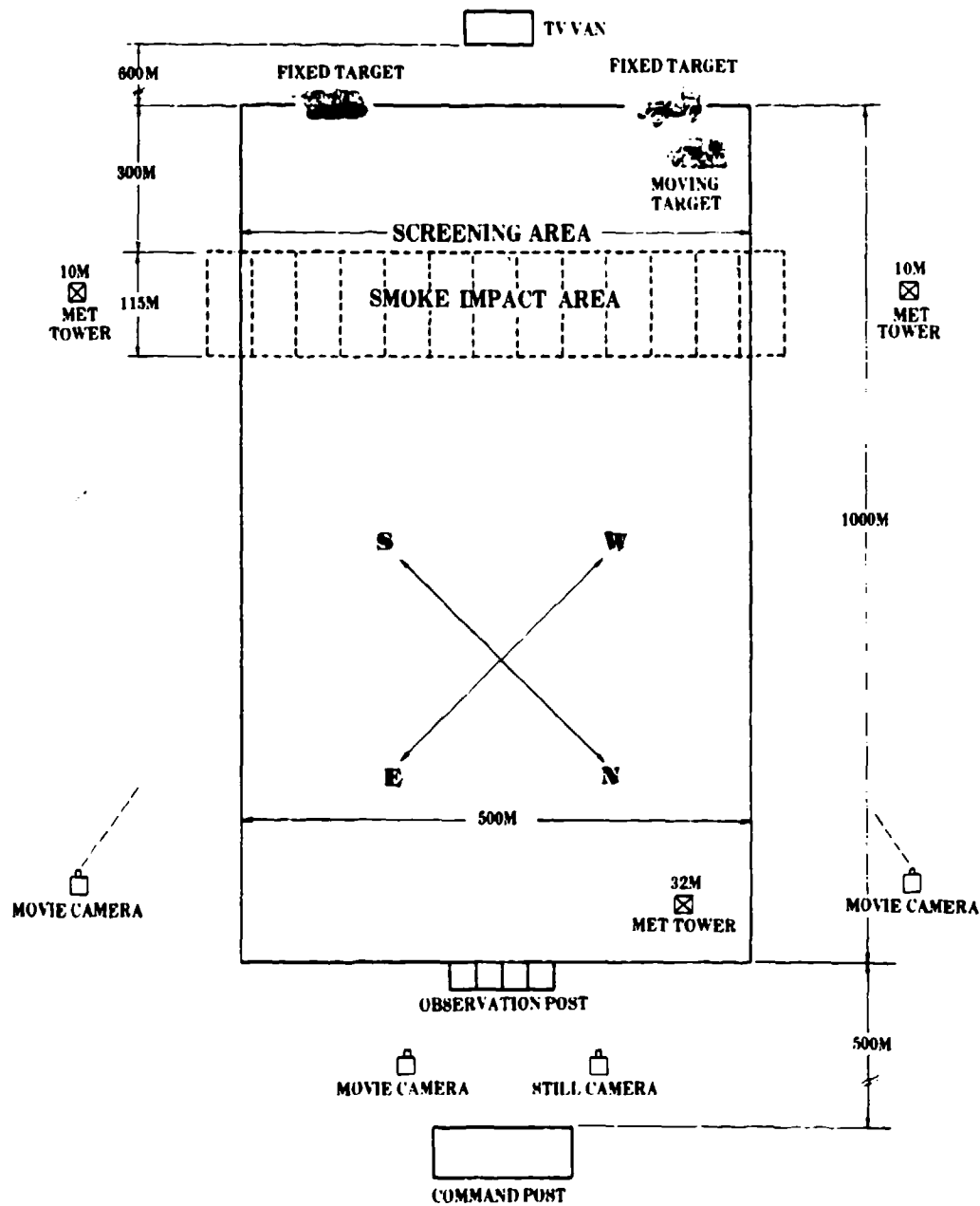


FIGURE 1. TEST GRID FOR KWIK SMOKE TESTS PHASE I DPG, UTAH

**UNCLASSIFIED**

B-2

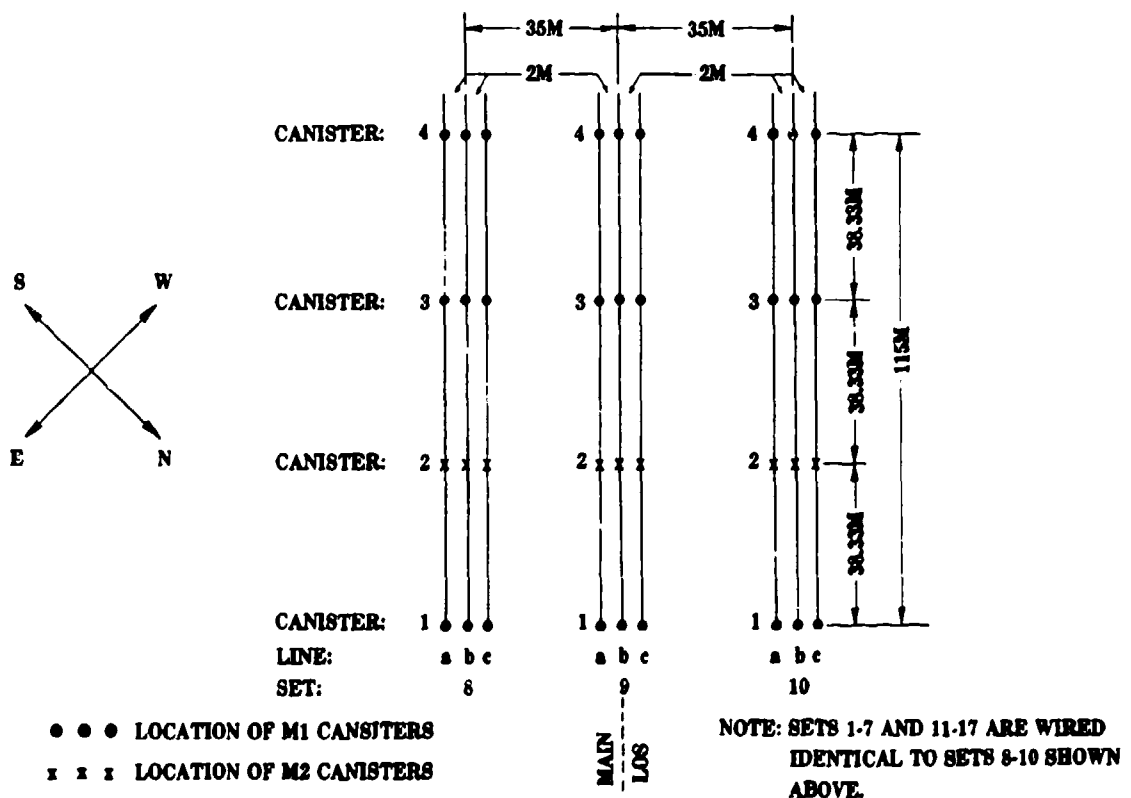


FIGURE 2. CENTER PORTION OF HC ARRAY AT SMOKE IMPACT AREA (SETS 8-10).

**UNCLASSIFIED**

## UNCLASSIFIED

MUNITION EXPENDITURES  
FOR HC SMOKE  
DPG TESTS

ID	= DPG
LATITUDE	DEG = N 40.2
LONGITUDE	DEG = W 112.7
ALTITUDE	KM = 1.3
JULIAN DATE	DAY = 259
ZULU TIME	HR = 21
CEILING	M = 7620.0
CLOUD COVER	% = 10
VISIBILITY	KM = 48.3
PRECIPITATION	= NO
TEMPERATURE	DEG = 28.3
DEWPPOINT	DEG = 1.7
WIND DIRECTION	DEG = 180.0
WIND SPEED	KTS = 10.0
ROUGHNESS ELEMENT	CM = 27.0

PASQUILL STABILITY CATEGORY C  
RELATIVE HUMIDITY 17.9

VISIBLE:

METERS MIN  
SCREEN LENGTH/DURATION: 500 6

HC SMOKE SCREEN

155MM HOWITZER

VOLLEY GUNS RATE/ SPACING	ROUNDS
MIN	METERS
INITIAL: 6	84
SUSTAIN: 6 .5	84 18

FIGURE 3. KWIK OUTPUT FOR TRIAL 12.

UNCLASSIFIED

**UNCLASSIFIED**

B-2

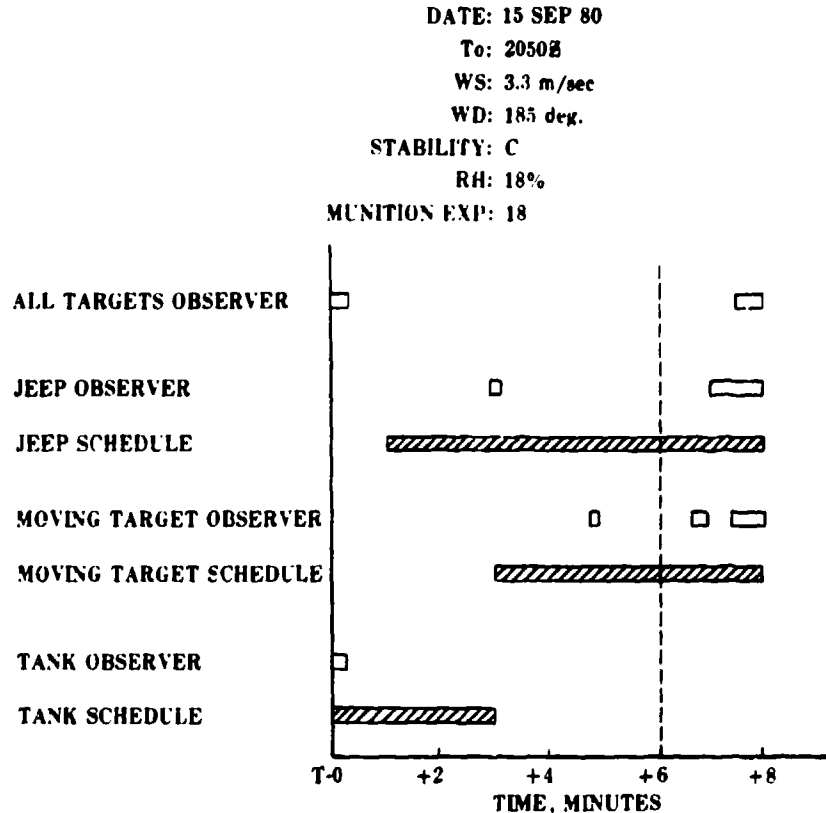


FIGURE 4. TARGET OBSERVER ASSESSMENT. KWIK I TEST  
TRIAL No. 12 DPG, UTAH

**UNCLASSIFIED**

453

**UNCLASSIFIED**

B-2

TABLE 1. OBSCURATION ASSESSMENT - KWIK PHASE I, DPG  
GROUP 2 (NEUTRAL)

<u>TARGET</u>	<u>SCREEN BUILDUP (MIN:SEC)</u>	<u>TRIAL NO. 5</u>		
		<u>TARGET SCHEDULE (MIN:SEC.)</u>	<u>TARGET OBSERVED (MIN:SEC.)</u>	<u>OBSCURATION (%)</u>
Tank (T)	*	4:30	0:00	100
Jeep (J)	*	2:30	0:12	92
Moving (M)	1:12	5:00	0:12	100
All (A)	*	5:00	0:15	<u>99</u>
			MEAN	98
<u>TRIAL NO. 6</u>				
T	2:00	3:00	2:00	100
J	2:00	5:00	1:18	93
M	1:40	3:00	1:40	100
A	2:00	5:00	2:00	<u>100</u>
			MEAN	98
<u>TRIAL NO. 7</u>				
T	*	2:30	0:00	100
J	1:00	4:00	1:15	92
M	*	5:00	0:00	100
A	1:00	6:00	1:00	<u>100</u>
			MEAN	98
<u>TRIAL NO. 8</u>				
T	*	2:00	0:00	100
J	< 1:00	5:00	0:00	100
M	0:30	6:00	0:30	100
A	0:30	6:00	0:18	<u>100</u>
			MEAN	100
<u>TRIAL NO. 12</u>				
T	0:18	3:00	0:18	100
J	< 1:00	5:00	0:15	95
M	*	3:00	0:15	92
A	0:18	6:00	0:18	<u>100</u>
			MEAN	97
<u>TRIAL NO. 15</u>				
T	0:45	6:00	0:45	100
J	1:30	6:00	3:30	56
M	2:00	6:00	2:15	93
A	1:48	6:00	3:45	<u>54</u>
			MEAN	76

\*Buildup time incomplete or undetermined

**UNCLASSIFIED**

**UNCLASSIFIED**

B-2

TABLE 2. MUNITION EXPENDITURE ASSESSMENT - KWIK PHASE I

## GROUP 1 (UNSTABLE) 2.3-2.8 M/S

<u>TEST NO.</u>	<u>KWIK</u>	<u>FIELD MANUAL</u>	<u>GAIN/LOSS</u>	<u>WIND</u>
11	12	12	0	QTR/HEAD
13	15	12	-25	VARIABLE
17	9	8	-12	VARIABLE
18	10	10	0	CROSS/QTR
			NET LOSS	- 9.3

## GROUP 2 (NEUTRAL) 3.3-5.8 M/S

5	9	11	18	QUARTERING
6	9	9	0	QTR/CROSS
7	9	8	-12	QTR/CROSS
8	9	10	10	CROSS/QTR
12	18	18	0	QTR/HEAD
15	8	9	11	QUARTERING
			NET GAIN	4.5

## GROUP 3 (NEUTRAL TO STABLE) 6.0-6.8 M/S

9	18	17	- 6	QTR/HEAD
10	27	29	7	QUARTERING
19*	7	12	42	CROSS/QTR
20	12	11	- 9	CROSS/QTR
21	9	10	10	CROSS/QTR
22	12	14	17	CROSS/QTR
			NET GAIN	10.2

\*E CATEGORY

**UNCLASSIFIED**

# UNCLASSIFIED

B-3

## COMPARISONS BETWEEN THE UPGRADED MODEL ACT II AND RECENT SMOKE WEEK TESTS

Robert A. Sutherland  
Atmospheric Sciences Laboratory  
USA Electronics Research and Development Command  
White Sands Missile Range, New Mexico 88002

### ABSTRACT

Results of comparisons between the field experiments of Smoke Week II and the performance of an upgraded smoke obscuration model ACT II are presented. The results include comparisons of both path integrated obscuring concentration (CL) derived from transmission data and directly measured path radiance (brightness) data. The comparisons include two trials for white phosphorus (WP), hexachloroethane (HC) and fog oil (FO) obscurants.

### 1. INTRODUCTION

In recent years the Army electro-optical community has become concerned with the problem of accurately modeling the effects of smoke obscuration in realistic battlefield environments. This has lead to a large inventory of smoke obscuration models (Sutherland, et al., 1981) but a relatively large dearth remains of studies comparing model results with actual field data. Although some models are reasonably accurate in modeling transmission or direct radiation (Hoock, et al., 1981) none have been demonstrated to be valid for the more difficult problem of modeling the diffuse or "path" radiance (Figure 1) which is required for the computation of contrast transmission.

The often overriding significance of the diffuse radiation (and contrast) in the real world is often obvious from casual observations such as the apparent disappearance of stars in the daytime or by the interference caused by headlight backscatter in fog.

The connection between these occurrences and those which will certainly be experienced by electro-optical devices (including the eye-brain) in the smoked battlefield is immediately obvious, demonstrating the significance of the problem to the military mission and subsequently the need for accuracy and validation in models describing the phenomenon.

In the latter respect the modeling community is fortunate in that a large block of path radiance data does exist from the series of tests conducted by the U.S. Army and often referred to as "Smoke Weeks."

Historically the problem of path radiance and its significance to visible perception has been recognized by the Army modeling community for several years. As early as 1972 an unpublished manuscript described a smoke obscuration model SOM which was reported to compute visible contrast and was later accepted as the Joint Technical Coordinating Group for Munitions Effectiveness (JTCG/ME) working model. This early model was expanded by at least two groups, one leading to the development of the model SOM II

# UNCLASSIFIED

457

THIS PAGE IS BLANK-NOT FILMED

# UNCLASSIFIED

B-3

(JTCG/ME SAWG Document, 1979), and another to ASLSOM which was further modified to become the ACT\* model (Gomez, et al., 1979) which is the direct forerunner of the present model, hence the acronym ACT II.

The major purpose of this paper is to present the results of comparisons between the ACT II model and measurements conducted during Smoke Week II. Details of both the model (Sutherland and Hoock, 1981) and the data (Dugway Proving Ground Report, 1978) can be found elsewhere. This paper contains brief descriptions of both elucidating salient features relevant to the interpretation of the results.

## 2. THE MODEL

Simply viewed the major computational objective of the model is to describe the propagation of radiant energy along a given line of sight described by the position of a target ( $r_0$ ) and an observer ( $r$ ) as sketched in Figure 1. Mathematically the problem is approached by applying the following formal solution to the radiative transfer equation (Chandrasekhar, 1960):

$$R(r) = R(r_0)e^{-\mu(r,r_0)} + \int_{r_0}^r [J(\theta,\phi) + (1-\bar{\omega}_g)B(\lambda,T)]e^{-\mu(r,r')} dr' \quad (1)$$

where the optical depth ( $\mu$ ) is in general a function of the obscurant mass extinction coefficient ( $\alpha$ ) and obscurant concentration ( $C(r')$ ) in accordance with the following definition:

$$\mu(r,r') = \int_{r'}^r \alpha C(r) dr \quad (2)$$

which for constant  $\alpha$  as assumed in the model reduces to the more commonly referred product  $\alpha CL$  where  $CL$  is the path integrated obscurant concentration.

The first term on the right side of Equation (1) is simply the direct radiation mentioned in the introduction. The term(s) inside the integral represent the diffuse or "path" radiance which accounts for both scattering into the line of sight via the "source" function ( $J(\theta,\phi)$ ) and for (thermal) emission via the "Blackbody" function ( $B(\lambda,T)$ ) where  $\theta,\phi$  are the zenith-azimuth directions of the target-observer line of sight,  $\lambda$  is the wavelength and  $T$  is the obscurant temperature.

For visible wavelengths the major computational load of the model is the determination of the source function which except for trivial cases cannot be computed analytically, leaving the modeler to devise some acceptable approximating scheme. The method used in the model is a variant of the single scattering approximation wherein the source function is assumed comprised of appropriately weighted contributions from all directions (sun, sky, terrain, etc.) over the entire environmental sphere. That is:

---

\*The acronym ACT derives from the developing agencies Atmospheric Sciences Laboratory, Chemical Systems Laboratory and TRASANA.

# UNCLASSIFIED

## UNCLASSIFIED

$$J(\theta, \phi) = \frac{1}{4\pi} \int_{4\pi} P(\theta_s) L(\theta', \phi') e^{-\mu(r, r_s)} d\Omega' \quad (3)$$

where  $L(\theta', \phi')$  is the ambient radiance from the direction  $(\theta', \phi')$  which is known (in part) from measurements in the Smoke Week data base and  $\theta_s$  is the scattering angle computed geometrically from the direction angles  $(\theta, \phi; \theta', \phi')$ . In Equation (3)  $r_s$  is the distance to the particular source assumed infinity (actually 10,000 meters) for sky sectors and appropriately calculated for terrain sectors. The phase function  $P(\theta_s)$  is an intrinsic property of the scattering medium which can be computed theoretically for inventory smokes (Shirkey, et al., 1980a) and are tabulated elsewhere (Shirkey, et al., 1980b). The phase function and single scattering albedo ( $\bar{\omega}_o$ ) are related by the following normalization convention:

$$\frac{1}{4\pi} \int_{4\pi} P(\theta_s) d\Omega = \bar{\omega}_o \quad (4)$$

For inventory smokes in visible scenarios the emission term of Equation (1) can be neglected. The reason for this is twofold, the first being that the Blackbody function is insignificant at visible wavelengths for any realistic obscurant temperature and the other being that the single scattering albedo is near unity (hence  $1 - \bar{\omega}_o \approx 0$ ). Thus thermal emission can be safely ignored in the validation studies to follow. It is instructive to note however that for infrared scenarios the sense of the above conclusions are reversed because in the infrared for inventory smokes  $\bar{\omega} \approx 0$  (Sutherland and Shirkey, 1980) and hence according to Equations (3) and (4) the source function approaches zero so that in the infrared the source function becomes negligible and the emission term dominates. This is a major physical difference between modeling the visible and the infrared. The model as now developed does treat the infrared, however, data comparable to that of the Smoke Weeks is as yet not available for validation studies. This is however an area of continued research in both modeling and in testing. (Smoke Week III reports measurements in the infrared but results are not yet available.)

For the special case of computing  $R(r_o)$ , the radiance at the target (or background) surface, the procedure is straightforward under the assumption of a Lambertian reflecting surface. That is:

$$R(r_o) = \frac{a}{\pi} \int_{2\pi} L(\theta', \phi') \cos(\theta_s) e^{-\mu(r, r_s)} d\Omega' \quad (5)$$

where (a) is the surface reflectivity or "albedo" and  $\theta_s$  in this case is the reflection angle referenced to the outward normal to the surface.

A similar expression excluding the factor  $a/\pi$  is used to compute the (smoke free) surface irradiance:

UNCLASSIFIED

**UNCLASSIFIED**

$$E_{sfc} = \int_{2\pi} L(\theta', \Omega') \cos(\theta' s) d\Omega' \quad (6)$$

In both Equations (5) and (6) note that the integration is carried out only over the forward hemisphere in order to avoid contributions from the rear or below the surface.

An aspect of the problem which causes major complexity is the fact that the entire environmental sphere must be considered in computing scattered and reflected radiation. This is especially complex for path radiance computations since a further integration is required along the line of sight from the target to the observer. The approach taken in the model is to divide the sky and terrain hemispheres into discrete angular sectors of equal solid angle and then to carry out the integrations numerically. The effect of surface albedo is accounted for by assuming a uniform radiance of magnitude ( $a E_{sfc}/\pi$ ) for each terrain sector. The model nominally requires 32 sectors for each hemisphere. Parallel point sources such as the sun or moon are then superimposed at the appropriate angular locations.

### 3. THE DATA (SMOKE WEEK II)

The Smoke Week II tests were conducted in November 1978 at Eglin Air Force Base, Florida, during conditions of general fair weather with varied degrees of cloud cover. Simultaneous meteorological and (smoke) cloud data were obtained for sixteen separate trials, six of which were selected for detailed comparisons between model and data.

Although the major purpose of the tests was to assess electro-optical sensor performance, it is significant to the modeling community that the data base also contains detailed radiation measurements of sun and sky plus (smoke) cloud path radiance measurements in the visible. Certain instrumental difficulties rendered similar infrared measurements unusable.

In this section certain points concerning the trials will be elucidated which are relevant to the interpretation of the model-data comparisons to follow. A more detailed description of the trials can be found elsewhere (Dugway Proving Ground Report, 1978).

Figure 2 is a sketch of the general geometrical configuration used in the trials. Usually the munitions are detonated at some distance (~75-100 meters) upwind from a crosswind line of sight described by the target and observer locations in Figure 2.

The immediate concern of this study is with simultaneous path radiance (actually photometric brightness, see later) and path integrated concentration (CL) along (nearly) parallel lines of sight. The CL data are actually obtained by backcalculating transmission obtained at a wavelength of 3.4 micrometers. A discussion of possible inconsistencies in obtaining CL in this manner rather than by direct chemical measurement is given elsewhere (Hoock, 1980).

**UNCLASSIFIED**

# UNCLASSIFIED

B-3

Radiance measurements were performed, for each event, by first aligning the photometer sequentially on a series of three targets; a white painted panel, an olive drab (OD) painted panel, and the natural background described as brown and green with trees and short vegetation. During the event the photometer is aligned to a black cavity providing a background of essentially zero for visible radiation so that path radiance is the directly measured quantity.

It is significant for some purposes to note that although the path radiance and CL measurements are simultaneous, the lines of sight are displaced by approximately six meters with the path radiance line to the south (Figure 2).

During (or slightly before or after) each trial measurements were also obtained at equally spaced angular locations over the sky hemisphere (37 measurements altogether). In using the Smoke Week data it is essential to realize that the unreduced sky radiance data refer to a field of view of  $1^{\circ}$  requiring conversion to a unit steradian for input to the model. The data may require further multiplication by a factor of  $\pi$  (however, the model as now coded uses these data in a relative sense normalizing to the measured surface irradiance via Equation (6)).

Some caution is required in directly comparing model and data because although the sky radiance data is assumed as standard radiometric ( $\text{Watt}/\text{m}^2 \cdot \text{sr}$ ) as required by the model the cloud brightness measurements are photopic. This requires a conversion assuming the response function for photopic vision (Stimson, 1974) which is approximated as:

$$R = R_0 \exp \left[ -\frac{1}{2} \left( \frac{\lambda - \lambda_0}{\sigma} \right)^2 \right] \quad (7)$$

where

$$R_0 = 673 \text{ lumen/watt}$$

$$\lambda = 0.56 \text{ micrometers}$$

$$\sigma = 0.043 \text{ micrometers}$$

This response function is then integrated over all wavelengths to yield the following conversion constant:

$$E(\text{Lumens}) = (2\pi)^{\frac{1}{2}} \sigma R_0 E(\text{Watt}) \quad (8)$$

This conversion itself could introduce some error due to departures of the underlying spectrum. For atmospheric work however, the error is usually slight since the solar spectrum closely approximates that defining the lumen (a blackbody at the melting point of platinum). Although some error is certainly introduced due to the ambient (blue) sky.

Some other definitions useful in making the radiometric-photopic conversion are (Stimson, 1974):

$$1 \text{ Candle} = 1 \text{ lumen/sr}$$

$$1 \text{ Footcandle} = 1 \text{ lumen}/\text{ft}^2$$

$$1 \text{ Footlambert} = (1/\pi) \text{ candle}/\text{ft}^2$$

(9)

461

# UNCLASSIFIED

**UNCLASSIFIED**

Table I lists other meteorological inputs measured during the test which are required as inputs for the model, mainly for the transport and diffusion portion described in detail elsewhere (Sutherland and Hoock, 1981).

TABLE I: METEOROLOGICAL INPUTS TO THE MODEL FROM SMOKE WEEK II DATA BASE

	TRIAL					
	1	17	8	24	16	21
8M Wind Speed (M/S)	4.1	3.2	2.4	4.0	5.7	3.8
8M Wind Direction	116.3	141.0	144.4	125.9	142.2	134.1
Power Law Exponent	0.11	0.10	0.06	0.10	0.06	0.10
1M Air Temperature ( $^{\circ}$ C)	23.6	24.4	24.7	25.0	24.7	24.4
Gradient ( $^{\circ}$ C/M)	-3.36	-0.27	-0.23	-0.40	-0.23	-0.27
Mixing Height (M) <sup>1</sup>	400.	800.	400.	200.	200.	200.
Temperature (Mix. Hgt., $^{\circ}$ C) <sup>2</sup>	**	**	**	**	**	**
Stability Category	C	B	C	D	C	B
Relative Humidity (%)	52	48	52	71	52	48
Dew Point Temperature ( $^{\circ}$ C) <sup>2</sup>	**	**	**	**	**	**
Surface Irradiance(Ly/Min)*	0.82	0.72	0.59	0.82	0.47	0.65
Surface Temperature ( $^{\circ}$ C) <sup>1</sup>	24.0	24.4	24.9	25.4	25.1	23.6
Surface Reflectivity <sup>1</sup>	0.25	0.25	0.25	0.25	0.25	0.25
Surface Roughness <sup>3</sup>	0	0	0	0	0	0
Reflection Coefficient <sup>3</sup>	1	1	1	1	1	1

\* Ly/Min = 697 Watt/M<sup>2</sup>  
 1 Estimated from available data  
 2 Optional input (not needed if other data given)  
 3 Default options employed

## 4. RESULTS

Table II summarizes the results of the measured and modeled initial (smoke free) conditions for the six trials studied. It is of some significance to note the clear agreement between the measured and modeled surface irradiance. This is not particularly surprising since the model essentially normalizes the measured sky radiances from a priori knowledge of the measured surface irradiance. The results here simply demonstrate that the numerical computations are performed with satisfactory precision. Earlier the model used the data in an absolute sense which led to errors on the order of three. This was assumed due to sharp variations in sky radiance which might occur

**UNCLASSIFIED**

# UNCLASSIFIED

B-3

in the real world. Subsequent investigations however have shown an unusual persistence indicating perhaps a systematic error in the sky radiance data. It is possible that the "error" here may be due to some confusion over the system of mixed units of the Smoke Week data base. In any case the method of the model now essentially circumvents errors due to such misunderstandings.

Table II further demonstrates good agreement with the olive drab target radiance which also holds (not shown) for both the white target and background. The reflectivities were estimated from the a posteriori data by assuming the white target to be 100% reflective. This yielded a value of 0.26 for the background and 0.24 for the OD target, thus both were assigned the nominal value of 0.25 for all trials. This same value was assumed for surface albedo.

TABLE II: SUMMARY OF RADIATION MEASUREMENTS MADE DURING SMOKE WEEK II FOR TRIALS USED IN THE COMPARISON

TRIAL NO.	DATE	SMOKE TYPE	SOLAR ZENITH	SURFACE IRRADIANCE	LUMINANCE (Cd/m <sup>2</sup> )			
			AZIMUTH	(W/m <sup>2</sup> )	BKG	TGT(WH)	TGT(OD)	
1	11/6/78	HC	51.5°	151.9°	572(562)*	2295	4111	1507(1521)*
17	11/13/78	HC	52.9°	212.0°	502(496)	1610	14732	2535(2664)
08	11/10/78	WP	59.4°	221.2°	411(415)	1816	16100	2398(2444)
24	11/15/78	WP	49.8°	168.9°	572(591)	1466	5499	1466(1828)
16	11/6/78	F0	63.7°	229.5°	328(325)	1439	16100	2569(2326)
21	11/15/78	F0	53.5°	154.3°	453(468)	2056	5173	1610(1347)

\* Values in parentheses indicate modeled results.

Table III summarizes the results of measured and modeled path integrated concentrations and path luminance for six cases studied. Generally the agreement (-50-100%) between measured and modeled CL product is as good or perhaps superior to similar transport and diffusion models (Hoock, et al., 1981).

For Trial 1 (Figure 3) the agreement between measured and modeled path radiance is surprisingly good considering all the vagaries of the real world which usually haunt the atmospheric modeler in an adverse way. An interesting feature of the model demonstrated by the results is the increased luminance near the edge of the cloud. This is a real effect often observed in nature under partly cloudy sky conditions and is the origin of the "silver linings" of poetry and song, although no such romanticism has previously been suggested for smoke clouds. A closer examination of the data may or may not verify the existence of this effect to the reader mainly because of the apparent random

# UNCLASSIFIED

# UNCLASSIFIED

B-3

nature of the measured data. A discussion of the significance of this and associated features of the model, to electro-optical sensor performance in the smoked battlefield is deferred pending further research.

In examining the remainder of Table III it is clear that a nominal agreement on the order of 50 to 100% holds with the possible exception of Trials 24 and 21 where the model appears to be especially low. The reason may be due to the 90% cloud cover, however, at this point the matter is open to speculation but will be more fully pursued in the future.

TABLE III: SUMMARY OF RESULTS OF MODEL AND DATA COMPARISONS FOR SIX TRIALS OF SMOKE WEEK II. CL COMPARISONS REFER TO PEAK VALUES; PATH LUMINANCE RESULTS ARE ESTIMATED AVERAGES

TRIAL NO.	CLOUD COVER	SMOKE TYPE	CL ( $\text{M}^2/\text{GM}$ )		PATH LUMINANCE ( $\text{Cd}/\text{M}^2$ )	
			DATA	MODEL	DATA	MODEL
01	30%	HC	4.2	3.6	3000	2500
17	0%	HC	16.0	7.5	3200	2200
08	10%	WP	12.0	13.9	3500	2500
24	90%	WP	20.5	18.5	6000	1000
16	10%	F0	2.6	2.1	2800	1800
21	90%	F0	1.6	2.0	4000	1000

## 5. CONCLUSIONS

In summary it appears that the model performs reasonably well for realistic comparisons with test data although the modeled radiances may be systematically low. This may be a manifestation of the neglect of multiple scattering which must certainly be of some significance for the situations modeled. On the other hand the model does appear to predict qualitatively features of the overall behavior of smoke clouds in a reasonable and realistic manner. Further research is required to examine and assess the significance of both model and test results.

**UNCLASSIFIED**

B-3

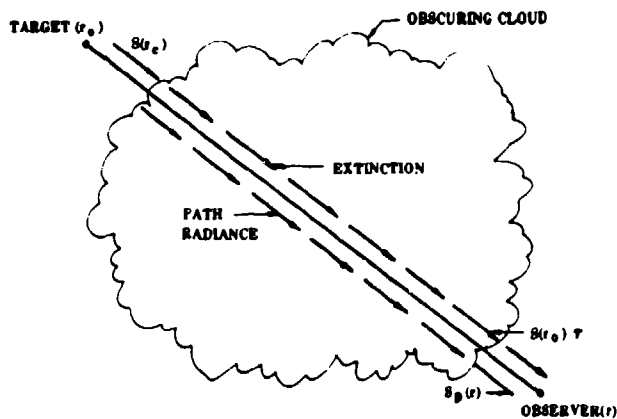


FIGURE 1. SKETCH DEMONSTRATING EXTINCTION (DIRECT RADIATION) AND PATH RADIANCE (DIFFUSE RADIATION).

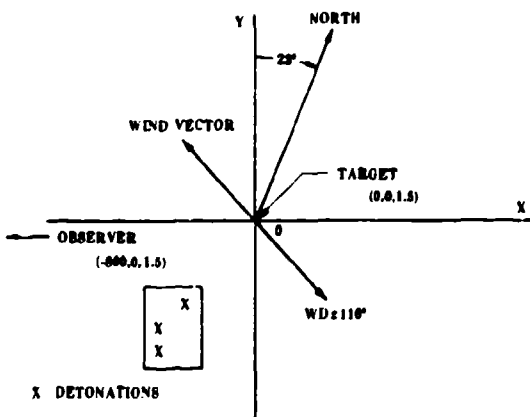


FIGURE 2. SKETCH OF THE SMOKE WEEK II TEST CONFIGURATION.

**UNCLASSIFIED**

465

UNCLASSIFIED

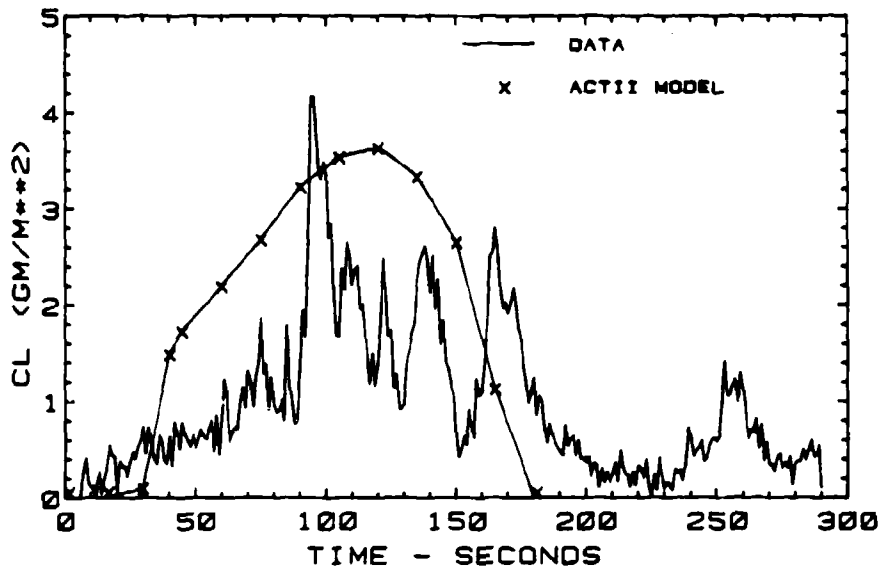


FIGURE 3a. TRIAL 01 SMOKE WEEK II  
Results of comparisons of path integrated concentration

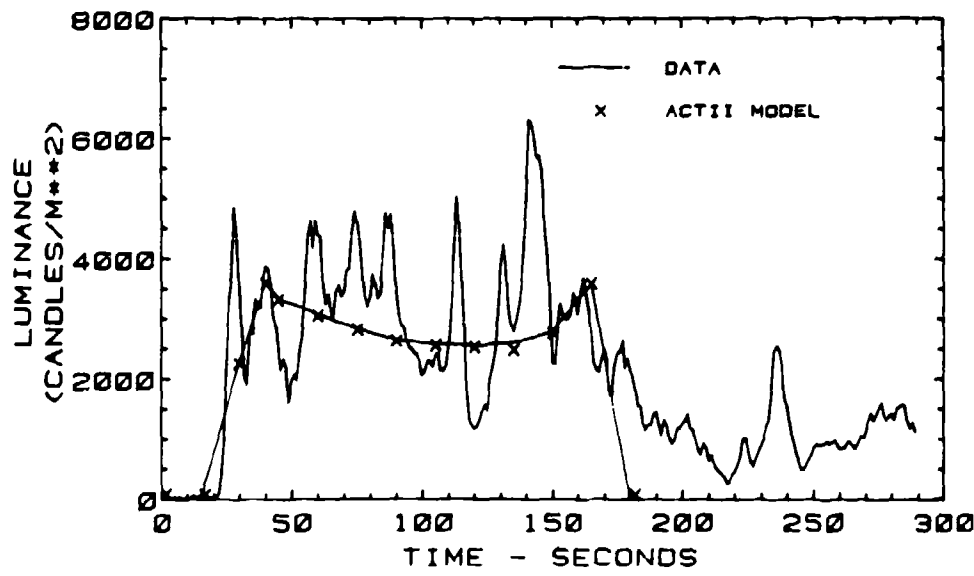


FIGURE 3b. TRIAL 01 SMOKE WEEK II  
Results of comparisons for path brightness

UNCLASSIFIED

# UNCLASSIFIED

B-3

## 6. REFERENCES

- Chandrasekhar, S., 1960: Radiative Transfer, Dover Press Publications, Inc., New York (second edition).
- Gomez, R. B., R. Pennsyle, and D. Stadtlander, 1979: "Battlefield Obscuration Model, ACT I,"  
Proceedings of the Smoke/Obscurants Symposium III, Harry Diamond Laboratories, Adelphi, MD.
- Hoock, D. W., 1980: "An Analysis of CL Profiles from the Inventory Smoke Munitions Test (Phase IIa)(U),"  
Proceedings of the Smoke/Obscurants Symposium IV, CONFIDENTIAL, Harry Diamond Laboratories,  
Adelphi, MD.
- Hoock, D. W., R. A. Sutherland, and D. A. Clayton, 1981: Comparison of EOSAEL 80 SMOKE Model with Test Data, ASL-TR (in press), Atmospheric Sciences Laboratory, White Sands Missile Range, NM.
- Shirkey, R. C., A. Miller, G. H. Goedecke, and Y. K. Behl, 1980a: Single Scattering Code AGAUSX: Theory, Applications, Comparisons, and Listing, ASL-TR-0062, Atmospheric Sciences Laboratory,  
White Sands Missile Range, NM.
- Shirkey, R. C., D. A. Clayton, and D. M. Quintas, 1980b: "Phase Function Data File PFNDT," Chapter 16  
in EOSAEL 80, Volume II: User's Manual, (R. C. Shirkey, Editor), Atmospheric Sciences Laboratory,  
White Sands Missile Range, NM.
- Shirkey, R. C. and R. A. Sutherland, 1980: "Aerosol Phase Function Data Bases," Chapter 16 in EOSAEL 80, Volume I: Technical Documentation (L. D. Duncan, Editor), Atmospheric Sciences Laboratory,  
White Sands Missile Range, NM.
- Stimson, A., 1974: Photometry and Radiometry for Engineers, Wiley and Sons, New York.
- Sutherland, R. A., and D. W. Hoock, 1981: An Improved Smoke Obscuration Model - ACT II, ASL-TR (in press), Atmospheric Sciences Laboratory, White Sands Missile Range, NM.
- Sutherland, R. A., D. W. Hoock, and R. B. Gomez, 1981: An Evaluation of U.S. Army Electro-Optical Obscuration Models and Data Bases, ASL-TR (in press), Atmospheric Sciences Laboratory, White Sands Missile Range, NM.
- DPG Final Test Report on Smoke Week II at Eglin Air Force Base, Florida (U), Volumes I and II, DPG-FR-78-317, CONFIDENTIAL, Dugway Proving Ground, UT, 1978.
- Smoke Obscuration Model II (SOM II) Computer Code Volume II - Analyst Manual, Publication of the Joint Technical Coordinating Group for Munitions Effectiveness Smoke Aerosol Working Group (JTCG/ME SAWG) Document 61 JTCG/ME-78-9-2, 1979.

# UNCLASSIFIED

# UNCLASSIFIED

B-4

## BATTLEFIELD ENVIRONMENT LASER DESIGNATOR WEAPON SYSTEM SIMULATION (BELDWSS) TEST AND SIMULATION RESULTS

ROBERT E. ALONGI  
DR. ROBERT E. YATES  
MISSILE COMMAND  
REDSTONE ARSENAL, ALABAMA

### ABSTRACT

The Redstone Test Facility at Redstone Arsenal, Alabama has recently completed a series of model tests of the HELIFIRE missile, the Ground Laser Locator Designator, and the Avionics System for AH64, TADS (Target Acquisition Designation System). These evaluations were conducted in both transient CM aerosols and in adverse weather. Performance of the various test items will be given as well as BELDWSS results. A description of the range test facility and data reduction system will also be presented.

### 1. INTRODUCTION

The Battlefield Environment Laser Designator Weapons System Simulation (BELDWSS) is a digital simulation program comprised of a union of three major elements:

- o The battlefield environment
- o The reflected laser energy signature of threat vehicles
- o The designation/delivery system dynamics

It is a program for treating system level problems in an obscurant environment. This is of primary benefit to developers of Electro-optical (EO) weapon systems. The program includes specialized tests to develop and validate models of environments and subsystems, integration of models into an overall weapon system simulation and weapon system performance analysis, as illustrated in Figure 1. The battlefield environment includes transient aerosols (such as smoke and dust), natural aerosols (such as rain and fog), human factors affecting designation system performance, tactical exercise maneuver (red and blue forces), electronic warfare effects, and terrain/forest masking.

A number of simulation models are incorporated within the BELDWSS program. One of these is the Target Signature Model (TSM). It defines the laser energy reflectance characteristics of threat vehicles. Another is a six-degree-of-freedom delivery system model coupled with a Monte Carlo statistical technique to determine the weapon trajectory and impact conditions. BELDWSS actually simulates a one delivery system on several targets engagement. It is not a force-on-force simulation such as CARMONETTE which calculates exchange ratios. Rather, BELDWSS models all known effects in the engagement of targets with laser semi-active systems in a battlefield environment.

# UNCLASSIFIED

469

**UNCLASSIFIED**

BELDWSS determines the probability-of-hit ( $P_H$ ) and all delivery system conditions required to determine the probability of attaining a kill given a target hit ( $P_{K/H}$ ). In addition, BELDWSS provides the capability to determine target availability, conditions along the line of sight to the target, target aspect, target range, etc. (See Figure 2). These conditions can easily be used for parametric studies of other electro-optical or radio frequency systems. Many engagement scenarios can be accepted.

The BELDWSS simulation is implemented on the Laser Designation Battlefield Obscuration Simulator (LDBOS) and is being exercised in the conduct of laser semi-active weapon system analysis studies. Results of the system analysis studies are used to relate critical performance parameters in lieu of using high cost live firings to obtain performance information. Model credibility is a key concern when system performance is determined by simulation instead of live missile firings. To assess model credibility, extensive validation field experiments were conducted with emphasis placed on evaluating subsystem hardware and obscurant models in an instrumented battlefield environment containing various realistic levels of obscurants.

The validation effort has continued through both a subsystem and a system level field experimentation program. Subsystem tests included system hardware such as designators and seekers, transient aerosols and natural or steady state aerosols. The data gathered during the field experiments is being used to validate the models in BELDWSS. System level validation is being accomplished through eight live firings in the various environments. Currently, seven firings have been successfully conducted to accomplish the system level validation. The designation systems modeled include both airborne and ground systems. The preproduction TADS airborne designation system has also been extensively tested, and there have been limited RPV and mast mounted sight parametric studies conducted using specification values. Further, the ground designators (GLLD, MULE and LTD) have been modeled with supporting field test data. The TSM has been validated with field test data that measure the reflectance characteristics of two threat vehicles.

**UNCLASSIFIED**

# UNCLASSIFIED

B-4

BELDWSS was developed by MLCOM during the period from 1975 through 1981 by means of a four phase program.

- o Phase I - established baseline system simulation and initial problem definition
- o Phase II - developed appropriate obscurant models
- o Phase III - developed subsystem models and validated models exercised in obscurant environments
- o Phase IV - conducted system validation firings in obscurants

## 2. VALIDATION METHODOLOGY

The process of validation consists of comparison analyses. The results of field experiments are compared with predicted results generated by computer simulation. For aerosols, validation is accomplished by establishing the degree to which the models predict transmittance, backscatter reflectance, and visibility. Geometric and environmental conditions similar to the field tests initialize the model.

The criteria to be used in determining how accurately the model must predict the obscurant characteristics is determined by performing sensitivity studies. These evaluate the obscurant effect on overall weapon system performance. The predictive performance is reviewed and evaluated by experts to assess degree of validity. Figure 3 is an example of the predictive method of validation. Models of the seeker and the designation system are also validated in this manner.

Some of the other models (the operator decision logic and the battlefield scenario models in particular) are not easily validated. These models are based on a very large number of defining assumptions including considerations such as:

- o The type of battlefield conditions simulated
- o The method of utilizing the designation system in a combat situation
- o How a designator operator would react when an obscurant occurs
- o The method of utilizing the data in the models

The validity of these models can only be assessed by considering the synergistic effect of the complete set of assumptions. Further, such validation process must be subjected to independent evaluation by outside critics. An overview of the validation concept for the BELDWSS models is presented in Figure 4.

# UNCLASSIFIED

**UNCLASSIFIED**

## 3. TRANSIENT AEROSOL MODELS

Transient aerosol models for which data was collected for validation consisted of:

<u>MODEL TITLE</u>	<u>TRANSIENT AEROSOL TYPE</u>
HEDUST	Artillery dust and debris (or artillery deployed CM Smoke)
TRACKS	Dust created from vehicular motion
BURN	Aerosol clouds created from burning targets, petroleum fire, etc.
SMOKE	Aerosols created from placed CM Smoke devices with a finite burn time (L8A1 red phosphorus, smoke pots, PWP-plasticized white phosphorus, etc.)

These models simulate three different types of aerosol clouds as follows:

- o aerosols created in a very short period of time  
(HEDUST puff model)
- o aerosols created at a fixed point on the terrain with a finite burn rate (SMOKE and BURN)
- o aerosols emitted over a finite period of time by a vehicle moving on the terrain (TRACKS dust, fog oil, etc.)

The models simulate the transport and diffusion of the cloud mass in the presence of a prevailing wind. The diffusion rate is governed by the atmospheric stability (Pasquill's Stability Category) in the battle area.

## 4. RANGE AND VALIDATION FACILITIES

Field validation experiments were conducted at Range TA-3, Redstone Arsenal and at Range C-72, Eglin AFB. The range TA-3 Redstone Arsenal facilities provided a unique opportunity to perform weapon system tests in natural and transient aerosol environments on an instrumented range.

**UNCLASSIFIED**

## UNCLASSIFIED

### 4.1 REDSTONE ARSENAL FACILITIES

Subsystem validation, Phase III, was conducted on MICOM, Range TA-3, as depicted in Figure 5. The TADS, GLLD and HELLFIRE seeker hardwares were evaluated in this range facility. As an example of the type of field experiment, a typical validation measurement might consist of the following sequence. A transient aerosol event (i.e., smoke) is initiated at Point 14 on Figure 5. The aerosol dynamics are measured, and the concentration pathlength of the aerosol along a line of sight is determined. The propagation and scatter of the projected laser energy is measured. The transmission at visible, laser, television, and FLIR wavelengths are measured, as well as the laser energy returns and the seeker response to these returns. The target illumination/tracking performance of the TADS and/or GLLD are measured against a variety of targets (tactical and others). In addition, meteorological data is recorded.

The test process involves recording approximately 250 simultaneous measurements at a rate of 20 measurements per second. Each of these data is time correlated with range IRIG timing. The collection, verification, formatting and combination of these data is automated and processed via three slave and one master digital computers.

These field experiments facilities enabled, for the first time, the simultaneous collection of the the data set sufficient for development and validation of the BELDWSS subsystem models.

### 4.2 EGLIN AFB FACILITIES

System level validation, Phase IV, is being accomplished through a live missile firing program at Eglin AFB (Figure 6). These live firings, all in obscurant environments, are only a limited subset of the subsystem experiment which was adopted for the system level program. These system level validation missile firings are scheduled to be completed by the end of April 1981. Currently, seven of the eight missiles have been fired. The program is proceeding on schedule.

## UNCLASSIFIED

**UNCLASSIFIED**

## 5. TEST AND SIMULATION RESULTS

Validation of the BELDWSS models are maturing through the analysis of the results from the Phase III and Phase IV measurement program. The Phase III activities were focused on validation of the transient aerosol and natural environment models. Phase IV validated the total weapon system model using eight live missile firings. Seven firings have been completed to date.

The Phase III Aerosol model validation achievements are illustrated by the comparison of simulation results with the test results. Sample results are given for energy transmission through the aerosol cloud for two different aerosols. These are L8A1 (red phosphor) (Figure 7) and track dust (Figure 8). These examples illustrate the excellent agreement between the model predictions and the test results for each of four signal wavelengths. Not only do the transmission values show good agreement, but the time profiles agree also. With this level of aerosol modeling success, the Phase IV system validation was undertaken.

The Phase IV validation was accomplished with live missile firings in obscurant environments. The results to date are given in Table 1. Weapon system performance was evaluated with three manmade obscurants (fog oil, red phosphor and HE dust) plus one natural environment (rain). All HELLPIRE missile tests were successful in providing valuable data for model validation. Several tests indicated that the seeker momentarily tracked the obscurant during the missile flight. No degradation in weapon system performance was detected as a result, only on one occasion did the missile fail to impact the target. System parameters were monitored during testing to assure that weapon system performance boundaries were probed. On the one occasion where the missile impacted short of the target, an unusual concentration of obscurant obliterated the target less than one second before launch and this concentration level increased through missile impact.

**UNCLASSIFIED**

# **UNCLASSIFIED**

B-4

## **6. CONCLUSIONS**

The BELDWSS program has clearly demonstrated the advantages of using the concept of simulation, combined with limited validation testing under rigidly controlled conditions, for electro-optical system performance evaluation. Under this concept, performance limitations can be identified early for prompt, cost effective corrective action. Applications to future generation weapon systems is projected and advantageous. For example, near term plans include incorporation of the simulation of the TOW II weapon system.

The validity of the BELDWSS system performance prediction has been demonstrated. Results from the field test experiments and the comparisons of the test results with model predictions clearly verify the accuracy of BELDWSS through:

- o Subsystem performance modeling (Phase I & II)
- o Smoke and obscuration modeling (Phase III)
- o Total weapon system simulation (Phase IV)

With the maturity of the BELDWSS simulation, the ability to predict accurately the weapon system performance in a variety of battlefield environments is assured. As new EO systems are developed and product improvements are applied to existing systems, it seems clear that the BELDWSS method of test validation and simulation will continue to satisfy the critical analysis and evaluation needs of Army missile weapon systems.

# **UNCLASSIFIED**

## UNCLASSIFIED

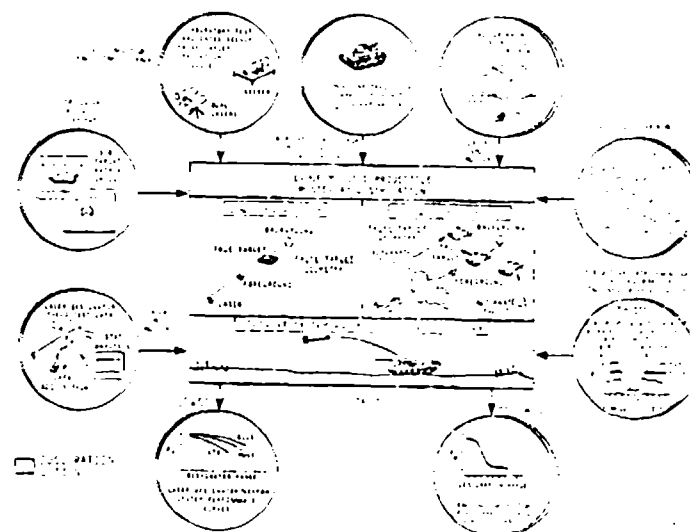


**FIGURE 1. BELDWSS MODELS.** Specialized tests validate the LDWSS/BELDWSS weapon system simulation.

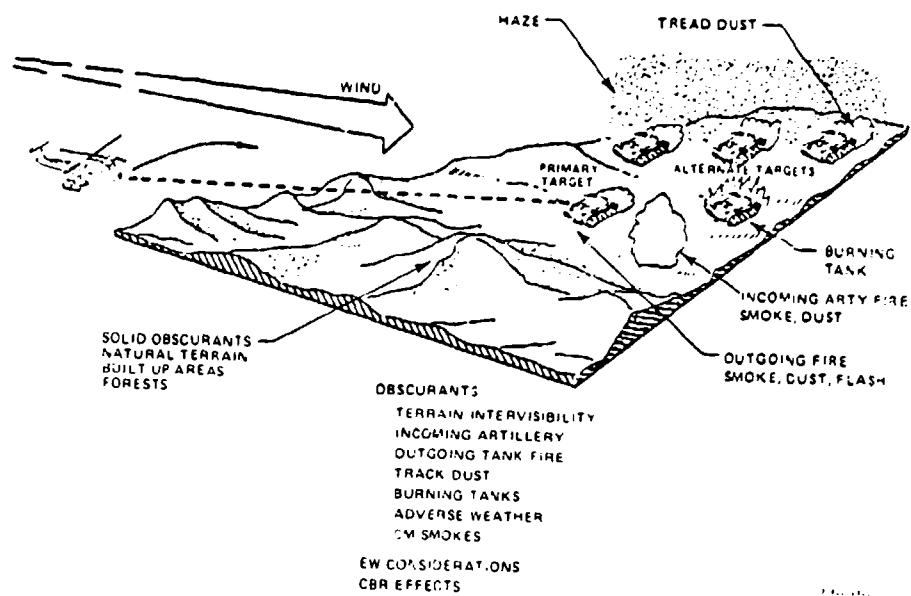


**FIGURE 2. SIMULATED BATTLEFIELD.** The Beldwss models the weapon system in the dirty battlefield environment.

UNCLASSIFIED

UNCLASSIFIED

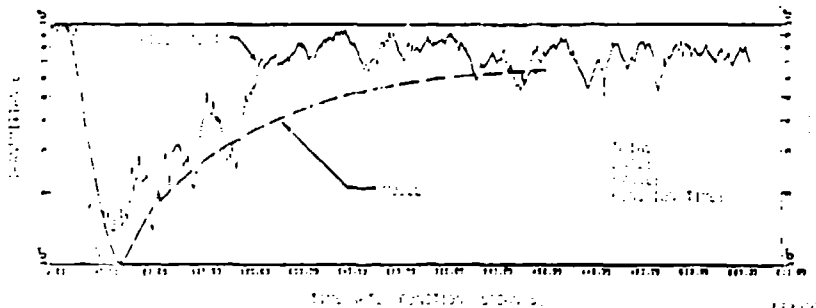


**FIGURE 3. PREDICTIVE DATA COMPARISON.** Comparison of field test results with model results is the foundation for the predictive method of model validation.

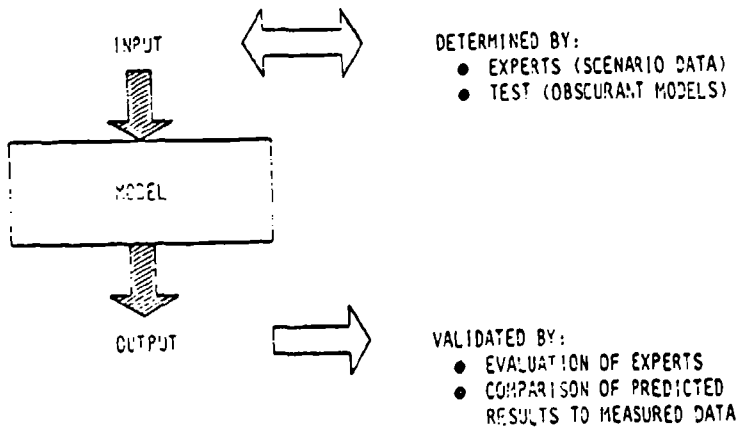


**FIGURE 4. MODEL VALIDATION METHODOLOGY.** The BELDWSS model validation process requires qualitative concurrence of experts and quantitative comparison of model with test results.

UNCLASSIFIED

**UNCLASSIFIED**

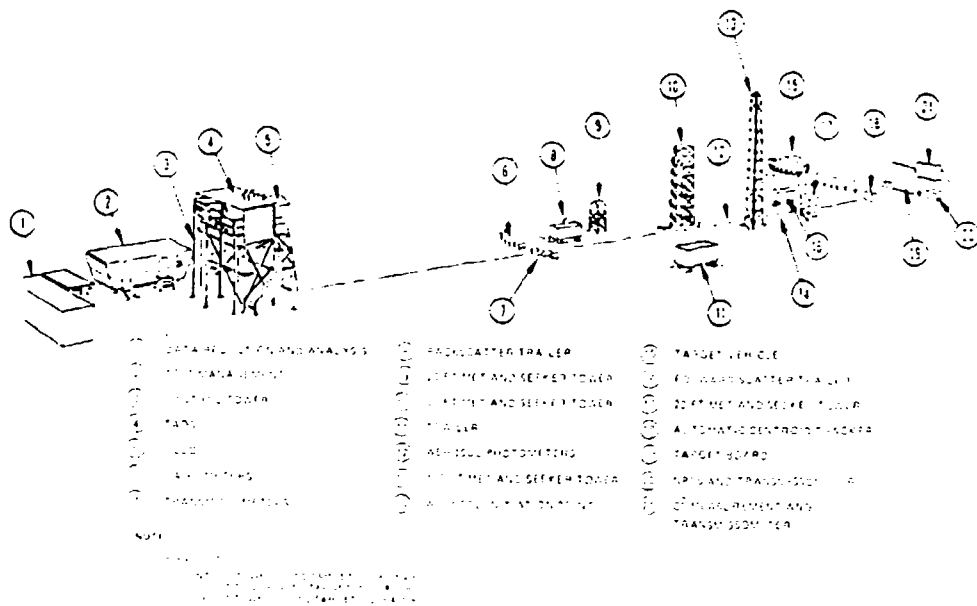


**FIGURE 5. BATTLEFIELD ENVIRONMENT RANGE FACILITY.** The instrumented test facilities at Redstone Arsenal are configured to provide maximum insight into EO weapon system performance on the dirty battlefield.

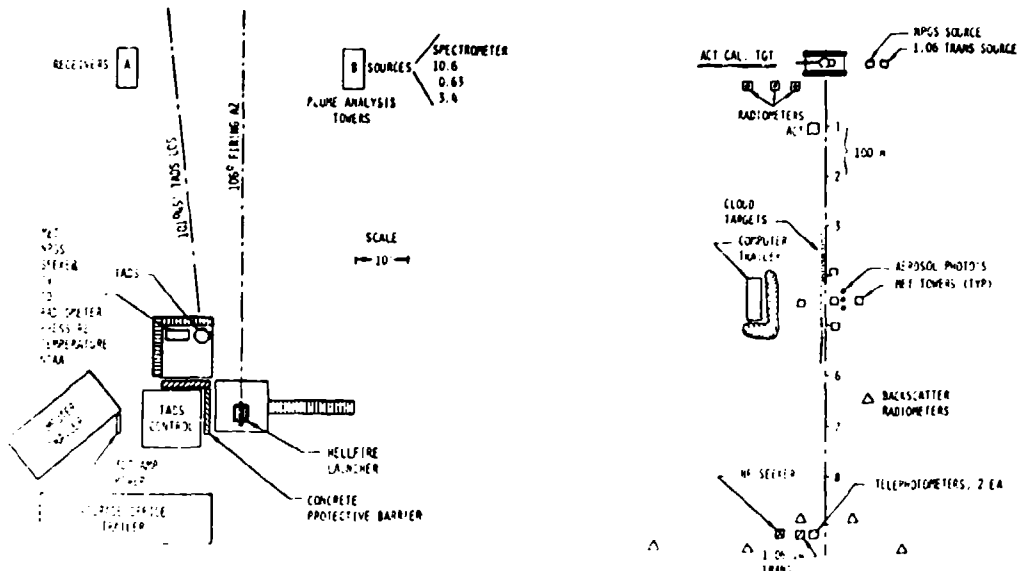


FIGURE 6. MISSILE LAUNCH RANGE FACILITY. Range facilities at Eglin AFB permit evaluation of EO weapon systems in obscurants during missile flight.

**UNCLASSIFIED**

UNCLASSIFIED

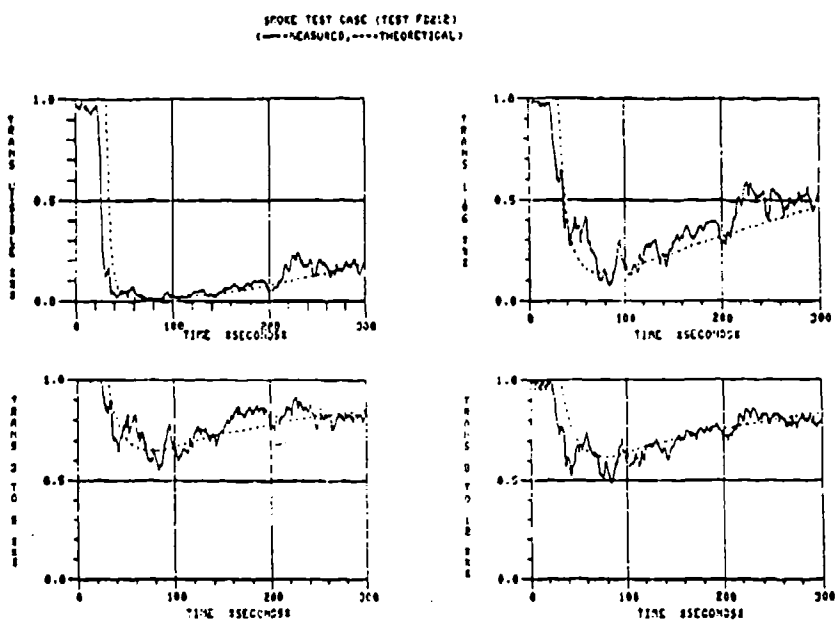


FIGURE 7. SMOKE MODEL VALIDATION RESULTS. The validity of smoke models in BELDWSS are demonstrated.

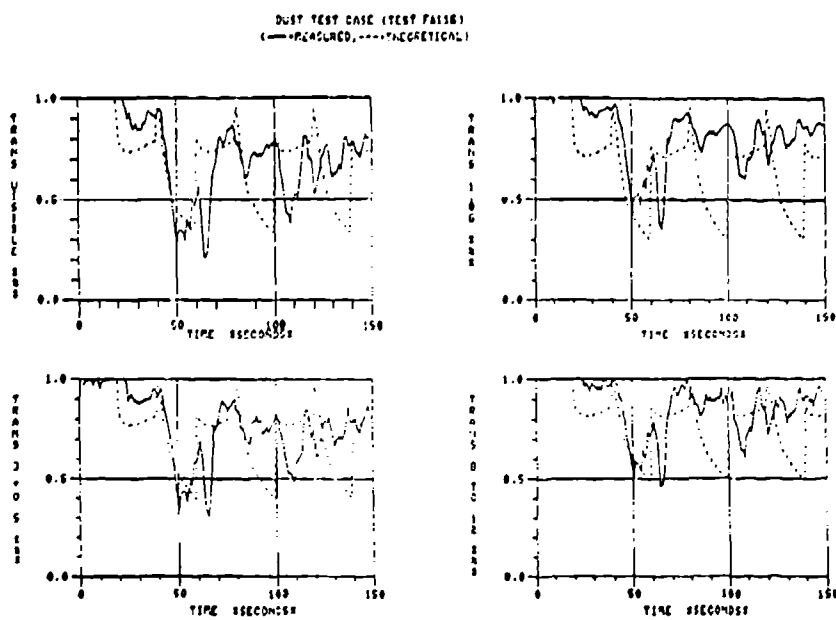


FIGURE 8. TRACK DUST MODEL VALIDATION RESULTS. The validity of track dust models in BELDWSS are demonstrated.

UNCLASSIFIED

**UNCLASSIFIED**

TABLE I. PHASE IV FLIGHT TEST RESULTS

BFO MISSION	DESIGNATION PROCESS	DATE	TARGET IMPACTED	MEAN ENERGY TRANSMISSION 1.06
Fog Dill #1	FLIR Manual Track	24 FEB 81	NO	Extremely Low
LBAI #1 (Red Phosphor)	FLIR Auto Track	12 MAR 81	YES	Very Low
LBAI #2 (Red Phosphor)	TV Manual Track	19 MAR 81	YES	Very Low
HE Dust #1 (Simulated Artillery)	FLIR Manual Track	21 MAR 81	YES	Very Low
Fog Dill #2	TV Manual Track	24 MAR 81	YES	Moderate
HE Dust #2 (Simulated Artillery)	TV Manual Track	26 MAR 81	YES	Moderate
Rain #1	TV Manual Track	1 APR 81	YES	Low

**UNCLASSIFIED**

# UNCLASSIFIED

B-7

## SENSITIVITY OF CALCULATED TRANSMITTANCES IN ARTILLERY PRODUCED DUST CLOUDS TO VARIATIONS IN MODEL INPUTS

Melvin G. Heaps and Donald W. Hoock  
Atmospheric Sciences Laboratory  
USA Electronics Research and Development Command  
White Sands Missile Range, New Mexico 88002

### ABSTRACT

The modeling of the transmission of visible and infrared radiation through artillery produced dust clouds depends on several quantities, processes and assumptions which are parameterized either as scaling laws and multiplicative factors or are specified directly as input values. Computer models by their very nature are deterministic, delivering single-valued outputs for specific inputs. In reality the input quantities are themselves not always well known, and many other parameters are simply best estimates within a range of possible choices. Several parameters from the different phases of dust cloud transmission problem have been varied within appropriate ranges. The more important parameters which can cause wide variations in the calculated transmittance are

- wind direction, which affects the position of the cloud with respect to the transmission line of sight
- the fraction of the actual crater mass remaining airborne, which affects the degree of obscuration
- the dust particle size distribution within the cloud, which affects the wavelength dependence of the obscuration.

Comparison with test data from the Dusty Infrared Test (DIRT) series show that current models are now able to correctly simulate many effects in dust cloud transmittance. Such comparisons have also shown a need for further improvements in the following areas

- initial (<3s) dust cloud development, models generally show more rapid transmittance drop-offs in this time frame than the data would indicate for explosions on the transmission line of sight
- inclusion of large turbulence eddies in dust cloud growth and movement, transmittance data often show "holes" appearing in clouds
- a better determination of the ground-hugging, non-buoyant dust skirt, most transmission measurements occur within 3 m of the surface
- inclusion of variation of meteorological parameters for long persisting (>1 min) dust clouds.

### 1. INTRODUCTION

The modeling of artillery and high explosive produced dust clouds and the resultant transmission of visible and infrared radiation through these clouds can be divided into three phases. The first phase deals with cratering and initial cloud properties and determines how much material is put into the cloud. The second phase deals with transport and diffusion of the resulting dust cloud and is important in determining the density of the dust cloud and its position with respect to the transmission line of sight. The third phase deals with the transmission of visible and infrared radiation through the dust aerosol and depends upon the particle size distribution and the composition of the material in the cloud.

In modeling the transmission through dust clouds there are certain quantities which are desired inputs to the models, but which may not always correspond to directly measured (or measurable) quantities. Table I shows some parameters which are commonly used in modeling, either as inputs or internally carried quantities, along with a comment about what quantity is actually measured. Uncertainties arise

UNCLASSIFIED

# UNCLASSIFIED

B-7

in determining a best value to be used because either the measurement itself yields a large range of possible values and an interpolation is then required, or the quantity can not be readily measured and an "educated guess" must be made.

TABLE I. MODELING PARAMETERS

NEED TO KNOW	WHAT IS MEASURED
Crater Volume	Apparent Crater Diameter(s) and Depth
Mass Lofted	No Direct Measurements
- Cloud and Dust Skirt	(Debris Measurements - Indirect)
Energy Partitioned (To Initial Cloud)	No Direct Measurements (Cloud Rise Rates - Indirect)
Pasquill Category	Estimated from Solar Insolation, Cloud Cover and Wind Speed
Wind Speed and Direction	Wind Speed and Direction (Often at Different Location)
Particle Size Distribution (In the Cloud)	Particle Size Groups (Sand/Silt/Clay)  Sieve and Hydrometer Sizing (Soil) Impactor Sampling (Cloud) Real Time In-Situ Sampling (Cloud)

The effect on the resultant transmission of the range of values of the model input parameters shall be studied here. The standard for comparison shall be the measured transmission through artillery produced dust clouds. The desired model output is the calculated transmittance at selected visible and infrared wavelengths. Selected inputs from each of the three phases of the dust cloud transmission problem shall be varied to determine their effects on and importance to the resultant transmittance.

# UNCLASSIFIED

# UNCLASSIFIED

B-7

## 2. SELECTION OF TEST DATA AND MODEL PARAMETERS

The test data shall be taken from the Dusty Infrared Test - II (DIRT-II) Program (Kennedy, 1980) conducted at White Sands Missile Range, NM, in July 1979. The test series consisted of single explosions from tube delivered (live fire) artillery rounds, statically detonated artillery shells, and statically detonated bare charges. From the many cases available, this report shall use selected cases of 105 mm and 155 mm shells. The quantity used for comparison shall be the transmittance through the artillery produced dust clouds (Curcio, et al., 1980). Figures 1 and 2 are examples of the transmittance at visible and infrared wavelengths versus time for statically detonated 105 mm and 155 mm shells.

The dust cloud transmission model used is one being developed under the auspices of the US Army Atmospheric Sciences Laboratory (Thompson, 1979; Thompson, 1980a; Thompson, 1980b). While this specific model can neither (and need not) represent all the various inputs required by different models nor identically parallel all algorithms and methods of solution used, it is a reasonable representation of the state of the art in dust cloud obscuration modeling (Heaps, 1980a; Heaps, 1980b). The main objective is to select a representative subset of potential input parameters and determine the sensitivity of the modeled transmittance to their variation.

The first phase of dust cloud modeling deals with cratering and the properties of the initial (i.e., essentially instantaneous) cloud. Several scaling laws have been developed which relate the apparent crater volume to the explosive charge type and positioning. Typical variations of actual crater volumes and the mean predicted crater volume are  $\pm 30\%$ ; that is about a factor of two difference between the smaller and large crater volumes for a given soil type. The next question deals with how much of the actual crater volume becomes airborne in the dust cloud, as opposed to being distributed as crater ejecta about the rim. Current estimates are that 25% of the apparent crater volume actually enters the cloud, but there is certainly another factor of two in variance inherent here. The basic quantity which needs to be determined is how much material is actually in the cloud, and this is a function of the apparent crater volume, the fraction which enters the cloud and an accurate determination of soil type. The basic parameter used here shall be called the lofted crater mass ( $L_{cm}$ ), which shall be used as multiplicative factor relating the volume of soil lofted to the explosive charge weight,

$$M(m^3) = 0.25 L_{cm} W^{1.111} \quad (1)$$

# UNCLASSIFIED

## UNCLASSIFIED

8-7

where  $M$  is the amount lofted ( $\text{m}^3$ ) and  $W$  is the explosive charge (in pounds of TNT).  $L_{\text{cm}}$  has a median value of 0.03 for artillery shells, but can vary between 0.01 and 0.075.

The initial (i.e., "instantaneous") size of an artillery dust cloud is usually scaled to an equivalent radius, determined from shock wave theory, which is approximately the radius of a sphere whose size is determined by the amount of explosive energy available to do work expanding the cloud against atmospheric pressure. For artillery shells this equivalent radius is on the order of 2-3 m. The initial cloud is often not spherical, particularly for cased and shaped charges, and thus an ellipsoid may be chosen for the initial cloud shape. However, the subsequent growth and diffusion of the cloud begins to obscure the effects of any initial shape within a few seconds. Thus, the effects of incorrectly scaling the initial cloud shape are felt to be less than the possible variation in the parameter governing the lofted crater mass ( $L_{\text{cm}}$ ), and these effects would be most noticeable only in the early period of dust cloud growth.

Visual examination of high explosive and artillery produced dust clouds shows that a non-buoyant base cloud or dust skirt accompanies the formation of the buoyantly rising main dust cloud. For modeling purposes this initial base cloud is given three times the horizontal dimensions and the same vertical extent as the initial buoyant main dust cloud. The airborne mass of the base cloud or dust skirt is taken to be 10% that of the main cloud. The subsequent diffusion and transport of the base cloud or dust skirt are taken to be independent, though governed by the same physics and meteorology, of the main cloud; the base cloud is taken to be "cold" and therefore has no subsequent vertical rise other than by diffusion. Because most lines of sight for electro-optical instruments are near the ground, the base cloud or dust skirt plays a large role in the resultant dust cloud obscuration effects. Because the base cloud is initially scaled to the main cloud, the potential errors and variation of parameters inherent in the formulation of the main cloud are also present for the base cloud.

Therefore, the variations possible in the first phase of dust cloud modeling, which governs cratering and initial cloud properties, center primarily in the areas of determining the amount of actual material in the cloud, defining the shapes of the initial base and main cloud, and determining the airborne mass of the base cloud or dust skirt. The largest uncertainty is in the parameter  $L_{\text{cm}}$ , which scales the amount of material in the dust cloud as a function of soil type. This parameter shall be varied to represent the largest range of uncertainties present in the first phase.

## UNCLASSIFIED

# UNCLASSIFIED

B-7

The second phase of dust cloud modeling deals with transport and diffusion, is influenced heavily by meteorological parameters, and determines the distribution and position of the cloud with respect to the optical line of sight. There are four parameters and quantities which influence this phase of the modeling problem. The first, the energy partitioned  $E_p$ , represents that fraction of energy of the initial explosion which is available for the rise and expansion of the main cloud. Current best estimates place the value of  $E_p$  at 25-30%, but there is certainly a factor of two variability depending on explosive charge type, placement and soil characteristics.

The next three quantities express the dependence of this phase of dust cloud modeling on meteorological quantities. The Pasquill category represents a quantification of atmospheric stability in six discrete steps from very unstable to very stable (the conventional Pasquill categories A through F). This parameter is estimated from meteorological observations of wind speed, cloud cover and solar insolation. Its use within the model is to select sets of values to be used in the diffusion of the base cloud and of the main cloud after its buoyant rise and expansion phase. The final two quantities are the wind speed and wind direction. These can be measured directly (though usually not precisely where the cloud is at any given moment) and used as inputs to the dust cloud model. In practice these quantities are usually held constant or averaged over periods of one or two minutes, which are the normal lifetimes of single artillery dust clouds.

The third phase of dust cloud modeling deals with the transmission of radiation through the dust cloud and depends primarily upon the composition and particle size distribution of the cloud. The composition of the soil and its optical properties (i.e., wavelength dependent indices of refraction) can be determined to some degree from soil samples. In addition the current model allows that 30% of the explosive charge ends up as micron sized carbon particles which are evenly distributed throughout the cloud. An actual determination of the cloud's particle size distribution has proved to be a difficult problem. Attempts have been made to measure the particle size distribution "in-situ" at various tests (Kennedy, 1980; Fernandez and Pinnick, 1980; Mason, 1980; Lindberg, 1979), but results are not yet felt to be reliable or representative. Soil samples and soil sieving techniques can give a reasonable representation of the gross size distribution of the soil in its natural state, but it is unclear whether the explosion itself preserves this "natural" size distribution. In order to be able to adequately model a wide range of soil type, the current model uses an easily and commonly measured parameter which is the percentage composition of the soil as sand, silt and clay. Sand represents particles of size 50-2000 $\mu\text{m}$ , silt represents particles of size 2-50 $\mu\text{m}$ , and clay represents particles of size  $<2\mu\text{m}$ . Representative particle size distributions and indices of refraction are assigned to each

# UNCLASSIFIED

485

**UNCLASSIFIED**

group. The composition of the initial cloud is then related directly to the soil composition, with an added small component of carbon. Subsequent settling of the larger size particles as time progresses will then cause a change in the relative composition of the cloud and also in its optical properties.

Table II gives the size parameters or quantities which shall be varied in subsequent simulations of test data. Where it is applicable, the average value of the parameter and its range are also given.

TABLE II

PARAMETER	VALUE USED
Crater Mass Lofted ( $L_{cm}$ ) (relates the amount of material lofted to the size of the explosive charge; a function of charge type, placement and soil type).	$\bar{L}_{cm} = 0.06-0.075$ range: 0.01 - 0.075
Energy Partitioned ( $E_p$ ) (a measure of the fraction of explosive energy available for rise and expansion of the main cloud; a function of charge type, placement and soil type).	$\bar{E}_p = 0.25$ range: 0.125 - 0.5
Pasquill Category (a quantification of atmospheric stability affecting diffusion of the cloud).	A - F (value estimated from meteorological observations) range: ± one category
Wind Speed	Measured (average) Value range: ± 0.5 - 1 m/s
Wind Direction	Measured (average) Value range: ± $10^{\circ}$
Particle Size Distribution (present distribution for different soil components are used).	Based on percentage composition of sand, silt and clay in the soil. range: ± 10 - 20% of measured values

**UNCLASSIFIED**

**UNCLASSIFIED**

B-7

## 3. COMPARISON OF MODELED VARIATIONS WITH TEST DATA

The test data shown in Figures 1 and 2 illustrate two points which should be noted. First, the rather jagged or stochastic nature of the actual transmission data is due to turbulence and the many small inhomogeneities actually present within the cloud; often large eddies are present which give brief "transmission holes" in the dust cloud. It is beyond the state of current computer codes to model anything but a continuum approach to the effects of turbulence and therefore simulated transmission data appear as smooth curves. Second, the actual data often show larger transmittances at infrared than at visible wavelengths, as Figures 1 and 2 show. This particular feature, while frequently observed, is by no means consistently present even within all test series.

Two test cases have been chosen to illustrate the variation one might expect between actual and simulated transmission data when the input quantities to the model are changed. The first case, already shown in Figure 1, is for a 105 mm shell detonated a reasonable distance from the line of sight whose cloud was carried across that line of sight at a somewhat oblique angle. This second case is for a larger 155 mm shell detonated closer to the line of sight, whose cloud was carried almost parallel to, but slightly away from the line of sight. Table III gives the basic input data for each case.

TABLE III

PARAMETERS	B-7 (105 mm)	A-11 (155 mm)
Distance from line of sight	19.5 m east	10.4 m west
Height of line of sight above detonation point	7.5 m	7.5 m
Estimated Pasquill Category	B	B
Wind Speed	2.4 m/s	3.7 m/s
Wind Direction	165°	36°
Angle of wind w.r.t. line of sight	41° (across)	10° (away)
Soil type	silty clay with varying amounts of sand; composition taken as 25% sand, 50% silt, 25% clay	
Indices of refraction	$\lambda = 0.55\mu\text{m}$	$\lambda = 10.37\mu\text{m}$
Clay	1.52 - 0.0007i	2.16 - 0.149i
Silt	1.55 - 0.0001i	2.35 - 0.0315i
Sand	1.55 - 0.0001i	2.35 - 0.0315i
Carbon	1.75 - 0.44i	2.22 - 0.726i
Type of explosive charge	statically detonated artillery shell placed with nose tip on the ground at an angle of about 11° with the surface	

**UNCLASSIFIED**

487

UNCLASSIFIED

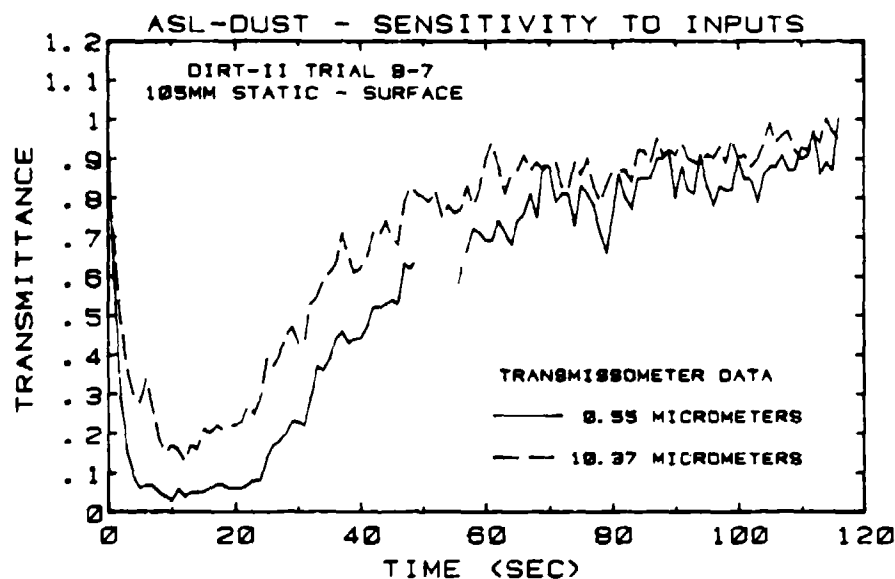


FIGURE 1. DIRT II TRIAL B-7 TRANSMISSOMETER DATA  
105 MM static round at .55 and 10.37 micrometers.

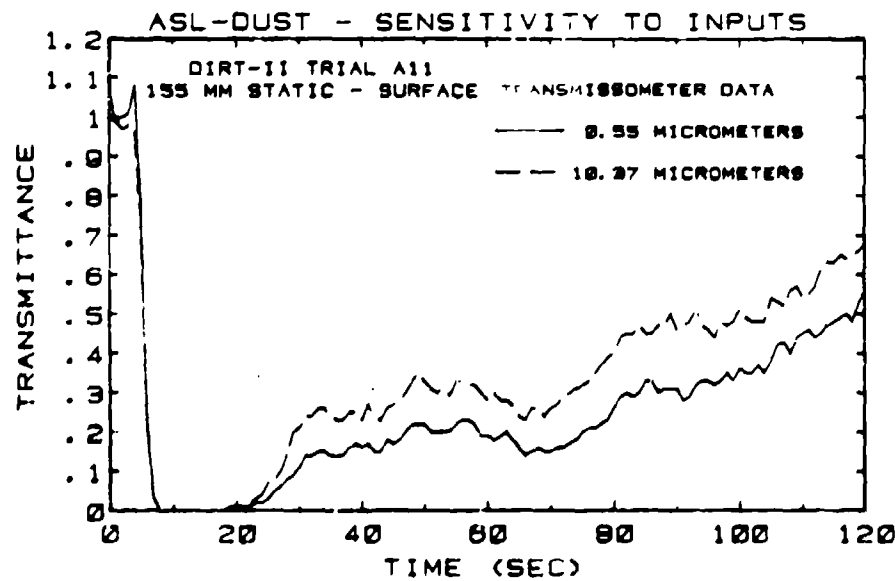


FIGURE 2. DIRT II TRIAL A11 TRANSMISSOMETER DATA  
155 MM static round at .55 and 10.37 micrometers.

UNCLASSIFIED

## UNCLASSIFIED

B-7

Figures 3 through 6 show the simulated transmittances for 105 mm (trial B-7) and 155 mm (trial A-11) explosions. The visible (0.55 $\mu$ m) and infrared (10.37 $\mu$ m) transmittances are shown separately. The parameter which has been varied is the lofted crater mass,  $L_{cm}$ . The larger values were taken from the averaged crater sizes for all statically detonated 105 mm and 155 mm shells respectively. The smaller values of  $L_{cm}$  were chosen as a lower limit for the types of desert soils present in the Dusty Infrared Test (DIRT) series. As might be expected, the measured  $L_{cm}$ 's for the respective sets of trials give the better representation of the measured transmittances.

Figures 3 and 4 show that the early time modeled transmittances do not drop off as rapidly as the test data would indicate. Examination of numerous cases of similarly placed charges (i.e., more than 10 m from the line of sight, such that the cloud is not initially in the line of sight) shows a similar trend. The indication is that the size and expansion of the base cloud or dust skirt are not correctly modeled for the first few seconds of the dust cloud's lifetime. In contrast, for dust clouds which are very close to the line of sight, similar to Figures 5 and 6 and other cases which were examined, the modeled transmittances dropped off more rapidly than the measured ones. The indication here is that the transmissometer may not have responded accurately during the initial seconds of rapid transmission decrease. Thus, comparisons between simulated and measured data for times less than approximately three seconds may not always be valid.

Figures 3 through 6 show that the larger values for the lofted crater mass factor ( $L_{cm}$ ) provide the better simulation of the transmission data. Because the main cloud rises eventually several tens of meters above the surface, while the base cloud stays within several meters of the surface, the main cloud moves out ahead of the base cloud or dust skirt due to the normal wind shears present in the atmospheric boundary layer. Thus for trials such as B-7, shown in Figures 3 and 4, where the cloud is blown across the line of sight, the obscuration at later times is due primarily to the base cloud; the main cloud is above and beyond the line of sight at these later times. In trial A-11, Figures 5 and 6, the bulk of the obscuration at earlier times is caused by the main cloud, because the track of the two clouds so closely parallels the line of sight. The main cloud, while above the line of sight, is still expanding down into it; after about 40 seconds the base cloud also begins to diffuse up into the line of sight and causes the majority of the obscuration after this time. The decline in the rate of improving transmittance seen in Figures 5 and 6 after 60 seconds is due to the base cloud diffusing up into the line of sight while the larger particles (>80 $\mu$ m) of the main cloud are beginning to settle down into the line of sight.

## UNCLASSIFIED

489

UNCLASSIFIED

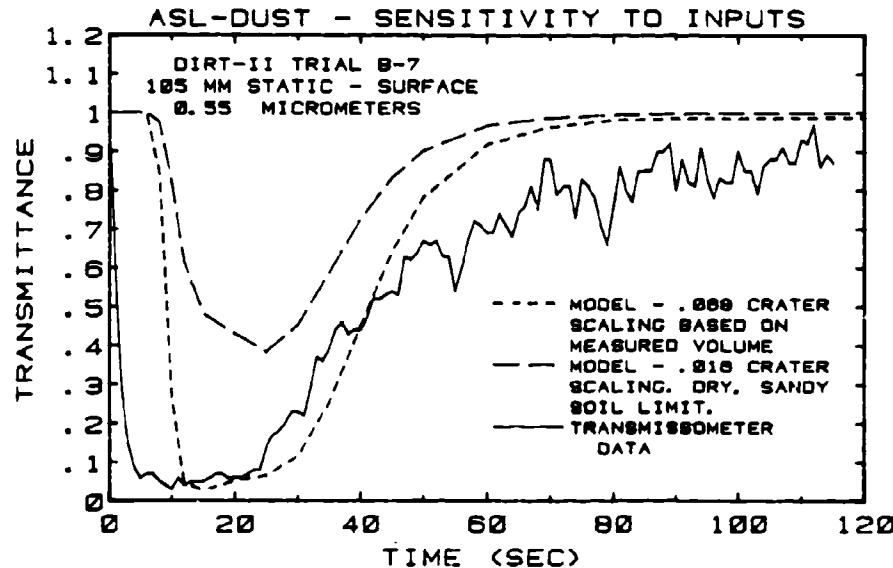


FIGURE 3. DIRT II TRIAL B-7 CRATER SCALING.  
Variation in crater scaling factor.

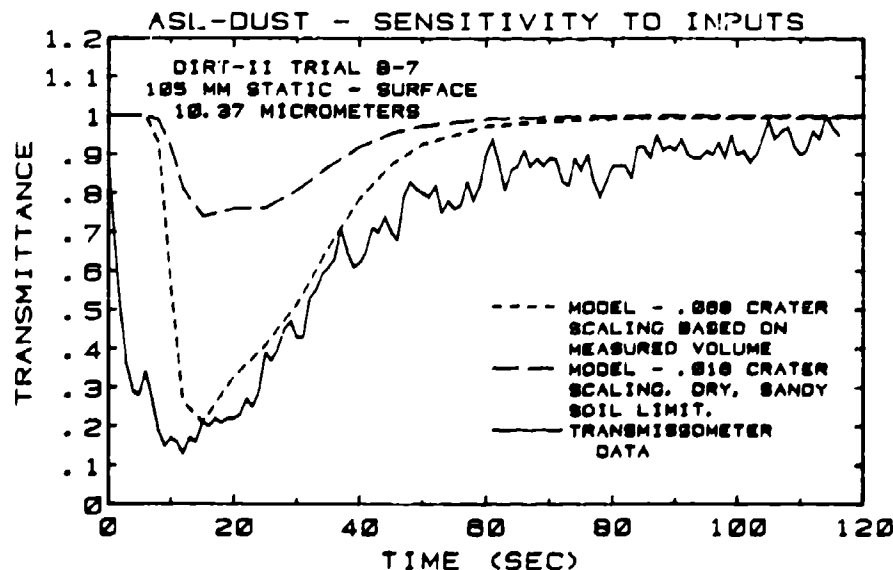


FIGURE 4. DIRT II TRIAL B-7 CRATER SCALING.  
Variation in crater scaling factor.

UNCLASSIFIED

**UNCLASSIFIED**

B-7

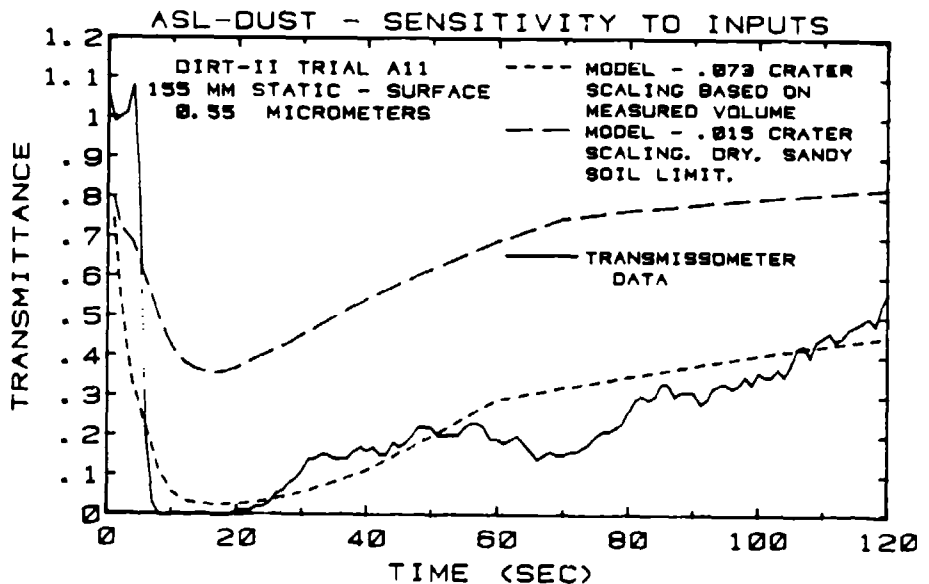


FIGURE 5. DIRT II TRIAL A11 CRATER SCALING.  
Variation in crater scaling factor.

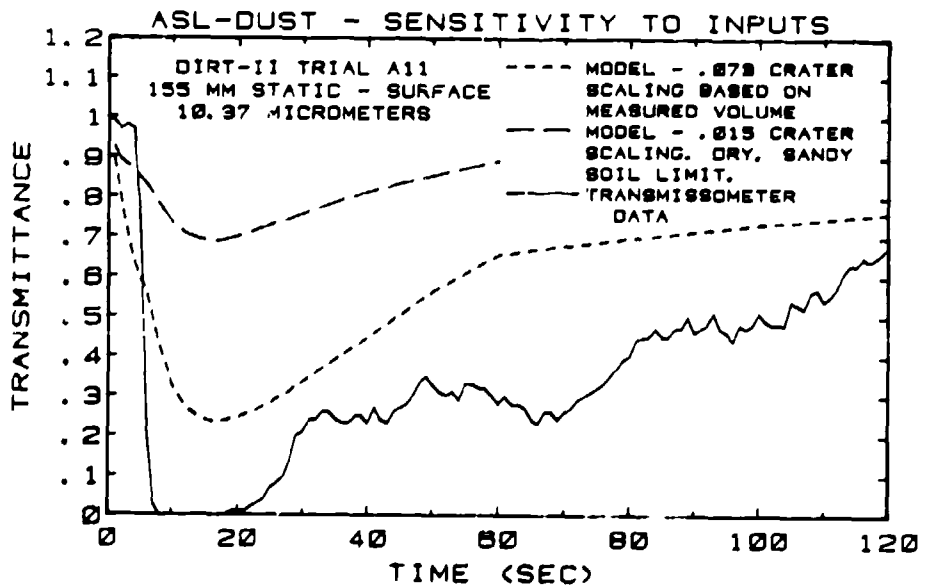


FIGURE 6. DIRT II TRIAL A11 CRATER SCALING.  
Variation in crater scaling factor.

**UNCLASSIFIED**

491

# UNCLASSIFIED

B-7

Figures 7 through 10 show the effect of varying the energy partitioned fraction,  $E_p$ . It can be seen that as the  $E_p$  fraction increases the simulated transmittances decrease. This is due to two reasons. The first is because the initial size of the main cloud, and hence the base cloud or dust skirt, is scaled to the amount of energy "available" to the cloud from the explosion. Thus, the initial base cloud is larger and extends into the line of sight to a greater extent. The second reason is that, although the main cloud is rising at a somewhat more rapid rate it is also expanding at a more rapid rate such that the amount of material in the line of sight due to the main cloud is slightly increasing.

Figures 11 through 14 show the effect of varying the Pasquill category. This parameter is varied in a step-like manner and the range of simulated transmittances show the importance of making an initially reasonable estimate. The Pasquill parameter primarily controls the diffusion of the base cloud and, after the rise and expansion phase, of the main cloud. The effect of changing the Pasquill category to more unstable conditions is to increase the rate of diffusion (expansion) of the cloud which in turn causes more material to be diffused into the line of sight. Thus changing the Pasquill category from B-A decreases the simulated transmittance. Figures 12 and 14 indicate that for infrared transmission a change in the Pasquill category to a more unstable value at later times gives a somewhat better fit to the data. This may indicate that the diffusion of the larger particles in the late-time cloud has been underestimated.

Figures 15 through 18 show the effect of varying the wind speed. The general effects are small, particularly when the cloud tends to parallel the line of sight, as in Figures 17 and 18. When the wind is more of a cross wind to the line of sight, the entire profile just slides over a few seconds in time, which is what one would expect. Of course the two profiles are not absolutely identical due to small differences in the respective speeds of the main and base clouds.

Figures 19 through 22 illustrate the effects of changing the wind direction. The differences are larger here for slight changes in wind direction than they were for the previous changes in wind speed. For trial A-11, Figures 19 and 20, where the cloud path nearly parallels the line of sight, a slight change in direction causes a very large change in the simulated transmittances. In this instance the cloud path is only  $5^\circ$  from the line of sight; for the earlier part of the infrared transmission profile in Figure 20 the altered wind direction gives a better fit to the data. In reality, the wind direction and speed do vary slightly on time scales of a few seconds; these are two causes of the stochastic nature of the actual transmission data.

**UNCLASSIFIED**

B-7

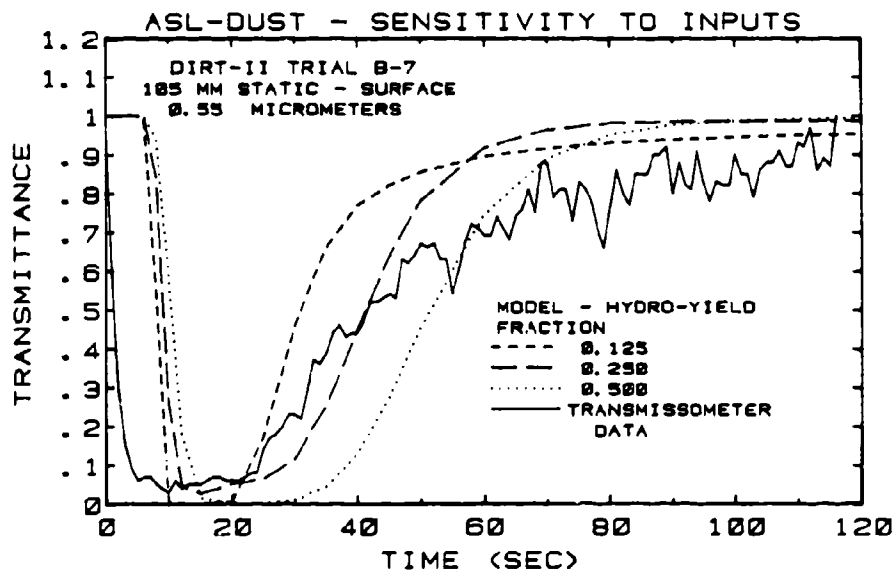


FIGURE 7. DIRT II TRIAL B-7 HYDRO-YIELD FACTOR.  
Variation in hydro-dynamic energy fraction.

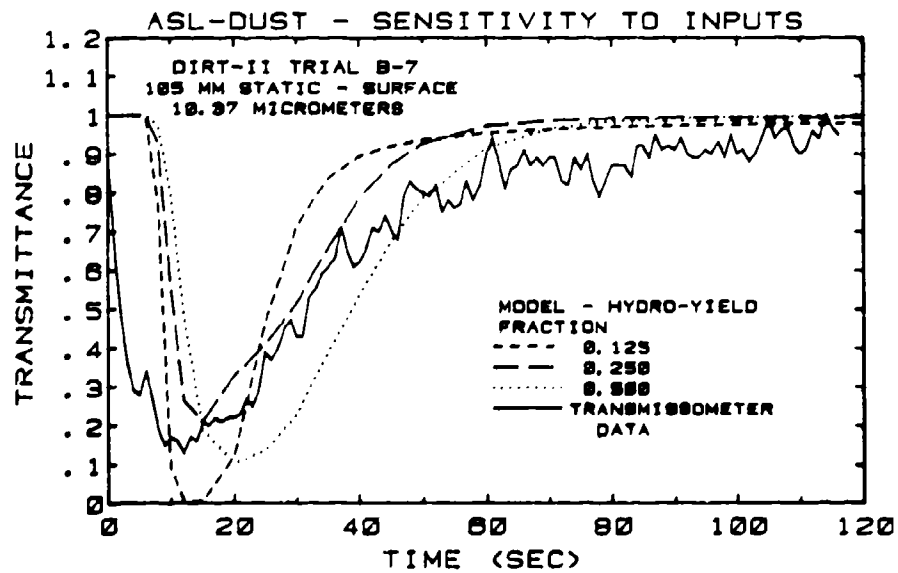


FIGURE 8. DIRT II TRIAL B-7 HYDRO-YIELD FACTOR.  
Variation in hydro-dynamic energy fraction.

**UNCLASSIFIED**

493

UNCLASSIFIED

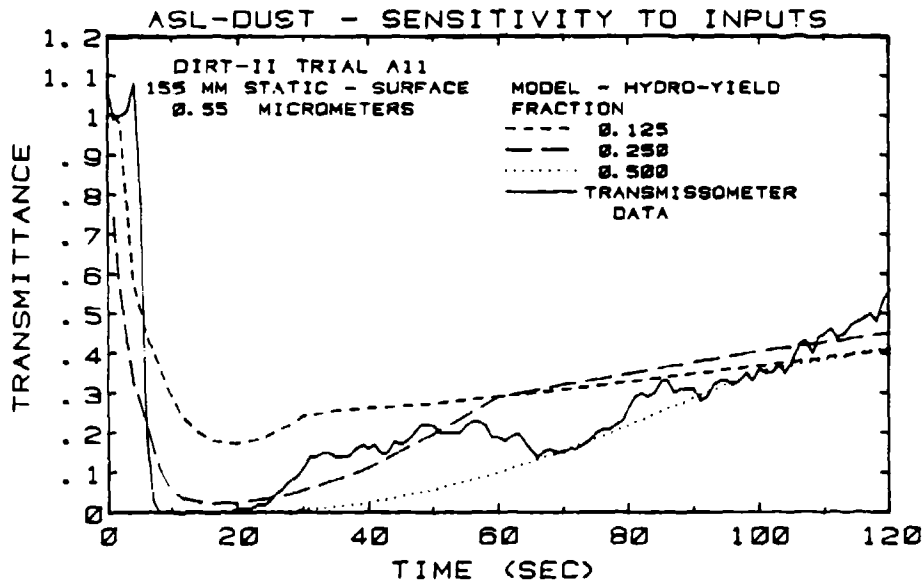


FIGURE 9. DIRT II TRIAL A11 HYDRO-YIELD FACTOR.  
Variation in hydro-dynamic energy fraction.

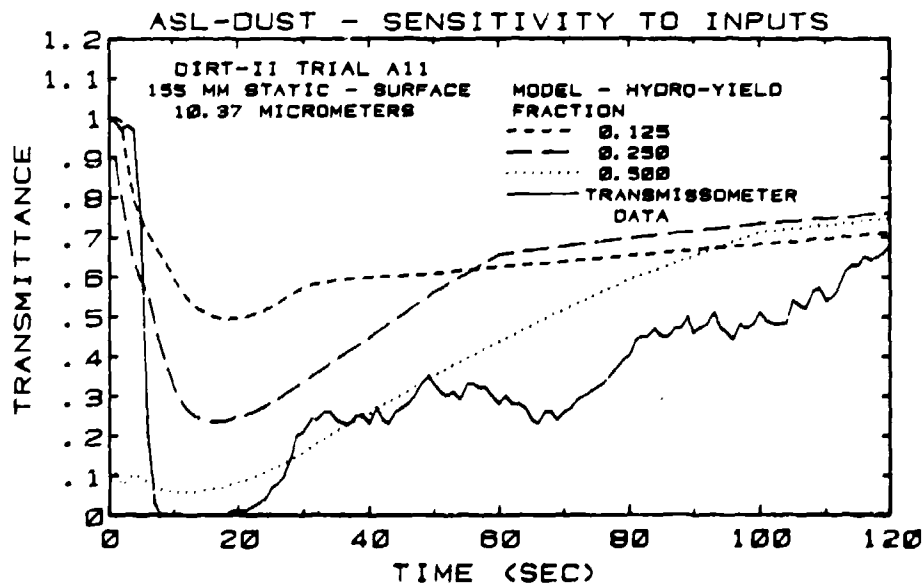


FIGURE 10. DIRT II TRIAL A11 HYDRO-YIELD FACTOR.  
Variation in hydro-dynamic energy fraction.

UNCLASSIFIED

**UNCLASSIFIED**

B-7

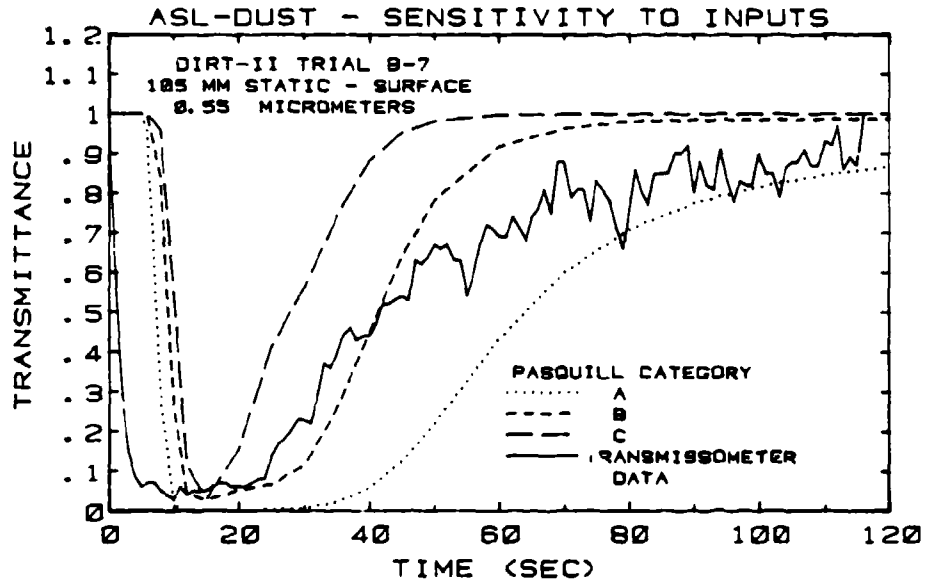


FIGURE 11. DIRT II TRIAL B-7 PASQUILL CATEGORY.  
Variation over Pasquill Stability Categories.

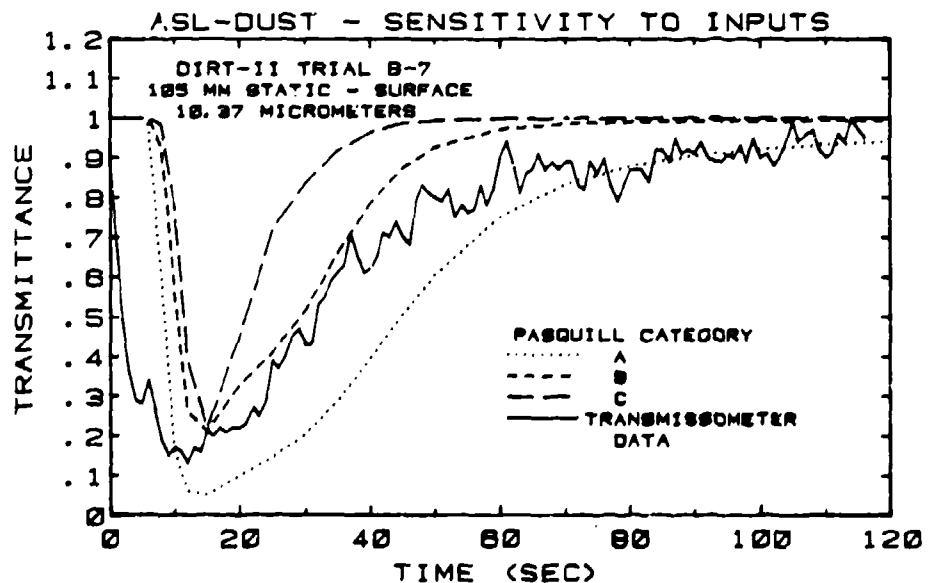


FIGURE 12. DIRT II TRIAL B-7 PASQUILL CATEGORY.  
Variation over Pasquill Stability Categories.

**UNCLASSIFIED**

495

UNCLASSIFIED

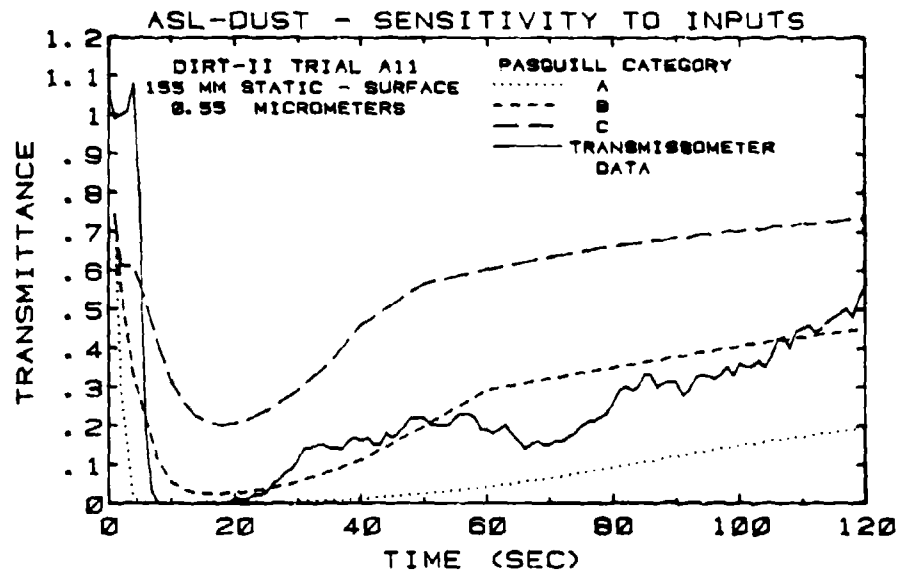


FIGURE 13. DIRT II TRIAL A11 PASQUILL CATEGORY.  
Variation over Pasquill Stability Categories.

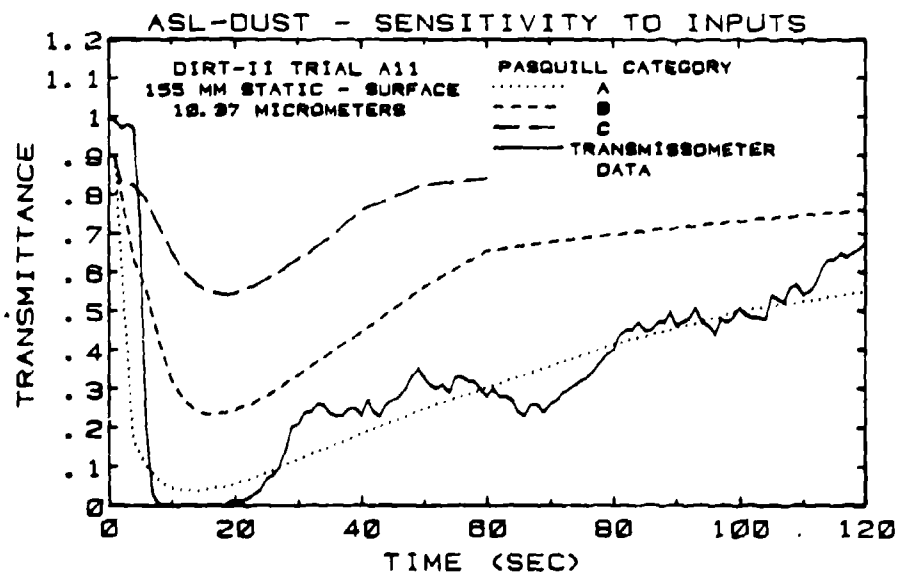


FIGURE 14. DIRT II TRIAL A11 PASQUILL CATEGORY.  
Variation over Pasquill Stability Categories.

UNCLASSIFIED

**UNCLASSIFIED**

B-7

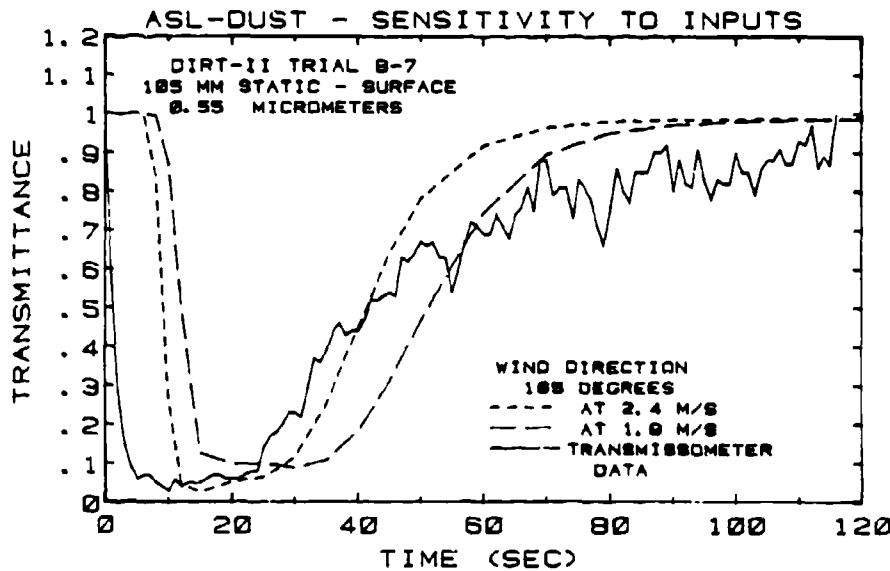


FIGURE 15. DIRT II TRIAL B-7 WINDS  
Variation in wind speed with constant direction.

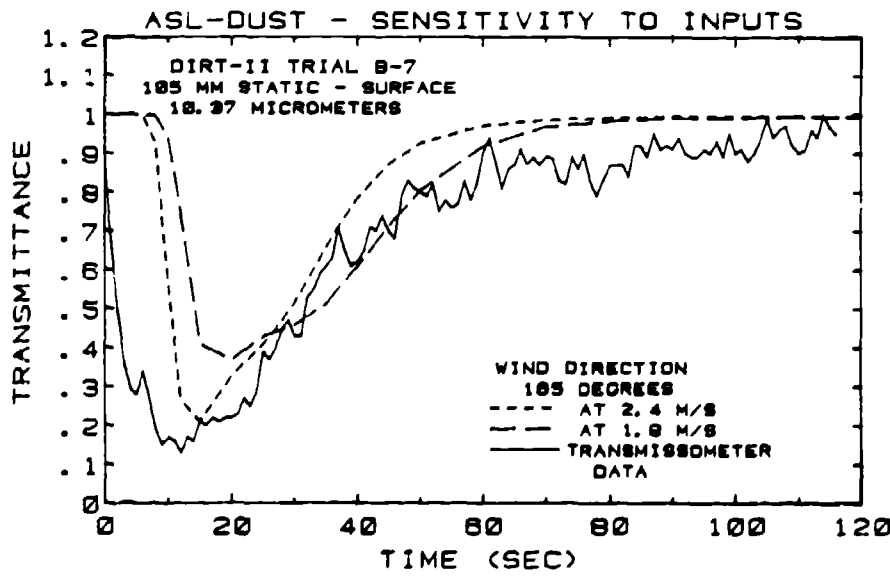


FIGURE 16. DIRT II TRIAL B-7 WINDS  
Variation in wind speed with constant direction.

**UNCLASSIFIED**

UNCLASSIFIED

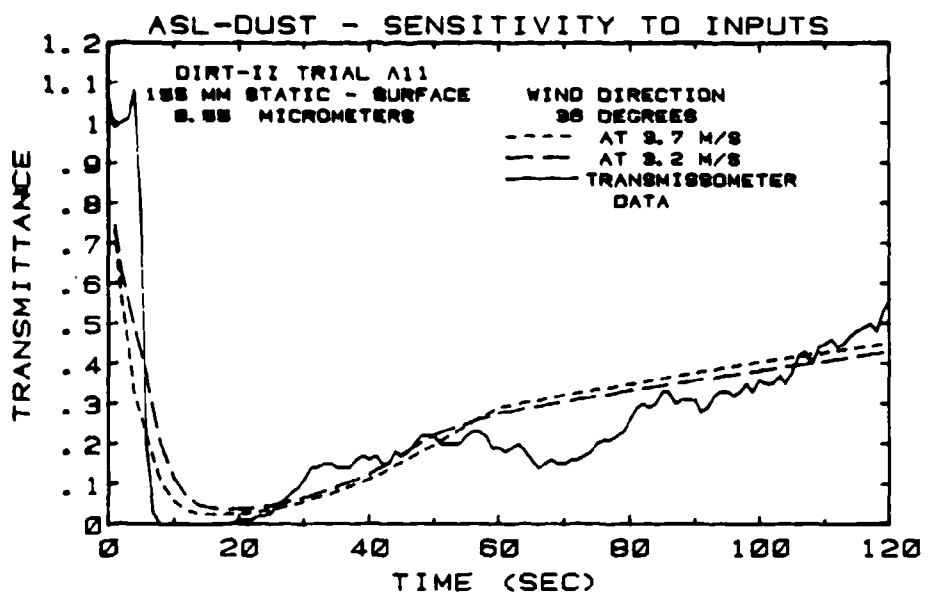


FIGURE 17. DIRT II TRIAL A11 WINDS  
Variation in windspeed with constant direction.

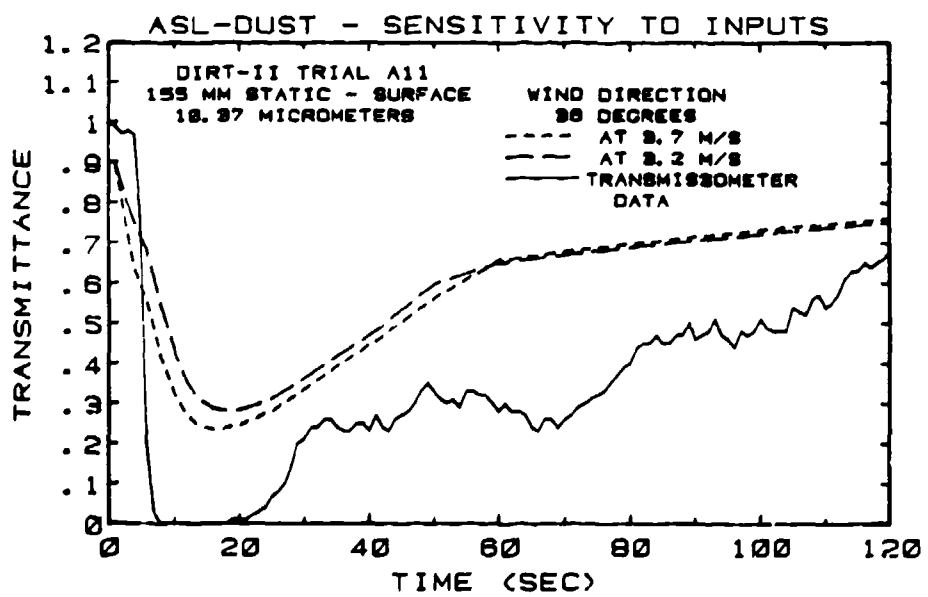


FIGURE 18. DIRT II TRIAL A11 WINDS  
Variation in windspeed with constant direction.

UNCLASSIFIED

**UNCLASSIFIED**

B-7

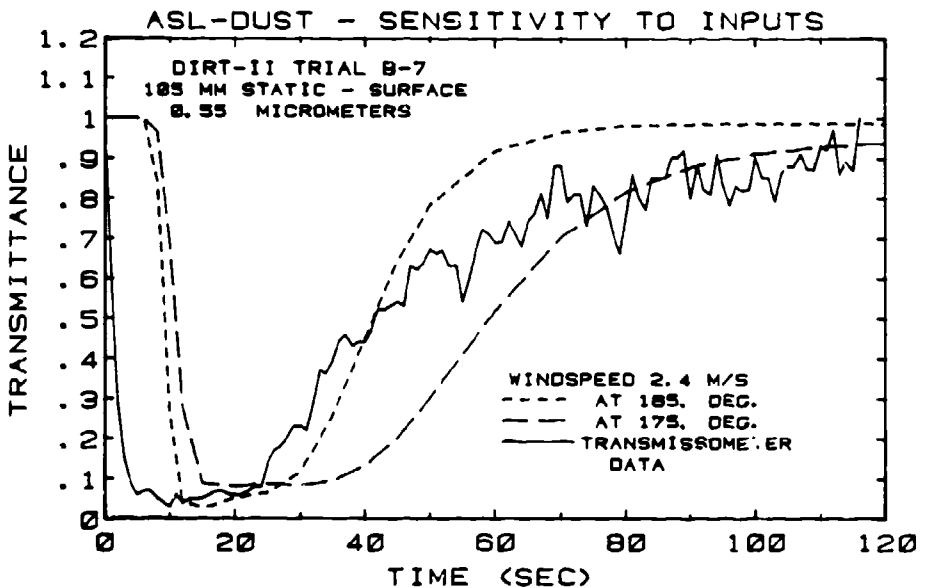


FIGURE 19. DIRT II TRIAL B-7 WIND DIRECTION  
Variation in wind direction at constant windspeed

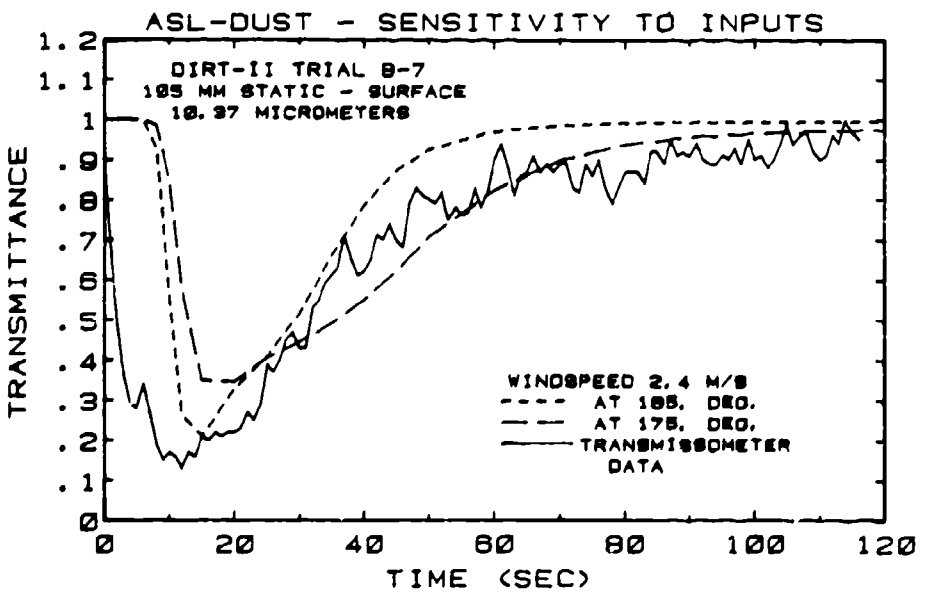


FIGURE 20. DIRT II TRIAL B-7 WIND DIRECTION  
Variation in wind direction at constant windspeed

**UNCLASSIFIED**

**UNCLASSIFIED**

B-7

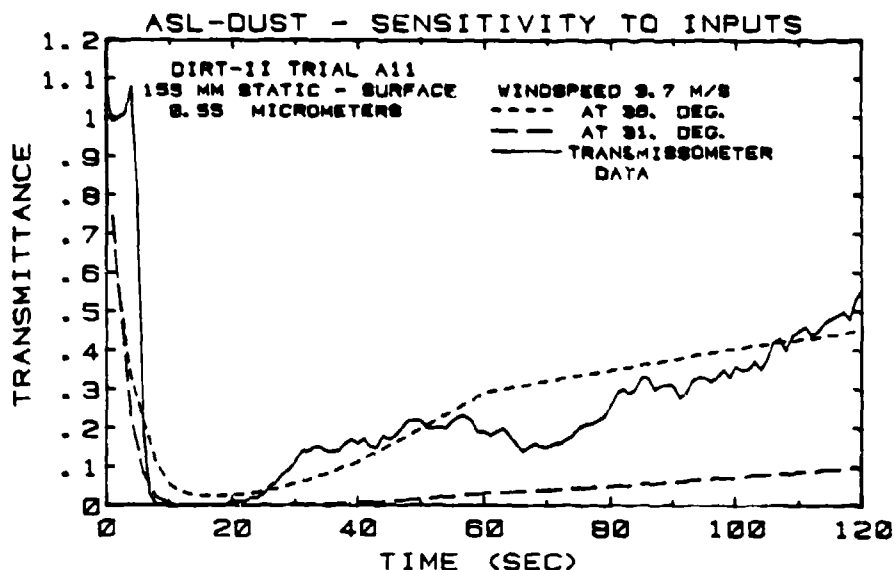


FIGURE 21. DIRT II TRIAL A11 WIND DIRECTION.  
Variation in wind direction with constant speed.

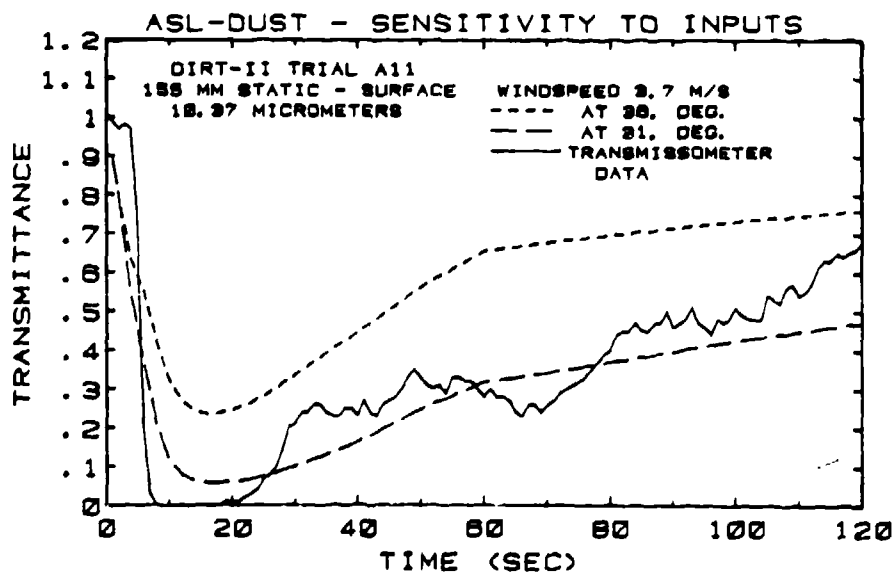


FIGURE 22. DIRT II TRIAL A11 WIND DIRECTION.  
Variation in wind direction with constant speed.

**UNCLASSIFIED**

## UNCLASSIFIED

B-7

Figures 23 through 26 show the changes in simulated transmittance for a change in soil composition, and hence particle size distribution. The best initial estimate for the soils of the DIRT-II series was a composition of 25% clay, 50% silt and 25% sand. In order to define a soil with a particle size distribution weighted toward smaller sizes, a composition of 80% clay, 12% silt and 8% sand was selected. Figures 23 through 26 show generally lower simulated transmittances for this second soil composition. This is to be expected because the smaller sizes tend to give an overall larger cross section to mass ratio. Also the ratio of visible to infrared transmittances is smaller for the second soil composition. Again this is to be expected because of the greater proportion of clay-sized particles (mean diameter 0.5um) causes relatively more extinction in the visible range. Further comments on the effect of the particle size distribution on the mass extinction coefficient are made in the next section.

The preceding examples of statically detonated 105 mm and 155 mm rounds, trials B-7 and A-11, are for periods of low to moderate windspeed and for wind directions within about  $40^{\circ}$  of the transmissometer line of sight. Two trials of live-fire 155 mm rounds are now considered for periods of somewhat higher windspeed and for a larger angle between the wind direction and the line of sight.

Both trials are for surface detonations using superquick point detonating fuzes. The impact point for trial ARTY A-3 of the DIRT-II test was 28 meters from the test area central line. The wind was 5 meters/second at  $330^{\circ}$ , about  $55^{\circ}$  from the transmissometer line of sight. Trial ARTY A-7 was for an impact only 2.3 meters from the central line at a windspeed of 4.6 meters/second, comparable to ARTY A-3, but with wind direction of  $360^{\circ}$ . This wind direction, about  $25^{\circ}$  from the transmissometer line of sight, was comparable to that of the static detonated rounds already considered. Figures 27 and 28 show the sensitivity of predicted transmission to a  $10^{\circ}$  variation in wind direction.

From these figures it is clear that the sensitivity for trial ARTY A-7 is comparable to that for the static rounds shown previously in Figures 19 through 22. This is due primarily to the comparable wind directions with respect to the line of sight. For trial ARTY A-7, however, the variation in transmission is much smaller. Thus, at wind directions approaching cross wind to the line of sight the uncertainty or fluctuation in wind direction is less critical.

It is interesting to note that the time and duration of obscuration are very similar between trials ARTY A-3 and ARTY A-7, despite the large difference in impact distance from the central line.

## UNCLASSIFIED

501

**UNCLASSIFIED**

B-7

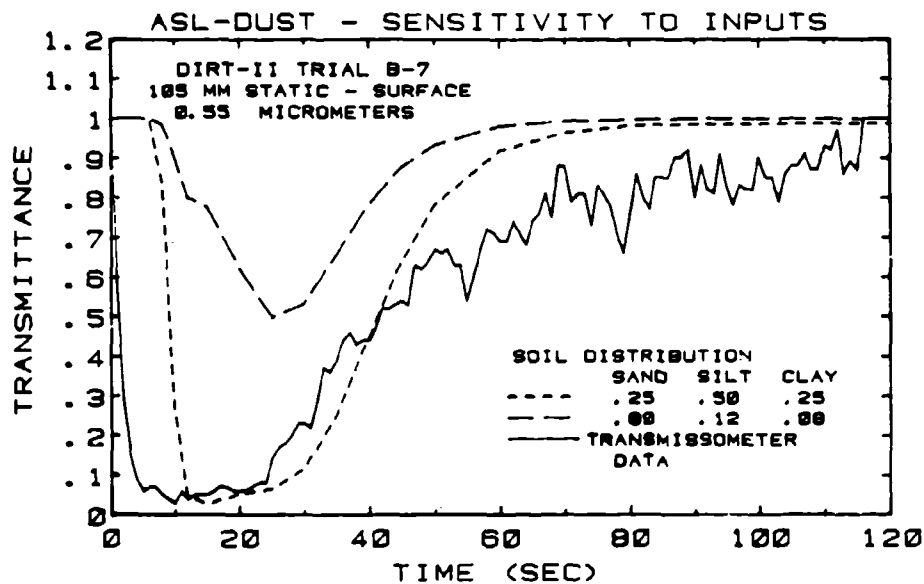


FIGURE 23. DIRT II TRIAL B-7 SOIL DISTRIBUTION  
Variation of percentage sand, silt and clay.

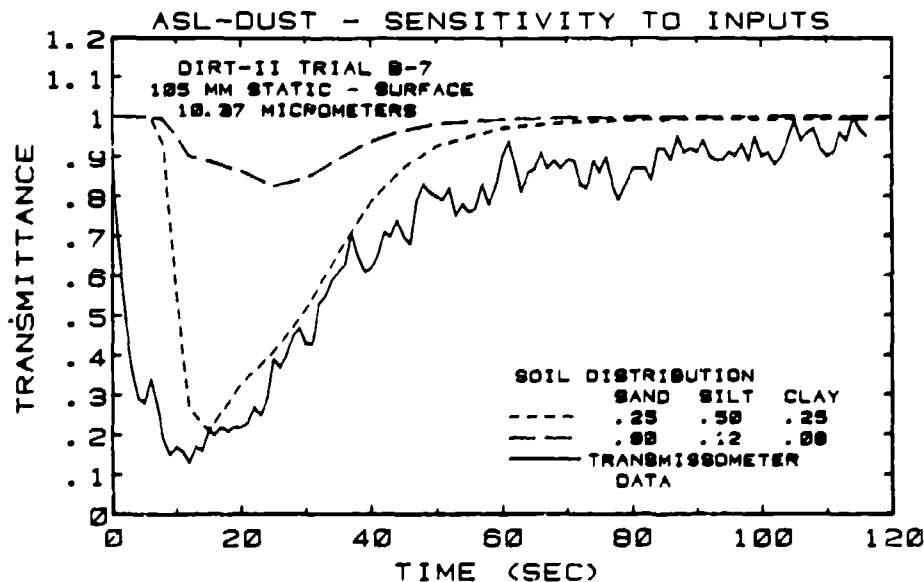


FIGURE 24. DIRT II TRIAL B-7 SOIL DISTRIBUTION  
Variation of percentage sand, silt and clay.

**UNCLASSIFIED**

**UNCLASSIFIED**

B-7

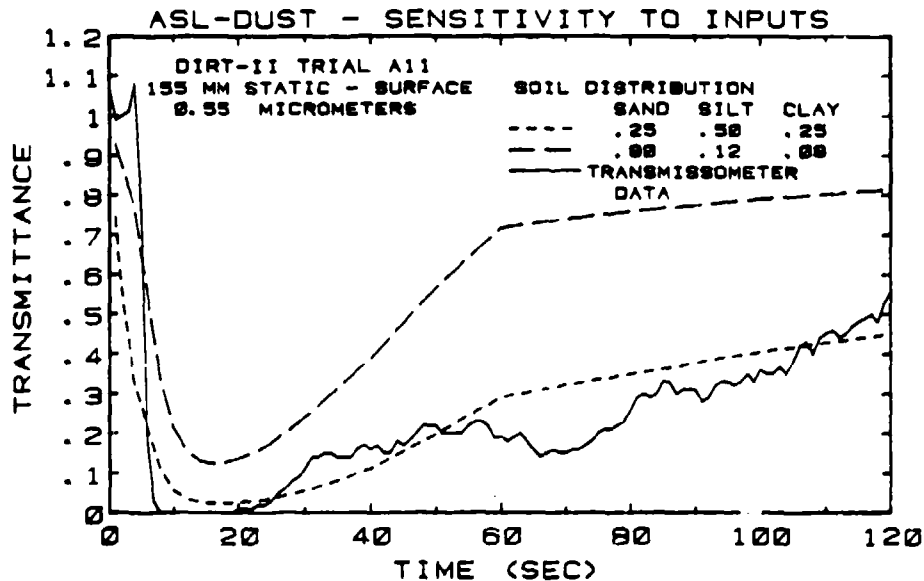


FIGURE 25. DIRT II TRIAL A11 SOIL DISTRIBUTION  
Variation of percentage sand, silt and clay.

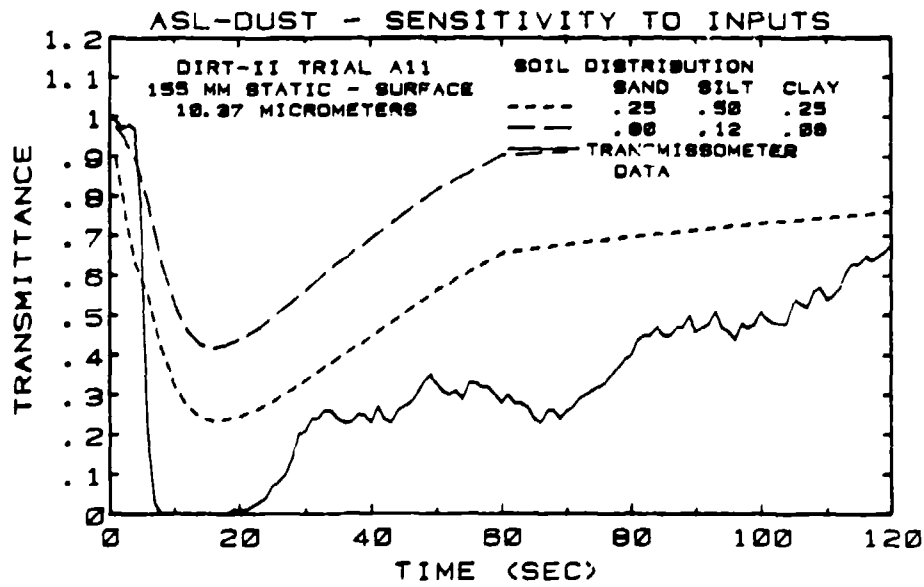


FIGURE 26. DIRT II TRIAL A11 SOIL DISTRIBUTION  
Variation of percentage sand, silt and clay.

**UNCLASSIFIED**

UNCLASSIFIED

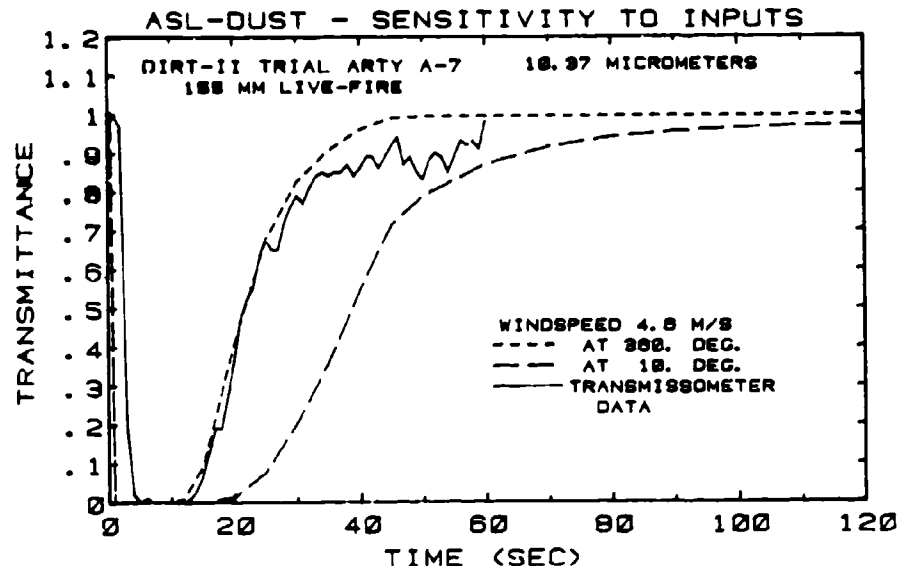


FIGURE 27. DIRT II ARTY A-7, WIND DIRECTION  
Variation in wind direction at constant windspeed

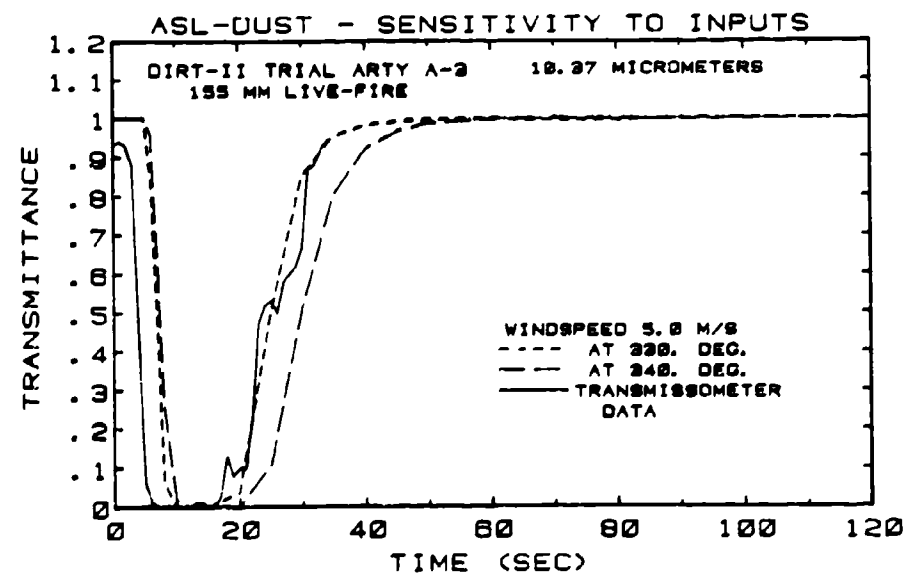


FIGURE 28. DIRT II ARTY A-3, WIND DIRECTION  
Variation in wind direction at constant windspeed

UNCLASSIFIED

## UNCLASSIFIED

B-7

This is due in part to the elevated transmissometer optical path which parallels the central line at a height of approximately 8 meters above the surface. As mentioned previously, the model predicts an initial reduction in transmittance which is too early for trial ARTY A-7 and too late for trial ARTY A-3. Detailed analysis of the model prediction of cloud positions suggests that the error in the former case may be due to a modeled initial buoyant rise which is too rapid.

Figures 29 and 30 show the change in predicted transmission for a 0.6 and 0.5 meters/second variation in windspeed. The effect is small, as expected for downwind distances of less than 30 meters. Trial ARTY A-3 does show a shift in the onset of obscuration of the magnitude expected for an increase in windspeed from 5.0 to 5.5 meters/second over a downwind distance of 28 meters.

Variation under a change in Pasquill category results in significant changes in predicted transmission, as shown in Figures 31 and 32. Stability affects the rate of diffusion of the cloud into the line of sight. This was discussed for the static detonated rounds.

Figures 33 and 34 display the predicted obscuration for the crater scaling factor determined directly from measurements of average live-fire 155 mm crater dimensions and that predicted for a very dry, sandy soil. The variation results in a factor of 6 change in the quantity of lofted soil. The lower bound represents a reasonable "a priori" choice which might be made for a desert-like soil. The measured dimensions obviously give a better agreement with the data. Thus, this example again emphasizes the sensitive dependence of the level of dust obscuration on the crater size, and its importance in the modeling effort.

### 4. TIME DEPENDENCE OF LOFTED DUST SIZE DISTRIBUTIONS AND MASS EXTINCTION

Most current dust obscuration models assume that a constant mass extinction coefficient can be applied throughout the lofted cloud. A mass extinction coefficient represents the volume extinction ( $m^{-1}$ ) per unit mass concentration ( $g/m^3$ ) within the cloud. It is an appealing scaling quantity because it separates the modeling approach into transport/diffusion prediction (which provides the mass concentration at each point along an optical path) and electromagnetic propagation calculation (which integrates the simple product of the concentration and wavelength dependent mass extinction coefficient over the line of sight to provide the optical depth). The application of a constant mass extinction coefficient throughout the cloud has generally been successful for smoke obscurants. However, it is

## UNCLASSIFIED

505

UNCLASSIFIED

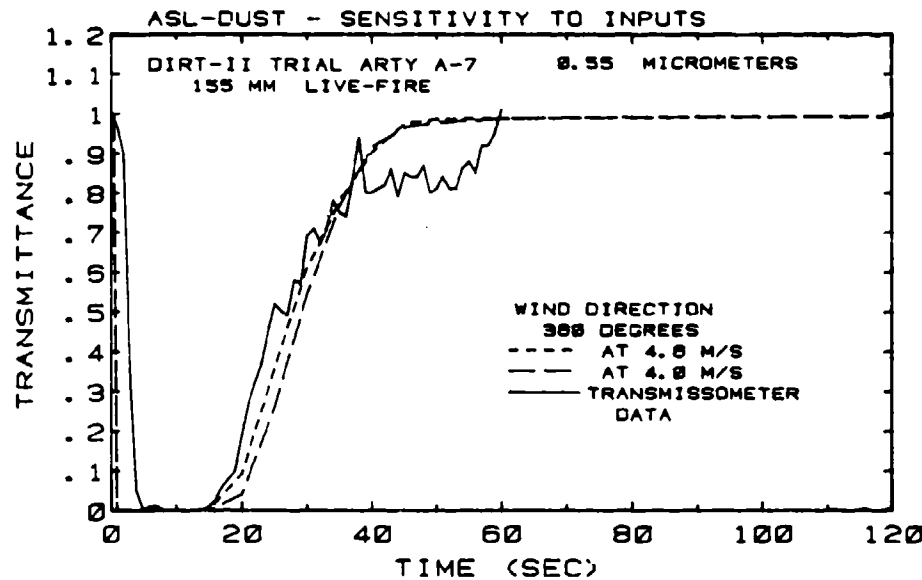


FIGURE 29. DIRT II ARTY A-7, WINDS  
Variation in windspeed with constant direction

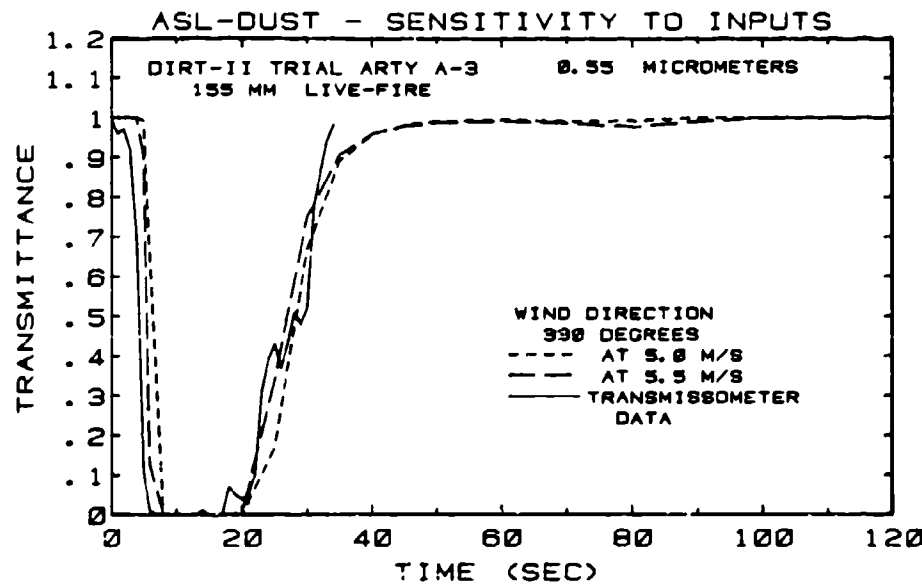


FIGURE 30. DIRT II ARTY A-3, WINDS  
Variation in windspeed with constant direction.

UNCLASSIFIED

**UNCLASSIFIED**

B-7

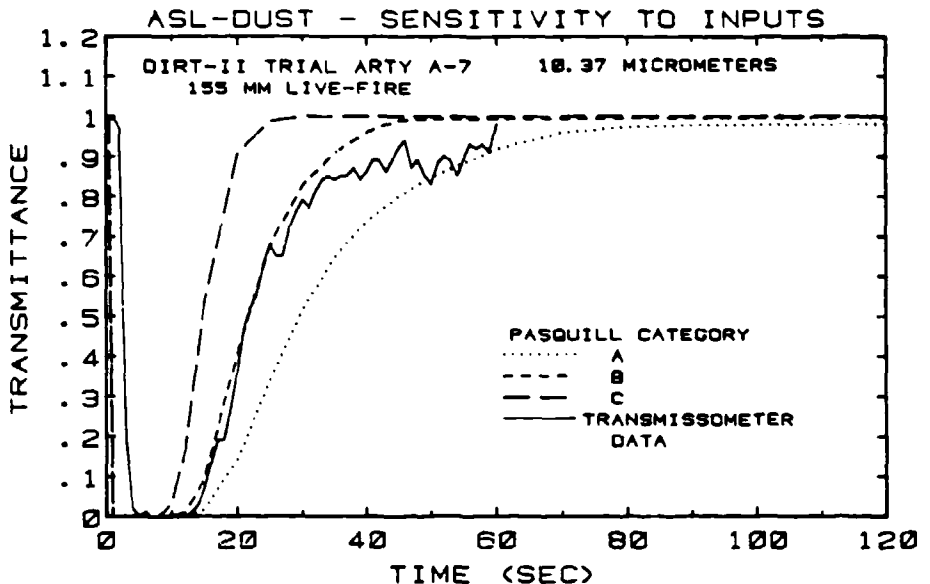


FIGURE 31. DIRT II ARTY A-7 PASQUILL CATEGORY.  
Variation over Pasquill Stability Categories.

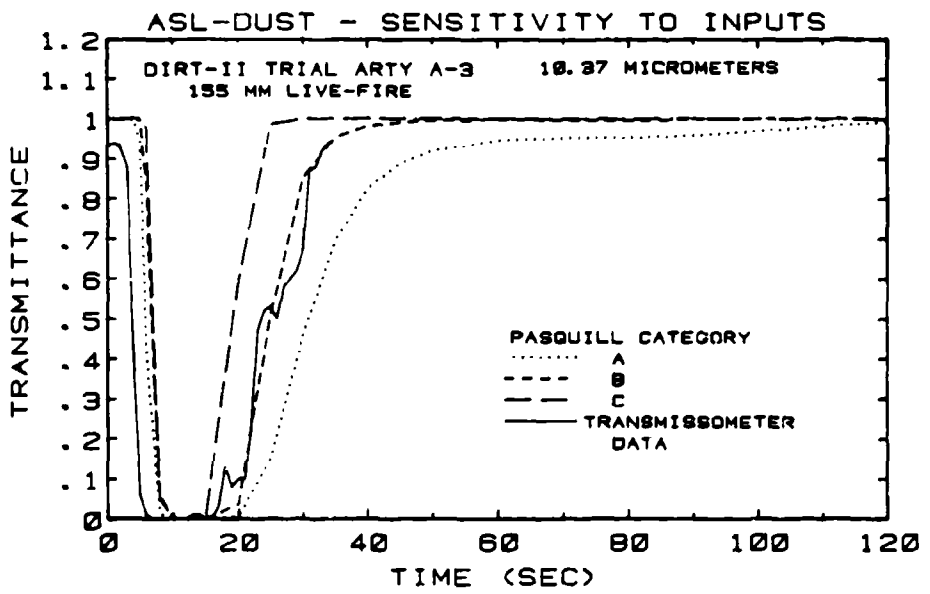


FIGURE 32. DIRT II ARTY A-3 PASQUILL CATEGORY.  
Variation over Pasquill Stability Categories.

**UNCLASSIFIED**

507

UNCLASSIFIED

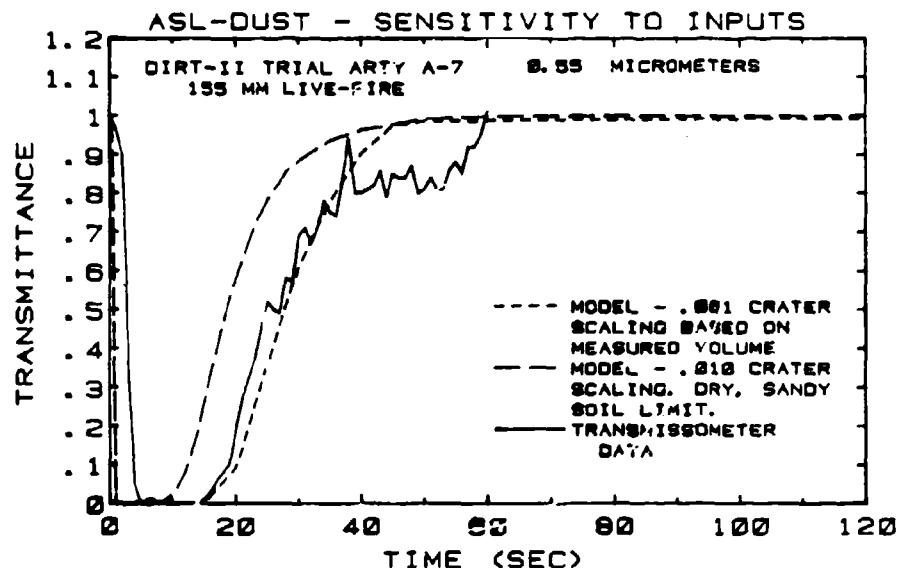


FIGURE 33. DIRT II ARTY A-7 CRATER SCALING.  
Variation in crater scaling factor.

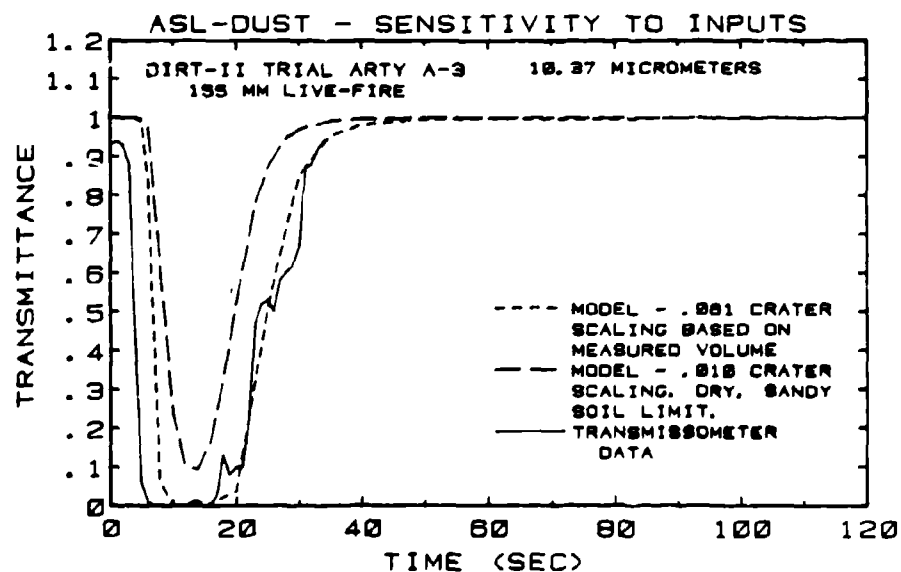


FIGURE 34. DIRT II ARTY A-3 CRATER SCALING.  
Variation in crater scaling factor.

UNCLASSIFIED

## UNCLASSIFIED

B-7

not clear that it is as applicable to dust clouds, where gravitational settling will eventually produce significant changes in the optical properties of the lofted dust. Sensitivity to gravitational settling will now be addressed.

The present model permits an extremely detailed investigation of the time dependence of size distributions and mass extinction coefficient within the lofted cloud. The initial size distribution of in-situ soil is partitioned into a series of "bins" ranging from 1 micrometer diameter particles to particles larger than 200 micrometers in diameter. For the present study 19 intervals were chosen. The theoretical extinction at each wavelength is computed from Mie theory for the particles at each interval. Transport and diffusion of each size range is treated separately, with the inclusion of an appropriate gravitational settling velocity. Thus, the model predicts the fallout of the larger particles with time and the resulting change in extinction properties for different regions within the overall cloud.

The present study assumes the in-situ soil to be that of the DIRT-II site, which is approximately 25% clay (less than  $2\mu\text{m}$ ), 50% silt ( $2$  to  $50\mu\text{m}$ ) and 25% sand (greater than  $50\mu\text{m}$ ). Internally the model assigns size distributions to each soil range. Clay is taken to be log-normal with mean diameter  $0.5\mu\text{m}$  and sigma of 2.3. Silt is taken to be log-normal with mean diameter of  $25\mu\text{m}$  and sigma of 1.4. Sand is assumed to be power law distributed over diameters from  $100$  to  $1000\mu\text{m}$  with exponent 4. These assignments are somewhat arbitrary but provide a reasonably smooth overall distribution. The motivation in model development based on these size ranges is to provide contact with simple observables.

Assigned refractive indices are given in Table III. The HE produced carbon component, nominally scaled as 0.3 pounds per pound of TNT, is assumed log-normal with mean diameter of  $0.5\mu\text{m}$  and sigma of 2. The carbon component is mixed with the dust size intervals for the purpose of diffusion computations. Table IV shows the relevant distribution and extinction parameters for the initial lofted dust cloud.

The analysis will now focus on the particular case of trial ARTY A-3. The type and depth of burst of the munition does affect the initial upward dynamic velocities of the soil, and meteorological conditions can affect the time required for the various size components to reach the ground. However, this trial is fairly representative of the magnitude of the effects which will be considered.

## UNCLASSIFIED

509

**UNCLASSIFIED**

TABLE IV. INITIAL LOFTED SIZE GROUP PARAMETERS

DIAMETER ( $\mu\text{m}$ )	MASS FRACTION	MASS EXTINCTION ( $\text{m}^2/\text{g}$ )		FALL VELOCITY (m/s)
		0.55 $\mu\text{m}$	10.4 $\mu\text{m}$	
1.0	0.00716	2.702	0.0333	.00
2.0	0.02258	0.965	0.0556	.00
3.0	0.02378	0.584	0.1243	.00
5.0	0.03498	0.422	0.295	.00
7.0	0.02098	0.328	0.344	.00
10.0	0.01642	0.271	0.225	.01
20.0	0.02996	0.216	0.125	.03
30.0	0.09829	0.192	0.0945	.07
40.0	0.14480	0.185	0.0852	.13
50.0	0.12210	0.182	0.0805	.20
60.0	0.07047	0.181	0.0790	.28
70.0	0.03139	0.180	0.0779	.38
80.0	0.01214	0.179	0.0771	.49
100.0	0.00600	0.179	0.0764	.74
120.0	0.03902	0.178	0.0757	1.02
140.0	0.03550	0.178	0.0753	1.31
160.0	0.03381	0.177	0.0750	1.61
180.0	0.03363	0.177	0.0748	1.91
200.0	0.04220	0.154	0.0654	2.20

Figure 35 shows the time dependence of the lofted mass over 120 seconds. The main cloud buoyantly lifts approximately 90% of the dust. Over 120 seconds most of the main cloud remains lofted, and little change is observed in the total airborne mass. The base cloud, however, is not buoyant. A large percentage of its mass is thus deposited on the ground over a relatively short period of time. Since the line of sight is often within a few meters of the ground on the battlefield, the base cloud is of particular importance.

Figure 36 shows the change in mass distribution with time. The initial mass median diameter is 47 $\mu\text{m}$ . After 25 seconds the mass median diameter is reduced to 35 $\mu\text{m}$  in the main cloud and to 25 $\mu\text{m}$  in the base cloud with virtually no particles larger than 140 $\mu\text{m}$  in the main cloud and none larger than 70 $\mu\text{m}$  in the base cloud. After 120 seconds the distribution has further shifted, with a 34 $\mu\text{m}$  mass median diameter in the main cloud and 7 $\mu\text{m}$  in the base cloud. All particles larger than 110 $\mu\text{m}$  in the main cloud and larger than 45 $\mu\text{m}$  in the base cloud have been deposited on the ground.

**UNCLASSIFIED**

B-7

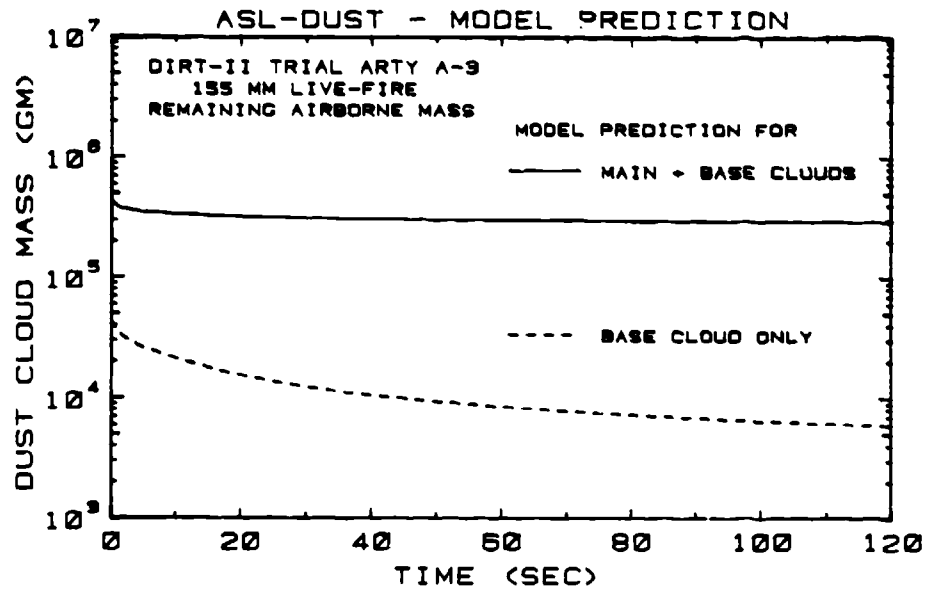


FIGURE 35. DIRT II ARTY A-3 REMAINING LOFTED DUST  
Predicted lofted mass profile for main and base clouds

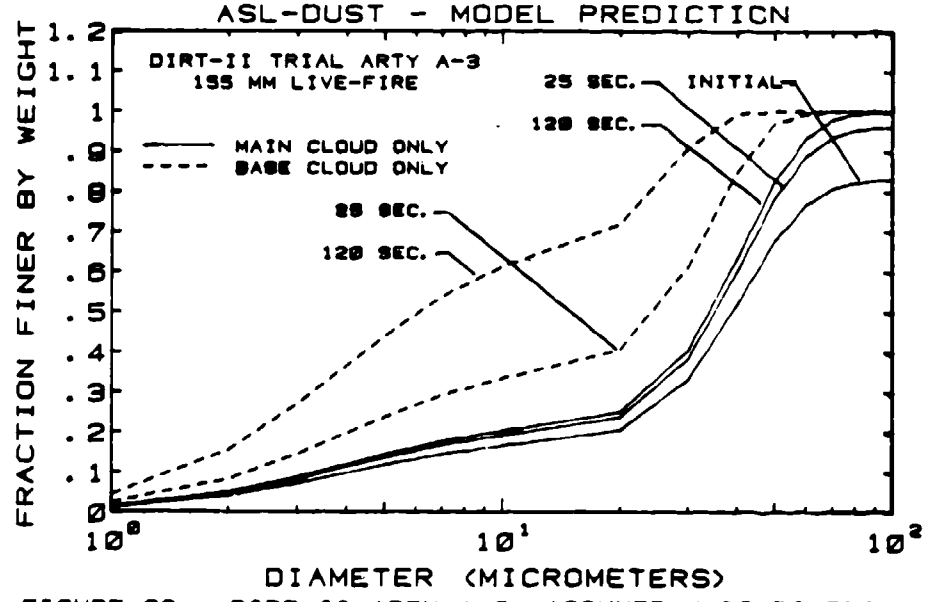


FIGURE 36. DIRT II ARTY A-3. ASSUMED MASS DISTRIBUTION  
Predicted shift in distribution due to settling.

**UNCLASSIFIED**

# UNCLASSIFIED

B-7

The extinction produced by the dust cloud is different for each wavelength and is very dependent on the size, number and refractive index of the dust particles, as can be seen in Table IV, with greatest weight from the smaller particles due to their larger numbers. Thus the loss of the larger, more massive particles has a lesser effect on the change in extinction than would the corresponding loss in mass of small particles. Figure 37 shows the predicted value of the mass extinction coefficient with time. In computing the values in Figure 37 we have purposely averaged over only the remaining lofted dust. The values thus represent the extinction coefficient which would be the measured average of a large number of samples throughout the main and base clouds. Over 120 seconds the predicted average mass extinction for all remaining lofted mass increases from  $0.26 \text{ m}^2/\text{g}$  to  $0.29 \text{ m}^2/\text{g}$  at 0.55 micrometers wavelength and from  $0.10 \text{ m}^2/\text{g}$  to  $0.11 \text{ m}^2/\text{g}$  at 10.4 micrometers wavelength. An average only over the base cloud predicts an increase to  $0.50 \text{ m}^2/\text{g}$  in the visible and  $0.16 \text{ m}^2/\text{g}$  at 10.4 micrometers wavelength.

Greatest variation in mass extinction coefficient occurs when one considers the change at a single point or along a narrow optical path. Figure 38 shows the computed mass extinction coefficient for the transmissometer line of sight during the period from 8 to 30 seconds when obscuration is appreciable. Detailed examination of the predicted positions of the size components shows that the base cloud passes almost entirely below the optical path, while the main cloud passes through and somewhat above the optical path. As a result, extinction is due primarily to the lower portion of the main cloud which is more concentrated with the larger size groups than is the upper part of the main cloud or the base cloud. The mass extinction increases from  $0.20 \text{ m}^2/\text{g}$  to  $0.27 \text{ m}^2/\text{g}$  and then returns to a value of  $0.20 \text{ m}^2/\text{g}$  in the 0.55 micrometer wavelength region. The corresponding change for 10.4 micrometers wavelength is from  $0.083 \text{ m}^2/\text{g}$  to a maximum of  $0.101 \text{ m}^2/\text{g}$  and returns again to  $0.083 \text{ m}^2/\text{g}$ .

Sensitivity of the mass extinction parameter to the evolution of the cloud and the position of the line of sight within it seems to indicate that a single, constant mass extinction parameter is insufficient to characterize an artillery produced dust cloud. An error in this quantity of  $\pm 50\%$  results in an error range in transmittance of  $T^{0.5}$  to  $T^{1.5}$ .

**UNCLASSIFIED**

B-7

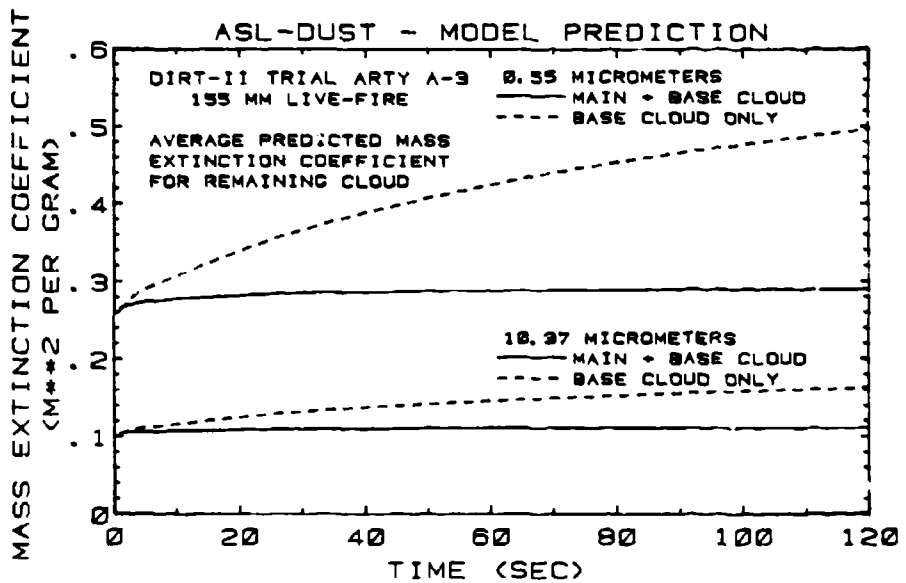


FIGURE 37. DIRT II ARTY A-3, MASS EXTINCTION  
Predicted mass extinction coefficient for lofted cloud

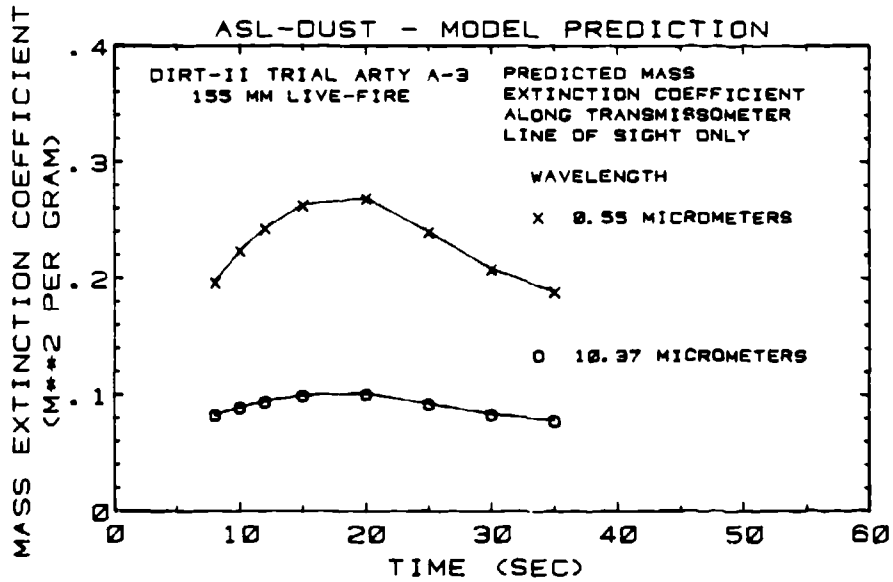


FIGURE 38. DIRT II ARTY A-3, MASS EXTINCTION  
Predicted mass extinction coefficient along line of sight

**UNCLASSIFIED**

# UNCLASSIFIED

B-7

## 5. CONCLUSIONS

The first phase of dust cloud modeling governs the cratering and initial cloud properties. The largest uncertainty lies in the correct determination of the actual amount of crater material which is lofted and remains airborne. Of secondary importance is the shape and size of the initial buoyant cloud and non-buoyant dust skirt. Using the lofted crater mass parameter,  $L_{cm}$ , as the variable, comparisons with test data showed that the larger values of  $L_{cm}$  gave the better fits. This is mainly because a cased artillery shell gives a larger crater than an equivalent bare charge for a given placement and soil type.

The second phase of dust cloud modeling deals with transport and diffusion. Four parameters were varied here. The first, the explosive energy partitioned to the initial cloud,  $E_p$ , influences the initial size of the main cloud, and hence the base cloud which is scaled to the main cloud, and the rise and expansion of the main cloud during its buoyant period. Increasing  $E_p$  tends to reduce the calculated transmittance because the larger base cloud and more rapidly expanding main cloud usually place more mass into the transmissometer line of sight. The second parameter  $P_s$ , the Pasquill category, is a quantification of atmospheric stability. Allowing the Pasquill parameter to assume higher values, i.e., to represent a more unstable or turbulent atmosphere, is similar in its effect to increasing the previous parameter  $E_p$ . Higher values of  $P_s$  tend to cause lower simulated values of transmittance because more of the cloud is able to diffuse into the line of sight.  $P_s$  is varied in discrete steps, while nature varies in a continuous manner; therefore a certain amount of care should be taken in correctly estimating a value of  $P_s$  to be used for modeling. The third parameter, the wind speed, directly affects the transport of the cloud. But its variation within a reasonable range was shown to have a small effect, particularly when the cloud's path was more or less parallel to the line of sight. The fourth parameter, the wind direction, also affects the transport of the cloud. However, small variations of the wind direction were found to produce large changes in simulated transmittance, in this case particularly when the cloud path was along the line of sight. Therefore, of the four parameters in the transport and diffusion phase of dust cloud modeling,  $E_p$  and  $P_s$  were found to have similar effects, the wind speed was found to be of minor importance, and the wind direction was of major importance.

The third phase of dust cloud modeling deals with transmission through the cloud. The important quantities here are the particle size distribution and the indices of refraction. The particle size

# UNCLASSIFIED

# UNCLASSIFIED

B-7

was chosen as the parameter to be varied. The best approach has been to divide the soil up into component parts, such as sand, silt and clay, which can be determined from soil analysis, and then assign a particle size distribution and set of refractive indices to each component. These sets of size distributions are then taken to be present in the initial cloud in the same proportion as in the soil. The variation of the soil components can then change the relative transmittances of visible and infrared wavelengths.

Gravitational settling was found to have a major influence on the mass extinction coefficient at different points within the cloud. A given mass of small dust particles was found to provide greater extinction than the same mass of large particles. Thus, as larger particles settle downward, the remaining body of the cloud has higher extinction per unit remaining lofted mass.

Thus, all three phases of modeling of dust clouds from artillery explosions are sensitive to model parameters which can not always be specified with high precision. The magnitudes of the changes in transmission produced by reasonable changes or uncertainties are comparable in several of these model parameters. Areas have been identified in which further model development is necessary. These include the early dynamic phase of cloud formation, variations in density within the cloud, and variation in meteorological parameters over the time scale considered.

## 6. REFERENCES

Curcio, J. A., K. M. Haught, and M. A. Waytko, 1980: "Transmittance Measurement at DIRT-II," Chapter 6 in Dusty Infrared Test - II (DIRT-II) Program, ASL-TR-0058, (B. W. Kennedy, Editor), Atmospheric Sciences Laboratory, White Sands Missile Range, NM.

Fernandez, G., and R. G. Pinnick, 1980: "Particle Size Measurements," Chapter 8 in Dusty Infrared Test II (DIRT-II) Program, ASL-TR-0058, (B. W. Kennedy, Editor), Atmospheric Sciences Laboratory, White Sands Missile Range, NM.

Heaps, M. G., 1980a: "Evaluation of Cratering Parameters on Transmission Through Artillery Produced Dust Clouds (U)," Proceedings of the Smoke/Obscurants Symposium IV, Volume 2, DRCM-SMK-T-001-80, CONFIDENTIAL, Harry Diamond Laboratories, Adelphi, MD.

Heaps, M. G., 1980b: "The Effect of Meteorological Parameters on Artillery Produced Dust Cloud Size, Growth, and Transport (U)," Proceedings of the Smoke/Obscurants Symposium IV, Volume 2, DRCM-SMK-T-001-80, CONFIDENTIAL, Harry Diamond Laboratories, Adelphi, MD.

# UNCLASSIFIED

515

**UNCLASSIFIED**

- Kennedy, B. W., Editor, 1980: Dusty Infrared Test - II (DIRT-II) Program, ASL-TR-0058, Atmospheric Sciences Laboratory, White Sands Missile Range, NM.
- Lindberg, J. D., Compiler, 1979: Measured Effects of Battlefield Dust and Smoke on Visible, Infrared, and Millimeter Wavelength Propagation: A Preliminary Report on Dusty Infrared Test - I (DIRT-I), ASL-TR-0021, Atmospheric Sciences Laboratory, White Sands Missile Range, NM.
- Mason, J., 1980: "Site Characterization for the MBCE/DIRT-II Battlefield Environment Tests," Chapter 9 in Dusty Infrared Test - II (DIRT-II) Program, ASL-TR-0058, (B. W. Kennedy, Editor), Atmospheric Sciences Laboratory, White Sands Missile Range, NM.
- Thompson, J. H., 1979: Models for Munitions Dust Clouds, ASL-CR-79-0005-2, Atmospheric Sciences Laboratory, White Sands Missile Range, NM.
- Thompson, J. H., 1980a: ASL-DUST: A Tactical Battlefield Dust Cloud and Propagation Code, Volume 1 - Model Formulations, ASL-CR-80-0143-1, Atmospheric Sciences Laboratory, White Sands Missile Range, NM.
- Thompson, J. H., 1980b: ASL-DUST: A Tactical Battlefield Dust Cloud and Propagation Code, Volume 2 - User's Manual, ASL-CR-80-0143-2, Atmospheric Sciences Laboratory, White Sands Missile Range, NM.

**UNCLASSIFIED**

# UNCLASSIFIED

B-8

## PARAMETERIZATION OF THE DISPERSION OF BATTLEFIELD OBSCURANTS

By

W. D. OHMSTEDE & E. B. STENMARK  
Battlefield Environment Division  
US Army Atmospheric Sciences Laboratory  
White Sands Missile Range, New Mexico

### ABSTRACT

Problems of short-term dispersion of battlefield smoke and dust are particularly sensitive to source properties and boundary layer structure. These complexities render questionable the utility of the usual Gaussian plume model; however, a stochastic modeling approach has been found useful in this regard. The aerosol dispersion is simulated by a finite number of pseudo particles whose motion is statistically consistent (within the limits of current knowledge) with the elementary Lagrangian properties of the lower boundary layer.

A scheme has been devised for systematic parameterization of a discrete set of model solutions. The boundary layer structure is functionally characterized in terms of two parameters; namely, stability and wind speed categories. Given the source properties, stochastic model solutions are then determined corresponding with these discretized parameters. Finally, a mathematical process is used to create a single multivariate model from the discrete set of model solutions, resulting in a fast and compact "model of a model." The computational speed and simplicity of this model renders it ideal for combat simulation problems where very large numbers of line-of-sight-obscuration calculations are required.

### 1. INTRODUCTION

Battlefield obscurants, in particular smoke munitions, can impact heavily on the effectiveness of extant and proposed weapon systems. Since models are a viable tool in system evaluations and war gaming, there is a need to develop simple but realistic battlefield diffusion models to relate propagation conditions to meteorology.

The obscuration effectiveness of smoke munitions depends in part on their design and composition. Although many of the older munitions are highly exothermic, newer designs produce aerosols with little buoyancy and thus they act as ground level sources. Non-buoyant smokes are more effective in reducing ground level intervisibility. A dispersed munition (area or multi-point source) is also more effective as a consequence of spatial diversity. Aside from these controllable design features, the smoke efficacy is also profoundly affected by atmospheric conditions. The wind direction alone is often the deciding factor between obscuration or not; and the wind speed and turbulence contribute to the smoke transport and vertical cloud growth. In most instances, the obscuration due to a single smoke munition is short-lived due to relatively rapid atmospheric dispersion.

The objective of this report is to describe the development of a simple model that provides a systematic parameterization of short-term dispersion from ground level sources with particular application to smoke munitions.

# UNCLASSIFIED

**UNCLASSIFIED**

## 2. DISPERSION MODELING

Gifford<sup>1</sup> has noted that there are three approaches from which useful working models of atmospheric diffusion can be derived by analytical techniques. These are statistical theory, gradient-transfer or K-theory, and similarity theory. Of these, the first has seen the most use because of ease of application. This approach, as manifest in the ORG-17 report by Milley,<sup>2</sup> has in the past dominated the characterization of smoke and chemical munition behavior. However, the conventional statistical theory has shortcomings when applied to the battlefield obscuration problem. Because of the brevity of smoke obscuration, it is essential that correct modeling of the source function in space and time be assured in order to obtain accurate modeling of the smoke distribution. The commonly used assumption that the pollutant soon "forgets" the detailed source properties is not a valid justification for the gross simplification of the source function as is manifest in most statistical theory models.

The problem of ground level sources has long been the nemesis of the conventional statistical theory approach. Ambiguities arise since the plume/puff obviously cannot be transported downwind by the speed at the source since the wind vanishes at ground level. This may not be significant for intermediate and long range diffusion problems but is serious for short-term dispersion. Indeed, the extreme inhomogeneity of the wind and turbulence (particularly scale properties), as manifest in the surface boundary layer, calls into question the very basis for the conventional statistical theory approach. Neither the gradient-transfer nor similarity theory approaches appear as viable options for modeling battlefield obscuration because the former is inapplicable to short-term diffusion, and the latter lacks generality.

Seeking an alternative, the authors,<sup>3</sup> following the lead of Hanna<sup>4</sup> and others, applied a relatively simple pseudoparticle model to the problem of simulating battlefield dispersion of smoke. The success of that effort encouraged the authors to further apply the approach to the development of the simple smoke obscuration model described here. The solution simulates the actual dispersion by tracing the life histories of a finite number of pseudoparticles which act as surrogates for small parcels of the real aerosol. The trajectory of a particle can be determined by Lagrangian time integration of its velocity. The velocity of the pseudoparticle is the sum of the mean velocity, at the position of the

**UNCLASSIFIED**

**UNCLASSIFIED**

particle, and a turbulent velocity fluctuation.

$$U_i(t) = \bar{U} [z_i(t)] + U'_i(t), \quad (1)$$

where  $U_i$  is the  $x$ -component velocity of the  $i$ -th pseudoparticle,  $\bar{U}$  is the mean velocity. The fluctuation is itself a sum of an inertial velocity which remembers its past history and a stochastic velocity which is completely random. For model implementation with finite time step  $dt$ , the memory is expressed in the next equation by an exponential Lagrangian correlation function  $R_L$  with Lagrangian time scale  $T_L$ .

$$U'_i(t) = U'_i(t-dt) \cdot R_{Lx}(dt/T_{Lx}) + U''_i(t) \quad (2)$$

The random fluctuation  $U''$  has a guassian distribution with variance

$$\overline{(U'')^2} = \overline{(U')^2} \cdot [1 - R_{Lx}^2(dt/T_{Lx})], \quad (3)$$

where the fluctuation variance on the right is the prescribed local Eulerian value. The trajectories of the pseudoparticles for a prescribed wind and turbulence structure can be evaluated by the following equation

$$x_i(t) = x_i(t-dt) + \frac{1}{2} dt \cdot [U_i(t) + U_i(t-dt)] \quad (4)$$

when the initial time, position, and velocity are specified. The initial conditions are derived from the smoke munition source properties except that the initial particle velocity is taken to be a random variable, related to the turbulence structure, added to any systematic source emission velocity. Complex source properties are not difficult to handle with this approach.

The concentration field of the real aerosol can be estimated by evaluating the local pseudoparticle statistics in small but finite space/time boxes in the region of interest. Generally, a very large number of pseudoparticles is required for the simulation to obtain a reasonably smooth concentration field. Herein lies the major shortcoming of this model approach. Even though the model algorithm is simple to implement, huge amounts of computer core or mass storage are required to save all the results. In some instances the CPU time may also be excessive. Consequently, this approach is not suitable for general modeling use. However, if one is willing to settle for a reasonable set of solutions for various "type" situations, the model can be executed and the results analyzed definitively.

**UNCLASSIFIED**

## UNCLASSIFIED

It is sufficient for the purposes of weapon system evaluation that the smoke obscuration be determined for selected smoke munitions and typical atmospheric conditions which might be encountered on the battlefield. Since the munition properties are already discretely designed, our objective can be achieved if a systematic categorical parameterization of the wind and turbulence structure is specified.

## 3. BOUNDARY LAYER PARAMETERIZATION

No completely satisfactory means for parameterizing the boundary layer structure exists. The popular "similarity theory" is not suitable because it is only applicable to the relatively shallow surface boundary layer and is unnecessarily complicated for the purpose at hand. A more general characterization might be developed with second-order closure methods, but the results would likely be even more unwieldy. An acceptable alternative to the various theoretical formulations would be a straightforward empirical approach.

Dumbauld and Bjorklund<sup>5</sup> have published a scheme for boundary layer parameterization which has been found quite useful for diffusion applications. This method uses two parameters, the net radiation index (NRI), as proposed by Turner,<sup>6</sup> and the wind categorized in five classes from less than 1 meter per second to greater than 7 meters per second. This two-parameter categorical scheme has 35 ( $5 \times 7$ ) possible boundary layer states. In all cases, the wind speed ( $\bar{u}$ ) and turbulence ( $\sigma_A$ ,  $\sigma_E$ ) are represented as having power-law exponents, and 5-meter turbulence values have been assigned to each state by Dumbauld and Bjorklund as shown in Tables 1 and 2. This scheme quite likely lacks

TABLE 1

WIND POWER-LAW EXPONENT  $\beta$  FOR TRANSPORT/DIFFUSION MODELS

Mean Layer Wind Speed $\bar{u}$ (m/sec)	Net Radiation Index						
	4	3	2	1	0	-1	-2
$\bar{u} < 1$	.2	.2	.20	.20	.20	.20	.3
$1 \leq \bar{u} < 3$	.2	.17	.20	.20	.20	.20	.25
$3 \leq \bar{u} < 5$	.15	.15	.17	.17	.20	.20	.20
$5 \leq \bar{u} < 7$	.10	.10	.15	.15	.15	.15	.15
$\bar{u} \geq 7$	.05	.10	.10	.10	.15	.15	.15

TABLE 2

TURBULENCE PARM.,  
TRANSPORT'D(a) Ten-Minute Standard Deviations of  $(\sigma_A)$  and Corresponding Values of the N RI Angle in DegreesExponent  $m$ 

Wind Speed at 5 Meters (m/sec)	Net Radiation Index							
	$\sigma_A$ m	$\sigma_A$ m	$\sigma_A$ m	$\sigma_A$ m	$\sigma_A$ m	$\sigma_A$ m	$\sigma_A$ m	
$\bar{u} < 1$	26	-1.09	26	-1.09	21	-1.33	15	-1.12
$1 \leq \bar{u} < 3$	26	-1.09	22	-1.26	16	-1.23	11	-1.12
$3 \leq \bar{u} < 5$	19	-1.22	16	-1.23	13	-1.03	9	-1.20
$5 \leq \bar{u} < 7$	14	-1.05	11	-1.17	11	-1.17	8	-1.45
$\bar{u} \geq 7$	9	-1.06	9	-1.37	8	-1.10	8	-1.45

(b) Standard Deviation of the Wind Elevation Angle in Degrees ( $\sigma_E$ ) and Corresponding Values of the Power-Law Exponent  $n$ 

Wind Speed at 5 Meters (m/sec)	Net Radiation Index							
	$\sigma_E$ n	$\sigma_E$ n	$\sigma_E$ n	$\sigma_E$ n	$\sigma_E$ n	$\sigma_E$ n	$\sigma_E$ n	
$\bar{u} < 1$	4.7	.10	4.7	.10	7.0	.07	5.0	0
$1 \leq \bar{u} < 3$	4.7	.10	4.4	.13	5.3	.07	3.7	0
$3 \leq \bar{u} < 5$	6.3	.15	5.3	.15	4.3	.13	3.0	0
$5 \leq \bar{u} < 7$	4.7	.20	3.7	.20	3.7	.15	2.7	0
$\bar{u} \geq 7$	3.0	.25	3.0	.20	2.7	.20	2.7	0

## UNCLASSIFIED

**UNCLASSIFIED**

generality and is probably biased towards the conditions one would encounter in a dry continental situation (western U.S. deserts). Its applicability to a moist maritime regime (e.g., Western Europe) may be in question. In particular, Klug<sup>7</sup> has expressed doubts about the utility of the NRI for European applications. Even so, the Dumbauld-Bjorklund scheme surely spans most of the typical and some of the extreme conditions which might be encountered by a weapon system on the battlefield.

For the problem at hand, it is necessary to parameterize the vertical distribution of the wind speed ( $\bar{u}$ ), the standard deviations of the longitudinal, lateral, and vertical turbulence fluctuations ( $\sigma_u$ ,  $\sigma_v$ ,  $\sigma_w$ ) and the corresponding Lagrangian time scales. As far as it goes, the Dumbauld-Bjorklund scheme has been adapted to this end. The longitudinal turbulence is evaluated by assuming that  $\sigma_u/\sigma_v = 2.5/2.3$ . The most difficult problem is to parameterize the Lagrangian time scales. This is little wonder since these are largely unmeasurable quantities in the boundary layer near ground level where the turbulence structure is especially inhomogeneous. Any parameterization of Lagrangian time scales is highly speculative. Generally, the assumption is made that the Lagrangian time scales are proportional to ratios of Eulerian length scales divided by the standard deviations of the respective velocity fluctuations. The Eulerian length and Lagrangian time scales for the vertical motion are restricted by the proximity to the ground. The Eulerian length scale tends to increase linearly with height, although this is modulated by the effects of stability. Hansen<sup>8</sup> has proposed relationships for the Lagrangian time scales which are based on similarity theory. Maintaining the spirit of the Hansen approach but the thrust of the Dumbauld-Bjorklund scheme, the Lagrangian time scales for the problem at hand are modeled by categorical two-parameter, power-law relationships.

#### 4. SOLUTIONS OF PSEUDOPARTICLE DISPERSION

At this point, let us consider a few examples. Figure 1 shows the simulated burn rate for a 155 MM M2 canister of HC smoke.<sup>9</sup> This is essentially a non-buoyant point source at ground level - a relatively simple munition. The smoke is emitted over a 76 second period.

Figure 2 illustrates, in the downwind-vertical plane, the smoke cloud from the canister at 50 and 200 seconds after the start of the burn. There is a 2 to 1 vertical exaggeration. The atmospheric conditions are NRI equal 0 and wind speed of 2M/sec. Only 800 particles have been used but that is enough to illustrate the general appearance of the cloud. It should be noted that the cloud has a distinct slope due to the wind shear. Particles near the ground tend to drag behind while particles higher up are running away.

**UNCLASSIFIED**

UNCLASSIFIED

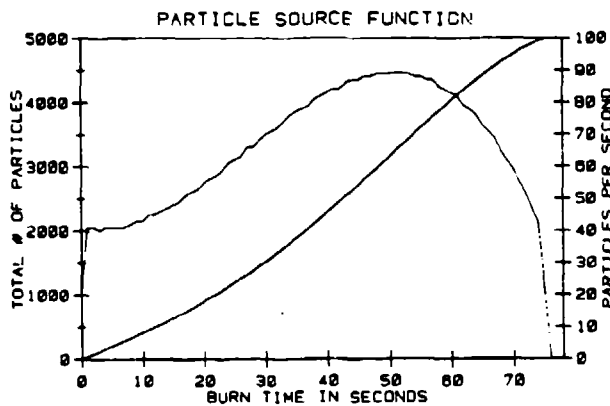


Figure 1. Particle Source Function for 155 MM M2 Canister. Release Rate (thin line), Accumulative number (thick line).

Figure 3 represents the same situation except for a NRI of 4. Naturally there is more vertical growth of the cloud due to the instability. As shown in these illustrations, the pseudoparticle dispersion model is a viable approach for realistic simulation of battlefield smoke obscuration. The representation of complex source properties such as the XM825 should be elementary, and the model readily copes with heterogeneous boundary layer structures. The boundary layer parameterization, combined with the dispersion model, provides the means for the categorical representation of a wide range of obscuration effects from various smoke munitions. Solutions have been calculated for several selected smoke munitions. The vast amounts of resultant pseudoparticle space/time position data have been further analyzed and reduced to estimates of the smoke concentration at the centers of gravity of a relatively large number of discrete space/time boxes in the region of interest. Even at this stage, a very large amount of highly specific data exists which must be further generalized to achieve the objective. This generalization is done by creating a model of the model.

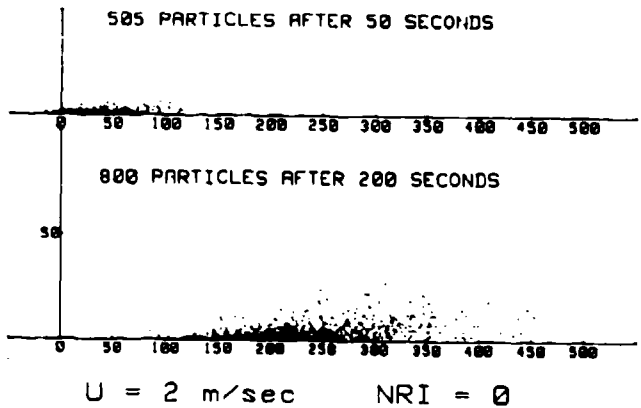


Figure 2. Downwind-vertical plane projection of pseudoparticle positions at 50 and 200 seconds following initiation of particle release. Two times vertical exaggeration. 0 Net Radiation Index (Neutral), 2m/sec. wind at 5m.

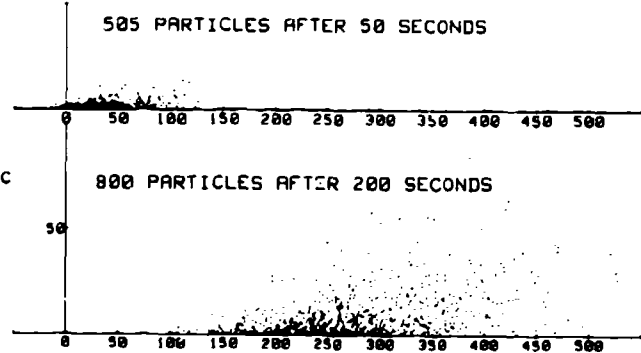


Figure 3. Same as Figure 2 except 4 Net Radiation Index (unstable).

UNCLASSIFIED

**UNCLASSIFIED**

## 5. MODEL OF A MODEL

Goldstein and Dushane<sup>10</sup> have described the concept of a mathematical process that they call reprogramming and which can be applied to the simplification of quite complex computer models. Briefly, the concept involves the representation of one dependent variable, which is a single-valued function of a number of independent variables, by a piecewise continuous hypersurface which is constructed from the intersection of hyperplanes. The proposition is that the complex functions can be locally approximated by simple linear functions, provided there are enough of the latter. The process involves the analysis of a finite number of discrete data points for the selection of the hyperplane coefficients so as to minimize the squared-error of fit to the values of the dependent variable.

For our problem, the smoke concentration is a function of the space/time variables, wind speed, NRI, and munition type. The latter two are strictly categorical variables and therefore are not used as continuous independent variables. The wind speed is a hybrid variable; we have chosen to model it as continuous to obtain a more general model. For each combination of munition type and NRI, the gross properties of the cloud are calculated as functions of time and wind speed. Two examples are illustrated in Figure 4. We presume a sloping axis to the cloud. In the Figure, XBAR and shift are the downwind position of the intersection of the axis with the ground, and the shift of that axis with height, respectively. Sigma X and sigma Z are the square roots of the X and Z second-moments, respectively. Sigma X is determined relative to the sloping axis and sigma Z relative to the ground. These properties behave peculiarly during the munition burn, but settle down soon after. The next step is to normalize the particle position data relative to the gross cloud properties. The particle concentrations in an array of normalized bins are calculated. These concentrations are further normalized by means of a simple

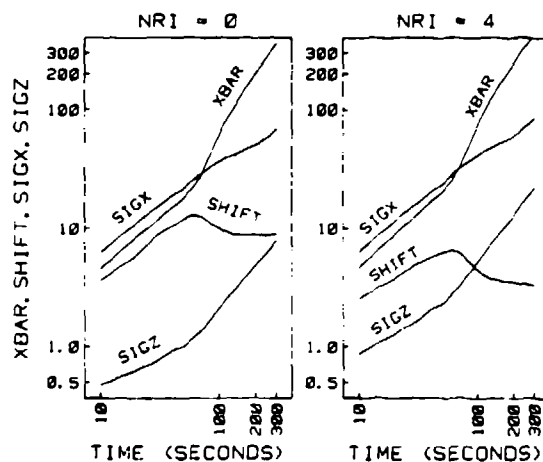


Figure 4. Gross statistical properties of the particle cloud as a function of time for the cases illustrated in figures 2 and 3.

XBAR: Downwind distance from source of the cloud axis intersection with the ground.

SHIFT: Shift of cloud axis with height (inverse of axis slope).

SIGX: Square root of along-wind, second moment relative to cloud axis.

SIGZ: Square root of vertical second moment relative to ground.

**UNCLASSIFIED**

**UNCLASSIFIED**

bivariate quadratic rational function. From these data, a set of hyperplane coefficients is generated to represent the normalized concentration as a function of time, normalized position and wind speed at five meters. This process of repro-modeling provides us with a single multivariate model from the discrete set of model solutions, resulting in a fast and compact "model of a model."

Figure 5 gives a rough idea of what is being done with the repro-modeling. Illustrated is one munition, NRI, wind speed, and time. The lines are the repro-model representation of the contours of the cross wind integrated concentration for the smoke cloud. This can be almost as easily translated into transmission through the cloud at a given wave length; thus, relating propagation conditions to meteorology.

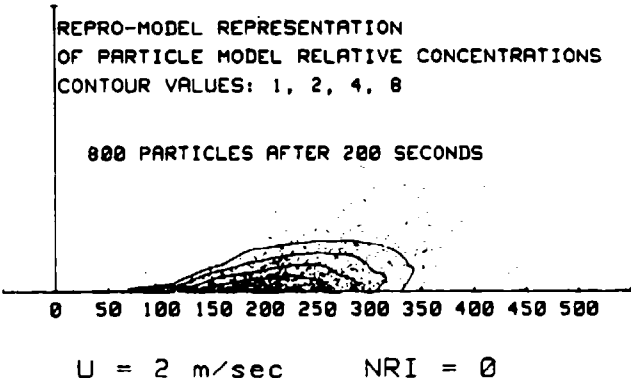


Figure 5. Relative concentration contours for repro-model solution corresponding with figure 2. Four times vertical exaggeration.

## 6. CONCLUSION

The stochastic pseudoparticle approach is a very powerful method for simulating the dispersion of atmospheric aerosols. It is intellectually honest; one pretty much knows where he stands with this model approach. It offers the opportunity to relate the dispersion to measurable atmospheric variables which furthermore can be modeled or parameterized.

The idea of modeling a model is intriguing. There are numerous models which are basically sound but too complicated for operational use. But, if some compromise can be made in regard to generality, repro-modeling provides a method for translating a finite number of model solutions for various categories of conditions into a usable operational model. Of course, there will be errors in the repro-model fit, but with sufficient care and effort, these ought to be reducible to acceptable limits in the light of other uncertainties associated with the problem.

**UNCLASSIFIED**

**UNCLASSIFIED**

The repro-modeling of the stochastic model solutions leads to a very elementary but realistic model for the parameterization of battlefield obscurants. The computational speed and simplicity of this model renders it ideal for combat simulation problems where very large numbers of line-of-sight-obscuration calculations are required.

## 7. REFERENCES

1. Gifford, F. A., January 1981, "Horizontal Diffusion in the Atmosphere: A Lagrangian-Dynamical Theory", LA-8667-MS, Los Alamos Scientific Laboratory, Los Alamos, NM.
2. Milley, G. H., May 1958, "Atmospheric Diffusion and Munition Expenditures", ORG Study Nr. 17, Army Chemical Center, MD (319109).
3. Ohmstede, W. D., and E. B. Stenmark, 1980, "A Model for Characterizing Transport and Diffusion of Air Pollution in the Battlefield Environment," conference papers: "Second Joint Conference on Applications of Air Pollution Meteorology," American Meteorological Society.
4. Hanna, S. R., 1978, "A Statistical Diffusion Model for Use with Variable Wind Fields," Proceedings of American Meteorological Society, Fourth Symposium on Turbulence, Diffusion, and Air Pollution.
5. Dumbauld, R. K., and J. R. Bjorklund, 1977, "Mixing-layer Analysis Routine and Transport/Diffusion Routine for EPAMS, Technical Report ECOM-77-2, US Army Atmospheric Sciences Laboratory, White Sands Missile Range, NM.
6. Turner, D. B., 1964, J Appl Meteorol, 3:83-91.
7. Klug, W., 1969, Staub-Reinhaltung der Luft, 29, 142-147.
8. Hansen, F. V., September 1979, "Engineering Estimates for the Calculation of Atmospheric Dispersion Coefficients, ASL Internal Report, US Army Atmospheric Sciences Laboratory, White Sands Missile Range, NM.
9. "Basic Smoke Characterization Test," March 1978, US Army Dugway Proving Ground, Dugway, UT.
10. Goldstein, G. B., and T. Dushane, 1976, "Repro-modeling Applied to the Simplification of TARCOM Computer Models," Technical Report No. 12242, TSC-PD-A156-1, US Army Tank-Automotive Research and Development Command, Warren, MI.

**UNCLASSIFIED**

# UNCLASSIFIED

B-9

## ERROR BOUNDS FOR SMOKE OBSCURATION MODELS (U)

Marvin D. Smith, James R. Rowland and D. Mark Anderson  
Division of Engineering, Technology and Architecture  
Oklahoma State University  
Stillwater, OK 74078

### ABSTRACT (U)

(U) A Stochastic Utilization and Performance Extension Routine (SUPER) has been developed as a general model for providing error bounds for smoke obscuration models. This error model has been applied to the Smoke Effectiveness Manual Model (SEMM) to determine error bounds on concentration-length (CL) due to random variations in wind speed. This combined error/smoke obscuration model, referred to as the SUPER/SEMM model, uses Monte Carlo simulation techniques to help identify the probability density of CL for selected ranges of wind speed variations. Confidence intervals are determined from these Monte Carlo runs to provide the desired error bounds. Using a given anti-tank guided missile (ATGM) threshold, a probability of obscuration curve is determined as a function of observation time.

(U) Comparisons are made between existing smoke data and the SUPER/SEMM model to determine whether these error bounds contain the expected percentage (95%) of the observed smoke data. Implications with regard to model evaluations are discussed.

### 1. INTRODUCTION (U)

(U) Virtually all smoke obscuration models developed to date produce nominal, or average, outputs when given nominal inputs [1-4]. These deterministic models require as inputs such information as average wind speed, average temperatures and average humidity readings. Clearly, random variations occurring in these inputs affect corresponding values of output variables. Yet deterministic models ignore random influences and provide only average output responses. Differences between deterministic model outputs and field test data are difficult to assess because the extent of expected random fluctuations about the deterministic model output responses is not known.

(U) A more suitable methodology is to form a stochastic model which allows random variations but is based on a deterministic model structure. Using the same structure for stochastic models as for the deterministic models insures that first principles have been primary in their construction. However, the incorporation of random variations in the stochastic model permits a more realistic comparison with field test data. Additional inputs required for the stochastic model are variances and correlations of all random inputs. These random inputs propagate through the stochastic model to yield corresponding random variations in the output. Therefore, error bounds can be formed for these expected output random variations.

(U) This paper describes a Stochastic Utilization and Performance Extension Routine (SUPER) which provides error bounds for smoke obscuration models. While generally applicable to a broad class of smoke obscuration models, SUPER is applied exclusively in this paper to the Smoke Effectiveness Manual Model (SEMM). Error bounds corresponding to 95% confidence intervals are calculated for concentration-length (CL). These error bounds are then transformed to yield a curve of probability of obscuration

# UNCLASSIFIED

527

## UNCLASSIFIED

versus observation time. This curve provides a range of obscuration probabilities rather than only the average time obscured as obtained from the deterministic model (SEMM).

## 2. THE SUPER MODEL (U)

(U) The Stochastic Utilization and Performance Extension Routine (SUPER) developed here can be applied to a general deterministic model to yield expected error bounds on its output variables. Figure 1 shows the structure of the Monte Carlo version of the SUPER model in a wrap-around fashion incorporating SEMM. This application to SEMM, referred to as SUPER/SEMM, is typical of the range of applications for which the SUPER model concept can be used. In each of these applications, the existing deterministic model forms the core of the combined stochastic model.

(U) SUPER/SEMM requires sample time functions of random inputs such as wind speed. In addition to mean values, variances and correlations of these random inputs are required. Uniformly-distributed pseudorandom numbers can be easily generated on the digital computer and then transformed to Gaussianly-distributed pseudorandom numbers with zero mean and unity variance. Inserting the desired mean and variance and holding these generated values constant over small time intervals yields a discrete-time approximation to a Gaussian white noise process. A shaping filter can be used to achieve the desired correlation property. For example, correlated wind speed sample functions can be obtained from

$$\begin{aligned}\dot{x}_1 &= x_2 \\ \dot{x}_2 &= -(\alpha^2 + \beta^2)x_1 - 2\alpha x_2 + 2\alpha w_c(t) \\ u(t) &= \alpha x_1 + x_2\end{aligned}\quad (1)$$

where  $\alpha = 0.0063$  and  $\beta = \pi/110$  in consistent units. In (1),  $w_c(t)$  is the Gaussian white noise process,  $x_1$  and  $x_2$  are internal state variables, and  $u(t)$  is the correlated random input (wind speed). The use of these wind speed sample functions is shown in Figure 1.

## 3. THE SEMM MODEL (U)

(U) While the SUPER model is applicable to a broad class of smoke obscuration models, its specific application to SEMM in the remainder of this paper makes it important to consider the inputs and outputs of SEMM more carefully. Examining these SEMM inputs and outputs provides the necessary interface between the deterministic model and the wrap-around SUPER model, as shown in Figure 1.

(U) The key equation in SEMM for CL is

$$\begin{aligned}CL = \sum_{I=1}^{NBURST} \frac{Q_{AI}}{\pi \sigma_x(I) \sigma_y(I) \sigma_z(I)} * A^{1/2} * \exp \left\{ -\frac{1}{2} \left[ \left( \frac{x+S*DX-x_{cent}}{\sigma_x(I)} \right)^2 \right. \right. \\ \left. \left. + \left( \frac{y+S*DY-y_{cent}}{\sigma_y(I)} \right)^2 + \left( \frac{z+S*DZ-z_B}{\sigma_z(I)} \right)^2 \right] \right\} \quad (2)\end{aligned}$$

**UNCLASSIFIED**

B-9

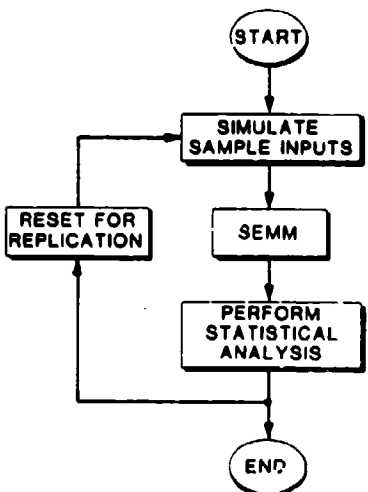


FIGURE 1. SUPER/SEMM: MONTE CARLO VERSION (U)  
(Unclassified)

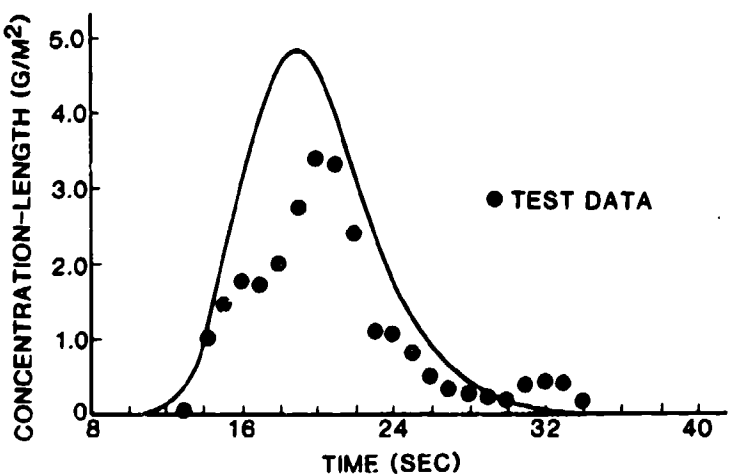


FIGURE 2. SEMM RESULTS FOR SMOKE PHASE IIA TRIAL 5 (U)  
(Unclassified)

**UNCLASSIFIED**

**UNCLASSIFIED**

where  $Q$ ,  $\lambda$ , and  $\Omega$  are munition parameters,  $DX$ ,  $DY$ , and  $DZ$  are direction cosines, and  $A$  and  $S$  are functions of the burst centroid location ( $x_{cent}$ ,  $y_{cent}$ ,  $z_B$ ) and its standard deviations. These standard deviations at any time  $t$  are

$$\begin{aligned}\sigma_x &= 0.1522 \left( \frac{Ut + A}{1.0} \right)^{.9294} \\ \sigma_y &= 3.41 \left( \frac{Ut + B}{100} \right)^\alpha \\ \sigma_z &= 1.35 \left( \frac{Ut + C}{20} \right)^\beta\end{aligned}\tag{3}$$

where the exponents  $\alpha$  and  $\beta$  are functions of the temperature gradient and  $U$  is the average wind speed. Values of  $A$ ,  $B$ , and  $C$  are given by

$$\begin{aligned}A &= 1.0 \left( \frac{\sigma_{xs}}{.1522} \right)^{1/.9294} \\ B &= 100 \left( \frac{\sigma_{ys}}{3.41} \right)^{1/\alpha} \\ C &= 20 \left( \frac{\sigma_{zs}}{1.35} \right)^{1/\beta}\end{aligned}\tag{4}$$

where  $\sigma_{xs}$ ,  $\sigma_{ys}$ , and  $\sigma_{zs}$  are initial standard deviations. Further details are given in [1].

(U) Figure 2 shows a curve of CL along a particular line-of-sight for Smoke Phase IIA, Trial 5, together with corresponding field test data. The inherent question arising in the evaluation of SEMM results in comparison with test data is how to quantify expected random variations in CL. Using SEMM alone yields no answer to this question; SUPER/SEMM provides the desired error bounds.

#### 4. ERROR BOUNDS FROM SUPER/SEMM (U)

(U) The Monte Carlo version of SUPER/SEMM shown in Figure 2 was used to obtain error bounds for the case considered in Figure 1. Ensemble-averaged results for CL were obtained for 100 simulation runs with randomly-generated wind speed time functions. The mean wind speed was 3.9 m/s with a standard deviation of 8% of the mean. Variations among the CL curves are indicated by Figure 3 with this typical shape shown at a selected point in time. A mean value of CL, designated by  $\hat{\mu}_{CL}$ , is estimated as  $\hat{\mu}_{CL}$ . Error bounds are denoted as  $\hat{\mu}_{CL} - K_1 \hat{\sigma}_{CL}$  and  $\hat{\mu}_{CL} + K_2 \hat{\sigma}_{CL}$ , which are 95% confidence intervals. Values of  $K_1$  and  $K_2$  define the relative positions of the error bounds with respect to the estimated mean  $\hat{\mu}_{CL}$ .

**UNCLASSIFIED**

B-9

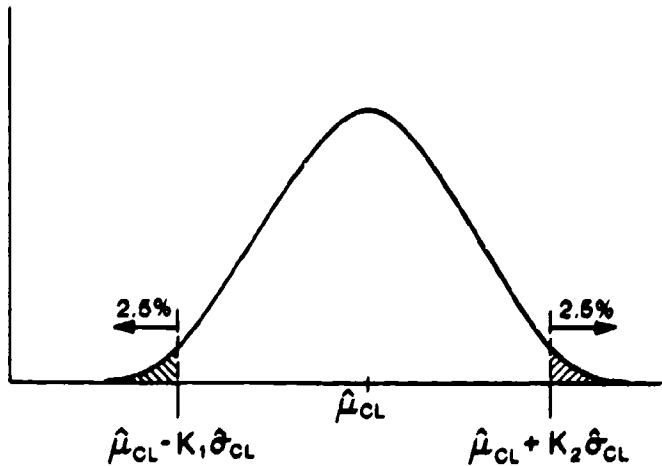


FIGURE 3. TYPICAL ERROR BOUNDS FROM SUPER/SEMM AT A POINT IN TIME (U)  
(Unclassified)

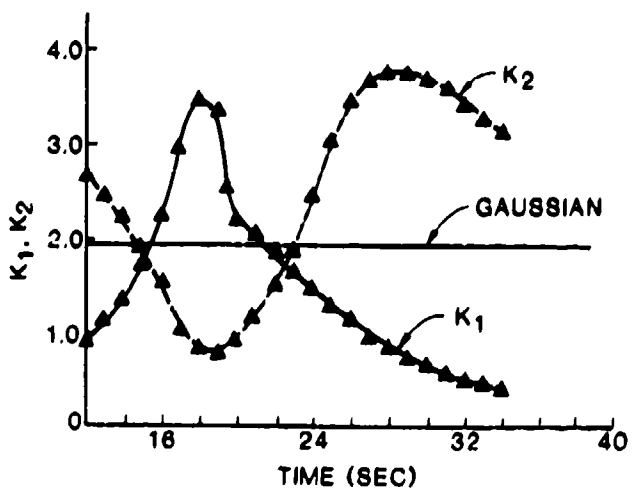


FIGURE 4. COMPARISONS FOR ERROR BOUNDS WITH GAUSSIAN AS A FUNCTION OF TIME (U)  
(Unclassified)

**UNCLASSIFIED**

531

**UNCLASSIFIED**

Values of  $K_1$  and  $K_2$  vary in time as shown in Figure 4. Moreover, these error bound parameters also vary as the wind speed standard deviation to mean wind speed ratio changes (Figure 5). Clearly, the probability density functions for CL are non-Gaussian for this line-of-sight considered.

(U) Error bounds from SUPER/SEMM for CL versus time are shown in Figure 6. An anti-tank guided missile (ATGM) threshold at  $1.14 \text{ g/m}^2$  is also shown. The percent of CL values above the ATGM threshold at a given point in time corresponds to the probability of obscuration at that time. What is needed is some indication of the length of time for which the target is obscured. This information is important in deciding whether a sufficient obscuring screen has been obtained.

##### 5. PROBABILITY OF OBSCURATION FROM SUPER/SEMM (U)

(U) A curve of probability of obscuration versus time is shown in Figure 7. Time differences across this curve at selected constant values of probability of obscuration can be identified as observation times. These probability of obscuration values can then be plotted as a function of the corresponding observation time to yield the curve shown in Figure 8. The vertical line at a time interval of approximately 12 seconds was determined by SEMM, indicating an average time interval of obscuration of 12 seconds. On the other hand, this entire curve from SUPER/SEMM provides information on the probability of obscuration for other time intervals as well. For example, probabilities of obscuration of 97%, 64%, and 13% correspond to time intervals of 5, 10, and 15 seconds, respectively. Moreover, SUPER/SEMM specifies that a twelve-second interval corresponds to a probability of obscuration of only 42%, a value not obtainable from SEMM alone.

(U) Figure 9 shows a comparison of actual test data with SEMM and SUPER/SEMM. Observe that the sample mean CL curve from SUPER/SEMM is slightly closer to the test data than the corresponding SEMM curve. More importantly, approximately 95% of the test data lies within the 95% error bounds of SUPER/SEMM. Similar results, not shown here, were obtained for 80% error bounds. These SUPER/SEMM curves were obtained by using wind speed data with a mean of 3.9 m/s and a standard deviation of 8%. Wind speed curves were not available for the exact time during which this single munition was tested. However, some wind speed data are available for tests involving multiple munitions. The extension of SUPER/SEMM to these multiple munition cases will help to evaluate SEMM more completely.

##### 6. EXTENSIONS (U)

(U) The concept of determining error bounds for concentration-length can be extended to include three-dimensional lines-of-sight using SUPER with an appropriate deterministic model. This added capability would enable probability of obscuration values to be determined for air-to-ground observations. In addition, multiple munitions can be incorporated into this model, together with other inputs (humidi-

**UNCLASSIFIED**

UNCLASSIFIED

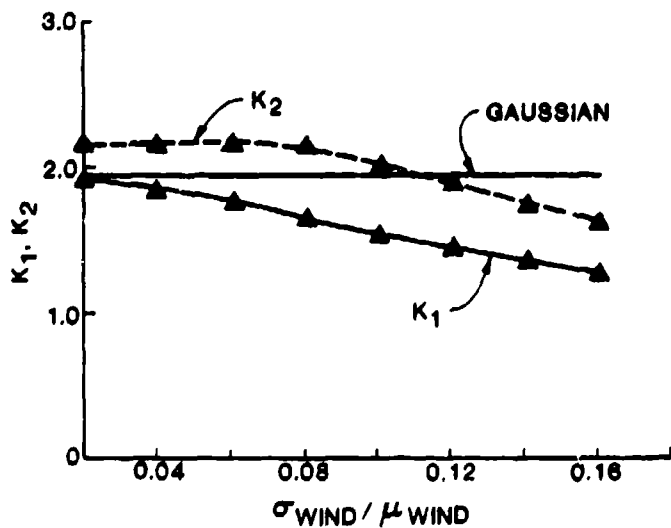


FIGURE 5. VARIATIONS IN ERROR BOUNDS FOR DIFFERENT WIND SPEED CHARACTERISTICS (U)  
(Unclassified)

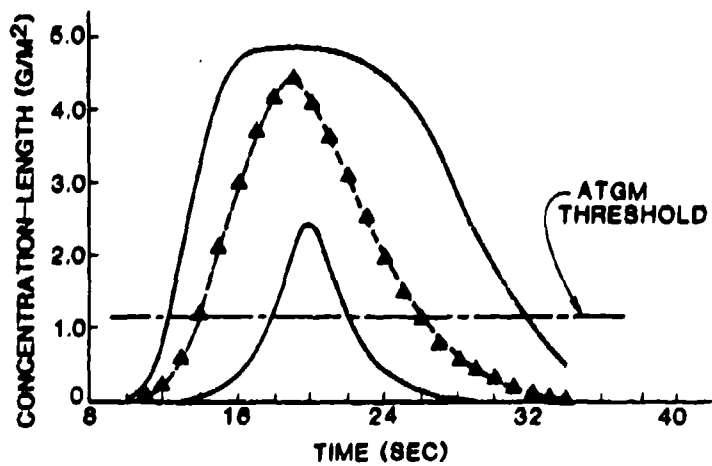


FIGURE 6. SUPER/SEMM RESULTS WITH ATGM THRESHOLD (U)  
(Unclassified)

UNCLASSIFIED

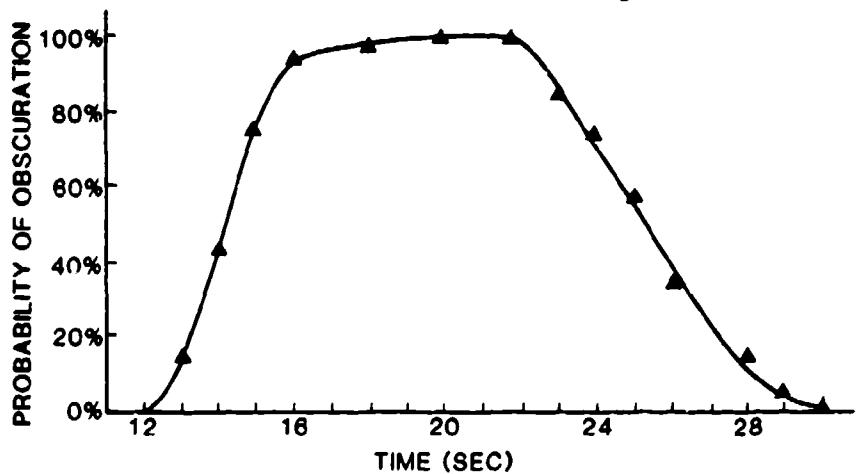
**UNCLASSIFIED**

FIGURE 7. PROBABILITY OF OBSCURATION VERSUS TIME (U)  
(Unclassified)

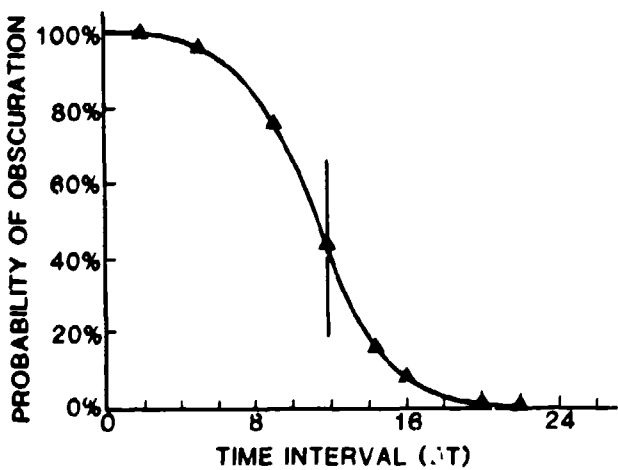


FIGURE 8. PROBABILITY OF OBSCURATION VERSUS DURATION OF OBSERVATION TIME (U)  
(Unclassified)

**UNCLASSIFIED**

**UNCLASSIFIED**

B-9

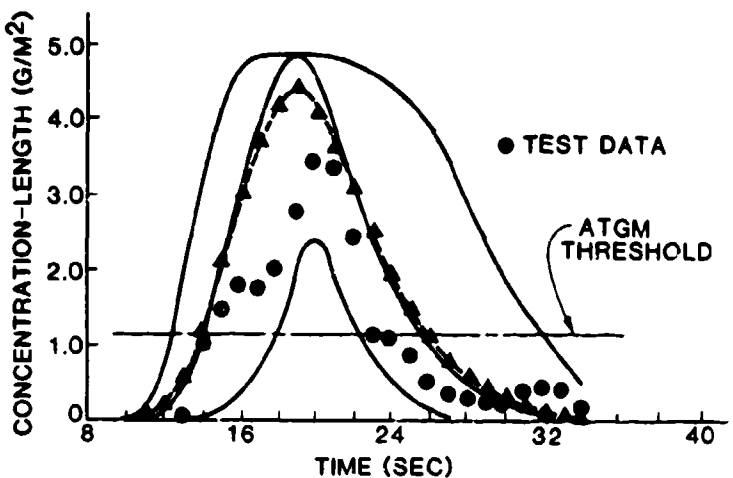


FIGURE 9. COMPARISONS BETWEEN TEST DATA, SEMM RESULTS, AND SUPER/SEMM RESULTS (U)  
(Unclassified)

ty and temperature variations) and other outputs (concentration and transmittance).

(U) The Monte Carlo version of SUPER was utilized in this paper to provide stochastic error bounds. Yet the deterministic model to which SUPER was applied was itself a direct model. What is needed is a direct algorithm for the SUPER model which can be applied easily to existing direct deterministic models. This direct algorithm computes the mean and variance of random outputs by forming expected values directly. A considerable savings in execution time is possible. Due to the large number of calculations required with the Monte Carlo approach, a far greater practical utility of the SUPER model can be achieved by using the direct technique.

(U) A final extension might include the development of an efficient computer program for the SUPER model to be used on a small computer or hand calculator to predict error bounds on smoke models. Such a unit could be used in the field to determine the number and placement of munitions to achieve the desired obscuration. In addition to the combat analyst, the tactical user can use this program as a strategic tool. Both users can benefit from the direct version of the SUPER model for determining error bounds.

**UNCLASSIFIED**

535

**UNCLASSIFIED**

## 7. CONCLUSIONS (U)

(U) The SUPER model has been developed in this paper as a general concept applicable to a broad class of deterministic smoke obscuration models. Results obtained using the SUPER model yield error bounds about the average model output. For example, SUPER/SEMM results presented in this paper provided 95% error bounds about an average concentration-length (CL). From these error bounds on CL, the probability of obscuration was determined as a function of observation time. Previously, SEMM indicated only an average value of time the target was obscured (12 seconds) with no quantitative measure of the probability of obscuration for this time duration. SUPER/SEMM determined that probability of obscuration to be 42% and provided corresponding probabilities of obscuration for other observation times as well.

(U) The application of SUPER/SFMM to the multiple munitions case should provide a useful evaluation of SEMM. Extensions to other deterministic models are planned for further evaluations and comparisons.

## 8. REFERENCES (U)

1. Robert M. Marchetti, "A Transport and Diffusion Model for Smoke Munitions", U.S. Army Materiel Systems Analysis Activity, Aberdeen Proving Ground, Maryland, March, 1979. (U)
2. Bruce W. Fowler and Thomas B. Owens, "A Parametric Model for the Effect of White Phosphorus Smoke on Target Detection: I, Model Development", Technical Report C-79-Advanced Systems Concept Office, USAMICOM, October, 1979. (U)
3. Marvin D. Smith and James R. Rowland, "Comparisons Between Theoretical and Empirical Models for Smoke Obscuration", Proceedings of the Smoke/Obscurant Symposium III, Harry Diamond Laboratory, Adelphi, Maryland, April 26-27, 1979, Paper A-11. (U)
4. Marvin D. Smith, James R. Rowland, J. Mark Richardson, Mark A. McDonald, "Stochastic Models for Smoke/Obscurants", Proceedings of the Smoke/Obscurant Symposium IV, Harry Diamond Laboratory, Adelphi, Maryland, April 22-23, 1980. (U)

**UNCLASSIFIED**

# UNCLASSIFIED

B-10

MMTRN: MILLIMETER WAVE PROPAGATION MODEL FOR RAIN,  
FOG AND SNOW EXTINCTION AND GASEOUS ABSORPTION

Douglas R. Brown

US Army Atmospheric Sciences Laboratory

White Sands Missile Range, New Mexico 88002

## ABSTRACT

A computer model, MMTRN, is presented which models fog/cloud extinction, water vapor and oxygen absorption from 10 GHz to 1500 GHz, and rain and snow extinction from 10 GHz to 500 GHz. Backscatter cross-sections for rain, fog, and snow are also included. Water vapor and oxygen absorption are modeled using line-by-line techniques, fog is represented as a Rayleigh aerosol. Rain and snow are modeled with  $aR^b$  relationships. This code is compact and is suitable for use in millimeter radar performance models.

## 1. INTRODUCTION

Models of millimeter wave atmospheric extinction have traditionally required large amounts of computer storage and execution time in order to provide the flexibility and accuracy necessary in a research oriented model. MMTRN has been developed as a small, quick program to provide the scientist, engineer, or system performance modeler with results which have accuracies linked to the experimental data variability, and commensurate with a simplified input data requirement. MMTRN does not attempt to demonstrate state-of-the-art models, but to use the physical understanding developed therein in simplified models of reasonable accuracy.

MMTRN routines calculate the attenuation of millimeter waves by water vapor and oxygen absorption, cloud, fog, and ice fog bulk absorption and backscatter, rain extinction and backscatter, and preliminarily, snow extinction and backscatter. Smoke and dust are not modeled in MMTRN due to security reasons (this is an unclassified code) and due to a lack of sufficient data. The included effects are modeled for all frequencies from 10 GHz (3.1 cm) to 500 GHz (.62 mm), and water vapor absorption can be extended to 1500 GHz (200  $\mu$ m). Temperature limitations vary widely for the individual calculations and will be discussed with the modules. Because no doppler broadening is included, or trace gases included, pressure (and therefore height) limitations should keep calculations above 100 torr (133 mB) total pressure.

# UNCLASSIFIED

## UNCLASSIFIED

## 2. MMTRN MODULES

## 2.1. Absorption by Water Vapor.

Water vapor absorption is calculated using a simplified line-by-line code where the contribution of each local water vapor line is summed to give the total absorption at a given frequency. This procedure can be defined by the equation for  $\alpha$ , the absorption coefficient in dB/km

$$\alpha(v) = \sum_{i=1}^N S_i C_s(T) W(\text{Species}) \phi(v, v_i, \gamma_i)$$

where  $S_i$  is the strength of the  $i^{\text{th}}$  line,

$C_s(T)$  is a temperature correction factor for the line strength,

$W(\text{Species})$  is the column density for the given species,

$\phi(v, v_i, \gamma_i)$  is the line absorption shape factor or the line profile,

$v_i$  is the center frequency for the  $i^{\text{th}}$  line

and  $\gamma_i$  is the pressure and temperature corrected line half width.

For water vapor, the line parameters,  $S_i$ ,  $\gamma_i$ , etc. were the AFGL line parameters<sup>1</sup>. A total of 56 lines are included, selected over the interval from 22 GHz to 2250 GHz on the basis of line strength. A cutoff was defined as the curve  $g(v)$ :

$$g_{\max} = g(v_i) = 10^{-2} S(v_i)$$

$$\text{and } g(v_i \pm 150\text{GHz}) = 10^{-1} g_{\max}$$

where  $v_i$  is the line frequency and  $S(v_i)$  is the line strength. The contribution of each line to  $g(v)$  was graphed and all lines whose strength was greater than  $g(v)$  were included. Lines to 2250 GHz were included to represent the contribution of strong line wings in the windows. Errors in this procedure, when compared with line-by-line calculations using 212 lines, were less than 1%.

The calculation of the line profile  $\phi(v, v_i, \gamma_i)$  was carried out using the Super Kinetic line profile<sup>2</sup>. This technique agrees reasonably with standard condition water vapor absorption data without the use of an added "continuum" contribution. It does not yet, however as with all treatments, adequately

## UNCLASSIFIED

B-10

represent the temperature and pressure dependence of the "anomalous" absorption. The profile is defined by:

$$\phi_{sk}(v, v_o, \gamma_o) = \frac{\text{NORM}}{\pi\gamma} \left[ \left( \frac{v_o^2 - v^2}{2\gamma v} \right)^2 + 1 \right]^{-1} \quad |v - v_o| \leq \Delta v$$

$$= x \frac{\text{NORM}}{\pi\gamma} \left[ \left( \frac{v_o^2 - v^2}{2\gamma v} \right)^3 + 1 \right]^{-1} \quad |v - v_o| \geq \Delta v$$

where  $x$  is defined such that  $\phi_{sk}$  is continuous at  $v=v_o \pm \Delta v$  and NORM is a normalization parameter. The parameters  $\gamma$  and  $\Delta v$  are variable, and give the best fit to water vapor when  $\gamma = 1.88$  and  $\Delta v \approx 10Y$ .

The line half widths are corrected for self broadening and temperature.

The only model limitation in this case is that fact that only pressure broadening is considered. Therefore, where doppler broadening begins to become important (at low pressures) this model should not be used without modification.

A comparison of selected experimental data and the calculation by MMTRN is shown in Figure 1. The data point at 60 GHz does not include the oxygen absorption which is included in MMTRN.

## 2.2. Absorption by Oxygen

Gaseous absorption by oxygen is treated using the method of Liebe, Gimmesad and Hopponen<sup>3</sup>. This technique uses a line-by-line technique modified to include the effects of line overlapping in the 60 GHz oxygen band.

The procedure differs from the water vapor line-by-line calculation fundamentally only in the line profile employed. A modified Van Vleck-Weisskopf<sup>4</sup> profile is used of the form

$$\phi(v, v_o, \gamma, I^\circ) = \frac{v}{v_o} \left( \frac{\gamma - (v_o - v) I^\circ p}{(v_o - v)^2 + \gamma^2} + \frac{\gamma - (v_o + v) I^\circ p}{(v_o + v)^2 + \gamma^2} \right)^{-1}$$

UNCLASSIFIED

**UNCLASSIFIED**

where  $I^*$  is the line interference factor and  $p$  is the atmospheric pressure. The result is a narrowing of the lines due to the line overlap.

For this model, 36 oxygen lines are included. Line data was taken from Liebe et al. The contribution by oxygen to the molecular absorption is calculated for frequencies below 140 GHz. Oxygen is ignored for frequencies above 140 GHz.

### 2.3. Bulk Absorption and Backscatter by Cloud, Fog, Ice Fog

Aerosol sizes for fog and clouds (without precipitation) are small, generally below 50  $\mu\text{m}$  for the larger particles, and are therefore well within the Rayleigh regime for millimeter waves. Due to the relative dependences of Rayleigh scattering and bulk attenuation on the wavelength, and water indices of refraction, scattering contributes much less than bulk attenuation, and can be ignored. In this case the attenuation coefficient  $\kappa$  (dB/km) is

$$\kappa = 4.343 \int_{\text{all sizes}} N(D) \sigma_e'(D) dD$$

where  $N(D)$  is the size distribution for fog/cloud and  $\sigma_e'(D)$  is the Rayleigh approximation for absorption:

$$\sigma_e'(D) = \pi^2 D^3 \text{Im} \left( -\frac{\frac{m^2-1}{m^2+2}}{\lambda} \right) \quad \lambda^{-1}$$

where  $m$  is the complex index of refraction for water and  $\text{Im}$  denotes the imaginary part. Noting that

$$\int D^3 N(D) dD = \frac{6}{\pi} \sum_i V_i = \frac{6}{\pi} V_{\text{total}}$$

where  $V_i$  is the volume of the  $i^{\text{th}}$  particle, and  $V_{\text{total}}$  is the total volume of all the particles per unit volume of space, we see that for water

$$V_{\text{total}} = \omega / \rho \omega$$

where  $\omega$  = total liquid water content and  $\rho$  = water density ( $\sim 1$ ), we have

**UNCLASSIFIED**

B-10

$$\kappa = \frac{81.86\omega}{\lambda} \quad \text{Im} \quad \left( -\frac{m^2-1}{m^2+2} \right)$$

Units are  $[\kappa] = \text{dB/km}$ ,  $[\lambda] = \text{mm}$ ,  $[\omega] = \text{gm/m}^3$ .

The indices of refraction for liquid/frozen water are computed using the method of Ray<sup>5</sup>. Ice fogs are calculated when temperature is below -30°C.

The liquid water content,  $\omega$ , has natural upper limits for fogs of about 1.5 gm/m<sup>3</sup> and for clouds near 4 gm/m<sup>3</sup>. If specific values of  $\omega$  are not known, they may be inferred roughly from

$$\omega = 5.95 \times 10^{-3} \times V^{-1.33}$$

where  $V$  is the visual range in km.

Water fog absorption with and without the background gaseous absorption is shown in Figure 2. Figure 3 shows the absorption due to ice fog. It should be noted that the complex index of refraction for ice is poorly known at such low temperatures. Also, the interaction of water vapor and fog may cause non-linear, i.e. anomalous, effects and attenuation may differ from these predictions.

Fog backscatter cross-section,  $\gamma$ , is defined for a Rayleigh scatterer,

$$\gamma = \frac{\pi^5 |\kappa|^2}{\lambda^4} \int D^6 N(D) dD \times 10^{-6} \text{ m}^2/\text{m}^3$$

where  $\kappa = \left( -\frac{m^2-1}{m^2+2} \right)$ ,  $\lambda$  : wavelength in mm,  $D$  is in mm, and  $N(D)$  is in units  $\text{m}^{-3} \text{ mm}^{-1}$ . An exponential distribution for  $N(D)$  is assumed,

$$N(D) = N_0 e^{-\alpha D}$$

because the  $D^6$  weighting makes the errors in  $N(D)$  for small  $D$  ignorable. Using the relationship between visibility and liquid water content,

**UNCLASSIFIED**

## UNCLASSIFIED

$$\omega = 5.95 \times 10^{-3} \times V_r^{-1.33}$$

and Koschmeider's relationship,

$$\kappa V_r = 3.912$$

we can compute  $\beta$ ,

$$\beta = 1.21462 \times 10^{-6} |\kappa|^2 \omega^{1.75} \lambda^{-6} \text{ m}^2/\text{m}^3.$$

Figure 4 shows the backscatter cross-sections for liquid and ice fogs.

#### 2.4. Rain Extinction and Backscatter.

It is generally accepted that Mie scattering by dielectric water spheroids provides an accurate model of millimeter wave scattering by rain<sup>6</sup>. Such codes are too complex to fit the requirements of size and speed for MMTRN. Also, to use the full power of Mie scattering calculations, raindrop number densities are required which are seldom measured accurately in the field. Instead, if drop-size models, such as Laws Parsons, are invoked, a significant reduction in realism and therefore accuracy is made. As these dropsize models are used extensively, it is reasonable to use a rain extinction model which matches this accepted loss of accuracy. In MMTRN this is accomplished by employing the  $\kappa = aR^b$  (dB/km) relationship, where R is rainrate in mm/hr, as discussed by Olsen, Rogers and Hodge<sup>7</sup>. The dropsize distribution used for general conditions is that of Laws and Parsons<sup>8</sup>.

The parameters a,b calculated by Olsen et al for temperatures of -10°C, 0°C, and 20°C and various frequencies were fit for frequency by a power law,

$$a = a_1 f^{\beta_a}$$

$$b = b_1 f^{\beta_b}$$

where f is frequency in GHz, and interpolated for temperature between -10°C and +20°C. Beyond these bounds temperature was set at -10°C or 20°C, respectively.

UNCLASSIFIED

# UNCLASSIFIED

B-10

Large discrepancies of predicted extinction versus measured attenuation are common, supposedly due to variations in the real dropsize distribution from the assumed mode. Figure 5 shows an example of this. The predicted extinction using the various dropsize models was a Mie scattering calculation. Because of this large variation between measured data and calculation, MMTRN was validated with Mie scattering computations, not experimental data. Figure 6 shows the agreement at 100 GHz. Figure 7 shows the extinction due to rain and gaseous absorption.

The rain backscatter cross-section was computed using Mie scattering codes and also fit to a power law,

$$\sigma = \alpha R^\beta \text{ m}^2/\text{m}^3$$

where R is again rainrate in mm/hr. The coefficients  $\alpha$ ,  $\beta$  were fit by polynomials and depend upon frequency and temperature. Sample calculations are shown in Figure 8.

## 2.5. Snow Extinction and Backscatter

Attempts to model snow extinction and particularly backscatter immediately confront the problems of an extremely limited experimental data set and an equally scarce theoretical literature. This is true for frozen hydrometeors in general<sup>9</sup>. The model in MMTRN is therefore a preliminary one, based upon the few available data and eagerly awaiting new results.

The snow extinction model again uses a  $\kappa = aS^b$  relation, where S is equivalent rain rate in mm/hr, that is, the melted snow rate. The data were taken from the following references: Robinson<sup>10</sup>, Babkin et al<sup>11</sup>, Nishitsuji<sup>12</sup>, Oomori and Aoyagi<sup>13</sup>, Malinkin et al<sup>14</sup>, Richard et al<sup>15</sup>. Three cases were defined, dry, moist and wet snow, although accurate delineation of the snow types was impossible due to the poor snow characterization during the measurements. The differentiation of extinction by snowtype seen in Figure 9 at frequencies below 50 GHz is represented by the data. The inversion of this at frequencies above 140 GHz is expected on theoretical grounds due to the relationship between cross-section and snowflake mass for the different snowtypes. The frequency at which this actually occurs is not known.

The lack of adequate data (the model is presently based on nine data points) to specify the behavior of the a and b coefficients required the use of similarity arguments between the characteristics

# UNCLASSIFIED

543

# UNCLASSIFIED

B-10

of the coefficients for rain and snow. The expectation is that averaging over the flake or drop distribution minimizes the differences in the scattering phase functions between snowflakes and raindrops.

No millimeter snow backscatter data was found in the literature. As a temporary model for snow backscatter, the Rayleigh scattering results of Imai et al<sup>16</sup>, Gunn and Marshall<sup>17</sup>, and Yagi et al<sup>18</sup> were employed. This model is therefore quite incorrect for frequencies above 30 GHz and should not be employed in its present form.

As this paper was being written, no data were available from the SNOW ONE test. As soon as the data are available, the MMTRN snow models will be updated.

### 3. CONCLUSION

As a final demonstration of the capabilities of MMTRN the following atmosphere was modeled:

Temperature	275°k
Humidity	100%
Fog liquid water content	0.05 gm/m <sup>3</sup>
Rain rate	4.0 mm/hr
Wet snow rate	2.5 mm/hr

Figure 10 shows the comparison between the background gaseous absorption and the full calculation. The calculation of 330 frequency points including backscatter took 26 seconds on an H.P. 1000/45 computer.

MMTRN is presently the basis of the EOSAEL<sup>19</sup> millimeter module, and is being used at the Atmospheric Sciences Laboratory in a millimeter radar performance model.

**UNCLASSIFIED**

## REFERENCES

- <sup>1</sup> McClatchey, R. A., W. S. Benedict, S. A. Clough, D. E. Burch, R. F. Calfee, R. Fox, L. S. Rothman, and S. S. Garing, 1973, "AFCRL Atmospheric Line Parametric Compilation," AFCRL-TR-0096.
- <sup>2</sup> Brown, D. R., and D. E. Snider, 1979, "H<sub>2</sub>O Near Millimeter Absorption: The Effect of Line Shape Variations," Proceedings of the Workshop on Millimeter and Submillimeter Atmospheric Propagation Applicable to Radar and Missile Systems, Redstone Arsenal, RR-80-3.
- <sup>3</sup> Liebe, H. J., G. G. Gimmetad, J. D. Hopponen, 1977, "Atmospheric Oxygen Microwave Spectrum - Experiment versus Theory," IEEE Transactions Antennas and Propagation, 25:377.
- <sup>4</sup> Van Vleck, J. H., and V. F. Weisskopf, 1945, "On the Shape of Collision-Broadened Lines," Review Modern Physics, 17:227.
- <sup>5</sup> Ray, P. S., 1972, "Broadband Complex Refractive Indices of Ice and Water," Applied Optics, 11:1936.
- <sup>6</sup> Kobayashi, H. K., "Atmospheric Effects on Millimeter Waves," ASL-TR-0049, January 1980.
- <sup>7</sup> Olsen, R. O., D. V. Rogers, and D. B. Hodges, 1978, "The  $aR^b$  Relation in the Calculation of Rain Attenuation," IEEE Transactions Antennas and Propagation, AP-26:318.
- <sup>8</sup> Laws, J. O., D. A. Parsons, 1943, "The Relation of Raindrops to Intensity," Trans Am Geophy Union, 24:452.
- <sup>9</sup> Kobayashi, H. K., "Effect of Hail, Snow and Melting Hydrometeors on Millimeter Radio Waves," ASL-TR-xxxx (in preparation)
- <sup>10</sup> Robinson, N. P., 1955, "Measurements of the Effect of Rain, Snow and Fog on 8.6 mm Radar Echoes," Proceedings IEEE, London, 203B:709.
- <sup>11</sup> Babkin, Yu. S., I. A. Iskhakov, A. V. Sokolov, L. I. Stroganov, and Ye. V. Sukhonin, 1970, "Attenuation of Radiation at a Wavelength of 0.96 mm in Snow," Radio Engineering and Electronic Physics, 15:2171.

**UNCLASSIFIED**

**UNCLASSIFIED**

<sup>12</sup>Nishitsuji, A., 1971, "Method of Calculation of Radio-Wave Attenuation in Snowfall," Electronics and Communications in Japan, 54-B:74.

<sup>13</sup>Oomori, T., and S. Aoyagi, 1971, "A Presumptive Formula for Snowfall Attenuation of Radio Waves," Electronics and Communications in Japan, 54-B:34.

<sup>14</sup>Malinkin, V. G., A. V. Sokolov, and Ye. V. Sukhonin, 1976, "Attenuation of Signal at the Wave-length  $\lambda = 8.6$  mm in Hydrometeors," Radio Engineering and Electronics Physics, 21:1.

<sup>15</sup>Richard, W. W., J. E. Kammerer, and R. C. Reitz, 1977, "140-GHz Attenuation and Optical Visibility Measurements of Fog, Rain and Snow," Ballistics Research Laboratory, Memorandum Report ARBRL-MR-2800, Aberdeen Proving Ground, MD 21005.

<sup>16</sup>Imai, I., M. Fujiwara, I. Ichimura, and Y. Toyama, 1955, "Radar Reflectivity of Falling Snow," Paper in Meteorology and Geophysics Japan, 6:130.

<sup>17</sup>Gunn, K. L. S., and J. S. Marshall, 1958, "The Distribution with Size of Aggregate Snowflakes," Journal of Meteorology, 15:452.

<sup>18</sup>Yagi, T., H. Uyeda, and H. Seino, 1979, "Size Distribution of Snowflakes and Graupel Particles Observed in Nagaoka, Niigata Prefecture," Journal of the Faculty of Science, Hokkaido University Ser. VII, 6:79.

<sup>19</sup>Duncan, L. D., ed. "EOSAEL 80, Vol. I, Technical Documentation," ASL-TR-0072, January 1981.

<sup>20</sup>Keizer, W., J. Snieder, C. deHaan, "Rain Attenuation Measurements at 94 GHz: Comparison of Theory and Experiment," DPP Symposium, Neubiberg bei München, Germany, 1978.

**UNCLASSIFIED**

B-10

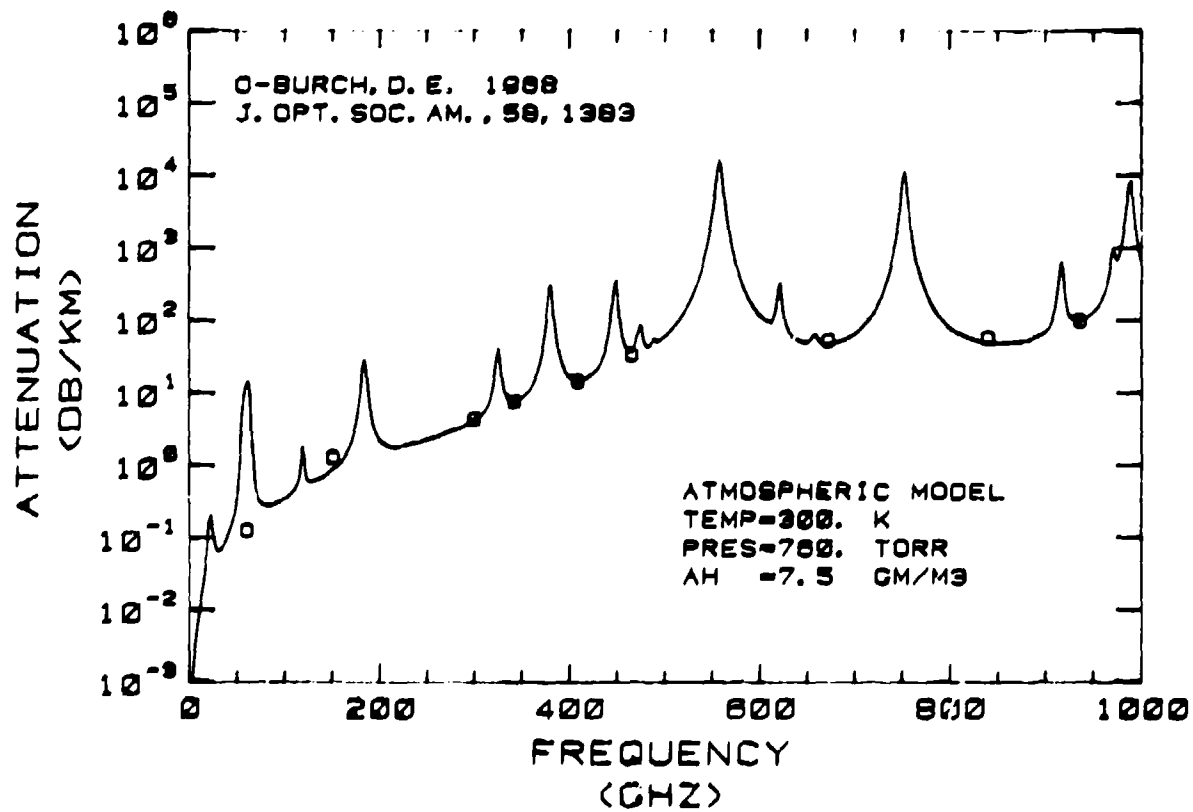


FIGURE 1: (U) Comparison of MMTRAN H<sub>2</sub>O and O<sub>2</sub> Absorption and Experimental H<sub>2</sub>O Data

**UNCLASSIFIED**

547

UNCLASSIFIED

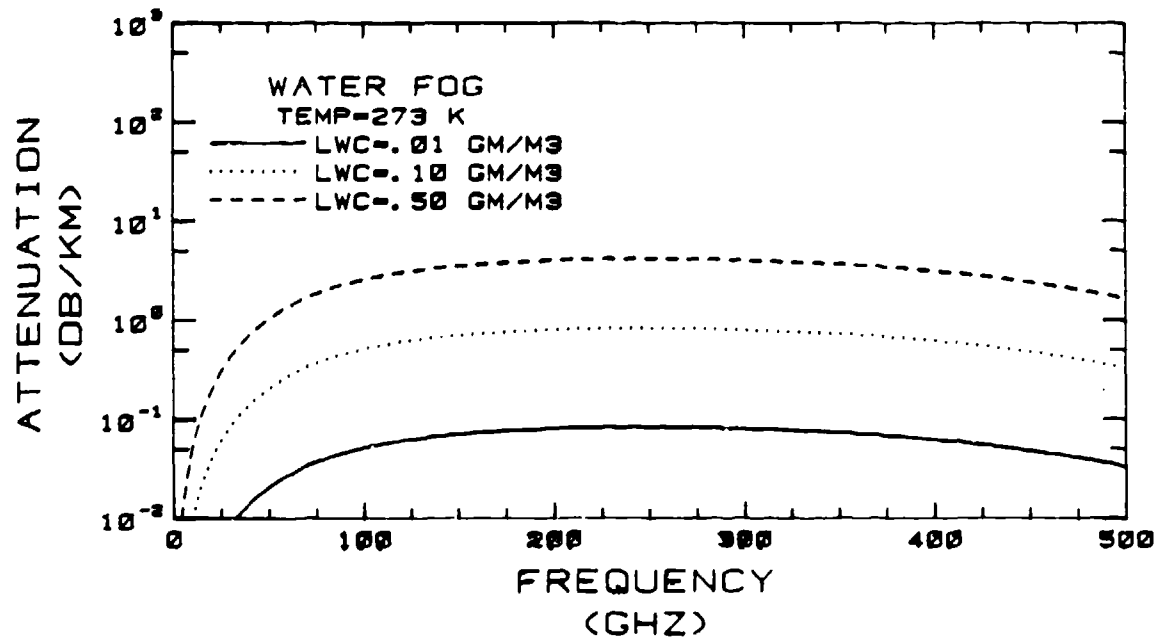


FIGURE 2a: (U) MMTRN Water Fog Absorption

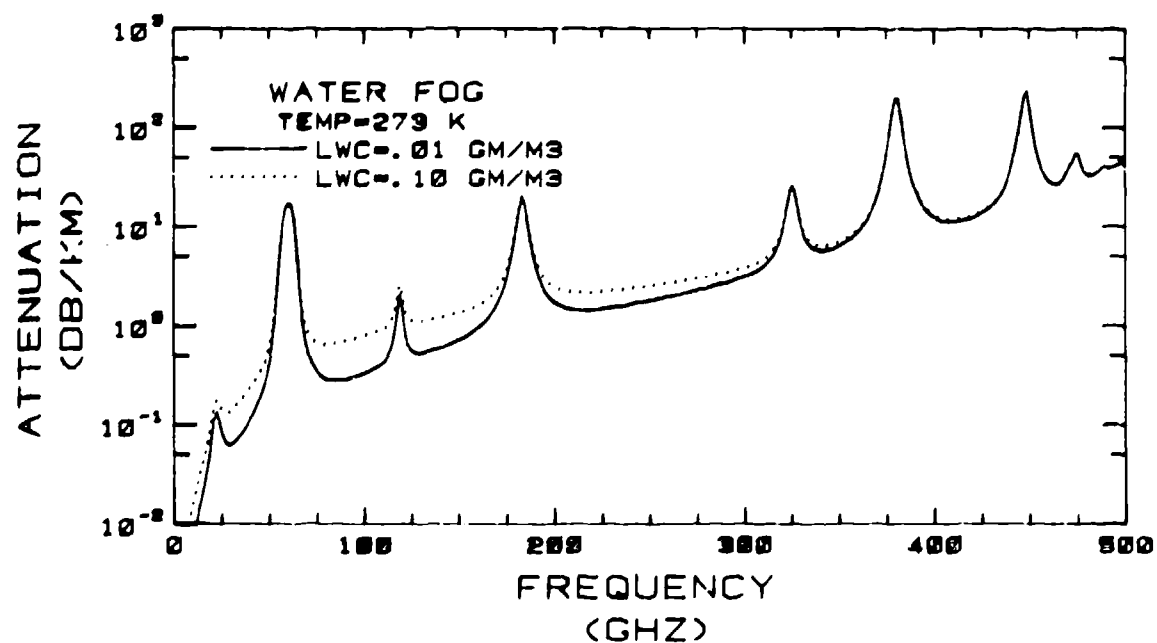


FIGURE 2b: (U) Water Fog Plus Gaseous Absorption

UNCLASSIFIED

**UNCLASSIFIED**

B-10

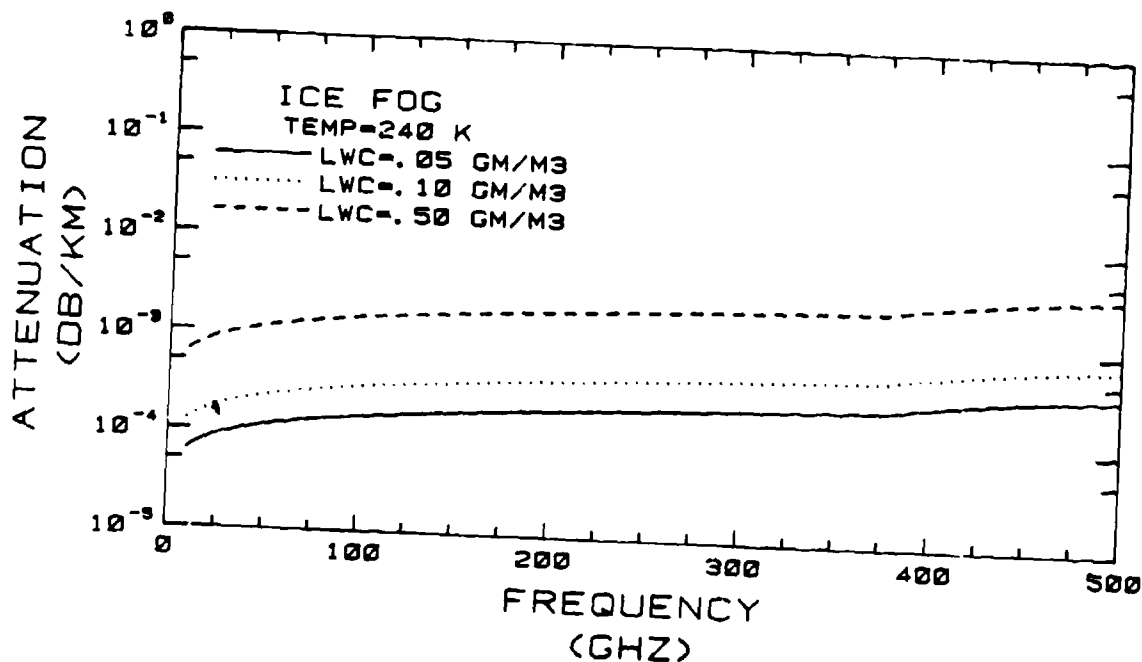


FIGURE 3: (U) MMTRN Ice Fog Absorption

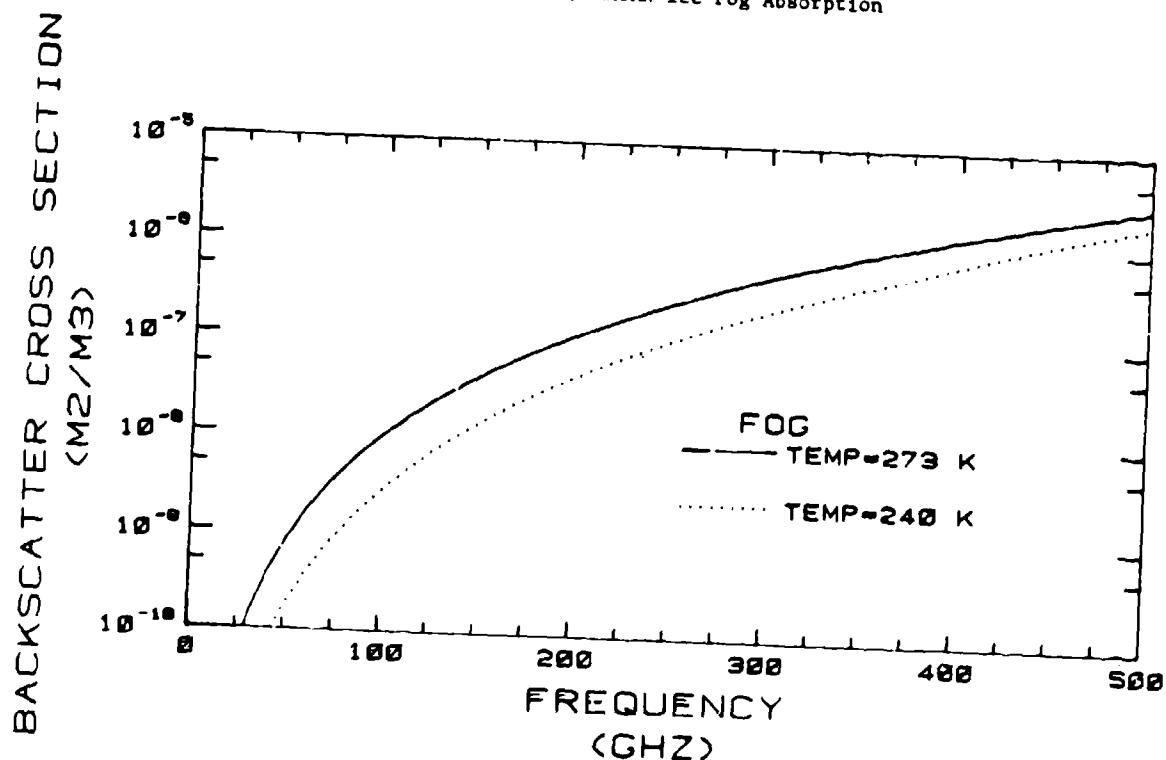


FIGURE 4: (U) Water and Ice Fog Backscatter Cross-Section, for 1  $\text{gm}/\text{m}^3$  LWC

**UNCLASSIFIED**

549

UNCLASSIFIED

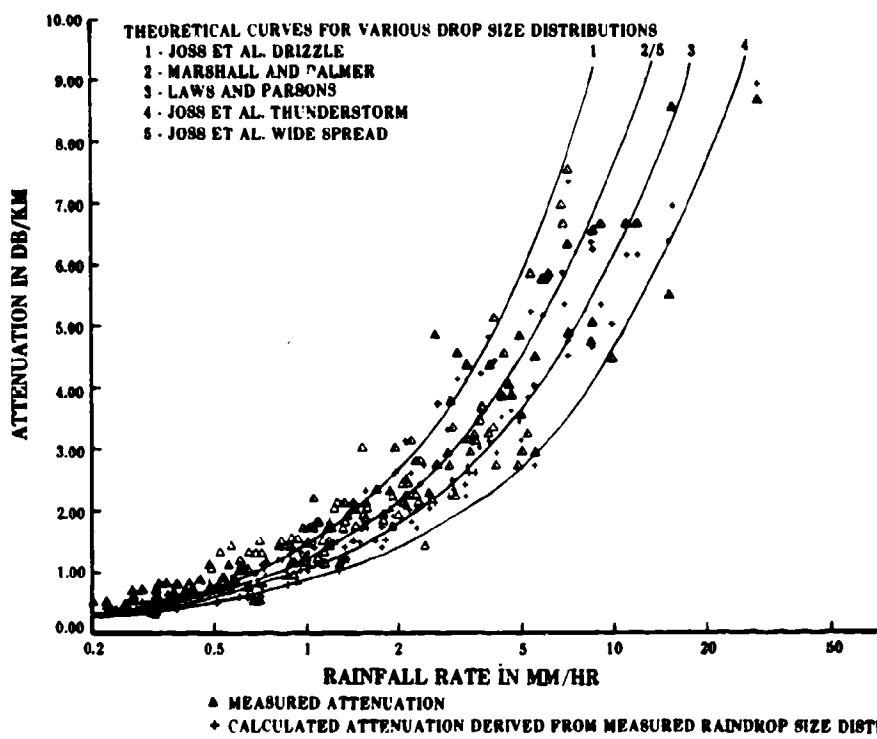
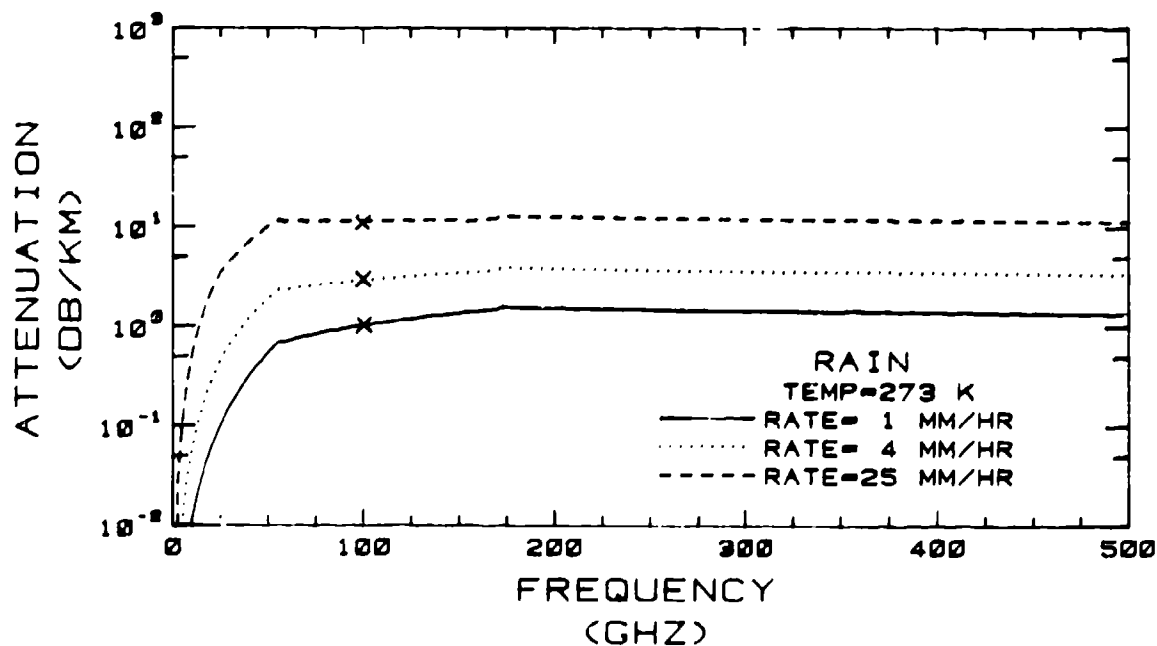
FIGURE 5: (U) Measured and Calculated Rainfall Attenuation at 94 GHz Keizer et al<sup>20</sup>

FIGURE 6: (U) Comparison of MMTRN and Mie Scattering Rain Extinction

UNCLASSIFIED

**UNCLASSIFIED**

B-10

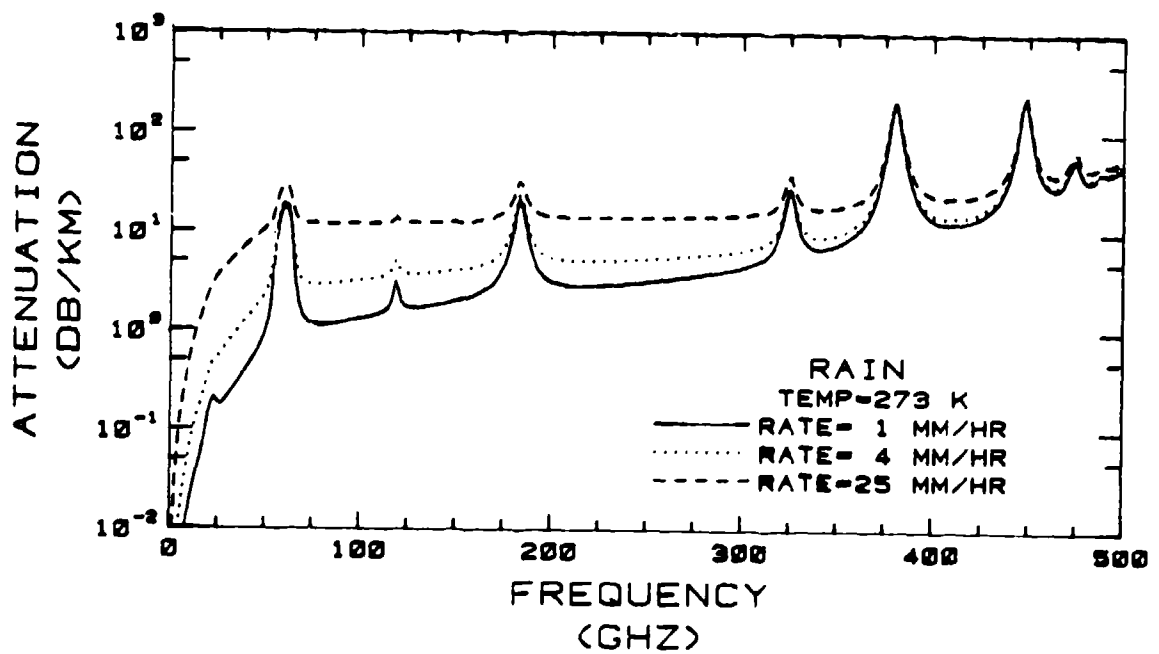


FIGURE 7: (U) Rain and Gaseous Attenuation

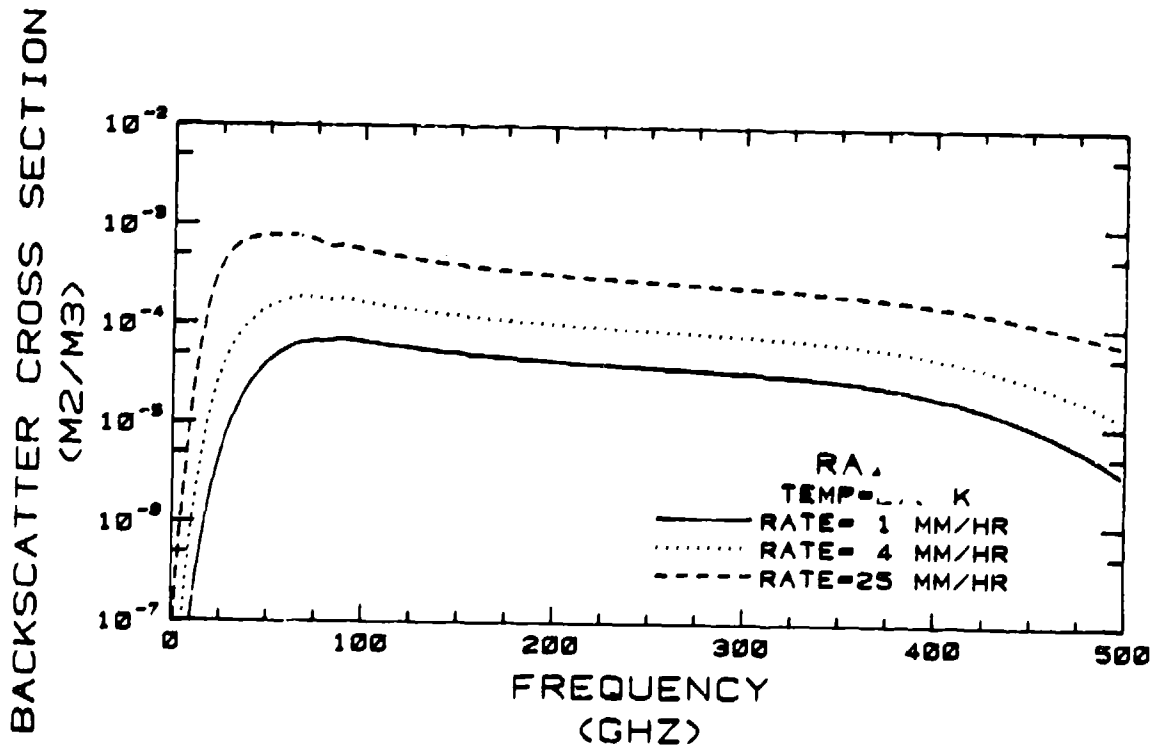


FIGURE 8: (U) Rain Backscatter Cross-Section

**UNCLASSIFIED**

551

UNCLASSIFIED

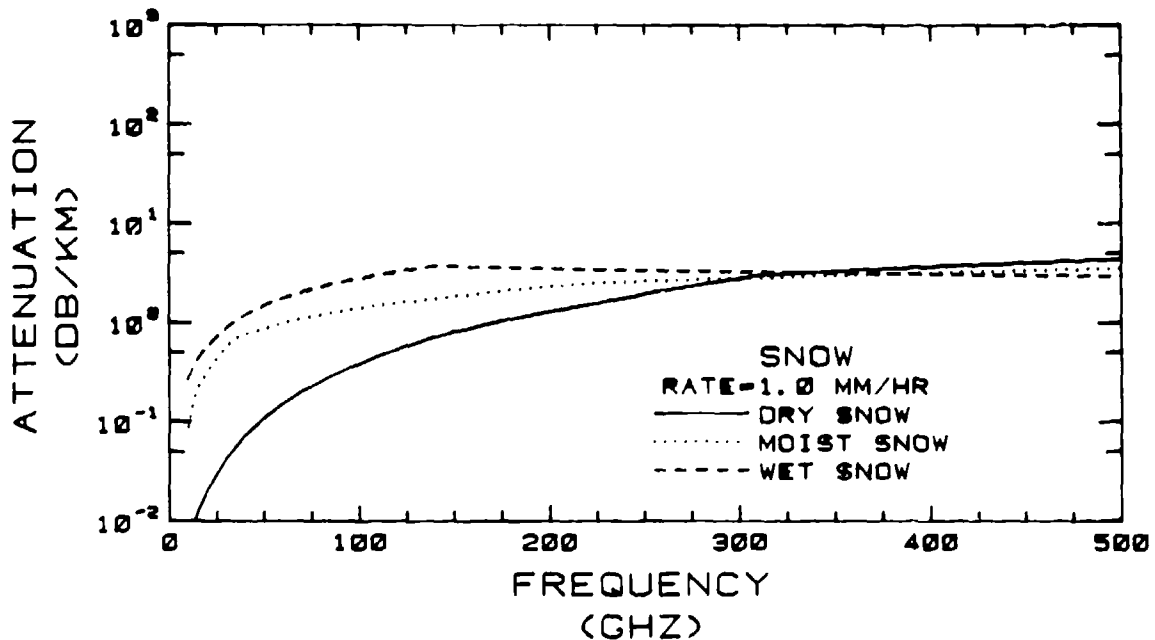


FIGURE 9a: (U) MMTRN Snow Attenuation

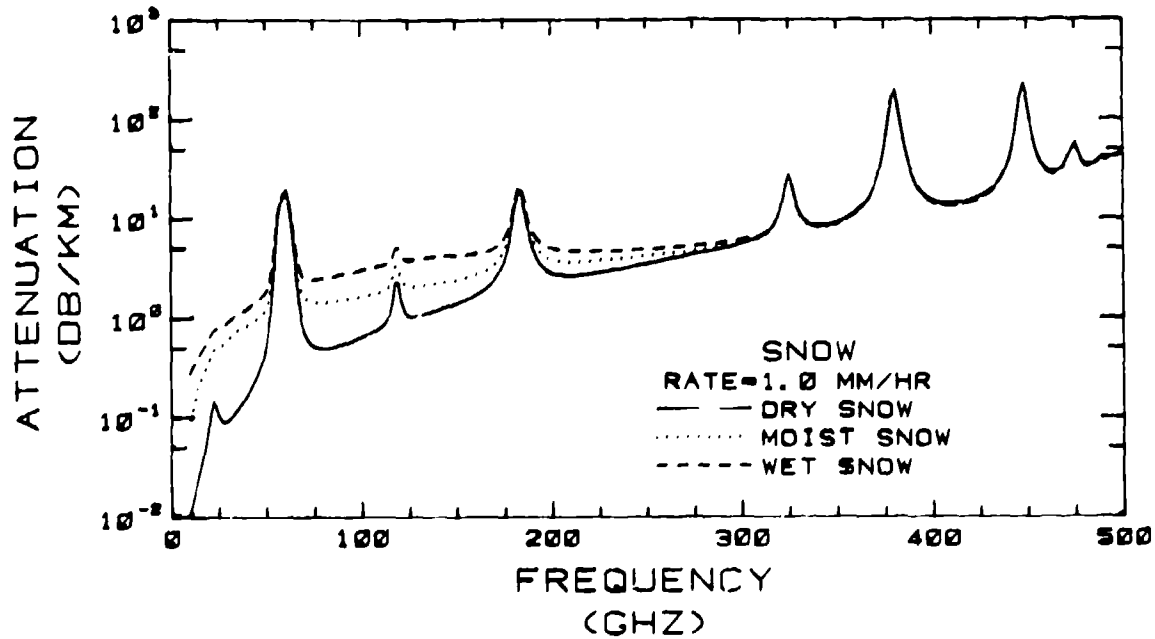


FIGURE 9b: (U) Snow Plus Gaseous Attenuation

UNCLASSIFIED

**UNCLASSIFIED**

B-10

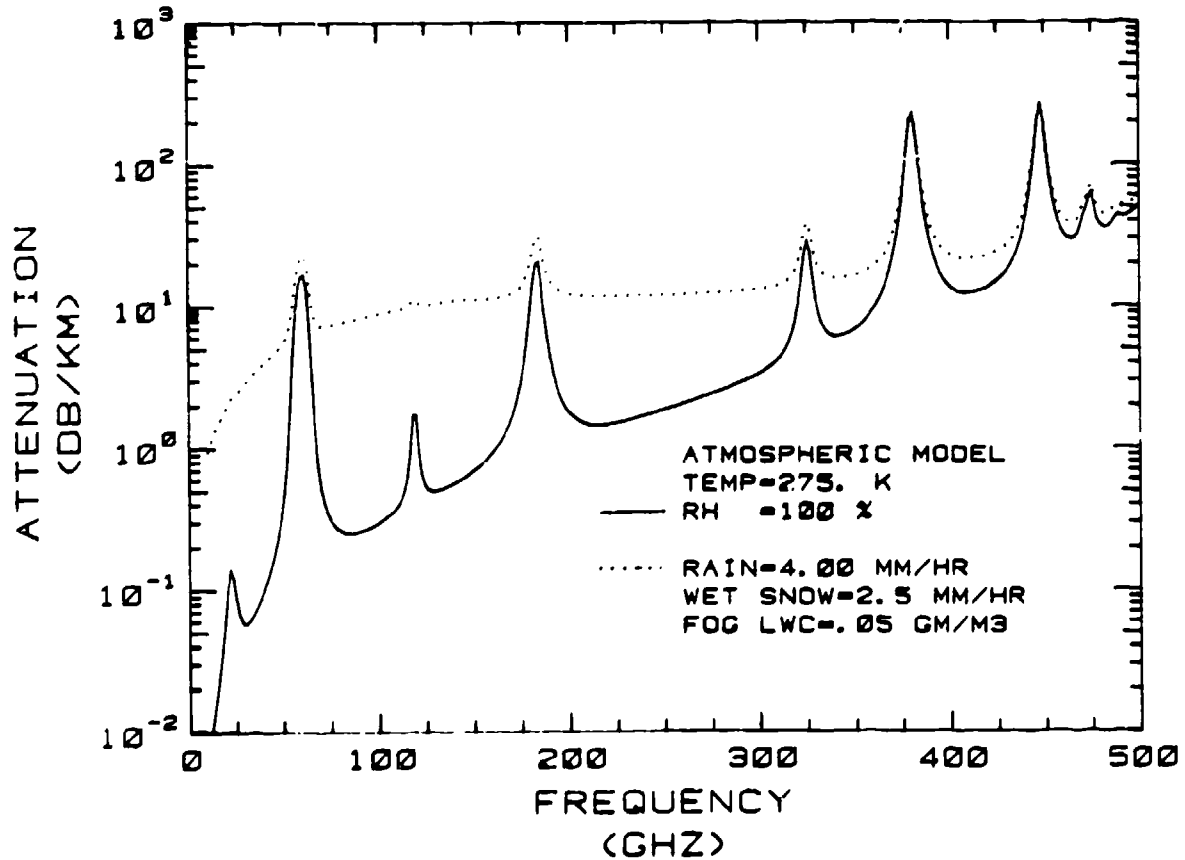


FIGURE 10: (U) Comparison of Adverse Weather Attenuation and Background Gaseous Absorption

**UNCLASSIFIED**

# UNCLASSIFIED

## EXTINCTION BY SMOKES AT VISIBLE, INFRARED AND MILLIMETER WAVELENGTHS

Janon F. Embury  
Chemical Systems Laboratory  
Aberdeen Proving Ground, MD 21010

### ABSTRACT

Current military inventory screening smokes such as white phosphorous and fog oil consist of polydispersions of spherical liquid particles, while experimental infrared and millimeter wavelength screening smokes consist of polydispersions of either flakes or fibers. The theory that describes scattering by individual nonspherical particles is complex. However, a major simplification occurs for a cloud of randomly oriented polydisperse nonspherical particles. The extinction spectra is shown to consist of two distinct regions. The first occurs at shorter wavelengths where extinction is independent of refractive index and depends only on particle size and shape. At longer wavelengths the extinction spectra are independent of size but depend on particle refractive index and shape. Experimental data support these simplifications. For any convex smoke particle, the extinction coefficient can be maximized by maximizing the surface area per unit mass. The wavelength range over which maximum extinction extends can be increased by appropriate choice of refractive index and shape such as metal filaments and flakes.

All inventory and experimental military smokes consist of a collection of aerosol particles which are nonuniform in size and orientation. This considerably simplifies the extinction spectra produced by a smoke cloud. The extinction spectrum for each particle individually is complicated and depends on size and orientation as well as shape and refractive index. However, when single particle spectra are superimposed to form the extinction spectrum of a smoke cloud, the narrow peaks and troughs of individual particle spectra are averaged out and a smoother cloud spectrum emerges.

Generally the cloud spectrum becomes flat at wavelengths somewhat shorter than the refractive index modulus multiplied by the smallest particle dimension. At wavelengths somewhat longer than this, the spectrum becomes Rayleigh with peaks located where the refractive index undergoes anomalous dispersion. The height of each peak is limited to the extinction plateau level at shorter wavelengths. At the shorter wavelengths in the plateau region, extinction is independent of complex refractive index and depends only on particle shape and size as represented by the particle surface area per unit mass. This applies to convex particles and the convex envelope around reentrant particles. On the other hand, in the Rayleigh region extinction depends on particle shape and complex refractive index and is independent of particle size. The transition region between the averaged resonance plateau and Rayleigh region looks like a combination of these two regions because the smaller particles in the polydispersion have a Rayleigh spectrum while the larger particles in

# UNCLASSIFIED

**UNCLASSIFIED**

the polydispersion have flat spectra. For the typically broad polydispersions which we aerosolize in our test chamber, the transition region often extends throughout much of the infrared from 2.5 microns to 14 microns wavelength.

Examples of aerosols which exist in the averaged resonance region producing flat spectra throughout the infrared are metal flakes and fibers. Dielectric spherical, irregular, flake and fiber particles produce Rayleigh spectra in the infrared when the mass median diameter or thickness is less than about half a micron, while diameters greater than this produce transition region extinction spectra. Within the transition region, smaller particle Rayleigh spectra are superimposed over flat averaged resonance spectra of the larger particles. To obtain flat spectra in the infrared with dielectric particles it is necessary to have fairly monodisperse samples with diameters or thicknesses greater than several microns, or typically polydisperse samples with mass median diameters or thicknesses so large that the aerosol settles out of the chamber volume in less time than is required to obtain a spectral radiometer scan. Conductive irregular or spherical particles often possess Rayleigh spectra in the infrared, but flat spectra commence above smaller particle dimensions than for dielectric particles.

Starting with a particle much larger than the wavelength in question and reducing its size we can increase its surface area to mass ratio, thereby improving its ability to extinguish radiation until an upper limit is realized which is the Rayleigh limit where all material becomes optically active. At visible wavelengths this upper limit would be greatest for metal spheres, while at infrared and millimeter wavelengths the upper limit would be greatest for metal flakes or fibers.

A generalized extinction spectrum would have a flat top at shorter wavelengths, while at longer wavelengths there would be a slope inversely proportional to wavelength for an absorber and inversely proportional to wavelength to the fourth power for a dielectric. Onto this slope is superimposed the structure originating from the wavelength dependence of the refractive index. As the particle size is reduced, the flat spectral top moves upward, but the wavelength at which the negative slope commences gets shorter. Thus, the cost for higher extinction is a reduction in the wavelength breadth of the extinction. Only by choosing a flake or fiber shape and a metallic composition can the onset of the negative slope be pushed out to a maximum wavelength, thereby maximizing extinction breadth and permitting the flat spectrum top to be maximized by size reduction. For a metal flake of a given thickness, the onset of negative slope begins at a wavelength four times greater than for a metal fiber having a diameter equal to the flake thickness.

**UNCLASSIFIED**

**UNCLASSIFIED****SOME ASPECTS OF LIGHT SCATTERING FROM CLOUDS  
OF REGULARLY AND IRREGULARLY SHAPED PARTICLES**

D.K. Anker\*  
Logica Limited  
64 Newman St., London

**ABSTRACT**

This paper presents an overview of the work presently being carried out in the theoretical study of scattering of radiation from irregularly shaped aerosols. The problem considered is that when the incident wavelength is of similar order to particle size. The particles under study are spherical, cylindrical or disc-shaped and their complex refractive indices can vary over a wide range to cover dielectrics or metals. The scattering cross-sections are obtained in the single-particle case and are then fed into a cloud model using a Monte-Carlo simulation package. Initial results are shown to indicate good agreement with experiment. Further work involving finite element techniques to tackle arbitrary shapes is outlined.

\* This work was carried out under contract ML32B/326 for the Chemical Defence Establishment, Porton Down, Wiltshire.

**UNCLASSIFIED**

**UNCLASSIFIED**

## I. INTRODUCTION

At CDE, the screening and transmittance properties of clouds of various particle types (e.g. droplets, smokes and aluminium flakes) have been studied. The results obtained by modelling single particle scattering have been fed into a radiative transfer model to examine the backward and forward scattering from clouds of these particles.

Particle types considered so far have been spheres, cylinders and circular discs. Cloud shapes have been either parallel slabs or half conical.

Scattering from spheres is well-understood, and it has been shown that clouds of slightly non-spherical particles can be accurately modelled by clouds of spheres, (c.f. Greenberg 1979), the main difference arising in the backscatter cross-section. The spherical scattering will be a maximum or minimum, for randomly oriented particles, depending on the refractive index. Clearly, the reason for good agreement is due to the averaging effect over all possible random orientations, smoothing over irregularities. Therefore, when using the results of single spherical scattering in our radiative transfer simulation, the results are expected to be in reasonable agreement with experiment. This is borne out in a later section.

However, there are certain particle types which have a regular shape but tend to take up a given alignment when falling with terminal velocity in a fluid (e.g. air). This is true for needle-like particles which fall with their axis of symmetry almost horizontal. The theory behind this is well-known in fluid-mechanics (c.f. H. Lamb, 1932).

Further, investigation of particles with internal structure has begun with the simple problem of multi-layered spheres, with each layer of material having a different refractive index. An extension of the programme to more elaborate internal structure (such as honeycombed or channelled) awaits further development using finite element analysis.

**UNCLASSIFIED**

Different refractive indices,  $m = m' + im''$ , for the spherical materials have been studied, ranging from dielectrics (with  $0.1 \leq m' \leq 15$ ) to metals (with the absorptive index  $-10 \leq m'' \leq 0$ ). Attention has been focused on a more limited range, the results of section 4 being for 38% sulphuric acid with  $m = 1.214 - i 0.252$  at wavelength,  $\lambda$ , equal to  $8.0 \mu\text{m}$ .

Radii, again, have been arbitrary, but the resonant region has been of most interest.

Turning to irregular particles, ie particles with edges, the one most under examination at present is the arbitrarily thin, circular conducting disc. These have been studied in an attempt to model flakes of aluminium. They have been separated out as particles for research in their own right due to the inability of spheroidal particles to model them accurately. Their tendency to align horizontally as they fall with steady motion means that averaging over all random orientations will give incorrect results. Some work has already been done on discs with finite thickness and low conductivity by Wei and Chu (1980). However, some problems arise in taking the thickness arbitrarily thin or allowing conductivity to grow large.

## 2. SINGLE PARTICLE SCATTERING

The scattering theory for homogenous spherical particles of complex refractive index is thoroughly documented in textbooks (e.g. J. Stratton (1941)). Scattering from a concentric multi-layered sphere can also be explained, using Mie theory. Therefore, in this section we shall briefly consider two more interesting particle types: the thin circular conducting disc, and arbitrarily shaped inhomogenous particles such as honeycombed spheres or channelled spheres. The first of these particle types has been studied to model thin aluminium flakes. The second particle type, the honeycombed and channelled spheres, are examined since several atmospheric dust particles are of this type (e.g. fly-ash from coal and oil fired power stations).

Considering the disc problem, some progress has been made. The major difficulty lies in solving numerically the integral equation for the induced current,  $J$ , in the disc.

**UNCLASSIFIED**

## UNCLASSIFIED

Summarising the theory, the electromagnetic field,  $E$ , impinging on a perfectly conducting disc, can be expressed:

$$\underline{E} = \underline{E}_0 + \frac{1}{4\pi i \epsilon_0 \omega} (\nabla \nabla \cdot + k^2) \int_{S'} \underline{G} \cdot \underline{G} dS' , \quad (1)$$

where  $\underline{E}_0$  is the incident field,

$$G \text{ is the Green's Function } = \frac{e^{-ik|\underline{R}-\underline{R}'|}}{|\underline{R}-\underline{R}'|}$$

$S'$  is the surface of the disc,  $0 \leq R' \leq a$ ,

$k = 2\pi/\lambda$ ,  $\lambda$  = incident wavelength.

If the problem is restricted to the surface of the conducting disc, no electric field,  $E$ , can exist. Also, all operators are reduced to two-dimensional operators in the surface of the disc.

It can be shown that, by expressing the radial current,  $J_r$ , azimuthal current,  $J_\phi$ , and charge density,  $\rho$  ( $= \nabla' \cdot \underline{J}$ ), in terms of Fourier sums in  $\phi$ , the following set of equations result from equation (1),

$$e^{-\frac{i}{k} (n+1)\pi} ( \text{MODE } \sec \theta_0 + i (1-\text{MODE}) ) J_{n+1} (kr \sin \theta_0) + A_n J_{n+1} (kr) \\ + k^2 \int_0^a r' a_n G_{n+1} dr' = 0 \quad (2)$$

$$e^{-\frac{i}{k} (n-1)\pi} ( \text{MODE } \sec \theta_0 - i (1-\text{MODE}) ) J_{n-1} (kr \sin \theta_0) + A_n J_{n-1} (kr) \\ + k^2 \int_0^a r' a_n G_{n-1} dr' = 0 \quad (3)$$

$$e^{-\frac{i}{k} (n+1)\pi} \tan \theta_0 \text{ MODE } J_n (kr \sin \theta_0) + A_n J_n (kr) + k \int_0^a r' C_n G_n dr' = 0 \quad (4)$$

for  $n = 0, \pm 1, \dots$

## UNCLASSIFIED

where

$$\text{MODE} = \begin{cases} 1 & \text{if TM-mode,} \\ 0 & \text{if TE-mode,} \end{cases}$$

$\theta_0$  = angle between incident radiation and axis of symmetry,

$J_n$  = Bessel function of 1st kind of n-th order,

$$G_n = \int_0^{2\pi} G(t) \cos nt dt,$$

$$J_r = \frac{1}{2} \sum_{n=-\infty}^{\infty} (a_n + b_n) e^{inx},$$

$$J_z = -\frac{1}{2} \sum_{n=-\infty}^{\infty} (a_n - b_n) e^{inx},$$

$$\rho = \sum_{n=-\infty}^{\infty} \rho_n e^{inx},$$

$A_n$  is unknown but is related to  $a_n, b_n$  via

$$\rho = \Psi' \cdot J$$

It can easily be deduced that in the Rayleigh region, the expressions for the O(1) current components are:

$$J_r = \frac{4}{3\pi^2} (a^2 - r^2)^{\frac{1}{2}} \left\{ \cos \theta_0 \text{ MODE } \cos \theta_0 + (1-\text{MODE}) (1 - \frac{1}{2} \sin^2 \theta_0) \sin \theta_0 \right\} + O(ka)$$

$$J_z = \frac{irk^{-1} \sin \theta_0 (1-\text{MODE})}{\pi^2 (a^2 - r^2)^{\frac{1}{2}}} + \frac{4}{3\pi^2} (a^2 - r^2)^{-\frac{1}{2}} \left[ \left\{ a^2 - \frac{1}{4} r^2 + (r^2 - \frac{1}{4} a^2) \sin^2 \theta_0 \right\} X \right. \\ \left. (1-\text{MODE}) \cos \theta_0 - \left\{ a^2 - \frac{1}{4} r^2 \right\} X \right. \\ \left. \cos \theta_0 \text{ MODE } \sin \theta_0 \right] + O(ka)$$

UNCLASSIFIED

## UNCLASSIFIED

where

$k = 2\pi/\lambda$ , and  $\lambda$  = wavelength of incident light,

$r$  = radial distance from disc centre,

$a$  = radius of disc

$\theta_0$  = vertical angle of incident radiation

$$\text{Mode} = \begin{cases} 0, \text{ TE-Mode} \\ 1, \text{ TM-Mode} \end{cases}$$

The total scattering cross-section becomes,

$$\sigma_{\text{TOT}} = \frac{128 k^4 a^4}{27 \pi^2} \left\{ 1 + \left( \frac{1}{4} (1-\text{MODE})^2 - \text{MODE}^2 \right) \sin^2 \theta_0 \right\}$$

It should be noted that, although the expression for the total scattering cross-section is finite and non-zero, the azimuthal current reaches infinitely large values as the disc edge is approached,

$$J_\phi \rightarrow (a^2 - r^2)^{-\frac{1}{2}}$$

This immediately points to a boundary layer problem, in which the current is brought under control by a rapid change across a very narrow annulus around the disc edge. In fact the corresponding problem in acoustics is considered by Crighton and Leppington (1973). They considered sound impinging on a semi-infinite plate of vanishing thickness,  $2a$ , and found a layer building up at the edge of width  $O(ka)$ . Within this layer, the velocity potential became zero at the exact plate edge.

Without full analysis, for our model, we have computed  $J_\phi$  up to a thin layer at the edge, wherein the  $J_\phi$  is approximated by a linear function from its value at the inner edge of this layer, to zero at the exact disc edge. The integration scheme for calculating  $J_r$ ,  $J_\phi$  is involved and complicated, and is described elsewhere, Anker (1981),

**UNCLASSIFIED**

but is based on work by Jones and Allami.

In order to check that a sufficient number of Fourier modes for  $J_r, J_g$  were taken, use of the Optical Theorem was made in order to obtain a comparison to the total cross-section calculated using the full 3-d integration of the bi-static cross-section.

$$\sigma_{TOT} = \frac{4\pi}{k} \text{Im}(F)$$

$$\sigma_{BIS} = |F|^2$$

$$\sigma_{TOT} = \int_0^{\pi} d\theta \int_0^{2\pi} d\phi \sin\theta \sigma_{BIS}$$

where  $F(\theta, \phi)$  = scattering amplitude.

So far, results in the Rayleigh region look promising, but larger radii discs have yet to be fully tested.

As soon as satisfactory results are obtained for the disc, it is thought that their incorporation into the RTSP will be the next step in comparing results with experiment.

As for arbitrarily shaped particles, the only general approach, which does not require expansions in many spherical harmonics or make other more restrictive assumptions about size and shape, is the global finite-element method outlined by Yeh, Ha, Dong and Brown (1979).

### 3. RADIATIVE TRANSFER SIMULATION PACKAGE

To model the transmission of light through a cloud of particles, an elementary, though quite flexible approach was taken. With the passage of, for example laser light in mind, the scattering of a coherent beam of photons was modelled by a Radiative Transfer Simulation Package (RTSP) using Monte-Carlo techniques.

**UNCLASSIFIED**

**UNCLASSIFIED**

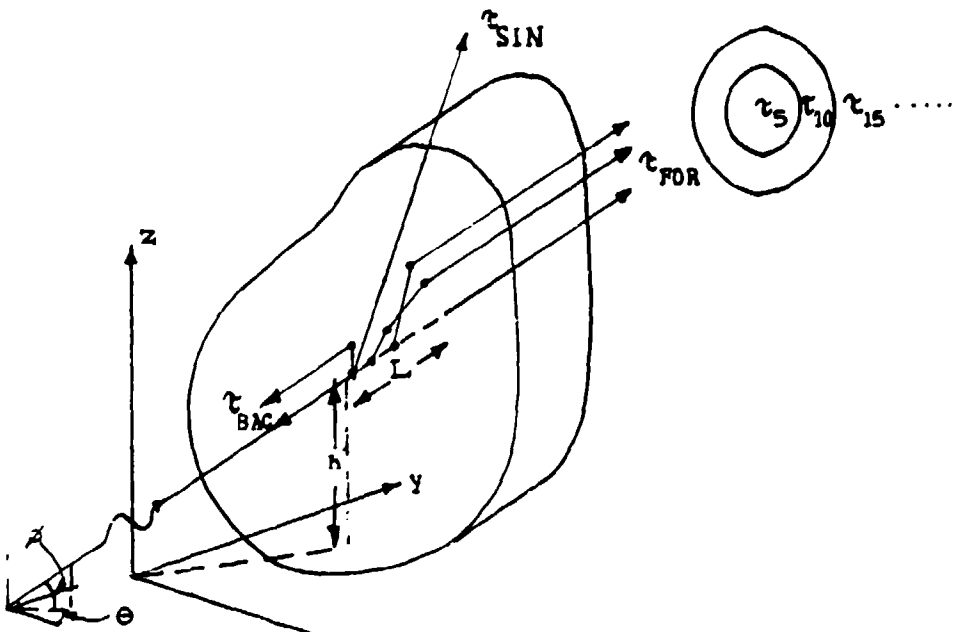
The exact macroscopic solution to the problem cannot be found for any general cloud shape, any particle size-distribution, material distribution, or number distribution in 3-d. We therefore have looked at other methods of solution and focused on a Monte-Carlo technique. The method involves tracking simulated photons from collision to collision within the cloud. The assumption that the photons do not interact with each other during their passage through the cloud (coherence) allows simplifications, in that photons travel in straight lines between collisions with cloud particles. (If necessary, we can relax this constraint in a later version of the RTSP, but a larger sample of input photons will be required to model photon-photon interactions). Theoretically, if the inter-particle distances are several times larger than the wavelength of input light, interference effects should be almost negligible.

In the next section the experimental results are compared to those of the RTSP, where inter-particle spacing is  $O(10^{-4} \text{ m})$  and the incident wavelength,  $\lambda$ , is  $O(10^{-6}\text{-}10^{-5} \text{ m})$ .

In the RTSP, each photon is followed from the point at which the beam of incident radiation strikes the cloud, until it either is absorbed or escapes from the cloud (back into the air or into the ground which is assumed perfectly absorbing). When the photon is emitted from the cloud, various scores are incremented. There is a score kept for photons contributing to each of the forward-scattering,  $\tau_{\text{FOR}}$  total -scattering,  $\tau_{\text{TOT}}$ , and single-scattering,  $\tau_{\text{SIN}}$  totals. Additionally, if scattering into angular boxes is required, scores are kept for each angular box. An illustration of these scattering coefficients is given in figure 1. The backscattered photons are also observed.

The simulation must continue until the lowest of these scores is above some specified value. The higher the value, the more accurate the results. In fact, the scattered photons emitted from the cloud satisfy a binomial distribution, and it can be shown that the accuracy in counting these random events (either the photon is emitted with probability  $p$  or not emitted with probability  $1-p$ ) is  $n^{-1}$ , where  $n$  is the number of successful events, given  $np^{-1}$  trial events.

UNCLASSIFIED



$\tau_{FOR}$  = Forward Scattering

$\tau_{BAC}$  = Backward Scattering

$\tau_{5i}$  = Scattering into angular box  $5(i-1) \leq \theta < 5i$ ,  $i=1, \dots, 18$

$\tau_{SIN}$  = Single Scatter

$$\tau_{TOT} = \text{Total Scattering} = \tau_{FOR} + (\tau_5 - \tau_{FOR}) + \sum_{i=2}^{18} \tau_{5i}$$

$h$  = height of entry above ground.  $0^\circ \leq \theta \leq 360^\circ$ ,  $-90^\circ \leq \phi \leq 90^\circ$

$\theta, \phi$  define angle of incidence

$L$  = Cloud Thickness

FIGURE I. RTSP SCATTERING COEFFICIENTS

UNCLASSIFIED

**UNCLASSIFIED**

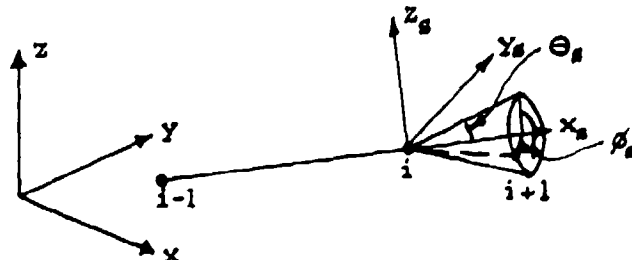
As well as the scattering coefficients of the cloud, two other points of interest are noted: the number of collisions undergone by each photon, the point of exit from the cloud.

The incident beam is specified by 3 parameters shown in figure I; the angle of incidence which requires the  $\theta, \phi$  values and the height of entry,  $h$ , above ground.

For the parallel slab, only the thickness,  $L$ , needs to be defined. For the half-cone model, refer to Evans and Jarvis(1980).

As the photon trajectory is followed through the cloud, it will collide a number of times with the cloud particles. At the  $i$ -th collision, probabilities of several scattering parameters are used to calculate, in Monte-Carlo fashion: scattering angle, distance to the  $(i+1)$ -th collision and scatterer-type.

The scattering angle consists of two angles, as shown in Figure II.



$X_s$  = line of sight between  $(i-1)$ -th collision and  $i$ -th collision,

$Z_s$  = axis perpendicular to  $X_s$  in  $X_s - Z$  plane,

$\theta_s$  = azimuthal scattering angle,

$\phi_s$  = conical scattering angle.

FIGURE II. RTSP SCATTERING ANGLE

**UNCLASSIFIED**

The probability of scattering into angle  $\theta$  is given by

$$P(\theta) d\theta = \frac{\text{INTEN}(\theta)}{Q_{\text{SCA}}} \frac{2 \sin(\theta)}{R^2} d\theta,$$

$R$  = radius of scatterer in reduced units,

$Q_{\text{SCA}}$  = Scattering efficiency,

$\text{INTEN}(\theta)$  = Scattering Intensity

A cumulative distribution is formed,

$$F(\theta) = \sum_{x=0}^{x=\theta} P(x)$$

the discrete sum replacing the exact integral in the above equation.

To select angle  $\theta$ , a random number,  $r$ , is chosen,  $0 \leq r \leq 1$ , and the cumulative distributions are scanned and  $F(\theta_{i+1})$  is chosen with  $F(\theta_i) \leq r \leq F(\theta_{i+1})$ .

To determine  $\phi$ , since its probability distribution is uniform, a random number between 0 and  $2\pi$  is chosen.

The inter-collision distance is chosen by taking the path length,  $D$ , from the last collision to the edge of the cloud, and dividing it into equal segments. The cumulative distribution for the distance is

$$F(x_M) = \sum_{i=1}^M \frac{1}{d} e^{-i \Delta/d}$$

where  $d$  = mean free path,

$M$  = No. divisions of path length,  $D$ ,

$\Delta = D/M$ .

**UNCLASSIFIED**

**UNCLASSIFIED**

Then, a random number,  $r$ , is again chosen  $0 \leq r \leq 1$  and  $F(r_{m+1})$  is chosen,  $F(r_m) \leq r \leq F(r_{m+1})$ .

Finally, choice of scatterer type in a polydispersed cloud depends on whether the particles have a Rosin-Rammler distribution or log-normal distribution. The  $n$  particle types are arranged in ascending radius,  $r$ , where

$$r_1 < r_2 < \dots < r_n.$$

radius ranges are then defined,

$$\left[0, \frac{1}{2}(r_1 + r_2)\right], \left[\frac{1}{2}(r_1 + r_2), \frac{1}{2}(r_2 + r_3)\right], \dots, \left[\frac{1}{2}(r_{n-1} + r_n), r_n\right]$$

For each range, the probability of a particle radius,  $r_i$ , lying within it, is computed and associated with the relevant type identifier,  $\frac{1}{2}(r_{i-1} + r_i) \leq r_i \leq \frac{1}{2}(r_i + r_{i+1})$ .

**4. EXPERIMENTAL RESULTS**

The results of the RTSP were firstly compared with the results predicted using the simple theory of Beer-Lambert,

$$T = e^{-\alpha CL}$$

where,

- $T$  = transmittance,
- $\alpha$  = mass extinction coefficient,
- $C$  = aerosol concentration,
- $L$  = radiation path-length.

Various values for each of  $\alpha$ ,  $C$  and  $L$  were taken and the transmittance,  $T$ , was compared with  $T_{FOR}$  from the RTSP. Results within 2% agreement were found in several simple cases. An example of one of these test runs is shown in table 1.

**UNCLASSIFIED**

## UNCLASSIFIED

TABLE 1. PREDICTED TRANSMITTANCE VALUES FOR  
A 38% SULPHURIC ACID AEROSOL.

$$\lambda = 8.0 \mu\text{m}, \quad L = 3\text{m}, \quad \phi = 0^\circ, \quad \theta = 0^\circ$$

Aerosol Concentration / g m <sup>-3</sup>	Forward Transmittance RTSP (Parallel slab, log-normal distribution)	Transmittance Beer-Lambert ( $\alpha = 0.303 \text{ m}^2 \text{g}^{-1}$ )
0.1	0.9119	0.9130
0.2	0.8304	0.8337
0.4	0.6934	0.6952
0.8	0.4841	0.4833
1.2	0.3363	0.3329
1.6	0.2330	0.2349

With the RTSP appearing to give results as expected, it was then run to simulate experimental data.

Experimental measurements of a scattered beam of light through a cloud of 38% Sulphuric Acid droplets with refractive index  $m = 1.214 - i 0.252$  at wavelength  $8.0 \mu\text{m}$  are shown in Figure 3 (reproduced from Carlon and Anderson (1979) and Evans and Jarvis, (1980)).

UNCLASSIFIED

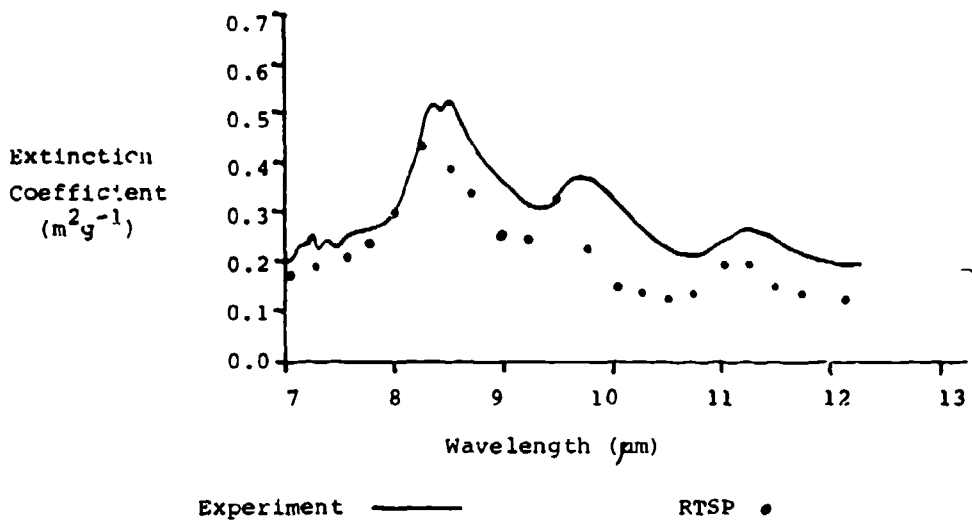
**UNCLASSIFIED**

FIGURE III. RTSP AND EXPERIMENTAL DATA

In the RTSP the cloud parameters were taken as follows: depth = 3.0m, height of beam entry = 1.5m, normal incidence. The aerosol parameters were: geometric mean radius for a log-normal distribution =  $0.424 \mu m$ , geometric standard deviation for a log normal aerosol size distribution = 1.5.

The experimental parameters were not altogether too clear from Carlon and Anderson's paper, but values similar to those above were inferred (c.f. Evans and Jarvis (1980) for details).

The RTSP results shown are significantly lower than the corresponding experimental results. There are several possible reasons for this disagreement which we expect to resolve with both further runs of the RTSP and clearer definition of experimental parameters.

The RTSP assumes uniform cloud concentration of particles across the cloud. This is unrealistic, and so a Gaussian distribution is being incorporated to model the cloud out on the field.

**UNCLASSIFIED**

**UNCLASSIFIED**

The assumption of particle size distribution is also somewhat suspect. Further, more tightly controlled experimental work must be done before a more definite comparison with the RTSP results can be made. However, some of the quantitative features are certainly present in the RTSP. In Evans and Jarvis (1980),  $\lambda = 0.63 \mu\text{m}$ , the cloud is shown to be scattering, while at  $\lambda = 8.0 \mu\text{m}$ , it is strongly absorbing in agreement with Carlon and Anderson (1979).

**UNCLASSIFIED**

**UNCLASSIFIED**

REFERENCES

Anker, D.K. "Thin Disc Scattering Package", Internal Report Logica Ltd., London (1981)

Carlon, H.R., and Anderson, D.H. "Aerosol Spectroscopy in the Infrared".  
U.S. Army Edgewood Arsenal, Aberdeen Proving Ground (1979).

Crighton and Leppington, "Singular Perturbation Methods in Acoustics: Diffraction by  
a Plate of Finite Thickness", Proc. Roy. Soc., 335A, 313-339, (1973).

Greenberg, J.M. "Light Scattering by Irregularly Shaped Particles", Editor, D. Schuerman,  
Plenum Press, N.Y. (1980).

Lamb, H. "Hydrodynamics" 6th edition. Cambridge University Press (1932).

Stratton, J., "Electromagnetic Theory", McGraw Hill, (1941).

Weil, H. and Chu, C.M. "Scattering and Absorption by Thin Flat Aerosols", Applied  
Optics, 19, 12, 2066-2071, (1980).

Yeh, C., Ha, K., Deng, S.B., and Brown, N.P. "Single-mode Optical Waveguides", Applied  
Optics, 18, 10, 1490-1504 (1979).

# UNCLASSIFIED

B-13

## A SEMIQUANTITATIVE MODEL FOR THE PREDICTION OF THE PERSISTENCY OF MULTICOMPONENT OIL SMOKES

by  
Glenn O. Rubel

### 1. INTRODUCTION

To model accurately the time-dependent obscuration efficiency of military screening smokes, knowledge of the evolving particle size distribution function is required. The dynamics of an oil aerosol is controlled by such processes as nucleation, coagulation and heterogeneous condensation/evaporation. Both nucleation and droplet vapor transfer are dependent on the vapor pressure of the liquid comprising the droplet. For multicomponent oils such as fog oil SGP-2, #2 diesel fuel, and PEG 200, the vapor pressure of the bulk liquid is composition dependent. Recently, Baek et al.<sup>1</sup> measured the evaporation rates of several multicomponent oils under vacuum and found an approximate relationship between vapor pressure and species molecular weight.

The purpose of this study is to provide experimental data on the evaporation rates of fog oil SGP-2, #2 diesel fuel, and PEG 200 droplets at one atmosphere.

From the evaporation data, vapor pressure/molecular weight correlations have been developed and compared to those relationships derived from vacuum evaporation.<sup>1</sup> Satisfactory agreement has been found, indicating the vapor pressure correlations to be a function of the specific material and not the particular process under study. In addition, from the evaporation data, correlations of vapor pressure and the percent mass evaporated are developed for the multicomponent oils. The data indicate that, while the evaporation rates of the mixture oils differ significantly, all oils can be characterized by a power law relationship between vapor pressure and percent mass evaporated.

A semiquantitative model is presented for the evaporation of multicomponent oil smokes. Continuum diffusion theory, coupled with Milburn's<sup>2</sup> analysis of evaporating water clouds, predicts that the persistency of any smoke is a function of cloud radius and specific cloud liquid. It is shown that (1) #2 diesel fuel evaporates an order of magnitude faster than PEG 200 and even more quickly than fog oil SGP-2, (2) a cloud of PEG 200 will evaporate at the same rate as one of fog oil for the first 10% mass evaporated and, thereafter, the persistency of the fog oil cloud exceeds that of PEG 200, (3) the persistency of all oil smokes increases with increasing cloud radius.

# UNCLASSIFIED

573

# UNCLASSIFIED

B-13

It is additionally shown that the mixture vapor pressure of fog oil SGF-2 will vary considerably from stock to stock. Finally, it is demonstrated that the vapor pressure of recondensed fog oil SGF-2 is about twice as high as the vapor pressure of the prevaporized fog oil. One possible explanation for this finding is that the oil mixture is undergoing thermal cracking during the vaporization process.

## 2. EXPERIMENTAL PROCEDURE

The experimental technique developed by Schweizer and Hanson<sup>3</sup> and later modified by Frickel et al.<sup>4</sup> was used to measure the evaporation rates of individual multicomponent oil droplets. A schematic of the experimental setup is illustrated in figure 1. The liquid droplet is electrostatically atomized by applying a high direct-current voltage to a capillary tube filled with the liquid of interest. The droplet is horizontally stabilized in the chamber by applying an alternating-current voltage across a bihyperboloidal electrode. The charged droplet is centered vertically in the chamber by applying a gravity-balancing direct-current voltage. The droplet diameter is determined optically by using a 35-mm objective in conjunction with a Vicker Image Eye Splitter. Successive droplet masses are found from the time-dependent balancing voltage by assuming constant charge number. Rubel<sup>5</sup> showed that, by controlling the temperature of the chamber and the chamber replenishment rate, the instantaneous vapor pressure of the evaporating droplet can be determined as a function of percent mass evaporated.

## EXPERIMENTAL SETUP

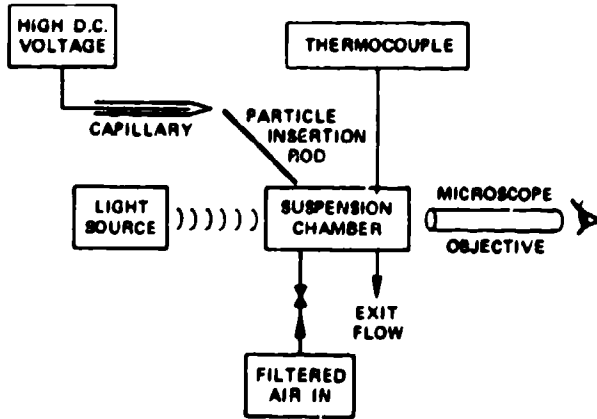


Figure 1. Experimental Setup for the Measurement of the Evaporation

Rates of Multicomponent Oil Droplets

# UNCLASSIFIED

B-13

## 3. RESULTS

3.1 Correlations of Vapor Pressure and Percent Mass Evaporated. Figure 2 shows the evaporation rates of fog oil SGP-2, #2 diesel fuel, and PEG 200 droplets evaporating at a temperature of 40° C. The ordinate  $M_e$  is the percent mass evaporated and is defined as:

$$M_e = (1 - M_R) \times 100 \quad (1)$$

where

$$M_R = M(t)/M(t_0).$$

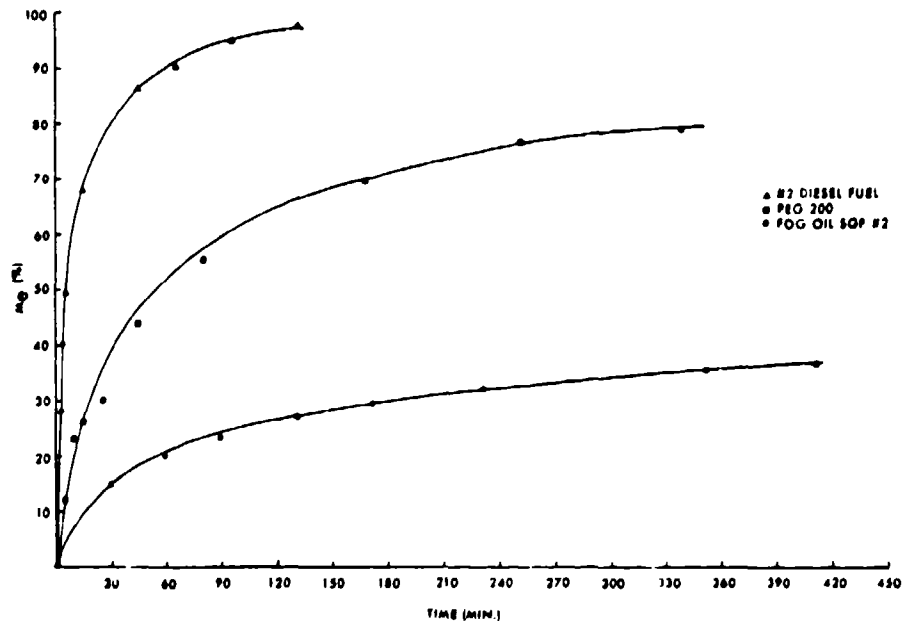


Figure 2. Percent Mass Evaporated as a Function of Time for Various Multicomponent Oils as Derived from Droplet Evaporation Studies

The initial droplet mass,  $M(t_0)$ , is determined from the optically measured diameter and the previously known material bulk density. In the present data, the material density is assumed invariant during evaporation.

# UNCLASSIFIED

575

# UNCLASSIFIED

B-13

Clearly, #2 diesel fuel is considerably more volatile than PEG 200, and fog oil SGP-2 is the least volatile oil. To gain further appreciation for the differences in the multicomponent oils, the correlations of vapor pressure and percent mass remaining are found. Rubel<sup>5</sup> showed that, by numerically solving for the mass decay rate and employing continuum diffusion theory, the total vapor pressure of the droplet as a function of percent mass remaining could be obtained. Figure 3 presents the vapor pressure data in logarithmic coordinates for the three oils of interest. The data indicate a strong linear dependence between the logarithmic percent mass remaining and the logarithmic vapor pressure.

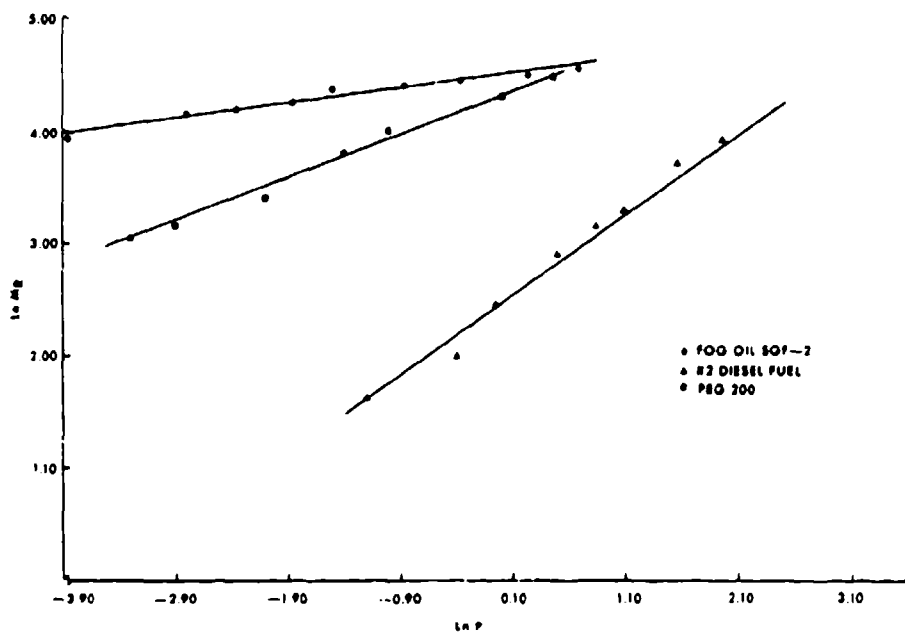


Figure 3. Percent Mass Remaining Versus Droplet Vapor Pressure  
as Derived from Droplet Evaporation Rate Measurements  
and Continuum Diffusion Theory

**UNCLASSIFIED**

B-13

A least-squares linear regression analysis of the data permits the following relationships:

## Fog oil SGF-2

$$\ln P = -3.348 \ln I + 7.452 \ln M_R \quad 50 \leq M_R \leq 100$$

## #2 Diesel Fuel

$$\ln P = -3.213 + 1.310 \ln M_R \quad 10 \leq M_R \leq 100 \quad (2)$$

## PBG 200

$$\ln P = 1.070 \ln I + 2.462 \ln M_R \quad 20 \leq M_R \leq 100$$

The above relations are valid at  $T = 40^{\circ}\text{C}$  and account for 98% of the data field. This characteristic linear relationship has been found to be valid for other homologous series such as dibasic esters and mineral oil.<sup>6</sup> The characteristic vapor pressure curves reveal that, while PBG 200 and fog oil SGF-2 exhibit similar volatilities during the early stages of evaporation, fog oil becomes progressively less volatile than PBG 200 as evaporation proceeds. These findings are consistent with the yield performance measurements made by Vervier and Anderson.<sup>7</sup>

3.2 Persistency of Multicomponent Oil Smokes. Measurements by Vervier and Anderson<sup>7</sup> indicate fog oil, diesel fuel, and PBG 200 smokes are comprised primarily of micron- and submicron-sized oil droplets. The employment of data derived from supermicron-sized droplet evaporation may seem inappropriate for oil cloud modeling. However, it is demonstrated in the appendix that, if the multicomponent oil constitutes a thermodynamically ideal solution, then the derived vapor pressure correlations are independent of the initial droplet diameter studied.

The class of equation (2) may be cast into the general form

$$P = a(M_R)^b \quad (3)$$

which when substituted into the continuum mass flux relation gives

$$\frac{dM}{dt} = \frac{-2\pi \overline{DM}_W \left(\frac{6}{\pi D}\right)^{1/3} a M^b + 1/3}{RT M(t_0)^b} \quad (4)$$

**UNCLASSIFIED**

**UNCLASSIFIED**

Integration of equation (4) results in the evaporation law for isolated multicomponent oil droplets

$$M(t)^{2/3} - b - M(t_0)^{2/3} - b = -A(t-t_0) \quad (5)$$

$$A = \frac{2\pi D M_w T_0}{R T M(t_0)^b} \left( \frac{6}{5} \right)^{1/3} b^{(2/3 - b)}$$

where

If  $b = 0$ , which implies constant droplet vapor pressure, the multicomponent evaporation law reduces to the single component evaporation law.

The cloud droplets comprising an oil smoke do not evaporate as isolated oil droplets. As the entire cloud evaporates, a source of vapor is generated which tends to retard the evaporation rate of existing droplets. The vapor concentration and temperature field surrounding the oil droplets is a complex function of multicomponent droplet evaporation, and molecular and turbulent diffusion. An accurate model which incorporates the previously mentioned processes would be intractable and beyond the scope of this study. Furthermore, even if a detailed model was constructed, the results would be at most semiquantitative due to the statistical nature of turbulence. For this reason, an approximate method is used to predict the persistency of oil obscuring smokes.

The cloud persistency model is based on the analysis developed by Milburn<sup>2</sup> for the evaporation of water clouds. Milburn considered the problem of an evaporating water cloud undergoing molecular diffusion to a vapor-free environment. Assuming the droplets achieve steady state conditions instantaneously, Milburn solved for the vapor and temperature fields inside and outside a water cloud. Under the condition of a free boundary, a cloud equation was developed and solved for during the early stages of evaporation. It was shown that the cloud evaporated either internally or at the cloud perimeter depending on the cloudiness factor  $\delta^2$  where

$$\delta^2 = 4nR_c^2 r_0 / \pi \quad (6)$$

If  $\delta^2 \gg 1$  the cloud evaporates primarily at the cloud perimeter. For cloud particle number concentrations of  $10^6$  P/cc the cloudiness factor greatly exceeds unity, implying oil clouds primarily evaporate at the perimeter. It would seem reasonable to state that the persistency of an oil smoke is governed by the evaporation rates of the oil droplets situated at the perimeter of the cloud.

# UNCLASSIFIED

B-13

Milburn derived an evaporation law for such droplets and found that the evaporation rate of perimeter droplets is  $(\pi\delta)^{-1}$ , the evaporation rate of isolated droplets. Consequently the persistency of oil smokes is approximated by equation (5) by taking into account the cloudiness factor  $\pi\delta$ .

Figure 4 depicts the evaporation of fog oil SGP-2, #2 diesel fuel, and PBG 200 clouds at 25° C. Mixture vapor pressures have been extrapolated from 40° C to 25° C using the Clausius Clapeyron equation. The persistency of the oil clouds is parameterized with respect to cloud radius R.

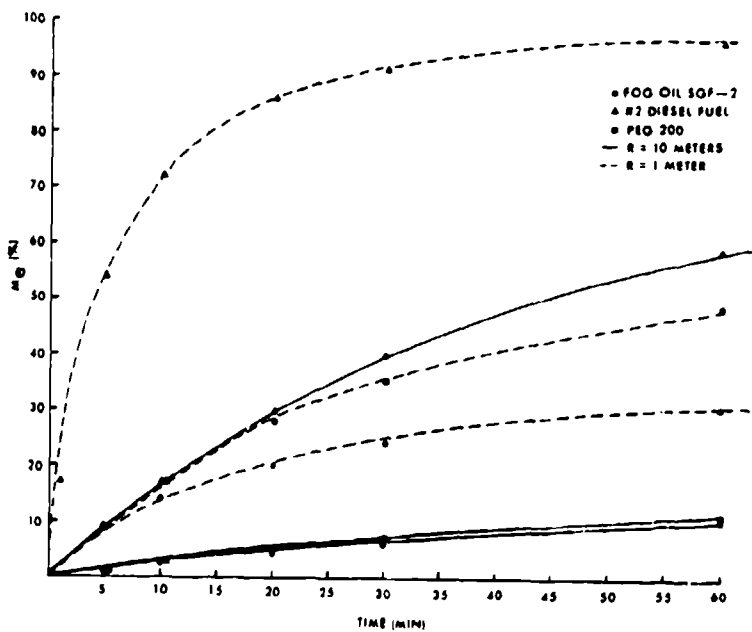


Figure 4. Multicomponent Oil Cloud Persistency Values As Calculated from a Semiempirical Model Based on Milburn's Analysis of Evaporating Water Clouds and Vapor Pressure Correlations Derived from Droplet Evaporation Studies

# UNCLASSIFIED

**UNCLASSIFIED**

Inspection of figure 4 provides several conclusions. First the persistency of #2 diesel fuel is significantly less than the persistency of either PEG 200 or fog oil SGF-2. Over a one-hour period, fog oil SGF-2 persists the longest; however, over the first 10% mass evaporated, fog oil and PEG 200 persist for approximately the same amount of time. These findings are consistent with previous field observations. The fact that PEG 200 and fog oil evaporate similarly over the first 10% mass evaporated can be predicted from figure 3. Here PEG 200 and fog oil SGF-2 possess similar vapor pressures over the initial phases of evaporation. As evaporation proceeds, the vapor pressures diverge and so do the persistency characteristics as seen in figure 4.

Second, the greater the cloud radius, the greater the cloud persistency. This is true of all oil smokes, although the persistency level is more sensitive to cloud radius for the more volatile liquids. In fact, an order of magnitude increase in cloud radius of a #2 diesel fuel smoke will cause the evaporation rate of such a cloud to match the evaporation rate of a relatively nonvolatile fog oil cloud. This is due to the dependence of the evaporation rate on the square of the cloud radius and on the vapor pressure to the first power.

It must be emphasized that the persistency model is, at best, semiquantitative. The model developed by Milburn is strictly valid over the first 20% mass evaporated. However, the relative persistency characteristics of the oil smokes, as predicted from the present model, is most probably still valid.

3.3 Variation in the Vapor Pressure of the Fog Oil SGF-2 Mixture as a Function of Supply. Fog oil SGF-2 is composed of a mixture of hydrocarbons with a molecular weight range from 250 to 400 gm/mole. The production specifications of fog oil generally involve pourability, thermal stability, and viscosity. Since the specifications do not relate to mixture vapor pressure there might exist a significant variation in fog oil SGF-2 depending on the particular supplier. The US Army is supplied with fog oil SGF-2 from three primary sources: (1) Delta Petroleum, (2) Witco Chemical Company, and (3) Phipps Product Co. To test for variation in vapor pressure among the various stocks of fog oil SGF-2, the evaporation rates of these oils are measured. Equation (7) shows the correlation of vapor pressure and percent mass evaporated for the #1, #2 and #3 supplies. Again the characteristic linear relationship is apparent for all three oils. Supply #1 possesses the lowest vapor pressure for a given percent mass evaporated while #3 is only slightly more volatile. However, supply #2 is significantly more volatile than #1 and #3 supplies. In fact, the vapor pressure of supply #2 is an order of

# UNCLASSIFIED

B-13

magnitude higher than the vapor pressure of supply #1 for percent mass evaporated exceeding 50%. This variation in mixture vapor pressure will have an impact on the persistency of the oil smoke. It may be concluded that for purposes of maximum obscuration, supply #1 would be the most efficient smoke producing liquid.

Applying a linear least-square regression analysis to the data of figure 5, the following correlations are obtained,

## Fog oil SGF-2

$$\ln P = -4.44E1 + 9.887 \ln M_R \quad \#1$$

$$\ln P = -2.237E1 + 5.251 \ln M_R \quad \#2 \quad (7)$$

$$\ln P = -2.427E1 + 5.403 \ln M_R \quad \#3$$

3.4 Comparison of Vapor Pressure Properties of Prevaporized and Recondensed Fog Oil. The vaporization of fog oil SGF-2 is achieved by elevating the temperature of the liquid to its boiling point. For the multicomponent oils, the boiling point is a function of the component molecular weight, with the heavier molecules characterized by the higher boiling points. In the field and in laboratory studies, generator vaporization temperatures are established by the complete vaporization of the liquid; i.e., the vaporization temperature is set at the boiling point of the component having the highest molecular weight. Consequently, those species with lower molecular weights are superheated beyond their normal boiling points. This condition introduces the possibility of thermal decomposition and a change in the mixture properties as a result of vaporization.

To investigate the possibility of thermal decomposition through generator vaporization, the vapor pressure of prevaporized and recondensed fog oil SGF-2 is determined. The recondensed fog oil is obtained by impaction on a cascade impactor. Linear least-square regression analysis allows the recondensed fog oil to be characterized by

$$\ln P = 4.371E1 + 9.887 \ln M_R \quad (8)$$

# UNCLASSIFIED

**UNCLASSIFIED**

A comparison of equation (8) with equation (7), reveals that the recondensed fog oil for supply #1, the oil under study, possesses a vapor pressure approximately twice as high as the prevaporized fog oil. Two remarks should be made. First, estimation of the persistency of the fog oil cloud based on prevaporized bulk properties can seriously overestimate the lifetime of these oil clouds. Whenever possible, the recondensed fog oil property, as in equation (8), should be employed. Second, the effect of generator temperature on the chemical and physical properties of the fog oil cloud should be pursued.

## 4. CONCLUSIONS

4.1 A semiquantitative model was developed which predicts the relative persistency of clouds of fog oil SGP-2, PEG 200, and #2 diesel fuel in an open atmosphere.

4.2 Model calculations predict the order of increasing persistency of various multicomponent oil smokes as #2 diesel fuel, PEG 200, and fog oil SGP-2.

4.3 Calculations also indicate that, while PEG 200 and fog oil SGP-2 evaporate similarly over the first 10% mass evaporated, for subsequent degrees of evaporation the persistency of fog oil exceeds that of PEG 200 considerably.

4.4 Evaporation data indicate that the mixture vapor pressure of the three distinct supplies of fog oil SGP-2 vary greatly. Consequently, the persistency values of fog oil SGP-2 will vary significantly from stock to stock.

4.5 The vapor pressure of recondensed fog oil is approximately twice as high as that of the bulk fog oil. Therefore, the use of bulk properties to predict fog oil persistency values would be incorrect.

**UNCLASSIFIED**

**UNCLASSIFIED**  
LITERATURE CITED

B-13

1. Baek, S.H., Harvis, J.E., and Brock, J.R., "Method for Measuring Evaporation Rates of Complex Oil Mixtures with Low Ambient Vapor Pressure", *Review of Scientific Instruments*, 51, 1980.
2. Milburn, R.H., "Theory of Evaporating Water Clouds", *J. Colloid Sci* 12, 378-388, 1957.
3. Schweizer, J.W., and Hanson, D.N., "Stability Limit of Charged Droplets", *J. Colloid, Int. Sci*, 35, (3), 1971.
4. Frickel, R.H., Schaffer, R.E. and Stamatoff, J.B., "Chambers for the Electrodynamic Containment of Charged Aerosol Particles", ARCSL-TR-77041, 1978.
5. Rubel, G.O., "On the Evaporation Rates of Multicomponent Oil Droplets", (Accepted for publication in *J. of Colloid Int. Science*).
6. Coburn, J.P., A.S.L.E., *Trans.*, 12, 129, (1969).
7. Vervier, J.J., and Anderson, D.H., "Laboratory Study of Vaporization/Condensation Smoke Materials", ARCSL-TR-79037, 1979.

**UNCLASSIFIED**

## UNCLASSIFIED

## APPENDIX

Under what conditions will the correlation between derived vapor pressure and percent mass evaporated be independent of the initial droplet diameter studies? To answer this question the following flux rate is introduced.

$$\frac{dn(m,t)}{dt} = \frac{-2\pi D(m)P^*(m)d\delta(m)n(m,t)}{KTn_T(t)} \quad (a)$$

Since components of similar character have a tendency to form ideal solutions,\* it is proposed that the homologous series of hydrocarbon molecules is an ideal mixture. Therefore, the solution vapor pressure is modeled according to Raoult's law as:

$$\delta(m) = 1$$

From equation (a) the relative density of two distinct components is expressed as a power law

$$\frac{n(m,t)}{n(m,t_0)} = \left[ \frac{n(\tilde{m},t)}{n(m,t_0)} \right]^{D(m)P(n)/D(\tilde{m})P(\tilde{m})} \quad (b)$$

For brevity the following variable  $\mu(m)$  is introduced for the relative density of component m

$$\mu(m) = n(m,t)/n(m,t_0) \quad (c)$$

The fractional mass remaining, the ratio of the instantaneous mass to the original mass  $M_0$ , is

$$\frac{M(t)}{M(t_0)} = \frac{\sum_m m n(m,t)}{\sum_m m n(m,t_0)} \quad (d)$$

The discrete form of the mixture solution is used for illustrative purposes; however, the following result can be derived from continuous arguments as well.

\*Glasstone, S., "Textbook of Physical Chemistry, 2nd Ed., 625-627, 1940.

# UNCLASSIFIED

B-13

From (b) and (c), (d) may be rewritten as

$$\frac{M(t)}{M(t_0)} = \frac{\sum_m X(m, t_0) \mu(\tilde{m}, t_0)^D(m) P^\circ(m) / D(\tilde{m}) P^\circ(\tilde{m})}{\sum_m X(m, t_0) \mu(m, t_0)} \quad (e)$$

where  $X(m, t_0)$  is the initial mole fraction of component  $m$ . Equation (e) states that the fraction of species  $m$ ,  $\mu(m, t)$ , is solely determined by the initial mole fraction  $X(m, t_0)$ , and the fraction of total mass remaining. Consequently, two droplets of different initial size but with the same initial composition will be characterized by the same relative density of component species, at the same mass fraction.

The total droplet vapor pressure can be written according to Dalton's law as:

$$P(t) = \sum_m P^\circ(m) X(m, t) \quad (f)$$

From equations (b) and (c), equation (f) is rewritten as:

$$\frac{P(t)}{P(t_0)} = \frac{\sum_m P^\circ(m) X(m, t_0) \mu(\tilde{m}, t)^D(m) P^\circ(m) / D(\tilde{m}) P^\circ(\tilde{m})}{\sum_m X(m, t_0) \mu(\tilde{m}, t)^D(m) P^\circ(m) / D(\tilde{m}) P^\circ(\tilde{m})} \quad (g)$$

Since  $\mu(m, t)$  is solely a function of initial mole fraction  $X(m, t_0)$  and percent mass remaining, the total droplet vapor pressure is also a sole function of  $X(m, t_0)$  and  $M(t)/M(t_0)$ . Therefore, it may be concluded that the correlations of vapor pressure and percent mass evaporated are independent of the initial droplet diameter studied.

**UNCLASSIFIED**

## GLOSSARY OF TERMS

a,b	vapor pressure correlation constants
d	droplet diameter
D	oil vapor diffusion coefficient
m	molecular mass of component m
M( $t_0$ )	initial droplet mass
M(t)	instantaneous droplet mass
$M_e$	fractional mass evaporated
$M_R$	fractional mass remaining
n	droplet number concentration
$n(m,t)$	solution density of component m
$N_T$	total number of solution components
P	total droplet vapor pressure
$P^*(m)$	equilibrium vapor pressure of component m
R	gas constant
$r_0$	initial droplet radius
$R_c$	cloud radius
t	time
T	temperature
$\delta^2$	cloudiness factor
$\delta(m)$	activity coefficient of component m
$\rho$	droplet density
$X(m,t)$	solution mole fraction of component m

# UNCLASSIFIED

## SCREEN, AN EOSAEL 80 MODEL FOR SMOKE MUNITION EXPENDITURE BASED ON TARGET ACQUISITION PROBABILITY

Donald W. Hoock  
Atmospheric Sciences Laboratory  
USA Electronics Research and Development Command  
White Sands Missile Range, New Mexico 88002

### ABSTRACT

This paper provides an introductory description of the SCREEN model included in the Electro-Optical Systems Atmospheric Effects Library 1980 (EOSAEL 80). The model predicts the required number and placement of 105 mm and 155 mm HC and bulk WP smoke munitions required to produce and maintain a screen of given spatial extent and time duration. The criteria for obscuration may, optionally, be defined as the desired maximum probability of target acquisition for a user defined scenario and for certain representative electro-optical imaging devices. SCREEN combines the KWIK munition expenditure model developed at the Atmospheric Sciences Laboratory (ASL), modified to utilize the EOSAEL 80 natural aerosol extinction model XSCALE, and an inverted formulation of the Night Vision and Electro-Optics Laboratory (NVEOL) Target Acquisition Model to provide threshold transmittance as a function of target acquisition probability.

### 1. INTRODUCTION

The most recent version of the Electro-Optical Systems Atmospheric Effects Library 1980 (EOSAEL 80) (Duncan, 1980; Shirkey, 1980) has incorporated a smoke munitions expenditure model, SCREEN. The purpose of this paper is to provide an overview of the model and the concept employed to more directly connect predicted smoke screen requirements to target acquisition probabilities.

Acquisition is a result of successful interpretation of information transfer above some limiting threshold. Use of smoke in battle continues to be an effective means of intentionally raising this threshold to reduce or deny acquisition by electro-optical systems. For imaging systems the threshold can be defined in terms of a limiting probability derived from a mixture of factors including the inherent limitations of human perception, the response of the electro-optical system, natural atmospheric degradation, available ambient illumination, target range and dimensions, scene contrast or thermal signature, background clutter and, of course, intentional intervening obscuration. Any single factor may be dominant. Thus, a successful model for smoke munitions expenditure must weigh all relevant effects to determine what additional obscuration, if any, is necessary for a particular probabilistic goal.

SCREEN addresses the above factors through modification and combination of three existing models: KWIK, an Army Atmospheric Sciences Laboratory smoke munition expenditure model (Umstead, et al., 1979), the Army Night Vision and Electro-Optics Laboratory Target Acquisition Model (Draft NVEOL Technical Report, 1980; Lawson, et al., 1978), and XSCALE (Duncan and Lindberg, 1981), the Army Atmospheric

UNCLASSIFIED

**UNCLASSIFIED**

Sciences Laboratory EOSAEL 80 model for adverse weather extinction coefficient scaling. The modified forms of the first two models form the submodules CWIC and ITAM of SCREEN, and each is discussed below.

## 2. CWIC

CWIC, an acronym for Cross Wind Integrated Concentration, is a version of KWIK modified to include XSCALE for adverse weather corrections and to accept a more general threshold criteria for screening. The present version of this model predicts the number, spacing and replenishment rate of 105 mm and 155 mm Hexachloroethane (HC) and bulk White Phosphorus (WP) smoke munitions required for broad band screening in the separate spectral regions of the visible, near, mid and far infrared wavelengths. Status of validation tests and further development of this model are reported elsewhere in these proceedings (Pena, 1981; Engebos, 1981).

CWIC accepts a simple set of inputs including screen requirement (downwind length and time duration), scenario (target and observer positions and average terrain roughness height) and meteorology (windspeed and wind direction). In addition, the user must provide relative humidity (or temperature and dew point), Pasquill category (or cloud height, cloud amount, latitude, longitude, date and time of day) and visibility (if adverse weather corrections are to be applied).

The model utilizes scaling of a cloud produced by unit continuous and near instantaneous smoke sources precomputed for each munition type during model development. Pasquill category and surface roughness parameterize the diffusion rate for the cloud. Relative humidity provides the hygroscopic dependent scaling of the smoke yield. Windspeed and wind direction are then included to define the effective optical depth through the cloud. The munition spacing is determined as the maximum downwind distance for the limiting value of the optical depth sufficient to reduce transmission below a defined level. Duration of effective screening for single munitions is internally defined for each munition type. As a result of precomputations and assumed scaling relationships, the model executes quickly with modest computer resource requirements.

Figures 1 through 4 show the predicted munition expenditure required for an arbitrary scenario as a function of varying transmission thresholds. The example is for a 1 km screen of 5 minutes duration, a windspeed of 5 m/s, a target to observer range of 2 km cross wind, Pasquill category C, 50% relative humidity, and 10 cm average surface roughness. The step function appearance of the predictions is due

**UNCLASSIFIED**

B-15

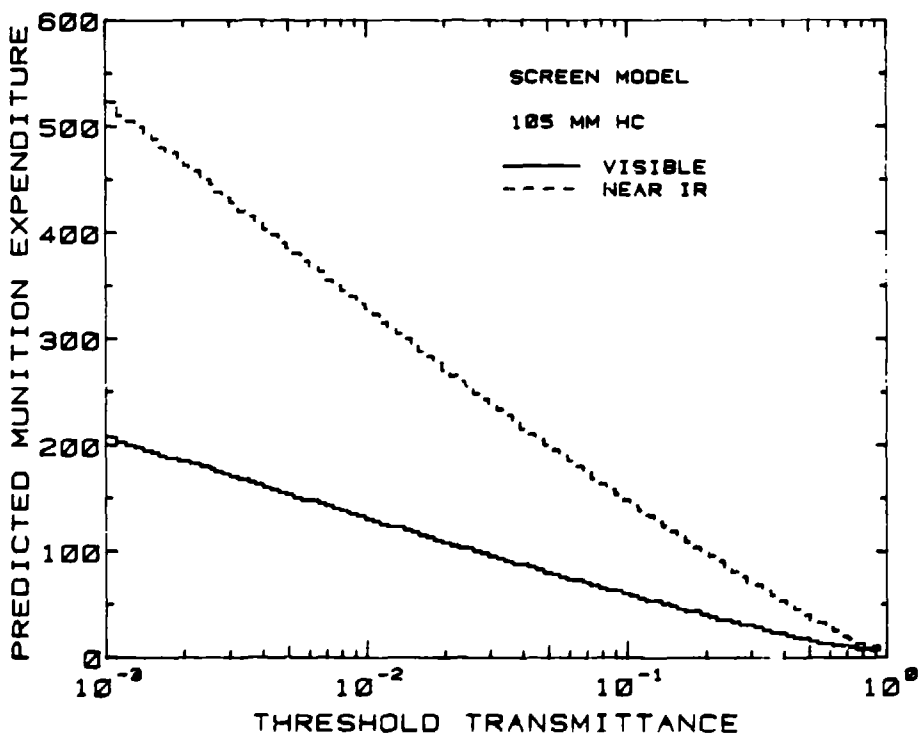


FIGURE 1. SENSITIVITY TO TRANSMISSION THRESHOLD  
105 mm HC munition. Example scenario: 1 km screen,  
5 minute duration, 2 km range, cross-wind,  
wind speed 5 m/s. Pasquill category C, relative  
humidity 50%. Adverse weather not included.

**UNCLASSIFIED**

589

UNCLASSIFIED

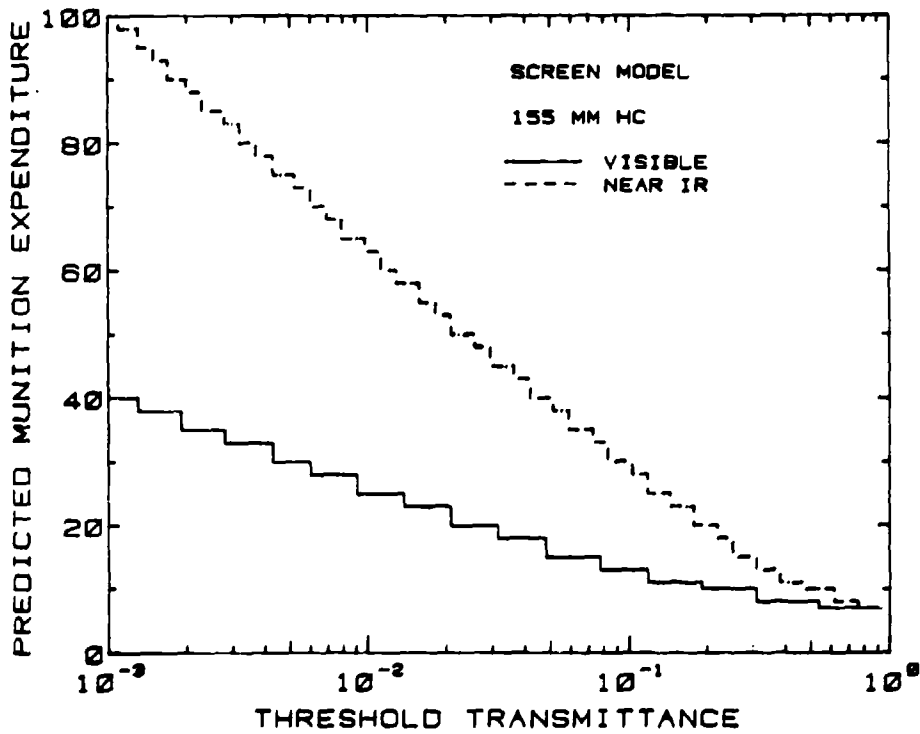


FIGURE 2. SENSITIVITY TO TRANSMISSION THRESHOLD  
155 mm HC munition. Example scenario: 1 km screen,  
5 minute duration, 2 km range, cross-wind,  
wind speed 5 m/s, Pasquill category C, relative  
humidity 50%. Adverse weather not included.

UNCLASSIFIED

**UNCLASSIFIED**

8-15

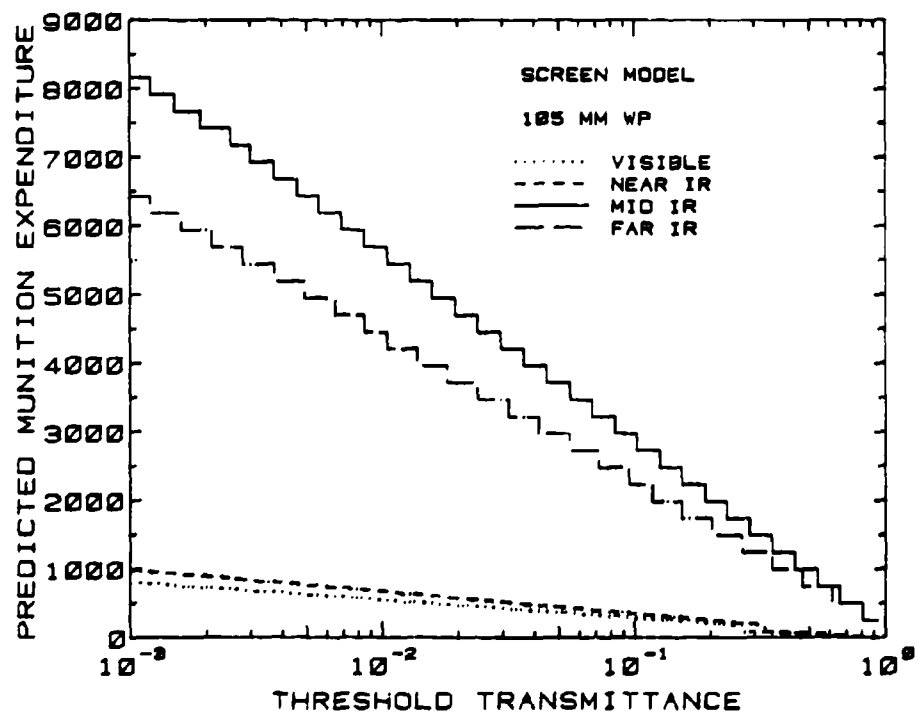


FIGURE 3. SENSITIVITY TO TRANSMISSION THRESHOLD  
105 mm WP munition. Example scenario: 1 km screen,  
5 minute duration, 2 km range, cross-wind,  
wind speed 5 m/s, Pasquill category C, relative  
humidity 50%. Adverse weather not included.

**UNCLASSIFIED**

591

UNCLASSIFIED

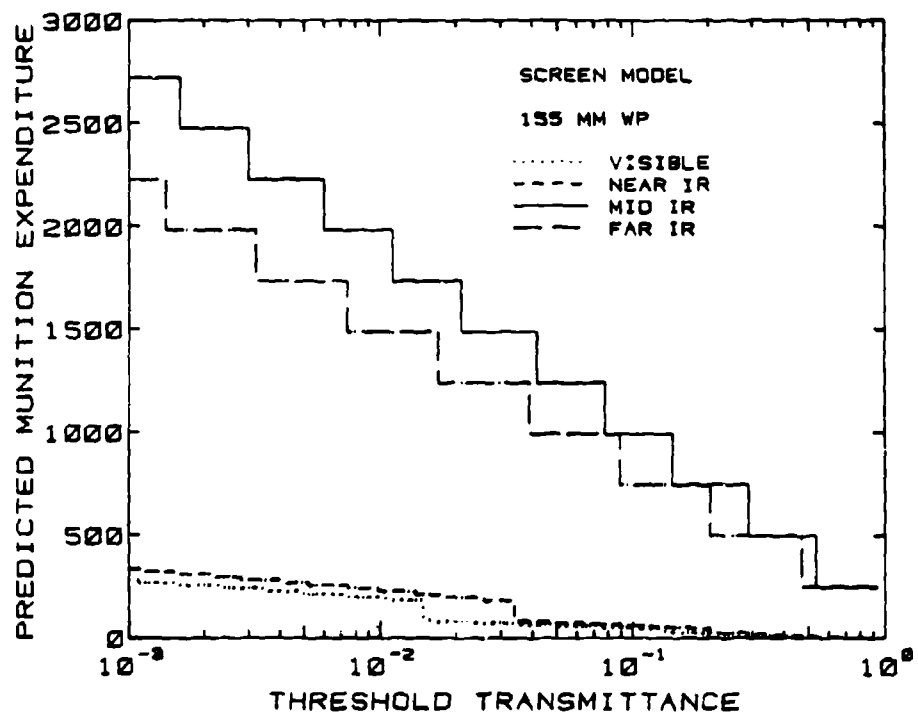


FIGURE 4. SENSITIVITY TO TRANSMISSION THRESHOLD  
155 mm WP munition. Example scenario: 1 km screen,  
5 minute duration, 2 km range, cross-wind,  
wind speed 5 m/s, Paquill category C, relative  
humidity 50%. Adverse weather not included.

UNCLASSIFIED

# **UNCLASSIFIED**

B-15

to upward rounding to the nearest whole munition and is compounded by required replenishment rates. Apparent major differences in requirements are due mainly to the different fill weights of smoke available from each munition type and wavelength dependence of extinction coefficients. The original model fixed the screen threshold criteria at 5% combined atmospheric and smoke transmission. It can be seen from these figures that the number of munitions required is sensitive to the threshold adopted.

The contribution to extinction from adverse weather aerosols (haze, fog, rain and snow) is computed for input visibility. Extrapolation to corresponding extinction in the infrared is accomplished through the EOSAEL 80 XSCALE model. XSCALE provides empirical relationships derived from an extensive data base. Aerosol characteristics are keyed to the parent air mass for fogs. Thus, CWIC addresses the factors of smoke and natural aerosols (or visibility) effects on obscuration.

### **3. ITAM**

The original 5% threshold transmittance of the KWIK model was an arbitrary value. Obviously the actual threshold depends on the application purpose of the screen, the target signature and the device types present. Therefore, the SCREEN model incorporates a second module, ITAM, to relax the threshold restriction and to allow analysis more relevant to electro-optical device testing and design criteria including the other obscuration factors listed in the introduction.

ITAM (an acronym for Inverse Target Acquisition Model) is a modified version of the Night Vision and Electro-Optics Laboratory Target Acquisition Model. The original model predicts an acquisition probability for given input scenario, sensor and atmospheric visibility. Modification was required to invert the computation sequence for SCREEN. Thus, the user inputs a desired maximum acquisition probability threshold, and the model then determines the transmission threshold required to reduce the probability of acquisition to this level.

The devices considered include thirteen imaging systems which operate in the visible through the far infrared. These include aided and unaided eye, day television, image intensifiers and various thermal weapon sights or FLIR's. These devices should be taken as representative of the general types which might be utilized in a screening environment and to permit analysis of the dependence of effective screening on varying scenarios.

# **UNCLASSIFIED**

**UNCLASSIFIED**

The computation process begins with the determination of the resolution (in terms of line pairs or resolvable cycles) required at the display for the given acquisition level and input probability of acquisition. This step is independent of the device type. The acquisition level specifies the number of line pairs required for 50% of observers to achieve successful acquisition. The level may be assigned a numerical value according to task (Table I) (Lawson and Shields, 1980). Thus this step incorporates the limitations of human perception. The higher the level of the task (or the greater the background clutter which also increases the level) the greater the resolution required. As a result, higher acquisition levels require less screening. An example is shown in Figure 5 for a thermal system. Similarly, to prevent the most primitive acquisition task, that of detection in an uncluttered background, larger numbers of smoke munitions are required.

TABLE I. ACQUISITION LEVELS

TASK	ACQUISITION LEVEL
Detection (highly visible)	< 1
(uncluttered)	1
(highly cluttered)	2-3
Orientation	1.4
Classification	2.5
Recognition	3-4
Identification	6.4

The second step in the model requires user definition of the range and linear dimension of the target. The required minimum resolvable line pairs per milliradian subtended by the target is computed from the absolute number of line pairs of the preceding step. A greater range or smaller target requires greater resolution and thus affects the screening threshold.

The third step introduces specific device response to the resolution requirement. Devices are identified by a number code in SCREEN. In addition to the number, the user must specify the field of view mode (wide or narrow) and ambient illumination of the scene for non-thermal devices. The model uses device dependent parameterized curves to relate the temperature difference or contrast, depending on the device, required at the device aperture for the number of line pairs per milliradian. For

**UNCLASSIFIED**

**UNCLASSIFIED**

B-15

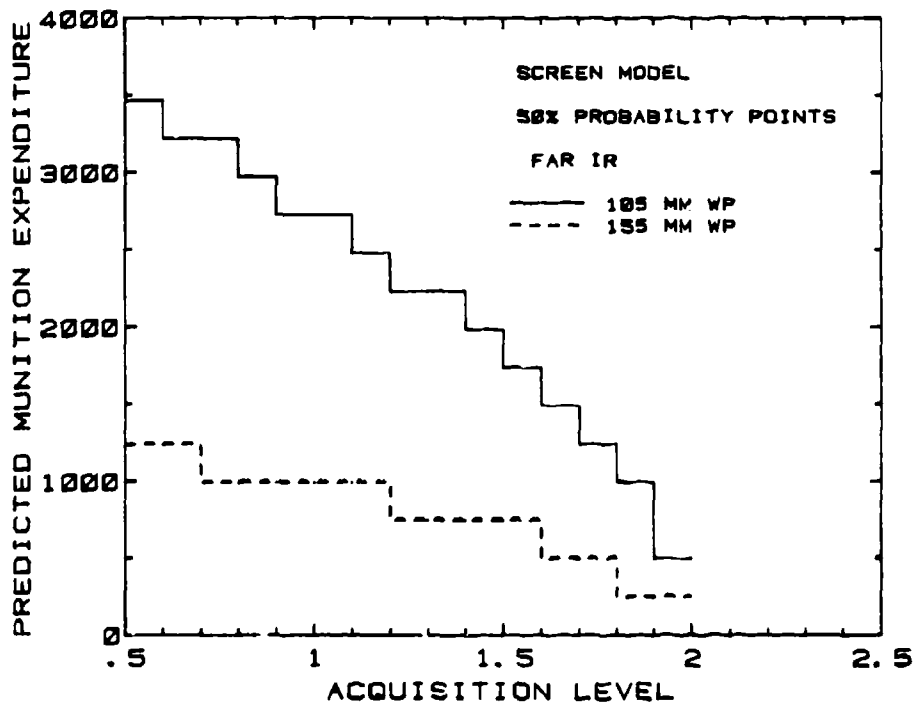


FIGURE 5. SENSITIVITY TO ACQUISITION LEVEL  
105 mm and 155 mm WP munitions. IR device.  
Same screen as in Figures 1-4, with further inputs  
of 2.3 m high target at 2 km, temperature or  
contrast of target of 2., wide FOV, ambient light  
of 50 ft candle, and sky/ground ratio 1.

**UNCLASSIFIED**

595

**UNCLASSIFIED**

those devices operating in the visible wavelength region, interpolation is performed between modeled ambient illumination levels. This interpolation has been designed to provide the same interpolating fraction as the original Target Acquisition Model. Figure 6 shows an example of the dependence of expenditures on ambient illumination for a particular device and scenario.

The final step in ITAM is to determine the transmittance through the atmosphere which will reduce the contrast or temperature difference at the target to that minimum required at the device for the initially specified acquisition probability. The user must provide the intrinsic contrast or temperature difference between the target and its background. At visible wavelengths the scattering of ambient illumination into the field of view contributes to contrast reduction. The model therefore requires the user to specify a sky to background ratio, or more properly the path radiance to background luminance ratio. Values of 1 to 2 are typical for light haze, but for dense smoke clouds, calculations with the ACT II smoke model (Sutherland, 1981) suggest that ratios on the order of 5 to 7 may be more proper when sunlight and skylight reflect off the surface of the cloud. Figure 7 shows an example of the effect of the sky to ground ratio.

Figures 8 and 9 show examples of the expenditure requirements as a function of probability of acquisition as predicted by the SCREEN model. Table II summarizes the minimum input requirements of the model.

TABLE II. MODEL INPUTS

<u>CWIC</u>	<u>ITAM</u>
Screen Length	Intrinsic Contrast or Temperature Difference
Screen Duration	Target Range
Target Range, Azimuth and Elevation	Target Dimension
Terrain Roughness	Probability of Acquisition
Adverse Weather Type	Acquisition Level
Windspeed	Device Code and Mode
Wind Direction	Ambient Illumination
Visibility	Sky/Background Ratio
Relative Humidity (or Temperature and Dewpoint)	
Pasquill Category (or Cloud Height and Amount, Latitude, Longitude, Date and Time)	

**UNCLASSIFIED**

B-15

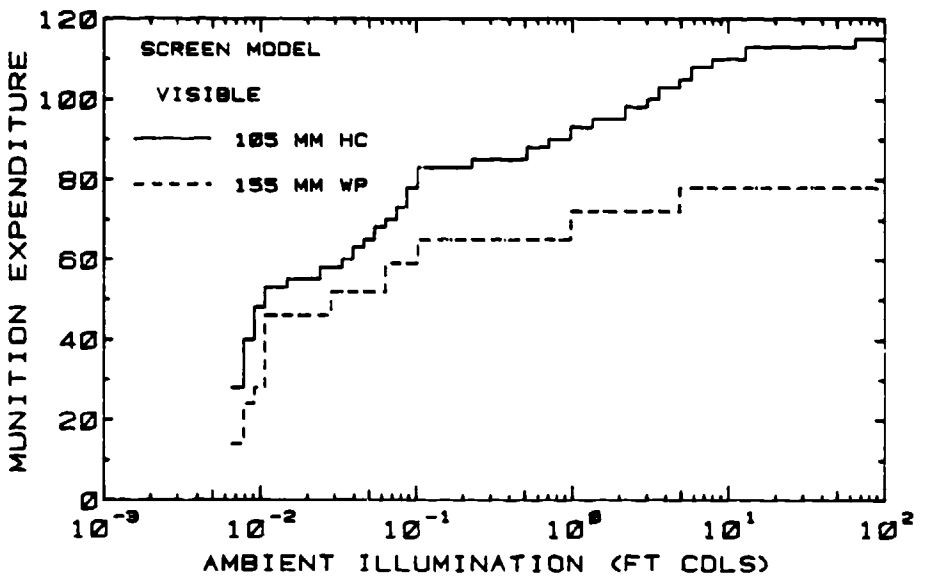


FIGURE 6. SENSITIVITY TO AMBIENT ILLUMINATION  
Scenario of Figures 1-5. 0.4-0.7 micrometers.

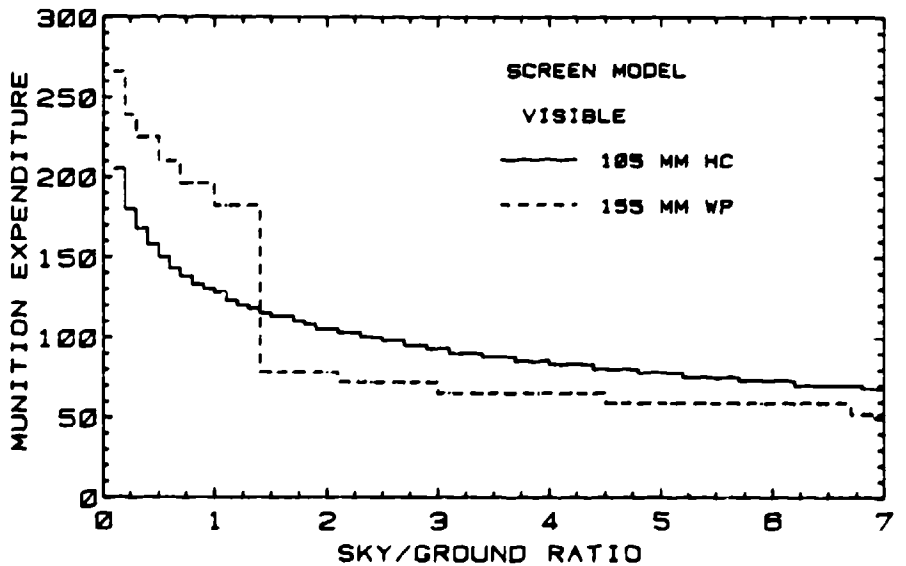


FIGURE 7. SENSITIVITY TO PATH/BACKGROUND RATIO  
Also known as "sky-to-ground ratio", the ratio  
of the scattered light into the FOV to the back-  
ground luminance. Same scenario as Figures 1-5.

**UNCLASSIFIED**

597

UNCLASSIFIED

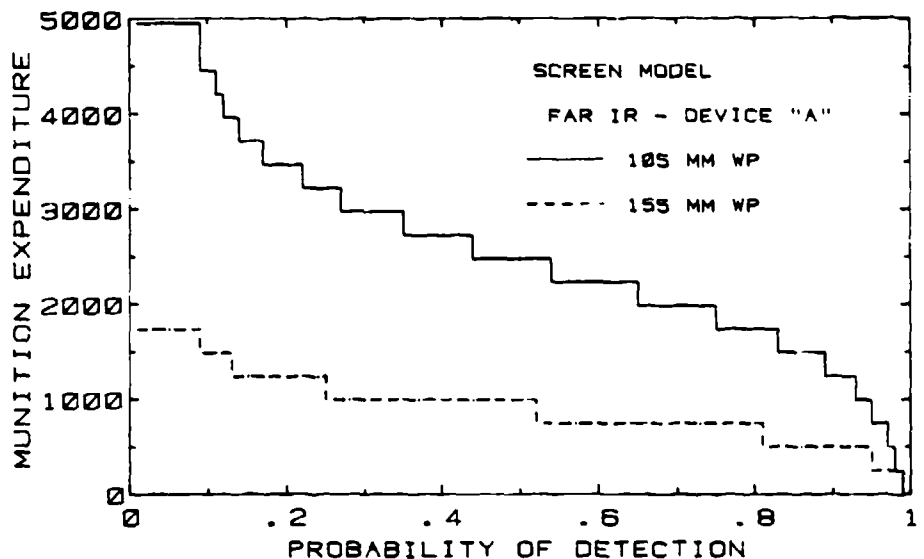


FIGURE 8. PREDICTION FOR DETECTION PROBABILITY  
Scenario of Figures 1-5. Acquisition level 1.

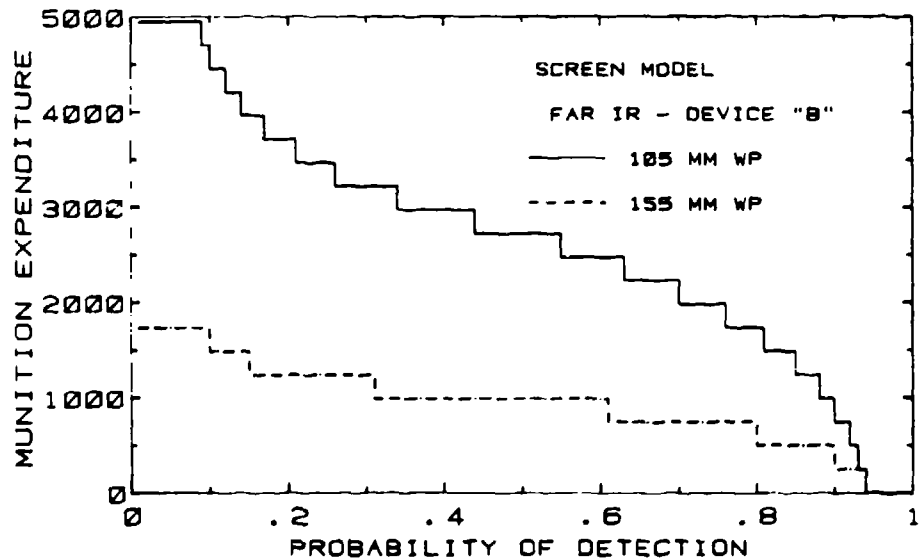


FIGURE 9. PREDICTION FOR DETECTION PROBABILITY  
Scenario of Figures 1-5. Acquisition level 1.

UNCLASSIFIED

# UNCLASSIFIED

B-15

## 4. CONCLUSIONS

SCREEN is a user-oriented model contained in EOSAEL 80. It is designed to allow flexible control of input variables and produces readable tabular output. The model provides a more direct connection between the reduction in transmission provided by a smoke screen and requirements of electro-optical systems, allowing the magnitude of various effects to be evaluated which also contribute to the obscuration process.

## 5. REFERENCES

- Duncan, L. (Editor), 1980: EOSAEL 80, Volume I: Technical Documentation, ASL-TR-0072, Atmospheric Sciences Laboratory, White Sands Missile Range, NM.
- Duncan, L. D. and J. D. Lindberg, 1981: Air Mass Considerations in Fog Optical Modeling, ASL-TR-0075, Atmospheric Sciences Laboratory, White Sands Missile Range, NM.
- Engebos, B., 1981: Plans for the Evaluation of Smoke Munition Expenditure Models, Proceedings of the Smoke/Obscurants Symposium V, Harry Diamond Laboratories, Adelphi, MD.
- Lawson, W. R., I. Cassidy, and J. Ratches, 1978: A Search Model, Proceedings of the IRIS Specialty Group on Imaging.
- Lawson, W. R., and F. Shields, 1980: "EO System Evaluation at NVEOL," Night Vision and Electro Optics Laboratory, Fort Belvoir, VA (presentation at Symposium of Visual Modeling and Evaluation of Electro Optical Systems, Royal Military College, Swindon Wilts).
- Pena, R., 1981: Munition Expenditure Model Verification KWIK Phase I, Proceedings of the Smoke/Obscurants Symposium V, Harry Diamond Laboratories, Adelphi, MD.
- Shirkey, R. C. (Editor), 1980: EOSAEL 80, Volume II: User's Manual, ASL-TR-0073, Atmospheric Sciences Laboratory, White Sands Missile Range, NM.
- Sutherland, R. A., 1981: Comparisons Between the Upgraded Model ACT II and Recent Smoke Week Tests, Proceedings of the Smoke/Obscurants Symposium V, Harry Diamond Laboratories, Adelphi, MD.
- Umstead, R. K., R. Pena, and F. Hansen, 1979: KWIK: An Algorithm for calculating Munition Expenditures for Smoke Screening/Obscuration in Tactical Situations, ASL-TR-0030, Atmospheric Sciences Laboratory, White Sands Missile Range, NM.
- Combat Simulation Target Acquisition Model and Data Input (U), CONFIDENTIAL, 1980, Draft NVEOL Technical Report, Night Vision and Electro Optics Laboratory, Fort Belvoir, VA.

# UNCLASSIFIED

599

# UNCLASSIFIED

B-16

## COMPUTED PATH TO BACKGROUND LUMINANCE RATIOS FOR OBSCURING SMOKE CLOUDS

Donald W. Hoock and Robert A. Sutherland  
Atmospheric Sciences Laboratory  
USA Electronics Research and Development Command  
White Sands Missile Range, New Mexico 88002

### ABSTRACT

The mathematical relation between transmittance and contrast transmission for wavelengths in the visible and near visible includes the ratio of the path to background luminances between target and observer. Some models for electro-optical systems performance at these wavelengths require this ratio as an input, e.g., the Night Vision and Electro-Optics Laboratory (NVEOL) Target Acquisition Model and the Electro-Optical Systems Atmospheric Effects Library (EOSAEL) SCREEN Model.

For the case of both target and observer immersed in a uniform atmosphere which degrades visibility this quantity, known commonly as sky-to-background ratio, is available from widely known tables and models. However, smoke clouds in the field of view present a special problem due to reflected ambient illumination. Therefore, the ACT II smoke model and the EOSAEL 80 aerosol phase function data base have been used to compute values of the path to background luminance ratio for representative scenarios involving white phosphorus (WP) smoke. Results may be used as input estimates to those systems performance models which require this ratio in the presence of smoke. Results also demonstrate the significant advantage to be gained on the battlefield by considering contrast transmission rather than the more ordinary direct transmission.

### 1. INTRODUCTION

A companion paper (Hoock, 1981) points out the sensitivity of current smoke screening and visual perception models to a quantity referred to as the sky-to-background ratio, or more properly the path-to-background luminance ratio, P/B, at visual wavelengths. Another paper (Sutherland, 1981) examines the origins of this quantity for smoke clouds and describes the validation of a model which can provide P/B. The present paper provides quantitative estimates which can be used to satisfy input requirements for this ratio in the EOSAEL 80 smoke munition expenditure model, SCREEN (Duncan, et al., 1981). It also lends insight into certain atmospheric phenomena of general importance to the smoke/obscurants modeling community.

The sheer complexity of the problem, which involves angular functions of both the scattering medium and the distribution of ambient radiation (illumination), prevents at present any quick and simple algorithm for generally determining the appropriate P/B ratio. For this reason the paper is limited to a few typical scenarios. However, computations for other specialized scenarios can be carried out with the model ACT II, described in detail elsewhere (Sutherland and Hoock, 1981; Sutherland and Clayton, 1981).

# UNCLASSIFIED

# UNCLASSIFIED

B-16

## 2. PROBLEM DEFINITION

Contrast is defined in most models as

$$C(s) = \frac{L_T(s) - L_B(s)}{L_B(s)} \quad (1)$$

where  $s$  is some distance along a line of sight,  $L_T$  is the radiance (luminance) incident toward the observer from the target and  $L_B$  the same quantity from the direction of the background. The term luminance ( $\text{candles/m}^2$ ) refers to radiance ( $\text{watt/m}^2 \cdot \text{sr}$ ) weighted by the spectral response of the human eye and in the context of this paper can be used interchangeably.

The contrast at a distance  $s$  can be related to the inherent contrast  $C(0)$  by

$$C(s) = \frac{C(0)}{1 + S_g(\tau^{-1} - 1)} \quad (2)$$

where  $\tau$  is the path transmission and  $S_g$  is the sky-to-background ratio. This ratio is more properly defined as

$$S_g = \frac{L_p(s)}{L_B(0)(1 - \tau)} \quad (3)$$

$L_p$  is the path radiance, which, simply stated, is radiation scattered into the field of view from sources over the entire environmental sphere including sun (or moon), sky and terrain. The appearance of the sky itself is a manifestation of path radiance and is also referred to as diffuse radiation. The significance of path radiance to problems of the real battlefield lies in the reduction in contrast which in turn reduces probability of target acquisition. The quantity  $L_p/L_B(0)$  is the path-to-background luminance ratio (P/B). The term contrast transmission is often applied to the ratio

$$\tau_c = \frac{C(s)}{C(0)}. \quad (4)$$

The remainder of this paper deals with the various relationships between the quantities of equations (1) through (4) for an intervening smoke cloud in the line of sight.

# UNCLASSIFIED

# UNCLASSIFIED

B-1E

## 3. EXAMPLES AND DISCUSSION

The following scenarios were chosen for computational examples. The sun is assumed to produce a beam flux of 380 watts/m<sup>2</sup> at the surface with a uniform sky producing an additional 380 watts/m<sup>2</sup>, giving a total surface irradiance of 760 watts/m<sup>2</sup> (one-half solar constant), close to that measured during the Smoke Week Tests. The surface reflectivity is assumed 0.25 and the background reflectivity 0.1. A single 105 mm White Phosphorus (WP) M60A2 smoke round (1.74 kg) or a single 81 mm WP M375A2 round (0.795 kg) is detonated on the surface at a point midway between a target and observer separated by 1 km as sketched in Figure 1. The line of sight is horizontal, 1.5 meters above the surface. Meteorological conditions are taken to be a 5 m/s windspeed with 18% relative humidity and neutral stability conditions. To remove much of the complication introduced by the transport of the cloud, the observer and target are assumed to move downwind at 5 m/s such that the cloud remains in the field of view. The cloud is allowed to undergo the usual modeled diffusion (i.e., expansion in size) but for convenience the buoyant rise mechanism of the model is bypassed so that the cloud remains near the surface.

Smoke optical constants: mass extinction coefficient, single scattering albedo, and phase functions are those compiled for WP in the EOSAEL 80 library. Molecular and adverse weather aerosol extinction are ignored so that effects are entirely those due to smoke. Only single scattering is considered.

Figure 2 presents the physical changes with time resulting from the cloud expansion. Originally the cloud, modeled as a Gaussian, is small and thus the concentration at the centroid is high. The volume ( $4\pi/3 \sigma_x \sigma_y \sigma_z$ ) increases with time and thus the concentration decreases. Figure 3 shows the path integrated concentration (CL) between the target and observer continually decreasing with time as one would expect. Thus far, the results contain nothing new and are typical of current transport and diffusion models.

A more interesting relationship, however, is displayed in Figures 3 and 4 for the path luminance. These predictions were obtained from the ACT II model. The path luminance is initially at a nominally low value. It then increases monotonically until approximately 200 seconds for the M60A2 and approximately 130 seconds for the M375A2. It then decreases monotonically eventually reaching zero as the cloud dissipates (not shown). Intuitively perhaps one might have assumed that the path luminance is a monotonic function of CL, the cloud being brighter the higher the smoke concentration. The fact that

# UNCLASSIFIED

**UNCLASSIFIED**

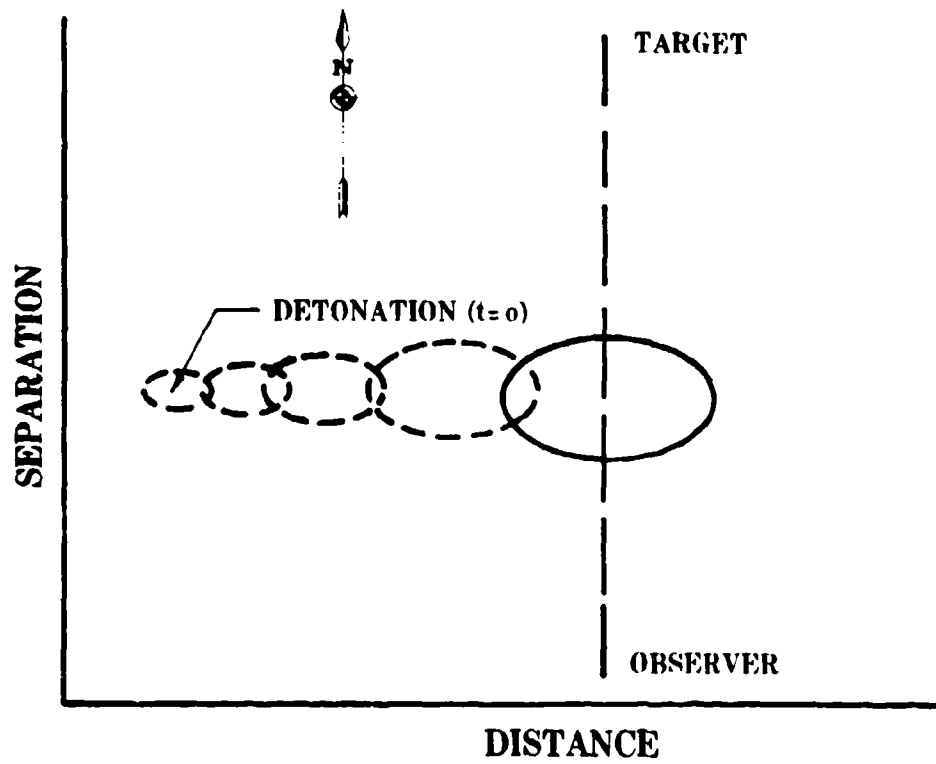


FIGURE 1. SKETCH SHOWING SCENARIO GEOMETRY USED FOR THE EXAMPLES.

**UNCLASSIFIED**

UNCLASSIFIED

B-16

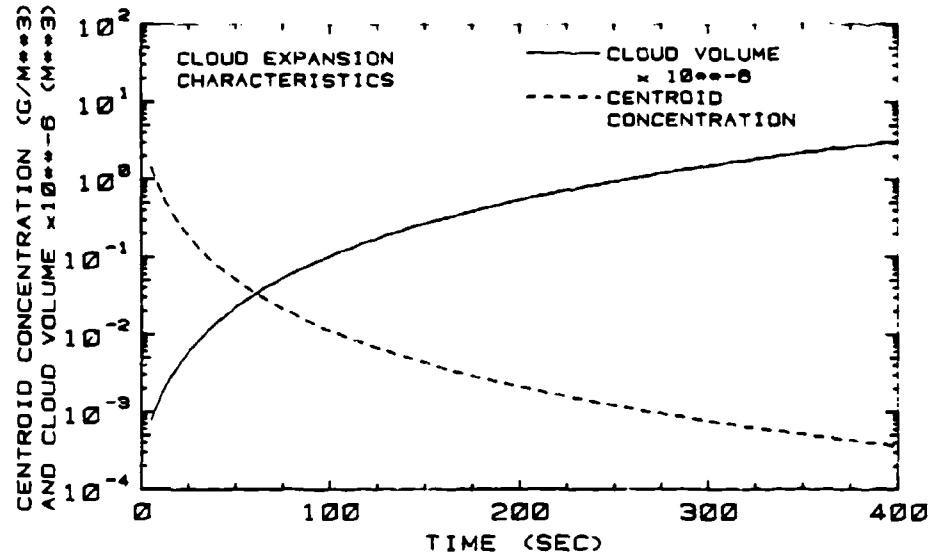


FIGURE 2. SMOKE CLOUD VOLUME AND CENTROID CONCENTRATION  
Volume and Gaussian centroid density prediction for a 105  
mm WP (M80A2). Neutral stability. 18% RH, 5 m/s wind speed

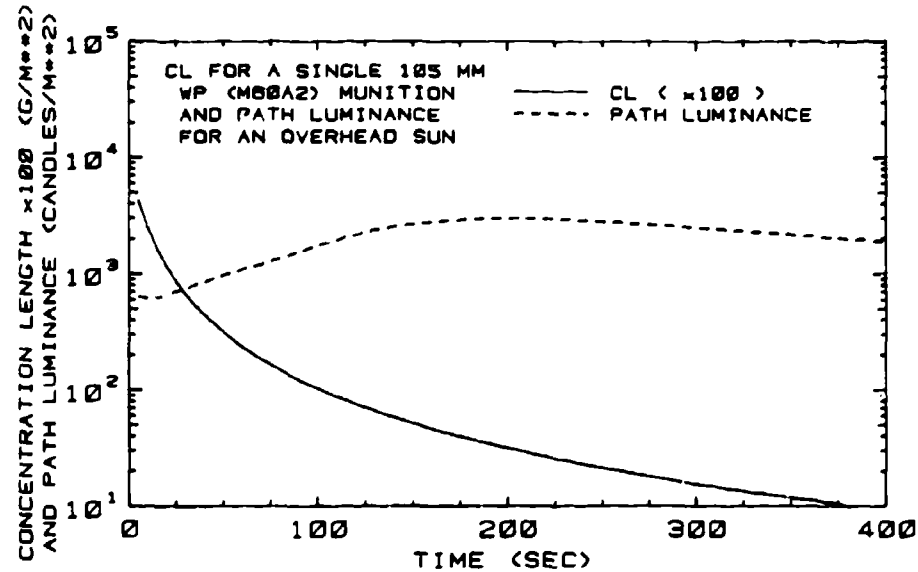


FIGURE 3. CONCENTRATION LENGTH AND PATH LUMINANCE.  
Integrated path concentration (CL) and path luminance  
for the scenario of Figures 1 and 2.

UNCLASSIFIED

605

UNCLASSIFIED

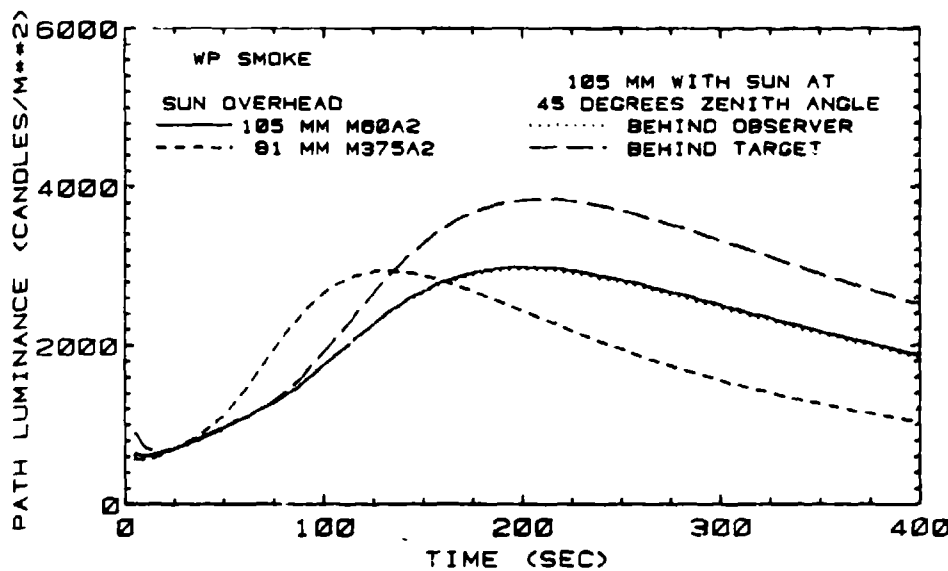


FIGURE 4. PATH LUMINANCE FOR FOUR EXAMPLES.  
Path luminance for sun overhead and at 45 degrees zenith  
behind the observer and behind the target.

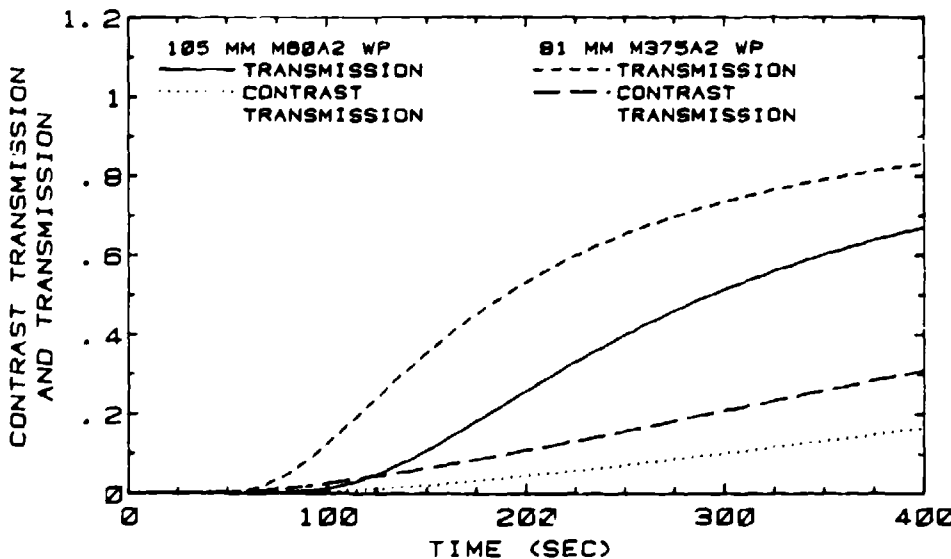


FIGURE 5. TRANSMISSION AND CONTRAST TRANSMISSION.  
Overhead sun and scenario of Figures 1 and 2 for single  
105 mm M80A2 and 81 mm M375A2 smoke munitions.

UNCLASSIFIED

UNCLASSIFIED

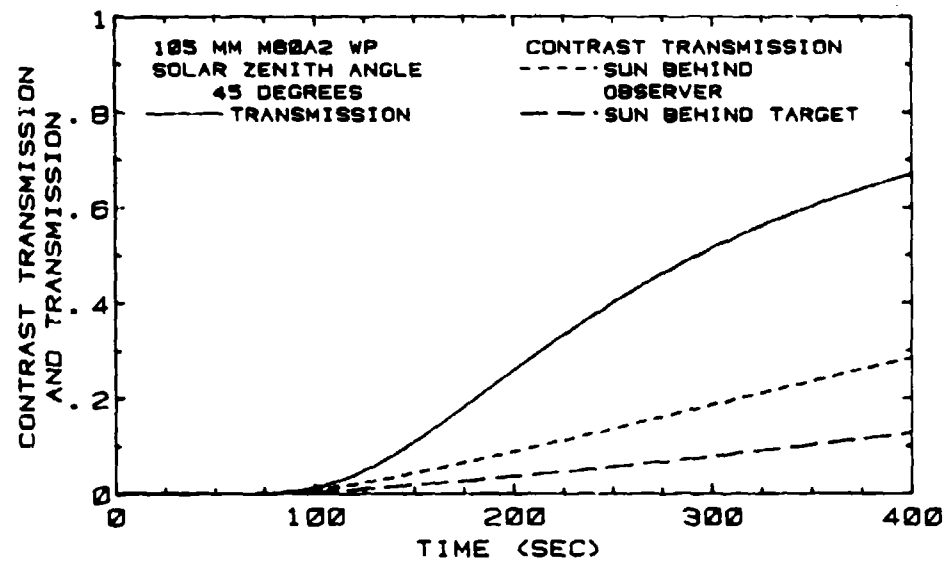


FIGURE 6. TRANSMISSION AND CONTRAST TRANSMISSION.  
Scenario of Figures 1 and 2 for a single 105 mm M68A2  
smoke munition. Solar zenith angle 45 degrees.

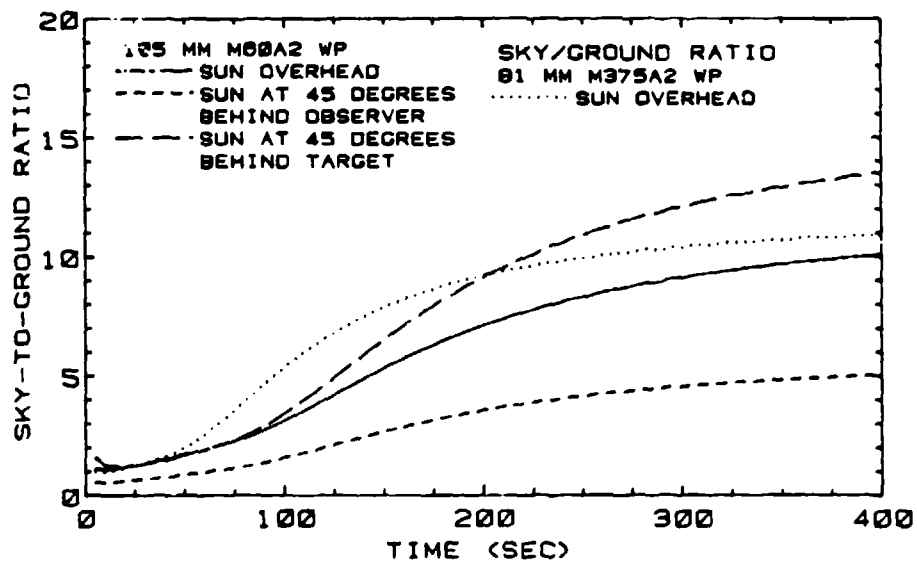


FIGURE 7. SKY-TO-GROUND RATIO  
Sky-to-ground ratio for the four cases shown previously.  
The background reflectivity is 0.1

UNCLASSIFIED

## UNCLASSIFIED

B-16

this is clearly not so is demonstrated in the figures. This emphasizes a fundamentally important difference between transmission and path luminance. (Both quantities are necessary to determine contrast transmission.) Transmission is determined by the properties of the obscurant solely along the path of propagation, whereas path radiance is a manifestation of the obscurant properties of the entire cloud and ambient illumination.

Referring again to the figures, the underlying physical explanation of the result is that the initial dense cloud blocks both direct and indirect light from the surroundings which would otherwise intersect the line of sight and scatter into the field of view. Thus, even though the line of sight contains a large quantity of scattering material (smoke), the luminance is actually lowered. Later, as the cloud expands and becomes less dense, more light from the surroundings (sky, sun and terrain) reaches the line of sight and scatters into the field of view causing increased brightness. Eventually the medium becomes less dense to the point that the scattering process itself is less effective and the path luminance decreases.

Figures 5 and 6 show the time dependence of the transmission and contrast transmission for the computational examples. Note that the peak in path luminance occurs at a transmission level of about 25%. This transmission level, normally considered to be well above perception thresholds in models which neglect path luminance, is well above the contrast transmission value, which is kept small by the path luminance. Only much later does the contrast transmission return to values near 100%.

Figures 4 through 6 also demonstrate the asymmetry in the acquisition process along a target and observer line of sight. The sun is shown for the cases of 45 degree zenith angles both behind the target and, for a separate example, behind the observer. The ordinary transmissions in both directions are equal. However, the contrast transmission from target to observer differs from that for the observer to the target. One or the other will thus have an "optical advantage" and will in essence acquire the other first. This is the major difference in the importance of path luminance considerations over simple transmission threshold arguments applied to the realistic battlefield.

Interestingly, the results of Figures 4 through 6 clearly show a distinct optical advantage in having the sun to the rear. This result quantitatively reinforces an old military rule to "attack with sun at the rear." This rule will generally hold in screening with current inventory smokes (WP, HC, and Fog Oil); however, smoke or obscurants producing significant backscatter could force a reversal.

## UNCLASSIFIED

608

**UNCLASSIFIED**

B-16

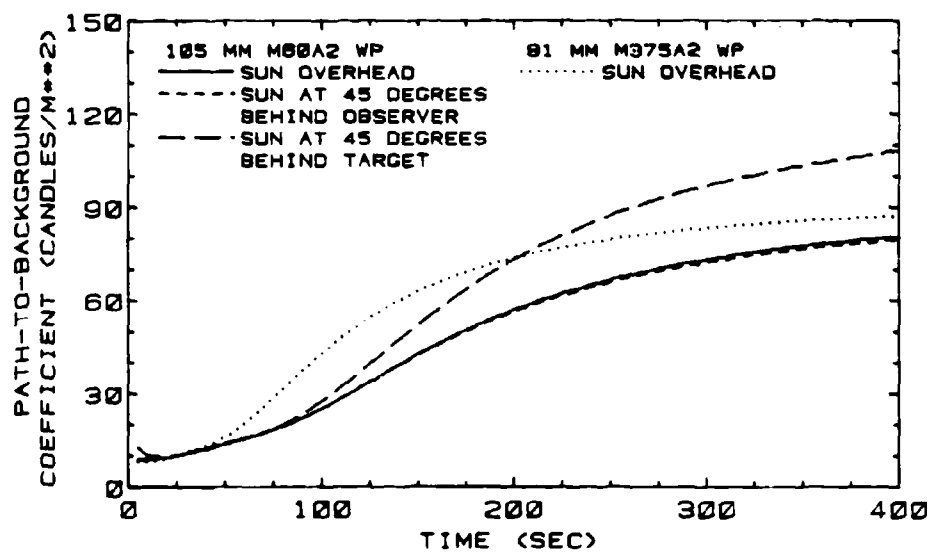


FIGURE 8. PATH-TO-BACKGROUND COEFFICIENT  
Scaled sky-to-ground ratio (for unit background luminance  
of 1 candle/m<sup>-2</sup>) and the four preceding ones.

**UNCLASSIFIED**

**UNCLASSIFIED**

Figures 7 and 8 provide a quantitative estimate of the sky to background ratio required by acquisition models in the presence of smoke. The values in Figure 7 are dependent upon the background reflectivity assumed 0.1 in this case. They range from about 1 to 10 over the period of time shown, and vary inversely with the background reflectivity. Therefore, for scaling purposes, Figure 8 shows the value of the P/B ratio for an absolute background luminance of 1 candle/m<sup>2</sup>. A model user can estimate a reasonable value for a given screening transmission threshold by comparison between figures. However, for an accurate value for a specific scenario a full model computation is required.

**4. CONCLUSIONS**

For acquisition modeling of a smoke obscured scenario at visual wavelengths, transmission is generally insufficient as the only required quantity. Contrast transmission must also be taken into account.

Path luminance through smoke is not monotonically dependent on smoke concentration. It depends on properties of the entire cloud.

Acquisition ability between a target and observer is rarely symmetric. Atmospheric effects will generally give one side the advantage.

The path to background ratio increases as the cloud dissipates, although precise values require non-trivial modeling based on a number of inputs, particularly background reflectivity.

# UNCLASSIFIED

B-16

## 5. REFERENCES

- Duncan, L. D. (Editor), 1981: EOSAEL 80 Volume I: Technical Documentation, ASL-TR-0072, Atmospheric Sciences Laboratory, White Sands Missile Range, NM.
- Hooock, D. W., 1981: SCREEN, An EOSAEL 80 Model for Smoke Munition Expenditure Based on Target Acquisition Probability, Proceedings of the Smoke/Obscurants Symposium V, Harry Diamond Laboratories, Adelphi, MD.
- Sutherland, R. A., 1981: Comparisons Between the Upgraded Model ACT II and Recent Smoke Week Tests, Proceedings of the Smoke/Obscurants Symposium V, Harry Diamond Laboratories, Adelphi, MD.
- Sutherland, R. A. and D. A. Clayton, 1981: An Improved Smoke Obscuration Model ACT II, Part 2: User's Guide, ASL-TR-(in press), Atmospheric Sciences Laboratory, White Sands Missile Range, NM.
- Sutherland, R. A. and D. W. Hooock, 1981: An Improved Smoke Obscuration Model ACT II, Part 1: Theory, ASL-TR-(in press), Atmospheric Sciences Laboratory, White Sands Missile Range, NM.

# UNCLASSIFIED

611

# UNCLASSIFIED

B-17

## OBSCURATION EFFECTS OF WINDBLOWN DUST

Mary Ann Seagraves  
Atmospheric Sciences Laboratory  
USA Electronics Research and Development Command  
White Sands Missile Range, New Mexico 88002

### ABSTRACT

Naturally occurring or windblown dust causes periods of low visibility, particularly in arid regions, and can be a source of obscuration of electro-optical devices operating in the visible or infrared spectral regions. Occurrence of windblown dust and factors influencing the injection of soil into the atmosphere by the wind are described. Characteristics of the dust affecting atmospheric optical properties discussed include particle number density, particle size distributions, and complex index of refraction. The time variation of extinction through a Middle East dust storm derived from single scattering calculations is given.

### 1. INTRODUCTION

Naturally occurring windblown dust and sand in the atmosphere can be a source of obscuration in many areas of the earth. However, it is most likely to occur in the arid and semiarid regions which comprise approximately one-third of the earth's land surface (Figure 1). The characteristics of arid lands which cause them to be susceptible to windblown dust include:

- (1) lack of soil moisture and vegetation to hold soil particles to surface,
- (2) high surface wind speeds due to small surface friction caused by lack of vegetation, and
- (3) atmospheric instability resulting from intense heating at the earth's surface.

In the Middle East, windblown dust frequently causes obscurations. Figure 2 shows the annual number of occurrences of visibility reduced to less than 11 kilometers by blowing dust for one hour or greater duration (Hinds and Hoidale, 1975) for selected locations in the Middle East. It should be noted that more than one occurrence could take place in a day if there was an intervening period of increased visibility. However, this was seldom the case in the data used for this analysis. The comparable number of occurrences for the main post area of White Sands Missile Range, NM, is 13 per year, as compared to 208 per year for Nasiriyah, Iraq. Similarly, the annual number of occurrences of visibility less than 1 kilometer due to a dust storm of one hour or greater duration is shown in Figure 3. The comparable number of occurrences at White Sands is one per year.

Late spring and early summer months are the periods when windblown dust most often occurs in most Middle Eastern countries. Figure 4 shows the frequency of occurrence of dust reported at Abadan, Iran, which is located at the northern end of the Persian Gulf. At Abadan, as at most Middle East stations,

# UNCLASSIFIED

613

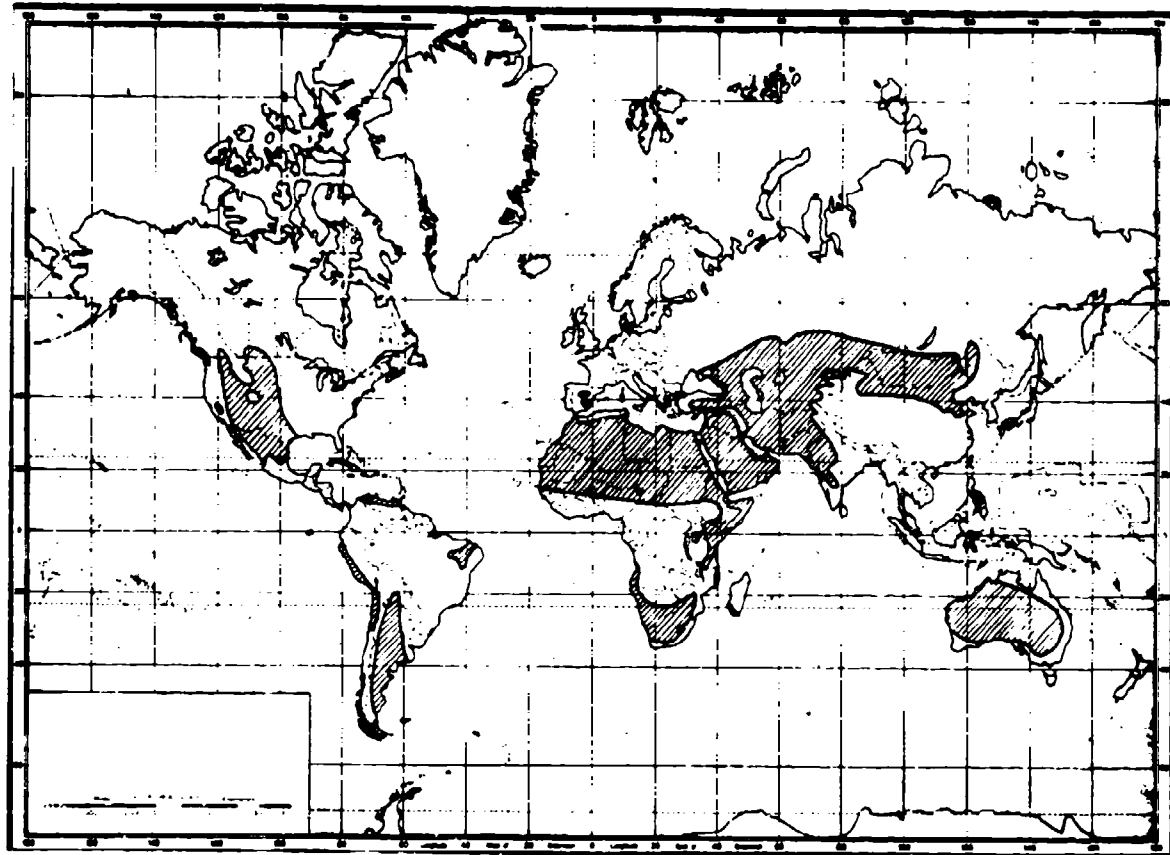
**UNCLASSIFIED**

FIGURE 1. ARID AND SEMIARID REGIONS OF THE WORLD.

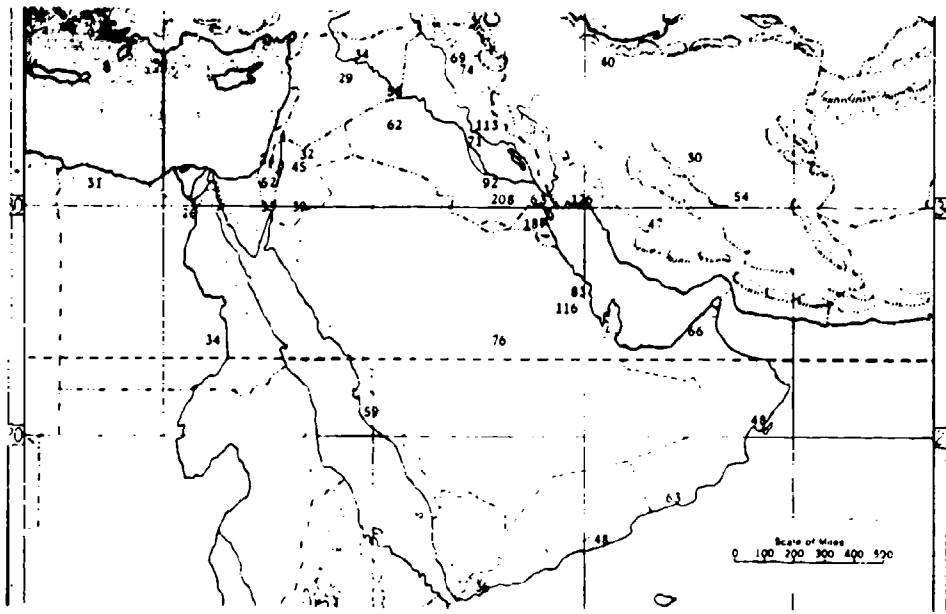


FIGURE 2. ANNUAL NUMBER OF OCCURRENCES OF VISIBILITY LESS THAN 11 KM DUE TO BLOWING DUST OF ONE HOUR OR GREATER DURATION.

**UNCLASSIFIED**

# UNCLASSIFIED

B-17

dust is reported with greatest frequency during the afternoon hours (12-17 hours LST). Figure 5 depicts the total percentage of the time in which visibility is reduced to low levels at Abadan in July during afternoon hours. For example, 10% of the time visibility is 3 km or less.

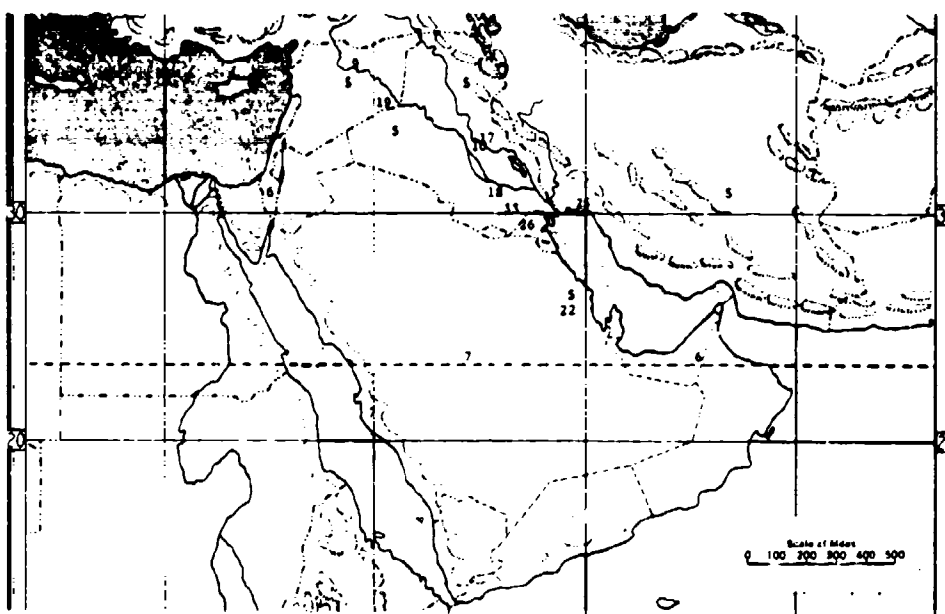


FIGURE 3. ANNUAL NUMBER OF OCCURRENCES OF VISIBILITY LESS THAN 1 KM DUE TO DUST STORM OF ONE HOUR OR GREATER DURATION.

## 2. MOVEMENT OF SOIL BY WIND

The factors which influence the injection of soil particles into the atmosphere by the wind are numerous and subject to complex interactions. Some of the more important of these factors are listed in Table I (Chepil, 1945). The influence of any of these factors may be positive or negative and one factor may counteract the influence of another in any situation, which greatly increases the complexity of models and prediction schemes. For example, wind turbulence increases the degree of wind erosion. Yet the erosion of a rough surface, where turbulence is stronger, is much less than that of a smooth surface where the mean wind speed is greater.

# UNCLASSIFIED

615

UNCLASSIFIED

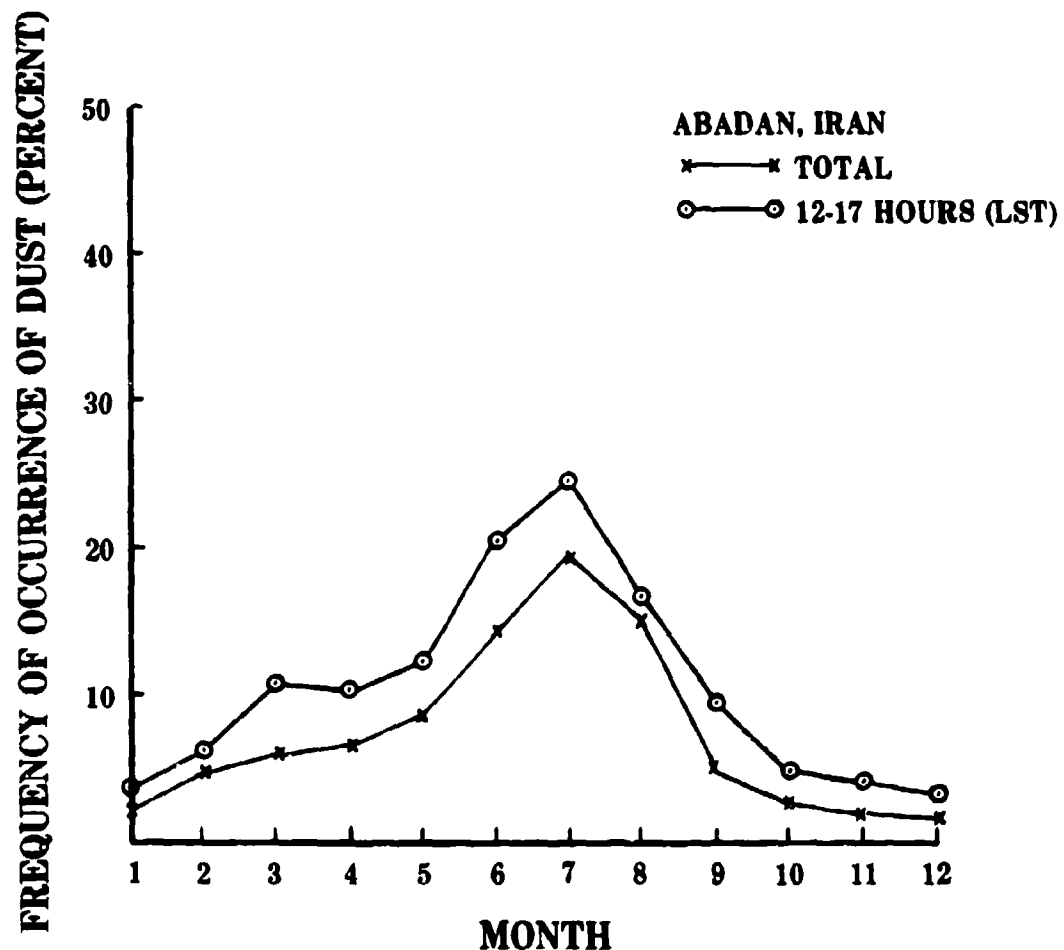


FIGURE 4. PERCENT FREQUENCY OF OCCURRENCE OF DUST BY MONTH AT ABADAN, IRAN.

TABLE I. FACTORS INFLUENCING MOVEMENT OF SOIL BY WIND

- |                     |                 |                       |
|---------------------|-----------------|-----------------------|
| 1. Air              | 2. Ground       | 3. Soil               |
| a. velocity         | a. roughness    | a. structure affected |
| b. turbulence       | b. cover        | organic matter, lime  |
| c. density          | c. obstructions | content, and texture  |
| d. viscosity        | d. temperature  | b. specific gravity   |
| e. moisture content | e. topography   | c. moisture content   |

UNCLASSIFIED

**UNCLASSIFIED**

B-17

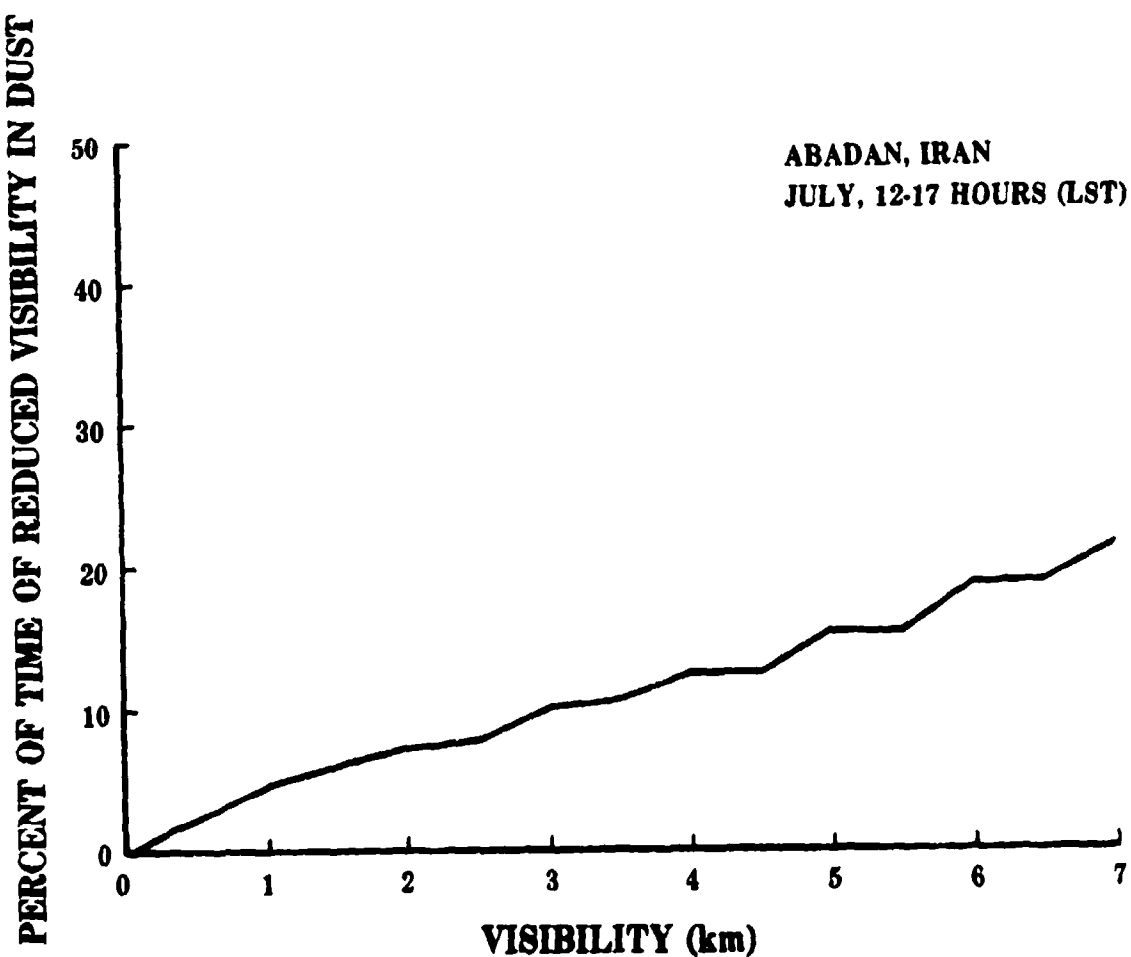


FIGURE 5. PERCENT OF TIME OF REDUCED VISIBILITY DURING JULY 12-17 HOURS (LST) AT ABADAN, IRAN.

### 3. AEROSOL CHARACTERISTICS AFFECTING ATMOSPHERIC OPTICAL PROPERTIES

The characteristics of atmospheric aerosols or airborne dust particles which most strongly affect the optical properties of the atmosphere are:

- (1) particle size distribution
- (2) particle number density or concentration,
- (3) complex index of refraction, and
- (4) particle shape.

The particle size distribution is an important factor in the transfer of radiation through the atmosphere since with a more narrow distribution the dependence of extinction on wavelength is stronger, while with a broad distribution extinction becomes independent of wavelength. It has been

**UNCLASSIFIED**

617

UNCLASSIFIED

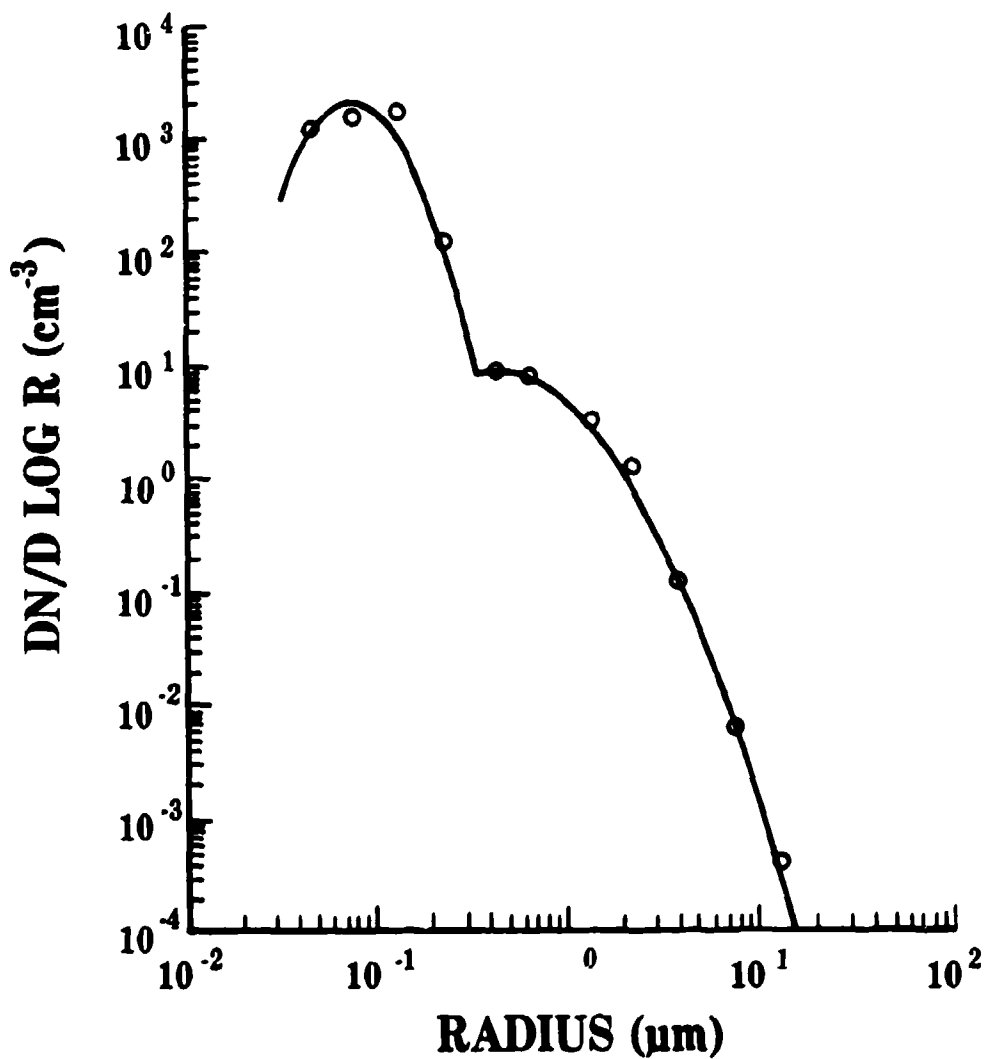


FIGURE 6. TYPICAL SIZE DISTRIBUTION OF AIRBORNE DUST (Patterson and Gillette, 1977a).

found that for visible wavelengths the particles which contribute most to extinction are those in the size range  $0.62 < r < 20 \mu\text{m}$  (Patterson, et al., 1976) while larger ones contribute more significantly at longer wavelengths. Although the size distribution of the soil particles in the atmosphere is a function of the parent soil, it is not identical to the surface soil size distribution. Measurements have indicated that the size distribution is generally multimodal (Patterson and Gillette, 1977a) as illustrated in Figure 6. This multimodality characteristic may be explained by considering the physical processes involved in causing soil particles to leave the surface of the earth and enter the atmosphere. In 1941, R. A. Bagnold (1941) presented a theoretical discussion of these processes which is still accepted as valid.

UNCLASSIFIED

**UNCLASSIFIED**

B-17

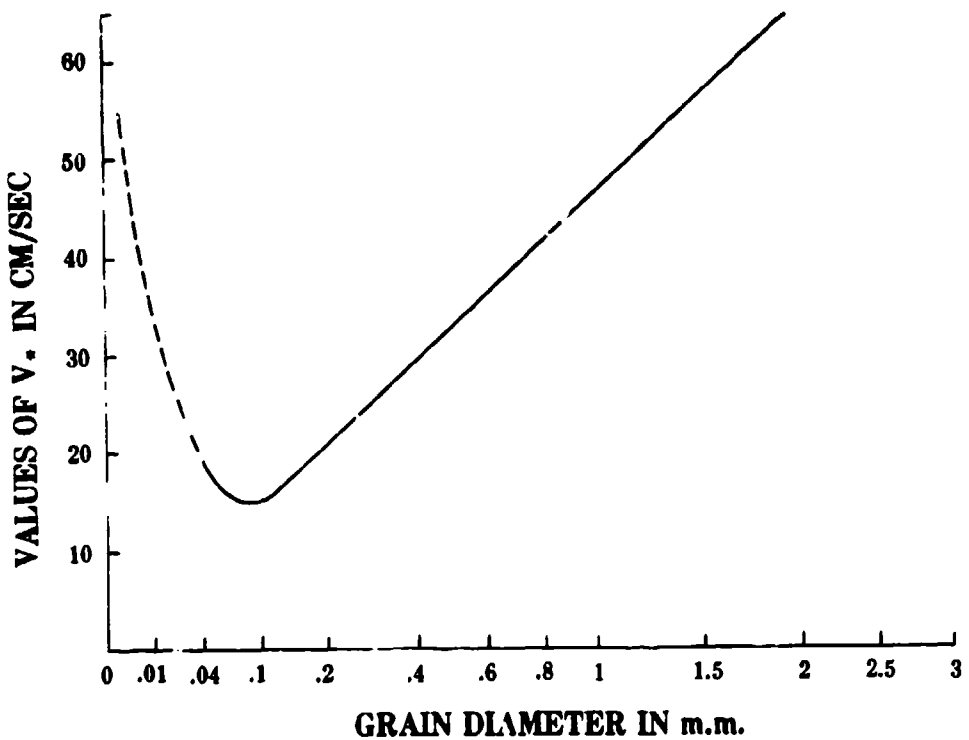


FIGURE 7. SIZE OF PARTICLE SUSCEPTIBLE TO MOVEMENT BY WIND VS FRICTION VELOCITY  $V_*$ .  
 $V_*$  is related to wind velocity  $V$  at altitude  $Z$  by  $V = 5.75V_*\log(Z/k)$   
where  $k$  is roughness length (after Bagnold, 1941).

According to Bagnold there is an optimal size ~0.1 mm diameter for particles to be susceptible to movement by the wind as shown in Figure 7. Smaller particles are less likely to be injected into the air by wind because of their reduced cross-sectional area while larger particles will be more difficult to be picked up because of their increased mass. These particles which are picked up directly by the wind comprise the "saltation mode" and are carried along by the wind in a series of short bounces. The peak value in the size distribution for this mode is the radius between 10 and 100  $\mu\text{m}$ . The saltation mode particles have a fairly high fall velocity as shown in Figure 8 and disappear rapidly from the overall size distribution as the wind decreases.

The suspension mode consists of smaller particles injected into the atmosphere when larger particles such as those in the saltation mode bounce on the surface or strike agglomerates causing small pieces to break off. These particles generally have a radius mode between 1 and 10  $\mu\text{m}$  and fall much more slowly than saltation mode particles since the viscosity of the atmosphere tends to retard

**UNCLASSIFIED**

## UNCLASSIFIED

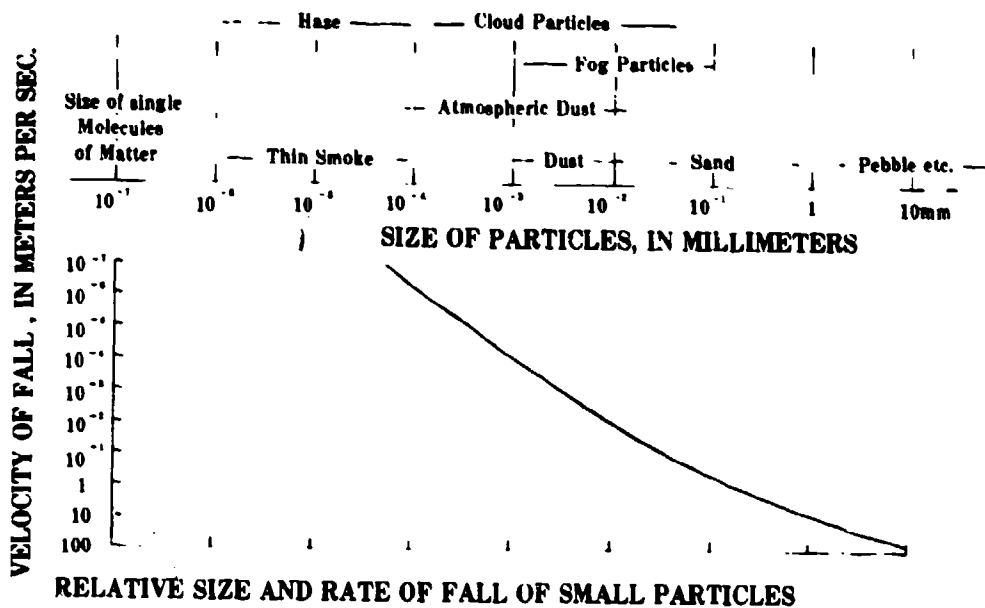


FIGURE 8. RELATIVE SIZE AND RATE OF FALL OF SMALL PARTICLES (after Bagnold, 1941).

their descent. This mode generally appears somewhat later in a storm and tends to reach an equilibrium size distribution which is approximately constant with wind speed (Gillette, et al., 1974).

The particles comprising suspension mode are the most important to constituting the optical properties of the atmosphere with the saltation mode particles being less significant. Two other modes which are usually negligible from an optics viewpoint are the surface creep mode and the background mode. The particulates comprising the surface creep mode range in size from 0.5mm to 1.0mm in diameter and tend to roll and slide along the surface. The background mode consists of particles from .02 to  $0.5\mu\text{m}$  in diameter. It appears to always be present in the atmosphere and is unrelated to the other modes in composition.

Models of the particle size distributions of naturally occurring dust usually use lognormal or power-law distributions (Schutz and Jaenicke, 1974; Gillette, et al., 1972; Gillette, 1974; Blifford and Gillette, 1971). It appears that a reasonably realistic size distribution model would be one composed of overlapping lognormal distributions, one for each particle mode to be included (Gillette, 1974; Blifford and Gillette, 1971).

UNCLASSIFIED

# UNCLASSIFIED

B-17

Within a single storm the particle number density or concentration is highly variable horizontally if the winds are strong and/or gusty. One observation of dust cloud mass concentration made using lidar backscatter data showed variations of over a factor of eight (Barber, 1979). The mean mass concentration is strongly correlated to the mean friction velocity which is a function of the horizontal wind speed, height above the surface, and roughness of the surface. Of course, the erodibility of the soil is also an important factor (Shinn, et al., 1974). Variations in the concentration are related to fluctuations in vertical wind speed which result from turbulent flow. However, because of the inertia of the particles, one cannot be sure that they are traveling with the atmospheric flow; but their behavior will be dependent upon the size of the particles in relation to the scale of the turbulence and upon the interactions of the particles when the concentration is high (Hidy and Brock, 1970).

The distribution of dust with height is strongly influenced by the thermal stratification (Karenblatt and Golitsyn, 1974). Under convective conditions such as exist during the initial and active stages of a dust storm, the concentration of the suspension mode particles tends to a constant value to large heights. For stable conditions the concentration of these particles diminishes exponentially with height. The saltation mode particles will be found only in the lowest few meters above the surface and only during periods of strong surface winds.

Efforts have been made to relate visibility directly to mass concentration of airborne dust particles (Patterson and Gillette, 1977b) using the relationship  $MV^Y = C$ , where M is mass concentration, V is visibility, and Y and C are constants. It was found that there was no single value of C that was generally applicable for relating mass concentration and visibility.

The complex index of refraction is dependent upon the chemical composition of the dust particles. Calculations have shown that extinction of visible and near-infrared radiation by airborne dust is nearly independent of the complex index of refraction over a reasonably wide range of realistic atmospheric values (Jennings and Gillespie, 1978). In the middle infrared region (8-12 $\mu$ m) extinction is more strongly dependent upon the complex index of refraction and both the real and imaginary parts are more variable with soil type than at shorter wavelengths. Measurements have shown that for certain soil types, especially clays, absorption makes a significant contribution (25-50%) to total extinction in the middle infrared regions (Carlon, 1980) implying that the imaginary part of the index of refraction is critical in this region. Studies by Gillette and Walker (1977) have shown that for at least some soil types, the saltation mode particles are usually quartz and the suspension mode usually consists of various clay minerals. Clay particles are more fragile than quartz and thus tend to break

# UNCLASSIFIED

621

**UNCLASSIFIED**

into smaller pieces when sandblasted during windy conditions. As a result, the most optically significant particles tend to be of types of clay, for which the complex index of refraction can vary considerably in the middle infrared region. Thus, it is difficult to make statements about the optical properties of dust in the 8-12 $\mu\text{m}$  wavelength region which would have application in a variety of geographical locations.

The irregular shapes of dust particles affects the radiative transfer properties of the atmosphere and adds another level of complexity to the already complex problems of modeling. The standard Mie scattering theory applicable for spherical particles is generally thought to give satisfactory results for total extinction calculations but is unsatisfactory for calculating scattering patterns and back-scatter amounts. There are currently computation techniques being developed (Chylek, et al., 1976; Pollack and Cuzzi, 1980) for handling the nonspherical shapes which should prove useful in future modeling efforts.

**4. MECHANISMS FOR REMOVAL OF DUST FROM ATMOSPHERE**

The saltation mode particles are generally removed rather rapidly by direct fallout and this mode tends to disappear with decreasing wind speed. The suspension mode particles fall out much more slowly and may be transported hundreds of kilometers from their place of origin before being removed from the atmosphere. Rainout and washout are mechanisms which can cause removal of the smaller particles. Small hygroscopic particles may be removed by fallout by encountering air containing moisture which will cause them to increase in size by absorption of moisture and thus fall faster.

**5. ESTIMATES OF EXTINCTION DURING A DUST STORM**

On 6 June 1977, a Sharav (Khamsin) dust storm occurred in the Negev desert of Israel, brought on by the passage of a low pressure system coming from the North Africa deserts (Levin, et al., 1980). The dust appeared first at high altitudes and then later was observed at the surface. The horizontal visibility ranges from 40 to 50 kilometers in the morning hours until about 1100 LST when it decreased and ranged from 1 to 10 kilometers.

During the course of the storm and for the two days following the storm measurements were made at the Wise Astronomical Observatory of Tel Aviv University near Mitzpe Ramon (latitude 30.596 N, longitude 34.762 E, 890 meters MSL). Aerosol size distributions were measured with a Royco optical

**UNCLASSIFIED**

# UNCLASSIFIED

B-17

counter. The imaginary part of the index of refraction was found for a period of time which included the storm. These data have been analyzed and discussed by Levin (1980).

To obtain estimates of the extinction and scattering which would occur during Sharav conditions, Mie calculations have been made and some of the results are presented in Figures 9 and 10. The particle size distributions used in calculations were power law distributions with parameters as Levin derived from his measurements. The complex indices of refraction used were as found by Levin, if available, or else typical values for desert aerosols. Values of the various parameters used are given in Table II.

TABLE II. DATA PARAMETERS USED IN MIE CALCULATIONS

Date/Time	Number Density (particles/cm <sup>3</sup> )	Power Law Distribution Parameters	
		C	B
6/6/1'00	31	10.60	1.38
/1130	32	10.13	1.46
/1230	58	7.93	1.97
/1330	53	13.80	1.71
/1405	29	5.91	2.19
/1550	23	5.54	2.13
/1630	17	3.14	2.27
6/7/0805	9	0.85	2.48
/0900	6	0.53	2.55
/1200	5	0.56	2.30
/1405	5	0.37	2.48
/1700	8	1.56	1.98
6/8/0845	4	2.63	2.17
/1145	3	0.74	1.74
/1630	13	2.17	2.03

Wavelength	Complex Index of Refraction
0.55μm	1.55-0.0051
1.06μm	1.55-0.0041
4.0μm	1.55-0.0041
10.6μm	1.7 -0.21

Particle Radius Maximum = 10μm

Particle Radius Minimum = 0.2μm

Particle Density = 2.5 gm/cm<sup>3</sup>

Path Length = 1 km

# UNCLASSIFIED

623

UNCLASSIFIED

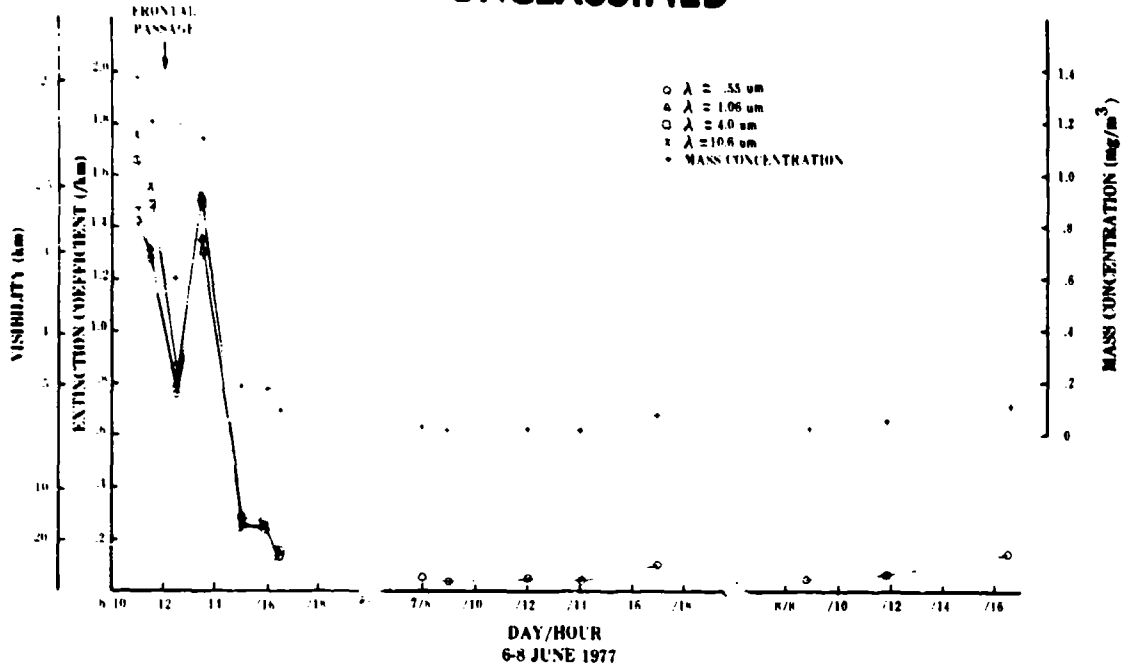


FIGURE 9. EXTINCTION COEFFICIENT, VISIBILITY, AND MASS CONCENTRATION DURING SHARAV CONDITIONS.

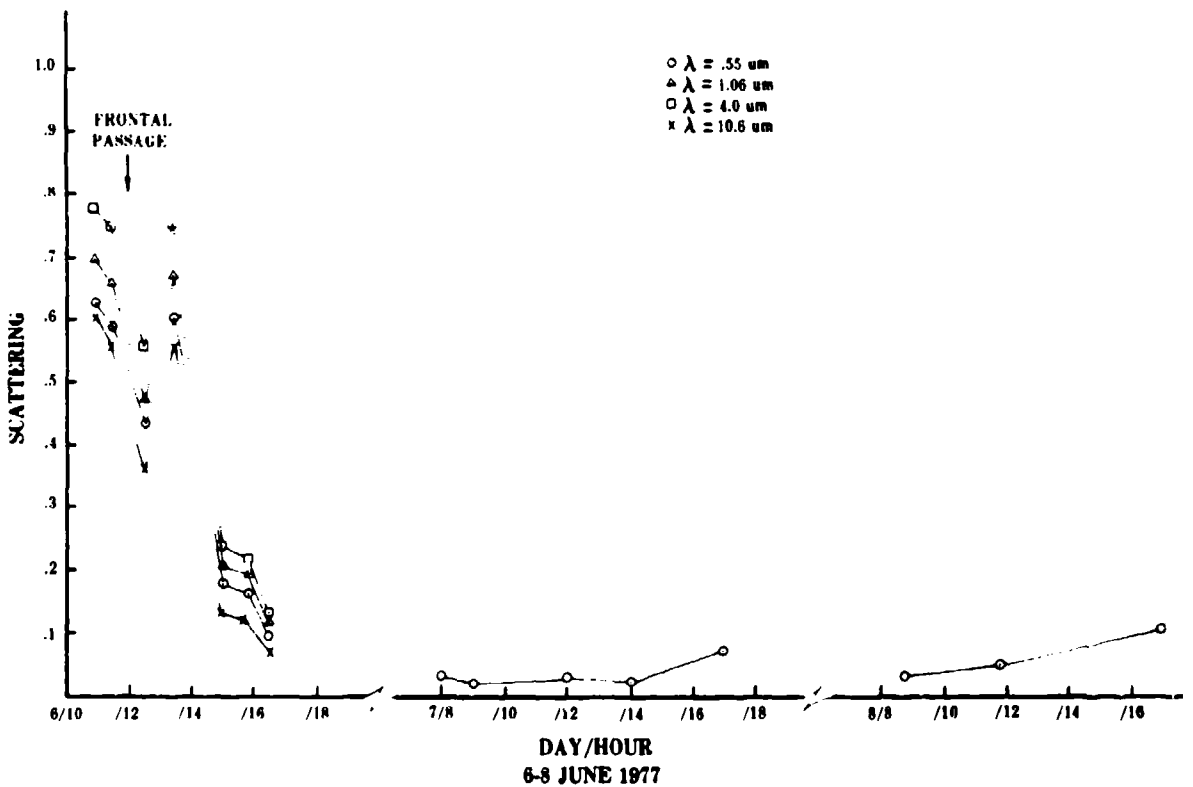


FIGURE 10. ATMOSPHERIC SCATTERING DURING SHARAV CONDITIONS (1 km path).

UNCLASSIFIED

# UNCLASSIFIED

B-17

The Mie calculations were done in four wavelengths: 0.55, 1.06, 4.0, and 10.6 micrometers. However, in Figures 9 and 10 only data for 0.55 micrometer are shown for 7 and 8 June because the data points for the other wavelengths were very nearly identical to the 0.55 micrometer data points. Note that scattering shown in Figure 10 is for a geometric path length of one kilometer.

The total extinction increases with increasing wavelength during the early part of the storm, while for scattering, the 10.6 micrometer wavelength undergoes less effect than the other wavelengths calculated. However, the absorption at 10.6 micrometers is greater than at other wavelengths, making the total extinction at 10.6 micrometers greater.

In addition to these calculations, Mie scattering calculations were also made by using the measured particle size distributions (instead of power law distributions). The magnitudes of the extinction and scattering found were comparable to or smaller than those derived from the power law distributions.

These results are most likely degraded somewhat by the use of some assumptions necessary for the Mie calculations, namely, that the dust particles are spherical, uniformly distributed, and have uniform complex indices of refraction, and that multiple scattering effects are negligible. The impact of these assumptions is not well known for such conditions. However, the results given here provide estimates of the magnitudes of the effects that dust storms can have on electromagnetic radiation.

## 6. CONCLUSIONS

The optical properties of atmosphere laden with windblown dust are strongly dependent upon the dust particle size distribution and the number density (which may be highly variable within a dust cloud). In the middle infrared spectral region the complex index of refraction which is variable with soil composition is also an important factor. The determination of the relationship between the optical properties of a dust cloud and measurable meteorological parameters requires a knowledge of the processes causing wind erosion and the interrelationships between various surface and atmospheric characteristics.

Single scattering calculations based on particle size distributions made during a Middle East dust storm have shown that extinction during the early stages of the storm is greater for middle infrared wavelengths than for near infrared or visible wavelengths. This results from the increased

# UNCLASSIFIED

625

**UNCLASSIFIED**

absorption of middle infrared wavelengths by airborne dust particles. As the storm decreases, the larger particles tend to settle out leaving primarily suspension mode particles. The extinction during this time is less wavelength dependent, with reduced scattering effects at the longer wavelengths being offset by more absorption than that occurring at shorter wavelengths.

There are several important parameters for which sufficient data is not available from which to construct and evaluate models. Among these are detailed number density and particle size distribution measurements showing the spatial variations in both the horizontal and vertical. Another is transmittance measurements through dust clouds whose other properties have also been measured.

**7. REFERENCES**

- Bagnold, R. A., 1941: The Physics of Blown Sand and Desert Dunes, Chapman and Hall, London.
- Barber, T. L., 1979: Short-time Mass Variation in Natural Atmospheric Dust, ASL-TR-0045, Atmospheric Sciences Laboratory, White Sands Missile Range, NM.
- Barenblatt, G. I., and G. S. Golitsyn, 1974: "Local Structure of Mature Dust Storms," Journal of the Atmospheric Sciences, 31:1917-1933.
- Blifford, I. H., Jr., and D. A. Gillette, 1971: "Applications of the Lognormal Frequency Distribution to the Chemical Composition and Size Distribution of Naturally Occurring Atmospheric Aerosols," Water, Air, and Soil Pollution, 1:106-114.
- Carlon, H. R., 1980: "Contributions of Particle Absorption to Mass Extinction Coefficients (0.55-14 $\mu$ m) of Soil-Derived Atmospheric Dusts," Applied Optics, 19:1165-1172.
- Chepil, W. S., 1945: "Dynamics of Wind Erosion: I. Nature of Movement of Soil by Wind," Soil Science, 60:305-320.
- Chylek, P., G. W. Grams, and R. G. Pinnick, 1976: "Light Scattering by Irregular Randomly Oriented Particles," Science, 193:480-482.
- Gillette, D. A., 1974: "Production of Fine Dust by Wind Erosion of Soil: Effect of Wind and Soil Texture," Atmosphere-Surface Exchange of Particulate and Gaseous Pollutants Symposium, ERDA, CONF-740921.
- Gillette, D. A., I. H. Blifford, Jr., and C. R. Fenster, 1972: "Measurements of Aerosol Size Distributions and Vertical Fluxes of Aerosols on Land Subject to Wind Erosion," Journal of Applied Meteorology, 11:977-987.

**UNCLASSIFIED**

# UNCLASSIFIED

B-17

- Gillette, D. A., I. H. Blifford, Jr., and D. W. Fryrear, 1974: "The Influence of Wind Velocity on the Size Distributions of Aerosols Generated by the Wind Erosion of Soils," Journal of Geophysical Research, 79:4068-4075.
- Gillette, D. A., and T. R. Walker, 1977: "Characteristics of Airborne Particles Produced by Wind Erosion of Sandy Soil, High Plains of West Texas," Soil Science, 123:97-110.
- Hidy, G. M., and J. R. Brock, 1970: The Dynamics of Aerocolloidal Systems, Pergamon Press, Oxford, England.
- Hinds, B. D., and G. B. Hoidal, 1975: Boundary Layer Dust Occurrence II: Atmospheric Dust Over the Middle East, Near East and North Africa, ECOM-DR-75-4, Atmospheric Sciences Laboratory, White Sands Missile Range, NM.
- Jennings, S. G., and J. B. Gillespie, 1978: Mie Theory Sensitivity Studies - The Effects of Aerosol Complex Refractive Index and Size Distribution Variations on Extinction and Absorption Coefficients, Part II: Analysis of the Computational Results, ASL-TR-0003, Atmospheric Sciences Laboratory, White Sands Missile Range, NM.
- Levin, Z., J. H. Joseph, and Y. Mekler, 1980: "Properties of Sharav (Khamsin) Dust-Comparison of Optical and Direct Sampling Data," Journal of Atmospheric Sciences, 37:882-891.
- Patterson, E. M., and D. A. Gillette, 1977a: "Commonalities in Measured Size Distributions for Aerosols Having a Soil-Derived Component," Journal of Geophysical Research, 82:2074-2082.
- Patterson, E. M., and D. A. Gillette, 1977b: "Measurements of Visibility vs Mass Concentration for Airborne Soil Particles," Atmospheric Environment, 11:193-196.
- Patterson, E. M., D. A. Gillette, and G. W. Grams, 1976: "The Relation Between Visibility and the Size-Number Distribution of Airborne Soil Particles," Journal of Applied Meteorology, 15:470-478.
- Pollack, J. B., and J. N. Cuzzi, 1980: "Scattering by Nonspherical Particles of Size Comparable to a Wavelength: A New Semi-Empirical Theory and Its Application to Tropospheric Aerosols," Journal of Atmospheric Sciences, 37:868-881.
- Schutz, L., and R. Jaenicke, 1974: "Particle Number and Mass Distributions Above  $10^{-4}$  cm Radius in Sand and Aerosol of the Sahara Desert," Journal of Applied Meteorology, 13:863-870.
- Shinn, J. H., N. C. Kennedy, J. S. Koval, B. R. Clegg, and W. M. Porch, 1974: "Observations of Dust Flux in the Surface Boundary Layer for Steady and Nonsteady Cases," Atmosphere-Surface Exchange of Particulate and Gaseous Pollutants Symposium, ERDA, CONF-740921.

# UNCLASSIFIED

**UNCLASSIFIED**

AREA C

SMOKE/OBSCURANT TECHNOLOGY AND HARDWARE DEVELOPMENT

**UNCLASSIFIED**

PRECORING PAGE BLANK-NOT FILMED

**UNCLASSIFIED**

THE OPTICAL PROPERTIES OF PHOSPHORUS SMOKE IN  
THE 7-14  $\mu\text{m}$  INFRARED

M.E. MILHAM

D.H. ANDERSON

CHEMICAL SYSTEMS LABORATORY

ABERDEEN PROVING GROUND, MARYLAND

**ABSTRACT**

As a result of the recent renewal of interest in the optical properties of military smokes, extensive measurements of the extinction spectra of white/red phosphorus (WP/RP) have been made in the 3-5  $\mu\text{m}$  and 7-14  $\mu\text{m}$  spectral regions. Lorenz-Mie calculations and experimental measurements on o-phosphoric acid have shown that the smoke particles produced by burning phosphorus in the open atmosphere are not composed of o-phosphoric acid, but instead are composed of complex oxyphosphorus acids. The extinction of phosphorus smoke can be calculated with reasonable accuracy by using the optical constants of o-phosphoric acid in the 3-5  $\mu\text{m}$  infrared, but not in the 7-14  $\mu\text{m}$  infrared. In this study a new method of determining optical constants from extinction spectra will be briefly described and applied to phosphorus smoke in the 7-14  $\mu\text{m}$  infrared. Extinction spectra and the corresponding optical constants for phosphorus smoke will be presented as a function of relative humidity. Because the complex oxyphosphorus acids which are present in the smoke droplets evolve with time toward simpler chemical species, the extinction of phosphorus smoke in the 7-14  $\mu\text{m}$  infrared is time dependent. The time dependent extinction spectra and optical constants will be presented and the optical constant data will be examined for insight into the chemical nature of phosphorus smoke. Finally, the effective extinction coefficients for phosphorus smoke across the 7-14  $\mu\text{m}$  band will be presented as functions of relative humidity and time.

**UNCLASSIFIED**

**UNCLASSIFIED**

## I. INTRODUCTION

The extinction spectra of phosphorus smoke in the 7-14  $\mu\text{m}$  spectral region are of special interest because the oxyphosphorus compounds in the smoke droplets are optically active in this region, and thus, the extinction spectra taken under different environmental conditions contain much useful information about the changing chemical and physical properties of the smoke droplets. This paper presents a study of the infrared optical properties of phosphorus smoke in the 7-14  $\mu\text{m}$  spectral region. We define the broad term optical properties to mean experimentally determined extinction spectra and three additional quantities derived from the spectral extinction - the optical constants  $n(\lambda)$ ,  $k(\lambda)$  and the effective or integrated extinction across the 7-14  $\mu\text{m}$  band. Since phosphorus smoke is hygroscopic, the moisture content of the atmosphere in which the smoke is disseminated has a strong influence on the extinction. A change in the atmospheric relative humidity changes the particle size distribution, the optical constants, and the density of the particles. Phosphorus smoke is also chemically unstable and, as a result, the extinction of phosphorus smoke in the 7-14  $\mu\text{m}$  band is time dependent.

In the first part of this paper, we will review the changes in the spectral extinction of phosphorus smoke with relative humidity and with time, and in the second part, we will present the optical constants and effective extinction across the 7-14  $\mu\text{m}$  band which were derived from the spectral extinction measurements.

The test facility used to make these measurements was the DARCOM Smoke Characterization Facility (Figure 1), which is part of the Chemical Systems Laboratory located at Aberdeen Proving Ground, MD. The spectral extinction was measured by burning a known amount of phosphorus - either white or red phosphorus (WP/RP) - in the 190  $\text{m}^3$  chamber; the phosphorus smoke was stirred continuously in order to maintain a uniform aerosol concentration. An Exotech model 10-24 radiometer with a circular variable filter monochromator was used to scan the 7-14  $\mu\text{m}$  region at the rate of 15 scans per minute; the path length through the aerosol was 6.1 m. Particle size samples were taken with an Andersen model 2000 cascade impactor, and the aerosol mass concentration was determined from samples taken on glass fiber filters. A moisture absorbing "train" containing magnesium perchlorate desiccant is used for a gravimetric

**UNCLASSIFIED**

**UNCLASSIFIED**

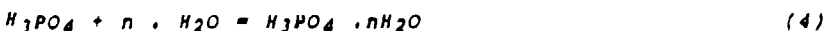
determination of absolute and relative humidity. The extinction spectra were determined by a Beer's law analysis

$$\alpha(\lambda) = -1/CL \ln \{I(\lambda)/I_0(\lambda)\} \quad (1)$$

where  $\alpha(\lambda)$  = extinction coefficient at wavelength  $\lambda$ , ( $m^2/gm$ )  
 $C$  = aerosol concentration, ( $gm/m^3$ )  
 $L$  = optical pathlength, ( $m$ )  
 $I(\lambda)$  = measured spectral intensity with smoke in the chamber, (volts)  
 $I_0(\lambda)$  = measured spectral intensity with no smoke in the chamber, (volts)

Figure 2 shows a typical phosphorus extinction spectrum which is characterized by extinction peaks located near 8  $\mu m$  and 10  $\mu m$  with a relative extinction minimum between the peaks and a "shoulder" near 11  $\mu m$ ; beyond 11  $\mu m$  the extinction falls rapidly to a relatively constant level. One of the remarkable aspects of the unaged phosphorus smoke spectra is the general reproducibility of the spectral profile. Phosphorus, when burned alone or in formulations which contain organic polymeric binders, catalysts, and oxidizers, produces spectra of the same characteristic shape, somewhat dependent on relative humidity, but otherwise easily recognized as those of phosphorus smokes.

The formation of a phosphorus smoke is usually described by the chemical equations:



The validity of this formation mechanism is easily tested by an experiment in which a solution of  $\alpha$ -phosphoric acid is sprayed into the test chamber; the extinction spectrum is determined and compared with the phosphorus extinction spectrum<sup>1</sup>. Figure 3 shows the results of such an experiment compared with a spectrum calculated from Lorenz-Mie theory by using the optical constants<sup>2</sup> for 65% (by weight)  $\alpha$ -phosphoric acid. The

**UNCLASSIFIED**

**UNCLASSIFIED**

measured particle size distribution was represented by a log-normal distribution with a mass median diameter (MMD) of 3.3  $\mu\text{m}$  and a geometric standard deviation ( $\sigma_g$ ) of 2.0. While there is excellent agreement between the measured and calculated spectrum for o-phosphoric acid, this clearly is not a phosphorus smoke spectrum. The chemistry of the smoke formation must be more complex than indicated by Equations 2-4. Certainly, the hydration of o-phosphoric acid to produce the final smoke droplets cannot be correct, and if the reaction of phosphorus pentoxide with water to produce o-phosphoric acid has any validity, it cannot occur directly. Instead, the reaction must proceed through the formation of intermediate compounds which are optically active in the 7-14  $\mu\text{m}$  region.

**II. DEPENDENCE OF PHOSPHORUS SMOKE****EXTINCTION ON RELATIVE HUMIDITY**

Figure 4 shows the changes to the white phosphorus extinction spectrum which occur when the relative humidity increases from 23% to 85%; these spectra were obtained by burning FISCHER NF grade WP in the chamber. Figure 5 shows the calculated extinction of o-phosphoric acid for eight relative humidities (concentrations)<sup>3</sup> as well as the extinction spectrum for water<sup>4</sup> (100%RH). The behavior of the extinction for phosphorus smoke and o-phosphoric acid aerosols is typical of hygroscopic materials and becomes more waterlike as the relative humidity increases. The 85% RH spectrum for WP has changed substantially from the lower RH spectra; however, it is not nearly as waterlike as the 82% RH o-phosphoric acid spectrum. Therefore, it would appear that the uptake of water for phosphorus smoke is less than for o-phosphoric acid at the same relative humidity, and the transition of phosphorus smoke to waterlike spectra occurs for a relative humidity which is higher than the corresponding relative humidity for o-phosphoric acid.

**III. TIME DEPENDENT EXTINCTION SPECTRA FOR PHOSPHORUS SMOKE**

In order to examine the variation of the phosphorus smoke extinction with time, an experiment<sup>5</sup> was conducted in which 51.1 gm of red phosphorus were burned in the test chamber. The resulting phosphorus smoke was held in the chamber for 280 min. after the phosphorus ignition and scanned continuously with the Exotech radiometer. Measurements of the aerosol concentration, relative humidity, and particle size distribution were made at various times throughout the test; Table I shows the results of these measurements as a function of time. The concentration measurements are presented as values of the concentration - path length product (CL). The phosphorus smoke behaved

**UNCLASSIFIED**

**UNCLASSIFIED**

in a predictable fashion for a hygroscopic material; the mass median diameter (MMD) of the smoke particles increased with time while the relative humidity inside the chamber decreased slightly (7.2%). The extinction spectra taken during twenty-eight sampling periods were determined by a Beer's law analysis of the radiometer data. The values of the transmitted intensity with aerosol in the chamber were determined by averaging 75-80 radiometer scans for each of the sampling periods. The intensity with no aerosol in the chamber was determined by averaging fifty radiometer scans taken before the phosphorus ignition with fifty scans taken after the aerosol was vented at the end of the test. The intrasample variability of the scans was not statistically significant. The resulting extinction spectra are shown in Figures 6,8-12.

Figure 6 shows the overall spectral changes which occur in the 7-14  $\mu\text{m}$  phosphorus smoke extinction as time increases. The extinction spectra taken up to 16.9 min. after the phosphorus ignition show little change in spectral shape. Thereafter, the spectral signature changes slowly, and the overall level of extinction tends to rise as the 8  $\mu\text{m}$  peak disappears and the magnitude of the 10  $\mu\text{m}$  extinction peak increases at first and then falls to a somewhat lower level. The location of the extinction peak near 10  $\mu\text{m}$  also shifts to longer wavelengths as the smoke ages; this shift is probably due to the increase in particle size which results from coagulation and growth of the aerosol. The location of the "shoulder" was relatively stable throughout the duration of the test, although it tends to become somewhat indistinct as the smoke ages. In the region beyond 12  $\mu\text{m}$ , the extinction tends to rise throughout the test, as would be expected, since this region is sensitive to the increase in hydration of the aerosol which is taking place.

Figure 7 shows the predicted extinction spectra that would have been obtained if the smoke particles in Figure 6 had been pure o-phosphoric at the same relative humidity. These spectra were computed<sup>5</sup> using the particle sizes predicted from a simple Smoluchowski model of coagulation and a drop-growth model for o-phosphoric acid and phosphorus smoke<sup>6</sup>. The o-phosphoric acid spectra are not in good agreement with the phosphorus spectra at any time, but the agreement is better for the phosphorus smoke near the end of the test. Apparently, the smoke droplets are evolving slowly toward o-phosphoric acid. Figures 8-12 show the detailed spectral changes that occurred during the test.

**UNCLASSIFIED**

**UNCLASSIFIED****IV. DETERMINATION OF OPTICAL CONSTANTS**

In the preceding sections, we have seen how the extinction spectra of phosphorus smoke vary with the relative humidity and with time. From these extinction spectra we would now like to derive the optical constants ( $n, k$ ) which are, respectively, the real and imaginary components of the spectral complex refractive index<sup>7</sup>.

$$N(\lambda) = n(\lambda) - ik(\lambda) \quad (5)$$

The procedure for deriving the optical constants from the extinction spectra should meet three criteria: (1) the polydispersity of the aerosol should be accounted for, (2) the optical dispersion of the material should be taken into account, and (3) the optical constants which are found should be the unique ( $n, k$ ) pair which characterizes the optical behaviour of the material. A complete description of the method of obtaining the optical constants from extinction measurements is contained in reference 7. In the development that follows we take a heuristic approach to the problem.

Figure 13 shows a flow chart of the algorithm for finding the optical constants from extinction spectra. This algorithm is an iterative procedure which, after an initial estimate of  $n(\lambda)$ , fits the  $k(\lambda)$  spectrum to the measured extinction spectrum by assuming that the extinction coefficient increases monotonically with  $k$  and then uses a subtractive Kramers-Kronig (SKK) analysis to establish a new estimate for  $n(\lambda)$ . The  $a_e(\lambda)$  are the measured values of the spectral extinction and the values of  $a_c(\lambda)$  are computed from Lorenz-Mie theory by integrating over the particle size distribution

$$a_c(\lambda) = \frac{3}{2\rho} \int [Q_e(N(\lambda), X)/D] dM \quad (6)$$

where  $Q_e$  = the efficiency factor for extinction

$X = \pi D/\lambda$ , the size parameter

$\rho$  = density of the particulate material, (gm/cm<sup>3</sup>)

$D$  = particle diameter, (μm)

$dM$  = mass size distribution function of the particles

For this study the mass size distribution was described by the log-normal distribution function

**UNCLASSIFIED**

# UNCLASSIFIED

C-1

$$dN = (2\pi \ln^2 \sigma_g)^{-1/2} \exp \left( \ln^2(D/D_m)/2\ln^2 \sigma_g \right) d\ln D \quad (7)$$

where  $D_m$  = mass median diameter

$\sigma_g$  = geometric standard deviation

- In order to assure that  $a_c(\lambda)$  is monotonically increasing with respect to  $k$ , it is necessary: (1) to restrict  $k$  to the range 0 to  $\sqrt{2}$  and (2) to place some limits on the particle size distributions. The restriction on the range of  $k$  poses no difficulty since most condensed matter has  $k$  values which lie in this region. Table II shows values of the mass median size parameter,

$$x_m = \pi D_m / \lambda \quad (8)$$

below which the extinction coefficient will be monotonic with respect to  $k$ . Table II shows that the extinction coefficient will be monotonic with respect to  $k$  for the range of optical constants and particle sizes likely to be encountered in nearly all practical problems in the 7-14  $\mu\text{m}$  spectral region. The initial estimate of  $n(\lambda)$  is taken to be 1.3, and the initial estimate of  $k$  is  $k_0 = \sqrt{2}/2$ .

The Kramers-Kronig relationship between  $n(\lambda_0)$  and the  $k(\lambda)$  spectrum is given by:

$$n(\lambda_0) = 1 + \frac{2\lambda_0^2}{\pi} P \int_0^\infty \frac{k(\lambda)d\lambda}{\lambda(\lambda_0^2 - \lambda^2)} \quad (9)$$

where  $P$  indicates the Cauchy principal value is to be taken. The integral in Equation 9 is to be evaluated over the entire electromagnetic spectrum, and since  $k(\lambda)$  is known only over a finite region ( $\lambda_{\min} < \lambda < \lambda_{\max}$ ) of the spectrum, it is necessary to extend the  $k$ -spectrum beyond the wavelength region where the data are known experimentally.

# UNCLASSIFIED

**UNCLASSIFIED**

The inaccuracies introduced by extending the k-spectrum can be reduced to relative insignificance by employing a subtractive Kramers-Kronig analysis (SKK). Assume that the real part of the refractive index  $n(\lambda_1)$  is known and subtract the KK expression for  $n(\lambda_1)$  from the KK expression for  $n(\lambda_o)$  in order to obtain the subtractive Kramers-Kronig relationship<sup>4,8-9</sup>:

$$n(\lambda_o) = n(\lambda_1) + \frac{2(\lambda_1^2 - \lambda_o^2)}{\pi} P \int_0^\infty \frac{\lambda k(\lambda) d\lambda}{(\lambda_o^2 - \lambda^2)(\lambda_1^2 - \lambda^2)} \quad (10)$$

The integral is now evaluated by letting  $k(\lambda) = k(\lambda_{min})$  for  $0 < \lambda < \lambda_{min}$  and  $k(\lambda) = k(\lambda_{max})$  for  $\lambda_{max} < \lambda < \infty$ . In general, these are not good physical approximations for  $k(\lambda)$  in the spectral regions where  $k(\lambda)$  has not been measured; but, as mentioned previously, this approximation will have an insignificant effect on the result produced by the SKK algorithm.

Let us now apply this algorithm to the two extinction spectra shown in Figure 3. First, we shall apply this method to the computed o-phosphoric acid extinction spectrum to see how accurately we can recover the values for  $n(\lambda)$  and  $k(\lambda)$  which were used to compute the spectrum. The results of the calculation are shown in Figures 14 and 15; the difference between the values computed from the extinction spectrum and the known values of  $n(\lambda)$  and  $k(\lambda)$  is less than one percent across the 7-14  $\mu\text{m}$  band. When the experimentally determined extinction spectrum from Figure 3 is analyzed, the optical constants shown in Figures 16 and 17 are obtained. For purposes of comparison, the known values of the optical constants for 65% o-phosphoric acid are also plotted in these figures. Figures 18 and 19 show the percent difference between  $n(\lambda)$  and  $k(\lambda)$  as determined from the extinction spectrum and the known values for 65% o-phosphoric acid. Figure 20 shows the percent difference between the computed and measured extinction spectra of Figure 3; notice that the spectral structure of the percent difference for the extinction spectra is very similar to the spectral structure of the percent difference for  $k(\lambda)$  (Figure 19). This suggests that the differences between the computed and the known values of the optical constants are due to experimental error in measuring the extinction spectrum and the particle size distribution.

In order to apply this method to phosphorus smoke, a value for  $n(\lambda_1)$  within the 7-

**UNCLASSIFIED**

**UNCLASSIFIED**

C-1

14  $\mu\text{m}$  band is required for the SKK analysis. This estimate was made by choosing  $n(\lambda_1)$  at an isosbestic wavelength, a wavelength for which  $n(\lambda)$  is independent of the solution concentration, for o-phosphoric acid solutions. Figures 21 and 22 show a plot of the optical constants for eight different concentrations of o-phosphoric acid<sup>2</sup> and water<sup>4</sup> (0% o-phosphoric acid). An inspection of Figure 21 shows that there is an isosbestic point at a wavelength of 7.1  $\mu\text{m}$  where  $n = 1.31$ ; this is the  $n(\lambda_1)$  value which was used in the determination of the optical constants of phosphorus smoke. Since the phosphorus smoke droplets are very likely composed of complex oxyphosphorus acids, it is expected that this isosbestic point should be quite a good estimate of  $n(\lambda_1)$  for phosphorus smoke. The effect of making an error in  $n(\lambda_1)$  is to displace the  $n(\lambda)$  curve by the amount of the error (Equation 10) but to leave the spectral shape unaltered;  $k(\lambda)$  is also affected by such an error, but to a much smaller extent than  $n(\lambda)$ .

**V. OPTICAL CONSTANTS FOR PHOSPHORUS SMOKE**

Our method of determining the optical constants from extinction spectra, which was described in the previous section, was applied to the phosphorus extinction spectra taken at 23, 52, and 85 percent relative humidity (Figure 4). The optical constant results are shown in Figures 23, 24 and should be compared with  $n(\lambda)$ ,  $k(\lambda)$  for o-phosphoric acid (Figures 21, 22).

The optical constant method was also applied to the extinction spectra which were measured as phosphorus smoke aged (Figures 6,8-12). The optical constants were computed for the extinction spectra obtained at 10.7, 49.3, 167., and 279. min. and are shown in Figures 25,26. It is readily apparent that there are few points of similarity between the optical constants for o-phosphoric acid and these optical constants.

Figure 27 shows an extinction spectrum for o-phosphorous acid ( $\text{H}_3\text{PO}_3$ ) ; this spectrum is distinctly different from either the o-phosphoric acid or the phosphorus smoke spectra. The optical constants which were determined from this spectrum are shown in Figures 28,29; there are some similarities between these optical constants and those obtained for phosphorus smoke at 279 min.

Figures 30, 31 are plots of the optical constants for phosphorus smoke at 279.

**UNCLASSIFIED**

**UNCLASSIFIED**

min., 50%  $\alpha$ -phosphoric acid, and 64%  $\alpha$ -phosphorous acid. The  $\alpha$ -phosphoric acid and  $\alpha$ -phosphorous acid optical constants show a definite correlation with the 279. min. phosphorus smoke optical constants. These chemical species ( $H_3PO_4$ ,  $H_3PO_3$ ) are certainly present in the phosphorus smoke at 279. min., although there are likely other species present also. The most probable method for the formation of  $\alpha$ -phosphorous acid is through the production of trivalent phosphorus oxides during the uncontrolled burning of the phosphorus<sup>1</sup>. Therefore, Equation 2 must be regarded as an incomplete description of the uncontrolled oxidation of phosphorus in the atmosphere.

**VI. EFFECTIVE AND 10.6  $\mu m$  EXTINCTION OF PHOSPHORUS SMOKE**

The effective or integrated extinction across a spectral band has been previously defined as 10,11

$$\alpha_{eff} = -\frac{1}{CL} \ln \left[ \frac{\int e^{-\alpha(\lambda)CL} S(\lambda) D(\lambda) d\lambda}{\int S(\lambda) D(\lambda) d\lambda} \right] \quad (11)$$

where  $S(\lambda)$  = spectral signature of the source

$D(\lambda)$  = spectral detector response curve

For these calculations, the source function was a 3000K black body and the detector response curve was the HgCdTe used in previous calculations<sup>10,11</sup>. For extinction spectra with significant spectral structure, such as 7-14  $\mu m$  phosphorus smoke spectra,  $\alpha_{eff}$  decreases as the value of the concentration-pathlength product increases. Figure 32 shows  $\alpha_{eff}$  for phosphorus smoke as a function of relative humidity for concentration-path length products ranging from 0.1 to 20. gm/m<sup>2</sup>; Figure 33 shows the  $\alpha_{eff}$  calculations for  $\alpha$ -phosphoric acid. Similar calculations were made for the time varying phosphorus extinction spectra; the results of these calculations are shown in Figure 34. Figure 35 shows the predicted  $\alpha_{eff}$  for  $\alpha$ -phosphoric acid aerosols as a function of time.

The performance of phosphorus smoke at the 10.6  $\mu m$  CO<sub>2</sub> laser wavelength is shown in Figures 36,37. Figure 36 shows a comparison of the phosphorus smoke extinction with the  $\alpha$ -phosphoric acid extinction as a function of relative humidity and Figure 37

**UNCLASSIFIED**

# UNCLASSIFIED

C-1

shows a similar comparison as a function of time.

## VII. CONCLUSIONS

1. Phosphorus smoke extinction changes slowly as the relative humidity is increased from low to moderate values (23% to 52%), but a substantial decrease in the extinction has occurred when the relative humidity reaches 85%.
2. The transition of phosphorus smoke to waterlike spectral behaviour in 7-14  $\mu\text{m}$  region occurs at relative humidities which are higher than the corresponding transition for o-phosphoric acid.
3. At constant ambient conditions, the extinction spectra for phosphorus change with time; these spectral changes are a result of the changing chemical composition of the smoke droplets.
4. The optical constants of phosphorus smoke can be derived from the extinction spectra. Such optical constants have been found as functions of relative humidity and time.
5. The aged phosphorus smoke contains o-phosphoric and o-phosphorous acids as well as other oxyphosphorus species.
6. The effective extinction coefficient increases slightly for relative humidities between 23% and 52% and decreases for relative humidities between 52% and 85%.
7. The effective extinction coefficient increases as the phosphorus smoke ages.
8. The oxidation of phosphorus to produce  $\text{P}_2\text{O}_5$  with subsequent hydration to o-phosphoric acid is inadequate to describe the formation of phosphorus smoke.

# UNCLASSIFIED

641

## UNCLASSIFIED

TABLE I. CONCENTRATION, RELATIVE HUMIDITY, AND PARTICLE SIZE  
DISTRIBUTION VARIATION WITH TIME FOR PHOSPHORUS SMOKE (RP)

Concentration			
Time*	Path Length**	Relative Humidity	MMD( $\mu m$ ), $\sigma_g^{***}$
(min)	(gm/m <sup>2</sup> )	(%)	
0		69.3	
8.92	7.34		1.14, 1.55
39.7	5.98		
44.9		68.3	
77.8	5.23		
135.4	4.41		
263.1		62.1	
265.3			2.35, 1.54
271.7	2.29		

\* Time elapsed from phosphorus ignition to the midpoint of the sampling interval.

\*\* Pathlength = 6.1 m

\*\*\* MMD = mass median diameter

$\sigma_g$  = geometric standard deviation

**UNCLASSIFIED**

TABLE II. APPROXIMATE VALUES OF THE UPPER MONOTONICITY  
LIMIT FOR THE MASS MEDIAN SIZE PARAMETER

$\alpha_g$	$n$		
	<u>1.33</u>	<u>2.0</u>	<u>3.0</u>
1.1	3.55	1.35	0.89
1.4	3.55	1.41	0.81
2.0	4.68	1.78	0.89
3.0	9.77	3.39	1.23

**UNCLASSIFIED**

UNCLASSIFIED

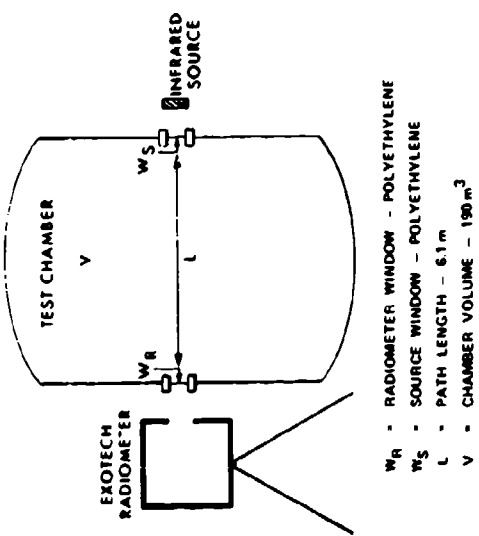


FIGURE 1. DARCOM SMOKE CHARACTERIZATION FACILITY.

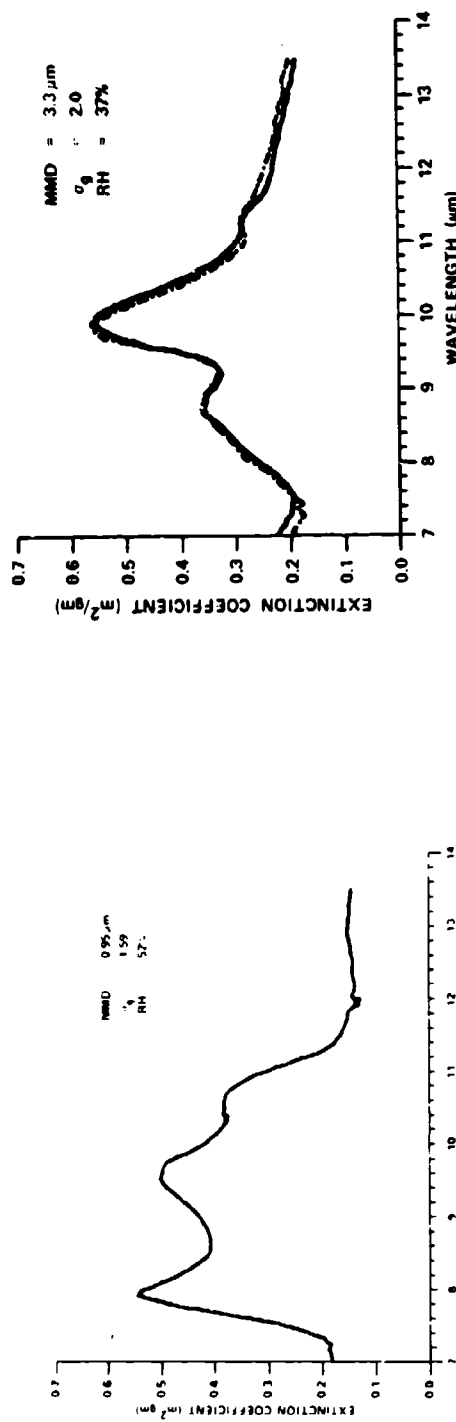


FIGURE 2. PHOSPHORUS EXTINCTION SPECTRUM.

FIGURE 3. COMPARISON OF THE EXPERIMENTALLY DETERMINED EXTINCTION SPECTRUM (DASHED LINE) WITH A COMPUTED EXTINCTION SPECTRUM (SOLID LINE) FOR 65% o-PHOSPHORIC ACID.

UNCLASSIFIED

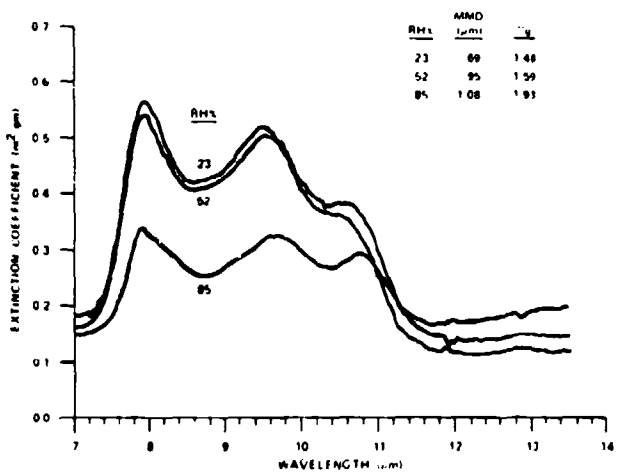
**UNCLASSIFIED**

FIGURE 4. EXTINCTION SPECTRA FOR PHOSPHORUS SMOKE (WP) AT THREE RELATIVE HUMIDITIES.

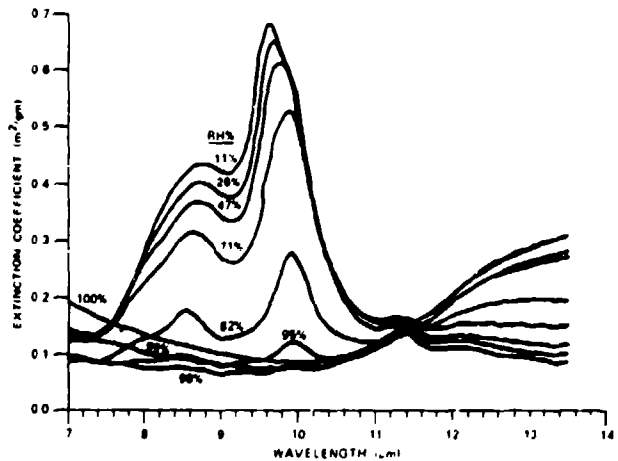


FIGURE 5. EXTINCTION SPECTRA FOR O-PHOSPHORIC ACID-WATER SYSTEM AT NINE RELATIVE HUMIDITIES.

**UNCLASSIFIED**

UNCLASSIFIED

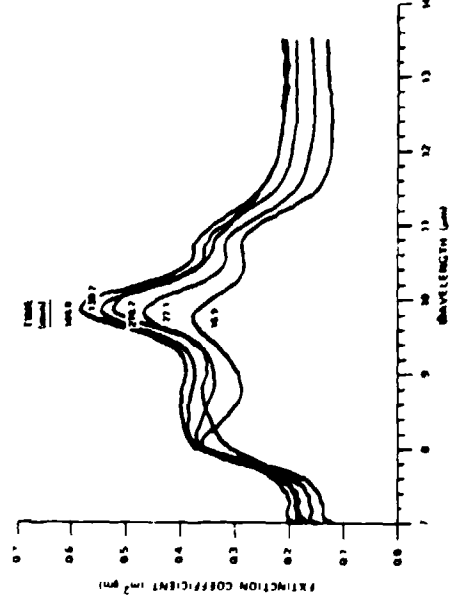


FIGURE 6. VARIATION OF PHOSPHORUS SMOKE EXTINCTION WITH TIME.

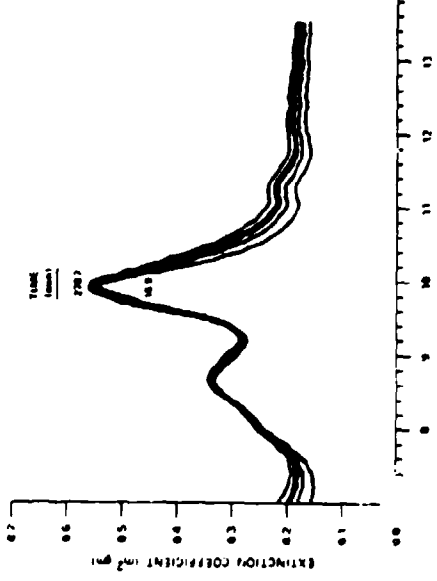


FIGURE 7. VARIATION OF  $\alpha$ -PHOSPHORIC ACID EXTINCTION WITH TIME.

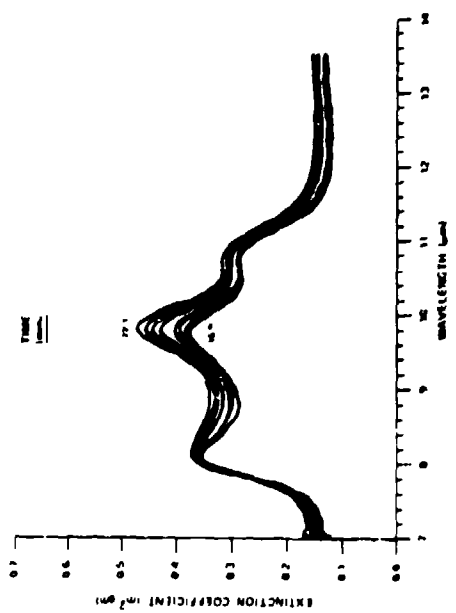


FIGURE 8. VARIATION OF PHOSPHORUS SMOKE EXTINCTION WITH TIME.

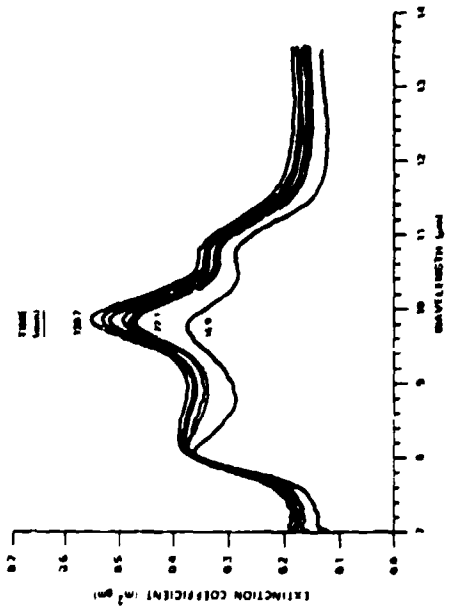


FIGURE 9. VARIATION OF PHOSPHORUS SMOKE EXTINCTION WITH TIME.

UNCLASSIFIED

**UNCLASSIFIED**

C-1

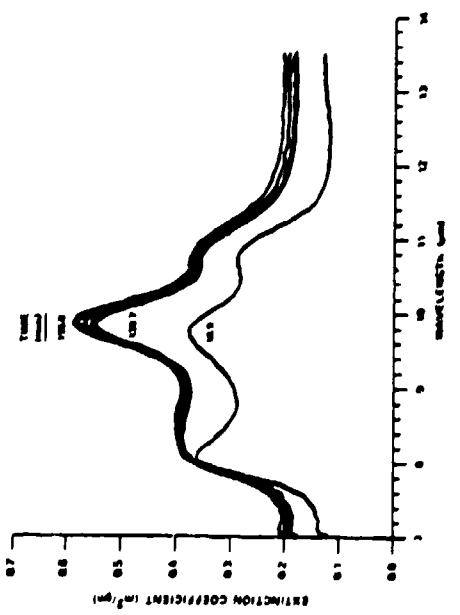


FIGURE 10. VARIATION OF PHOSPHORUS SMOKE EXTINCTION WITH TIME

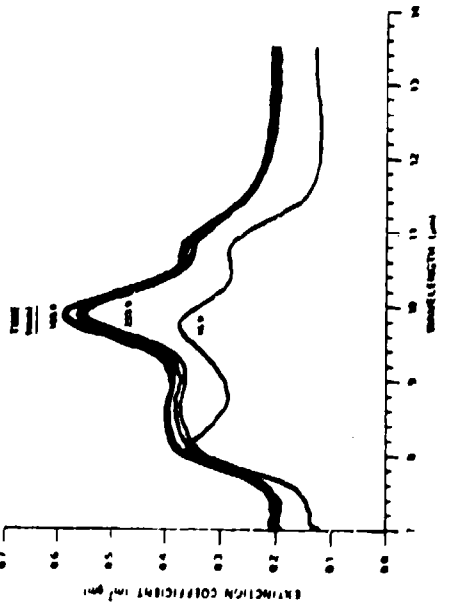


FIGURE 11. VARIATION OF PHOSPHORUS SMOKE EXTINCTION WITH TIME

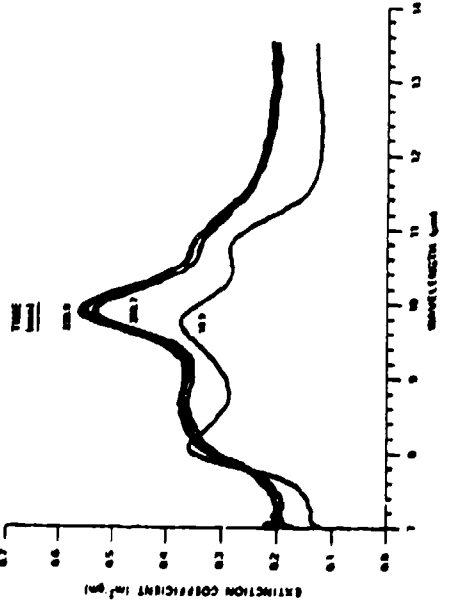


FIGURE 12. VARIATION OF PHOSPHORUS SMOKE EXTINCTION WITH TIME

**UNCLASSIFIED**

647

UNCLASSIFIED

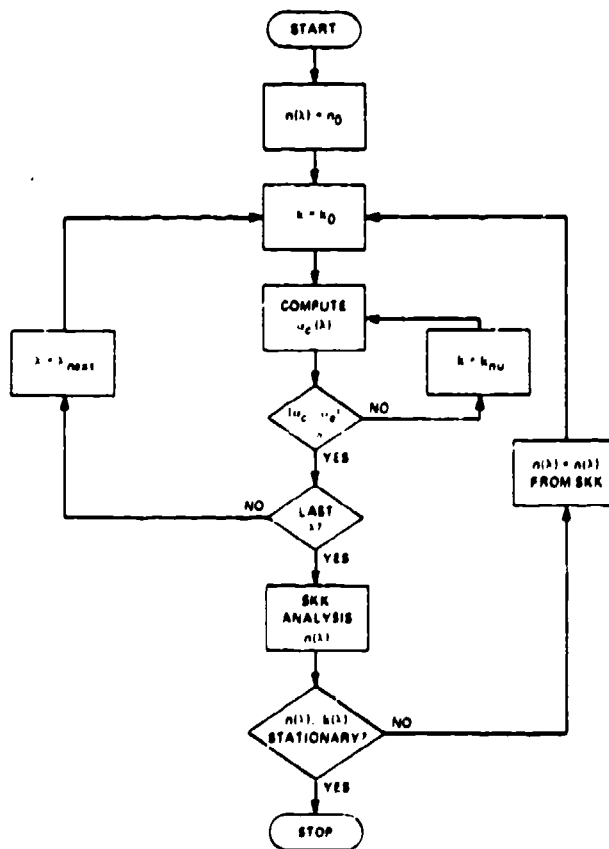


FIGURE 13. FLOWCHART OF THE ALGORITHM FOR DETERMINING THE OPTICAL CONSTANTS  $n, k$  FROM EXTINCTION MEASUREMENTS.

UNCLASSIFIED

UNCLASSIFIED

C-1

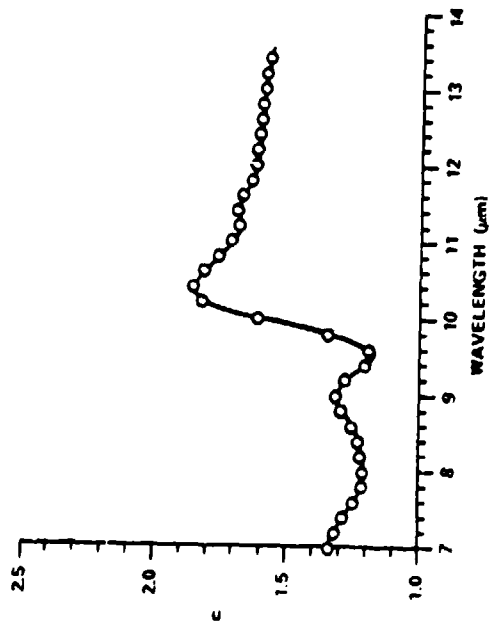


FIGURE 14. COMPARISON OF  $\alpha_{11}$  DERIVED FROM A SPECTRUM (CIRCLES) COMPUTED FROM LORENZ-MIE THEORY WITH THE REAL PARTS USED IN THE COMPUTATION (SOLID CURVE).

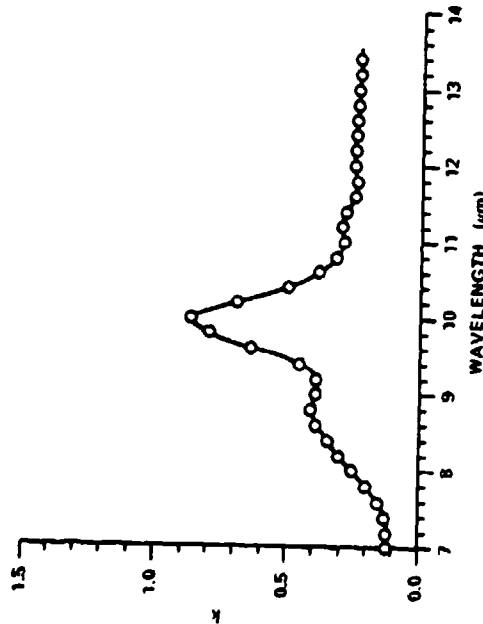


FIGURE 15. COMPARISON OF  $k_{11}$  DERIVED FROM A SPECTRUM (CIRCLES) COMPUTED FROM LORENZ-MIE THEORY WITH THE IMAGINARY PARTS USED IN THE COMPUTATION (SOLID CURVE).

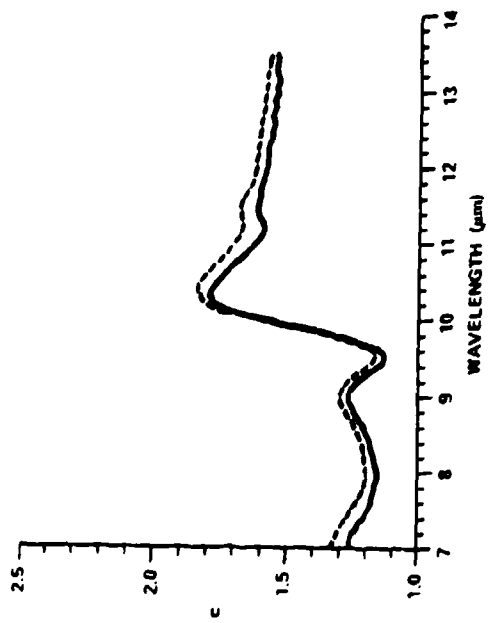


FIGURE 16. COMPARISON OF  $\alpha_{11}$  DETERMINED FROM EXTINCTION MEASUREMENTS (SOLID CURVE) WITH THE MEASURED VALUES FOR 65% O-PHOSPHORIC ACID (DASHED CURVE).

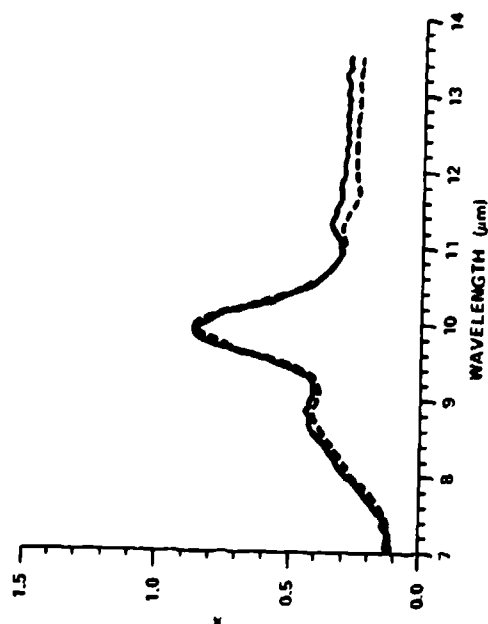


FIGURE 17. COMPARISON OF  $k_{11}$  DETERMINED FROM EXTINCTION MEASUREMENTS (SOLID CURVE) WITH THE MEASURED VALUES FOR 65% O-PHOSPHORIC ACID (DASHED CURVE).

UNCLASSIFIED

UNCLASSIFIED

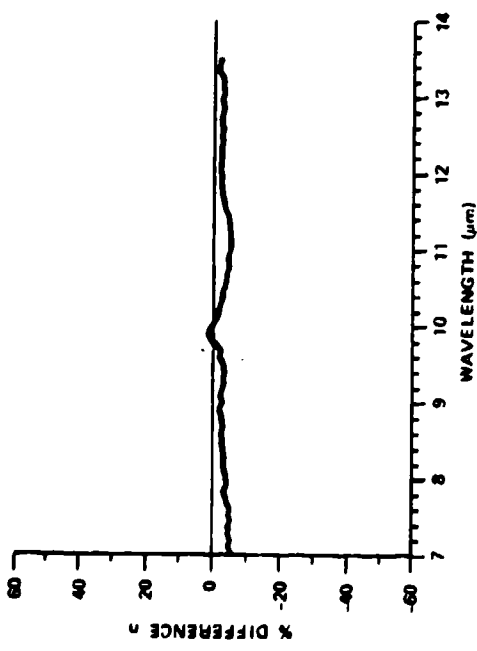


FIGURE 18. PERCENT DIFFERENCE BETWEEN  $n(\lambda)$  DETERMINED FROM EXTINCTION MEASUREMENTS AND THE VALUES OF  $n(\lambda)$  FOR 65%  $\alpha$ -PHOSPHORIC ACID.

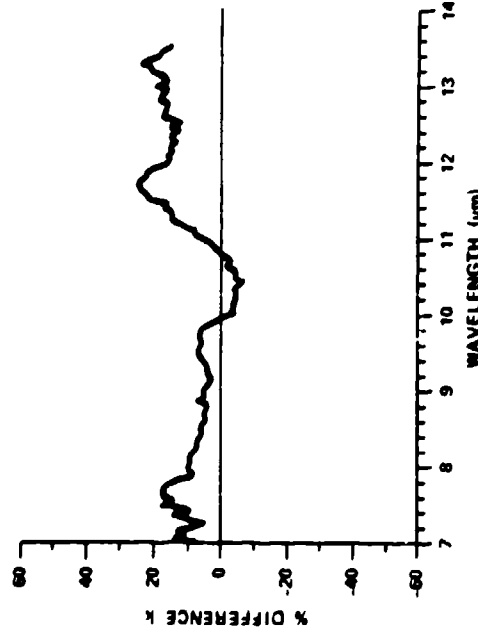


FIGURE 19. PERCENT DIFFERENCE BETWEEN  $k(\lambda)$  DETERMINED FROM EXTINCTION MEASUREMENTS AND THE VALUES OF  $k(\lambda)$  FOR 65%  $\alpha$ -PHOSPHORIC ACID.

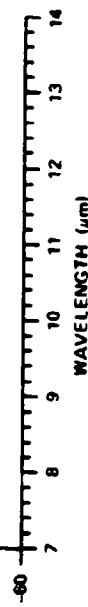


FIGURE 20. PERCENT DIFFERENCE BETWEEN THE COMPUTED AND MEASURED EXTINCTION SPECTRUM AS A FUNCTION OF WAVELENGTH.

UNCLASSIFIED

**UNCLASSIFIED**

C-1

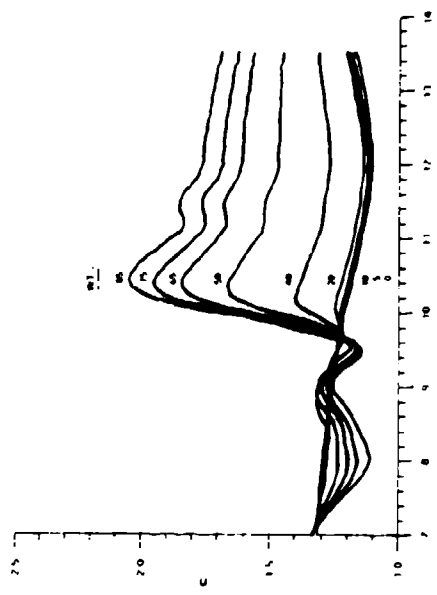


FIGURE 21. REAL PART OF THE REFRACTIVE INDEX FOR SOLUTIONS OF *o*-PHOSPHORIC ACID.

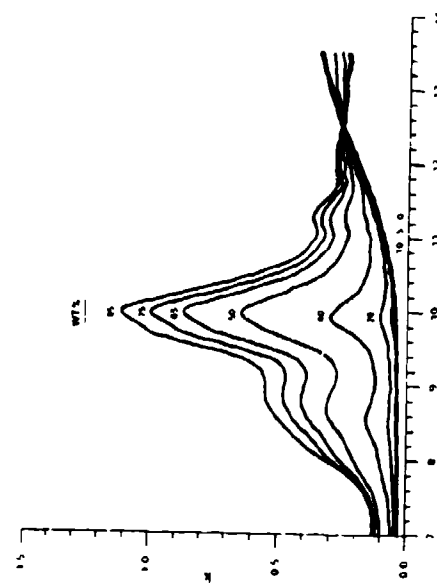


FIGURE 22. IMAGINARY PART OF THE REFRACTIVE INDEX FOR SOLUTIONS OF *o*-PHOSPHORIC ACID.

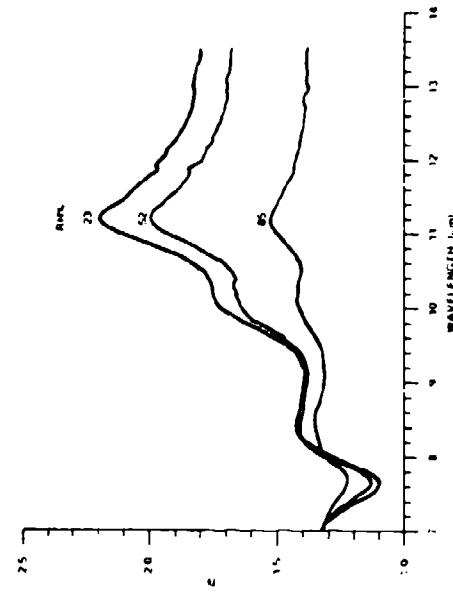


FIGURE 23. REAL PART OF THE REFRACTIVE INDEX FOR PHOSPHORUS SMOKE AS A FUNCTION OF RELATIVE HUMIDITY.

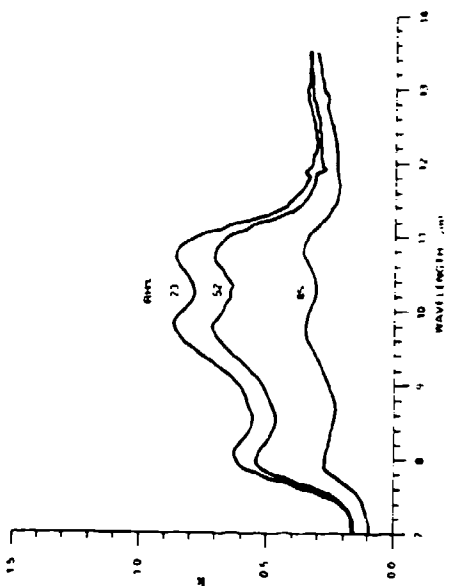


FIGURE 24. IMAGINARY PART OF THE REFRACTIVE INDEX FOR PHOSPHORUS SMOKE AS A FUNCTION OF RELATIVE HUMIDITY.

**UNCLASSIFIED**

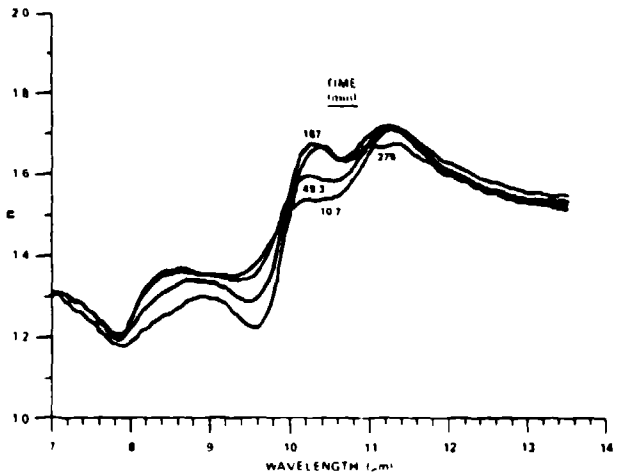
**UNCLASSIFIED**

FIGURE 26. REAL PART OF THE REFRACTIVE INDEX FOR PHOSPHORUS SMOKE AS A FUNCTION OF TIME.

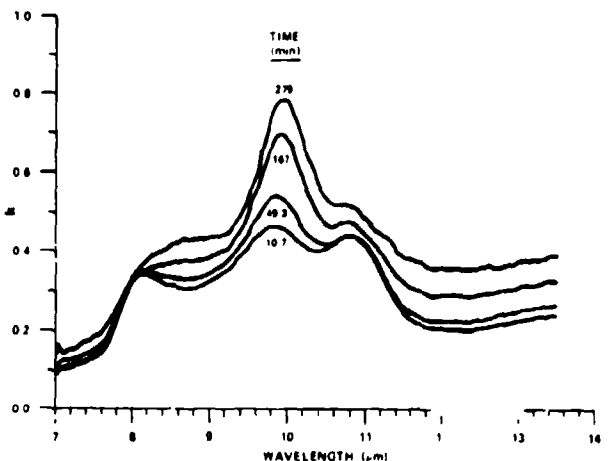


FIGURE 28. IMAGINARY PART OF THE REFRACTIVE INDEX FOR PHOSPHORUS SMOKE AS A FUNCTION OF TIME.

**UNCLASSIFIED**

**UNCLASSIFIED**

C-1

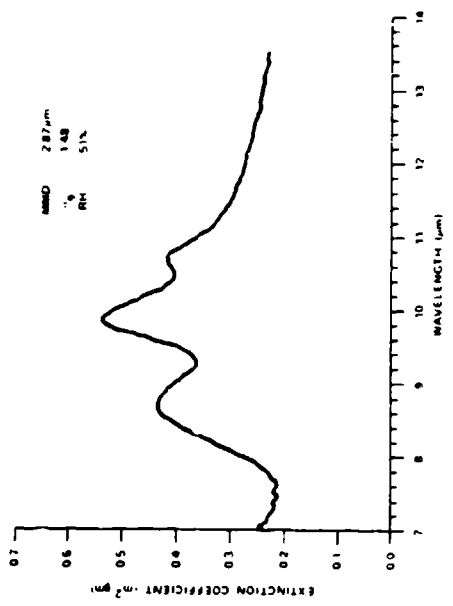


FIGURE 27. EXTINCTION SPECTRUM FOR O-PHOSPHOROUS ACID.

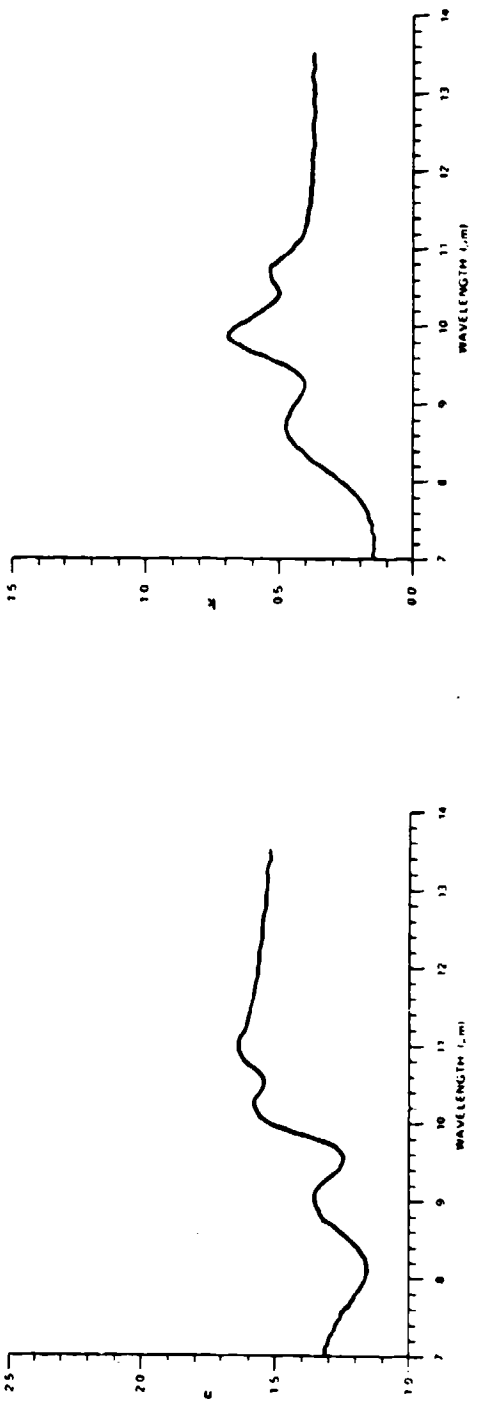


FIGURE 28. REAL PART OF THE REFRACTIVE INDEX FOR O-PHOSPHOROUS ACID (64%).

FIGURE 29. IMAGINARY PART OF THE REFRACTIVE INDEX FOR O-PHOSPHOROUS ACID (64%).

**UNCLASSIFIED**

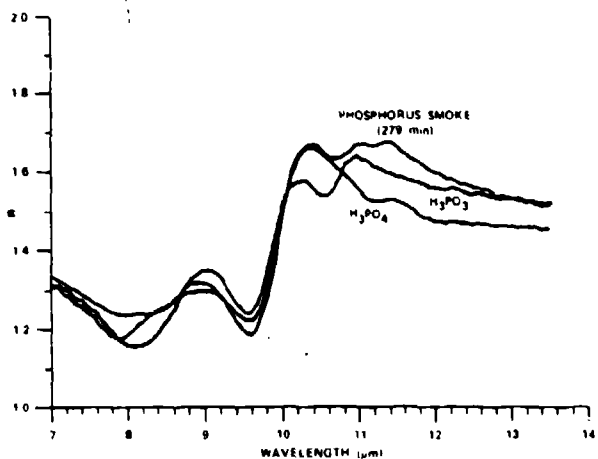
**UNCLASSIFIED**

FIGURE 30. COMPARISON OF  $n(\lambda)$  FOR PHOSPHORUS SMOKE,  
 $\alpha$ -PHOSPHORIC ACID AND  $\alpha$ -PHOSPHOROUS ACID.

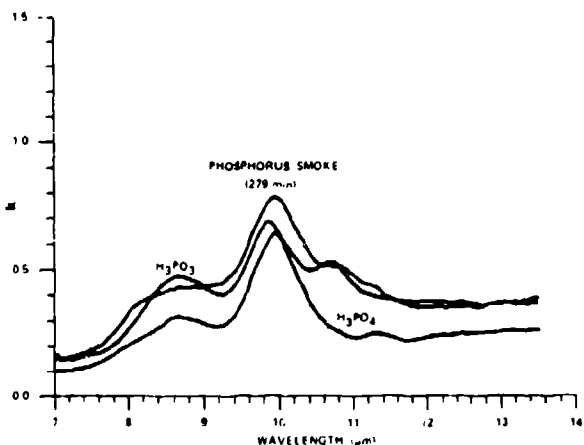


FIGURE 31. COMPARISON OF  $k(\lambda)$  FOR PHOSPHORUS SMOKE,  
 $\alpha$ -PHOSPHORIC ACID, AND  $\alpha$ -PHOSPHOROUS ACID.

**UNCLASSIFIED**

**UNCLASSIFIED**

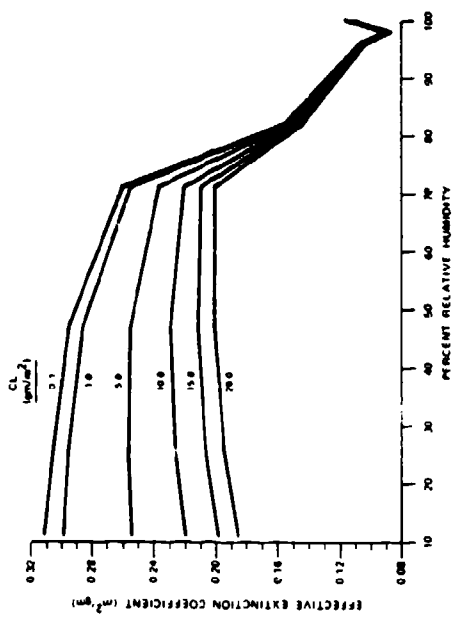


FIGURE 32. EFFECTIVE EXTINCTION FOR O-PHOSPHORIC ACID AS A FUNCTION OF RELATIVE HUMIDITY.

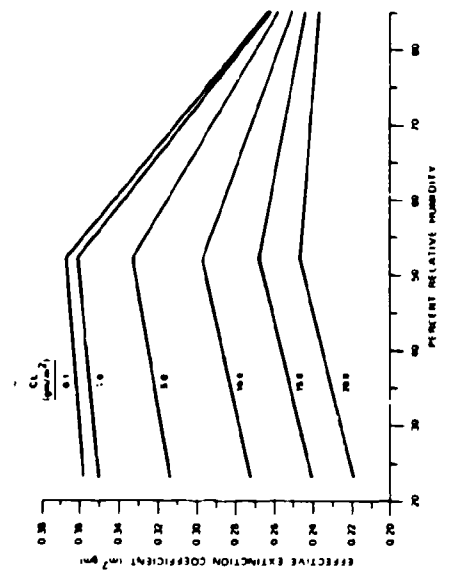


FIGURE 33. EFFECTIVE EXTINCTION FOR PHOSPHORUS SMOKE AS A FUNCTION OF RELATIVE HUMIDITY.

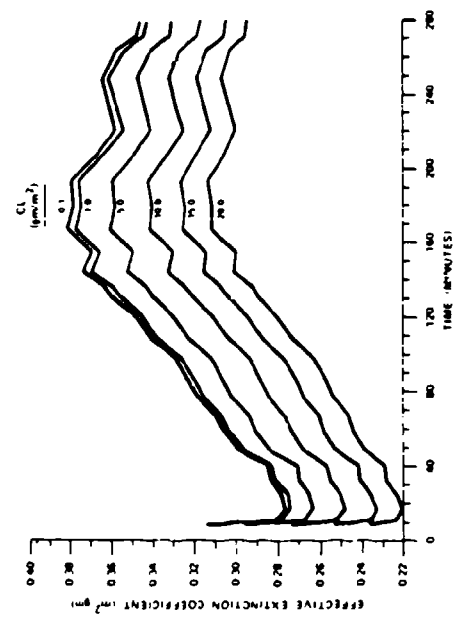


FIGURE 34. EFFECTIVE EXTINCTION FOR PHOSPHORUS SMOKE AS A FUNCTION OF TIME.

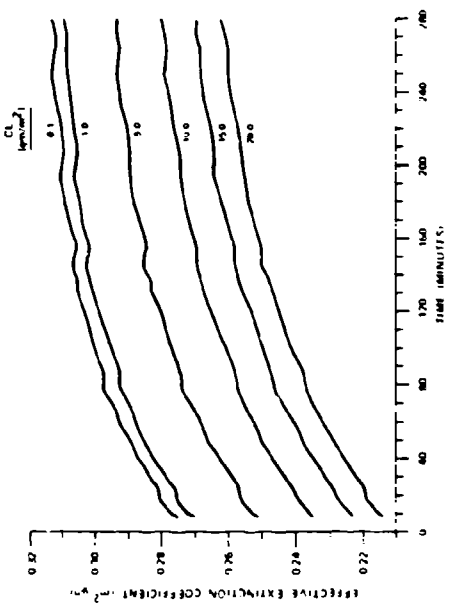


FIGURE 35. EFFECTIVE EXTINCTION FOR O-PHOSPHORIC ACID AS A FUNCTION OF TIME.

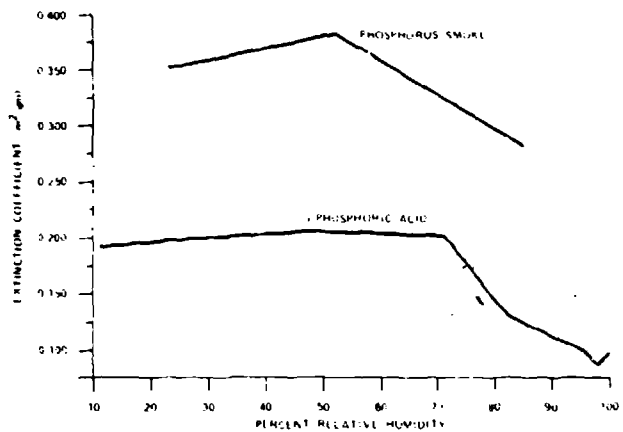
**UNCLASSIFIED**

FIGURE 36. COMPARISON OF THE EXTINCTION COEFFICIENT AT  $10.6\mu\text{m}$  FOR PHOSPHORUS SMOKE AND *o*-PHOSPHORIC ACID AS A FUNCTION OF RELATIVE HUMIDITY.

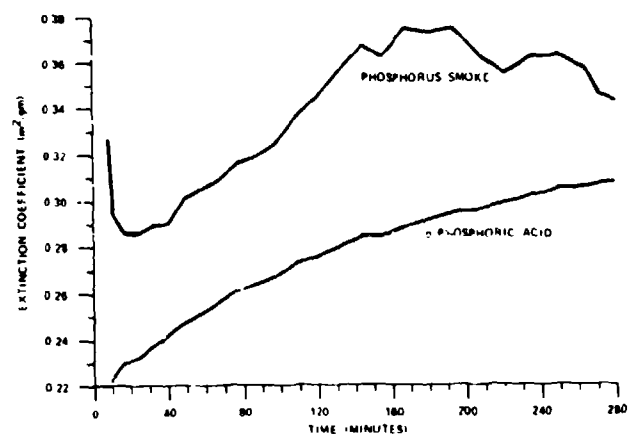


FIGURE 37. COMPARISON OF THE EXTINCTION COEFFICIENT AT  $10.6\mu\text{m}$  FOR PHOSPHORUS SMOKE AND *o*-PHOSPHORIC ACID AS A FUNCTION OF TIME.

**UNCLASSIFIED**

## REFERENCES

1. Milham, M.E., Anderson, D.H., Frickel, R.H., and Tarnove, T.L. New Findings on the Nature of WP/RP Smokes, ARCSL-TR-77067 (1977).
2. Querry, M.R. Molecular Crystalline Electromagnetic Properties of Selected Condensed Materials in the Infrared. Final Report DAAG-29-76-GS-0185 (1979).
3. Milham, M.E., Holst, G.C., and Anderson, D.H. A Parametric Study of the Propagation of CO<sub>2</sub> Laser Radiation Through Clouds of Phosphoric Acid Droplets. Proceedings of Smoke/Obscurants Symposium IV, DRCPM-SMK-T-001-80, Office of the Project Manager Smoke/Obscurants, APG, Md. (1980).
4. Hale, G.M. and Querry, M.R. Optical Constants of Water in the 200 nm to 200 μm Wavelength Region, Appl. Optics 12:555 (1973).
5. Milham, M.E. and Anderson, D.H. Time Dependent Extinction of Phosphorus Smoke, in preparation.
6. Rubel, G.O. Is Phosphoric Acid a Good Model for Phosphorus Smoke? Proceedings of Smoke/Obscurants Symposium IV, DRCPM-SMK-T-001-80, Office of the Project Manager Smoke/Obscurants, APG, MD (1980).
7. Milham, M.E., Frickel, R.H., Embury, J.E., and Anderson, D.H. Determination of Optical Constants from Extinction Measurements, ARCSL-TR-81031 (1981).
8. Bachrach, R.Z. and Brown, F.C. Exciton-Optical Properties of TiBr and TiCl. Phys. Rev. B1, 818-831 (1970).
9. Bachrach, R.Z. and Brown, F.C. Modified Kramers-Kronig Analysis of Optical Spectra. J. Opt. Soc. Am. 61, 1651-1655 (1971).
10. Stuebing, E.W. Deviations from Beer's Law Which Sometimes Prevent Defining a Single Overall Extinction Coefficient for a Smoke in Each Atmospheric Window. Proceedings of the Smoke/Obscurants Symposium II, DRCPM-SMK-T-004-78, Office of the Project Manager for Smoke/Obscurants, APG, MD. (1978).
11. Frickel, R.H., Rubel, G.O., and Stuebing, E.W. Relative Humidity Dependence of the Infrared Extinction by Aerosol Clouds of Phosphoric Acid, Proceedings of Smoke/Obscurants Symposium III, DRCPM-SMK-T-002-79, Office of the Project Manager Smoke/Obscurants, APG, MD (1979).

# UNCLASSIFIED

C-2

## REPLACEMENT OF HC SMOKE

Michael D. Smith  
Chemical Systems Laboratory  
Aberdeen Proving Ground, MD

### ABSTRACT

Medical research has shown that one of the components of HC smoke mix, hexachloroethane, is carcinogenic. In addition, the combustion products of HC are highly toxic. At Chemical Systems Laboratory, several programs are ongoing to replace HC in inventory smoke munitions. A Navy day/night signal formulation composed primarily of red phosphorus has been modified and adapted for use in the AN/M8 grenade. Red phosphorus is an effective white smoke producer of relatively low toxicity.

### 1. BACKGROUND

The HC smoke mix is a mixture of hexachloroethane, zinc oxide, and aluminum. Medical research conducted by Chemical Systems Laboratory and others has shown that HC mix poses a serious chronic health hazard to production personnel. Further, the combustion products are a potential acute hazard to personnel exposed to the smoke without protective gear. In addition, a report by the National Institute of Health (NIC-CB-TR-68, dated 1978) states that hexachloroethane is carcinogenic to male mice. Because of these toxicological considerations, a safer white smoke producing formulation is being sought for use in inventory smoke ammunition. Actions are now ongoing to replace HC mix in the AN-M8 smoke hand grenade and the ABC-MS smoke pot with a pyrotechnic red phosphorus (RP) smoke mix.

### 2. CANDIDATE SMOKE MIX EVALUATION

The candidate replacement RP smoke mix under study is an adaptation of a US Navy developed formulation which consisted of:

53% red phosphorus (RP)  
7% magnesium (Mg)  
34% manganese dioxide ( $MnO_2$ )  
3% zinc oxide ( $ZnO$ )  
3% linseed oil

This formulation is used in pyrotechnic devices which are used as Marine Location Markers. When this composition is ignited, the magnesium and the manganese dioxide react as a thermite to generate heat and vaporize the phosphorus. The phosphorus vapor then burns in the surrounding atmosphere to produce a dense white smoke and yellow flame.<sup>1</sup>

---

<sup>1</sup> Webster and Johnson. NWSC/CR/RDTR-22. New Potentials in Red Phosphorus Compositions. Aug 76.

# UNCLASSIFIED

# UNCLASSIFIED

C-2

Initial testing of this formulation at Chemical Systems Laboratory was performed in the M8 grenade. This item is a steel cylindrical can approximately 2.25 inches in diameter by 4.5 inches high. The standard M8 HC grenade is an end burner, i.e., the top surface of the mix is ignited and the flame propagates down through the smoke composition. Smoke is emitted through four, 0.312 inch diameter openings in the grenade top cover. Testing in this configuration produced burn (smoke emission) times in excess of the prescribed 90-135 seconds.

Various modifications were then made, both in the composition of the smoke mixture and the item configuration, to produce an acceptable grenade. The best tested configuration was like that of the M18 colored smoke grenade type, i.e., a core burner in which smoke is emitted through a 0.5 inch diameter hole in the center of the grenade base as well as through the four holes in the cover. Various alternate formulations were tested; in particular, aluminum, titanium, and boron were considered in place of moisture reactive magnesium. The formulation selected as the best to date contains the following:

8.5% Mg

32.5% MnO<sub>2</sub>

1.5% MgO (magnesium oxide)

3.0% linseed oil

The MgO was incorporated to replace ZnO as the toxicity of the latter is suspect. The improved M8 grenade as described has an average burn time of 2 minutes and contains approximately 1 pound of RP smoke mixture.

Additional studies were begun during this early development as well. Various starter mixtures were evaluated and high temperature storage stability of the smoke mix was assessed. These studies determined that the performance of the standard M8 grenade starter mixture was surpassed by that of another Navy composition. The most consistent grenade performance was observed when 25 grams of this Navy starter mixture consisting of 30% lead dioxide, 30% cupric oxide, and 40% silicon was used. High temperature storage of grenades at 160°F for 90 days indicated the need for a physical barrier between the starter mixture and the smoke mixture to prevent ignition problems. The continued use of the existing zinc starter cup in the improved grenades proved adequate as a barrier.

# UNCLASSIFIED

# UNCLASSIFIED

C-2

The improved M8 grenades appear to produce as much or more visible white smoke than do the M8 HC grenades, although comparative smoke production has not yet been quantified. The improved grenades, in addition to smoke, produce an intense flame at the orifices (the Navy formulation was developed as a day/night signal).

The performance of the improved M8 grenades was encouraging enough to begin a formal Product Improvement Program (PIP) in January 1980. Tasks are ongoing or planned to study alternative chemicals and formulations, alternative binders, chemical stability, and storage stability (surveillance), and to optimize grenade performance.

A backup formulation was developed and tested, in which calcium sulfate ( $\text{CaSO}_4$ ) substitutes for the manganese dioxide, and calcium carbonate ( $\text{CaCO}_3$ ) replaces the magnesium oxide in the primary candidate RP mix previously discussed. This alternate composition was developed at the recommendation of toxicologists who indicated that  $\text{MnO}_2$  and  $\text{MgO}$  may be health hazards in some situations. This backup formulation is only slightly inferior in performance as compared to the primary RP mixture.

Grenades made with both the primary and backup RP mixtures have been placed in a 1 year ambient surveillance program. Grenades field tested after 32 weeks storage still perform satisfactorily. Additional studies to determine the chemical stability of the smoke mix have just been initiated. Various binders, additives, coatings, or treatment processes will be compared to determine the most effective means of preventing chemical decomposition of the mix and thus increase the shelf life of the munition. For example, red phosphorus and magnesium metal are known to decompose in the presence of moisture, and some techniques to prevent its intrusion are required.

Alternative sources and grades of chemicals to those used in the initial development work are being evaluated in a parametric study. The objectives are to determine the effect of variability of the chemical ingredients on grenade performance and safety.

Alternate binders, other than linseed oil, are also being considered. In initial work, the newly loaded M8 grenades were placed in an oven at  $140^{\circ}\text{F}$  for 48-72 hours to "cure" the linseed oil. Efforts to minimize or eliminate this processing step are continuing. Side by side comparison of burning

# UNCLASSIFIED

661

# UNCLASSIFIED

C-2

grenades in which one was heat treated and the other was not, show no apparent difference in smoke production or burn times after 32 weeks ambient storage. The possibility of eliminating the linseed oil binder was considered, but a pressed slug of RP mix without the binder has very little mechanical strength. Dry binders like paraffin or microcrystalline waxes have been tested and show potential as an alternative to linseed oil.

## 3. PRODUCIBILITY STUDIES

A Manufacturing Methods and Technology (MMT) program was begun in October 1980 to study production processing methods for blending the new RP smoke mix. The batches of RP mix made to date have been small in quantity (1-20 lb) and laboratory size vertical planetary or twin-shell blenders have been used. Neither of these blenders are efficient and are not recommended to prepare larger quantities. A pilot plant size Airmix mixer (manufactured by Sprout-Waldron Division of Koppers Co., Inc.) already in place at CSL will be evaluated initially. This mixer is capable of blending dry material in seconds using compressed air alone. Plans are to determine the hazards associated with blending the known impact and friction sensitive RP mix in a laboratory size mixer prior to scaling up to the pilot plant model. Should the Airmix mixer prove unsafe or ineffective, alternate mixing equipment will be tested.

## 4. MEDICAL EVALUATION

When a final selection is made of a replacement smoke mix which meets the performance requirements in the M8 grenade (scheduled for late 1981) and the M5 smoke pot, the chemical components and combustion products will be thoroughly tested in a medical evaluation program. A medical evaluation plan (MEP) has already been prepared. The objective of this MEP is to assure that the RP smoke mix is free of both carcinogenic constituents and unacceptable levels of toxicity to industrial/troop personnel and the environment. The selection of primary and alternate candidate chemical ingredients is coordinated with the medical community to insure, as much as possible, that the candidate materials have a high probability of meeting the MEP objectives and criteria for a safe smoke. A phosphorus smoke producing replacement composition for HC was chosen primarily because medical research studies to date indicate that RP and phosphorus smokes are relatively low human health hazards.

# UNCLASSIFIED

# UNCLASSIFIED

C-3

## SMOKE/OBSCURANTS HEALTH EFFECTS RESEARCH

David L. Johnson, CPT, MSC

James C. Eaton

US Army Medical Bioengineering

Research and Development Laboratory

Fort Detrick, Frederick, MD

Increased requirements for employing smoke in support of combat operations and the need to be prepared to fight effectively in a smoke environment dictate that increasing numbers of soldiers will be exposed to smoke during field testing and training. Increased governmental regulation, public awareness, and the tendency to resort to litigation make it legal, ethical, and imperative that the health effects of Army smoke/obscurants be determined. The US Army Medical Bioengineering Research and Development Laboratory (USAMBRDL) has the mission to develop the health effects data base upon which The Surgeon General must rely in providing guidance for protection of health and the environment.

The program at USAMBRDL addresses the possible health hazards associated with troop exposures, industrial occupational operations and the environmental effects of manufacture, testing, deployment, storage, and demilitarization of smoke/obscurants, with primary emphasis on troop exposures. Because of resource limitations, extensive health effects evaluations are confined to smoke/obscurants already in the inventory or in the final stages of development. The normal progression of health effects studies begins with problem definition and initial health hazard assessment based upon currently available information. For assessment of health hazards to the soldier, it is necessary to obtain data on the chemical and physical characteristics of smokes as they are deployed in the field. These data are often quite different from those taken when evaluating the obscuring characteristics of aerosols. Because mammalian toxicologic studies of smoke/obscurant aerosols involve the greatest expenditure of resources, they must be designed to reflect realistic exposure scenarios in order to maximize the relevance of information derived.

Since the passage of the National Environmental Policy Act (NEPA) of 1969 and the Occupational Safety and Health Act (OSHA) of 1970, we have witnessed in the United States an explosive expansion of Federal regulatory control over industry in the areas of pollution control and health protection.<sup>1,2</sup> The impacts of these two Acts as well as the amended Federal Water Pollution Control and Clear Air Acts, the Toxic Substances Control Act (TSCA), and, most recently, the Resource Conservation and Recovery Act, are being felt daily by industry in the form of construction delays, stringent pollution

# UNCLASSIFIED

663

**UNCLASSIFIED**

control and workplace safety and sanitation standards, and seemingly unending reporting and record-keeping requirements.

As a Federal agency, the US Army has been directed through various executive orders to comply with many of the provisions of the Acts just mentioned.<sup>3</sup> We have been very fortunate in that we have been largely allowed to police our own operations through the services of the US Army Environmental Hygiene Agency and other internal groups, especially in the area of occupational health protection. Since the advent of TSCA, however, we have been subject to direct regulation by the US Environmental Protection Agency (with certain exemptions for national defense purposes).

The TSCA presents us with very definite requirements to provide health and environmental effects data for "new" chemical products or "significant new uses" of old products and to include requirements for information relating to manufacture, use, and ultimate disposal of these items.<sup>4</sup> These requirements, combined with those of the other Acts, form a set of legal obligations which we must satisfy if we are to remain within the law.

Aside from the legal requirement to provide health and environmental effects data, we are also morally obligated to protect the health of the individual worker and to act responsibly as the caretaker of the environment for the next generation.<sup>5,6</sup> Other factors are also of concern, such as the economic impact of future litigation resulting from present manufacture, use, and disposal practices -- including those relating to munitions.

Recognition of expanded requirements for the use of smokes and obscurants in support of combat and combat support operations and for the need to fight effectively in a smoke environment<sup>7</sup> dictates that increasing numbers of military personnel will be exposed to smoke and obscurant aerosols during field testing and training and that such testing and training will occur more frequently. Regulatory requirements, increased public awareness, and the tendency to resort to litigation thus make it imperative that health and environmental effects data be developed for smoke and obscurant munitions.

Although the primary responsibility for providing information necessary to permit health and environmental hazard assessments rests with the developer, the Project Manager for Smokes and Obscurants,<sup>8</sup> there are other sources of such information, both within and without the Army community. Traditionally, the Chemical Systems Laboratory has had and will continue to have a role in development of this type of data, as has the Human Engineering Laboratory. Ultimate responsibility for the management, interpretation, and performance of toxicologic studies to produce the data, however, resides in the Army Medical Department (AMEDD), specifically The Surgeon General (TSG). It is The Surgeon General who evaluates the data, sets appropriate health protection standards, and provides the safety release for Army presribing how an end-item can be safely employed in

**UNCLASSIFIED**

# UNCLASSIFIED

C-3

training. It is the mission of the US Army Medic Engineering Research and Development Laboratory (USAMBRDL), Fort Detrick, MD, to conduct the research necessary to develop the health effects data upon which TSC bases hazard assessments.

During the past few years USAMBRDL has conducted a number of studies of smoke/obscurant munition compounds and aerosols in support of PM-Smoke to provide the information necessary for evaluation of the toxic properties of inventory smokes and to ensure development of new munitions acceptable from both performance and health effects standpoints. Due to limited AMEDD resources, current research centers on two major types of effects: potential for inducing cancer (carcinogenesis) and incapacitating or irreversible toxic effects. Other effects are of concern (particularly performance decrement) but are not our primary focus. In addition, the previously mentioned resource limitations have forced us to concentrate on items already in the inventory or in the final stages of development. This is unfortunate since it is quite conceivable that early integration of health and environmental effects considerations into the selection of candidate materials would enhance eventual development of products acceptable from both performance and health protection standpoints and reduce overall materiel acquisition costs.

Studies conducted by USAMBRDL extend in scope from relatively simple paper studies such as problem definitions to very complex long-term mammalian toxicology studies involving repeated, intermittent exposures, multiple-dose schedules and assessment of numerous biological and/or behavioral endpoints. Studies frequently progress from the problem definition and production-and-use study stage to physical/chemical characterizations of compounds, acute exposure animal mortality studies, longer-term subchronic studies using multiple exposures, and often to the long-term subchronic studies mentioned above.

For assessment of health hazards to the soldier, it is necessary to obtain data on the chemical and physical characteristics of smokes as they are deployed in the field. These data are often quite different from those taken when evaluating the obscuring properties of aerosols. Because mammalian toxicology studies of smoke/obscurant aerosols involve the greatest expenditure of resources, they must be designed to reflect realistic exposure scenarios in order to maximize the quantity and quality of information derived. Materials currently under study include Fog Oil, Diesel Fuel, White Phosphorus/Felt, Red Phosphorus/Butyl Rubber, and colored smokes. Papers relating to the specifics of some of this work appear elsewhere in these Proceedings.

As with any experimental research, health effects research is expensive and its results may appear to condemn more than they exonerate. But there is value in revealing and quantifying health and environmental hazards associated with new developments. Such data may be entered into the cost-benefit equation, and if the costs and risks are found to outweigh the advantages, funds may be

# UNCLASSIFIED

665

**UNCLASSIFIED**

directed into more promising avenues. If the decision is in favor of the continued development and eventual deployment of the obscurant system, protective measures and devices may be prescribed or developed to prevent damage to the environment or to the health of the soldier or the industrial worker.

By careful selection of candidate materials we may avoid unnecessary expenditure of development resources on materials known to possess toxic properties or reduce those expenditures by detection of such effects through appropriate research early in the development cycle. In addition, we may help to avoid future costs to the government resulting from individual and class action damage suits, and may enhance the effectiveness of our fighting forces through removal of smoke/obscurant use restraints in training.

The requirement for conducting health and environmental effects research as an integral portion of project development is well established. It is up to both the medical and developmental communities then to see that the appropriate funding and administrative procedures are set in place to accommodate this requirement before we find ourselves in conflict with regulatory agencies outside the US Army.

**REFERENCES**

1. Bockrath, Joseph T. Environmental Law for Engineers, Scientists, and Managers. McGraw-Hill Book Company, New York, NY, 1977.
2. Clayton, George D. and Florence E. Clayton, eds. Patty's Industrial Hygiene and Toxicology, Volume I, 3rd ed. John Wiley & Sons, New York, NY, 1978.
3. Rowlett, Carl D. "The Role of Health/Environmental Hazard Assessments in the Development of Improved Smokes and Obscurants." In: Proceedings of the Smokes/Obscurants Symposium IV. Office of the Project Manager for Smokes/Obscurants, Aberdeen Proving Ground, MD, 1980.
4. Druley, Ray M. and Girard L. Ordway. Toxic Substances Control Act. Bureau of National Affairs, Washington, DC, 1977.
5. The Industrial Environment--Its Evaluation and Control. US Department of Health, Education, and Welfare, Washington, DC, 1973.
6. Canter, Larry W. Environmental Impact Assessment. McGraw-Hill Book Company, New York, NY, 1977.
7. "Employment of Smoke." US Army Training and Doctrine Command Pamphlet 525-3, Fort Monroe, VA, 26 September 1980.
8. Letter, Headquarters US Army Materiel Development and Readiness Command, 27 June 1979, Subject: Implementation of Toxic Substances Control Act (TSCA) Premanufacturing Health and Environmental Toxicity Testing Requirements.

**UNCLASSIFIED**

**UNCLASSIFIED**

AN INVESTIGATION OF AEROSOL MATERIALS  
THAT OBSCURE IN THE MIDDLE-TO-FAR INFRARED

Richard A. Kenley, Clyde L. Witham, and Kenneth M. Sancier  
SRI International, 333 Ravenswood Avenue, Menlo Park, CA

**ABSTRACT**

Since the end of World War II, the U.S. technology for production of screening smokes has undergone little change. During these years, however, there has been a wide proliferation of highly sophisticated battlefield devices that require line-of-sight contact with the target and that can, in principle, be defeated by the use of obscurants. Among them are such items as night-vision devices, laser range-finders, laser target designators, and optically tracked, wire-guided antitank missiles. These systems operate at wavelengths in the visible, near infrared (IR), and middle-to-far IR regions of the spectrum. Effective screening agents for the visible and near IR regions (0.4 to 1.2  $\mu\text{m}$  wavelength region) are currently available. There is a need to develop agents for obscuration in the middle-to-far IR (1.2 to 14  $\mu\text{m}$ ) region, however.

Investigations supported by the U.S. Army were performed to determine the IR extinction characteristics of various materials that could ultimately have potential as screening smokes. Both organic and inorganic materials were investigated in bulk samples using the KBr disc technique, and in aerosol form using a Wilks variable pathlength gas cell.

Aerosols were generated using various techniques, and optical and physical characterization measurements were made from a flow-through type aerosol test system. Aerosol size distributions were measured with a piezoelectric cascade impactor and with scanning electron micrographs of filter samples of the aerosol.

**UNCLASSIFIED**

**UNCLASSIFIED**

## 1. INTRODUCTION

The modern battlefield is characterized by the proliferation of sophisticated electrooptical devices for target acquisition, ranging, and identification. Such devices require line-of-sight contact with the target and can, in principle, be defeated by tactical obscurants. These systems operate at wavelengths in the visible, near infrared (IR), and middle-to-far IR regions of the spectrum. Conventional smokes effectively screen in the visible region of the spectrum, but are relatively transparent at longer wavelengths.<sup>1</sup>

Thus, a requirement exists for the development of aerosolizable materials that feature enhanced absorption or scattering in the atmospheric windows (3 to 5  $\mu\text{m}$  and 8 to 14  $\mu\text{m}$ ) of the IR spectrum.

Recent years have witnessed the development of a sound theoretical basis (*vide infra*) for predicting the effects of particle geometry and composition on IR extinction by aerosol clouds. With few exceptions, however, experimental validation of the theory has been lacking. Nor does the theory address the important relationships between physical-chemical material properties and dynamic aerosol properties such as dissemination efficiency and gravitational settling velocity.

Given these considerations, there is a clear need for preparation of various materials that model the theoretical requirements for high IR extinction as well as a need for direct determination of their spectral and aerosol properties. At SRI International, under contract to the Army Chemical Systems Laboratory (CSL), we have attempted to bridge this gap between theory and practice. We produced or obtained a variety of materials, determined IR spectra on bulk samples of the materials, and evaluated their suitability for aerosol dissemination. We provided several of the most promising materials to CSL for determination of aerosol IR spectra. Our objectives were to provide an experimental verification of theoretical aspects of IR extinction by aerosols and to rate candidate materials with respect to potential practical application as battlefield obscurants.

We have found, in consonance with theory, that thin disc-shaped particles represent a promising class of materials for high IR extinction. Specifically, metal flakes and crystalline graphite are reasonable candidates for further development as tactical screening agents. In the following, we give a brief description of the principles underlying our investigations and detail the findings of our work.

**UNCLASSIFIED**

## 2. MODELS FOR ENHANCED IR EXTINCTION BY AEROSOL PARTICLES

The transmitted intensity of a beam of electromagnetic radiation penetrating an aerosol is reduced via scattering and/or absorption of the radiation by the particles that comprise the cloud. The Beer-Lambert law\* (1),

$$-\log(\%T) = \alpha CL \quad (1)$$

relates the transmitted intensity to the aerosol concentration, the optical pathlength, and the extinction coefficient,  $\alpha$ .

The definition of the extinction coefficient,

$$\alpha = \frac{(\text{Geometric Cross Section, } G)(\text{Extinction Efficiency, } Q)}{(\text{Mass, } \rho V)} \quad (2)$$

indicates that increasing the extinction efficiency or increasing the ratio of cross-sectional area to mass enhances extinction. Both extinction efficiency and the ratio of cross-sectional area to mass are dependent on particle size; as the particle diameter becomes smaller, the area-to-weight ratio becomes larger, thus enhancing extinction. There is a limit to the enhancement, however, by the extinction efficiency. For particles much larger than the wavelength of incident light, both the scattering and absorption components of extinction are inversely proportional to the particle diameter. (For a cloud of polydisperse particles, the extinction efficiency is essentially constant at two.) As the particle diameter approaches the wavelength, extinction peaks and then diminishes with decreasing particle size. As the particle becomes much smaller than the wavelength (Rayleigh region), the scattering component of extinction drops rapidly (inverse cube of diameter), whereas the absorption component tends to plateau.

For a given mass (or volume) of aerosol particles larger than the wavelength, the extinction coefficient can be increased by varying particle shape and thus increasing the ratio of geometric cross section to mass ( $Q$  will not change). Embury<sup>2,3</sup> has calculated cross-sectional areas for various particle shapes, and we have included excerpts of that information in Table I. (For most practical aerosol clouds, these results should also apply to the region of particle size close to the wavelength.) Since a sphere is the geometry having the least surface area per volume, any shape different from the sphere represents an increase in the surface-area-to-mass ratio. The average geometrical cross-sectional area for a set of randomly oriented particles is one-fourth the surface area. Thus, the cross-sectional area is directly proportional to the surface area. From Table I, it is evident that for various shapes geometric cross-section-to-mass ratios increase significantly over that of spheres with increasing aspect (length-to-diameter, radius-to-thickness) ratios. A hollow sphere is a special case of the general hollow particle, and the increase in cross section of the hollow sphere to mass over that of a solid sphere  $[(G/V)/(G/V)]_s$  is just

---

\* Nomenclature is given in Section 7.

**UNCLASSIFIED**

**UNCLASSIFIED**

$(r^2/9t^2)^{1/3}$ . The hollow sphere is also a special case of the general puffed (or foamed) particle. For a spherical foamed particle, the  $[(G/V)/(G/V)]_s$  is just the inverse of the solids fraction,  $1/f$ .

Figure 1 is a plot of the parameters that affect the  $[(G/V)/(G/V)]_s$  ratio for various shapes. The figure demonstrates that to increase the  $[(G/V)/(G/V)]_s$  ratio by a factor of 10, filament length-to-diameter ratios must exceed 2500. For a disc, an aspect ratio of about 300 is needed, and for a shell, the thickness should be about 1/100 the radius to achieve the same increase. If a solid sphere can be foamed or puffed out so that 90% of the puffed material is voids, the  $[(G/V)/(G/V)]_s$  ratio will also increase by a factor of 10.

In practice it may be difficult to effectively disperse filaments with aspect ratios as high as 2500. Very thin hollow particles with sufficient strength or stability may be difficult to manufacture. Thin discs, in the form of flakes, and puffed particles are probably the most tractable shapes to deal with physically and exhibit the greatest dependence of geometric-cross-section-to-mass ratio on particle geometry.

Significant enhancement of the extinction coefficient for particles with diameters less than the wavelength of incident light (Rayleigh region) cannot be achieved simply by changing particle shape because the extinction efficiency becomes a very strong function of the complex index of refraction as well as the aspect ratio. Embury has noted<sup>5</sup> that the extinction coefficient can be changed by coating ellipsoidal particles with materials of a different index of refraction. These calculations predict that extinction is enhanced when a dielectric material is coated with a highly conductive material such as metal.

Since extinction in the Rayleigh region is such a strong function of the complex index of refraction, it should also be possible to select materials with enhanced extinction on the basis of refractive indexes. The imaginary component of the refractive index governs light absorption and relates to the magnetic permeability and electrical conductivity of materials ( $n' = 2\sigma \mu_m f'$ ). Thus, highly conductive materials, such as metals or doped semiconductors, should absorb strongly at IR wavelengths. Metals also reflect efficiently in the IR region.

For dielectric materials, complex refractive indexes are generally unknown, making prediction of extinction efficiencies difficult. It is known, however, that for dielectrics, frequencies of maximum absorption correlate with chemical functional groups. Empirical correlations of absorption bands with chemical structure are available (e.g., see Table II) and permit the selection of inorganic and organic compounds that are likely to feature strong absorption in the spectral regions of interest.

In summary, theory predicts that particle geometries and refractive indexes can contribute to enhanced IR extinction. In seeking appropriate materials to model these effects we elected to examine the following:

**UNCLASSIFIED**

# UNCLASSIFIED

C-4

- Dielectrics: inorganic and organic compounds featuring absorption bands in the 3 to 5  $\mu\text{m}$  and 8 to 14  $\mu\text{m}$  regions.
- Foamed particles: expanded graphite.
- Coated dielectrics: copper-coated polymer microspheres and copper-coated mica flakes.
- Thin discs: metal flakes (spherical metal particles were examined for comparison) and crystalline graphite.
- Semiconductors: doped ZnO semiconductors.

## 3. EXPERIMENTAL DETAILS

### 3.1 MATERIALS

3.1.1 COMMERCIALLY AVAILABLE MATERIALS. Table III summarizes sources and descriptions of materials obtained from commercial sources.

3.1.2 EXPANDED GRAPHITE. Several samples of graphite powder were intercalated with nitric acid and exfoliated by rapid heating to yield expanded particles. Details follow.

Sample 3043-027. A 0.0370-gm ( $3.08 \times 10^{-3}$  mole carbon) sample of graphite powder used as a lock lubricant (Schage Lock Co.) was read over the surface of a tared Petri dish. The Petri dish was placed in a dessicator containing  $\text{CaCl}_2$  and exposed to vapors from a beaker of 70%  $\text{HNO}_3$ . After 18 hours, the total sample weight was 0.04070 gm. The amount of intercalated  $\text{HNO}_3$ , by difference, was 0.0137 gm ( $0.217 \times 10^{-3}$  mole).

Sample 3043-68. A 7.59-gm (0.63 mole carbon) sample of graphite powder (Alfa Ventron) was immersed for 2 hours in 30 ml of 70%  $\text{HNO}_3$ . The liquid  $\text{HNO}_3$  was filtered, dried at 25°C for 15 to 30 min and the remaining sample weight was 7.88 gm, corresponding to 0.28 gm ( $4.48 \times 10^{-3}$  mole) of intercalated  $\text{HNO}_3$ .

Sample 3043-71. A 5.81-gm (0.487 mole carbon) sample of (Schlage) graphite powder was immersed for 2 hours in a mixture of 70%  $\text{HNO}_3$ -30% oleum. The acid was filtered, dried at 25°C for 15 to 30 min and the remaining sample weight was 12.91 gm, corresponding to 7.10 gm (0.113 mole) of intercalated  $\text{HNO}_3$ .

Sample 3043-90A. A 1.0892-gm (0.0908 mole carbon) sample of Southwestern grade 1636 graphite was suspended in 70%  $\text{HNO}_3$  for 18 hours. The sample was filtered, worked with water, and weighed. The product weighed 1.2174 gm, corresponding to 0.1282 gm (0.0020 mole) of intercalated  $\text{HNO}_3$ .

Sample 3043-90B. The intercalated graphite (3043-90A) was divided into two fractions. One fraction was untreated. The other (3043-90B) was exfoliated by spreading small amounts of the powder on a 300°C hot plate.

3.1.3 COPPER-COATED MICROSPHERES. Solid poly(methyl methacrylate), PMMA, microspheres were prepared and copper-coated by an electroless deposition method. Solid copper microspheres were prepared similarly.

# UNCLASSIFIED

**UNCLASSIFIED**

Preparation of Solid PMMA Microspheres (Sample 11751-9). An 80-gm sample of PMMA resin (Dupont Elvacite 2009) was dissolved in 240 gm of  $\text{CH}_2\text{Cl}_2$  and 80 gm of ethyl acetate. The solution was emulsified in a Waring blender with 600 g of aqueous 10% gum arabic, stirred at high speed in a Virtris homogenizer for 10 minutes, then stirred in an open beaker at ambient temperature until the organic solvents evaporated. The gum arabic was diluted to 5% with demineralized water. The microspheres were centrifuged and washed six times with water, isolated by filtration and air drying, then resuspended in water. The average particle size of the microspheres was 2  $\mu\text{m}$ .

A 20-gm sample (11751-7) was also prepared using this technique.

Preparation of Copper-Coated Solid PMMA Microspheres (Sample 11751-26-1). A 20-gm sample of PMMA microspheres (11751-9) was slurried in water and dispersed in 200 ml 2%  $\text{SnCl}_4$ , and 1% HCl, then stirred for 20 minutes at room temperature, followed by filtration and washing with water. The wet microspheres were dispersed in 600 ml of 0.005%  $\text{PdCl}_2$ , in 1% HCl, stirred 20 minutes, filtered, and washed with water and dried at 25°C. The microspheres were then redispersed in 8.6 liters of water containing  $\text{CuSO}_4 \cdot 5\text{H}_2\text{O}$  (88 gm), Rochelle Salt (440 gm), and NaOH (123 gm). The suspension was stirred at room temperature, and 176 gm of 37%  $\text{H}_2\text{CO}$  solution added slowly by an addition funnel. The suspension was stirred until gas ( $\text{H}_2$ ) evolution was no longer evident. The copper-coated microspheres were then filtered, washed, and air-dried. The yield was 41.2 gm (97.2%).

Using this same general procedure, with minor modifications, two other samples (11751-26-2 and 11751-26-3) of copper-coated microspheres were prepared. Table IV summarizes the quantities of materials used to produce the copper-coated microspheres and the final yields.

Preparation of Solid Copper Microspheres (Sample 11751-28). Solid copper microspheres were prepared by the general procedure used for copper-coated PMMA microspheres (sample 11751-26-3) except that the sensitization step (treatment of PMMA microspheres with  $\text{SnCl}_4$ ) was omitted. Thus, 31.1 gm of an aqueous slurry of PMMA microspheres (8.0 gm of PMMA) was added to 240 ml of 0.005%  $\text{PdCl}_2$ , in 1% HCl and stirred 20 minutes. The microspheres were filtered, washed, and resuspended in 10 liters of an aqueous solution of 106 gm of  $\text{CuSO}_4 \cdot 5\text{H}_2\text{O}$ , 528 gm of Rochelle Salt, and 148 gm of NaOH. Next, 211 gm of aqueous 37%  $\text{H}_2\text{CO}$  solution was added dropwise. No deposition of copper occurred, and an additional 1.76 liters of aqueous  $\text{CuSO}_4 \cdot 5\text{H}_2\text{O}$  (35.2 gm), Rochelle Salt (35.2 gm), and NaOH (35.2 gm) was added, followed by 70 gm of 37%  $\text{H}_2\text{CO}$ . When the solution was warmed to 35° to 40°C, copper microspheres precipitated. The supernatant (containing suspended PMMA microspheres) was decanted, and the copper microspheres were isolated by filtration, washed with water, and dried. The yield was 35 gm (95%). The average diameter of the microspheres was approximately 5  $\mu\text{m}$ .

3.1.4 COPPER-COATED MICA. The general procedure for electroless deposition of copper on mica consists of four steps:

**UNCLASSIFIED**

# UNCLASSIFIED

C-4

- (1) Pretreatment with surfactant (poly ethoxylated quaternary ammonium chloride, Armak chemicals ethoquad C251) or polymer [either poly(acrylic acid) prepared in situ by persulfate-catalyzed polymerization at 50°C, or ethylene-maleic anhydride copolymer (Monsanto)] to break up agglomerates of mica.
- (2) Sensitization with a solution of 1.0 gm of  $\text{SnCl}_2 \cdot \text{H}_2\text{O}$  in 49 gm of water plus 4 ml of concentrated HCl.
- (3) Catalysis with a solution of 0.005%  $\text{PdCl}_2$  in 1% aqueous HCl.
- (4) Plating with an aqueous solution of  $\text{CuSO}_4 \cdot 5\text{H}_2\text{O}$ , Rochelle Salt, and NaOH to which is added 37% aqueous  $\text{H}_2\text{CO}$ .

Several samples of coated mica were prepared using various pretreatments and various copper-to-mica ratios. The copper-to-mica ratio was varied by changing the relative amounts of  $\text{CuSO}_4 \cdot 5\text{H}_2\text{O}$  and mica in the plating solution. Table V summarizes the reaction conditions used for copper-coated mica. The procedure for preparing sample 11751-27 is typical and is described below.

A 10-gm sample of mica (English Mica Co., C300) was pretreated by dispersing the mica in 150 ml of 1% Ethoquad C125, stirring for 15 minutes at room temperature, filtering, and washing with water. The sensitized mica was added to 300 ml of  $\text{PdCl}_2$  solution, stirred 20 minutes, filtered, and washed. The catalyzed material was then dispersed in 4 liters of water containing 40 gm of  $\text{CuSO}_4 \cdot 5\text{H}_2\text{O}$ , 56 gm of NaOH, and 200 gm of Rochelle Salt and stirred continuously while 80 gm of 37%  $\text{H}_2\text{CO}$  was added dropwise via an addition funnel. When gas ( $\text{H}_2$ ) evolution ceased, 1.2 liters of aqueous  $\text{CuSO}_4 \cdot 5\text{H}_2\text{O}$  (40 gm), NaOH (40 gm), and Rochelle Salt (40 gm) was added, followed by 80 gm of 37%  $\text{H}_2\text{CO}$  solution. After  $\text{H}_2$  evolution was completed, this step was repeated. Finally the copper-coated mica was filtered, washed with water, and air-dried. The yield was 38.6 gm (95% based on Cu plus mica).

3.1.5 DOPED SEMICONDUCTORS. Three electrically conductive  $\text{ZnO}$  pigments were studied. Two pigments (HC-016 and HC-238) were obtained from the New Jersey Zinc Company and one pigment (BS-F-1) from the St. Joe Minerals Corporation. These pigments are off-white with a slight grey or yellow hue.

## 3.2 METHODS

### 3.21. INFRARED SPECTRA. We obtained IR data on bulk materials using the KBr disc technique.

A 2- to 10-mg sample of test compound was added to approximately 1 gm of KBr (Baker Analytical reagent grade). The mixture was thoroughly ground with an agate mortar and pestle. A portion of the mixture was then placed in a stainless steel die and pressed into a 1.27-cm-diameter disc. The thickness of the disc was typically 0.1 cm and was accurately measured with a micrometer. The concentration of test compound in the disc was calculated from equation (3).

# UNCLASSIFIED

**UNCLASSIFIED**

$$\text{Concentration of } X = \frac{\text{gm } X}{\text{gm } X + \text{gm KBr}} \quad (\mu\text{m of disc})$$

$$\cdot [\frac{\pi}{4}(1.27)^2(\text{thickness})]^{-1}$$

IR spectra were measured for aerosols using a 20-m variable pathlength Wilks cell fitted with NaCl windows, and a Perkin Elmer 457 spectrophotometer. Mirrors in the Wilks cell were gold-coated, then overlaid with a silica coating to minimize surface marring of the mirrors. Aerosol was sampled at flowrates between 10 and 15 l/min. Particulate settling onto the mirrors of the Wilks cell was a problem, and after a 300 mg/m<sup>3</sup> concentration of bronze flakes was sampled for 1 hour, light transmission through the cell had been reduced by 37%. Typical sample times were 15 minutes, to allow for equilibration and the appropriate wavelength scan time. Extinction coefficient calculations were based on the average of a blank run before and after sampling. All measurements were made at pathlengths of 0.75 m or 9.75 m. The 0.75-m pathlength was calibrated by filling the Wilks cell with CO<sub>2</sub> and N<sub>2</sub>. The 9.75-m length was uncalibrated.

Because of problems associated with particulate coating of the mirrors in the Wilks cell, aerosol IR spectra were also obtained at CSL in a 70-m<sup>3</sup> chamber equipped with a Barnes IR Radiometer.

**3.2.2 AEROSOL GENERATION AND MEASUREMENT.** Figure 2 is a schematic of the flow-through aerosol test chamber designed and built for characterizing the aerosols. The chamber was constructed of 6-inch-diameter stainless steel tubing, and is 7.2 m long. All inlet air flows were supplied by a filtered compressed air source and metered by means of calibrated critical flow orifices. Aerosols dispersed in the system can be recovered by collection in a downstream bag filter. The bag filter can be bypassed if no aerosol recovery is required. All test chamber air (that is not removed by sampling) passes through a 24 by 24 inch HEPA filter for removal of particulate before being exhausted to the atmosphere. A blower is provided downstream of the filter to maintain the system at a slightly negative pressure (approximately 2 inches WC). By maintaining a negative pressure on the system, any leaks will be into the chamber, thus preventing escape of aerosol into the working area.

Under normal conditions the test chamber was operated with an airflow of 1415 liters per minute. The average duct velocity was 130 cm/second, and the residence time from the aerosol generator to the sample point was approximately 4.8 seconds. The test chamber was designed to maintain all particles less than about 200 μm in diameter in suspension (ignoring the effect of impaction at the 90-degree bends, which could remove up to 50% of the 200-μm-diameter particles) at a nominal flowrate of 1500 liters per minute. At that flowrate, the chamber is operated in a turbulent flow regime with a Reynolds number of 12,700. Thus, the aerosol is well mixed by the time it reaches the sample point. Two 3M Company Kr<sup>85</sup> sources of 20 mCi each were placed in the chamber just upstream of the dispersion nozzle to help mitigate the electrostatic effects due to the charging effect of the aerosol generator.

# UNCLASSIFIED

C-4

A helium-neon laser coupled with a PIN 5 silicon photodetector was mounted on the test chamber as a transmissometer. A combination of Kodak Wratten filters No. 29 and 52 was placed in the detector to reduce stray light. The transmissometer was used as a measure of aerosol generator stability (by monitoring changes in transmission with time) and as a measure of extinction of the test aerosol at 0.63  $\mu\text{m}$ . The laser and detector optics were kept clean by flowing filtered compressed air over the windows, at a flow-rate of 15 liters per minute.

Glycerine and siloxane aerosols were produced with a modified Mist-O-Gen ultrasonic generator. Glycerine was dissolved in water and the siloxanes were atomized as neat materials.

Powders were aerosolized by means of a proprietary grooved disc feeder and sonic velocity disperser developed by SRI International. The powder was unloaded pneumatically from the disc by an 85 l/min air stream and fed to the sonic velocity disperser operated at 70 psig and 1300 l/min. Tests performed on the disperser indicated essentially complete dispersion of nonfree-flowing powders at those conditions. Aerosol concentration in the chamber was varied by controlling the disc speed of the feeder. Concentration changes were monitored by the response of the He-Ne transmissometer.

Aerosol samples were taken on Nucleopore filters for gravimetric determination of concentrations and also for obtaining scanning electron micrographs. All airflows were measured using critical flow orifices. Particle size determinations in the aerosol were made with a California Measurements Piezoelectric Cascade Impactor (Model No. PC-2). The impactor was modified by removing the second stage orifice and impaction substrate to improve data interpretation. The impactor was operated at a nominal airflow rate of 250  $\text{cm}^3/\text{minute}$ . Sampling from the aerosol chamber was performed as close to isokinetic as possible.

## 4. RESULTS AND DISCUSSION

This section describes materials and spectral properties for bulk samples of classes of materials. Aerosol physical characteristics and aerosol IR spectral data for various classes of materials are discussed separately.

### 4.1 DIELECTRICS

Table VI summarizes IR spectral data for bulk samples of selected organic and inorganic materials. The table lists absorption maxima and extinction coefficients at the maxima plus extinction coefficients at 3.5, 9.6, and 10.6  $\mu\text{m}$ . Figures 3 and 4 are typical absorption spectra, respectively, for an organic compound (dibutyl butylphosphonate) and an inorganic compound (Mistron talc).

The table shows that fluorocarbons (Teflon 7C) and organophosphorus compounds (dibutyl butylphosphonate) featured several absorption bands in the regions of interest. The extinction coefficients were rather low, however, and did not exceed 0.3  $\text{m}^2/\text{gm}$ .

675

# UNCLASSIFIED

**UNCLASSIFIED**

Siliceous materials featured the most intense absorptions of any of the dielectric materials that we investigated. This was true both for organo-silicons such as hexamethyl disiloxane, and inorganic materials such as silica (Min-U-Sil and Cab-O-Sil), or silicate minerals (clay or talc).

A sample of talc (Cyprubond) showed one of the highest extinction coefficients ( $\alpha = 0.82 \text{ m}^2/\text{gm}$  at  $9.8 \mu\text{m}$ ) of any of the materials investigated in this work. Cyprubond is an inorganic silicate that has been treated with an organosilane, aminopropyl triethoxysilane. The organosilane bonds covalently to free hydroxyls in the talc. It is interesting to note that the  $9.8 \mu\text{m}$  wavelength extinction coefficient for Cyprubond was nearly double (0.82 versus  $0.44 \text{ m}^2/\text{gm}$ ) that of Mistron, an identical talc not treated with the organosilane. Similarly treated (silanized) versus untreated (Afton clay) samples of kaoline (another silicate) showed  $9.6 \mu\text{m}$  wavelength extinction coefficients ( $\alpha = 0.70$  and  $0.54 \text{ m}^2/\text{gm}$ , respectively) that differed by a factor of 1.3. The phenomenon thus appears to be real and may be a general property of silicates coated in this manner.

Although certain of these dielectrics exhibited reasonably high extinction coefficients, they shared a common deficiency. All the materials discussed above featured absorption bands in discrete wavelength regions. In all cases the materials were essentially transparent to a large part of the IR spectral region. This was especially true of siliceous materials, which absorbed strongly near  $9.6 \mu\text{m}$  but absorbed very weakly in almost all other regions of the spectrum. Such compounds might be useful obscurants in terms of countermeasures against electrooptical devices operating at specific wavelengths (e.g., at the  $9.6$  and  $10.6 \mu\text{m}$  lines of a  $\text{CO}_2$  laser). However, if extinction is integrated over the entire 3 to 5 and 8 to  $14 \mu\text{m}$  regions, total extinction would be marginal for most of these materials.

Some materials, such as coal and molybdenum disulfide, exhibited featureless absorption over the entire IR region. The extinction coefficients for these materials, though constant over the 3 to  $14 \mu\text{m}$  range, were nevertheless somewhat low; at  $10.6 \mu\text{m}$ ,  $\alpha = 0.096$ , and  $0.081 \text{ m}^2/\text{gm}$  for coal, and  $\text{MoS}_2$ , respectively. Graphite, however, combined broadband extinction with high extinction efficiency; at  $10.6 \mu\text{m}$   $\alpha = 0.26$  and  $0.85 \text{ m}^2/\text{gm}$  for Schrage and Asbury graphites, respectively.

#### 4.2 INTERCALATED AND EXPANDED GRAPHITES

As noted above, crystalline graphite exhibits intense broadband IR absorption. We can rationalize this behavior in terms of the relatively high conductivity (and hence high imaginary refractive index) of the material as well as the layered graphitic structure, which approximates the model for thin discs.

The planar graphite structure permits intercalation of small molecules within the interstitial spaces.  $\text{HNO}_3$ -intercalated graphite is highly conductive,<sup>5-9</sup> and we reasoned that this material might exhibit enhanced extinction due to conductivity effects. Table VI reveals, however, that this is not the case;  $\text{HNO}_3$ -intercalated Schrage graphite exhibited lower extinction coefficients than the original material except at  $7.19 \mu\text{m}$  where the  $\text{HNO}_3$  absorption band contributes to absorption.

# UNCLASSIFIED

C-4

We were also interested in HNO<sub>3</sub>-intercalated graphite, insofar as rapid heating of the material is known<sup>10-13</sup> to cause exfoliation of the intercalant and separation of the basal planes resulting in an expanded or foamed material. We investigated several materials and methods (see Section 3.1.2) for exfoliating graphite and found that Schläge and Southwestern graphites (see Table III) could be greatly expanded. Figures 5 and 6 are scanning electron micrographs (SEMs), respectively, of intercalated and expanded graphites. The figures clearly reveal the separation of planes in the expanded material.

Because the thickness-to-radius ratio of disc-like structures and the solids fraction of foamed particles strongly influence the geometric-cross-section-to-mass ratio (Figure 1), it seems likely that exfoliated graphites would feature enhanced extinction relative to nonexpanded material. Unfortunately, the expanded graphite lacks strength and is recompressed in preparing KBr discs for bulk spectra. Additionally, the expanded particles that we prepared are far too large (ca. 100  $\mu\text{m}$  in diameter) to permit aerosolization. Thus we have been unable to verify the predicted spectral properties of the expanded material. We consider that with additional development aerosolized expanded graphite could be obtained and believe this area warrants further investigation.

### 4.3 COATED DIELECTRICS

We investigated two types of coated dielectric materials. Polymer (PMMA) microspheres and mica served as substrates, and we used an electroless (chemical reduction) deposition process<sup>14-16</sup> to prepare thin copper coatings on either material. The advantage of the electroless deposition process is that all of the cupric ion added as starting material reduces to metallic copper on the surface of the substrate. This allows the application of very thin and even coatings to the substrate and permits the coating thickness to be easily controlled.

Table IV describes the samples of copper-coated PMMA microspheres prepared. Starting with 2- $\mu\text{m}$ -diameter solid PMMA microspheres, we prepared coated samples with copper-to-polymer ratios of 0, 1.1, 2.2, and 4.5. These ratios correspond to copper layers of 0.05, 0.1, and 0.2  $\mu\text{m}$ , respectively. Table VII summarizes the IR spectral properties of the bulk materials. The table lists extinction coefficients at the PMMA absorption maxima (5.85 and 8.9  $\mu\text{m}$ ) and also at 3.5, 9.6 and 10.6  $\mu\text{m}$ . The table shows that increasing the Cu-to-polymer ratio of the coated spheres transformed the particles from absorbers at discrete wavelengths (6.85 and 8.9  $\mu\text{m}$ ) to materials featuring broadband extinction (equal values for  $\alpha$  at all wavelengths). It also appeared that increasing the copper-to-polymer ratio from 2.2 to 4.5 did not increase extinction. This suggests that the 0.1- $\mu\text{m}$  layer of copper absorbed or reflected nearly all of the incident radiation and that increasing the layer thickness only contributed to a reduction in extinction coefficient normalized on a weight basis. The relatively low extinction coefficient for solid copper microspheres can be similarly rationalized.

# UNCLASSIFIED

677

# UNCLASSIFIED

C-4

Table VIII gives IR spectral data for copper-coated mica. The data are given at 3.5 and 10.6  $\mu\text{m}$  as well as at the 10.0  $\mu\text{m}$  absorption band of uncoated mica. The copper-coated mica was similar to the copper-coated PNMA microspheres in that increasing copper-to-mica ratios past 0.76 resulted in broadband extinction, but did not contribute to increased extinction normalized on a weight basis.

## 4.4 THIN DISCS

We obtained pigment grade aluminum, bronze, and copper flakes and recorded KBr disc IR spectra for all three materials. For comparison we also examined spherical aluminum and copper particles. Table IX summarizes the spectral data. Crystalline graphite can also be characterized as a disc-shaped material (as previously discussed). Spectral data for graphite samples are given in Table VI. Because all the metal samples exhibited broadband extinction, we calculated extinction coefficients at a single wavelength (10.6  $\mu\text{m}$ ). Table IX shows that the flakes exhibited considerably higher extinction coefficients than corresponding spheres. Moreover, absolute values for extinction coefficients were quite high, with the value for aluminum flakes ( $\alpha = 0.96 \text{ m}^2/\text{gm}$ ) being the highest of any material investigated. That aluminum flakes were superior to bronze and copper flakes in terms of extinction normalized on a mass basis probably relates to the relatively low density of aluminum [see equation (1)].

## 4.5 DOPED SEMICONDUCTORS

Highly doped, electrically conductive semiconductor pigments were proposed as screening smoke material because doping increases the charge carrier concentration of the semiconductor, resulting in a broad, intense absorption band in the IR. The modification of the electrical conductivity increases the complex index of refraction, thus enhancing the extinction efficiency.

IR spectra of several grades of commercially available aluminum-doped conductive zinc oxide pigments were measured with the KBr disc technique and are reported in Table X. The spectra were fairly broadband, and the materials produced a reasonably high extinction coefficient. Attempts were made to further enhance the conductivity of the commercial material by increased doping with hydrogen. Although conductivity was increased, it was determined to be a surface effect rather than an increase for the bulk material.

## 4.6 AEROSOL PROPERTIES AND SPECTRA

We investigated aerosol properties for selected materials. Initial work at SRI indicated the use of the Wilks variable pathlength cell for determination of IR spectra was complicated by sedimentation and collection of particles on the cell mirrors. Consequently most aerosol spectral data were recorded using the 70-m<sup>3</sup> chamber at CSL.

At SRI we investigated the following materials: glycerin, hexamethyl disiloxane, decamethyl tetrasiloxane, doped zinc oxide (HC-238), molybdenum disulfide, and bronze (MD 90) flakes. Table XI summarizes aerosol physical and spectral data for these materials.

# UNCLASSIFIED

C-4

Glycerine was aerosolized using an ultrasonic generator at a nominal concentration of 100 gm/m<sup>3</sup>, from a 10% by weight solution in water. Based on known generator characteristics, the nominal average diameter was about 2  $\mu\text{m}$ . As expected, strong absorption bands appeared at about 3.3 and 9.6  $\mu\text{m}$ . The extinction coefficient for the glycerine alone was estimated to be 0.1 m<sup>2</sup>/gm at 3.3  $\mu\text{m}$  and 0.08 m<sup>2</sup>/gm at 9.6  $\mu\text{m}$ . At 3.3  $\mu\text{m}$  the glycerine-water system has an extinction coefficient of about 0.15 m<sup>2</sup>/gm (see Table IX). These values are only approximate, since no specific determination of aerosol concentration was made.

Two liquid siloxanes (hexamethyl disiloxane, and decamethyl tetrasiloxane) were also generated in the ultrasonic aerosol generator, but it was evident that any aerosol vaporized before entering the test system. Qualitatively, the siloxanes exhibited strong absorption bands similar to those obtained for the bulk measurements. The actual vapor concentration in the system was unknown and therefore no extinction coefficients could be calculated.

Doped ZnO (HC-238) and MoS<sub>2</sub> were generated as aerosols with the sonic velocity disperser. Several runs were made at various aerosol concentrations to determine IR spectra and to evaluate the effect of the aerosol on the operation of the Wilks cell. Aerosol concentrations were determined gravimetrically from Nucleopore filters, and particle-size distributions were measured with a modified piezoelectric cascade impactor.

The aerosol IR spectra for doped ZnO were qualitatively similar to the spectra for the bulk material but exhibited a lower average total extinction (0.15 m<sup>2</sup>/gm). Molybdenum sulfide exhibited approximately the same extinction coefficient as ZnO.

Particle size distribution was reasonably close to log normal; the mass median diameter of the ZnO was 1.0  $\mu\text{m}$ , the mass median diameter of the MoS<sub>2</sub> was 2.1  $\mu\text{m}$ , and the standard geometric deviation was about 2.9 for the ZnO and about 2.6 for the MoS<sub>2</sub>. The size distributions as measured for the ZnO at both the low and high concentrations were identical, indicating consistent dispersion from the sonic velocity disperser.

The spectral data obtained for ZnO and MoS<sub>2</sub> are somewhat suspect because of a discovery that the mirrors in the Wilks cell may have been out of alignment. After the cell had been calibrated with CO<sub>2</sub>, it was determined that a pathlength of 0.75 m could be used with confidence, and this was done for measurement with the bronze (MD90) powder. The extinction coefficients measured for the bronze powder in the aerosol closely matched those found in the bulk measurement (0.3 as compared with 0.36 m<sup>2</sup>/gm).

Table XII summarizes aerosol spectral data obtained at CSL. Materials investigated included: bronze, aluminum and copper flakes, copper spheres, copper-coated mica, copper-coated PMMA microspheres, and crystalline graphite. The table gives extinction coefficients at four wavelengths and aerosol concentrations as a function of time after dissemination. The sonic velocity disperser was used to aerosolize all the

# UNCLASSIFIED

# UNCLASSIFIED

C-4

samples, and aerosol concentrations were determined gravimetrically. The table indicates that metal flakes, particularly aluminum flakes, exhibited strong extinction throughout the IR region. The Asbury graphite was also a strong absorber, essentially equalling the performance of the aluminum flakes. Copper spheres, and copper-coated dielectrics, though broad-band absorbers, exhibited relatively low extinction coefficients at 3.0 and 10.6  $\mu\text{m}$ . The increase in extinction coefficients with time reflects a changing size distribution of the aerosols due to relatively rapid sedimentation of large diameter particles.

Table XII also shows that for the same materials, aerosol extinction coefficients were considerably greater than values determined for bulk samples using the KBr disc technique. This probably resulted from more efficient dispersion of powders into individual particles on aerosolization with the sonic velocity disperser compared with dispersion of particles within a KBr powder by use of a mortar and pestle. This appears to be a general phenomenon and recommends that KBr disc data be interpreted as semiquantitative or only as lower limits to aerosol data.

## 5. CONCLUSIONS

Of 30 samples representing various geometries and material types we find that disc-shaped (flaked) materials, as a class, exhibit the highest IR extinction. Aluminum flakes and crystalline graphite in particular feature extinction coefficients of approximately  $2$  to  $3 \text{ m}^2/\text{gm}$ . Metal-coated dielectrics, metal spheres, and doped semiconductors are broadband obscurants, but their extinction coefficients are significantly lower than those for metal flakes or graphite. Inorganic and organic dielectrics featuring discrete IR absorption bands could have utility as countermeasures for single-wavelength electrooptical devices, but would absorb only a small fraction of the total light available in the atmospheric windows of the IR spectrum. Theoretical considerations provide for increased extinction with increasing aspect (radius-to-thickness) ratio of disc-shaped particles. Rapid exfoliation of  $\text{HNO}_3$ -intercalated graphite offers some promise for increasing aspect ratios by separation of basal planes in graphitic materials. However, development of suitable methods for generation of aerosols of exfoliated graphite requires further investigation.

The KBr disc method for determining IR spectra of bulk powders is semiquantitative at best. For a given material, extinction coefficients measured by the KBr disc method are generally lower by a factor of approximately two than values determined on aerosol samples.

# UNCLASSIFIED

# UNCLASSIFIED

C-4

## 6. REFERENCES

1. Harris, B. L., Shantz, F., and Wiseman, W. J., "Chemical in War," in Kirk-Othmer Encyclopedia of Chemical Technology. 3rd Ed., Vol. 5, pp 405-408. Wiley-Interscience, New York. 1979.
2. Embury, J., In Search of Strong Infrared Extinction in Aerosols. Proc. Army Science Conference, West Point, N.Y., 1980.
3. Embury, J., Light Scattering by Irregularly Shaped Particles. D. Schuerman, ed. Plenum Press, New York. 1980.
4. Sadler Collection of Standard Spectra, Sadler Research Laboratories, Philadelphia PA. 1965.
5. Fischer, J. E., Thompson, T. E., Foley, G.M.T., Guerard, D., Hoke, M., and Lederman, F. L., Optical and Electrical Properties of Graphite Intercalated with HNO<sub>3</sub>. Phys. Rev. Lett. 37, 769 (1976).
6. Fischer, J. E., Thompson, T. E., and Vogel, F., Free Carrier Plasma in Graphite Compounds. ACS Symposium Series, No. 21, American Chemical Society. 1975.
7. Yoffe, A. D., Electronic Properties of Two Dimensional Solids: The Layer-Type Transition Metal Dichalcogenides. Festkorperprobl. XIII, 1 (1973).
8. Di Salvo, F. J., Schwall, R., and Geballe, T. H., Superconductivity in Layered Compounds with Variable Interlayer Spacings. Phys. Rev. Lett. 27, 310 (1976).
9. Barz, H. E., et al., Superconductivity in Layered Structure Organometallic Crystals. Science, 168, 568 (1970).
10. Dowell, M. B., Exfoliation of Intercalated Graphites, I. Effect of Graphite Crystallinity. 12th Biennial Conference on Carbon, American Carbon Society. July 28 to August 1976, p. 31.
11. Dowell, M. B., Exfoliation of Intercalated Graphites, II. Structure, Porosity, and the Mechanism of Exfoliates. Ibid, p. 35.
12. Berger, D., and Maire, J., Propriétés Physiques du Graphite Expansé Recomprimé. Mater. Sci. Eng., 31, 335 (1977).
13. Berger, D., and Maire, J., Préparation de Certains Composés Lamellaires. Mater. Sci. Eng., 31, 331 (1977).
14. Goldie, W., Electro Copper Deposition. Plating, No. 11, 1069 (1974).
15. Lukes, R. M., The Chemistry of the Autocatalytic Reduction of Copper by Alkaline Formaldehyde. Plating, No. 11, 1066 (1964).
16. Kenley, R. A., Reyes, Z., and Andeen, G. S., Novel Tactical Obscurants Based on Hollow Microspheres. Chemical Systems Laboratory, Contractor Report ALCSL-CR-80050, June 1980.

# UNCLASSIFIED

681

**UNCLASSIFIED**

## 7. GLOSSARY

<u>Symbol</u>	<u>Description</u>	<u>Typical Units</u>
A	Area of each face of a regular polyhedron	m <sup>2</sup>
a	Edge length of cube	μm
C	Mass concentration	gm/m <sup>3</sup>
D <sub>o</sub>	Outside diameter of hollow sphere	μm
D <sub>p</sub>	Particle diameter	μm
f	Solids fraction of a foamed particle	Dimensionless
f'	Frequency	Hz
G	Average geometric cross-sectional area of an assemblage of randomly oriented particles	m <sup>2</sup>
(G/V) <sub>s</sub>	Ratio of average geometric cross section to volume for a solid sphere	m <sup>-1</sup>
j	Imaginary number (-1) <sup>1/2</sup>	Dimensionless
L	Path length	μm
l	Length of a cylinder or thickness of a disc	μm
N	Number of faces of a regular polyhedron	Dimensionless
n'	Imaginary part of the complex index of refraction	Dimensionless
Q	Extinction efficiency	Dimensionless
R <sub>o</sub>	Diffuse reflectance	%
r	Radius of sphere	μm
r <sub>i</sub>	Radius of inscribed sphere of a polyhedron	μm
r <sub>o</sub>	Radius of spherical particle before foaming	μm
Re	Reynolds number ( $D_p U_p / \mu$ )	Dimensionless
S	Surface area of particle	m <sup>2</sup>
T	Temperature	°C
t	Time	s
t <sub>s</sub>	Thickness of shell	μm
t <sub>1/2</sub>	Half-life	s
U	Particle settling velocity	cm/s
V	Volume	m <sup>3</sup>
V <sub>o</sub>	Volume of a particle before foaming	m <sup>3</sup>
α	Extinction coefficient	m <sup>2</sup> /gm
α <sub>k</sub>	Spectral absorption coefficient	m <sup>2</sup> /gm

**UNCLASSIFIED**

C-4

<u>Symbol</u>	<u>Description</u>	<u>Typical Units</u>
$\alpha_s$	Spectral scattering coefficient	$m^2/gm$
$\lambda$	Wavelength	$\mu m$
$\lambda_{max}$	Wavelength at maximum absorption	$\mu m$
$\mu$	Fluid viscosity	poises
$\nu_m$	Magnetic permeability	$\frac{weber}{m\cdot amp\cdot turn}$
$\rho$	Density	$gm/cm^3$
$\rho_u$	Density of metal coating	$gm/cm^3$
$\rho_p$	Density of polymer core	$gm/cm^3$
$\sigma$	Electrical conductivity	$(ohm\cdot cm)^{-1}$

**UNCLASSIFIED**

683

**UNCLASSIFIED****8. ACKNOWLEDGEMENTS**

This work was performed under U.S. Army contract DAAK11-79-C-0065. The authors wish to thank Bosco Lan, Zoila Reyes, and Marie Comas of SRI International for their valuable contributions. We also gratefully acknowledge Dr. Jannon Embury of the Army Chemical Systems Laboratory for his many helpful suggestions.

**UNCLASSIFIED**

## UNCLASSIFIED

C-4

TABLE I. GEOMETRIC CROSS SECTIONS FOR VARIOUS PARTICLE SHAPES<sup>a</sup>

Particle shape	Average geometric cross section <sup>b</sup> (G)	Geometric cross section per unit mass (G/pV)	Cross section to mass ratio relative to solid sphere [(G/V)/(G/V) <sub>s</sub> ]
Sphere	$\pi r^2$	$\frac{3}{4\pi r}$	1
Cube	$\frac{3a^2}{2}$	$\frac{3}{2a}$	$\left(\frac{6}{\pi}\right)^{1/3}$
Regular polyhedra	$\frac{NA}{4}$	$\frac{3}{4\pi r_1}$	$\frac{NA}{4\pi r_1^2}$
Thin long cylinder (l >> r)	$\frac{\pi r l}{2}$	$\frac{1}{2\pi r}$	$\left(\frac{2l}{9\pi}\right)^{1/3}$
Thin disc (r >> l)	$\frac{\pi r^2}{2}$	$\frac{1}{2\pi l}$	$\left(\frac{2r^2}{9\pi l}\right)^{1/3}$
Hollow particle (thin shell) <sup>c</sup>	$\frac{S}{4}$	$\frac{1}{4\pi l}$	$\left(\frac{S}{36\pi l^2}\right)^{1/3}$
Puffed particle <sup>d</sup>	$\frac{S}{4f^{2/3}}$	$\frac{S}{4f^{2/3} \rho V_o}$	$\frac{S}{(36\pi)^{1/3} f \rho V_o^{2/3}}$

<sup>a</sup>Nomenclature is given in Section 7.<sup>b</sup>This is the average cross-sectional area for an ensemble of random orientations of convex particles where every orientation has equal probability.<sup>c</sup> $t < 0.05r$ .<sup>d</sup>Shape of the puffed particle is unchanged from the particle before puffing.

UNCLASSIFIED

## UNCLASSIFIED

TABLE II. CHARACTERISTIC INFRARED ABSORPTION BANDS OF SOME ORGANIC AND INORGANIC COMPOUNDS

Vibration	Functional Group	Range ( $\mu\text{m}$ )	Example	Sadtler <sup>a</sup> Number
O-H Stretch	Alcohol	2.9-3.3	$\text{C}_2\text{H}_5\text{OH}$	4112
	Saccharide	2.9-3.3	D-Glucose	5455
	Carboxylic acid	3.3-3.6	$\text{C}_2\text{H}_5\text{COOH}$	125
	Phosphoric acid	3.3-3.6	$(\text{C}_2\text{H}_5\text{O})_2\text{P}(\text{O})\text{OH}$	9041
N-H Stretch	Amine	2.8-3.1	$(\text{C}_2\text{H}_5)_2\text{NH}$	12932
	Amide	2.9-3.2	$\text{C}_2\text{H}_5\text{C}(\text{O})\text{NH}_2$ $(\text{C}_2\text{H}_5\text{O})_2\text{P}(\text{O})\text{NH}_2$	3035 18706
	Ammonium	3.1-3.4	$\text{C}_2\text{H}_5\text{S}(\text{O})_2\text{NH}_2$ $(\text{NH}_4)_2\text{O}_2\text{P}(\text{O})\text{OH}$	5760 WT278K
C-H Stretch	Alkyl	3.3-3.6	$\text{C}_2\text{H}_{12}$	690
C-O Stretch	Saccharide	8.3-10.0	Cellulose	07033
P-O-C Stretch	Phosphate ester	9.5-10.5	$(\text{C}_2\text{H}_5\text{O})_2\text{P}(\text{O})\text{OH}$	9041
Si-O-Si Stretch	Siloxane	8.7-9.5	$[(\text{CH}_3)_2\text{CHSi}(\text{OC}_2\text{H}_5)_2]_2\text{O}$	11474
	Silicon dioxide	8.3-10.0	Silica gel	1760
	Silicates	8.7-10.0	$\text{Al}_2\text{O}_3 \cdot 2\text{SiO}_2 \cdot 2\text{H}_2\text{O}$ (Kaolin)	1759
S-O Stretch	Sulfonamide	8.3-9.5	$\text{C}_2\text{H}_5\text{S}(\text{O})_2\text{NH}_2$	5760
C-F Stretch	Fluorocarbon	7.7-9.1	$\text{C}_2\text{F}_{12}$	1870
C-Cl Stretch	Chlorocarbon	12.5-16.0	$\text{C}(\text{Cl}_3)\text{C}(\text{C}_2)_2\text{CH}(\text{C}_2)_2$	5143

<sup>a</sup>See Ref. 4.

## UNCLASSIFIED

C-4

TABLE III. DATA AND SOURCES FOR COMMERCIALLY AVAILABLE MATERIALS

Material	Trade name	Chemical formula	Physical form	Source
NiCrAl	Al	Al	Flakes Spheres	Atlantic Powdered Metals, Inc. SRI Particle Bank
SiC	SiO <sub>2</sub>	Si	Flakes	Bee Chemical Co.
SiC	SiC-Si	Si <sub>3</sub> N <sub>4</sub>	Flakes	Alcan Metal Powder, Inc.
Ti	Al	Ti	Powdered	SRI Particle Bank
Ti	Al	Ti	Flakes	Atlantic Powdered Metals, Inc.
Titanium Carbide	Titanium Carbide	Ti <sub>3</sub> C <sub>2</sub> (Ti <sub>2</sub> C <sub>3</sub> ) <sub>n</sub> (TiC <sub>2</sub> ) <sub>m</sub>	Liquid	Petrocarb Systems
Titanium Carbide	Titanium Carbide	Ti <sub>3</sub> C <sub>2</sub> (Ti <sub>2</sub> C <sub>3</sub> ) <sub>n</sub> (TiC <sub>2</sub> ) <sub>m</sub>	Liquid	K & K Chemicals
Titanium Carbide	Titanium Carbide	Ti <sub>3</sub> C <sub>2</sub> (Ti <sub>2</sub> C <sub>3</sub> ) <sub>n</sub> (TiC <sub>2</sub> ) <sub>m</sub>	Spun Liquid	SRI Particle Bank
Titanium Carbide	Titanium Carbide	Ti <sub>3</sub> C <sub>2</sub> (Ti <sub>2</sub> C <sub>3</sub> ) <sub>n</sub> (TiC <sub>2</sub> ) <sub>m</sub>	Amorphous	Alfa Ventron
Titanium Carbide	Titanium Carbide	Ti <sub>3</sub> C <sub>2</sub> (Ti <sub>2</sub> C <sub>3</sub> ) <sub>n</sub> (TiC <sub>2</sub> ) <sub>m</sub>	Crystalline	Astaire Miles
Titanium Carbide	Titanium Carbide	Ti <sub>3</sub> C <sub>2</sub> (Ti <sub>2</sub> C <sub>3</sub> ) <sub>n</sub> (TiC <sub>2</sub> ) <sub>m</sub>	Amorphous	Union Carbide
Titanium Carbide	Titanium Carbide	Ti <sub>3</sub> C <sub>2</sub> (Ti <sub>2</sub> C <sub>3</sub> ) <sub>n</sub> (TiC <sub>2</sub> ) <sub>m</sub>	Amorphous	Schläger Carb Co.
Titanium Carbide	Titanium Carbide	Ti <sub>3</sub> C <sub>2</sub> (Ti <sub>2</sub> C <sub>3</sub> ) <sub>n</sub> (TiC <sub>2</sub> ) <sub>m</sub>	Crystalline	SRI Powdered Graphite Co.
Titanium Carbide	Titanium Carbide	Ti <sub>3</sub> C <sub>2</sub> (Ti <sub>2</sub> C <sub>3</sub> ) <sub>n</sub> (TiC <sub>2</sub> ) <sub>m</sub>	Amorphous	U.S. Carbide
Titanium Carbide	Titanium Carbide	Ti <sub>3</sub> C <sub>2</sub> (Ti <sub>2</sub> C <sub>3</sub> ) <sub>n</sub> (TiC <sub>2</sub> ) <sub>m</sub>	Liquid	Peterson Systems
Titanium Carbide	Titanium Carbide	Ti <sub>3</sub> C <sub>2</sub> (Ti <sub>2</sub> C <sub>3</sub> ) <sub>n</sub> (TiC <sub>2</sub> ) <sub>m</sub>	Amorphous	Cypress Mining Co.
Titanium Carbide	Titanium Carbide	Ti <sub>3</sub> C <sub>2</sub> (Ti <sub>2</sub> C <sub>3</sub> ) <sub>n</sub> (TiC <sub>2</sub> ) <sub>m</sub>	Amorphous	English Mine Co.
Titanium Carbide	Titanium Carbide	Ti <sub>3</sub> C <sub>2</sub> (Ti <sub>2</sub> C <sub>3</sub> ) <sub>n</sub> (TiC <sub>2</sub> ) <sub>m</sub>	Amorphous	Alfa Ventron
Titanium Carbide	Titanium Carbide	Ti <sub>3</sub> C <sub>2</sub> (Ti <sub>2</sub> C <sub>3</sub> ) <sub>n</sub> (TiC <sub>2</sub> ) <sub>m</sub>	Amorphous	Cypress Mining Co.
Titanium Carbide	Titanium Carbide	Ti <sub>3</sub> C <sub>2</sub> (Ti <sub>2</sub> C <sub>3</sub> ) <sub>n</sub> (TiC <sub>2</sub> ) <sub>m</sub>	Amorphous	Cypress Mining Co.
Titanium Carbide	Titanium Carbide	Ti <sub>3</sub> C <sub>2</sub> (Ti <sub>2</sub> C <sub>3</sub> ) <sub>n</sub> (TiC <sub>2</sub> ) <sub>m</sub>	Ground	Papert
Titanium Carbide	Titanium Carbide	Ti <sub>3</sub> C <sub>2</sub> (Ti <sub>2</sub> C <sub>3</sub> ) <sub>n</sub> (TiC <sub>2</sub> ) <sub>m</sub>	Amorphous	Pennsylvania Glass and Sand
Titanium Carbide	Titanium Carbide	Ti <sub>3</sub> C <sub>2</sub> (Ti <sub>2</sub> C <sub>3</sub> ) <sub>n</sub> (TiC <sub>2</sub> ) <sub>m</sub>	Powder	Gabot Corp.
Titanium Carbide	Titanium Carbide	Ti <sub>3</sub> C <sub>2</sub> (Ti <sub>2</sub> C <sub>3</sub> ) <sub>n</sub> (TiC <sub>2</sub> ) <sub>m</sub>	Powder	New Jersey Zinc Co.
Titanium Carbide	Titanium Carbide	Ti <sub>3</sub> C <sub>2</sub> (Ti <sub>2</sub> C <sub>3</sub> ) <sub>n</sub> (TiC <sub>2</sub> ) <sub>m</sub>	Powder	New Jersey Zinc Co.
Titanium Carbide	Titanium Carbide	Ti <sub>3</sub> C <sub>2</sub> (Ti <sub>2</sub> C <sub>3</sub> ) <sub>n</sub> (TiC <sub>2</sub> ) <sub>m</sub>	Powder	St. Joe Minerals Corp.

Unknown  
Sources of material

UNCLASSIFIED

**UNCLASSIFIED**

TABLE IV. DESCRIPTION AND YIELD OF COPPER-COATED MICROSPHERES

Sample No.	Microspheres <sup>a</sup> sample size (gm)	CuSO <sub>4</sub> •5H <sub>2</sub> O used (gm)	Cu-to-Polymer Ratio <sup>b</sup>	Yield	
				(gm)	(%) <sup>c</sup>
11751-26-1	20	88	1.12	41.2	97.2
11751-26-2	14	123.2	2.24	39.4	86.8
11751-26-3	8	141	4.48	41.7	95.2

<sup>a</sup>Microsphere sample 11751-9 was core material.<sup>b</sup>Cu-to-polymer ratio = (gm CuSO<sub>4</sub>•5H<sub>2</sub>O)•(% copper in CuSO<sub>4</sub>•5H<sub>2</sub>O = 25.5)  
(gm polymer)<sup>-1</sup>.<sup>c</sup>% Yield = 100 x (yield, gm) [(gm polymer) + (gm CuSO<sub>4</sub>•5H<sub>2</sub>O)(% copper in  
CuSO<sub>4</sub>)]<sup>-1</sup>.**UNCLASSIFIED**

## UNCLASSIFIED

C-4

TABLE V. DESCRIPTION OF COPPER-COATED MICA SAMPLES

Sample No.	Pretreatment	Material Quantities Used			Yield	
		Mica (gm)	CuSO <sub>4</sub> •5H <sub>2</sub> O (gm)	Cu-to-Mica <sup>a</sup> Ratio	(gm)	(%) <sup>b</sup>
11751-13	Ethoquad <sup>c</sup>	1.0	2.0	0.51	--	--
11761-16	d	1.0	2.0	0.51	--	--
11751-18-1	d	1.0	1.0	0.26	--	--
11751-18-2	d	1.0	2.0	0.51	--	--
11751-20	d	1.0	3.0	0.76	1.7	97
11751-20A	Ethoquad PAA <sup>e</sup>	1.0	3.0	0.76	1.5	95
11751-24-1	Ethoquad	1.0	8.0	2.0	2.9	97
11751-24-2	EMA 21	1.0	8.0	2.0	2.8	93
11751-25	Ethoquad	1.0	12.0	3.0	3.8	95
11751-27	Ethoquad	10.0	120.0	3.0	38.6	97

<sup>a</sup>Cu-to-mica ratio = (gm CuSO<sub>4</sub>•5H<sub>2</sub>O) • (% copper in CuSO<sub>4</sub>•5H<sub>2</sub>O = 25.5 • (gm mica)<sup>-1</sup><sup>b</sup>Yield = 100 x (yield, gm) [(gm mica) + (gm CuSO<sub>4</sub>•5H<sub>2</sub>O) (% copper in CuSO<sub>4</sub>•5H<sub>2</sub>O)]<sup>-1</sup><sup>c</sup>Pretreatment procedure: disperse mica in 1% aqueous Ethoquad C125 (Armark Chemicals), using 15 ml solution per gm of mica, stir 15 min, filter, and wash with water.<sup>d</sup>Not pretreated.<sup>e</sup>Pretreatment procedure: disperse mica in 1% aqueous Ethoquad C125, add 1.0 gm acrylic acid per gm mica, add 40 mg ammonium persulfate, and heat to 50°C. After poly(acrylic acid) PAA is formed, dilute with 20 ml 2% aqueous NaOH, filter, and wash with water.<sup>f</sup>Pretreatment procedure: disperse mica in aqueous 2% NaOH containing ethylene-maleic anhydride copolymer (EMA 21, Monsanto), warm to 50°C with stirring, cool to room temperature, filter, and wash with water.

UNCLASSIFIED

UNCLASSIFIED

TABLE VI. BULK IR SPECTRAL AND PARTICLE SIZE DATA FOR TAILORED IR ABSORBERS

Sample	Measurement medium	Sample concentration ( $\text{g}/\text{L}$ )	Path- length ( $\text{cm}$ )	$\lambda_{\text{max}}^{\text{a}}$ ( $\mu\text{m}$ )	Extinction coefficient ( $\text{L}/\text{mol}\cdot\text{cm}$ )			Corrected Fisher diameter ( $\mu\text{m}$ )	Density ( $\text{g}/\text{cm}^3$ )
					$\lambda_{\text{max}}$	$\lambda_{\text{max}}$	$\lambda_{\text{max}}$		
Acrylate I tetrastearate	NBR (CHCl <sub>3</sub> )	2.8 21.7	1.4 0.10	3.35 <sup>c</sup> 7.92	b	b	0.10 < 0.01	0.096 0.33	0.071 < 0.01
Acryloyl triethylphosphonate	CHCl <sub>3</sub>	52.9	0.10	3.4 <sup>c</sup> 8.9	0.19	0.19	0.04	0.15	0.041
Acrylate (Solid)	NBR	3.5	1.4	9.4	0.49	0.01	0.48	0.27	3.45
Acrylate (Solid)	KBr	1.0	1.46	b	b	0.14	0.33	0.26	5.0
Acrylate (Solid)	KBr	9.34 <sup>d</sup>	9.89	b	b	0.77	0.85	0.85	1.9-2.1
Acrylate (Solid)	KBr	1.2	2.0	7.19	0.34	0.20	0.19	0.19	—
Acryloyl triethylphosphonate	CHCl <sub>3</sub>	27.1	0.10	11.8 <sup>c</sup> 5.0	0.44	0.01	0.24	3.012	—
Acrylonitrile diisobutane	KBr	1.5	1.23	7.7	0.35	0.12	0.54	0.23	—
Acrylonitrile (Viton Clad)	KBr	—	—	9.0	0.38	—	—	—	—
Acrylonitrile (Viton Clad)	KBr	1.0	1.14	11.7 <sup>c</sup> 9.0	0.44	0.15	0.70	0.28	—
Acrylonitrile diisobutane	NBR	3.26	0.86	b	0.13	0.081	0.071	0.476	4.8
Acrylonitrile (Viton)	NBR	0.32	1.5	9.80	0.41 + 0.06 <sup>e</sup>	< 0.01	0.19	0.057	2.75 <sup>f</sup>
Acrylate (t, propylene) solution (7%)	NBR	0.98	0.89	9.60	0.32 + 0.13 <sup>e</sup>	< 0.01	0.27	0.032	2.75 <sup>f</sup>
Acrylate (Gardasil)	NBR	18.4	0.94	8.3	0.013	< 0.01	< 0.01	30 <sup>h</sup>	2.3
Acrylate (Gardasil)	NBR	1.9	1.1	9.3	0.51	< 0.01	0.21	0.015	2.65
Acrylate (Gardasil)	NBR	1.2	1.4	9.0	0.52	< 0.01	0.25	< 0.01	2.65 <sup>i</sup>

<sup>a</sup>Wavelength at maximum absorption.<sup>b</sup>No apparent absorption maximum.<sup>c</sup>More than one maximum absorption wavelength exists.<sup>d</sup>See experimental details, Section 3.1.2.<sup>e</sup>Average of three determinations.<sup>f</sup>Assumed density.<sup>g</sup>As reported by the manufacturer, method unknown.

UNCLASSIFIED

**UNCLASSIFIED**

C-4

TABLE VII.  
INFRARED SPECTRAL DATA FOR COPPER-COATED SOLID  
POLY(METHYL METHACRYLATE) MICROSPHERES<sup>a</sup>

Sample	Cu-to-Polymer Ratio	Sample concentration (mg/cm <sup>3</sup> )	Pathlength (cm)	Extinction coefficient (m <sup>2</sup> /gm)			
				5.85 μm	8.9 μm	3.5 μm	9.6 μm
11751-7	0	0.94	1.25	0.22	0.14	0.034	0.042
11751-26-1	1.13	3.8	0.934	0.18	0.13	0.13	0.071
11751-26-2	2.24	2.1	1.30	0.12	0.12	0.14	0.12
11751-26-3	4.48	0.99	1.31	0.12	0.12	0.093	0.12
11751-28	∞	2.4	1.33	0.038	0.038	0.025	0.034

<sup>a</sup>All spectral obtained with KBr disc technique.

b Sample numbers refer to samples listed in Table IV.

**UNCLASSIFIED**

691

UNCLASSIFIED

TABLE VIII. INFRARED SPECTRAL DATA FOR COPPER-COATED MICA<sup>a</sup>

Sample No. <sup>b</sup>	Pretreatment <sup>c</sup>	Cu-to-Mica Ratio	Sample concentration (mg/cm <sup>3</sup> )	Pathlength (mm)	Extinction coefficient (m <sup>2</sup> /gm)	10.6 μm
11751-18-1	None	0.26	0.75	1.18	0.036	0.16
11751-18-2	None	0.51	1.8	1.20	0.13	0.20
11751-20	None	0.76	1.3	1.24	0.16	0.23
11751-20A	Ethoquad/PAA	0.76	1.5	1.29	0.13	0.17
11751-24-1	Ethoquad	2.0	3.3	1.46	0.17	0.21
11751-24-2	EMA 21	3.0	1.1	1.31	0.13	0.17
11751-25	Ethoquad	3.0	1.9	1.24	0.21	0.20
11751-27	Ethoquad	3.0	1.1	1.36	0.12	0.14
Mica	--	0	2.1	1.29	0.045	--

<sup>a</sup>Spectra obtained using KBr disc technique.<sup>b</sup>Sample numbers refer to samples listed in Table V.<sup>c</sup>Refer to Section 3.1-4 for details.

UNCLASSIFIED

## UNCLASSIFIED

C-4

TABLE IX. INFRARED SPECTRAL AND PARTICLE SIZE DATA FOR METAL FLAKES AND SPHERES

<u>Sample</u>	<u>Sample Concentration (mg/cm<sup>3</sup>)</u>	<u>Path length (mm)</u>	<u>Extinction coefficient (m<sup>2</sup>/gm) at 10.6 μm</u>	<u>Corrected Fisher diameter (μm)</u>	<u>Density (gm/cm<sup>3</sup>)</u>
Aluminum (1400 U)	0.46	1.25	0.96	0.729	2.71
Aluminum (spheres)	2.11	1.9	0.019	6.50	2.71
Bronze (MD90)	1.2	1.20	0.36	0.580	8.79
Bronze (MD98)	2.03	0.445	0.35	a	8.79
Copper (1400 U)	1.74	1.23	0.25	1.10	8.50
Copper <sup>b</sup> (spheres)	2.4	1.33	0.037	a	8.50

<sup>a</sup>Data not taken.<sup>b</sup>Sample S-11751-28, see Section 3.1.3.

UNCLASSIFIED

693

**UNCLASSIFIED**

TABLE X.  
BULK IR SPECTRAL AND PARTICLE SIZE DATA FOR SEMICONDUCTORS

Sample	Extinction coefficient ( $m^2/g$ )		Fisher diameter ( $\mu m$ )	Density ( $g/cm^3$ )
	3.5 $\mu m$	9.6 $\mu m$		
ZnO (HC-238)	0.99	0.18	0.18	5.47
ZnO (BS-F-1)	0.07	0.16	0.16	5.47
ZnO (HC-016)	0.05	0.955	0.055	5.47
ZnO (SP300)	< 0.01	< 0.01	< 0.01	5.47

**UNCLASSIFIED**

**UNCLASSIFIED**

C-4

TABLE XI. INFRARED AND AEROSOL PROPERTIES OF VARIOUS SMOKES

Sample	Aerosol concentration (mg/m <sup>3</sup> )	Aerosol mass median diameter (μm)	Aerosol extinction coefficient (m <sup>2</sup> /gm)			Bulk extinction coefficient (m <sup>2</sup> /gm)		
			3.5 μm	6 μm	9.6 μm	10.6 μm	3.5 μm	9.6 μm
Glycerine <sup>a</sup>	~ 100	~ 2	0.1	--	0.08	--	--	--
Glycerine + H <sub>2</sub> O <sup>a</sup>	~ 100	~ 2	0.15	--	--	--	--	--
ZnO (HC-23B)	60	1.0	0.17	0.15	0.07	0.07	0.09	0.18
	300	1.0	0.07	0.07	0.09	0.09	--	--
MoS <sub>2</sub>	300	2.1	0.07	0.08	0.13	< 0.01	0.13	0.081
Bronze flakes (ND90)	340	2.3	--	--	--	0.30	--	0.36

<sup>a</sup>These values are approximate; extinction coefficients estimated at 3.8 μm.

**UNCLASSIFIED**

## UNCLASSIFIED

TABLE XII. AEROSOL INFRARED SPECTRAL DATA<sup>a</sup>

Material	Designation	Time after dissemination (min)	Aerosol concentration (mg/m <sup>3</sup> )	Extinction coefficient (m <sup>2</sup> /gm)			
				0.63 μm	1.1 μm	3.0 μm	10.6 μm
Bronze flakes	MD98 <sup>b</sup>	9	2.5 × 10 <sup>3</sup>	c	c	0.35	0.38
		15.8	440	c	c	1.12	1.24
		18	360	c	c	1.24	1.30
Bronze flakes	ND90 <sup>b</sup>	0	595	c	c	0.66	0.69
		5	490	c	c	0.66	0.71
		15	227	c	c	0.82	0.87
Aluminum flakes	1400 L <sup>b</sup>	0	165	2.26	2.55	1.90	1.93
		2.5	160	2.16	2.40	2.15	2.38
		5.0	150	2.05	2.31	2.35	2.63
		10	120	1.99	2.49	2.40	2.63
		15	120	1.52	2.00	2.00	2.63
Copper flakes	1400 L <sup>b</sup>	0	810	0.917	1.69	1.01	1.06
		2.5	750	0.883	1.16	1.06	1.08
		5.0	630	0.877	1.28	c	c
		10	360	1.04	1.80	1.32	1.36
		15	240	1.16	2.65	1.49	1.53
		20	180	1.36	3.47	1.54	1.60
Copper spheres	11751-28	0	100	1.25	1.90	0.73	0.02
		2.5	50	2.26	3.44	0.94	0.04
		5.0	40	2.63	4.05	1.16	0.13
Copper-coated mica	11751-27	1.0	280	0.50	0.72	0.36	0.14
		3.0	120	0.94	1.4	0.63	0.35
		5.0	100	1.00	1.75	c	0.37
		10	60	1.16	2.8	0.73	0.38
PMMA solid microspheres	11751-9	0	710	1.48	1.93	1.28	0.16
		2.0	660	1.43	1.96	1.28	0.16
		3.0	630	1.43	1.99	1.30	0.16
		4.0	470	1.49	2.27	1.44	0.16
		5.0	290	1.62	2.67	1.60	0.16
Copper-coated microspheres (Cu-PMMA = 1.21)	11751-26-1	0	575	1.09	1.28	0.85	0.48
		2.5	520	1.08	1.30	0.85	0.48
		5.0	430	1.14	1.41	0.91	0.48
		10	245	1.40	1.82	1.5	0.74
		15	180	1.43	1.99	1.76	0.93
		20	51	1.64	2.31	c	1.24
Copper-coated microspheres (Cu-PMMA = 1.24)	11751-26-2	0	540	0.50	0.68	0.41	0.20
		2.5	405	0.55	0.78	0.45	0.23
		5.0	325	0.57	0.75	0.46	0.23
		10	190	0.71	1.05	0.53	0.20
Copper-coated microspheres (Cu-PMMA = 4.48)	11751-26-3	0	585	0.63	0.67	0.50	0.31
		2.5	345	0.79	0.89	0.71	0.37
		5.0	230	1.0	1.2	0.85	0.39
		10	130	1.1	1.6	1.1	0.42
		14.5	105	1.1	1.6	c	0.43
Ashley graphite	Micro 250 <sup>b</sup>	0	235	2.6	3.0	2.45	2.6
		5.0	230	2.8	3.0	2.4	2.6
		10	220	2.9	3.1	2.3	2.6

<sup>a</sup>Data obtained at CSL.<sup>b</sup>See Table III.

cNot determined.

**UNCLASSIFIED**

C-4

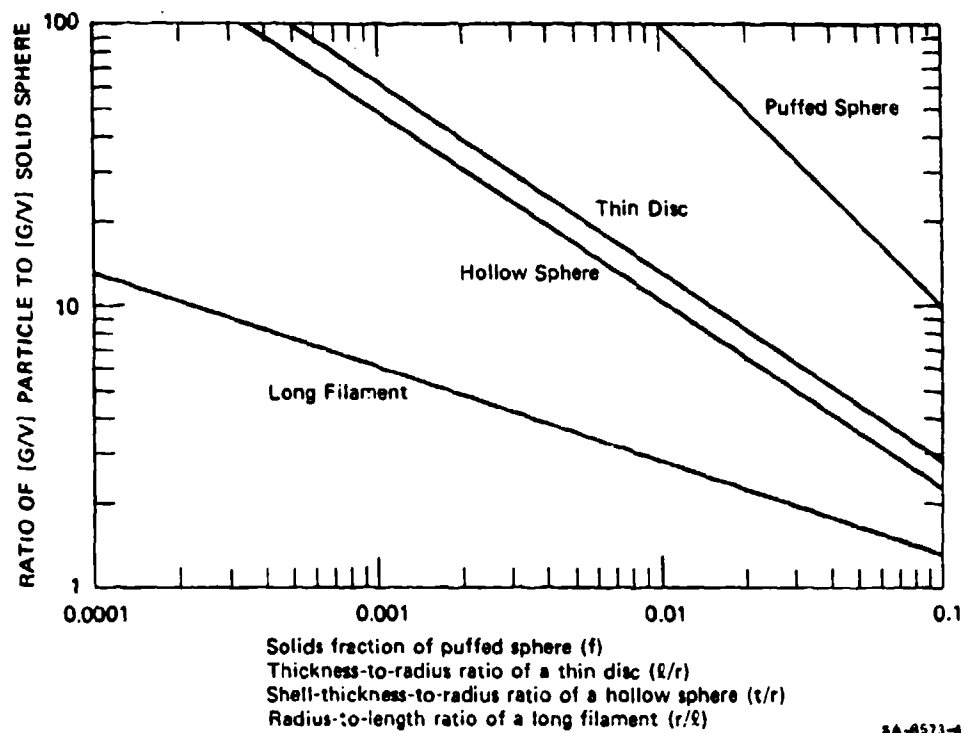


FIGURE 1. RATIO OF AVERAGE GEOMETRIC CROSS SECTION TO MASS FOR VARIOUS PARTICLE SHAPES RELATIVE TO A SOLID SPHERE.

**UNCLASSIFIED**

UNCLASSIFIED

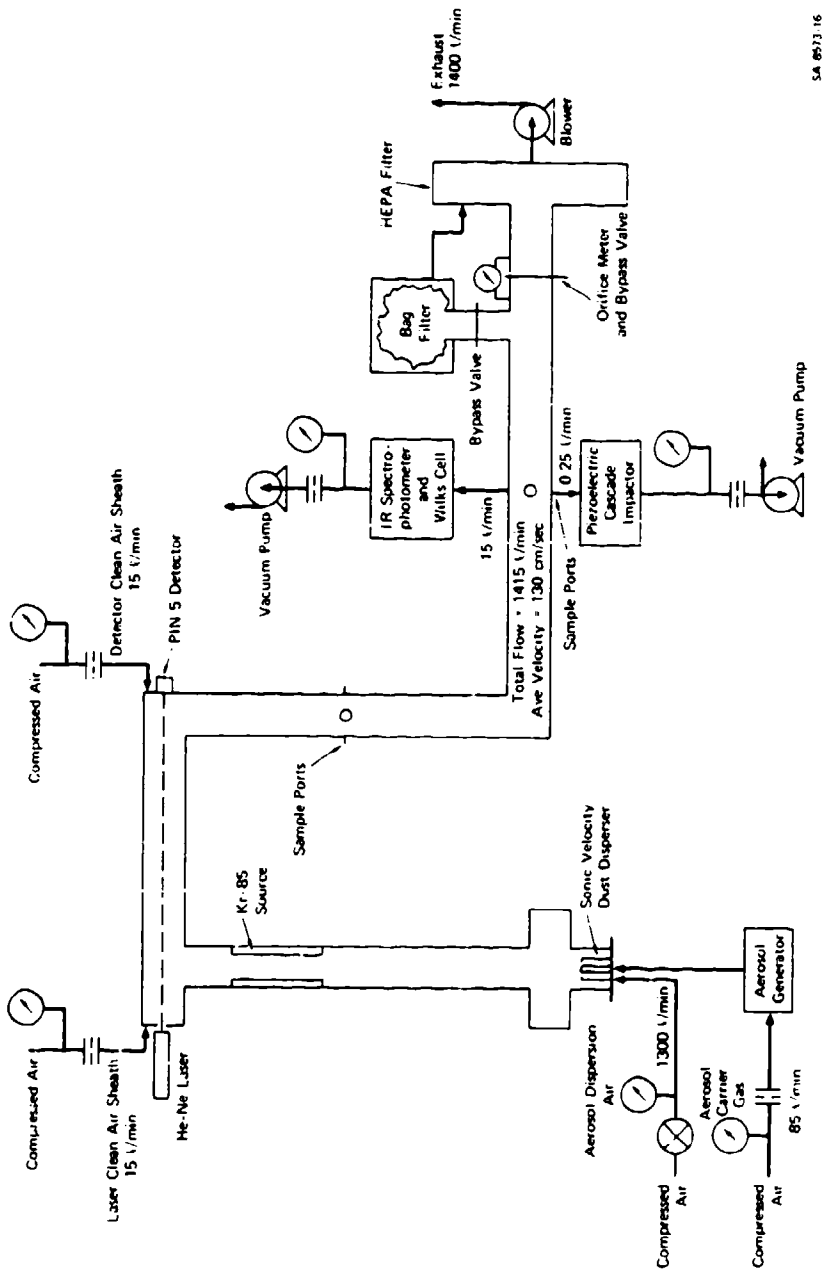
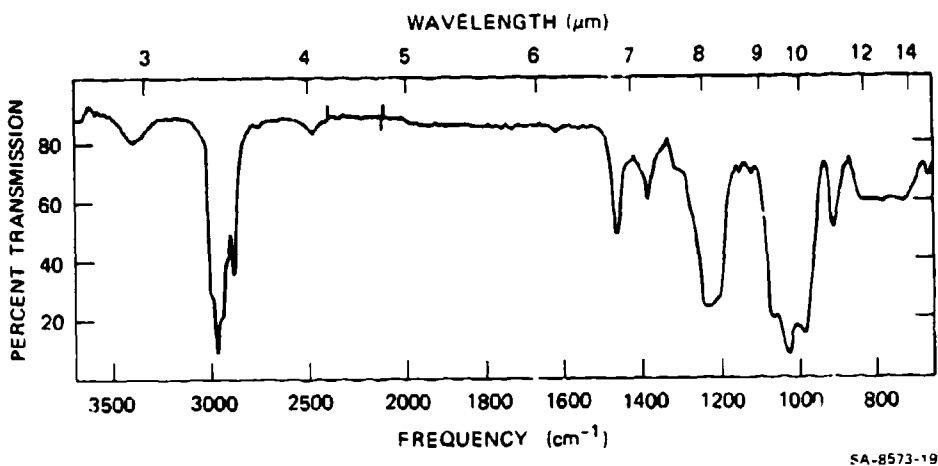


FIGURE 2. SCHEMATIC OF AEROSOL TEST SYSTEM.

UNCLASSIFIED

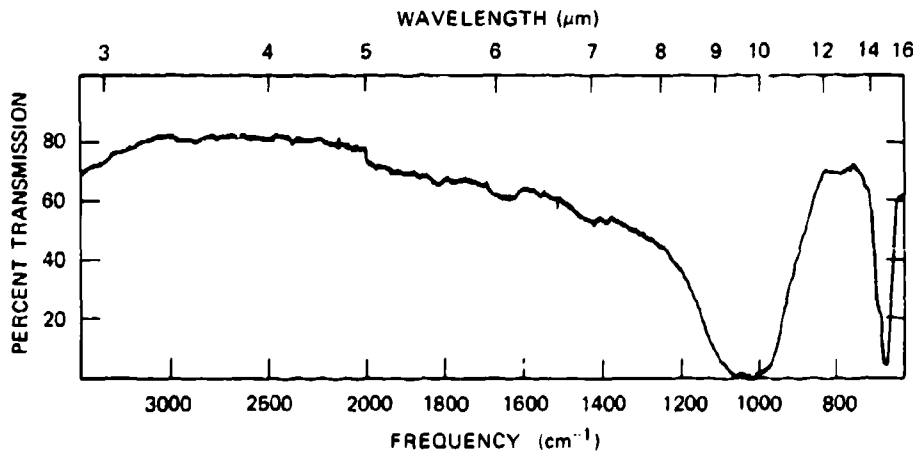
**UNCLASSIFIED**

C-4



SA-8573-19

FIGURE 3. IR SPECTRUM OF DIBUTYL BUTYLPHOSPHONATE ( $52.9 \times 10^3$  gm/m<sup>3</sup>) IN CHCl<sub>3</sub>.  
(Thickness =  $12 \times 10^{-3}$  m).



SA-8573-5

FIGURE 4. IR SPECTRUM OF MISTRONE TALC ( $8.8 \times 10^3$  gm/m<sup>3</sup>) IN KBr DISC.  
(Thickness =  $12 \times 10^{-3}$  m)

**UNCLASSIFIED**

C-4

UNCLASSIFIED

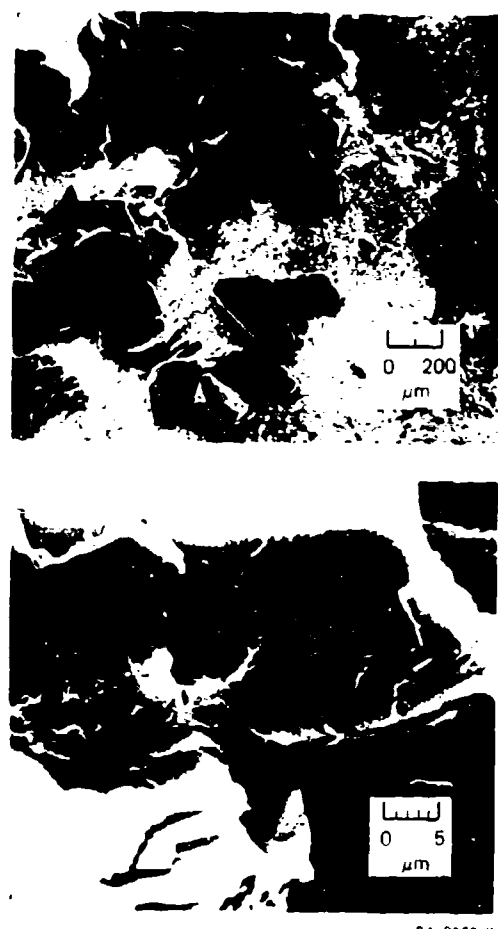
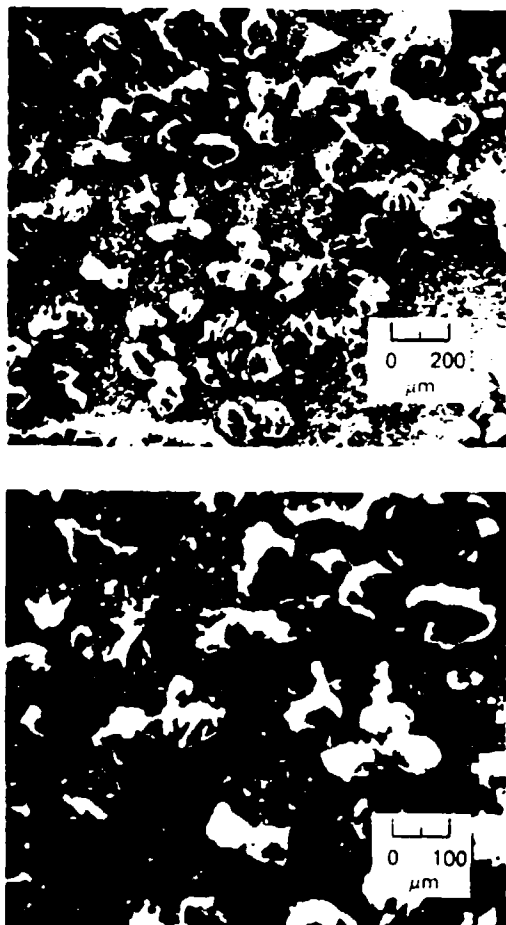


FIGURE 5 SCANNING ELECTRON MICROGRAPHS  
OF INTERCALATED GRAPHITE

UNCLASSIFIED

**UNCLASSIFIED**

C-4



SA-8573-11

**FIGURE 6 SCANNING ELECTRON MICROGRAPHS  
OF EXPANDED GRAPHITE**

**UNCLASSIFIED**

701

# UNCLASSIFIED

C-9

## Pyrotechnic Infrared Screening Mechanisms

Joseph A. Domanico  
Chemical Systems Laboratory, ARRADCOM  
Aberdeen Proving Ground, MD

### ABSTRACT

Of all protective smoke devices, infrared screening munitions are quickly assuming an increasingly important role in military technology. To maintain adequate defenses against hostile infrared imaging weapons and devices, a vast improvement in screening mechanisms is required due to the fact that infrared materials pose special problems in both packaging and current dissemination methods. This paper will present a technical overview of the work effort to devise infrared screening systems of the continuous source type. New dissemination technology and methods will be discussed for dissemination times of approximately 30 seconds to over 5 minutes. Both stationary and projected munition types will be presented.

The four dissemination techniques currently being investigated are 1) the rotating particulate dispenser 2) sublimable matrix types 3) thixotropic blends and 4) associated pyrotechnic formulations.

### 1. INTRODUCTION

There currently exists several development programs under the guidance of The Project Manager for Smoke for the purpose of designing smoke munitions to screen in the non-visible wavelengths. This paper will deal only with the efforts of Chemical Systems Laboratory to provide the smoke community with an infrared screening smoke pot.

Several proposed mechanisms for the design of an infrared smoke pot will be presented and an explanation of the "inner" workings provided.

### 2. GENERAL REQUIREMENTS

In designing mechanisms for an infrared smoke pot, it is best to define some general characteristics of both the physical parameters and the performance of the proposed pot. While these are by no means rigid requirements, they do aid in the comparison of several different types of mechanisms.

For the purpose of the evaluation of the various proposed mechanisms, the following operational characteristics will be used.

#### a. Operational Parameters

1. Produce a dense cloud of smoke within 30 seconds of functioning.
2. Cloud density and size roughly equivalent to current M5 HC smoke pot.
3. Provide both visual and infrared screening capability.
4. Smoke should last about 5 minutes in zero wind.

# UNCLASSIFIED

**UNCLASSIFIED**

5. Be capable of remote electrical ignition.
  
- b. Physical Parameters
  1. Weigh less than 25 kg.
  2. Be stackable or capable of chain ignition.
  3. Be less toxic than current HC smoke mix.
  4. Be waterproof and weatherproof.
  5. Be capable of rapid development.
  6. Be equally or less hazardous than the current HC smoke pot.
  7. Be capable of deployment while wearing standard NBC protective equipment.

**3. SYSTEM DESCRIPTIONS****3.1 PYROTECHNIC MECHANISM**

Of the four potential candidate systems mentioned above, the most desirable would be the simplest to fabricate and load. The production of infrared screening materials by pyrotechnic means would easily be the most direct and therefore the most simple. There exist several candidate materials for dissemination by pyrotechnics but only one will be discussed here, the pyrotechnic production of carbon from polystyrene.

By formulating a burning pyrotechnic mixture which contains polystyrene, it has been shown that a significant increase in the darkening of the smoke cloud results due to the presence of carbon in the smoke. This carbon is in the form of "charred" pieces of powdered polystyrene which are ejected by the pyrotechnic formulation.

As would be the case, this mechanism falls short of meeting the criteria for a viable infrared screening smoke due to the low alpha of the carbon produced and the parasitic effect of the burning pyrotechnic vehicle. However, the amount of visible smoke provided by this mixture is large enough to warrant the continued investigation of this method. If a material is found to possess a higher alpha, and thus require less material to provide an infrared screen, this mechanism may yet prove to be of great value. However, until such a material is found, this candidate must step aside for systems which promise higher returns in a shorter period of time.

**3.2 SUBLIMABLE MATRIX****UNCLASSIFIED**

## UNCLASSIFIED

C-9

Another pyrotechnic method which appears to have merit is the two compartment system. This system is not new to the pyrotechnic community, and in fact, is quite an old method. However, when applied to the practice of the dissemination of infrared screening materials, a new twist is added to complicate matters. The infrared screening material to be disseminated is heat sensitive and does not vaporize easily. Thus, the properties of the material which is to be disseminated are the worst possible. This simple method now becomes challenging to the point of being impossible.

To alleviate this problem somewhat, the infrared screening material is blended with a sublimable material which acts as a heat sink. If properly chosen, the sublimable material may additionally add to the screening effects in either or preferably both the visible and infrared spectrums. This reduces the parasitic properties of the sublimable, which by current design occupies approximately one-half the volume of the matrix.

Further information on the work performed under contract by the Shock Hydrodynamics Corporation for Chemical Systems Laboratory may be found in reference (1).

### 3.3 THIXOTROPIC BLENDS

By using a similar approach to the sublimable matrix system, the powdered infrared screening material may be added to a high vapor pressure liquid containing a thixotropic material. The liquid's effect on the material is to allow a higher packing density (thus making the proposed dissemination system more efficient per unit volume).

Two pyrotechnic systems are then added to the design, a pyrotechnically activated valve to begin dissemination of the screening material, and a pyrotechnic heat source to continue the dissemination at the desired rate. The heat source is necessary due to the cooling effect of the rapidly escaping gases of the carrier liquid.

Currently, a contract is being negotiated with The Energy and Minerals Research Corporation by Chemical Systems Laboratory in an effort to explore the feasibility of this proposed infrared screening mechanism.

### 3.4 THE WHIRLWIND DEVICE

The whirlwind device was the result of early exploratory efforts of Chemical Systems Laboratory to design a screening mechanism which was more efficient than any previously mentioned design.

## UNCLASSIFIED

705

**UNCLASSIFIED**

The device consisted of two compartments, the infrared screening agent chamber, and the pyrotechnic gas source chamber. While the actual workings of the device was a difficult task, the theoretical functioning of the device was simple. The screening agent was compacted into short cylinders with a non-solvent liquid and allowed to thoroughly dry. Several of these cylinders (each had a hole running through the length of it) were placed into the agent compartment of the device. The center hole of the cylinders allowed them to slip over a hollow tube which had a fine male thread on its outer surface. The upper end of this tube went through the top of the compartment where it joined a "t" shaped tube which was curved slightly. This curve was to allow the escaping gases from the pyrotechnic gas source to impart a rotating force to the tube. The lower end of the tube had a cutting blade fixed to it. As the pyrotechnic gas source burned, the escaping gases were vented into the center of the agent chamber causing a low pressure area at the base of the tube where the cutter blade was located. The gases continued up the tube and escaped from the device through the curved "t" tubing. This rotated the cutter blade which scraped some of the infrared screening agent from the block of the material. The scrapings were attracted to the low pressure areas at the center of the device and carried with the escaping gases out the curved "t" tubing. This action continued until both the infrared screening agent and the pyrotechnic were expended.

Yes, it is difficult to believe this device does work, but several tests of this device with actual infrared screening material has shown it to be effective in both the visible and infrared wavelengths.

**4. SUMMARY**

In comparing these mechanisms with each other and in examining their application to the development of an infrared screening smoke pot, careful consideration must be given before a logical choice can be made. Perhaps before any firm requirements can be agreed upon for the performance characteristics of this smoke pot, a retrospective look should be made at the existing visual pot, its design, its functioning, and the doctrine associated with its use. Only then can the application of these mechanisms be evaluated for the design of an infrared smoke pot.

# **UNCLASSIFIED**

C-9

## **REFERENCES**

1. E. A. Lawton, "Substrates for Pyrotechnic Dissemination of Infrared Screening Materials," Final Report, ARCSL-CR-81013, Shock Hydrodynamics Division, Whittaker Corporation, Contract No. DAAK11-80-C-0041 (1981).
2. Ronald O. Pennsyle, "A Parametric Study of Emission Rates Required for IR Screening From a Continuous Source," CSL Tech Note 79-5 (1979).
3. Marion K. Freeman, "Thixogel Technique for IR Obscuration," Energy & Minerals Research Company, Unsolicited Proposal (1980).

**UNCLASSIFIED**

# UNCLASSIFIED

C-10

## FEASIBILITY STUDY OF 2.75 INCH MULTISTAGE CHAFF WARHEAD

W. G. Rouse  
Chemical Systems Laboratory  
Aberdeen Proving Ground, Maryland

### ABSTRACT

#### 1. INTRODUCTION

Helicopters are particularly vulnerable to radar-directed gunfire. Chaff, which is aluminum or aluminized glass fibers, has long been used to defeat radar. A number of chaff delivery and dispensing systems have been developed to disperse the material in the air.

To escape radar detection, helicopter tactics dictate flying nap-of-the earth (NOE), but to acquire and destroy targets with the tube-launched, optically-tracked, wire-guided (TOW) missile or other weapons requires the helicopters to rise above NOE for 30 or more seconds. This approximate period of time is all that is required for enemy radar acquisition and gun direction to destroy the helicopter.

If a number of radar targets having approximately the same radar cross section (RCS), or scope image, were to appear on the scope, each would have to be examined for several seconds before the radar operator chooses one of them for the target, thereby giving the helicopter pilot more time to perform his task and render him less vulnerable to enemy fire. Hence, this is our interest in a decoy chaff warhead. The objective of this investigation, therefore, is to develop the technology required to provide a multistage decoy chaff warhead.

#### 2. DESIGN CONCEPT

The round selected for the decoy chaff investigation was the 2.75 inch warhead with the MK 49 MOD 3 rocket motor.

Previous tests of a fully loaded chaff 2.75 inch warhead at White Sands Missile Range indicated that it had an RCS value several times that of a helicopter. If this payload could be dispersed in several separate increments along the missile flight path, each would provide an RCS approximately

UNCLASSIFIED

709

**UNCLASSIFIED**

equal to that of a UH-1 or AH-1 series helicopter. The design concept and feasibility investigation was directed to this end.

## 3. HARDWARE DESIGN (FIGURE 1)

The chaff cassettes evolved to a cylindrical shape and are made of frangible acrylic material. The warhead base and nose cone are modified components from the M259 smoke warhead. The fuze is a modified WDU4A/A motor burnout fuze from the advanced development of the M259. The delay burster body is likewise a component of the early development of the M259. The beams and bulkheads are made of carbon steel assembled together with rollpins. These burster assemblies do not meet the fielding requirements of MIL-STD-1316, and additional development is required in this area.

Flight stability of the rocket with incremental dispersion of the chaff cassettes was considered to be a major problem. Not only does the center of gravity change, but also aerodynamic streamlining of the smooth cylinder is adversely affected as segments are blown away. In discussions with aerodynamic personnel, it was concluded that the best chance of success was to detonate cassettes in increments from rear to front. The warhead is designed, therefore, to function in this manner. The modified WDU4A/A fuze functions 1 1/2 seconds after launch, 400 meters downrange. This ignites the first burster assembly which functions 0.150 second later, expelling the aft cassette and igniting the delay of the second burster assembly. One and one-half seconds later, the second cassette is expelled and the third burster assembly delay is ignited, and so on. For sequences of five dispersing events, 0.150 second delay elements were used.

In several static tests, the function of one burster igniting the delay of the adjacent burster assembly was successfully demonstrated. In several tests conducted thus far, red or white talc has been used in place of chaff since it is considerably more visible, more available, and much less expensive.

The delay burster assemblies consist of an aluminum body with a pyrotechnic delay to provide a 0.150 and a 1.50 second delay after ignition. When the 1.50 second delay column has burned through, it ignites a MK 37 heat-sensitive detonator or 150 mg of lead azide which in turn detonates 5 1/2 inches of 25 grain/foot primacord. (These burster assemblies do not meet the fielding requirements of MIL-STD-1316 and additional development is required in this area). The primacord is placed inside a rubber tube which acts to suppress the flash, but not the detonating force. Past experience has

**UNCLASSIFIED**

# **UNCLASSIFIED**

C-10

shown that the flash melts and bonds the mylar wrapping surrounding the chaff cylindrical modules, thereby preventing them from dispersing the chaff fibers. The blast fragments the plastic modules and expels the chaff into the airstream.

## **4. TESTS (FIGURES 2, 3)**

All of the rounds fired demonstrated stable flight characteristics. Utilizing 1.5 second sequence spacing, it has been demonstrated that dispersion can take place for a period of three seconds after rocket motor burnout and over a range of 500 meters to 1500 meters from the point of launch. Utilizing .15 second delays, five sequential dispersions have been made starting at a range of about 500 meters and producing a cloud every 75 meters.

## **5. CONCLUSION**

The effort to date has successfully demonstrated that explosive dissemination of sequential partial payloads is feasible during rocket free flight without producing unstable flight. This concept has potential application for producing multiple chaff decoy clouds from a single warhead or providing a means of explosively distributing a payload over a significant portion of a rocket flight.

# **UNCLASSIFIED**

UNCLASSIFIED



FIGURE 11. HARDWARE. Multistage  
recoiled rocket.

UNCLASSIFIED

**UNCLASSIFIED**

3-10



FIGURE 3. - STARS AND STRIPES  
View from Launch Vehicle

**UNCLASSIFIED**

713

C-10

**UNCLASSIFIED**

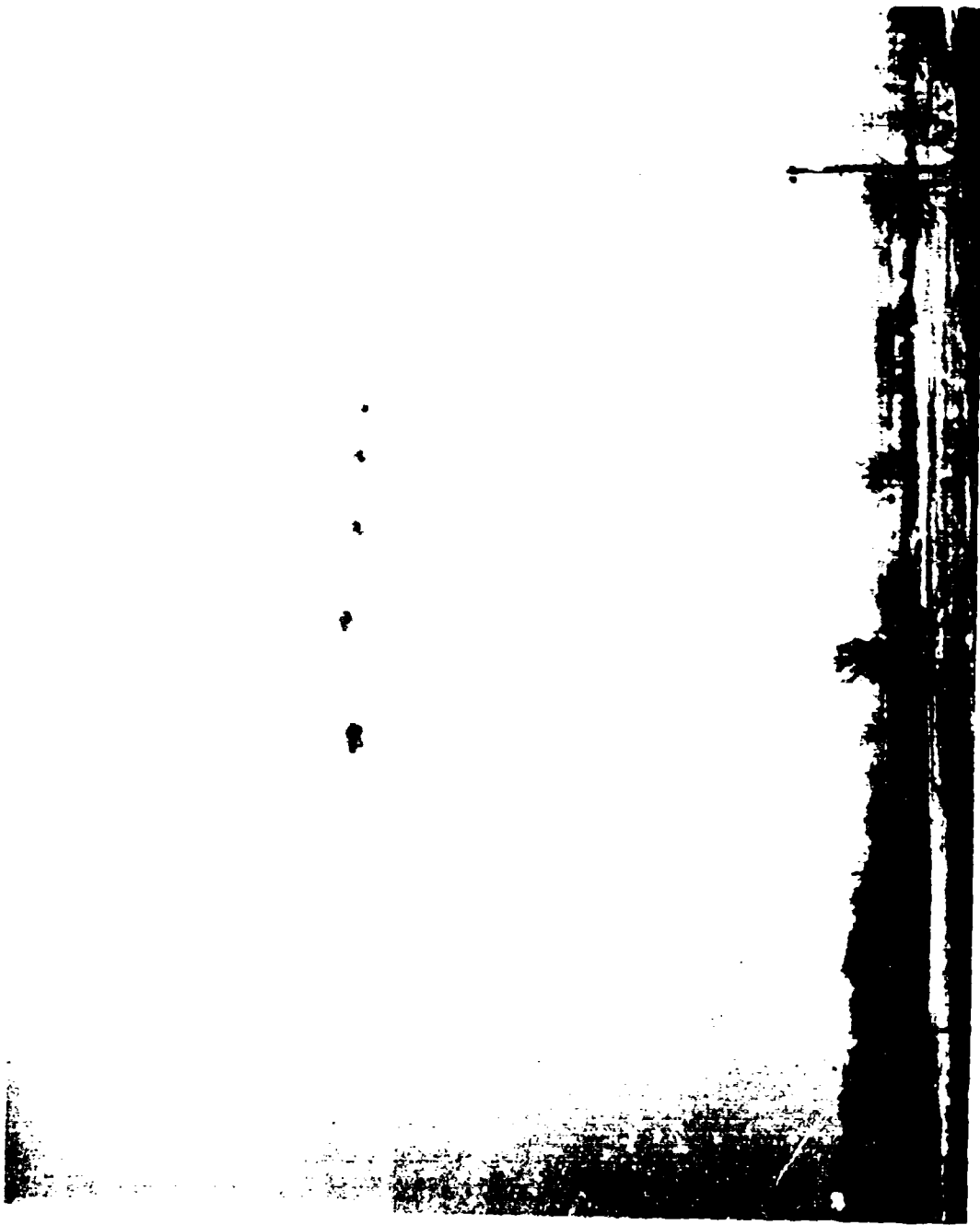


FIGURE 3. CLOUD SEPARATION.  
View across trajectory.

714

**UNCLASSIFIED**

# UNCLASSIFIED

## CLUTTER REJECTION TECHNIQUES FOR LASER SEMI-ACTIVE MISSILE SYSTEMS

HUEY F. ANDERSON  
Advanced Sensors Directorate  
US Army Missile Laboratory  
US Army Missile Command  
Redstone Arsenal, Alabama 35898

ROBERT J. POLGE  
University of Alabama, Huntsville  
Huntsville, Alabama

### ABSTRACT

Laser semi-active missile systems, a class of precision guided weapons, are utilized in terminal homing guidance applications. However, clutter signals due to atmospheric and aerosol backscatter degrade performance in both detection and guidance. This paper presents new clutter rejection techniques which improve system performance. Differences between target and clutter returns are investigated. On this basis two types of discrimination techniques are developed and evaluated. The first technique combines FFT processing, inverse filtering and adaptive detection. In the second technique, the digital filtering is performed in the time domain. The techniques have been applied to realistic data resulting in an improvement greater than 10 dB in signal-to-clutter ratio.

### 1. INTRODUCTION

In military applications, lasers offer advantages in pointing, tracking, bandwidth, immunity to electrical interference, etc. One such application is found by utilizing a well collimated laser beam to designate or illuminate a remote target. Radiation is reflected from the target such that a receiver/seeker intercepting the radiation can determine the guidance signals required to terminally home on the target. This type of system is called laser semi-active (LSA) terminal homing and constitutes one of several laser systems in the class of precision guided weapons.

System performance can be degraded by the transmitted pulse interacting with several elements in a tactical scenario, such as atmosphere, battlefield aerosols and backgrounds. These interactions produce backscatter signals (clutter) that can be detected as real targets or interfere with the detection of the real target signal. It is desired to reject or reduce the clutter signals to improve system performance. This paper addresses the phosphorus aerosol backscatter clutter problem.

# UNCLASSIFIED

**UNCLASSIFIED**

Common techniques used in the detection and discrimination process are based on peak power and relative time separation of target and clutter returns. Problems using these techniques can occur in realistic battlefield scenarios.

There are several other parameters that might be used in discriminating between target and clutter returns. Processing these parameters involve single pulses or a sequence of pulses. Possible factors in using single pulse processing are doppler effects, polarization effects, and pulse structure. When a coherent laser pulse is radiated to and reflected from a target, the radial velocity of the target can be determined by finding the frequency change in the return signal. This change in frequency is called doppler shift. The information contained in the doppler shift can be easily used to separate stationary clutter returns from moving targets. When aerosols are introduced between laser and target, doppler shifts associated with the overall cloud movement and the individual particle movement will also be present. The measurement and resolution of the particle doppler shift is beyond the state-of-the-art in instrumentation. Since aerosol cloud velocities are of the same order as expected vehicle velocities, separation of the two sources would be most difficult. This, coupled with a requirement for coherent sources and heterodyne receivers, makes this technique seem less promising.

It has been shown [1] that certain aerosols modify incident laser pulse polarization differently than do solid, manmade targets. The work primarily involves atmospheric cloud and linear polarization. Results show that linearly polarized laser radiation incident to thin atmospheric clouds produce scattered radiation that is linearly polarized the same as the incident wave. The radiation reflected from rough surfaces is nearly depolarized. In principle, the polarization component of the return signal orthogonal to that of the transmitted signal represents the target. All other components, due to cloud scattering and target, are rejected or eliminated by the receiver/analyizer. This technique has serious problems when dense aerosols are encountered since multiple scattering tends to depolarize the incident signal. Then, for battlefield aerosols, polarization detection and discrimination does not appear to provide the improvement desired.

Significant differences have been shown [2] to exist in the time structure of laser pulses returned from aerosols and targets. Included in these differences are pulse width, pulse rise and fall times, pulse modulation, and pulse amplitude. Spatial characteristics of battlefield aerosols are such that signal returns due to narrow input pulse widths are stretched in time. This is brought about by single and multiple scattering as the narrow pulse propagates through the aerosol. Since the

**UNCLASSIFIED**

# UNCLASSIFIED

C-11

transmitted pulse is not stretched in the forward direction, the target reflected signal is still a narrow pulse. Typical pulse shapes are shown in Figures 1 and 2 for aerosol and target returns. Pulse widths measured in SMOKE WEEK I and II showed that those due to aerosols were an order of magnitude larger than target returns. Further verification of these widths have been made after this experiment and circuitry were implemented to take advantage of these expected differences.

In many instances, the aerosol return is amplitude modulated with complex structure making pulse width discrimination ineffective. The nature of the modulation structure is determined by the non-uniformity of concentration along the propagation path. In addition, the target return may be superimposed on the aerosol return rendering pulse width discrimination of little use. It is now proposed that the entire pulse structure be utilized to improve discrimination and target detection. This concept is investigated and signal processing algorithms are developed.

## 2. SIGNAL PROCESSOR

Two signal processing techniques corresponding to the block diagram in Figures 3 and 4 have been developed and are incorporated as options in a computer program called "Processor." Mechanics of this program are found in [2]. The input signal includes target or clutter pulses generated by a Monte Carlo simulation. The processor shown in Figure 3 operates in the frequency domain and includes options for power spectral analysis and normalization. Signal-to-clutter improvement is investigated for inverse filtering with an optional receiver transfer function. The detection process is studied utilizing an adaptive technique based on frequency content.

The processor shown in Figure 4 operates in the time domain using digital recursive and non-recursive filters. Then the filtered pulse is transformed to the frequency domain by FFT processing for evaluation and in preparation for adaptive detection. As before, receiver transfer functions and normalization are optional.

## 3. INVERSE FILTERING

If characteristics of the clutter signal are known, inverse filtering can be used to eliminate or reduce the clutter signal. It is difficult to predict the clutter pulse structure in the time domain; however, it has been shown in [2] that clutter in the frequency domain is well behaved.

# UNCLASSIFIED

717

**UNCLASSIFIED**

and shows consistent trends from pulse to pulse. This result points strongly to inverse filtering for separating target and clutter signals. Three inverse filters were considered.

The frequency response of the ideal inverse filter  $G(\omega)$  is given by

$$G(\omega) = \frac{1}{S(\omega)}$$

where  $S(\omega)$ , in this case, represents clutter in the transform domain. This means that the impulse response of the clutter must be known *a priori*. Problems in applying this arises when the clutter signal reduces to zero. Then, the filter cannot be implemented. Remedies for this have been sought by placing certain restraints on the nature of the input signal. When the clutter signal power is assumed to be additive and the target signal power constant, it has been shown [3] that the optimum inverse filter is described by

$$G(\omega)^2 = K_1 \frac{\|E(\omega)\|^2}{\|L(\omega)\|^2}$$

where  $\|E(\omega)\|^2$  is the clutter power spectrum,  $\|L(\omega)\|^2$  is the target power spectrum and  $K_1$  a proportionality constant. This filter was implemented yielding very poor results. The primary problem with this method is the large variation encountered in target signal power.

Another optimum linear shift-invariant filter has been designed to restore a degraded signal with the least mean-square-error. It has been shown [4] that for statistically uncorrelated signal and clutter, the optimum filter frequency response is given by

$$G(\omega) = \frac{H^*(\omega) L(\omega) L^*(\omega)}{\|H(\omega)\|^2 L(\omega) L^*(\omega) + E(\omega) E^*(\omega)}$$

where  $H(\omega)$  is the receiver transfer function and \* denotes complex conjugate. Since phase information has not been retained in previous detection and processing, the above inverse filter transfer function reduces to

$$G(\omega) = \frac{\|H(\omega)\|}{\|E(\omega)\|^2 + \frac{1}{\|L(\omega)\|^2}}$$

This formula has been implemented into the filter section shown in Figure 3 and the Processor program described in [2].

**UNCLASSIFIED**

# UNCLASSIFIED

C-11

Since some degree of statistical correlation exists between target and clutter signals the filter cannot be considered optimum. However, significant improvement in signal-to-clutter ratios will result.

The clutter power spectrum shown in Figure 5 has been found to be typical and is used to compute the inverse filter transfer function shown in Figure 6.

## Signal-to-Clutter Improvement

The power spectrum has been selected for evaluating target signal-to-clutter improvement. This is first accomplished by comparing the total power in each signal. Until now, the signals being treated have represented optical intensity or optical power density (irradiance). After detection, the signals are actually electrical and should be considered as such in further processing. However, since discrimination and detection decisions are based on relative comparisons, neither units nor scales are important. Therefore, all tabulated power spectra values have been multiplied by  $10^{14}$  for convenience.

Execution of the inverse filter with a typical target signal and receiver transfer function yields the spectrum shown in Figure 7. A typical clutter signal pulse (C49 in ref [2]) was processed through the inverse filter resulting in the power spectrum shown in Figure 8. The receiver transfer function was also included in the computation.

To determine signal-to-clutter improvement attained by the inverse filtering process, a baseline of signal-to-clutter ratios before filtering was developed. The Processor program was used to compute the total power within the spectrum for several cases with the results given in Table 1. All computations were run with and without the receiver transfer function. This, in effect, shows the difference between using unlimited bandwidth and the relatively narrow bandwidth determined for the receiver. Then, signal-to-clutter ratios are determined and presented in Table 2. Notice that there are some cases where extra bandwidth does not provide an advantage. The improvement shown was determined by simply taking the ratio of the results of "without" to "with filter." In all cases, the inverse filtering significantly improved signal-to-clutter ratios. Maximum improvements of 5.6 dB and 8.3 dB were attained with and without the receiver transfer function, respectively. Further improvement in performance will be attained by combining this inverse filter with the adaptive detection technique discussed in Section 5.

## 4. DIGITAL FILTERING

Digital techniques are useful in studying linear systems in both time and frequency domains.

# UNCLASSIFIED

719

**UNCLASSIFIED**

The initial filtering is performed in the time domain, but processing and evaluating resultant outputs are performed in the frequency domain as indicated in Figure 4.

The first digital filter studied here is adapted from [4]. It is a recursive filter with two feedback loops and a single delay element as shown in Figure 9. The transfer function is given by

$$G(z) = \frac{1 - z^{-1}}{1 - kz^{-1}}$$

where  $z^{-1}$  is the unit delay operator. This corresponds to the difference equation

$$y(nT) = x(nT) - x(nT - T) + ky(nT - T),$$

which has been implemented in the Processor program with a sampling interval equal to 1.4 nanoseconds. The feedback parameter  $k=.8$  was selected based on an optimization analysis which includes digital filtering and adaptive detection. Sample target and clutter power spectral returns are shown in Figure 10 and Figure 11 after being modified by the double loop single delay (DLSD) filter. Notice that low frequency power spectra are attenuated and high frequencies are emphasized.

Signal power after processing with the DLSD filter is given in Table 3 for a typical target return and for several clutter returns. The values before filtering are also included. Values from these tables were used to determine signal-to-clutter ratios and improvement factors with and without a receiver transfer function and presented in Table 4. Note that the improvement can reach 10 dB. Values in the table also show that by extending receiver bandwidth ( $\| H(\omega) \| = 1$ ) further improvement is attained.

## 5. ADAPTIVE DETECTION

Significant improvement in signal-to-noise ratio has been attained using an inverse or a DLSD filter. Yet this is not sufficient and a simple threshold detection will produce too many errors. Therefore, an adaptive detection technique, operating in the frequency domain, was developed to use in combination with filtering as shown in Figure 8-10. The discrimination between target and clutter is made on the basis of relative power distribution between low and high frequencies. Let  $f_c$  be the

**UNCLASSIFIED**

**UNCLASSIFIED**

C-11

C-11

cutoff frequency dividing the spectrum bandwidth into low and high frequencies. Then the ratio of low frequency to high frequency power is significantly greater for clutter than for target pulses. This ratio varies randomly from pulse to pulse. However, if  $f_c$  is selected properly, based on typical pulses, the ratio will be almost always greater than one for clutter alone and less than one for target alone or target plus clutter.

An acceptable discrimination technique should nearly always produce target decisions when only target signals are input. It should also reject clutter when only clutter is present. When both are present, target decisions should nearly always be produced. The decision and cutoff frequency are determined by iterative executions of the Adaptive Detection subroutine of the Processor program. Performance of the adaptive detector was evaluated without and with the prefiltering.

**Detection Without Prefiltering**

The analysis was performed twice for the same sample set of pulses; first the receiver transfer function is included, then it is neglected in the analysis. In both cases several cutoff frequencies were tried.

Results of this analysis with receiver transfer function are given in Table . . . columns titled "Threshold" contain values that result from the low frequency integration : spectrum for a particular pulse. The columns with title "Signal" contain values that represent . . . high frequency portion of the power spectrum. For target signals, the high frequency values under "Signal" must be larger than the lower frequency values under "Threshold" for the correct decision to be made. However, if the input is a clutter pulse, the correct decision is made when pulses under "Threshold" columns are larger than values under "Signal" columns. The box around the power value indicates that the detection process works satisfactorily for the selected input pulse and cutoff frequency. Thus, the table shows that the adaptive detection process works well for target alone and clutter alone.

The same type of analysis is performed on target plus clutter pulses with the results given in the bottom portion of the clutter row. The values in the columns indicate that the target is not detected. Therefore, overall results show that the adaptive technique does not work well for the conditions stated (i.e., without filtering and with receiver transfer function). Even in the case of

**UNCLASSIFIED**

721

**UNCLASSIFIED**

target alone, detection does not occur if the cutoff frequency is increased to 3.5 mhz. This is because a large portion of the high frequencies is being attenuated by the receiver transfer function. Reduced bandwidth affects the target signals more than the clutter signals.

Results of the same analysis but without the receiver transfer function are shown in Table 6. Note that the decision process again works well for target and clutter signal taken separately. But, it also works very well with target and clutter signals in combination. Thus, the larger bandwidth has improved the detection performance. The only condition that did not provide the correct decision was target with clutter pulse C50. This is because clutter pulse C50 has significantly more total power than does the target pulse. Excess target signal using the adaptive detection technique is shown in the last column. This is determined by finding the amount,  $x$ , that the target signal can be reduced and still produce the correct decision. The limit case is given by

$$xT_a + C_a = xT_b + C_b$$

where  $T_a$  and  $T_b$  represent the target power above and below  $f_c$ . Similarly, the clutter power is divided into  $C_a$  and  $C_b$ . Given  $T_a$ ,  $T_b$ ,  $C_a$ , and  $C_b$ ,  $x$  is easily computed. Alternately one can say that the target strength could be reduced by  $(1-x)100$  in percent.

**Detection with Prefiltering**

In this section, the adaptive detection technique is combined either with inverse filtering or with loop delay filtering. In both cases, the simulation includes the receiver transfer function. Results for the combination of inverse filtering and adaptive detection are shown in Table 7 for two frequency cutoffs. For a cutoff frequency of 3.5 mhz all decisions are shown to be correct as indicated by the boxes around the power values. The last column indicates that correct decisions could be made even if the target signals were reduced from 40% to 96%. Thus, outcomes using inverse filtering provide true decisions for all sample cases treated and would also be correct with significant reductions in target signal levels. Of course, if the receiver bandwidth were increased, the performance would be even better.

Before evaluating the combination of DLSD filter and adaptive threshold detection, the best value for the feedback factor  $k$  must be determined. This was accomplished by selecting values for  $k$

## **UNCLASSIFIED**

between .5 and .98 and then performing the decision process for several target and clutter pulses. An example of the results are shown in Table 8 for one clutter pulse. The boxed in values show that  $k=.8$  is optimum for the selected set of clutter and target pulses.

Target and clutter pulses were processed after DLSD filtering yielding results shown in Table 9. Note that all decisions are correct for target and clutter signals alone as indicated by the boxed in power values. This combination also produces good results for target plus clutter except for the clutter pulse C50. The last column of Table 9 indicates that the target signal power can be reduced significantly and still provide the correct decision. Near equal performance is attained for both cut-off frequencies used. It is expected that by increasing the receiver bandwidth, target signal would be increased sufficiently over clutter signal to improve the detection process. The results given represent significant improvement over the results without prefiltering given in Table 5.

### **6. CONCLUSIONS**

The signal-to-clutter ratio can be improved using an inverse filter or a loop delay filter. In fact, inverse filtering alone produces a significant improvement in detection. An adaptive detection processing technique was also analyzed. Because of the bandwidth limiting effects of the receiver, the adaptive technique must be used in combination with inverse filtering. Using this combination, no detection errors occurred for all pulses considered.

### **REFERENCES**

1. Manz, J. E., "A Radar Cloud/Target Polarization Discrimination Technique," AFWL-TR-70-76, October 1970.
2. Anderson, Huey, "Target/Clutter Discrimination Techniques for Laser Semi-Active Missile Systems," US Army Missile Command Technical Report, RE-81-16, April 1981.
3. Cramer, Bruce, "Optimum Linear Filtering of Analog Signals in Noisy Channels," IEEE Transactions on Audio and Electroacoustics, Vol AV-14, No. 1, March 1966.
4. Urkowitz, Harry, "Analysis and Synthesis of Delay Line Periodic Filters," IRE Transactions on Circuit Theory, June 1957.

## **UNCLASSIFIED**

**UNCLASSIFIED**

Table 1. Total Power Signals With and Without Inverse Filtering

Case/Power	Inverse Filter		No Filter	
	W/Xfer	W/O Xfer	W/Xfer	W/O Xfer
T49	.407	1.03	1.34	3.52
C49	.094	.153	1.35	1.53
C50	.476	.71	6.7	6.8
C51	.14	.197	2.13	4.51
C52	.248	.402	2.62	5.69
C53	.040	.068	.575	1.25
C54	.204	.281	1.67	3.59

Table 2. Signal-to-Clutter Analysis Using Inverse Filtering

Clutter	NO FILTER		INVERSE FILTER		IMPROVEMENT	
	S/C Ratio W/Xfer	S/C Ratio W/o Xfer	S/C Ratio W/Xfer	S/C Ratio W/o Xfer	W/Xfer	W/o Xfer
C49	1.13	2.3	4.34	6.7	3.84	2.91
C50	.26	.52	.855	1.45	3.29	2.79
C51	.81	.78	2.91	5.23	3.59	6.71
C52	.66	.62	1.64	2.56	2.48	4.13
C53	3.02	2.8	10.3	15.2	3.41	5.43
C54	1.03	.98	2.0	3.67	1.94	3.74

**UNCLASSIFIED**

**UNCLASSIFIED**

Table 3. Total Power Signals with and without Double Loop Single Delay Filter

Case	DLSD Filter		No Filter	
	W/Xfer	W/o Xfer	W/Xfer	W/o Xfer
T49	.76	3.16	1.34	3.52
C49	.13	.34	1.35	1.53
C50	.83	1.4	6.7	6.8
C51	.23	.42	2.13	4.51
C52	.38	.73	2.62	5.69
C53	.05	.15	.575	1.25
C54	.28	.44	1.67	3.59

Table 4. Signal-to-Clutter Analysis Using Double Loop Single Delay Filter, K=.8

Clutter	No Filter		DLSD Filter		Improvement	
	S/C Ratio W/Xfer	S/C Ratio W/o Xfer	S/C Ratio W/Xfer	S/C Ratio W/o Xfer	S/C Ratio W/Xfer	S/C Ratio W/o Xfer
C49	1.13	2.3	5.9	9.4	5.18	4.09
C50	.26	.52	.92	2.3	3.54	4.42
C51	.81	.78	3.3	7.5	4.07	9.62
C52	.66	.62	2.0	4.4	3.03	7.10
C53	3.02	2.8	15.2	21.5	5.03	7.68
C54	1.03	.98	2.7	7.3	2.62	7.45

**UNCLASSIFIED**

**UNCLASSIFIED**

Table 5. Adaptive Detection Analysis With Receiver But Without Filters

Source/Freq Cutoff	Threshold		Signal	
	Frequency (mhz)	3.0 3.5	Frequency (mhz)	3.0 3.5
Target		.626 .725	.714	.612
C49		[1.29]	[1.30]	.065 .054
T&C1		1.92	2.03	.78 .67
C50		[5.65]	[5.70]	.408 .316
T&C1		6.28	6.43	1.12 .928
C51		[2.04]	[2.05]	.097 .085
T&C		2.67	2.78	.811 .697
C52		2.36	[2.41]	.276 .215
T&C1		2.99	3.14	.990 .827
C53		[.539]	[.546]	.035 .028
T&C1		1.17	1.27	.749 .64
C54		1.40	1.50	.289 .193
T&C1		2.03	2.23	1.00 .805

Table 6. Adaptive Detection Analysis Without Receiver or Filter

Source/Freq Cutoff	Threshold		Signal		$x/(1-x)100$	
	Frequency (mhz)	3.0 3.5	Frequency (mhz)	3.0 3.5	3.0	3.5
Target		.668 .793	[2.88]	[2.75]		
C49		[1.34]	[1.36]	.196	.182	
		2.01	2.15	[3.08]	[2.93]	.52/48 .60/40
C50		[5.91]	[5.98]	.960	.849	
T&C1		6.58	6.77	3.84	3.60	None None
C51		[2.11]	[2.13]	.268	.254	
T&C		2.78	2.92	[3.15]	[3.00]	.83/17 .96/4
C52		[2.46]	[2.52]	.622	.547	
T&C1		3.13	3.31	[3.50]	3.30	.83/17 None
C53		[.555]	[.564]	.121	.112	
T&C1		1.22	1.36	[3.00]	[2.86]	.20/80 .23/77
C54		[1.46]	[1.58]	.468	.351	
T&C1		2.13	2.37	[3.35]	[3.10]	.45/55 .63/37

**UNCLASSIFIED**

**UNCLASSIFIED**

C-11

Table 7. Adaptive Detection Analysis With Receiver and Inverse Filter

Source/Freq Cutoff	Threshold		Signal		$x/(1-x)100$	
	Frequency (mhz)	3.0	Frequency (mhz)	3.0	3.5	3.0
Target	.049	.094	.363	.3		
C49	.061	.066	.033	.029		
T&C1	.110	.160	.396	.352	.16/84	.16/84
C50	.300	.323	.186	.156		
T&C1	.349	.417	.549	.479	.60/40	.60/40
C51	.094	.098	.047	.043		
T&C	.143	.192	.410	.366	.24/76	.24/76
C52	.121	.143	.131	.109		
T&C1	.170	.237	.494	.432	.15/85	.15/85
C53	.021	.025	.019	.016		
T&C1	.070	.119	.382	.339	.04/96	.04/96
C54	.077	.120	.132	.095		
T&C1	.126	.214	.495	.418	.11/89	.11/89

Table 8. Loop Delay Filter Feedback Factor k Determination  
(With Receiver Transfer Function)

Source	THRESHOLD					
	k=.98		k=.95		k=.8	
	3.0	3.5	3.0	3.5	3.0	3.5
Target	.402	.532	.366	.509	.153	.243
C49	.689	.692	.367	.368	.064	.066
T&C1	1.09	1.22	.73	.88	.22	.31
SIGNAL						
Target	.756	.627	.770	.633	.604	.523
C49	.054	.052	.059	.059	.063	.062
T&C1	.806	.68	.83	.69	.67	.59

**UNCLASSIFIED**

**UNCLASSIFIED**

**Table 9. Adaptive Detection Analysis After Loop Delay Filtering  
(With Receiver Transfer Function, k=.8)**

Source/Freq Cutoff	Threshold		Signal		$x/(1-x)100$	
	Frequency (mhz)		Frequency (mhz)			
	G=2.2 3.0	G=1.4 3.5	G=1 3.0	G=1 3.5	3.0	3.5
Target	.34	.342	.604	.523		
C49	.14	.092	.063	.062		
T&C1	.48	.434	.67	.59	.18/82	.17/83
C50	1.2	.797	.293	.244		
T&C1	1.5	1.32	.897	.767	None	None
C51	.33	.321	.083	.071		
T&C	.66	.561	.687	.594	.94/6	.83/17
C52	.41	.302	.202	.167		
T&C1	.75	.643	.806	.690	.79/21	.75/25
C53	.04	.031	.035	.030		
T&C1	.37	.373	.639	.553	.02/98	.01/99
C54	.2	.192	.19	.146		
T&C1	.53	.532	.794	.669	.04/96	.25/75

**UNCLASSIFIED**

**UNCLASSIFIED**

C-1

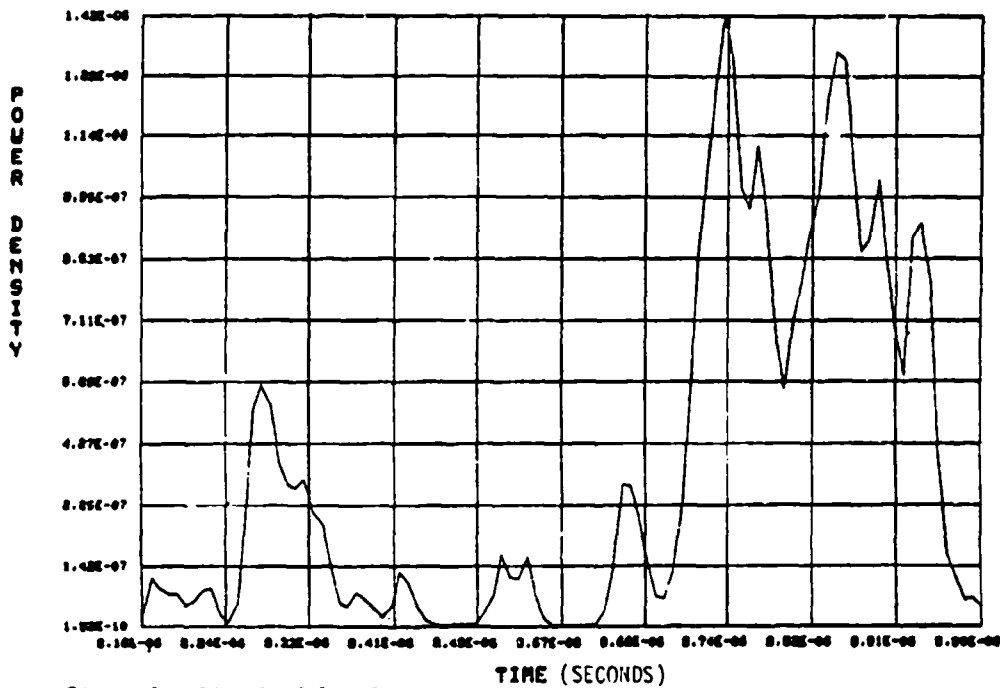


Figure 1. Time Profile of Clutter Pulse C49

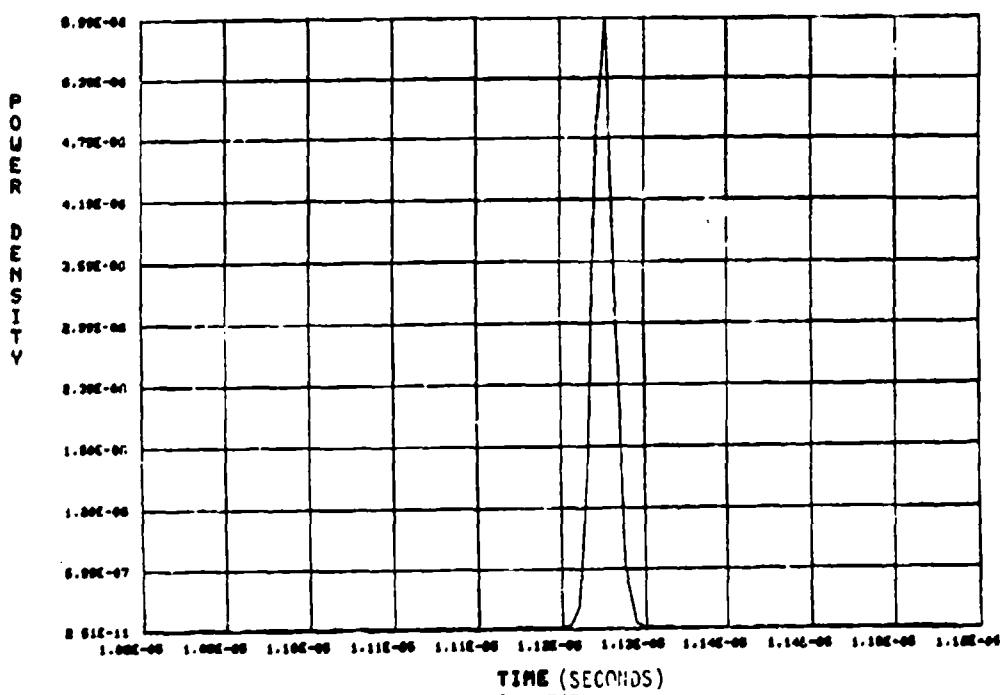


Figure 2. Time Profile of Target Pulse T47

**UNCLASSIFIED**

**UNCLASSIFIED**

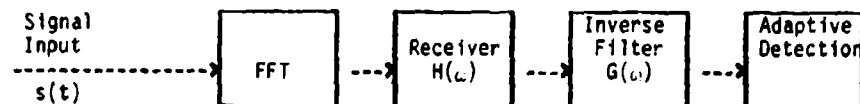


Figure 3. Processor for Frequency Domain Analysis

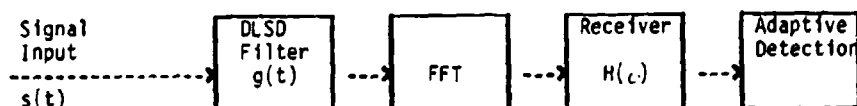


Figure 4. Digital Filter Processor

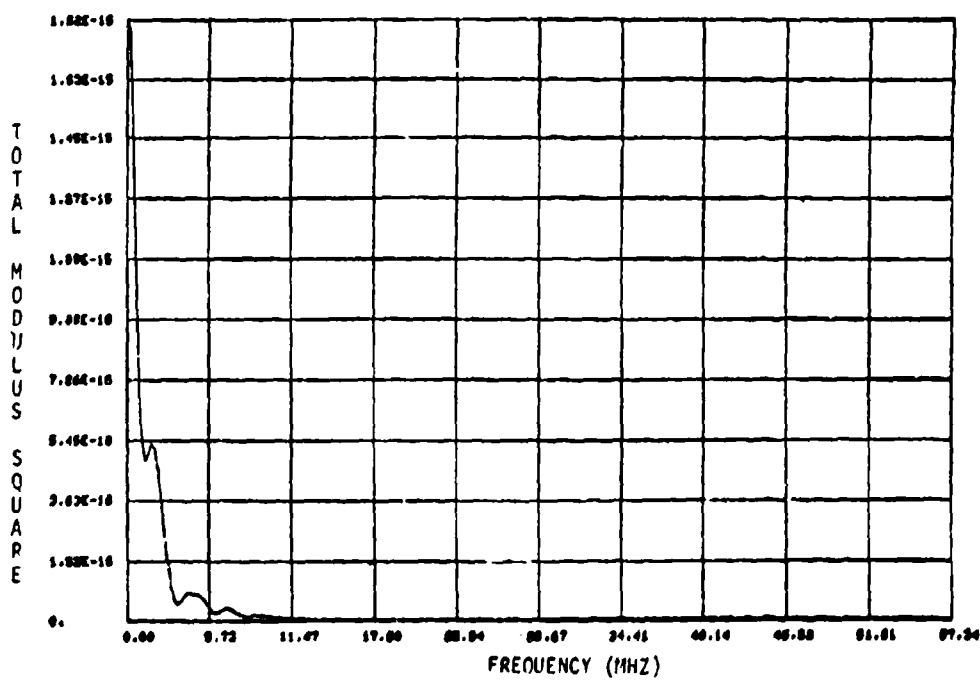


Figure 5. Average Clutter Signal Power Spectrum

**UNCLASSIFIED**

**UNCLASSIFIED**

C-11

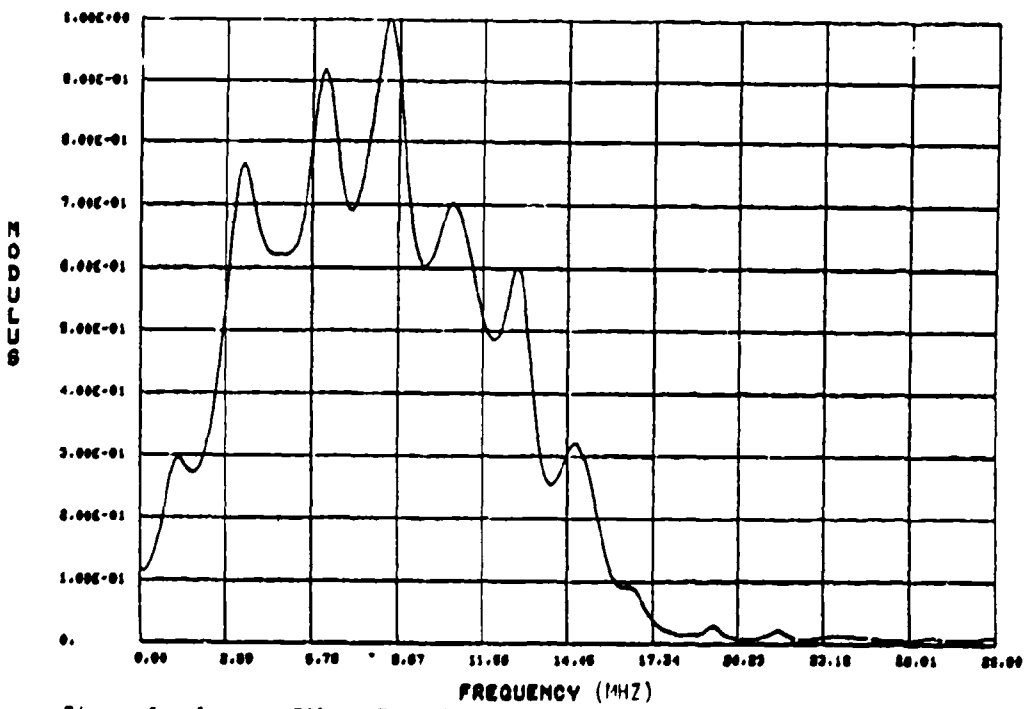


Figure 6. Inverse Filter Transfer Function

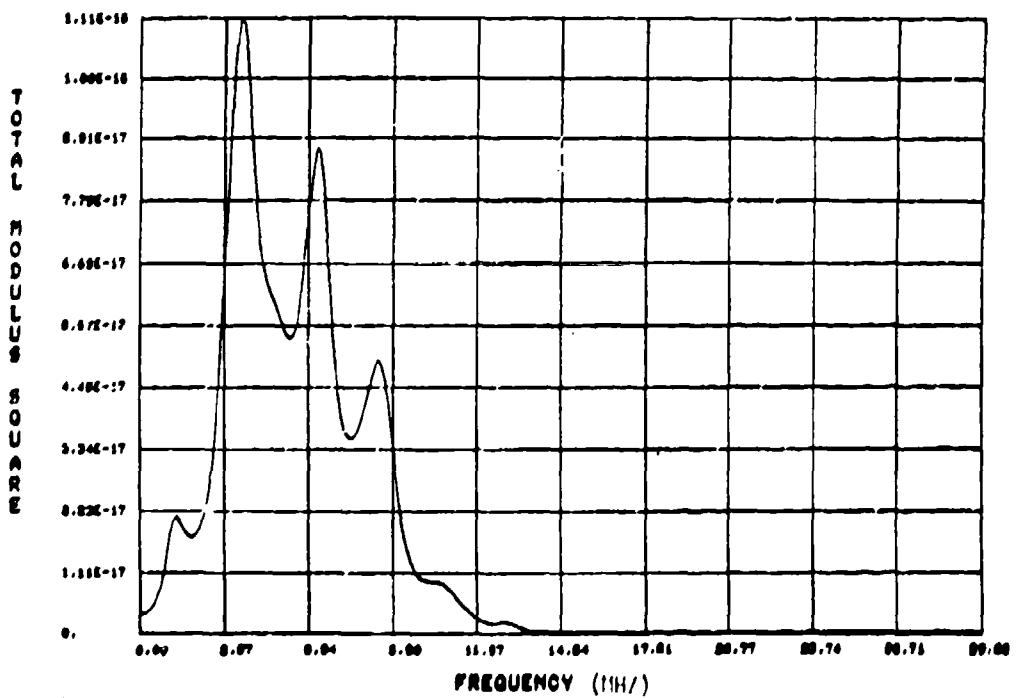


Figure 7. Target Power Spectrum With Receiver and Inverse Filter

**UNCLASSIFIED**

731

UNCLASSIFIED

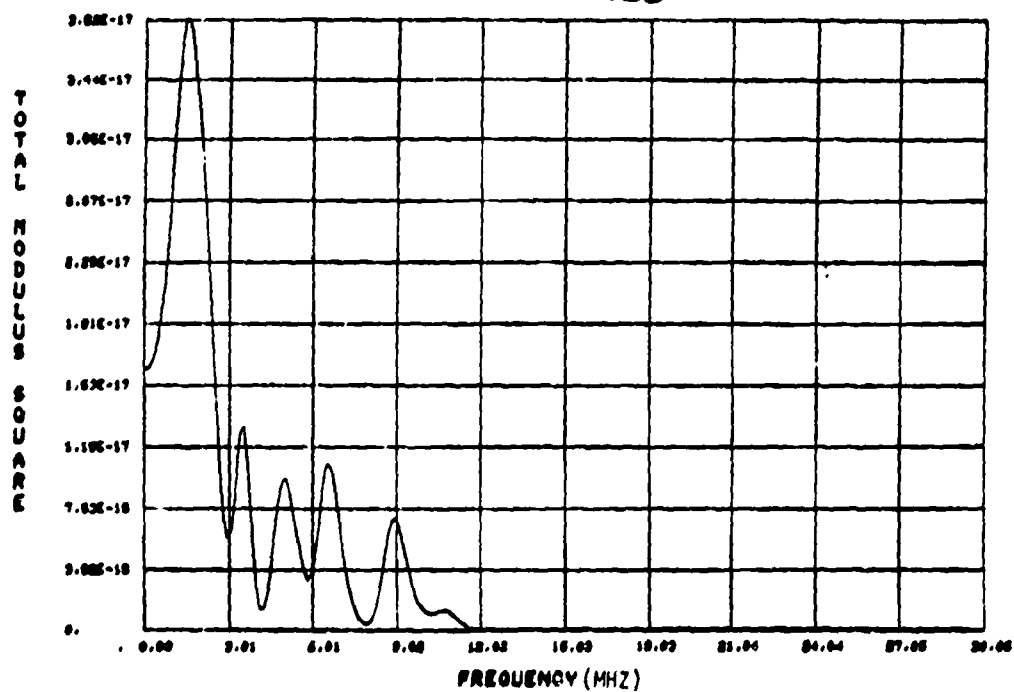


Figure 8. Clutter Pulse C49 Power Spectrum with Receiver &amp; Inverse Filter

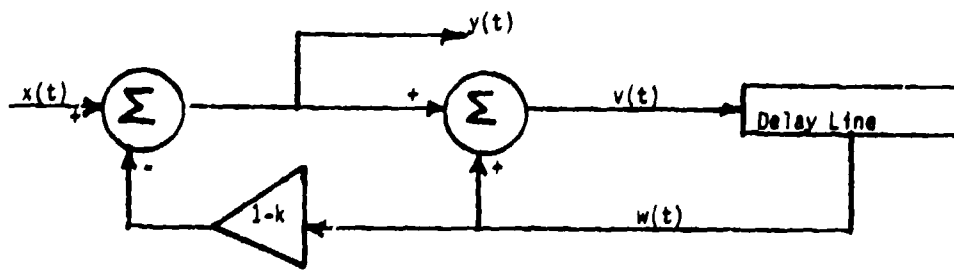


Figure 9. Double Loop Single Delay Digital Filter

**UNCLASSIFIED**

C-11

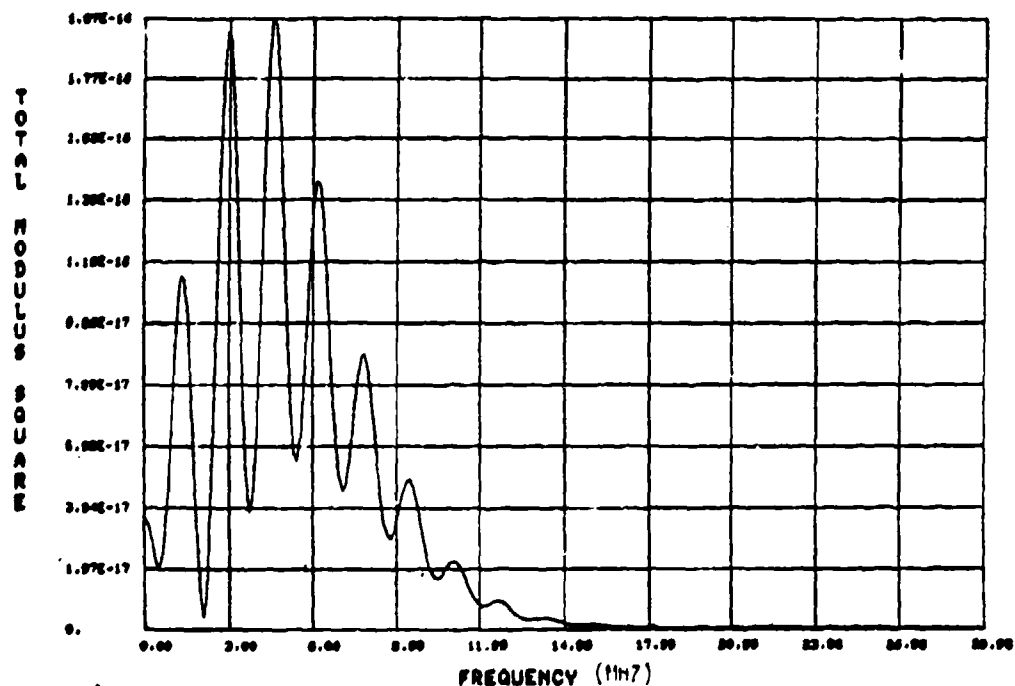


Figure 10. Power Spectrum of Target Pulse After DLSD Filtering

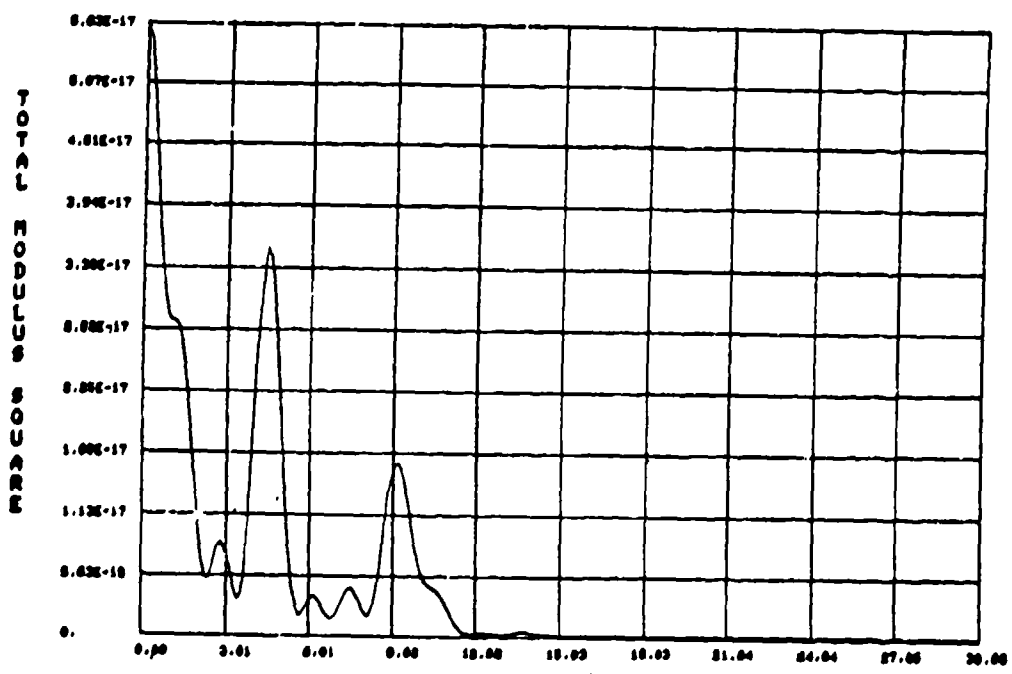


Figure 11. Clutter Pulse C49 Power Spectrum After DLSD Filtering

**UNCLASSIFIED**

733

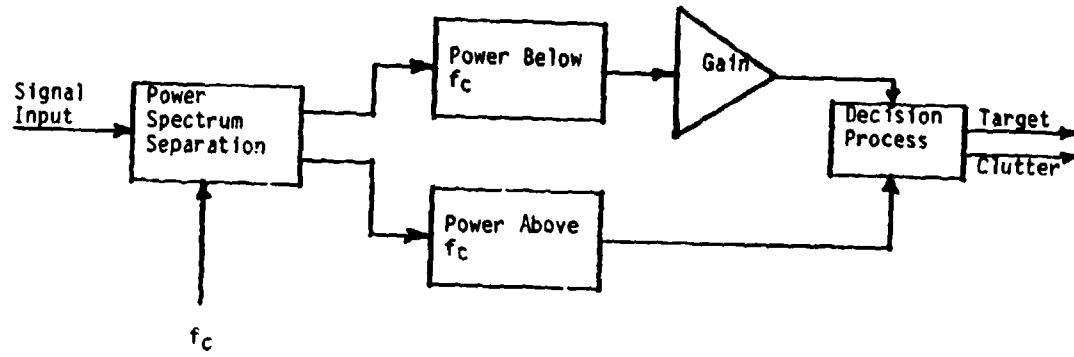
**UNCLASSIFIED**

Figure 12. Block Diagram of the Adaptive Detection

**UNCLASSIFIED**

# UNCLASSIFIED

C-12

## COPPERHEAD PERFORMANCE ON THE MODERN DIRTY BATTLEFIELD

Howard E. Weaver and George D. Minto  
Martin-Marietta Corporation  
Orlando, Florida 32885

### ABSTRACT

This presentation is made via a documentary film relating the story of how smoke tests beginning in November 1978 with the COPPERHEAD Semi-Active laser guided projectile led to a series of seeker improvements which were proved out in Smoke Week III in August 1980. The film highlights the fact that the initial seeker design was not optimized for operation on a dirty battlefield, but through a series of analyses and tests, pulse processing logic changes were made which result in an order of magnitude improvement in the ability to track in an obscured scene. The film proceeds in a step-by-step manner to describe the desired night-sight rule of thumb for determining call for fire, the COPPERHEAD pulse processing techniques in the initial design, results observed during tests in obscurants, design changes, test results with the changes, and final rule of thumb confirmation in SMOKE WEEK III. Effects of the seeker improvements on clear air performance will also be covered. The film makes no attempt to discuss tactics relative to smoke employment by the enemy.

UNCLASSIFIED

735

# UNCLASSIFIED

C-14

## PHYSICAL AND CHEMICAL CHARACTERIZATION OF SMOKE PRODUCED FROM WHITE PHOSPHORUS/FELT WEDGE

W. Bock, R. Butler, S. Katz, N. Rajendran and A. Snelson  
IIT Research Institute  
Chicago, Illinois

### ABSTRACT

Laboratory studies have been made to characterize physically (particle size) and chemically (composition) the smoke produced by U.S. Army white phosphorus/felt wedge munitions. The smokes for particle size analyses were generated at relative humidities from 5% to 75%. Particle size was determined at  $\approx 1 \mu$  (mass median diameter) independent of relative humidities  $\geq 10\%$ . Chemical analyses of smoke aerosols generated at relative humidities from 25% to 75% showed no obvious dependence on the latter. About 65% of the phosphorus in the aerosol is present as polyphosphoric acids ( $H_{n+2}P_2O_{3n+1}$ , where  $n = 1$  to 8, in relative abundance (n values)  $2 > 1 > 3 > 4 > 5 > 6 > 7 > 8$ ). The remaining  $\approx 35\%$  of the aerosol phosphorus appears to be present as polyphosphoric acids with  $n > 8$ . The gas phase associated with the aerosol was analyzed for inorganic and organic materials. Both types of species were found at low concentrations. A total of 25 were characterized.

The above study was sponsored by the U.S. Army Medical Bioengineering Research and Development Laboratory, Fort Detrick, Maryland, Mr. Jesse J. Barkley, Contract Officer. A detailed final report of this work will be available shortly.

# UNCLASSIFIED

737

# UNCLASSIFIED

C-15

## CHEMICAL AND PHYSICAL CHARACTERIZATION OF A DIESEL FUEL OBSCURANT FOR INHALATION TOXICOLOGY STUDIES

R. A. Jenkins, R. W. Holmberg, J. H. Moneyhun, and J. S. Wike  
Analytical Chemistry Division  
Oak Ridge National Laboratory  
Oak Ridge, Tennessee 37830

### 1. INTRODUCTION

The military has shown a renewed interest in the use of smokes and obscurants for screening purposes in warfare. This, coupled with present day concerns for environmental and occupational exposure safety has prompted the Army to investigate the risks associated with passive and/or accidental exposure to these smokes. As part of this program, the Department of Defense is supporting an investigation of the inhalation toxicology of one of these obscurants. In this case, the smoke is produced by diesel powered vehicles from diesel fuel with a system designated by the acronym VEESS (Vehicle Engine Exhaust Smoke System). Briefly, the same fuel that powers the vehicle is pumped into the exhaust manifold immediately downstream of the engine. The fuel vaporizes and the vapors are carried through the exhaust system and forcibly ejected, along with the normal exhaust gases, into the air. They condense to form an aerosol cloud which is used for screening. The size and cost of a large vehicle, such as a tank, as well as the amount of aerosol which the VEESS system produces, precludes its direct use in a laboratory environment. Therefore, we have undertaken a study employing exposures to a diesel fuel based smoke generated under similar circumstances, but on a much smaller scale. The purpose of the work described in this paper is (1) the development, construction, and evaluation of a diesel fuel based aerosol generator on a laboratory scale; (2) the chemical and physical characterization of the material to which the materials are exposed; (3) the comparison of test and field aerosols.

### 2. GENERATION/EXPOSURE SYSTEM

At the outset of the study, it was deemed important to be able to build into the laboratory-scale generator a chemical environment similar to that which exists in the exhaust system of the tank or other large diesel powered vehicle. It should be emphasized that the white obscurant cloud consists primarily of droplets of diesel fuel in the micron and submicron size range. The black, sooty particles and gaseous constituents of diesel exhaust constitute only a minor fraction of the cloud. However, the ability to study chemical interactions of the fuel with the exhaust gases was part of the design criteria of the generator.

Figure 1 is a schematic of the generation system. The generator itself consists of a 1 meter long section of stainless steel tubing (2.5 cm i.d.). A 1 kw Vycor immersion heater is mounted inside the tubing to simulate the manifold heating. The carrier gas, simulating the exhaust gas, passes along the heater where it is heated to 600°C. (Presently we are using nitrogen flowing at 10 l/min as a carrier

# UNCLASSIFIED

739

**UNCLASSIFIED**

gas. However, generation of the aerosol in the presence of other gases can be easily afforded by mixing those gases upstream of the generator.) The temperature of the Vycor heater is maintained by means of a thermocouple controller. Diesel fuel is pumped onto the end of the heater where it is volatilized and carried down the tube. Since the exposure chamber operates at a constant air flow (420 l/min), aerosol concentration is regulated by varying the injection rate of the diesel fuel using low volume metering pumps. Fuel flow rates from 0.5 to 10 ml/min produce aerosol concentrations of 1 to 20 g/m<sup>3</sup>. A thermostatically controlled heater surrounding the last two-thirds of the manifold is used to maintain the exiting vapor at 350°C. This acts to prevent premature condensation and to simulate the exhaust temperature of the manifold of the vehicle.

Figure 2 is a schematic of the entire exposure system. The generator is interfaced to the exposure chamber air supply through a glass pipe "T". The hot gases and vapors enter countercurrently into the downflowing air supply where they mix turbulently, and rapidly cool to form a dense aerosol cloud. The chambers used are of a modified NYU type, rectangular with tapered end sections, having a total volume of 1.4 m<sup>3</sup>. Conditioned air is fed into the chambers from the top and exhausts at the bottom. The chambers operate at a slight (10 mm H<sub>2</sub>O) negative pressure.

Initially, there was a problem with establishing a homogeneous distribution of the aerosol within the chamber. The incoming airstream was observed to jet straight from the inlet at the top of the chamber to the bottom of the chamber, bounce upwards off the bottom and return toward the bottom with a swirling motion. To avoid potential nonuniform exposure, an assembly consisting of a dispersing cone and two laminarizing screens was designed and installed in the upper tapered section of the NYU chamber. The screens consist of perforated aluminum plates with 10% free opening area. Thus, when smoke enters the chamber it is spread across the cone and then dispersed in the horizontal plane by the screens.

### 3. CHEMICAL CHARACTERIZATION OF THE FUEL

Because the chemistry of diesel fuels can vary considerably, it is conceivable that the relative toxicity of the aerosol could fluctuate with the fuel source. To provide a data base for comparison with future studies, and to monitor the stability of the material being bioassayed, routine physical and chemical characterization of the fuel is performed. For this particular study, all the diesel fuel was purchased at one time from one particular source (1). It is currently being stored in barrels refrigerated to 4°C. A standard protocol has been developed in fuel handling to reduce the impact of aging. When a new barrel of fuel is opened, it is allowed to come to ambient temperature (approximately 22°C), thoroughly agitated and aliquotted into five-gallon gas tight fuel cans. The individual cans are stored refrigerated until they are required for use in the animal exposures. When an individual fuel can is transferred to the inhalation exposure facility, remaining fuel from the previous exposures is discarded. In order to chemically and physically monitor the fuel, samples are collected weekly and

**UNCLASSIFIED**

# UNCLASSIFIED

C-15

subjected to several standard tests: viscosity (ASTM No. D-2615), refractive index, and simulated distillation (ASTM No. D-2887-73). Typical results of such characterization for the diesel fuel being used in this study are found in Table 1. While such information provides for a referenceable data base, it affords little detailed information as to the chemical composition of the material. Thus, a gross compositional profile of the fuel is obtained from the samples with high resolution gas-liquid chromatography (Figure 3). The most abundant individual species in the diesel fuel appear to be the straight chain saturated hydrocarbons C<sub>10</sub>-C<sub>22</sub>.

Formation of double bonds and oxidation products of the individual constituents are likely consequences of aging. In order to document such aging, UV/visible spectra are taken on each sample collected. A slight increase in optical absorption at 375 nm with continued air-fuel contact has been observed. We suspect that this is associated with the increasing yellowish appearance of the fuel as it ages. Diffuse reflectance Fourier transform infrared spectrometry is being investigated as a rapid means of characterizing chromophor formation in the fuel. A sample spectrum of the fuel is given in Figure 4. An increase in the infrared absorption in the region of 1550 cm<sup>-1</sup> appears to be associated with fuel aging. This may be due to C=C formation.

A more detailed chemical characterization of the fuel is afforded through a tiered analytical scheme, in which the diesel fuel is first separated by high performance liquid chromatography (HPLC) followed by gas chromatography. This approach has permitted characterization of the fuel as to the relative amounts of aromatic and aliphatic constituents by a procedure which is inherently more accurate and rapid than the standard method (ASTM 1319). In addition, it affords a depiction of the constituents according to compound and class. HPLC separation is accomplished by isocratic elution with hexane on a 5  $\mu$  silica column. The HPLC chromatogram provides for a gross comparison of the differences in fuels. In order to obtain the aliphatics:aromatics ratio value for a specific fuel, standardization according to refractive index sensitivity must be performed. This has been accomplished by choosing standard compounds which have specific refractive index absorbances close to those of the constituents eluting in each of the four or five major compound classes within the fuel. The compounds chosen for this standardization include dodecane, toluene, naphthalene, and 3,6-dimethylphenanthrene. The aliphatics: aromatics ratio obtained by this procedure gives values very close to those obtained by independent tests (29.3% aromatics by HPLC vs 30.5% by analysis supplied with the fuel).

In order to more lucidly visualize the individual compound classes, the specific HPLC fractions are collected and reduced in volume to 500  $\mu$ l in a manner so as to prevent loss of volatile constituents. An aliquot of the concentrate is subjected to high resolution gas chromatographic separation using a 30-meter SE-52 fused silica capillary column. The first fraction eluting from the HPLC consists predominantly of straight and branched-chain saturated paraffins. Concentrations of some of the normal par-

741  

# UNCLASSIFIED

**UNCLASSIFIED**

affins in the fuel are reported in Table 2. The second fraction eluting from the HPLC is predominantly substituted benzene compounds. The third fraction is comprised predominantly of two-ring aromatics, including alkylated naphthalenes, alkylated biphenyls, and small amounts of aromatic thiophenes. Major constituents of the fourth fraction include fluorene, alkylated fluorenes, phenanthrene, and alkylated phenanthrenes.

**4. PHYSICAL CHARACTERIZATION OF THE AEROSOL**

Particle size distributions have been estimated using a Mercer-Lovelace cascade impactor (2), operating at a flow rate of one l/min. Stage constants were calculated for measured jet diameters using Stokes parameters determined by Marple (3). Direct weighing of the impactor stages was found to be unreliable because of the small amounts of aerosol collected on each stage. Consequently, we have used a computer-assisted low resolution gas chromatographic technique for estimating the amount of diesel fuel aerosol collected on each stage. The glass stage plates are immersed in carbon disulfide to dissolve the fuel from the plate. An aliquot of the resulting solution is injected into the GC column (5% SP-2100 on 100-120 mesh Supelcoport® operated isothermally at 200°C). The entire quantity of partially resolved hydrocarbon constituents is eluted in 3 min. The flame ionization detector output is fed into an analog-to-digital converter. The resulting poorly resolved band of constituents is displayed on a graphics terminal with sufficient resolution to separate the small solvent ( $CS_2$ ) peak from the fuel peaks. The area under the fuel peak is integrated and the mass determined by comparing this area with standardized solution of the same fuel type. An example of aerosol particle size at a given aerosol concentration plotted on logarithmic probability coordinates is shown in Figure 5. Some growth in size occurs from the top to the bottom of the chamber. The particle size in the top of the chamber does not represent the "initial" size of the aerosol, since it has had time to grow prior to reaching this point in the system.

Small infrared backscatter probes are routinely used to monitor aerosol concentration at several points within the exposure chambers. These probes consist of proximity sensor chips which contain a light-emitting diode and phototransistor. The chips are approximately 1/4 inch in diameter and are placed on the end of a probe which may be positioned anywhere within the chamber. The chip detects the amount of light backscattered by the aerosol immediately in front of the probe. Voltage output from the probes is adjusted so that all respond equally to the same aerosol concentration. The output then can be related to aerosol concentration, as measured gravimetrically with Cambridge filter pad samples. The response of the sensor is linear over the aerosol concentration ranges of interest here. Use of this sensor (4) has been described for quantitation of animal exposures to tobacco smoke (5). The filling/emptying chamber dynamics are illustrated quantitatively in Figure 6. Two matched sensors were mounted in the chamber, one immediately above the first tier of cages and one just below the bottom tier. The

# UNCLASSIFIED

C-15

data in Figure 6 indicate that there is some lag time between the termination of fuel flow into the aerosol generator and final washout of the fuel from the chamber.

## 5. CHEMICAL CHARACTERIZATION OF THE AEROSOL

The obscurant cloud generated is an evaporation/condensation aerosol which undergoes a large dilution simultaneously with the condensation. Many of the more volatile constituents of the fuel have significant vapor pressures at ambient temperatures, and thus may partition themselves between the vapor and particle phases. This complicates sampling of the aerosol, since the method of sampling the cloud can ultimately affect the relative composition of the sample obtained. Samples of the particulate phase are collected on 44 mm diameter glass fiber Cambridge filter pads identical to those used in cigarette smoke analyses (6). At reasonably low sampling flows these filters are 99.95% efficient at collection of particles larger than 0.3  $\mu$  diameter. Flows of 2 l/min (linear velocity = 2.4 cm/sec) or less are employed in collection of aerosol samples.

Since animals are exposed to both the liquid and vapor phase of the aerosol, some independent measure of the concentration of each phase is desirable. Estimation of the concentration of particles in the aerosol is relatively straightforward. At sufficiently low flows, a known quantity of aerosol can be drawn across the filter and the increase in pad weight is taken as the mass of particles present in the sampled volume of aerosol. Determination of the quantity of vapor is more difficult, since it is difficult to assure that for a sample sufficiently large to weigh accurately, 100% recovery of all vapor phase constituents has occurred. Instrumental measurement of the vapor quantity posed substantial standardization and sample dilution problems. Thus, we have been attempting to use an indirect determination of the amount of fuel which does not recondense following aerosolization. This in turn, should be a good estimate of the relative fraction of vapor phase constituents in the aerosol. The change in the apparent concentration of a "non-volatile" tracer - one which has an extremely low vapor pressure at ambient temperatures - in the liquid phase of the aerosol can be used to determine this fraction through the following expression:

$$F = \frac{V-1}{V}$$

where

F = fraction of the fuel remaining in the vapor phase

V = the ratio of the concentration of tracer in the aerosol particulate phase to that of the tracer in the original fuel =  $[T_{part}]/[T_{fuel}]$

# UNCLASSIFIED

743

**UNCLASSIFIED**

In this case decachlorobiphenyl was chosen as the tracer. (It is also intended for use as a dosimetric tracer for diesel fuel aerosol deposition in the experimental animals.) In our experiments, no evidence of measurable quantities of this tracer in the vapor phase has been found following aerosolization. Results of the experiments (Table 3) indicate that, as the aerosol becomes more dilute, a greater fraction of the fuel remains uncondensed. However, over the particle concentration used in the subchronic exposures (0.45-5.0 mg/l), the relative fraction of vapor to particulate phases should not change substantially.

Aerosolization partitions the more volatile constituents of the fuel between the vapor and particle phase of the aerosol. This is illustrated graphically in Figure 7. Here a comparison of the high resolution gas chromatographic profiles of the liquid fuel and the liquid phase of the aerosol indicates a substantial decrease in the concentration of those constituents eluting before n-C<sub>12</sub>H<sub>26</sub>. Comparison of the quantities of the normal hydrocarbons in the fuel and aerosol is presented in Table 4. Again, the absence of the lower boiling constituents from the liquid phase of the aerosol is evident. Samples of the collected aerosol have also been subjected to the tiered HPLC fractionation/GC visualization scheme. Results of these studies also point to a diminished concentration of the more volatile constituents of the fuel in the liquid phase of the aerosol.

We are currently developing methods for the quantitative sampling of the vapor phase. The most promising of these appears to be the collection of the filtered vapor on small Tenax cartridges. The cartridges, containing approximately 1.8 ml of Tenax GC®, are thermally desorbed onto a nickel precolumn which is cryogenically cooled. The nickel column then is attached to an OV-101 glass capillary column and the resulting plug is chromatographed (7). Because the vapors are relatively concentrated (hundreds of micrograms/cc), the actual volume of aerosol sampled must be small to prevent breakthrough of individual constituents. Thus, to obtain a time averaged sample, infusion pumps are used to draw filtered aerosol through the Tenax cartridges at rates of a few cc/min.

Figure 8 compares the high resolution GC profile of the filtered vapors trapped on Tenax with that of the whole aerosol (the latter sample was obtained by removing the Cambridge filter upstream of the Tenax trap). Again, partitioning of the fuel constituents between the vapor phase and the liquid phase is evident.

Characterization of the animal exposure chamber atmospheres has not been limited to profiling methodologies. Analyses of specific constituents in the atmospheres had indicated acetaldehyde concentrations of 18-20 µg/l, carbon monoxide at approximately 2 ppm, and oxides of nitrogen (NO<sub>x</sub>) at approximately 1 ppm.

**UNCLASSIFIED**

## 6. CHEMICAL EVALUATION OF FIELD AEROSOLS

The system being used to expose animals in this study does not exactly mimic that used under field conditions because here, the diesel fuel is vaporized in a nitrogen carrier gas. In vehicular-based systems, oxygen and other constituents of the exhaust could react with diesel fuel to form compounds not present in the nitrogen-generated aerosol. As part of an effort to assess chemical differences between the vehicular-based diesel fuel aerosol and that used in the inhalation toxicology studies, ORNL participated in the Smoke Week III exercises held at Eglin Air Force Base during August of 1980. The purpose of our involvement was to collect chemical samples of the VEESS smoke and make comparisons as to the chemical composition of those smokes with that used in the inhalation toxicology studies.

Sampling systems used during the exercises were similar to those employed in the laboratory, i.e., glass fiber filter pads backed with Tenax traps. Samples of the gases were to be collected in gas sampling bays downstream of piston-driven flow-controlled pumps. In addition to the chemical samplers other analytical instrumentation was used. A chemiluminescent oxides of nitrogen analyzer provided on-line NO<sub>x</sub> concentration measurements. An Ecolyzer® was used to determine carbon monoxide levels. An activated charcoal trap backed with Tenax GC® was used to remove interfering organic volatiles from the sample. In addition, a Gayle/ORNL Optical Particle Concentration Monitor was used to provide instantaneous readout of particle concentrations. Because diesel fuels can differ in chemical composition, samples were collected from the M-48 tank's fuel tank immediately prior to the VEESS run.

In the one successful test in which we were able to obtain a few measurable samples of VEESS smoke, the amount of smoke crossing the sampler was highly variable. Continuous readout of the particle sensor monitoring aerosol droplet concentrations in the center of the ORNL sampling line indicated peak aerosol concentrations of only 160 mg/m<sup>3</sup>. However, during only 30% of the total test duration was the aerosol concentration above that minimally detectable (5 mg/m<sup>3</sup>). Peak concentrations of carbon monoxide were observed to be approximately 2 ppm. NO<sub>x</sub> concentrations were also observed to be highly variable, with peak concentrations of approximately 7 ppm. Again, this was thought to be due to the non-uniform concentration of smoke cloud being sampled. Because of the very low concentrations of smoke existing on the sampling grid at any one point, very few of the samples collected were amenable to chemical analysis. Of those which were collected, high resolution GC profiles of the liquid phase of the aerosol compared with those of the aerosol being tested in the ORNL study illustrate some important differences. Primarily, these differences exist in the concentration of the lower boiling constituents of the aerosol liquid phase. For example, in Table 5 are compared the relative n-paraffin concentrations for the VEESS fuel with those from the collected aerosol. As much as 30% of the amount of the n-paraffins (those eluting before n-C<sub>14</sub>H<sub>30</sub>) present in the fuel are absent from the liquid phase of the aerosol. This finding is qualitatively similar to the aerosol generated in the ORNL studies. However, the liquid phase of the ORNL-generated aerosol contains a relatively higher proportion of lower boiling constit-

**UNCLASSIFIED**

**UNCLASSIFIED**

uents than that of the VEESS aerosol. These differences may be as much as 20% by weight and may be due both to differences in temperature at which the particles were collected (31°C vs. 22°C at ORNL) and to the aerosol concentrations examined. Other major differences between the field test and the ORNL aerosol were ascribed to differences in the two fuel samples.

Studies to chemically characterize a more relevant aerosol have been limited to pilot experiments in which oxygen (present at concentrations approximately equal to those in the exhaust gas of the diesel engine) is added to the nitrogen carrier gas generating the aerosol. The most evident change involves a noticeable increase in infrared absorption of the liquid phase of the aerosol in the spectral region indicative of carbonyl formation. This phenomenon has been confirmed chemically (8), showing an approximately 5-fold increase in the gas phase carbonyl content in the oxygenated aerosol.

**7. ACKNOWLEDGEMENTS**

We gratefully acknowledge C. E. Higgins' idea for the unfiltered aerosol collection on Tenax®.

Research sponsored by the U.S. Department of Defense under Interagency Agreement DOE No. 40-4016-79, U.S. DOD Project Order No. 9600, under Union Carbide Corporation's contract W-7405-eng-26 with the U.S. Department of Energy.

**8. REFERENCES**

1. Phillips Chemical Co., Petrochemicals Division, 14D4 Phillips Bldg., Bartlesville, OK 74004.
2. Mercer, T. T., Tillery, M. I., and Ballew, C. W. (1962). A cascade impactor operating at low volumetric flow rates. AEC Research and Development Report LF-5, December 1962. (The impactor used was manufactured by the Sandia Research and Development Co., 1712 Virginia N.E., Albuquerque, NM, 87110.)
3. Marple, V. A. and Liu, Y. H. (1974). Characteristics of Laminar Jet Impactors. Env. Sci. & Tech. 8, 648.
4. Gayle, T. M., Higgins, C. E., and Stokely, J. R. (1979). A continuous smoke monitoring device for continuous animal exposure systems. In "Tobacco Smoke Inhalation Bioassay Chemistry," Oak Ridge National Laboratory Report ORNL-5424, p. 63.
5. Jenkins, R. A. and Gayle, T. M. (1980). An Instrumental Inhaled Smoke Dosimeter for the Quantitative Characterization of Aerosol Exposures, in "Pulmonary Toxicology of Respirable Particles, Proceedings of the Nineteenth Annual Hanford Life Sciences Symposium," Publication CONF-791002, pp. 68-86, available from NTSI, Springfield, VA 22161.
6. Wartman, W. B., Cogbill, E. C., and Harlow, E. S. (1959). Determination of Particulate Matter in Concentrate Aerosols. Application to "Tar" and Nicotine in Cigarette Smokes. J. Assoc. Off. Anal. Chem. 31, 1705-1709.

**UNCLASSIFIED**

C-16

7. Zlatkis, A., Brazell, R. S., and Poole, C. F. (in press). The role of organic volatile profiles in clinical diagnosis. Clin. Chem.
8. Maskarinec, M. P., Manning, D. L., and Oldham, P. (1981). Determination of vapor phase carbonyls by high-pressure liquid chromatography. J. Liq. Chrom. 4, 31-39.

**UNCLASSIFIED**

747

**UNCLASSIFIED**

TABLE 1. PHYSICAL PARAMETERS  
DIESEL FUEL - PHILLIPS REFERENCE

Kinematic Viscosity	3.335 centistokes
Refractive Index	1.477
Simulated Distillation	
Initial Boiling Point	112°C
Final Boiling Point	313°C
Average Boiling Point	235°C

TABLE 2. CONCENTRATIONS OF NORMAL PARAFFINS  
PHILLIPS REFERENCE FUEL

<u>Hydrocarbons</u>	<u>Concentration mg/g fuel</u>
n-C <sub>9</sub> H <sub>20</sub>	1.2
n-C <sub>10</sub> H <sub>22</sub>	5.5
n-C <sub>11</sub> H <sub>24</sub>	12.6
n-C <sub>12</sub> H <sub>26</sub>	12.8
n-C <sub>13</sub> H <sub>28</sub>	13.3
n-C <sub>14</sub> H <sub>30</sub>	16.0
n-C <sub>15</sub> H <sub>32</sub>	16.8
n-C <sub>16</sub> H <sub>34</sub>	19.1
n-C <sub>17</sub> H <sub>36</sub>	18.8
n-C <sub>18</sub> H <sub>38</sub>	10.7
n-C <sub>19</sub> H <sub>40</sub>	6.8
n-C <sub>20</sub> H <sub>42</sub>	2.6

**UNCLASSIFIED**

**UNCLASSIFIED**

C-15

TABLE 3. FRACTION OF FUEL REMAINING IN VAPOR PHASE  
FOLLOWING AEROSOLIZATION

<u>Particle Concentration mg/l</u>	<u>[DCBP]<sub>part</sub> [DCBP]<sub>fuel</sub></u>	<u>Fraction of Fuel Remaining in Vapor Phase, %</u>
0.45	1.25 ± 0.03	20
1	1.23 ± 0.04	18
3	1.21 ± 0.06	17
5	1.17 ± 0.05	14
8	1.08 ± 0.03	7

TABLE 4. EFFECT OF AEROSOLIZATION ON LIQUID PHASE COMPOSITION

<u>Hydrocarbon</u>	<u>% of Normal Paraffins</u>	
	<u>Phillips Fuel (Prior to Aerosolization)</u>	<u>ORNL Aerosol (Phillips Liquid Phase)</u>
n-C <sub>8</sub>	-	-
n-C <sub>9</sub>	1.1	-
n-C <sub>10</sub>	4.4	2.2
n-C <sub>11</sub>	8.6	4.6
n-C <sub>12</sub>	8.5	6.7
n-C <sub>13</sub>	10.0	9.3
n-C <sub>14</sub>	10.5	10.5
n-C <sub>15</sub>	13.1	14.1
n-C <sub>16</sub>	14.8	16.7
n-C <sub>17</sub>	12.9	15.5
n-C <sub>18</sub>	9.0	11.2
n-C <sub>19</sub>	4.5	5.6
n-C <sub>20</sub>	1.9	2.4
n-C <sub>21</sub>	0.6	1.0
n-C <sub>22</sub>	0.3	-

**UNCLASSIFIED**

**UNCLASSIFIED**

TABLE 5. COMPARISON OF LIQUID PHASE NORMAL PARAFFINS

<u>Hydrocarbon</u>	% of Reported Normal Paraffins	
	<u>VEESS Fuel</u>	<u>VEESS Aerosol</u>
n-C <sub>8</sub>	1.1	-
n-C <sub>9</sub>	1.3	-
n-C <sub>10</sub>	2.6	-
n-C <sub>11</sub>	5.8	-
n-C <sub>12</sub>	8.9	-
n-C <sub>13</sub>	12.1	2.5
n-C <sub>14</sub>	12.2	8.8
n-C <sub>15</sub>	12.0	15.0
n-C <sub>16</sub>	11.4	18.3
n-C <sub>17</sub>	9.1	15.8
n-C <sub>18</sub>	8.5	13.6
n-C <sub>19</sub>	5.1	8.7
n-C <sub>20</sub>	3.8	6.8
n-C <sub>21</sub>	2.4	4.2
n-C <sub>22</sub>	1.6	2.7
n-C <sub>23</sub>	1.0	1.5
n-C <sub>24</sub>	0.9	1.1
n-C <sub>25</sub>	0.5	1.0

**UNCLASSIFIED**

**UNCLASSIFIED**

C-15

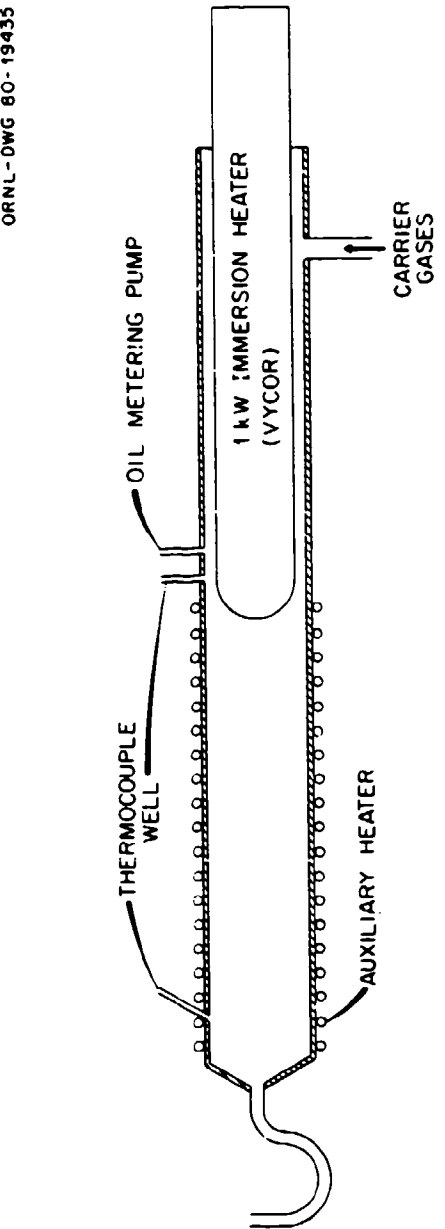


FIGURE 1. SCHEMATIC DIAGRAM OF DIESEL FUEL AEROSOL GENERATOR.

**UNCLASSIFIED**

751

**UNCLASSIFIED**

ORNL-DWG 80-19436

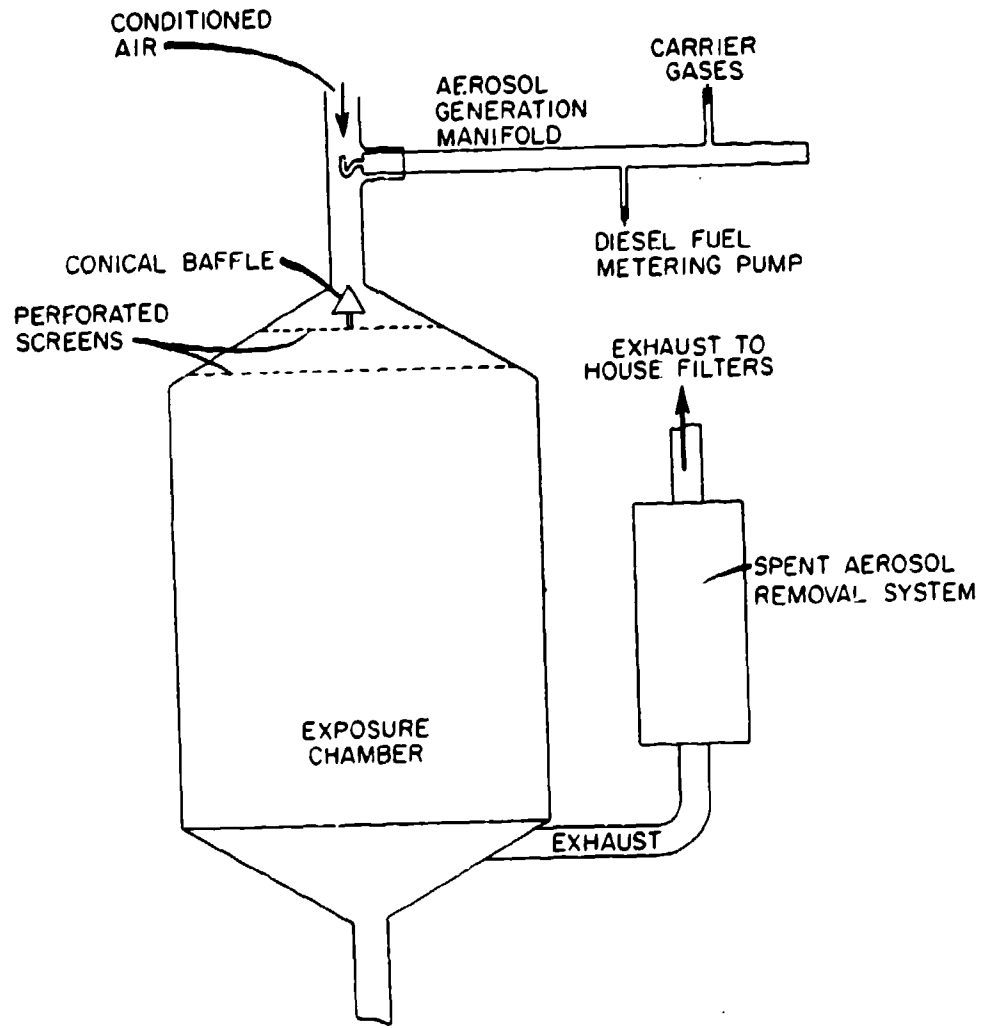


FIGURE 2. SCHEMATIC DIAGRAM OF COMPLETE EXPOSURE SYSTEM.

**UNCLASSIFIED**

**UNCLASSIFIED**

ORNL/BNL 81-9191

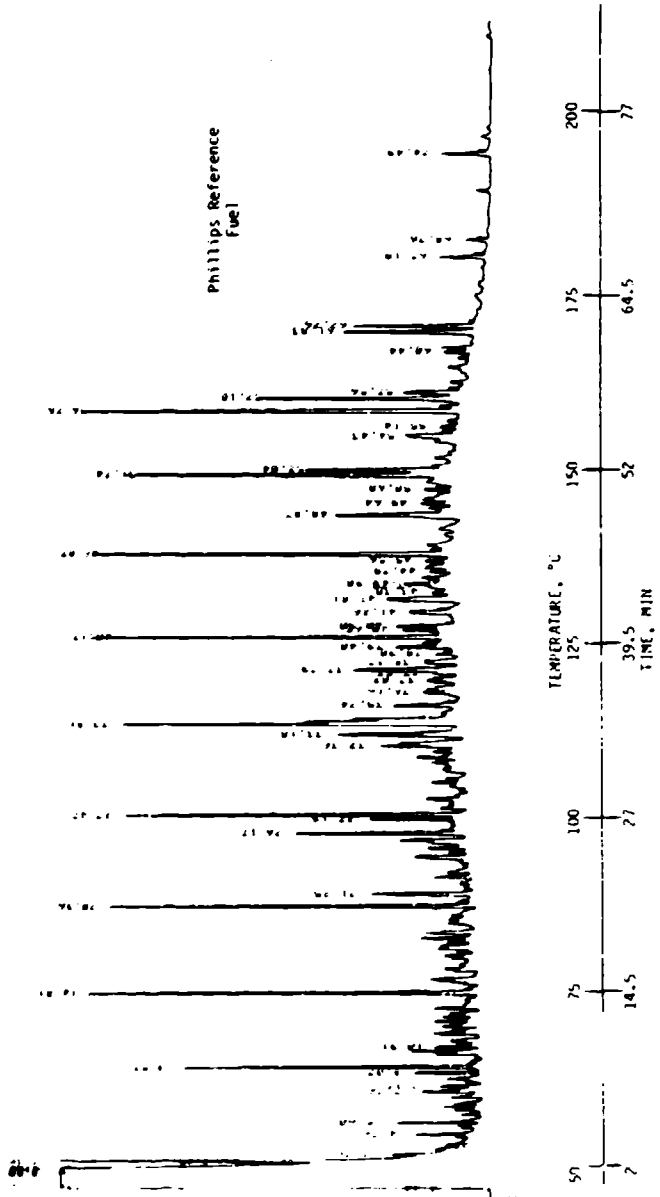


FIGURE 3. HIGH RESOLUTION GAS CHROMATOGRAPHIC PROFILE OF #2 DIESEL FUEL.  
Conditions: 30 m SE-52 coated fused silica column.  $\frac{1}{2}$  carrier gas @ 20 psi.  
2  $\mu$ l splitless injection, vented after 30 sec.

**UNCLASSIFIED**

C-15

UNCLASSIFIED

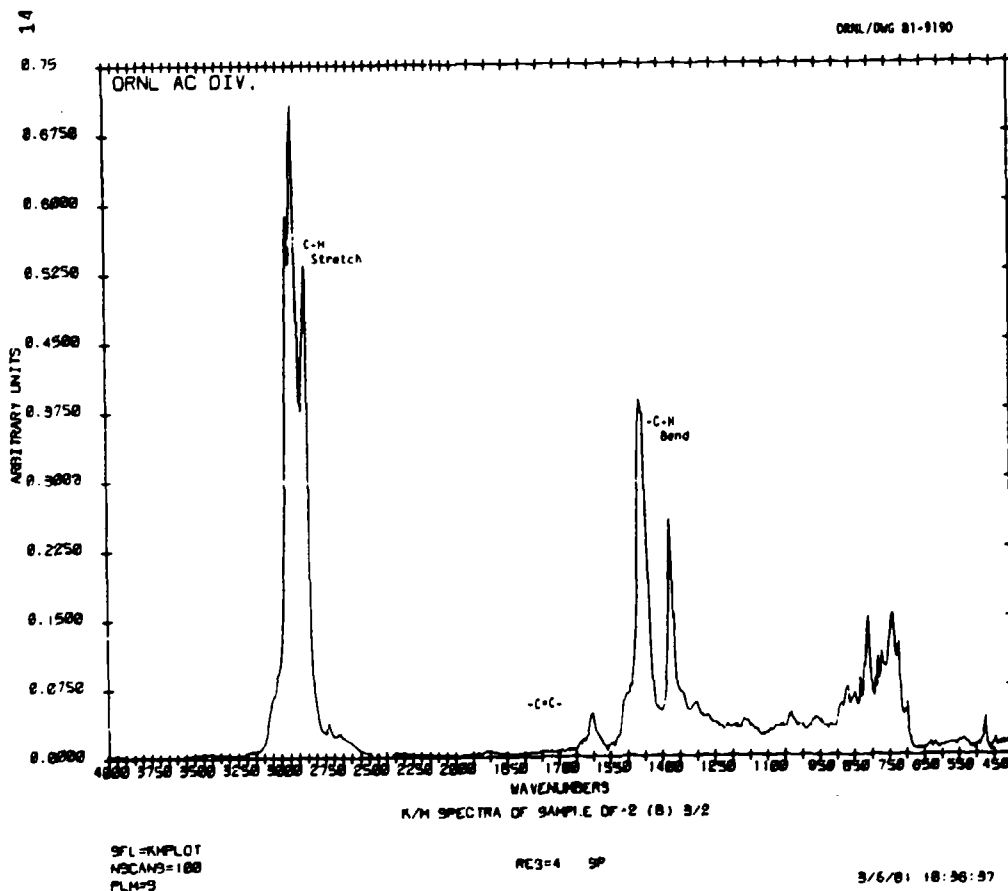


FIGURE 4. DIFFUSE REFLECTANCE FOURIER TRANSFORM INFRARED ABSORPTION SPECTRUM OF #2 DIESEL FUEL.

UNCLASSIFIED

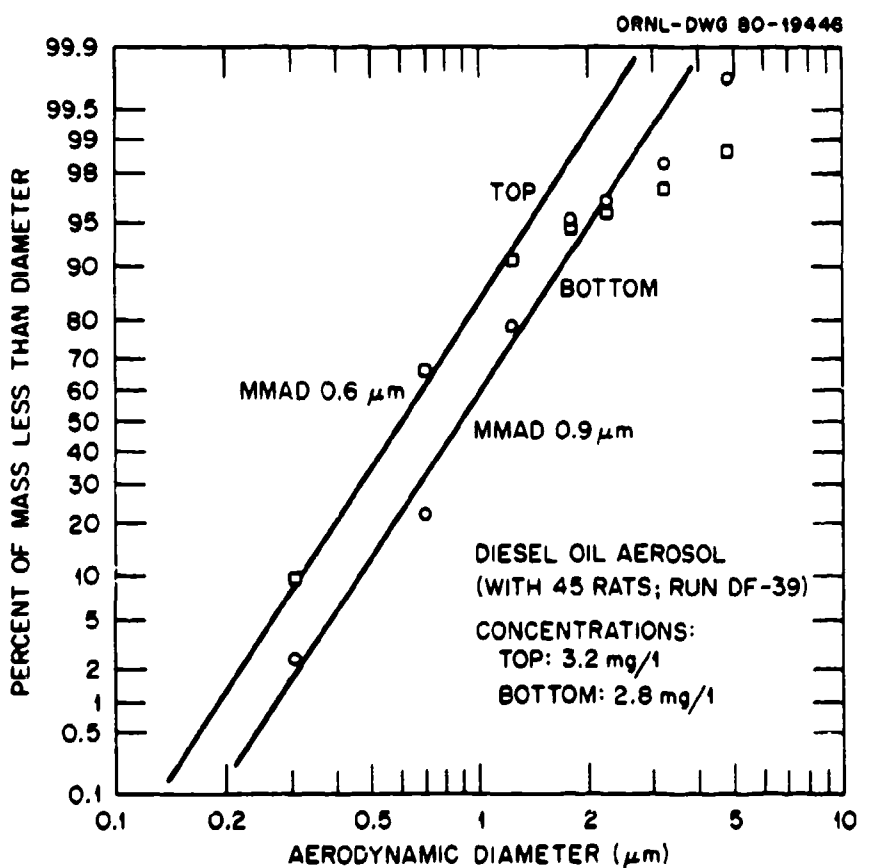
**UNCLASSIFIED**

FIGURE 5. PARTICLE SIZE AS DETERMINED BY CASCADE IMPACTION AT TOP AND BOTTOM OF EXPOSURE CHAMBER.

**UNCLASSIFIED**

UNCLASSIFIED

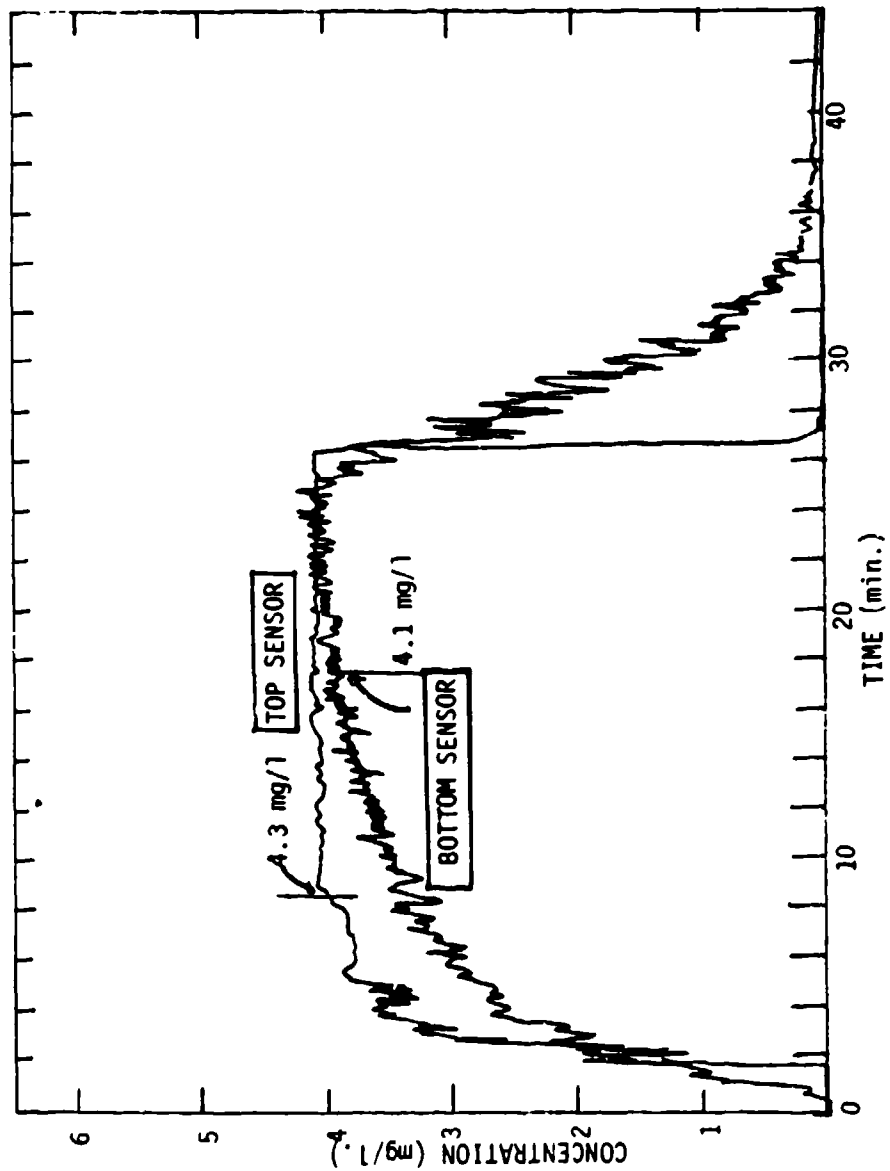


FIGURE 6. TWO CHANNEL RECORDING OF PARTICLE CONCENTRATION FROM DIESEL FUEL AEROSOL IN ANIMAL EXPOSURE CHAMBER.

UNCLASSIFIED

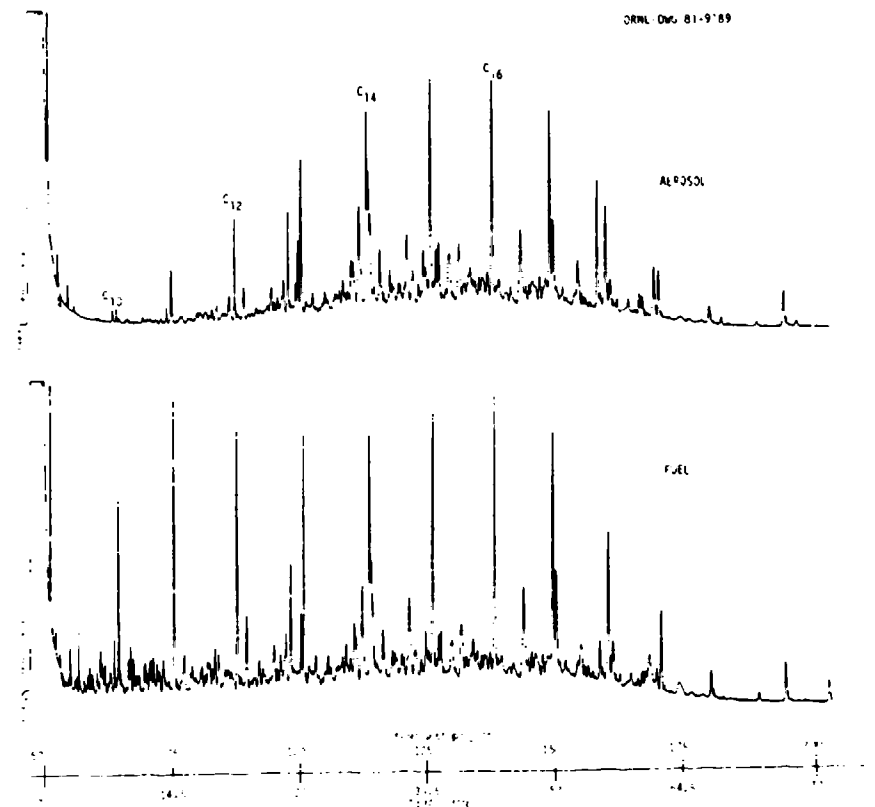
**UNCLASSIFIED**

FIGURE 7. COMPARISON OF HIGH RESOLUTION GAS CHROMATOGRAMS: LIQUID PHASE OF THE AEROSOL VS UN-AEROSOLIZED DIESEL FUEL.  
Conditions: Same as Figure 3.

**UNCLASSIFIED**

UNCLASSIFIED

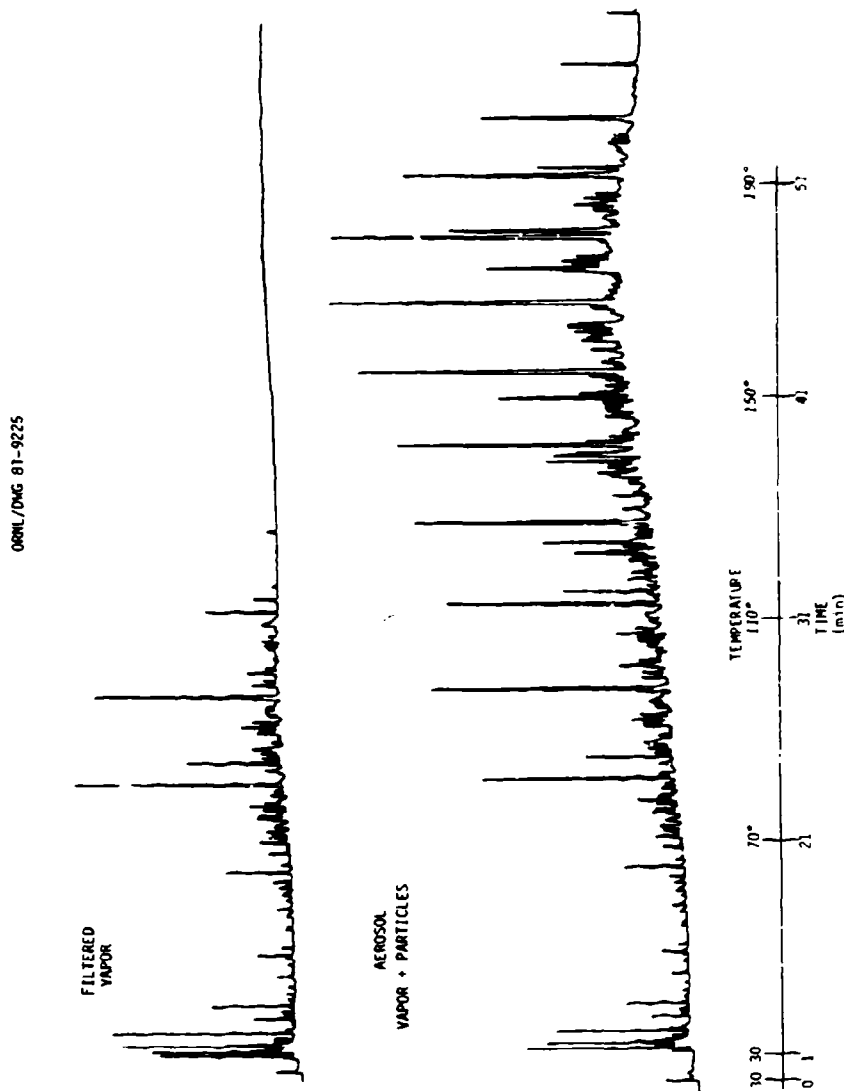


FIGURE 8. COMPARISON OF HIGH RESOLUTION GAS CHROMATOGRAMS OF VAPOR AND UN-FILTERED AEROSOL SAMPLES  
COLLECTED ON TENAX®.

Conditions: 50 m - OV-101 coated glass capillary column. He carrier gas.  
1.8 cc Tenax Desorbed @ 250°C for 10 min. He flow: 6 cc/min.

UNCLASSIFIED

# UNCLASSIFIED

C-16

## ACUTE EXPOSURES OF RATS TO AN INHALED AEROSOL OF DIESEL FUEL

W. Dalbey<sup>1</sup>, S. Lock<sup>1</sup>, B. Holmberg<sup>2</sup>, J. Moneyhun<sup>2</sup>, and M. Guerin<sup>2</sup>  
<sup>1</sup>Biology Division, Oak Ridge National Laboratory, Oak Ridge, TN 37830  
<sup>2</sup>Analytical Chemistry Division, Oak Ridge National Laboratory, Oak Ridge, TN 37830

### ABSTRACT

Diesel fuel aerosols, produced by volatilization of the fuel followed by rapid condensation in ambient air, are used as military obscurants. A toxicological evaluation of an aerosol generated under laboratory conditions is currently underway. Acute range finding exposures of 2, 4, and 6 hours duration have been carried out at aerosol concentrations from 2.67 mg/L to 16 mg/L. Deaths resulting from these exposures occurred within 48 hours. Apparent cause of death was pulmonary hemorrhage and edema. Data from these experiments were used in designing a study in which a series of repeated exposures are followed by measurement of selected biological endpoints shortly after the termination of exposure and at two weeks post-exposure. The endpoints were designed to examine pulmonary function, alveolar macrophage activity, neurological function and immunological function. Changes in body weight, blood chemistry and whole tissue morphology are also being examined. A pilot study involving repeated exposures has been completed and will be discussed along with the design and some preliminary results from the more extensive exposures.

### INTRODUCTION

There is currently little information on the potential health effects of aerosols of diesel fuel such as those used as visual obscurants. For this reason, we are currently exposing laboratory rodents to such an aerosol. The objectives of this research are twofold. The first is to characterize the aerosol produced in the laboratory from diesel fuel #2 under conditions of volatilization and condensation similar to those in the field. The second is to assess the biologic effects of acute and subchronic exposures of rodents to that aerosol under conditions which can be related to potential troop exposure.

In another article in this proceedings (Jenkins et al.), the chemical and physical characterization of the diesel fuel and its aerosol has been discussed. We will discuss the biologic data available to date here. This experiment is ongoing. Therefore, our presentation will deal mainly with experimental approach and data from initial exposures.

# UNCLASSIFIED

# UNCLASSIFIED

C-16

## EXPERIMENTAL ANIMALS

Sprague-Dawley rats (Charles River) of both sexes are used for all exposures. Upon arrival at our laboratory, animals go through a 2-week quarantine during which those positive for infection with Pseudomonas are killed. Some incidence of Kilham's rat virus, RCV, and SDA virus has been observed by serological testing. No gross evidence of infection has been observed.

Animals are housed in suspended wire mesh cages, one rat per cage. Food and water are provided ad libitum except during exposures. During exposures, the cages are placed into 2-m<sup>3</sup> chambers for whole-body exposure to the diesel fuel aerosol. Modifications in the chambers to accomplish uniform distribution of the aerosol have been described elsewhere (Jenkins et al., this proceeding). Aerosol concentration is monitored continuously by two infrared backscatter probes and periodically during each exposure by gravimetric determination. An interlock and alarm system prevents overexposure of the animals in case of a failure in the exposure system.

## ACUTE EXPOSURES

Range-finding exposures were conducted to determine concentrations of the aerosol which would be tolerated by the animals. As part of the second objective of this study, the assessment of biologic effects of exposure, we are attempting to define the relative importance of the concentration, duration, and frequency of exposure. Exposure durations selected to reflect the range occurring with human exposures are 2, 4, and 6 hours. Therefore, the range-finding study consisted of single exposures to varying concentrations for these three exposure durations.

Another objective of the acute exposures was to obtain an indication of whether one biologic endpoint, mortality, was related to the product of aerosol concentration (C) and duration (t) of exposure. One may assume that the Ct product is proportional to the actual dose of material retained by the animal and that a given biologic effect is related to that dose. This assumption can greatly simplify extrapolation of data related to the risk of exposures having various concentrations and durations. However, such an assumption is not always valid and may lead to inaccurate conclusions. For this reason, we have included a test of the relation of the Ct product to biologic endpoints wherever possible in our study, not as the main objective of the exposures but as a secondary one.

Each exposure group in the acute study consisted of five male and five female Sprague-Dawley rats, 12-14 weeks of age. Rats were exposed one time for either 2, 4, or 6 hr to concentrations ranging from 2.67 to 16 mg/liter. After exposure, symptoms which appeared to be related to the Ct product included

# UNCLASSIFIED

C-16

eye irritation, loss of coordination, apparent sedation, and labored breathing. Animals were observed for 2 weeks after exposure. All deaths occurred within the first 48 hr, primarily from pulmonary hemorrhage and edema, as observed during autopsy and in histologic sections of tissues taken at autopsy.

Mortality data are shown in Figure 1. Statistical analysis of these data (exploratory regressions of the proportions dying, and various transforms thereof including probit, logit, and arcsine) revealed that mortality was highly related to the Ct product ( $p = 0.0001$  and 83% of the variation in mortality was explained by Ct). The mortality response and transformations of it seem more nearly linear in log (Ct) than in Ct. Estimation of the influence of exposure duration on mortality by analysis of covariance showed that mortality was slightly greater with 2-hr exposure, but (1) exposure time accounted for less than 10% of the ability of a linear model based on log (Ct) to explain the mortality response and (2) there was no ordered relation of mortality to duration of exposure. Therefore, the dominant factor in predicting response is the Ct product.

## DESIGN OF REPEATED EXPOSURES

Since mortality after single exposures was essentially proportional to the Ct product, an estimate of the maximum tolerated dose (MTD) for multiple exposures was based on the Ct product. The lower confidence bound of the Ct product resulting in 1% mortality after single exposures was 8 hr·mg/L. Thus, 8 hr·mg/L was taken as the MTD, the "dose" expected to result in very little or no mortality after single exposures.

This MTD was used in the repeated exposures conducted to date. As stated before, one major purpose of these exposures is to help define the relative importance of aerosol concentration, duration of each exposure, and frequency of exposures. Exposure durations were selected as 2 and 6 hours. Concentrations were chosen to provide a Ct of 8 hr·mg/L for both exposure durations. The frequency of exposure was set at either 1 or 3 exposures per week. It was felt that 3 exposures per week would allow little time for recovery of the animals between exposure while 1 exposure per week could permit significant recovery from the acute effects of exposure before the subsequent dosing was given.

Thus the experimental design is a cube, as shown in Figure 2. Each corner of the cube represents one experimental group of animals and one set of exposure conditions. An additional set of four groups was originally in our design ( $Ct=8/3$ ) but it is not certain at this time if those groups will remain in the design. They will remain only if biologic effects after exposure to Ct of 8 are great enough to indicate a significant impact from exposures to a lower Ct. The study is conducted in blocks of 4

# UNCLASSIFIED

761

# UNCLASSIFIED

C-16

groups each, allowing time for data evaluation and changing the design between blocks. All groups receive a total of 9 exposures. Those exposed 3 times per week are treated for 3 weeks; those exposed once weekly are treated for 9 weeks. Biologic assays are performed within the first few days after the last exposure and again after 2 weeks without exposure. All controls are sham-exposed.

## DESCRIPTION OF BIOLOGIC ENDPOINTS

Another objective of the repeated exposures is to identify the more pronounced areas of toxicity resulting from exposure. Our approach to this question has been a battery of assays, some of which are performed on the same animal. These assays are listed below:

- Body weight and food consumption during and after exposures.
- Clinical chemistry on serum samples, blood cell and platelet counts, and specific gravity of urine.
- Alveolar macrophage (AM) function
  - 1) Number of lavaged AM's
  - 2) Phagocytic activity of AM's attached to glass
  - 3) Bactericidal activity of free cell population lavaged from lung
- Pulmonary function tests
  - 1) Pulmonary resistance
  - 2) Lung volumes
  - 3) Quasi-static pressure-volume curves
  - 4) Maximal exhaled flow-volume curves
  - 5) Multibreath nitrogen washout curves
  - 6) Carbon monoxide diffusing capacity
- Neurotoxicity screening assays
  - 1) Startle reflex
  - 2) Tail flick
  - 3) Forelimb grip strength
- Immunotoxicity assay: humoral antibody formation in response to bovine serum albumin challenge
- Morphology of respiratory tract and major organs
- Body weight, food consumption, clinical chemistry, and blood cell counts, urinary specific gravity, and histopathological examination of tissues are common to many toxicological studies in which the potential for systemic toxicity exists.

# UNCLASSIFIED

C-16

The alveolar macrophage and pulmonary function tests were chosen because of possible effects of retained aerosol on the respiratory tract. The alveolar macrophages are free ameboid scavengers which engulf particles deposited on the surface of the alveoli and aid in the destruction and clearance of those particles from the lung, generally via the trachea. This is a very important protective mechanism because the lungs are continually exposed to the exterior environment. If the phagocytic activity of the AM's is compromised, the animal would be less able to respond to a particulate challenge, such as a bacteria. The assays used here include the number of AM's which can be obtained by lavaging the lungs with a standard volume of saline. This number reflects the number of AM's in the lung. The competence of these AM's to phagocytize yeast and kill bacteria is measured in vitro.

The pulmonary function tests are generally designed to measure pulmonary mechanics in the living animal. Pulmonary resistance is an index of the resistance in the respiratory tract to air flow. Lung volumes and pressure-volume curves are included to measure the distensibility of the lung under nearly static conditions, generally a reflection of tissue characteristics. Flow-volume curves during maximal forced exhalations reflect the dynamic properties of the lung and can be used to detect relatively subtle alterations in the lower airways. Diffusing capacity reflects the overall capability to exchange gas (CO) across the lung.

Screening tests for toxicity in the nervous system include the startle reflex (measure of reflex response to an external noise), tailflick (responsiveness to heat stimulation of the tail as an index of damage to a peripheral pain reflex), and the forelimb grip strength (an index of voluntary muscle control in the anterior portion of the body).

The humoral antibody assay may reflect the ability of an exposed animal to respond to a foreign antigen.

## BIOLOGIC EFFECTS OF REPEATED EXPOSURES

At this time, exposure and biologic assays of the first half (2 groups) of the first block of 4 treatment groups have been completed. Thus, data are available for animals exposed to (1) 0 mg/l, 6 hr/exposure, 3 exposures/wk and (2) 4 mg/l, 2 hr/exposure, 3 exposures/wk. In both cases, animals were assayed just after the last exposure and after a 2-wk recovery period. No statistical analyses have been performed and animal numbers are not adequately large for direct comparison between exposed and untreated groups (4 rats per sex for each endpoint at each time of assay). The statistical strength of the experimental design lies in the large number of groups of animals rather than in direct comparison between any 2 groups.

# UNCLASSIFIED

763

# UNCLASSIFIED

C-16

However, some trends in the data are apparent at this time and may indicate effects of exposure. The number of viable alveolar macrophages lavaged from the lungs of exposed animals was greater than that obtained from sham-treated controls, as seen in Table 1. Numerous other cell types not normally observed in control animals were also present. This increase might be expected to result from the influx of diesel fuel particles into the lung. When an aliquot of the cell suspension containing the macrophages was allowed to settle onto a glass coverslip, a higher percentage of them attached to the glass (see Table 2). The ability of these cells to phagocytize yeast particles, however, was apparently reduced (Table 2). Thus, the diesel fuel causes a rather complex series of events involving changes in the number and type of free cells in the lung and their ability to engulf foreign particles.

The most definite alteration in pulmonary function is in the deflation pressure-volume curves, as seen in Figure 3. Here, change in lung volume is plotted against the pressure difference across the lungs (transpulmonary pressure) which inflates the lungs. The reference volume in this curve is residual volume, the volume of air remaining in the lungs after full deflation. The lungs of exposed animals did not appear to be as greatly distended at full inflation as were the lungs of sham-exposed controls. The difference in lung volume from residual volume to full inflation (the vital capacity) appeared to be less, indicating possible changes in the composition of the tissues in the lung resulting from exposure to diesel fuel aerosol. This trend was present in both sexes at both 2 days and 2 weeks after the last exposure.

Finally, there was an increase in the time of response in the tail flick assay (a decreased responsiveness to heat on the animal's tail). Some type of neurologic damage in the lower part of the body of exposed animals may have been responsible (see Table 3).

## ANCILLARY STUDIES

In addition to the core experiments described above, additional studies are underway. One involves quantifying the amount of aerosol retained in various areas of the respiratory tract in relation to exposure conditions. Rather than assuming that the effective dose of diesel fuel is proportional to the Ct product with both 2 and 6 hour exposures, we are measuring that dose. Decachlorobiphenyl, easily detected by gas chromatography, is used as a tracer for the particulate phase of the aerosol. In conjunction with the deposition study, other animals are injected with [<sup>3</sup>H]thymidine at intervals after diesel fuel. The thymidine is incorporated into DNA of dividing cells. Thus, areas of the respiratory tract where cell proliferation is increased to repair the damage done by the diesel fuel exposure may

# UNCLASSIFIED

C-16

be identified. This incorporation into DNA may be seen microscopically by autoradiography and quantified. Thus the primary site of a proliferative response, presumably a reflection of damage, may be determined.

Lastly, pulmonary resistance and breathing pattern during inhalation of diesel fuel are being measured. To date, animals have been anesthetized and a cannula tied in their trachea for these measurements during inhalation of the aerosol. Under these conditions, there is a sex-related increase in pulmonary resistance during exposure to diesel fuel aerosol, the females being more reactive (see Figure 4). This increase is probably reflex, initiated by receptors in the airways. The standard errors of the means shown in Figure 4 are large. Some animals responded much more than others. In fact, there may be a responder-nonresponder dichotomy. This possibility is being further investigated.

## CONCLUSIONS

A system was constructed to expose laboratory rodents to an aerosol of diesel fuel similar to that found under field conditions. Extensive chemical and physical characterization of that aerosol has been performed. An acute mortality study with single exposures showed that mortality was essentially proportional to the Ct product over the range of exposure conditions used. A Ct product of 8 hr·mg/L was chosen as a maximal tolerated dose and successive exposures to that Ct were begun. After 9 exposures, preliminary data indicate possible changes in alveolar macrophage function, pulmonary function, and one neurotoxicity screening test.

## ACKNOWLEDGEMENT

Research sponsored by the US Army Medical Research and Development Command, Fort Detrick, Frederick, MD 21701, under Army Project Orders 9600 and 0027 and by the Office of Health and Environmental Research, U.S. Department of Energy, under contract W-7405-eng-26 with the Union Carbide Corporation.

# UNCLASSIFIED

765

**UNCLASSIFIED**

C-16

TABLE I. MILLIONS OF Viable ALVEOLAR MACROPHAGES LAVAGED FROM THE LUNG (MEAN  $\pm$  S.E.)

	<u>Exposed</u>	<u>Nonexposed</u>
<u>2 days post-exposure</u>		
males	8.3 $\pm$ 4.1	3.9 $\pm$ 1.1
females	6.1 $\pm$ 2.8	2.4 $\pm$ 0.5
<u>2 weeks post-exposure</u>		
males	7.7 $\pm$ 2.1	3.6 $\pm$ 1.6
females	8.6 $\pm$ 1.9	1.5 $\pm$ 0.4

**UNCLASSIFIED**

C-16

TABLE II. PERCENT OF MACROPHAGES ATTACHED<sup>1</sup> AND BINDING INDEX IN PHAGOCYTOSIS ASSAY WITH YEAST. (MEAN  $\pm$  S.E.)

	Exposed		Nonexposed	
	attached	BI <sup>2</sup>	attached	BI
<u>2 days post-exposure</u>				
males	7.8 $\pm$ 2.6	5.6 $\pm$ 0.2	1.9 $\pm$ 0.4	10.6 $\pm$ 3.0
females	5.0 $\pm$ 0.6	4.6 $\pm$ 1.0	1.6 $\pm$ 0.4	11.8 $\pm$ 2.6
<u>2 weeks post-exposure</u>				
males	1.6 $\pm$ 0.3	3.7 $\pm$ 1.0	0.6 $\pm$ 0.1	6.8 $\pm$ 1.3
females	1.1 $\pm$ 0.2	4.5 $\pm$ 0.9	0.6 $\pm$ 0.1	5.8 $\pm$ 0.4

1) Percent of suspended cells which attached to glass coverslip during assay procedure.

2) Binding index is number of yeast per 100 alveolar macrophages.

**UNCLASSIFIED**

767

**UNCLASSIFIED**

C-16

TABLE III. RESULTS OF TAIL FLICK ASSAY: SECONDS TO REMOVE TAIL FROM HEAT SOURCE. (MEAN  $\pm$  S.E.)

	<u>Pre-exposure</u>	<u>2 days post-exposure</u>	<u>2 weeks post-exposure</u>
<b><u>Males</u></b>			
exposed	2.1 $\pm$ 0.1	2.8 $\pm$ 0.3	2.0 $\pm$ 0.2
nonexposed	2.3 $\pm$ 0.4	2.5 $\pm$ 0.3	2.4 $\pm$ 0.3
<b><u>Females</u></b>			
exposed	2.2 $\pm$ 0.3	2.2 $\pm$ 0.2	3.3 $\pm$ 0.5
nonexposed	2.0 $\pm$ 0.4	2.3 $\pm$ 0.3	2.5 $\pm$ 0.3

**UNCLASSIFIED**

C-16

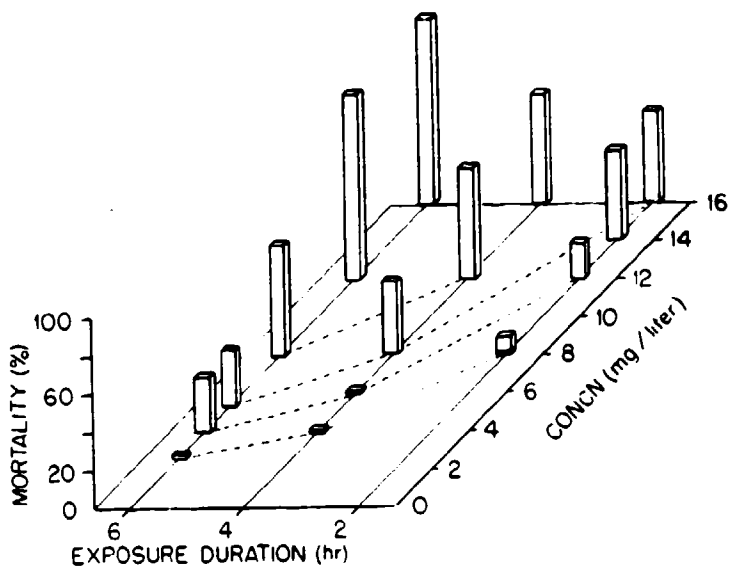


Figure 1. Three-dimensional plot showing percent mortality among groups of 10 rats after single exposures to varying combinations of concentration and duration. Dashed lines connect points of equivalent  $C_t$  products.

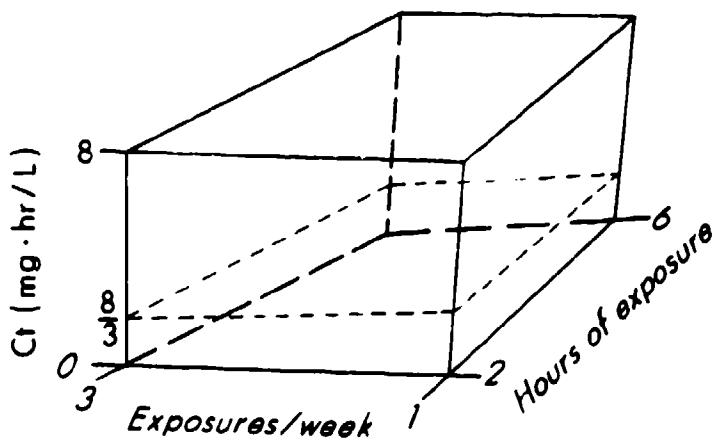


Figure 2. Experimental design of repeated exposures.

**UNCLASSIFIED**

769

UNCLASSIFIED

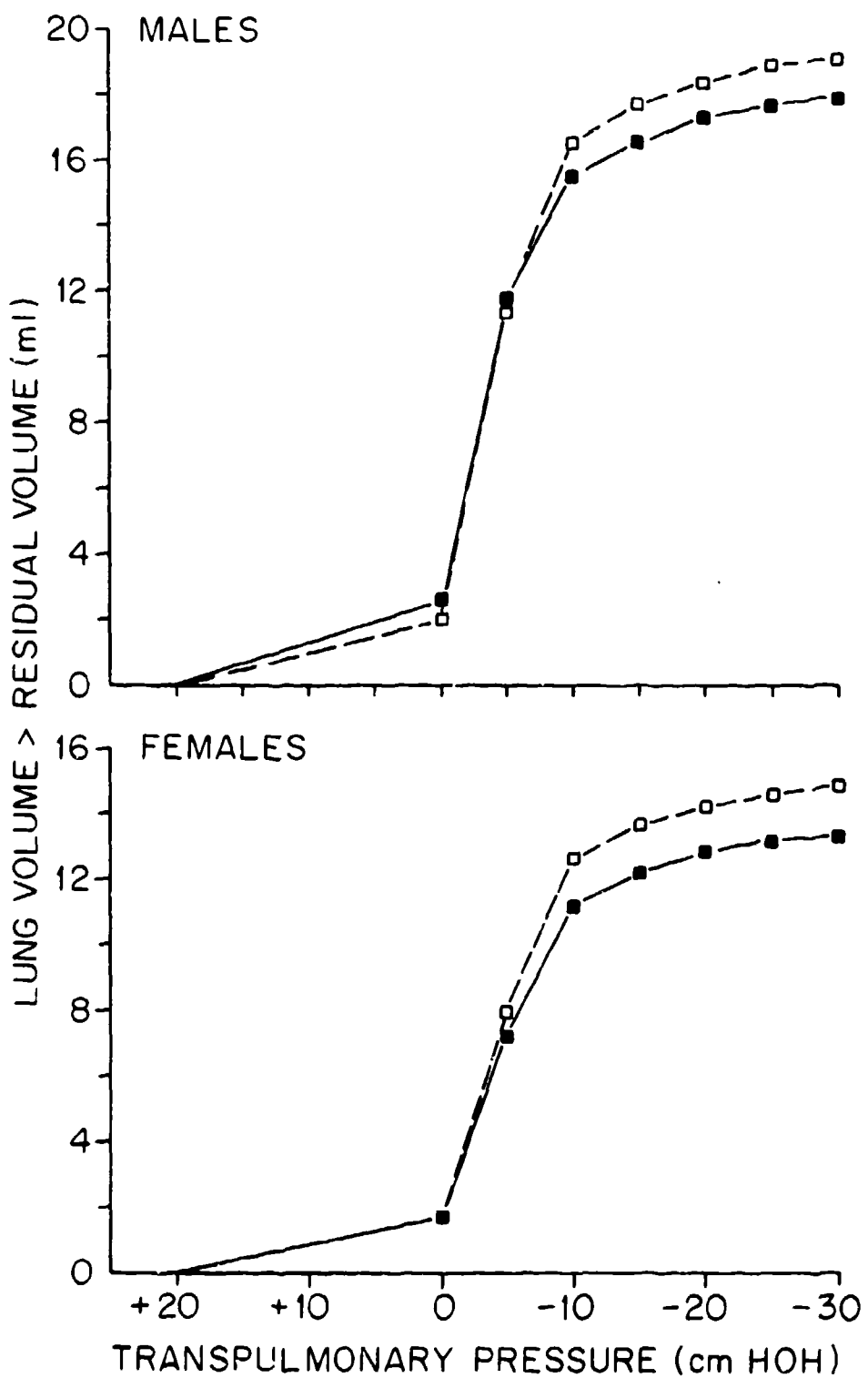


Figure 3. Quasistatic pressure-volume curves from exposed (■) and untreated (□) animals at 2 weeks after last exposure.

UNCLASSIFIED

UNCLASSIFIED

C-16

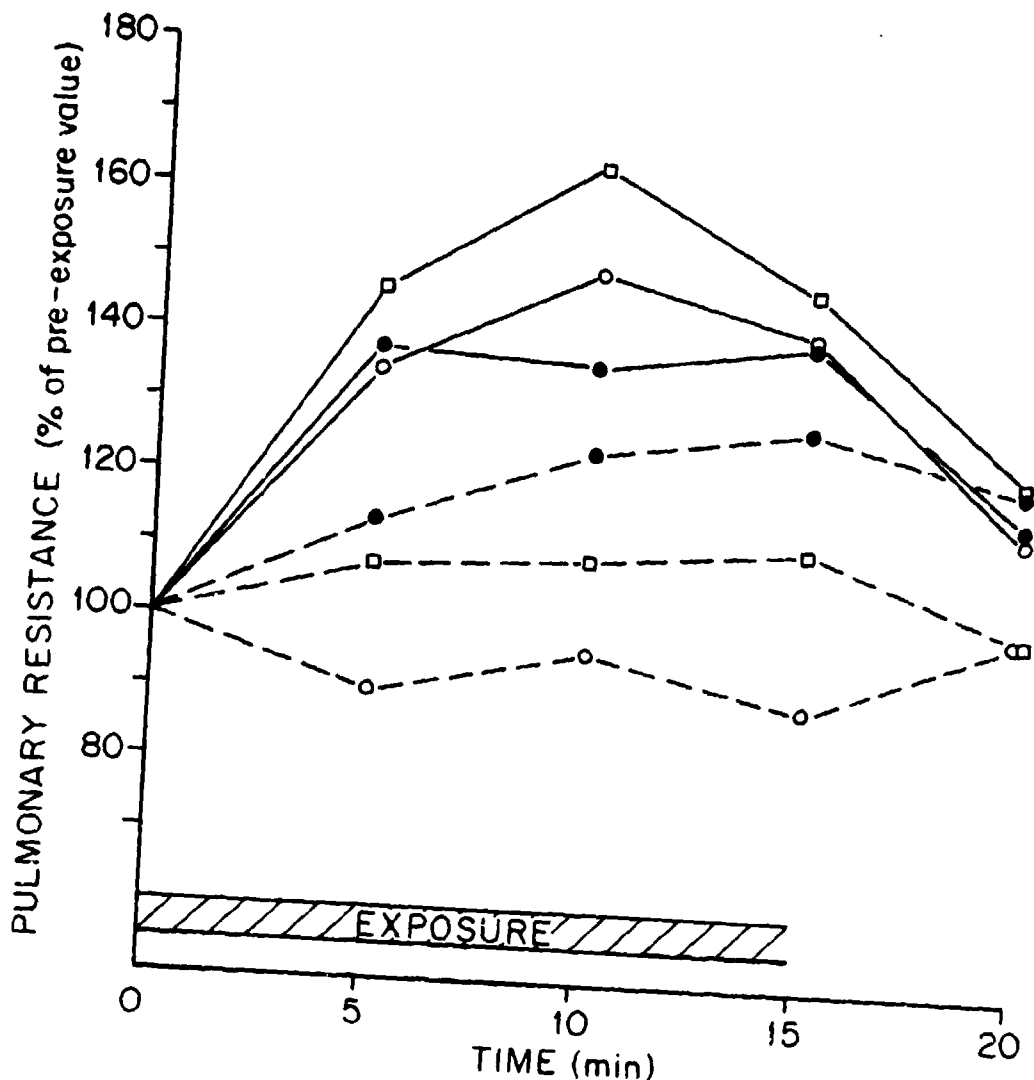


Figure 4. Pulmonary resistance during exposure to diesel fuel aerosol at 1/3 mg/L (○), 2 mg/L (●), and 4 mg/L (□). Solid lines represent females; dashed lines represent males. Data are means of resistance values expressed as percent of resistance for each rat before exposure began.

UNCLASSIFIED

# UNCLASSIFIED

C-17

## SUBSTITUTION OF NONTOXIC DYE IN M18 COLORED SMOKE GRENADES

Michael D. Smith  
Chemical Systems Laboratory  
Aberdeen Proving Ground, MD

### ABSTRACT

The current M18 yellow and green smoke grenades use component dyes benzanthrone and vat yellow 4. In 1979, a report issued by the National Cancer Institute stated that vat yellow 4 was proven carcinogenic to mice. Chemical Systems Laboratory identified a dye, D & C No. 11, which is certified by the Food and Drug Administration for use in drugs and cosmetics. New yellow and green smoke mixes incorporating this nontoxic dye were successfully developed and tested. This effort will reduce the health hazard to manufacturing and using personnel, and will result in an average annual estimated cost savings of \$450,000 due to the lower cost of the replacement dye.

### 1. DESCRIPTION

The standard M18 colored smoke grenade is a burning type munition used for signalling purposes. The grenade is a cylindrical metal container, 4.5 inches long by 2.5 inches in diameter. It contains approximately 325 gm of either green, red, yellow or violet pyrotechnic smoke mix. A standard M201A1 ignition fuze is screwed into a fuze adapter located on top of the grenade and serves to initiate functioning of the munition. The red, yellow, and violet smoke grenades have a single smoke emission hole in the bottom. The green smoke grenade has four smoke emission holes in the top (fuze end) in addition to a hole in the bottom. All emission holes are covered with tape to protect the smoke mix and starter mix from moisture.

The pyrotechnic configuration consists of a central core hole in the consolidated pyrotechnic smoke mix. The approved formulation contains sulfur as the fuel, potassium chlorate as the oxidizer, sodium bicarbonate as a coolant, and the appropriate color organic dye. Table I shows the composition of the standard M18 grenades.

### 2. PROBLEM

Research studies conducted to date indicate that the organic dyes in colored smoke pyrotechnic formulations pose potentially serious health hazards to occupationally exposed personnel. An Edgewood Arsenal Technical Report, EB-TR-74064, December 1974, stated that disperse red 9, vat yellow 4, and benzanthrone dyes are potential carcinogens and recommended that they be replaced. A National Cancer Institute Report, NCI-CG-TR-134, 1979, reported that vat yellow 4 was found to cause cancer in male mice. And, most recently, research conducted in 1980 by Oak Ridge National Laboratory revealed that

# UNCLASSIFIED

# UNCLASSIFIED

C-17

all four smoke dye mixes exhibited mutagenic activity in the crude (as commercially received) forms. These health effects are of concern as they give rise to a potential ban on production and use of colored smoke munitions.

## 3. SOLUTION

A solution to the health effects problem is the substitution of dyes which are noncarcinogenic and of minimal (reversible, nonincapacitating) toxicity to industrial personnel and the environment. Programs to identify and qualify candidate substitute dyes are now underway at Chemical Systems Laboratory. In order for a replacement dye to be acceptable, it must qualify both technically and medically.

## 4. SELECTION CRITERIA FOR COLORED SMOKE DYES

### 4.1 TECHNICAL EVALUATION

The M18 colored smoke signals produce smoke by volatilization of colored materials (organic dyes). The finely divided dyes are intimately combined with a pyrotechnic mixture of an oxidizer, a fuel, and a coolant. The heat produced by the reaction of the fuel and oxidizer volatilizes the dye which condenses outside the munition to form the colored smoke. A coolant chemical is added to regulate the rate of burning and lower the temperature of combustion so as to prevent excessive decomposition of the dye, evidenced by decolorization or flaming.

A suitable dye for the production of colored smokes must possess thermal stability, volatility, and purity of color.<sup>1</sup> A simple test can be used to assess a dye for these three properties simultaneously. A small amount of the dye is placed in a test tube and gently heated. If the dye shows indication of subliming or vaporizing readily, it may be of use, but if it melts long before vaporization or decomposes, it is not suitable for use in smoke mixtures. Not all dyes which give off

<sup>1</sup> Heath, G. D., "The Formation of Colored Smoke Colors, Part I of Review of Suitable Organic Dyestuff, PR 251", Great Britain, Sep 43.

# UNCLASSIFIED

# UNCLASSIFIED

C-17

colored vapors in this test will operate successfully in a smoke munition, but no dye which has failed the test tube trials has been found to function properly in smoke mixtures.<sup>2</sup>

Dyes which pass the preliminary test are then tested by mixing with a combustion mixture. The heat produced by the fuel mixture must vaporize the dye without destroying it. The dye should have a high flash point so that the dye is not inflamed. And in the absence of true sublimation, the melting and boiling points of the dye should lie close together to prevent any great amount of liquid dye being present in the munition, as the liquid will slow down or stop the combustion.<sup>2</sup>

The three chief factors which render a dye suitable for the production of a colored smoke (volatility, thermal stability, and color purity) are closely related to the chemical constitution of the dye.<sup>2</sup> In an early investigation of volatility and thermal stability of dyes, it was concluded that dyes containing amino or substituted amino groups, but not sulfonic groups or sulfonic groups in the form of sodium salts, were suitable for the production of colored smokes.<sup>3</sup> These conclusions were confirmed and amplified by a British investigator in a systematic survey of the common dyestuffs. This investigator formulated the following rules to predict the volatility and thermal stability of a given dye.<sup>1</sup>

- a. The molecular weight must not exceed 450.
- b. The most satisfactory dyes are members of the following series: Anthraquinone, azine, azo, quinoline, and xanthene.
- c. The following groups must be absent: Sulfonic, hydrochloride, nitro, nitroso, quaternary ammonium, and oxonium.
- d. The following groups may be present: Amino and substituted amino, alkyl, aryl, chloro, bromo, hydroxy, and alkoxy.
- e. The dye must not tend to undergo auto-condensation.

<sup>1</sup> Heath, G. E., The Formation of Colored Smoke Clouds, Part 1 of Review of Suitable Organic Dyestuff, PR 2547, Great Britain, Sep 43.

<sup>2</sup> Ray, Arthur B., Industrial and Engineering Chemistry, Vol 18, No. 1, Production of Colored Smoke Signals, 1926.

<sup>3</sup> Li, Y. H., and Shih, Chun. Journal of the Chinese Chem. Society, Vol 2, pp. 205-10, 1934.

# UNCLASSIFIED

# UNCLASSIFIED

C-17

Even when a particular dye possesses the required thermal stability and volatility, it does not necessarily follow that it will give a satisfactory colored smoke cloud. In order to act as a satisfactory signal, the color must be readily distinguishable under all conditions and sufficiently characteristic to avoid confusion with other colors. Dyes which are unacceptable by themselves may be useful in a mixture. For example, no single dye is presently known to give a green smoke, but a very satisfactory cloud results from the blending of suitable blue and yellow dyes.

The relationship between color and chemical constitution is complicated, since the color depends not only on the chromogen (color producing molecular group) and the auxochromes (substituent groups which intensify the color), but also on the relative position of these within the dye molecules. Nevertheless, the preceding rules may be sometimes usefully applied to members of a particular series.<sup>1</sup>

## 4.2 MEDICAL EVALUATION

Candidate replacement dyes with the requisite technical properties must also qualify as being non-oncogenic and of minimal toxicity.

A detailed medical evaluation program (MEP) has been planned which will provide for a toxicology data base to answer these questions. The MEP focuses on industrial site exposure to the worker and the environmental consequences of industrial waste and fallout during training. The US Army Medical Research and Development Command (USAMRDC) through the US Army Medical Bioengineering R&D Laboratory (USAMBRDL), Ft Detrick, Maryland, will provide the health hazard assessment required for the replacement smoke formulations.

## 5. TESTING OF SUBSTITUTE DYES

In July 1979, Chemical Systems Laboratory began a search for candidate substitute dyes. The search for a qualified replacement red dye for disperse red 9 has been frustrating. A literature search for red dyes which have the correct chemical and physical properties was performed. Of the more

---

<sup>1</sup> Heath, G. D., The Formation of Colored Smoke Clouds, Part 1 of Review of Suitable Organic Dyestuff, PR 2547, Great Britain, Sep 43.

# UNCLASSIFIED

# UNCLASSIFIED

C-17

than 120 red dyes evaluated, all but two were eliminated from further consideration for one or more of the following reasons: (a) has known hazardous health effects, (b) no longer commercially available, or (c) produces unsatisfactory colored smoke clouds. Two dyes which produced a satisfactory red smoke in preliminary testing are being evaluated further. Both are produced by Mobay Chemical Corporation and are known as Macrolex Red 1069 and Oil Red G Type F28. At this time little is known about the toxicology of these dyes as they are recent commercial developments.

Much greater success has been obtained in finding a replacement for vat yellow 4 dye. A dye was identified which produces an excellent yellow smoke cloud and is listed by the Food and Drug Administration for use in drugs and cosmetics. This dye, 2-(2-quinolyl)-1,3-indandione, (synonyms: chinoline yellow, D&C yellow 11, solvent yellow 33, quinoline yellow SS, CI No. 47000) has been under intensive evaluation at Chemical Systems Laboratory for over a year.

Chinoline has been tested as a replacement for both vat yellow 4 and benzanthrone dyes in both the yellow and green smoke formulations. In initial studies, the new dye was combined with various pyrotechnic ingredients in differing ratios in order to optimize smoke grenade performance and meet the requirements of MIL-G-12326. These formulations were then subjected to accelerated storage (12 weeks at 160°F) to assure the stability of the smoke mixes. The optimum formulas are presented in Table II.

After selection of the optimum improved formulations, grenades were produced for final performance testing. The purpose of the final test program was to evaluate and compare the performance of the improved yellow and green grenades with standard yellow and green M18 grenades. An outline of the test plan is presented as Table III.

Final testing was performed just recently by an independent evaluator, and while test data is still being analyzed, the improved yellow and green grenades appear acceptable in all technical aspects.

## 6. IMPLEMENTATION

When final technical approval is given to the improved mixes, necessary changes to the technical data package for the M18 grenade will be made so that the improved grenades can be produced. Of course,

# UNCLASSIFIED

# **UNCLASSIFIED**

C-17

the final acceptance for production of the improved smoke mixes may depend on health effects data from the medical evaluation program.

## **7. BENEFITS**

The most important benefit derived from the substitution of chinoline yellow dye into the yellow and green colored smoke grenades is a reduction (presumably) in the health hazards to occupationally exposed personnel. An additional benefit gained is a substantial cost savings. The chinoline yellow dye costs less than the dyes it replaces, so there is a savings of \$1.77 per yellow grenade and \$.49 per green grenade. The average annual savings based on projected grenade requirements is \$452,000.

# **UNCLASSIFIED**

UNCLASSIFIED

TABLE I. STANDARD LOADING FOR M18 COLORED SMOKE GRENADES

Smoke	Military Specification	Chemical Nomenclature	Identification of dyes		Component	M18 grenade formulations Weight (%)
			Trade Name			
Red	MIL-D-3284C 24 June 1971	1-Methylaminoanthraquinone	Disperse Red 9		Dye, Disperse Red 9 Sodium bicarbonate Potassium chlorate Sulfur	40 25 26 9
Yellow	MIL-D-0050029C(MU) 26 April 1968	Dibenzo (b, def) chrysene-7,14-dione	Dye, Vat Yellow 4		Vat Yellow 4 Benzanthrone Sodium bicarbonate Potassium chlorate Sulfur	14 24.5 33.0 20.0 8.5
	MIL-D-0050074C(MU) 9 May 1968	7H-Benz (de) anthracene-7-one	Dye, benzanthrone			
Green	MIL-D-003277(MU) 26 March 1968	1,4-Di-p-toluidinoanthraquinone	Dye, Solvent Green 3		Solvent Green 3 Vat yellow 4 Benzanthrone Sodium bicarbonate Potassium chlorate Sulfur	28 4 8 22.6 27 10.4
	MIL-D-0050029(MU) 26 April 1968	Dibenzo (b,def) chrysene-7,14-dione	Dye, Vat Yellow 4			
	MIL-D-0050074C(MU)	7H-Benz (de) anthracene-7-one	Dye, benzanthrone			
Violet	MIL-D-3691B 20 July 1970 (Violet smoke mix dyes preblended)	1,4-Diamino-2,3-dihydroanthraquinone (80 + 2%) 1-Methylaminoanthraquinone (20 + 2%)	Chemical name Disperse Red 9		Violet smoke mix Sodium bicarbonate Potassium chlorate Sulfur	42 24 25 9
Starter mix					Potassium Chlorate Sulfur Sodium bicarbonate Corn starch	43.2 16.8 30.0 10.0

UNCLASSIFIED

**UNCLASSIFIED**

C-17

TABLE II. IMPROVED LOADING FOR YELLOW AND GREEN M18 GRENADES

<u>Smoke</u>	<u>Component</u>	<u>Weight (%)</u>
Improved Yellow	Chinoline yellow dye	42
	Magnesium carbonate	21
	Potassium chlorate	22
	Powdered Sugar	15
Improved Green	Chinoline yellow dye	12.5
	Solvent green 3 dye	29.5
	Magnesium carbonate	18
	Potassium chlorate	24
	Powdered sugar	16

**UNCLASSIFIED**

# UNCLASSIFIED

C-17

TABLE III. TEST PLAN

A. ENVIRONMENTAL STORAGE TESTS

1. Hot - Dry @ +160°F, 5-10% RH
2. Wet - Hot @ +113°F, 85% RH
3. Extreme Cold @ -65°F
4. Cyclic. (Hot/Dry - Wet/Hot - Extreme Cold) weekly
5. Ambient (controls)

B. PACKAGED ROUGH HANDLING

1. High Altitude - low temperature
2. Transportation vibration
  - a. Hot, +160°F
  - b. Cold, -65°F
  - c. Room ambient
3. Bounce (Transportation Shock)
  - a. Hot, +160°F, preconditioned
  - b. Cold, -65°F, preconditioned
  - c. Room ambient
4. Five foot Drop Test
  - a. Hot, preconditioned +160°F
  - b. Cold, preconditioned -65°F
  - c. Room ambient

C. FUNCTIONAL EFFICIENCY TRIALS

1. Grenades after environmental storage. Precondition to operating conditions of AR 70-38.
2. Grenades after rough handling
  - a. Hot cyclic safety trials
  - b. Cold soak safety trials
  - c. Ambient (controls)

D. SMOKE COLOR IDENTIFICATION TESTS

# UNCLASSIFIED

# UNCLASSIFIED

C-18

## IMPROVEMENTS AND PROPOSED DEVELOPMENT OF ALKALI HALIDE SMOKES<sup>1</sup>

L. A. Mathews and P. St. Amand  
Naval Weapons Center  
China Lake, California 93555

### ABSTRACT

Alkali halide smokes produce hygroscopic nuclei by oxidizing an organic fuel with perhalates of the alkali metals in specially chosen combinations. These smokes have some advantages over conventional screening smokes in their overall adaptability to battlefield use, extended storage, safety and low toxicity.

Previous alkali chloride formulations used in weather modification research were limited as screening smokes because the nuclei that were generated picked up water rapidly only at relative humidities greater than 80%, thus limiting their use geographically. A program was therefore initiated to improve the deliquescence of these nuclei. Based on vapor pressure studies, modification of the previous alkali chloride formulation itself has increased the yields at lower relative humidities. The smokes are now effective over a wide range of relative humidities and can be used throughout most of the world a good part of the time.

It is proposed to explore the possibilities of using different binders and different additives to change the optical properties of the alkali halide smokes. New energetic pyrotechnic and explosive compositions will be devised for rapid and efficient dispersion. With a little experimentation using an explosive fuel binder, loadings for smoke grenades, bombs, and shells that also serve as anti-personnel devices can be developed. Using fuel binders such as polybutadiene or higher energetic binders, smoke rockets can be developed that will permit laying of either lateral curtains of smoke or stratus decks.

<sup>1</sup>Completion of this paper was precluded by the discovery of a formulation with significantly improved screening properties at low relative humidities.

# UNCLASSIFIED

783

# UNCLASSIFIED

C-19

## A LABORATORY INVESTIGATION OF AEROSOL AND EXTINCTION CHARACTERISTICS OF OBSCURANT SCREENS PRODUCED FROM ALKALI HALIDE PYROTECHNICS

J. T. Hanley and E. J. Mack  
Calspan Corporation  
Advanced Technology Center  
Buffalo, NY 14225

### ABSTRACT

Under contract with the Naval Air Systems Command (AIR-310), Calspan has been conducting an experimental investigation of the feasibility of producing stable, optical-obscurant screens (smokes and fogs) with artificially-generated hygroscopic aerosols at relative humidities of ~30 to 95%. The objectives of this investigation are to evaluate the physical, optical, chemical, and growth characteristics of aerosols generated from the Navy's Salty Dog pyrotechnic, and alternate formulations, as functions of humidity. The investigation has included individual-particle growth studies performed under the microscope and large-scale tests performed in Calspan's 590 m<sup>3</sup> chamber. Results from this investigation show that the Salty Dog pyrotechnic produces copious quantities of hygroscopic aerosols which exhibit significant growth at humidities above ~70%, producing increased aerosol mass yield and extinction. Data documenting particle growth, I.R. and visible wavelength extinction, mass yield, and hysteresis growth effects are presented. A limited comparison of Salty Dog and white phosphorus extinction yields is also presented.

### 1. INTRODUCTION

The scope of this effort is limited to an experimental evaluation of the efficiency of "Salty Dog" pyrotechnic aerosols as an alternative to white phosphorus in producing conditions of restricted visibility (i.e., smoke screens) at subsaturated humidities. In the experiments, smokes (fogs) are generated by burning a prescribed quantity of the pyrotechnic under prescribed humidity conditions within the well-mixed 590 m<sup>3</sup> chamber. In addition, the growth of individual particles as a function of RH was studied using a microscope, spider thread and a RH-controlled viewing chamber. In this paper, results of the experiments, i.e., aerosol size spectra, aerosol growth, mass loading and extinction as functions of relative humidity are presented. Extinction data are compared with data obtained in phosphorus pentoxide smokes, and particle growth data are compared with both measurements and theoretical estimates of the growth of pure salts.

#### 1.1 FACILITIES AND INSTRUMENTATION

Large-scale laboratory experiments are carried out in Calspan's 590 m<sup>3</sup> Chamber. The facility's large size (~9 m diameter by ~9 m high) minimizes wall effects, provides relatively long path lengths for extinction measurements, and provides for a useful aerosol lifetime of many hours. A complete air handling capability permits, as required, the removal of virtually all particulate and gaseous contaminants prior to each experiment, the introduction of specified aerosols, and control of humidity from 20 to 98% RH. A cut-away view of the chamber facility and a list of instrumentation pertinent to this investigation are provided in Figure 1 and Table 1, respectively. Specific details

# UNCLASSIFIED

785

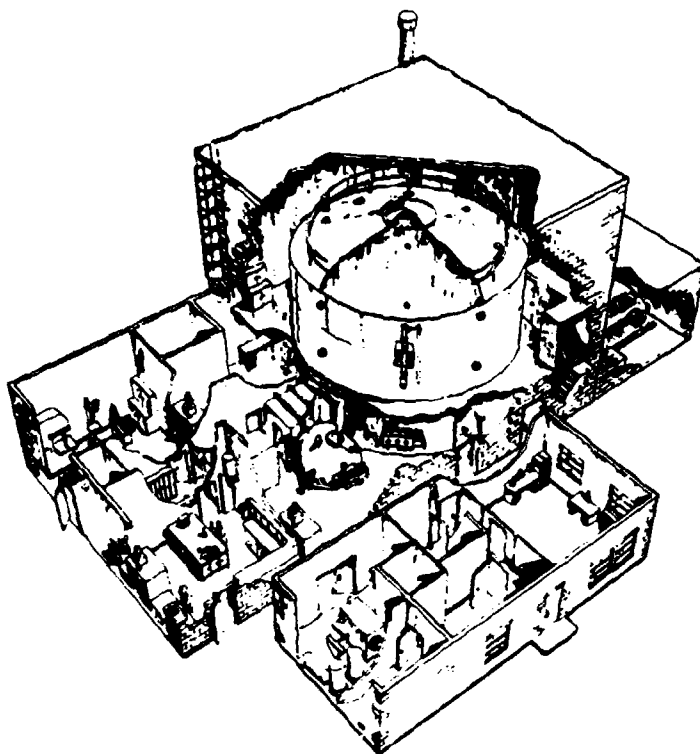
**UNCLASSIFIED**

Figure 1. Cut-Away View of Calspan's Chamber Facility.

Table 1  
INSTRUMENTATION USED IN LARGE-SCALE EXPERIMENTS

**EXTINCTION:**

	<u>Wavelength</u>	<u>Extinction Coefficient</u>
CALSPAN TRANSMISSOMETER	Visible, 0.4-0.5 $\mu\text{m}$ $\lambda$	$0.1 \text{ to } 0.001 \text{ m}^{-1}$
CALSPAN IR TRANSMISSOMETER	Continuously Variable, 2-12 $\mu\text{m}$ $\lambda$	$0.1 \text{ to } 0.001 \text{ m}^{-1}$
MRI NEPHELOMETER	Visible $\lambda$	$(8.0 \text{ to } 0.5) \times 10^{-4} \text{ m}^{-1}$

**AEROSOLS:**

GARDNER SMALL PARTICLE DETECTOR	TOTAL CONCENTRATION ( $> .0025 \mu\text{m}$ )
TSI ELECTRICAL AEROSOL ANALYZER	SIZE SPECTRA ( $.01-.75 \mu\text{m}$ dia)
ROYCO OPTICAL PARTICLE COUNTER	SIZE SPECTRA ( $.3-3. \mu\text{m}$ dia)
CALSPAN DROPLET SAMPLER (GELATIN REPLIC.)	SIZE SPECTRA ( $3.-50 \mu\text{m}$ dia)
CASELLA CASCADE IMPACTOR	ELEMENTAL CHEM. ANAL. VIA SEM
LO-VOL FILTER SAMPLER	MASS LOADING AND CHEM. ANAL.

**UNCLASSIFIED**

# UNCLASSIFIED

C-19

of the instrumentation and chamber facility may be found elsewhere (Ref. 1-3).

## 1.2 EXTINCTION MEASUREMENTS

Extinction produced by aerosol hazes is measured at visible wavelengths over a folded path of about 18 m. A lens collimated beam from an incandescent bulb powered by a regulated power supply is focused on a photomultiplier after traversing the chamber twice (reflection by a mirror at the opposite chamber wall). The detector photomultiplier is an RCA-4440 which has a peak sensitivity in the range 0.4-0.5  $\mu\text{m}$  wavelength. Two visible wavelength transmissometer systems are available at heights of  $\sim 1$  and 5 m above the floor.

A recently built IR transmissometer utilizes an 18 m path length, a 900°C black body source, and an HgCdTe detector operated at liquid nitrogen temperature. The chopped, collimated source beam is directed through the chamber (at a height of 1 m) and onto the detector by spherical front-silvered mirrors. Continuous measurements of extinction as a function of wavelength are obtained via a pair of variable wavelength filter wheels located in front of the detector. The spectral resolution of these filters is two percent over the wavelength interval from 2-12  $\mu\text{m}$ .

"Unattenuated" light intensities (i.e.,  $I_0$ ) are measured by both the visible and IR transmissometer systems prior to the introduction of aerosols into the chamber. Estimates of extinction are then obtained from the optical transmission data via Beer's law:

$$I = I_0 e^{-\beta x}$$

where  $I_0$  is the intensity of the incident light,  $I$  is the observed light intensity at some distance  $x$  through the aerosol medium, and  $\beta$  is the extinction coefficient of the aerosol cloud.

## 1.3 INDIVIDUAL PARTICLE GROWTH STUDIES

In an effort to gain further insight into the deliquescent growth properties of the pyrotechnic aerosols, an apparatus was assembled which allowed measurement of the growth of an individual particle as a function of RH. Individual particles, 20-40  $\mu\text{m}$  diameter, were mounted on a stretched spider thread filament (of  $\sim 1 \mu\text{m}$  dia) for viewing with the aid of a microscope. The specimen particle was placed in a viewing chamber through which air of carefully controlled and measured RH flowed. The accuracy and

# UNCLASSIFIED

787

**UNCLASSIFIED**

repeatability of the apparatus was determined through measurements of (and comparison with theoretical estimates) particles of pure NaCl and pure KCl. Details of the set-up may be found elsewhere (e.g., Ref. 3). Measurements of the growth characteristics of aerosol from three alternative formulations of "Salty Dog" were obtained, and the data demonstrate that the deliquescence properties of the aerosol can be managed.

#### 1.4 SMOKES FROM SALTY DOG AND ALTERNATE FORMULATION PYROTECHNICS

The basic aerosol used for producing conditions of restricted visibility at subsaturated humidities in these experiments was generated by pyrotechnic devices known as "Salty Dogs". The devices, developed at the Naval Weapons Center (Ref. 5) and designated CY85A, are said to be composed of "18% hydrocarbon binder, 5% magnesium, 10% sodium chloride, 65% potassium perchlorate and 2% lithium carbonate." When burned, the pyrotechnic produces copious quantities of hygroscopic aerosol ( $>10^{10}$  particles  $> 1.0 \mu\text{m}$  diameter per gram of payload). The aerosol begins to deliquesce at  $\sim 68\%$  RH, and extinction in the smoke increases by an order of magnitude as RH is increased from 70 to 95%. A total of 32 experiments with the standard Salty Dog formulation was conducted during FY 78 and 79.

In consonance with the Navy's increased interest in screening smokes, alternate formulations of the alkali halide pyrotechnics are being developed at NWC (Ref. 6) and tested at Calspan (Ref. 3 and 4). A total of 36 large-scale chamber tests on two new formulations, designated NWC 29 and NWC 78, was conducted during FY 80. Extinction measurements indicated that neither NWC 29 nor 78 produces greater extinction than standard Salty Dog and that NWC 78 may be slightly less effective due to its smaller dry yield factor.

### 2. RESULTS OF LARGE-SCALE LABORATORY EXPERIMENTS

#### 2.1 CHEMICAL ANALYSES OF THE OBSCURANT AEROSOLS

Low volume filter samples obtained for mass-loading measurements were analyzed to determine elemental composition of the aerosolized pyrotechnic. Analysis for K, Mg, Na, Ca and Li was performed by atomic absorption spectroscopy. Ion chromatography was used to determine Cl content. These results, together with the chemical composition of the bulk pyrotechnic (as provided by Dr. L. Mathews, NWC, China Lake) are presented in Table 2. As can be seen, the majority of the aerosol, by weight, for all formulations is Cl. The remainder being primarily a mixture of Na and K for NWC 78 and Salty Dog, and

**UNCLASSIFIED**

**UNCLASSIFIED**

C-19

Table 2

CHEMICAL COMPOSITION OF ALKALI HALIDE PYROTECHNICS AND SMOKES (BY WEIGHT)

	SALTY DOG CY85A	NWC #29	NWC #78
Bulk Pyrotechnic (NWC Analyses)	65% KC1O <sub>4</sub>	79% NaClO <sub>4</sub>	54% NaClO <sub>4</sub>
	10% NaCl	5% Mg	25% KC1O <sub>4</sub>
	5% Mg	2% LiCl	5% Mg
	2% Li <sub>2</sub> CO <sub>3</sub>	14% Binder	2% LiCl
	18% Binder		14% Binder
Measured Aerosol (Elemental) (Calspan Analyses)	51% Cl	68% Cl	75% Cl
	33% K	27% Na	12% Na
	10% Na	4% Mg	9% K
	6% Mg	<1% Li	3% Mg
	<1% Li	<1% K	<1% Li

Na for NWC 29.

## 2.2 EXTINCTION YIELD FOR THE ALKALI HALIDE PYROTECHNIC

2.2.1 VISIBLE WAVELENGTHS. The effectiveness of the NWC pyrotechnics in producing visible wavelength extinction was measured with the chamber's transmissometer. For comparison to the extinction produced by Salty Dog, more recent data obtained from tests of NWC 29 and NWC 78 are plotted in Figure 2 along with Salty Dog extinction data obtained in earlier tests (see Ref. 2). The results, on a per payload gram per chamber basis, are shown in the figure as a function of humidity. From these data, it is apparent that neither NWC 29 nor 78 produces greater extinction than Salty Dog, and the data suggest that NWC 78 may provide slightly less extinction per unit payload of pyrotechnic burned.

2.2.2 EXTINCTION AT IR WAVELENGTHS. Continuacis IR extinction measurements from ~2 to 12  $\mu\text{m}$  wavelength were made with the IR transmissometer. The instrument, designed and fabricated at Calspan, was installed in the chamber during the latter portion of the chamber tests, presenting an opportunity to obtain initial, limited data on the IR extinction spectra of the smokes. IR data were obtained for one test each of Salty Dog, NWC 29 and NWC 78 in which 50 g payloads were aerosolized at a humidity of 90-92%. While believed to be reasonably reliable, the data should be regarded as

**UNCLASSIFIED**

**UNCLASSIFIED**

C-19

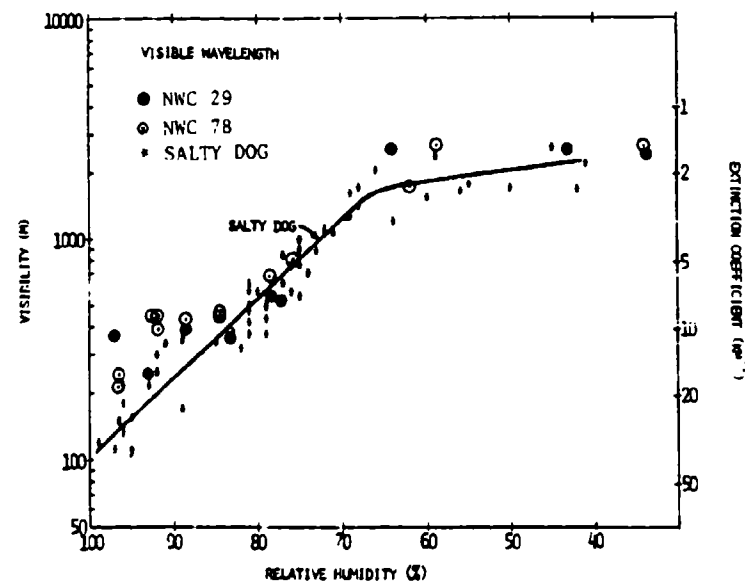


Figure 2. Chamber visibility and extinction as a function of humidity for one gram payloads of Salty Dog, NNC 29 and NNC 78.

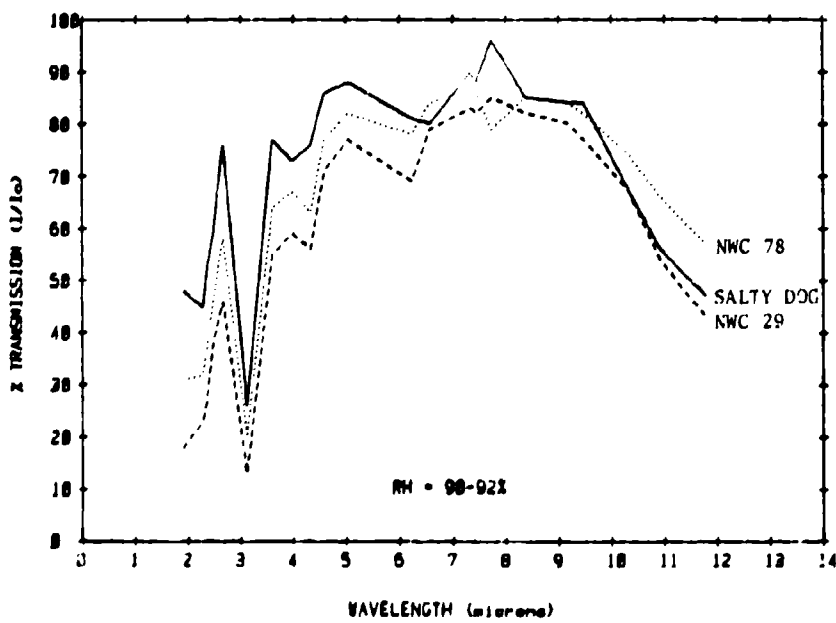


Figure 3. Chamber transmission spectra for 50 g payloads of Salty Dog and NNC 29 and 78.

**UNCLASSIFIED**

/90

# UNCLASSIFIED

C-19

preliminary only, since it was manually reduced at only a few discrete points. The spectra are shown in Figure 3.

## 2.3 PARTICLE SIZE SPECTRA AS A FUNCTION OF HUMIDITY IN THE ALKALI HALIDE SMOKES

In small payload experiments, particle size distribution data were obtained for the range of 0.01 to 3  $\mu\text{m}$  diameter over a range of relative humidities from 35% to 93%. Figure 4 presents the size distribution data for the three NWC pyrotechnics, normalized on a per payload gram basis within the 590  $\text{m}^3$  chamber. From the size spectra of Figure 4, it is apparent that all of the pyrotechnics produce aerosols which undergo significant growth at humidities above  $\sim 70\%$  RH. At lower humidities, little or no growth was observed. Additionally, Salty Dog appears to generate about twice the total number of particles as either NWC 29 or 78. However, NWC 29 and 78 produce a greater number of larger (i.e.,  $>1 \mu\text{m}$ ) particles per unit payload.

The average per-gram yields of the alkali halide pyrotechnics in terms of aerosol production and extinction are presented as functions of RH in Table 3. For standard Salty Dog (CY85A), total aerosol output is consistently  $\sim 8 \times 10^{13}$  particles per gram; at higher humidities the aerosols deliquesce, and greater numbers of larger aerosols (i.e.,  $>1.0 \mu\text{m}$  diameter) are observed, giving rise to increases in extinction. Note that for the "dry" aerosol tests (i.e., RH < 60%), the assumption of density comparable to NaCl (i.e.,  $\sim 2 \text{ g/cm}^3$ ) suggests that aerosol mass was  $\sim 0.5 \text{ g/g}$  pyrotechnic--i.e., that only half the pyrotechnic remained as an aerosol.

## 2.4 AEROSOL MASS YIELD OF THE NWC PYROTECHNICS

The mass yield of a pyrotechnic is defined as the ratio of the resultant cloud mass to the payload mass. For the chamber tests, the payload was always an accurately known quantity, being weighed shortly before burning. To obtain a measure of the cloud mass, filter samples of the resultant smokes were obtained, and the mass of the filter sample was then related to the total cloud mass by the ratio of the chamber to sample volume. Figure 5 presents the resultant yield data for NWC 29 and 78 as a function of humidity. The dashed segments of the curves occur in the region of initial significant particle growth. For this region, the data base is insufficient to clearly define the shape of the curve.

# UNCLASSIFIED

791

UNCLASSIFIED

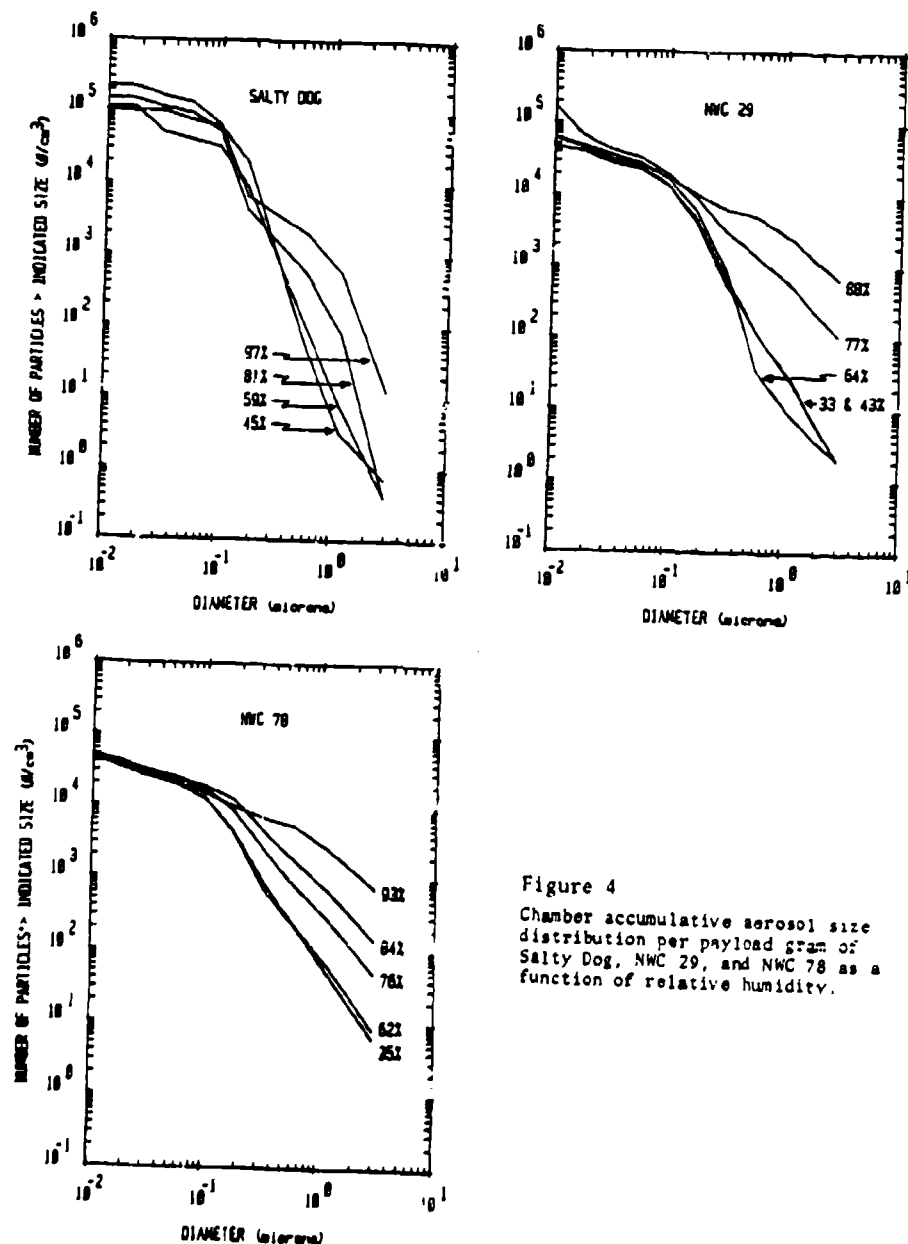


Figure 4  
Chamber accumulative aerosol size distribution per payload gram of  
Salty Dog, NWC 29, and NWC 78 as a  
function of relative humidity.

UNCLASSIFIED

**UNCLASSIFIED**

C-19

Table 3

AVERAGE AEROSOL AND EXTINCTION YIELD (PER GRAM OF PYROTECHNIC)  
AS FUNCTIONS OF RELATIVE HUMIDITY FOR NWC ALKALI HALIDE PYROTECHNICS

## SALTY DOG (CY85A)

<u>Humidity</u>	<u>Number of Tests</u>	<u>Number of Particles of Size &gt; Indicated Diameter</u>			<u>Aerosol Volume</u>	<u>Integrated Extinction Coefficient</u>
		<u>&gt;0.01 <math>\mu\text{m}</math></u>	<u>&gt;0.1 <math>\mu\text{m}</math></u>	<u>&gt;1.0 <math>\mu\text{m}</math></u>		
40-58%	6	$7.3 \times 10^{13} / \text{g}$	$2.0 \times 10^{13} / \text{g}$	$2.3 \times 10^{10} / \text{g}$	$0.28 \text{ cm}^3 / \text{g}$	$1.2 \text{ m}^2 / \text{g}$
60-69%	2	$8.0 \times 10^{13}$	$2.1 \times 10^{13}$	$8.4 \times 10^{10}$	0.34	1.5
70-77%	5	-	-	-	-	2.2
79-85%	6	$6.9 \times 10^{13}$	$2.4 \times 10^{13}$	$19.6 \times 10^{10}$	-	5.1
93-97%	5	$8.1 \times 10^{13}$	$3.3 \times 10^{13}$	$59.4 \times 10^{10}$	-	15.0

## NWC 29

33-64%	2	$3.3 \times 10^{13} / \text{g}$	$.87 \times 10^{13} / \text{g}$	$1.2 \times 10^{10} / \text{g}$	$0.15 \text{ cm}^3 / \text{g}$	$0.95 \text{ m}^2 / \text{g}$
77-88%	2	$6.8 \times 10^{13}$	$1.1 \times 10^{13}$	$86 \times 10^{10}$	-	5.1

## NWC 78

35-62%	2	$2.8 \times 10^{13} / \text{g}$	$.72 \times 10^{13} / \text{g}$	$3.3 \times 10^{10} / \text{g}$	$0.35 \text{ cm}^3 / \text{g}$	$0.96 \text{ m}^2 / \text{g}$
76-84%	2	$2.6 \times 10^{13}$	$1.0 \times 10^{13}$	$28 \times 10^{10}$	-	5.0
93%	1	$2.8 \times 10^{13}$	$.85 \times 10^{13}$	$150 \times 10^{10}$	-	9.6

**UNCLASSIFIED**

UNCLASSIFIED

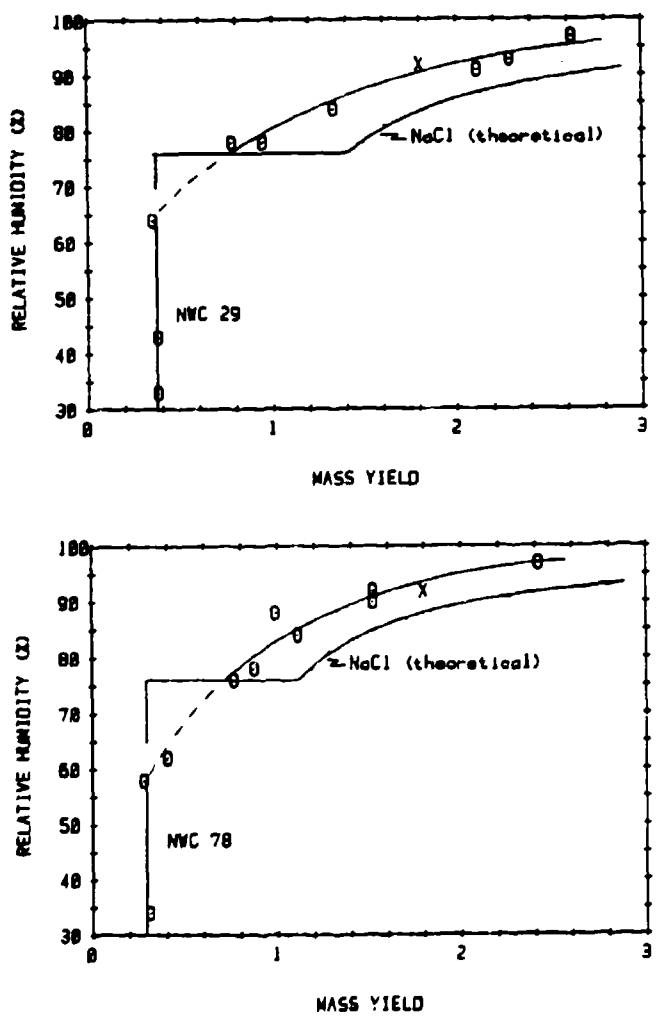


Figure 5 Mass yield for NVC 29 and NVC 78 as a function of humidity, and the theoretical yield of an NaCl aerosol having an assigned dry yield equal to that of the pyrotechnic.

UNCLASSIFIED

# UNCLASSIFIED

C-19

As can be seen, the measured dry yields of NWC 29 and 78 were approximately 0.38 and 0.50, respectively. These values are somewhat lower than the expected theoretical dry yields of 0.48 for NNC 29 and 0.495 for NWC 78 reported by NWC. The "X" shown on the figures represents a mass yield measurement from a single Salty Dog test at 92% RH. By the relative position of the curves to the "X", it is seen that NWC 29 produced a greater yield than NWC 78 at higher humidities, apparently due to the initially greater dry yield of NWC 29. The single Salty Dog data point precludes a definite conclusion as to its yield relative to that of NWC 29 and 78, however, it appears that neither NWC 29 nor 78 produces a significantly greater yield than Salty Dog. The lower yield of NWC 78, relative to that of the Salty Dog point, apparently accounts for the slightly lower yield in extinction also observed for NWC 78 (see Figure 2).

In addition to the measured mass yield curve, a theoretical yield curve (Ref. 7) is shown based on the assumption that all of the pyrotechnic dry yield aerosol is composed entirely of pure NaCl. As can be seen, for both NWC 29 and 78, the measured yield was less than the theoretical at humidities above the deliquescent threshold of NaCl (76%). The differences between theoretical yields for NaCl and measured yields for the pyrotechnics are attributed to the fact that the generated aerosol was not pure NaCl but rather a combination of several salts and, additionally, may contain a large fraction as insoluble, inert material, thereby reducing the effective mass yield and overall aerosol growth of the pyrotechnics.

### 3. RESULTS OF INDIVIDUAL PARTICLE GROWTH STUDIES

In an effort to gain further insight into the deliquescent growth characteristics of the aerosolized pyrotechnics, an apparatus was assembled which allowed the measurement of individual particle growth under controlled humidity conditions. The particles, observed through a microscope, were 20-40  $\mu\text{m}$  in diameter and mounted on a stretched spider thread filament of approximately 1  $\mu\text{m}$  diameter. The specimen particle was placed in a viewing chamber through which air of carefully controlled and measured humidity flowed. The apparatus and aerosol generation procedures are described in detail elsewhere (Ref. 3).

To determine the utility of the apparatus to allow repeatable and accurate measurement of deliquescent particle growth, initial tests were conducted using particles of pure NaCl and pure KCl. Samples were collected on spider thread filaments by spraying a concentrated solution mist of the salt (dissolved in distilled water) over the thread, with some droplets being caught by the thread. When dried, the dissolved salts crystallized into near perfect cubes about the thread.

# UNCLASSIFIED

795

**UNCLASSIFIED**

The growth of three NaCl and three KCl particles was measured as a function of RH, and the resultant growth curves are presented in Figure 6. Note for the NaCl particles, as the humidity was increased from a low value, the particles remained in the solid phase until reaching a deliquescence RH of ~77%. At this humidity, the particles completely dissolved, approximately doubling in diameter. As the RH was increased further, the droplets underwent additional growth. Upon lowering the RH, the hysteresis effect was observed where the particles existed as supersaturated solution droplets at humidities below their deliquescence RH. When the humidity was decreased to ~55%, the supersaturation could no longer be maintained and the droplets crystallized. The repeatability of these growth characteristics can be evaluated by comparison of the growth curves for all three NaCl particles. A similar set of measurements was obtained for pure KCl particles again showing a high degree of repeatability, except for the recrystallization RH. (Recrystallization of the droplet upon lowering humidity is a spontaneous nucleating event, and thus it was not expected that this value would be highly repeatable.)

To assess the accuracy of the measured growth curves, comparison was made of the measured results to those predicted by theory (Ref. 7). This comparison is shown at the bottom of Figure 6 and indicates that the measured values agreed very well with the theoretical deliquescence humidity and relative growth upon deliquescence; drop sizes were within 10% of the theoretical size expected at 90% RH.

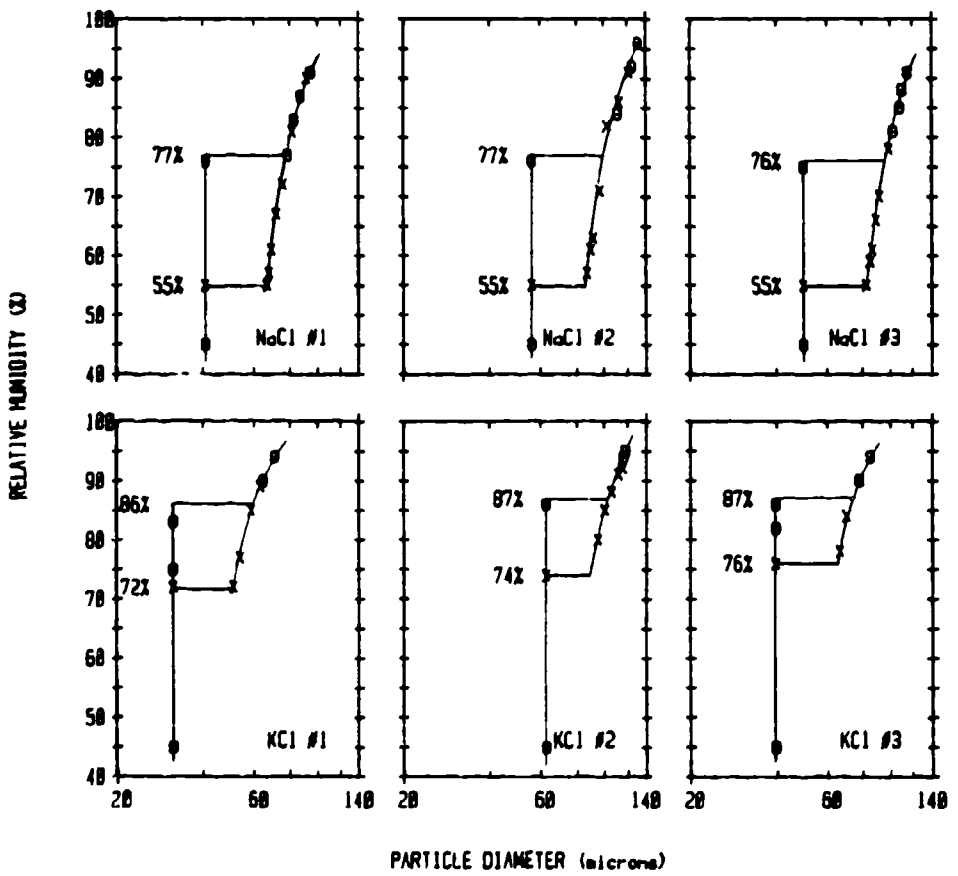
Following the successful tests with the pure salts, samples of Salty Dog, and NWC 29 and 78 were tested. The shapes of these pyrotechnic particles\* were very irregular in comparison to the near cubic shape of the pure KCl and NaCl specimens. Thus, measurement of the dry particle size was difficult, and the values reported below are based on best estimates of the particle size and may well be overestimates due to voids in the particle structure. The resultant growth curves for two particles of each of the three pyrotechnics are presented in Figure 7. Referring to the Salty Dog particles, at low humidities the particles were essentially all solid with no significant liquid present. (Apparently due to the trace presence of  $MgCl_2$  and  $LiCl$ , minute quantities of liquid water were detected on each particle at humidities as low as 40%.) As the humidity was increased above ~73%, measurable growth was observed as the particles began to dissolve. In the RH range of 73-80%, the particles were a mixture of solid undissolved salt and liquid salt solution co-existing in an apparent

\* Submicron particles produced by burning the pyrotechnics at low RH were collected on the specimen spider thread and allowed to agglomerate at high RH to produce recrystallized dry particles which were large enough (i.e., 20-40  $\mu m$  diameter) for viewing with an optical microscope.

**UNCLASSIFIED**

## UNCLASSIFIED

C-19

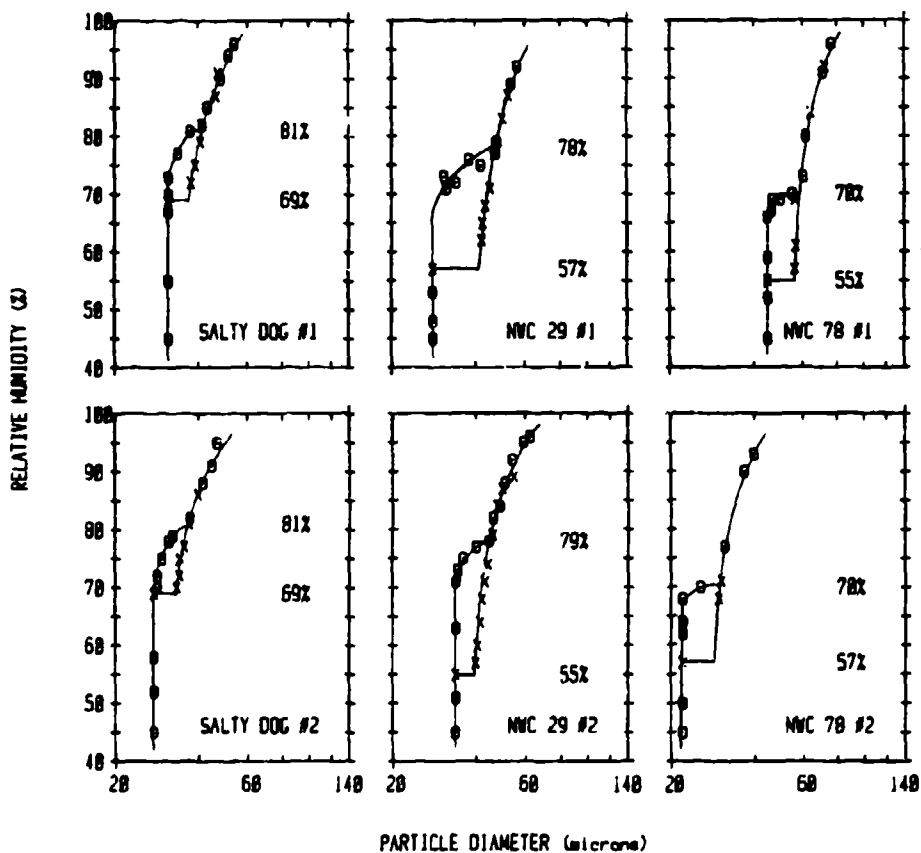


		Deliquescent RH	GROWTH RELATIVE TO DRY DIAMETER AT:	
			Deliquescent RH	90% RH
NaCl	Theory	76%	1.90	2.43
	Measured	77%	1.89	2.22
KCl	Theory	85%	1.89	2.13
	Measured	87%	1.82	1.93

Figure 6. Measured and theoretical (Low, 1969) particle diameter as a function of humidity for NaCl and KCl. Measurements made for increasing humidity are denoted by "O" and for decreasing humidity by "X".

UNCLASSIFIED

UNCLASSIFIED



	APPROXIMATE DELIQUESCENCE HUMIDITY	RH FOR COMPLETE DISSOLVING	RECRYSTALLIZATION RH	PARTICLE GROWTH FACTOR AT 90% RH
SALTY DOG	69%	81%	69%	1.6
NWC 29	70%	78%	~56%	1.8
NWC 78	68%	70%	~56%	1.6

Figure 7. Measured particle diameter as a function of humidity for Salty Dog, NWC 29 and NWC 78. Measurements made for increasing humidity are denoted by "O" and for decreasing humidity by "X".

UNCLASSIFIED

# UNCLASSIFIED

C-19

equilibrium state, differing from the behavior of pure salts (e.g., see Figure 6) which completely dissolve upon deliquescence. At a RH of 81%, the Salty Dog particles completely dissolved. Upon lowering the humidity, the hysteresis effect was observed until the RH was lowered to ~69% when the droplets underwent a complete phase transition from liquid supersaturated salt solution to solid crystal. It should be noted that the mixed state of liquid salt solution and solid salt was not observed in the hysteresis region. As with the pure salts, the measurements were very reproducible.

In comparison to Salty Dog aerosol, the NWC 29 specimens became completely dissolved at ~78% RH and recrystallized at 55-57%. The NWC 78 particles completely dissolved at ~70%, significantly lower than the RH required for Salty Dog aerosols, and recrystallized at 55-57%. These values are compared in the table at the bottom of Figure 7.

In summary, the individual particle studies indicate that, of the three formulations, NWC 78 produces aerosol having the most favorable growth characteristics. While particles of all three formulations began significant growth at approximately the same RH, NWC 78 completely dissolved at 70% as opposed to 81% and 78% for Salty Dog and NWC 29, respectively. Thus, it is expected that for the same dry size distribution, NWC 78 would produce larger droplets in the humidity range of 70 to 80% than would either NWC 29 or Salty Dog. Additionally, NWC 78 exhibited a much lower recrystallization humidity (55-57%) than did Salty Dog (69%) and, thus, would be expected to maintain larger droplet sizes than Salty Dog under decreasing humidities in the range 69-57%.

## 4. COMPARISON OF THE EXTINCTION CHARACTERISTICS OF ALKALI HALIDE SMOKES WITH THOSE OF WHITE PHOSPHORUS

In this section, the extinction yield produced by the NWC alkali halide pyrotechnics is compared to that of white phosphorus; two approaches are taken in the comparison. The most fundamental approach is based on the extinction produced by equal payloads of each pyrotechnic. This analysis is limited to comparison on the NWC pyrotechnics with reagent-grade white phosphorus and will compare their overall effectiveness, including the influence of dissemination efficiency. A second means of comparison is based on the extinction provided by equal amounts of airborne aerosol, and thus is independent of the means and efficiency of dissemination and provides information on which aerosol material is most effective in producing extinction.

UNCLASSIFIED

**UNCLASSIFIED**

## 4.1 COMPARISON OF VISIBLE WAVELENGTH EXTINCTION ON THE BASIS OF PAYLOAD MASS

Figure 2 earlier presented chamber measurements of visible wavelength extinction on a per unit payload mass basis for the three NWC pyrotechnics. Similar measurements for white phosphorus payloads (Ref. 2) are presented in Figure 8a along with the alkali halide aerosol data. The ordinate is termed the payload mass extinction coefficient defined as

$$\text{PAYLOAD MASS EXTINCTION COEFFICIENT} = \frac{\text{EXTINCTION COEFFICIENT}}{\text{PAYLOAD MASS/CHAMBER VOLUME}}$$

In the actual deployment of some obscurant munitions, it is volume not mass which limits the munition payload. Thus, for these munitions, a volume-normalized extinction parameter appears to have greater utility. Such a volume-normalized parameter is plotted in Figure 8b, where

$$\text{PAYLOAD VOLUME EXTINCTION COEFFICIENT} = \frac{\text{EXTINCTION COEFFICIENT}}{\text{PAYLOAD VOLUME/CHAMBER VOLUME}}$$

From Figure 8 it is seen that based on either payload mass or volume, pure, reagent-grade white phosphorus produces greater extinction than the alkali halide pyrotechnic smokes at all humidities. To obtain extinction comparable to that produced by reagent-grade white phosphorus,  $\sim 2$  times as much NWC pyrotechnic must be burned at 95% RH and  $\sim 10$  times as much is required at 60% RH. From the mass yield data presented in Figure 5, it is apparent that the reason for much (if not all) of the difference in extinction effectiveness between Salty Dog and white phosphorus at RH >80% is due to the low dry yield ( $\sim 0.3$ ) of the Salty Dog pyrotechnic.

## 4.2 COMPARISON OF VISIBLE WAVELENGTH EXTINCTION BASED ON QUANTITY OF AIRBORNE PYROTECHNIC MATERIAL

Added insight into the extinction efficiency of the alkali halide aerosols may be gained by comparing extinction based on the amount of material which actually becomes airborne to produce the smoke. Such an analysis provides a comparison based on the effectiveness of the pyrotechnic aerosol as opposed to the pyrotechnic itself. As before, volume (as opposed to mass) is used as the extinction normalizing quantity. The nominal volume of the airborne aerosol which originated directly from the pyrotechnic is used and, hence, does not include additional volume due to condensation, hydration, oxidation or particle shape. For example, in a cloud produced by a white phosphorus payload, the nominal volume is that only of the phosphorus in the cloud. For convenience, this

**UNCLASSIFIED**

**UNCLASSIFIED**

C-19

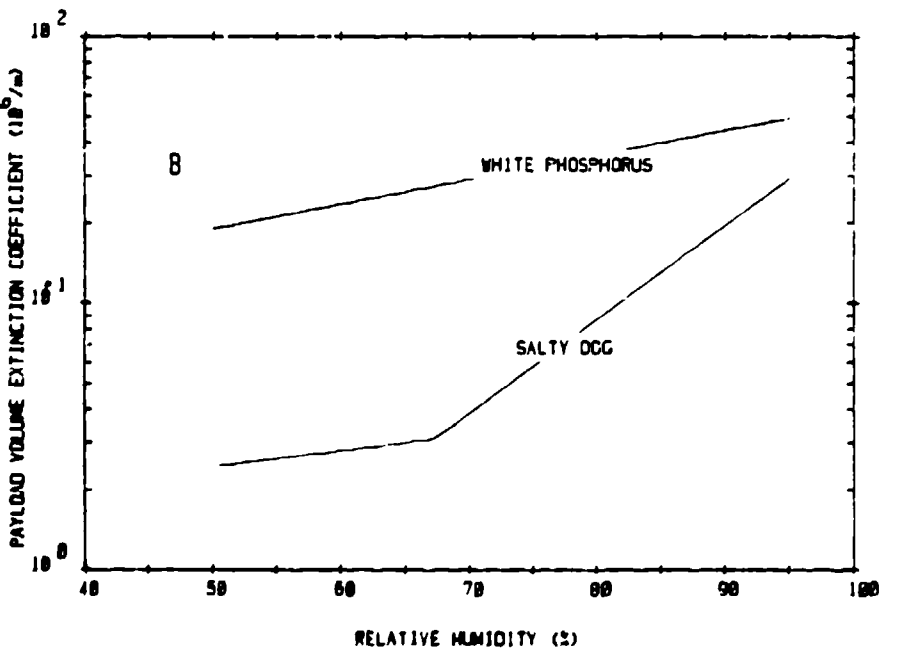
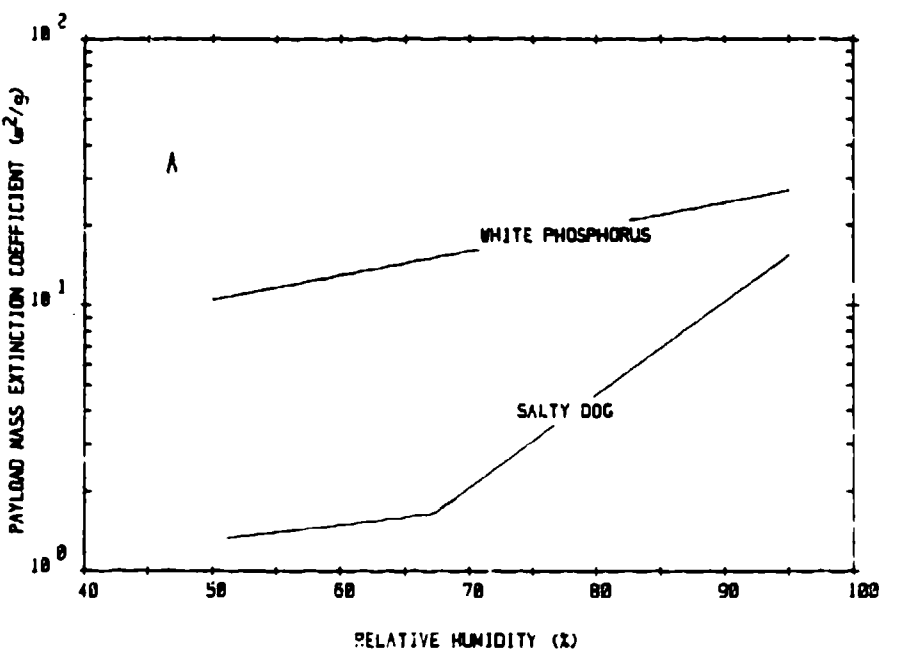


Figure 8. Mass (A) and volume (B) payload extinction coefficient as a function of relative humidity at visible wavelength for white phosphorus and Salty Dog.

**UNCLASSIFIED**

**UNCLASSIFIED**

measure of volume is referred to as the "dry" volume. Figure 9 presents the "dry" airborne volume extinction coefficient as a function of humidity at visible wavelength for Salty Dog and white phosphorus, where

$$\text{"DRY" AIRBORNE VOLUME EXTINCTION COEFFICIENT} = \frac{\text{EXTINCTION COEFFICIENT}}{\text{"DRY" AIRBORNE VOLUME/CHAMBER VOLUME}}$$

The "dry" airborne volume was computed by dividing the measured "dry" airborne mass by the density of the "dry" material.

From Figure 9 it is apparent that, on the basis of the aerosol itself, at humidities above ~80%, the Salty Dog aerosol produces a more dense screen than does the white phosphorus aerosol. This confirms the earlier conclusion that, at high humidities, the difference in extinction based on equal payloads of Salty Dog and white phosphorus is due to differences in dry yield rather than aerosol characteristics.

#### 4.3 COMPARISON OF IR WAVELENGTH EXTINCTION BASED ON QUANTITY OF AIRBORNE OBSCURANT MATERIAL

As previously indicated, some preliminary data were obtained on the IR extinction characteristics of the NWC alkali halide pyrotechnics at ~92% RH (Ref. 3). Limited IR data were also obtained in several white phosphorus tests. For the purposes of gross comparison, greatly-smoothed, volume-normalized IR extinction spectra for Salty Dog and reagent-grade white phosphorus (at ~92% RH) are plotted in Figure 10. It is readily apparent that the extinction effectiveness of both Salty Dog and white phosphorus decreases rapidly as wavelength increases from the visible into the IR, due principally to the relatively small particle sizes generated in these smokes. At longer IR wavelengths, extinction in the white phosphorus smoke is increased over that of Salty Dog aerosols due to P-O bond absorption. The data demonstrate that for visible wavelength obscuration, Salty Dog aerosols provide a viable alternative to white phosphorus while avoiding the hazards associated with the use of phosphorus.

The rapid decrease in extinction with increasing wavelength for the Salty Dog and phosphorus aerosol is primarily due to their relatively small sizes. The vast majority of particles generated by both of these materials are in the size range 0.01-1.0  $\mu\text{m}$  diameter, with ~30% of the particles in the size range 0.1-1.0  $\mu\text{m}$ . Thus, the aerosols, while effective scatterers at visible wavelengths by virtue of their enormous concentrations and small sizes, quickly become ineffective scatterers as

**UNCLASSIFIED**

C-19

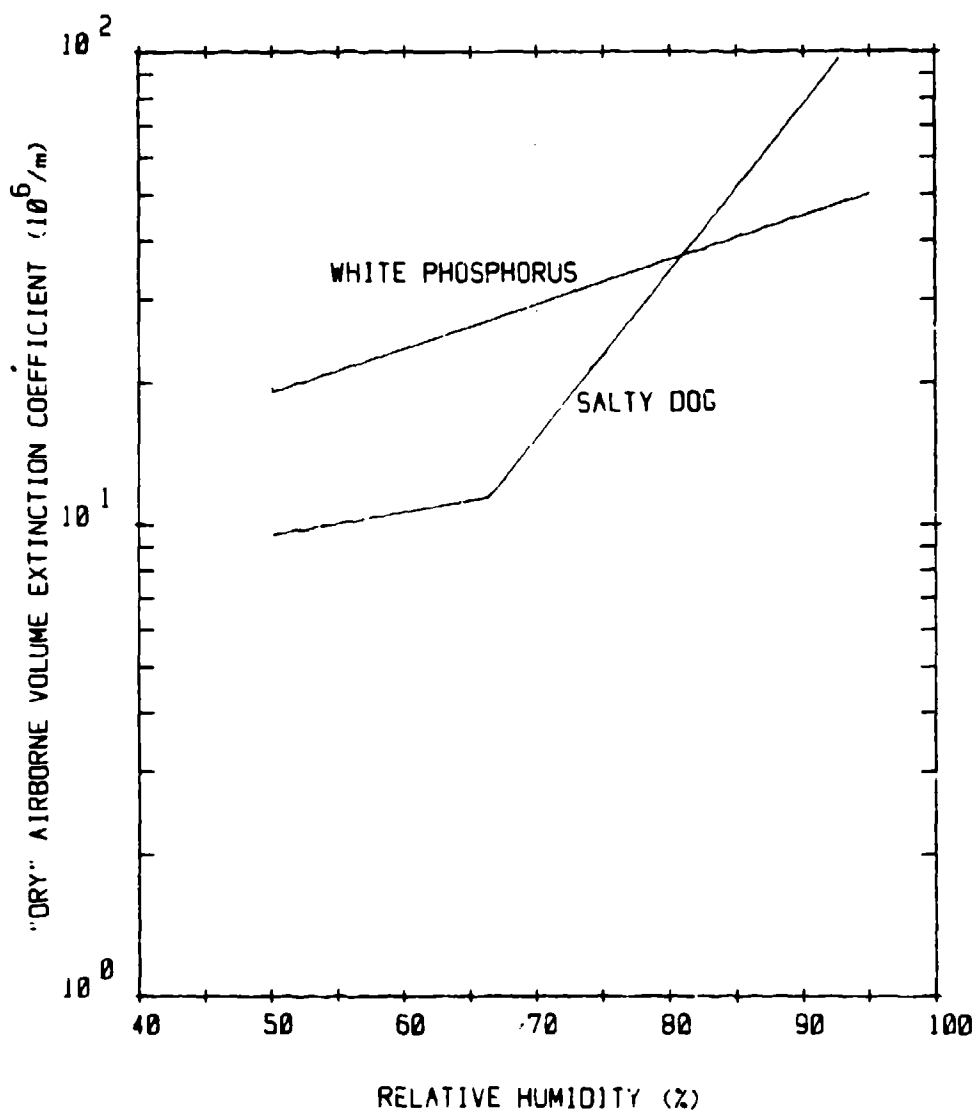


Figure 9. "Dry" airborne volume extinction coefficient as a function of relative humidity at visible wavelength for white phosphorus and Salty Dog.

**UNCLASSIFIED**

803

UNCLASSIFIED

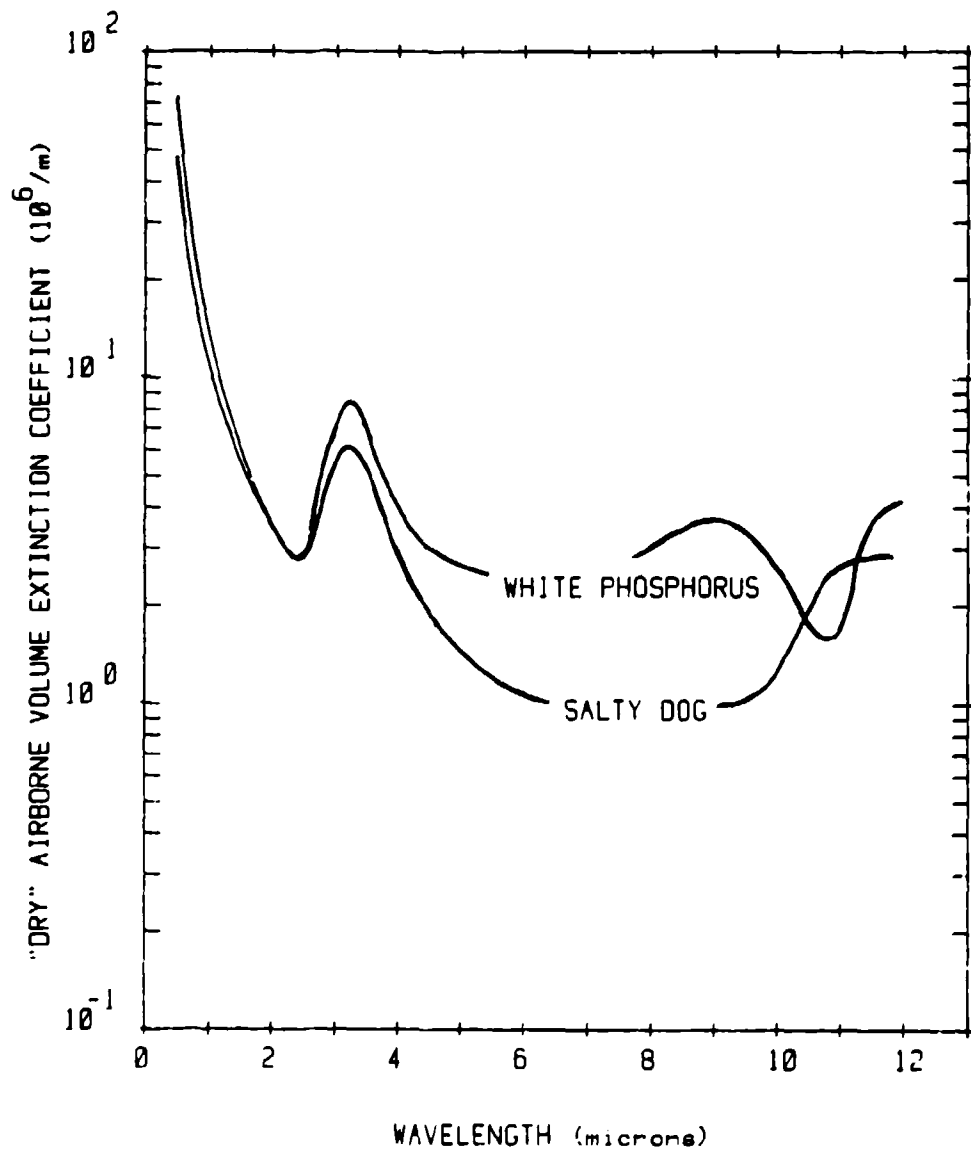


Figure 10. "Dry" airborne volume extinction coefficient as a function of wavelength (0.5-12 microns) at 92% RH.

UNCLASSIFIED

# UNCLASSIFIED

C-19

wavelength increases beyond the visible. With the advent of modern EO systems, obscuration at IR wavelengths has become increasingly important. Thus, efforts to increase the IR extinction efficiency of alkali halide smokes as an alternative to phosphorus are underway at this laboratory and at several Navy laboratories under NASC support.

## REFERENCES

1. Mack, E.J., R.J. Anderson and J.T. Hanley, 1978: "A Preliminary Investigation of the Production of Stable Fogs under Subsaturated Conditions," Calspan Report No. 6287-M-1, 103 pp Calspan Corporation, Buffalo, NY 14225
2. Mack, E.J. and J.T. Hanley, 1980: "A Laboratory Study of Artificial Fogs Produced under Subsaturated Conditions," Calspan Report No. 6510-M-1, 37 pp Calspan Corporation, Buffalo, NY 14225
3. Hanley, J.T. and E.J. Mack, 1980: "A Laboratory Investigation of Aerosol and Extinction Characteristics for Salty Dog, NWC 29 and NWC 78 Pyrotechnics," Calspan Report No. 6665-M-1, 40 pp Calspan Corporation, Buffalo, NY 14225
4. Hanley, J.T. and E.J. Mack, 1980: "A Laboratory Investigation of Aerosol and Extinction Characteristics for Salty Dog, NWC 29 and NWC 78 Pyrotechnics," NASC 310C Program Review, 29-30 Sep 80, Radnor, PA
5. Hindman, E.E. and O.E.R. Heimdal, 1977: "Water Droplet Fogs Formed from Pyrotechnically Generated Hygroscopic Aerosol Particles," 51st Colloid and Interface Science Symposium, Am. Chem. Soc., 19-22 June 1977, Grand Island, NY
6. Mathews, L.A. and P. St. Amand, 1980: "Alkali Halide Screening Smoke Formulations," NASC 310C Program Review, 29-30 Sep 80, Radnor, PA
7. Low, Richard D.H., 1969: "A Comprehensive Report on Nineteen Condensation Nuclei (Part I - Equilibrium Growth and Physical Properties)," Report No. ECOM-5249, 553 pp. U.S. Army Electronics Command, Fort Monmouth, NJ

# UNCLASSIFIED

805

# UNCLASSIFIED

C-20

## XM49 MECHANICAL, SMOKE GENERATOR

W. G. Rouse  
Chemical Systems Laboratory  
Aberdeen Proving Grounds, Maryland

### ABSTRACT

#### 1. INTRODUCTION

The XM49 Mechanical Smoke Generator (Figure 1) is currently in Advanced Development. It is being developed to replace the M3A3 Smoke Generator and provide a capability to produce smoke screens in the visual and Infra-red (IR) regions of the electromagnetic spectrum.

#### 2. DESIGN CONCEPT

Due to the differences in the screening materials (liquids requiring heat for vaporization for visual screening and small particles or powders for IR screening) the generator must utilize two different mechanisms to disperse the materials. To minimize weight and power requirements the generator is designed to have two separate modes of operation: One used to produce visual screens and the other to produce IR screens. To obtain simultaneous screening in the visual and IR spectra, generators operating in each mode are set up to have the resulting screens intermingle.

The XM49 Mechanical Smoke Generator is designed to produce visual screens with standard liquid hydrocarbon smoke materials utilizing the vaporization - condensation principle (Figure 2). When operating in the visual screening mode the generator produces white smoke at a nominal fuel consumption rate of 60 gallons per hour.

The generator produces IR screens by blowing candidate, particulate materials directly from a shipping container (Figure 3). When operating in the IR mode the generator disperses material at a rate of five to ten pounds per minute.

#### 3. FUNCTIONAL OPERATION

##### 2.1 VISUAL SCREENING MODE (FIGURE 4)

The generator obtains its power from a single cylinder two-cycle engine which drives an integral blower, a burner fuel pump, a smoke material pump and an electrical generator. The engine draws its fuel from a five-gallon fuel tank that is part of the generator. The blower provides air to the burner (combustion chamber) and provides the force to expel the vaporized smoke material from the generator. The burner fuel pump draws from the installed five-gallon fuel tank and supplies the fuel tank and supplies the fuel under pressure to the burner nozzle in the combustion chamber. The generator provides electrical power to the capacitive discharge igniter which provides high voltage to the spark generator near the burner nozzle. The electrical system is utilized during generator startup to ignite the burner in the combustion chamber. After burner ignition the electrical system is open circuited and the electric

# UNCLASSIFIED

**UNCLASSIFIED**

generator floats in an unloaded condition. The smoke material pump draws on an external supply tank of smoke material and supplies the smoke material under pressure to a manifold of six nozzles at the forward end of the smoke generator. During normal operation the fuel tank will provide fuel to the engine and burner for approximately one hour. This is approximately the same period that a 55 gallon drum of smoke material will provide smoke material to the injection nozzles. While the burner is operating a portion of the blower air flow is directed around the combustion chamber to limit external burner can temperatures. The flow of smoke material being vaporized cools the exhaust tube portion of the generator. As the mixture of hot air and vaporized smoke material leaves the generator, it is cooled by mixing with the atmosphere, producing a dense white smoke which is dispersed by wind and other environmental conditions producing the smoke screen.

#### 2.2 IR SCREENING MODE (FIGURE 4)

To operate the XM49 Smoke Generator to produce an IR screen, heat is not required nor desired. Therefore, the generator is used as a blower and the burner fuel pump, electric generator and smoke material pump idle on the line. The two-cycle engine draws fuel from the fuel tank and drives the blower which blows air through the burner can, discharging through the visual smoke discharge tube. Because transferring particles (powder) from one container to another is difficult and messy, a drum head discharger was designed that replaces the drum head of the screening material shipping container (Figure 5), and is clamped in position in the same manner as the original drum head. A flexible tube is clamped to the outlet tube of the generator and the inlet tube of the drum head discharger. The inlet tube has two slide valves used in operation.

The upper slide valve bypasses the airflow from the generator and is opened while the engine blower is brought up to operating speed. The lower slide valve admits air into the drum to allow particles to be blown out through the exit port. To stop particle dispersion the lower slide valve (inlet) is closed and the upper slide valve (bypass) is opened.

#### 4. CONCLUSION

The XM49 Smoke generator will provide a capability to produce smoke screens in either the visual or IR regions of the electro magnetic spectrum. Thus, within the capability of the smoke materials, XM49 smoke generators can be used to selectively screen the visual region, IR region or both regions.

**UNCLASSIFIED**

**UNCLASSIFIED**

C-20

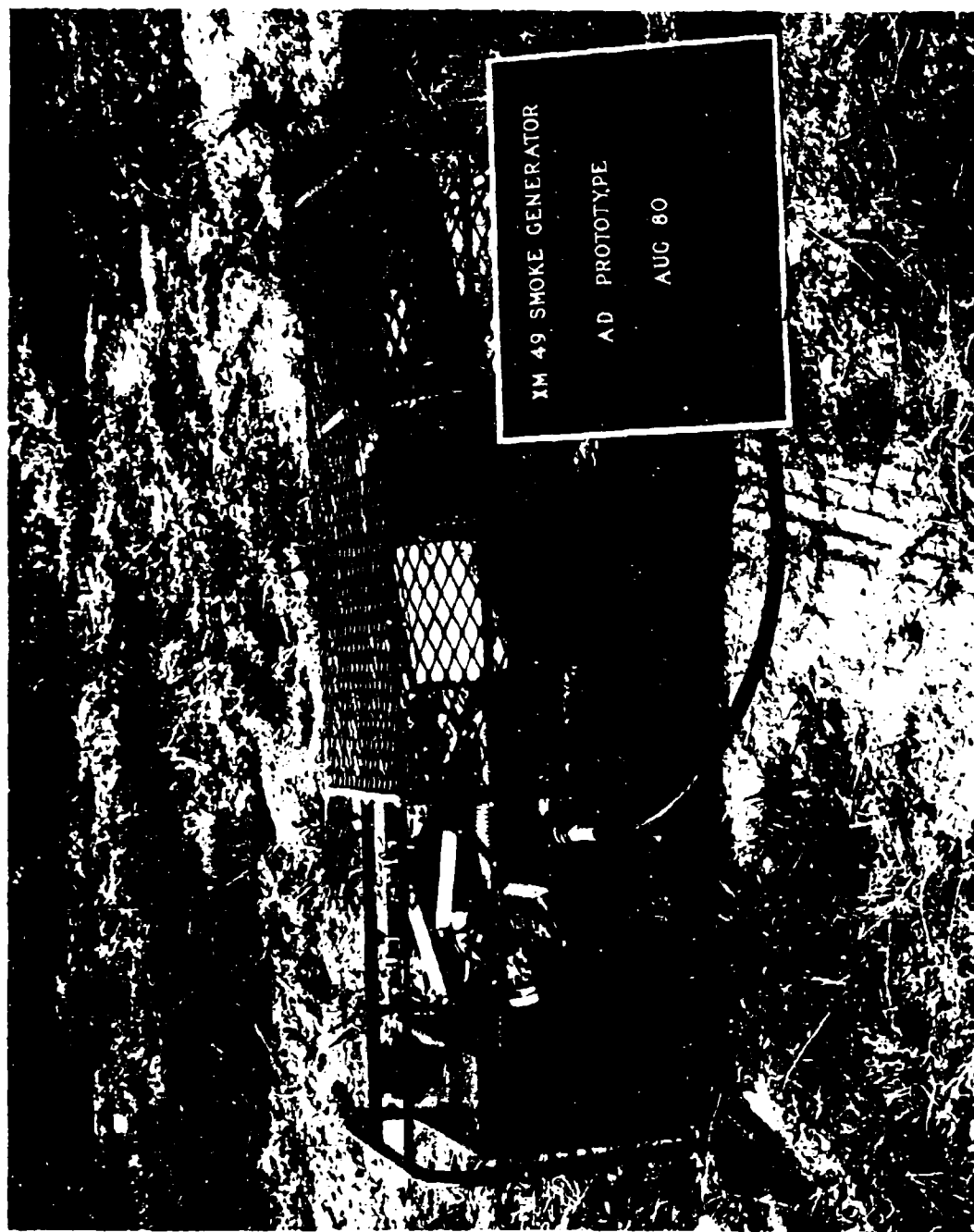


FIGURE 11. XM 49 SMOKE GENERATOR, AD PROTOTYPE.

**UNCLASSIFIED**

809

C-20

**UNCLASSIFIED**

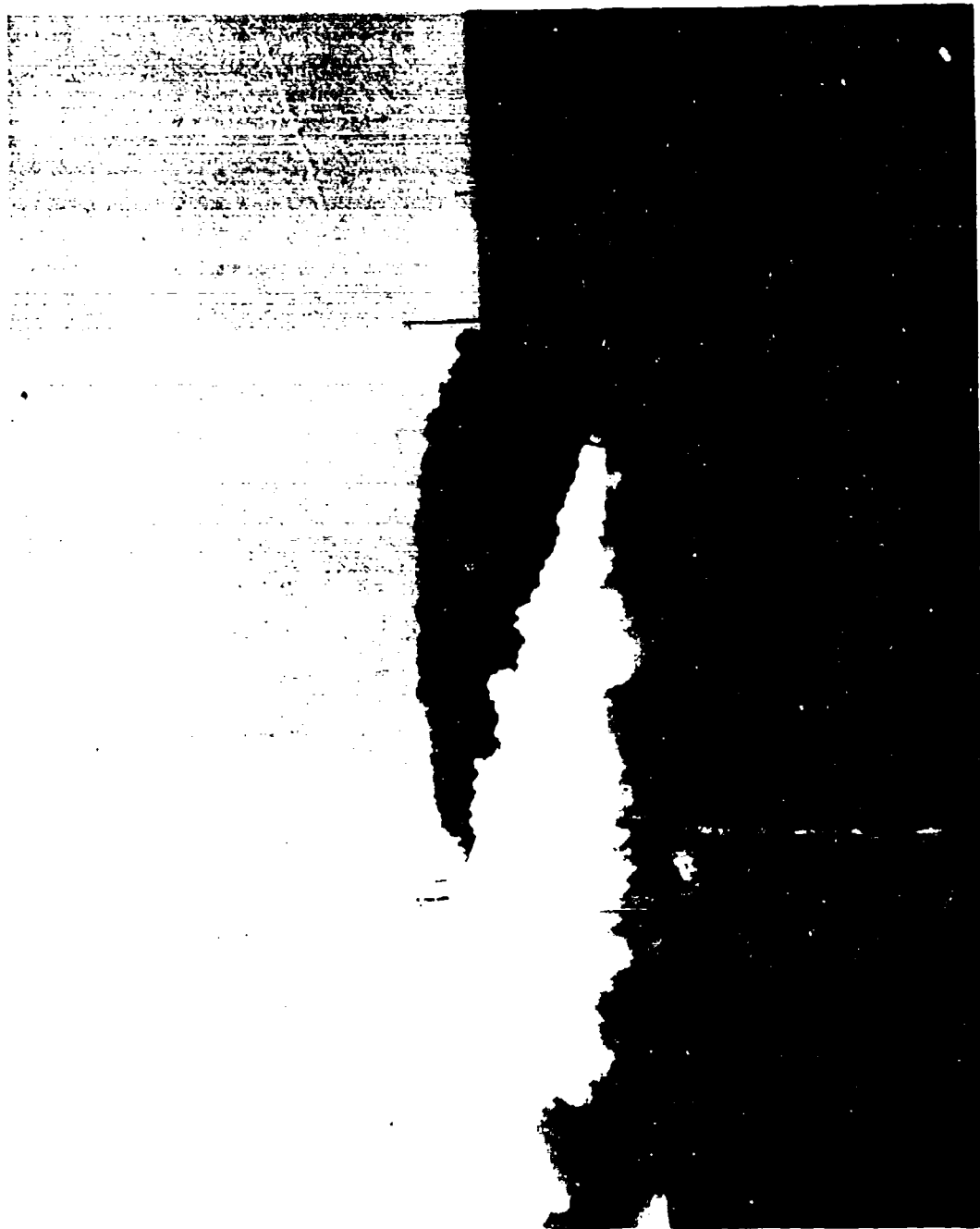


FIGURE 2. XM49 MECHANICAL SMOKE GENERATOR VISUAL SCREENING

**UNCLASSIFIED**

**UNCLASSIFIED**

S-20



FIGURE 3. XM49 MECHANICAL SMOKE GENERATOR - S

**UNCLASSIFIED**

311

**XM49 SMOKE GENERATOR**

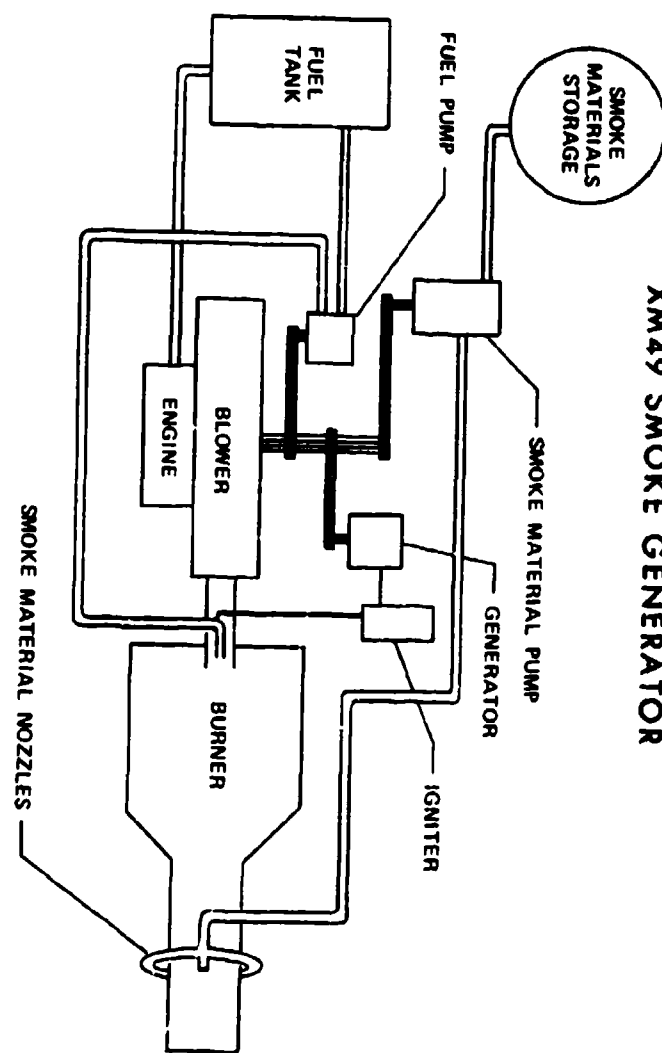


FIGURE 4. XM49 MECHANICAL SMOKE GENERATOR FUNCTIONAL SKETCH

**UNCLASSIFIED**

**UNCLASSIFIED**

C-20



FIGURE 5. XM49 MECHANICAL SMOKE GENERATOR

**UNCLASSIFIED**

813

# UNCLASSIFIED

Helicopter Smoke Countermeasure  
Grenade - Phase II

C-22

Joseph A. Domanico  
Chemical Systems Laboratory, ARRADCOM  
Aberdeen Proving Ground, MD

## ABSTRACT

A technical overview will be presented for the Helicopter Smoke Countermeasure Grenade Exploratory Development Program. Program requirements and objectives will be presented for both the experimental turret launcher and the latest design configuration of the smoke projectile.

The grenade development will be discussed during its past two year design cycle. Subsystem interdependencies will be shown as well as the grenade's relationship to the experimental launching system. Currently, this launching system is under contract to the Boeing Aerospace Company by Applied Technology Laboratory.

Future potential uses for the unique polyethylene projectile will be analyzed for other screening applications in both the visible and infrared spectral regions.

## 1. INTRODUCTION

Chemical Systems Laboratory, under the direction of Applied Technology Laboratory, is currently involved in exploratory development efforts for a rotary wing aircraft self-protection smoke system. Concurrently with this effort, Boeing Aerospace Company is developing a compatible turret launching system, also under the direction of Applied Technology Laboratory.

## 2. DESIGN REQUIREMENTS

In defining the objectives for the program, the main concern was to place the emphasis on the characteristics of the smoke cloud. A general description of those characteristics are:

1. Modified paraboloid shape.
2. Persistency of 1 minute in zero wind.
3. Cloud frontal size of 30 meters horizontal and 50 meters vertical.
4. Cloud position approximately 45 meters forward of the aircraft.
5. Extinction coefficient of 4.0 to 1.2 m<sup>2</sup>/gm at 0.4 to 1.1 um wavelength.

In meeting these described goals, the projectile system was defined with the following characteristics:

1. A total round weight equal to or less than 1.25 kg.
2. Red phosphorus as the smoke agent.
3. A projectile body of which only 20 percent or less remained unconsumed by the burst.
4. Electrical initiation.
5. A total projectile volume of 1100 cc.

UNCLASSIFIED

PRECEDING PAGE BLANK-NOT FILMED

**UNCLASSIFIED**

6. A pyrotechnic delay train of 1-3 seconds.

3. DESCRIPTION

To meet the above requirements and initial design criteria, several configurations were fabricated and tested. After comparison testing of these several designs and much deliberation by both Chemical Systems Laboratory and Applied Technology Laboratory, a specific design was chosen.

The projectile geometry chosen was a cylinder approximately 2.5 inches in diameter and 14 inches long. This projectile was to be made of polyethylene with several scorings running along the length of the projectile to aid in its break-up upon functioning. The final configuration chosen was a two piece projectile which was a mirror image of itself when viewed from the side. The ends of the projectile halves were modified so that when they were injection molded they became either "male" or "female". The use of a standard roll thread mechanism allowed the two halves to be pressed together to construct a single projectile. Additionally, a fill plug was molded into the base of the halves to allow the projectile to be filled after it was assembled. This was added to allow additional flexibility in the design. A one-piece thin walled and scored polyethylene tube ran the length of the projectile and was held in place by the mating of the two projectile halves. A solid polyethylene plug with the identical thread as the pyrotechnic fuze was placed opposite the fuze and sealed the burster well from the elements. The entire projectile was fabricated from polyethylene except for the aluminum fuze body.

It was decided to furnish each projectile with it's own firing tube due to the severe rough handling tests which ammunition must undergo for safety certification and to the fouling properties of black powder, which was chosen as the propellant. This tube was to be of extruded aluminum and welded to an aluminum module base. This module base possessed a straight thru female thread into which the propulsion unit was screwed.

The propulsion unit contained a high firing energy Atlas M-100 electric match connected to two concentric brass rings located at the outer base of the unit. The black powder was also contained in this unit. The unit was made of acrylic resin plastic rather than polyethylene due to polyethylene's poor performance when used with adhesives.

816  
**UNCLASSIFIED**

# UNCLASSIFIED

C-22

Finally, the projectile was to be held in place by a thin walled aluminum disk which would be fixed in place with an RTV type of cement.

Additionally, the main bursting charge for the red phosphorus smoke fill was chosen to be a modified form of photoflash powder. Due to the lack of a safe and arm device during this stage of the development process, a high explosive detonating type material was discarded for use in this round.

## 4. THE LAUNCHING SYSTEM

No description of a round of ammunition is complete without a description of the associated launching system. The current configuration of the launcher designed and built by Boeing Aerospace Company is a six shot design which shoots in a variety of modes. The standard mode is to fire two rounds (one each from both sides of the launcher) to produce a single cloud for protection.

To increase the flexibility of the system to meet the infinite possible needs for the system, the launcher also allows the operator to fire 1, 2, 4, or 6 rounds at the touch of a button. The launcher can traverse an arc of 270 degrees (centered to the front of the aircraft) and may be jettisoned in the event of a malfunction or damage. The current location of the launcher is on the underside of aircraft, forward of and between the landing skids. The low profile of the launcher prevents damage during landing.

## 5. FUTURE APPLICATIONS

The Helicopter Smoke Countermeasure Grenade System has aroused interest from other areas of the smoke community. It is currently being investigated as a potential candidate for a canopy smoke for secure ammunition sites, and as a vehicle for the testing of smoke material in other than the visible spectrum.

Added interest has also arisen since this projectile was fitted with a low impulse rocket motor and stabilized with flexible fins.

# UNCLASSIFIED

# **UNCLASSIFIED**

C-22

## **REFERENCES**

1. Tenney L. Davis, Ph.D., Chemistry of Powder and Explosives, Angriff Press, Hollywood, CA, 1975.
2. Karl O. Bauer, Handbook of Pyrotechnics, Chemical Publishing Co., Inc., New York, NY, 1974.
3. Dr. Herbert Ellern, Military and Civilian Pyrotechnics, Chemical Publishing Co., Inc., New York, NY, 1968.
4. Reverend Ronald Lancaster, M.A., Fireworks Principles and Practices, Chemical Publishing Co., Inc., New York, NY, 1972.
5. George M. Hess, "Aerosol Laser Passive Countermeasure Conceptual Development," Final Report, Boeing Aerospace, Seattle, WA (1979).
6. R. H. Kohl (Editor), Proceedings of the 1980 Smoke Symposium IV, DRCPM-SMK-T-001-80, Vols I & II, Harry Diamond Laboratory, Adelphi, MD (1980).
7. Engineering Design Handbook, Military Pyrotechnic Series, Part 1-4, Headquarters, US Army Material Command (1974).

**UNCLASSIFIED**

**UNCLASSIFIED**LASER-INDUCED SMOKE GENERATION

Richard W. Lapple  
USARRADCOM  
Aberdeen Proving Grounds, Maryland

**ABSTRACT**

A brief outline of smoke generation for Army material with respect to laser-induced methods is presented and applied by means of solid and liquid-to-smoke cannisters in combination with radiation cyclones.

Benchscale investigations of laser-induced particle emission have been carried out and well-quantified analytically since about 1962 (1-4). Pilot plant investigations involving study of laser rockets in static fire has gained in interest since about 1974 (5-10). The basic principle of laser-induced smoke generation is relatively simple: to chemically react laser photons and suitable smoke agents. The net result for static or rocket munitions is at least a 20% to 30% greater smoke agent payload with a far more economical use of mass and energy than chemical propulsion or dissemination. Binary laser-induced smoke munitions involve concurrent development of injection modules, a smoke agent cannister and a radiation cyclone cannister (a throttleable, self-contained laser energy storage battery).

**1. Smoke Agent Cannister**

The translation of existing technology into smoke generation is rather straight forward as far as concerns smoke agent conversion of the solid-to-smoke or liquid-to-smoke types as represented in figures 1 and 2, respectively. Atomization, nozzle operation (hydraulic, pneumatic and rotary or spinning disk atomizers) and dissemination determine liquid-to-smoke generation performance (11-14). In solid-to-smoke generation, jets of very high velocity negative, positive and neutral species are jettisoned as a result of intense surface heating; vapor and plasma subsequently expand from the laser interaction sites. Mass spectrometric studies have found typical particle velocities at 100-70,000 m/sec for laser energy densities between 0.5 to 700 J/cm<sup>2</sup>. By studying sites of laser-solid interaction, one can expect up to 15 gm/cm<sup>2</sup>.sec (4.1 lb/sec for 5 inch diameter projectile) dissemination rates for volatile substances even at 0.5 J/cm<sup>2</sup>, the lowest energy density studied (15).

**2. Radiation Cyclone Cannister**

The development of the radiation cyclone cannister for storage of laser energy represents an advance in the state-of-the-art of microminiaturization of energy sources and requires familiarity with the field of microphysical and translight particle mechanics (16). The charge-to-mass ratio of the photon may be determined from small-angle scattering theory and from the principles of microphysical particle mechanics (17):

$$(1) \cot d/2 = D/b \quad D = Qe_p/m_p c^2$$

where  $d$  is the angle of deflection,  $b$  is the impact parameter,  $e_p$  is the charge of the photon,

**UNCLASSIFIED**

**UNCLASSIFIED**

C-23

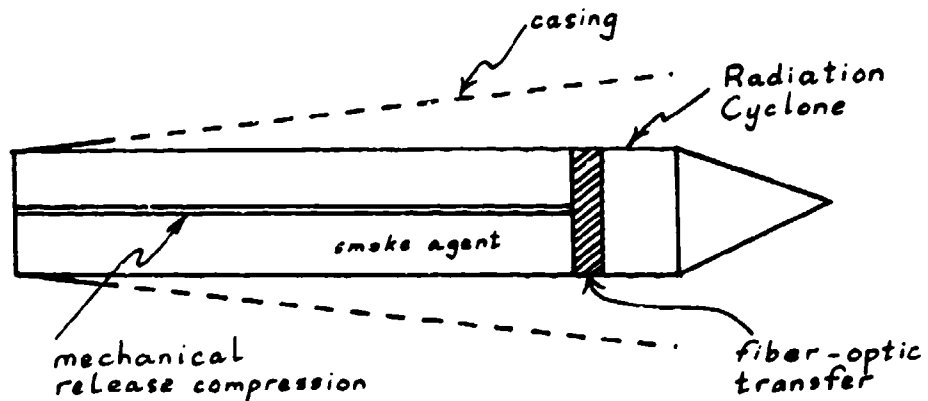


Figure 1. (U) Smoke Cannister or Projectile

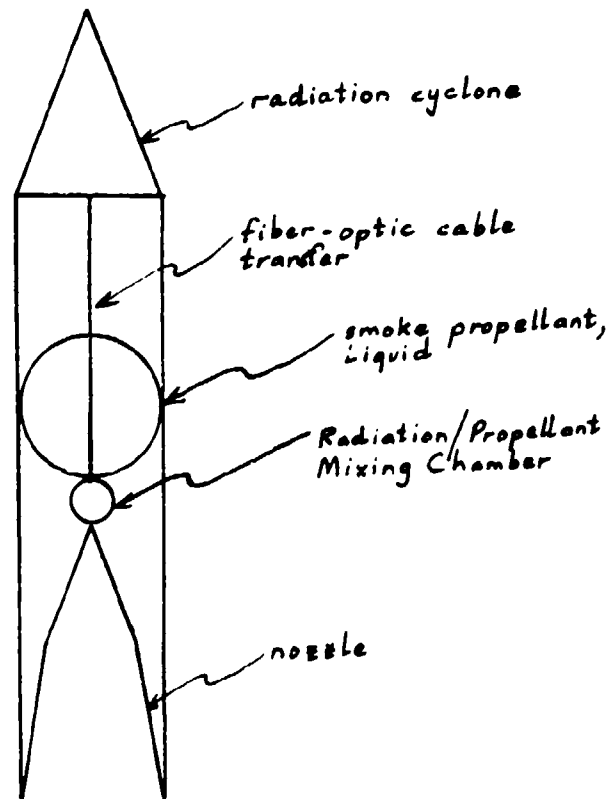


Figure 2. (U) Smoke Laser Rocket

## UNCLASSIFIED

$m_p$  is the mass of the photon,  $c$  is the velocity of light and  $Q$  is the charge of the deflecting body. In a spherical electrostatic field, electrodynamics determines the deflection of light as (18):

$$(2) \quad d = (4/c^2) (e/m_0) (a') (Q/b)$$

where  $e$  is the charge of the electron,  $m_0$  is the mass of the electron and  $a'$  is an experimental shape factor. Comparison of (1) and (2) yields:

$$(3) \quad e_p/m_p = (2a') (e/m_0) = e/m_0$$

This result was suggested and measured directly by Nobel Physics Laureate Johannes Stark in his experiments on the electrical deflection of light in 1945. Therefore, the radius of a cyclone of photons, induced by means of a permanent magnetic field, becomes:

$$(4) \quad R = (c/B) (e/m_0)^{-1} = 3 \times 10^8 / (5000 \text{ gauss} \cdot 1.75 \times 10^{11} \text{ coul/kg}) \\ = 3.4 \text{ mm}$$

## 3. References

1. H. J. Schwarz, H. Hora eds., Laser Interaction and Related Plasma Phenomena, Plenum, New York 1971 p. 85, R. E. Honig "Mass Spectrometric Studies of the Interaction of Laser Beams with Solids"
2. J. F. Ready, Effects of High-Power Laser Radiation, Academic, New York 1971
3. J. F. Ready, E. Bernal, "Mechanisms of Laser-Surface Interactions" Contract No. DA-18-001-AMC-1040(X), May 1969.
4. N. B. Basov, ed., Temporal Characteristics of Laser Pulses and Interaction of Laser Radiation with Matter, Consultants Bureau, New York (1977).
5. M. A. Minovitch (NASA CR 134,966) "Performance Analysis of a Laser Propelled Interorbital Transfer Vehicle" June 24, 1974.
6. K. W. Billman (NASA-SP-395) "Second NASA Conference on Laser Energy Conversion", 1976.
7. M. Huberman, et. al. (AD-A034-955) "Investigation of Beamed Energy Concepts for Propulsion", Oct. 1976.
8. P. K. Chapman (AD-A056-748) Nov. 1977 "Investigation of Laser Propulsion"
9. A. N. Pirri et. al (AD-A033-887) "The Fluid Mechanics of Pulsed Laser Propulsion"
10. F. J. Dyson, F. W. Perkins, Jr., SRI Report JSR-77-12 "JASON Laser Propulsion Study" Summer 1977
11. C. E. Lapple et. al. Contract DA-18-035-AMC-122(A) "Atomization--A Survey and Critique of the Literature"
12. D. E. Blake, C. E. Lapple Contract DA-18-035-AMC-122(A) "Bibliography on Electrostatic Phenomena in Aerosol Dissemination"
13. C. E. Lapple et. al. Contract DA-18-035-AMC-122(A) "Development of Aerosol Charge Analyzer"
14. C. E. Lapple Adv. Chem. Eng. 8, 1(1970) "Electrostatic Phenomena with Particulates"
15. F. S. Karn, et. al U. S. Bureau of Mines R. I. 7338 (1970) "Coal Investigations Using Laser Irradiation"
16. R. W. Lapple 2nd World Chemical Engineering Congress, Montreal Oct. 1981, "Microphysical and Translight Particle Mechanics"
17. R. M. Eisberg, Fundamentals of Modern Physics, Wiley, New York (1964) p. 104.
18. A. Giao Compt. Rend 224, 1212 (1947) "Sur la propagation de la lumiere dans un champ electrostatique".

UNCLASSIFIED

**UNCLASSIFIED**

19. J. Stark in A. Tiselius Nobel Lectures, Physics Vol. I., Elsevier, Amsterdam, 1967 p. 437; International Who's Who 1954-1956.
20. J. Stark Mitteilungen 1, 1947, (privat communication); see J. Stark Physik Haetter 3, 162 (1947) "Ueber den Einfluss des electrostatistischen Felds auf Licht"
21. J. Stark, Erfahrungen and Theorien ueber Licht and Elektron, G. H. Stifel, Traunstein, West Germany, 1950, (Translated by R. W. Lapple Practical Experience and Theories about Light and Electrons)
22. J. Stark Z. Phys. 133, 504 (1952) "Weitere experimentelle Untersuchungen ueber die Natur des Lichtes"
23. J. Stark Z. Phys. 136, 221 (1953) "Folgerungen ueber die Konstitution der Lichtenergie"

**UNCLASSIFIED**

# UNCLASSIFIED

C-27

## MULTISPECTRAL ABSORPTION AND SCATTERING PROPERTIES OF AN EXPERIMENTAL CHAFF CLOUD

J. R. Baskett, et al  
Delco Electronics  
Goleta, California 93017

### ABSTRACT<sup>1</sup>

This paper summarizes a program to establish a multispectral data base on the attenuation properties of a chaff like material produced by the Naval Weapons Center at China Lake, CA. The properties of the chaff cloud were examined at four radar and two laser frequencies. The extinction of all wavelengths was resolved into absorption and scattering losses, and the infrared cloud emission was measured. Both the experimental method and the data are summarized.

An abstract on this subject was sent for consideration for presentation at the Symposium, but was not received. Contractors and US government agencies which are registered users of DTIC may apply to DTIC on DTIC Form 1 for paper AD C022866 (Secret) (20 pages) which contains the material described by the above abstract. Representatives of foreign governments should apply through their embassies. DTIC users may apply on Form 55 for a related paper, AD C-22869-L (Classified) (25 pages), titled "Radar Absorbing Chaff: Material Properties and Performance at Microwave Frequencies" by S. B. Bowling of M.I.T./Lincoln Laboratory which deals with the system implications of the absorbing chaff material characterized by the preceding paper. It includes: a discussion of the material properties, a model for its absorption of energy between 3 and 94 GHz, the geophysical processes which affect its deployment in space, and suggestions for potential applications.

# UNCLASSIFIED

823

**UNCLASSIFIED**

AREA D

DOCTRINE AND TRAINING, CONCEPTS AND SYSTEMS EVALUATION  
AND ANALYSIS

**UNCLASSIFIED**

~~RECORDING PAGE BLANK-NOT FILMED~~

**UNCLASSIFIED**

## TRAINING SMOKE CONSIDERATIONS (MILES SYSTEM)

Robert H. Fricke  
Obscuration Sciences Section  
Physics Branch, Research Division  
Chemical Systems Laboratory  
Aberdeen Proving Ground, MD 21010

**ABSTRACT**

To achieve realism during training it is desirable to operate in a tactical screening smoke environment. However, conflicting requirements exist between training devices and tactical realism. For example, training devices that utilize lasers for operation/communication are adversely affected by smoke. It has been suggested that a visible-to-infrared extinction ratio of 10:1 is sufficient to permit the Mechanized Infantry Laser Engagement Simulation (MILES) system to operate in a smoke environment. Two alternatives exist to achieve this requirement: (a) modify existing smokes to increase the infrared transmission or (b) modify the MILES system to operate at a longer wave length. The current MILES system operates at 0.9 micrometers (GaAs laser). It is shown that only smokes with unusual optical properties will permit this ratio to exist for the current MILES system operating at 0.9 micrometers; however, by appropriate particle size control of current smokes (e. g. fog oil smoke) this ratio can be fairly easily achieved for systems operating at wave lengths greater than 1.5 micrometers.

**1. INTRODUCTION**

The Mechanized Infantry Laser Engagement Simulation (MILES) system incorporates a variety of simulated weaponry including firearms simulated by infrared lasers and detectors. It is desirable to use this system for training in smoke; however, the simulated firearms must continue to function in the smoky environment -- that is, the smoke must attenuate visible radiation but not that at the laser frequency. A 10:1 ratio between the visible and infrared extinction coefficients appears to be suitable for this purpose. In addition, it is required that the smoke be capable of attenuating visible radiation to 1% of its initial intensity in a 35 meter path. Using these criteria, optical properties have been calculated for smoke materials at laser wave lengths of 0.9  $\mu\text{m}$  (GaAs system now in use) and 1.55  $\mu\text{m}$  (proposed InGaAsP system).

The extinction coefficient  $\alpha$  is the ratio of the total optical cross section of a quantity of condensed-phase aerosol material to its mass. It is related to the transmitted radiation intensity by

$$1) \quad I = I_0 e^{-\alpha c L}$$

where  $I_0$  is the intensity of radiation incident on the aerosol cloud,  $c$  is the mass concentration of the condensed phase material of the aerosol (henceforth to be

**UNCLASSIFIED**

**UNCLASSIFIED**

called the aerosol or the aerosol material), and  $I$  is the intensity of radiation after it has travelled a distance  $L$  through the cloud. The optical efficiency  $Q$  is the ratio of the optical cross section of a particle (in this discussion spherical) to its geometric cross section.<sup>1</sup> For a single particle (or a monodisperse aerosol) the extinction coefficient is related to the optical efficiency by the relation

$$2) \quad \alpha = \frac{3Q}{2\rho D}$$

where  $\rho$  is the density of the aerosol material and  $D$  is the diameter of the particle. The extinction coefficient is the sum of contributions due to scattering and absorption of radiation by the particle, viz:

$$3) \quad \alpha = \alpha_{\text{sca}} + \alpha_{\text{abs}}$$

Here and subsequently  $\alpha$  is in  $\text{m}^2/\text{g}$ ,  $\rho$  is in  $\text{g}/\text{m}^3$ ,  $D$  and the wave length  $\lambda$  are in micrometers, the path length  $L$  is in meters, the concentration  $c$  of the aerosol is in  $\text{g}/\text{m}^3$ , and  $N$ , the number concentration of aerosol particles, is in particles/ $\text{m}^3$ .

The value of the extinction coefficient for a polydisperse aerosol is

$$4) \quad \alpha = \int \alpha(D)dc = \int_0^\infty \alpha(D) \left( \frac{dc}{d\ln D} \right) d\ln D$$

where  $\alpha(D)$  is the extinction coefficient for a monodisperse aerosol of diameter  $D$ .

Particle size distributions are assumed to be log normal:

$$5) \quad \frac{dc}{d\ln D} = \frac{c}{\sqrt{2\pi} \ln \sigma_g} e^{-\frac{1}{2} \left[ \frac{\ln(D/D_0)}{\ln \sigma_g} \right]^2}$$

where  $dc$  is the mass per unit volume of space in the size interval  $[\ln D, \ln D + d\ln D]$ ,  $c$  is the aerosol mass concentration,  $D_0$  is the mass median diameter (MMD), and  $\sigma_g$  is the geometric standard deviation.

The complex index of refraction is  $m = (n, k)$  where  $n$  is the usual refractive

# UNCLASSIFIED

D-1

index (ratio of the phase velocity in free space to that in the material) and  $k$  is a measure of absorption ( $k = \text{absorption coefficient} \cdot \lambda / (4\pi)$ ).

## 2. RAYLEIGH CALCULATIONS

Assuming that the particles are small, some idea of the possibilities involved can be derived from relatively simple calculations based on Rayleigh scattering and absorption. Let us assume for this purpose that the index of refraction of the aerosol material is the same for the laser frequency as for the visible. The extinction coefficients for a material of complex refractive index  $m = (n, k)$  are

$$6) \quad \alpha_{\text{abs}} = \frac{6\pi}{\lambda\rho} \text{Im}\left(\frac{m^2-1}{m^2+2}\right)$$

and

$$7) \quad \alpha_{\text{sca}} = 4\pi^4 \frac{D^3}{\lambda^4} \left| \frac{m^2-1}{m^2+2} \right|^2$$

for absorbers and scatterers respectively<sup>2</sup>. The extinction coefficient ratios (XCR)  $r_{\text{abs}}$  and  $r_{\text{sca}}$  are therefore

$$8) \quad r_{\text{abs}} = \frac{\lambda_{\text{ir}}}{\lambda_{\text{vis}}} \frac{\text{ir}}{\text{vis}}$$

for absorbers and

$$9) \quad r_{\text{sca}} = \frac{\lambda_{\text{ir}}^4}{\lambda_{\text{vis}}^4} \frac{\text{ir}}{\text{vis}}$$

for scatterers. The wave length  $\lambda_{\text{vis}}$  ranges from 0.4 to 0.7  $\mu\text{m}$ ; hence for absorbing smokes the XCR ranges from 1.3 to 2.3 for the GaAs (0.9- $\mu\text{m}$ ) system and from 2.2 to 3.9 for the InGaAsP (1.55- $\mu\text{m}$ ) system. For scatterers, the ranges are 2.7 - 25.6 and 24 - 225 respectively. An "average" XCR can be found by integrating over the visible range for a given infrared wave length:

$$10) \quad \bar{r} = \frac{\int_0^{\infty} (\lambda_{\text{ir}}/\lambda)^4 d\lambda}{\int_0^{\infty} d\lambda} = 14.12 \frac{\lambda_{\text{ir}}^4}{\lambda_{\text{vis}}^4}$$

# UNCLASSIFIED

829

## UNCLASSIFIED

Then

$$11) \quad \begin{aligned} \text{for } \lambda_{ir} = 0.9\mu\text{m} & \quad \bar{r} = 9.3 \\ \text{for } \lambda_{ir} = 1.55\mu\text{m} & \quad \bar{r} = 82. \end{aligned}$$

(It should be noted that this integration is valid only for dilute smokes. The wavelength integrated extinction coefficient is reduced at higher concentrations unless  $\alpha$  is independent of the wavelength.<sup>3</sup>) From these considerations it would appear that a non-absorbing smoke satisfactory for a 1.5- $\mu\text{m}$  system should be fairly readily available; however, for the 0.9- $\mu\text{m}$  system the XCR would have to be enhanced by suitable variation of the refractive index with wave length. Figure 1. shows the variation of the dimensionless product  $\alpha\lambda^4\rho/D^3$  with  $n$  for non-absorbers. Since attenuation increases with  $n$ , one might hope to achieve the 10:1 XCR by using a material whose refractive index decreases with increasing wave length. This is not an unusual phenomenon.

From the visible attenuation requirement and considerations on coagulation some inferences can be made regarding particle size requirements. A smoke whose particle number density  $N$  is substantially greater than  $10^{12}/\text{m}^3$  coagulates rapidly enough that the particle size of the smoke changes in minutes.<sup>4</sup> Let us therefore assume a maximum  $N$  of  $10^{12}/\text{m}^3$  and calculate the particle diameter necessary to meet the attenuation requirement. The requirement is

$$12) \quad I/I_0 = e^{-\alpha CL} < 0.01$$

We will (now and hereafter) assume an aerosol material density of  $1 \text{ g/cm}^3$ . Then

$$13) \quad \alpha C > \frac{\ln 100}{35} = 0.1316/\text{m}$$

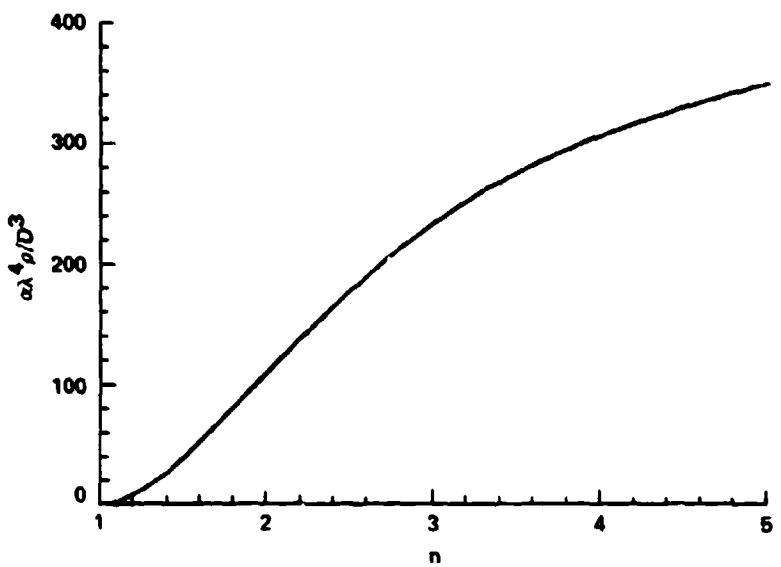
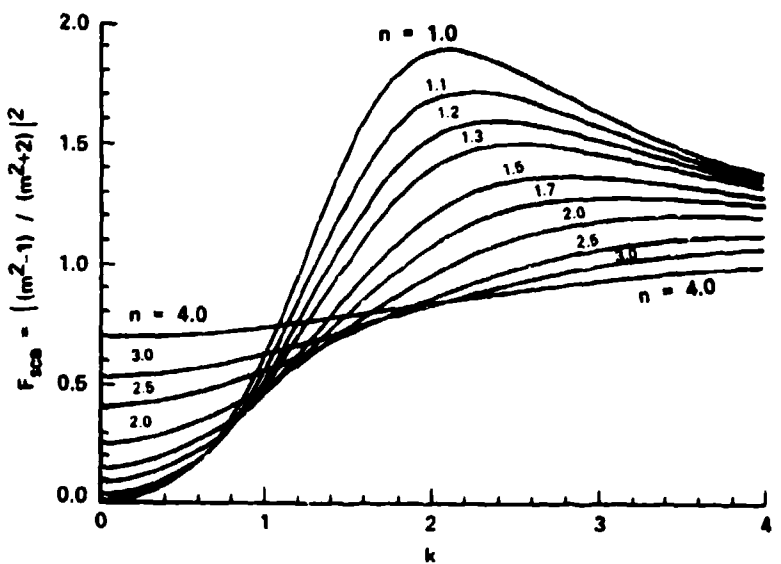
Inequality 13) can be written

$$14) \quad \frac{4\pi^4 D^3}{\lambda^4 \rho} F_{sca} \cdot N \cdot \frac{\pi}{6} \rho (D/10^4)^3 > 0.1316$$

where  $F_{sca} = \left| \frac{n^2 - 1}{n^2 + 2} \right|^2$  (see eq. 6). Then

UNCLASSIFIED

UNCLASSIFIED

FIGURE 1. DIMENSIONLESS SCATTERING COEFFICIENT  $\alpha \lambda^4 \rho / D^3$  VS  $n$  FOR NON-ABSORBERSFIGURE 2. SCATTERING FACTOR  $F_{sca}$  VS  $k$  FOR VARIOUS VALUES OF  $n$ .

UNCLASSIFIED

## UNCLASSIFIED

$$15) \quad D^6 > 0.1316 \cdot \frac{3}{2\pi^5} \lambda^4 \cdot \frac{10^{12}}{N \cdot F_{sca}}$$

Figure 2. shows  $F_{sca}$  as a function of  $k$  for values of  $n$  ranging from 1 to 4. If  $n$  is restricted to values  $> 1$ ,  $F_{sca} < 1.89$ , and since  $N < 10^{12}$ ,

$$16) \quad D > (0.1316 \cdot \frac{3}{2\pi^5} \lambda^4 \cdot \frac{10^{12}}{N \cdot F_{sca}})^{1/6} > 0.264\lambda^{2/3}$$

and the size parameter  $x$  ( $= \pi D/\lambda$ ) is governed by

$$17) \quad x > (\frac{0.1316 \cdot 3}{1.89 \cdot 2\pi^5})^{1/6} > 0.831/\lambda^{1/6}$$

Table I. shows the particle diameter and size parameters necessary for Rayleigh scatterers to meet the visible attenuation requirement.

TABLE I. RAYLEIGH SCATTERING PARTICLE SIZES

If $\lambda_{vis} =$	$D >$	$x >$
0.40μm	0.14μm	1.13
0.55	0.18	1.01
0.70	0.21	0.94

A similar calculation for absorbing particles yields

$$18) \quad D > 0.242\lambda^{1/3} \quad x > 0.759/\lambda^{2/3}$$

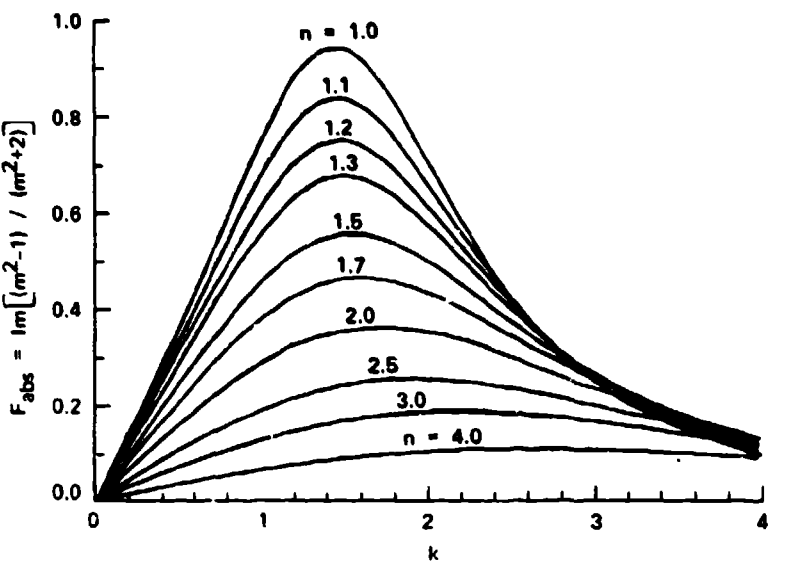
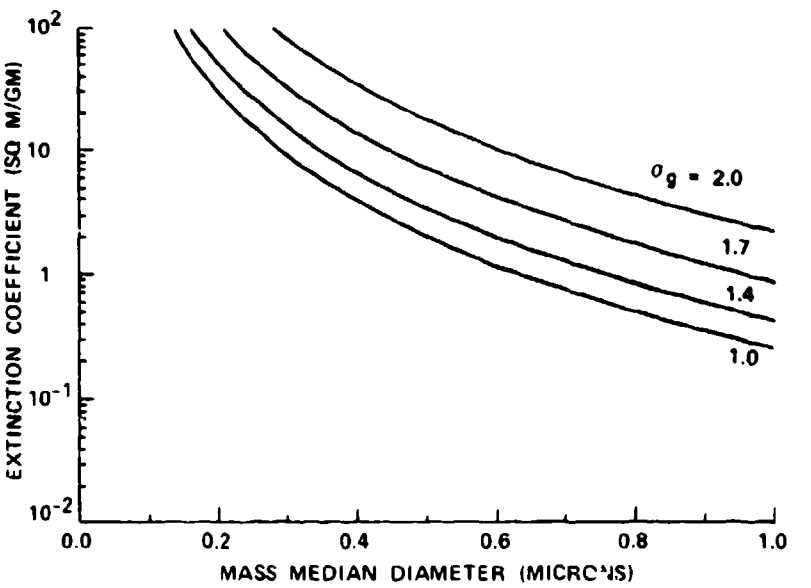
taking into account that for  $n > 1$  the maximum value taken by  $Im((m^2-1)/(m^2+2))$  is 0.944 (see Figure 3). Table II. shows the resulting requirements on  $D$  and  $x$ .

TABLE II. RAYLEIGH ABSORPTION PARTICLE SIZES

If $\lambda_{vis} =$	$D >$	$x >$
0.40μm	0.18μm	1.40
0.55	0.20	1.13
0.70	0.21	0.96

UNCLASSIFIED

UNCLASSIFIED

FIGURE 3. ABSORPTION FACTOR  $F_{\text{abs}}$  VS  $k$  FOR VARIOUS VALUES OF  $n$ .FIGURE 4. MINIMUM EXTINCTION COEFFICIENT TO MEET VISIBLE ATTENUATION REQUIREMENT VS MMD FOR VARIOUS VALUES OF  $\sigma_g$ 

UNCLASSIFIED

**UNCLASSIFIED**

If the initial number density of the cloud were  $10^{13}/\text{m}^3$ , the required particle diameters for scatterers would be reduced from those shown in Table I. by a factor of 0.7 but the particles would quickly coagulate to diameters about 1.5 times those shown in the table; for absorbers the required particle diameters would be about half those shown in Table II., and the particles would quickly coagulate to the sizes shown in that table.

The values of  $x$  listed in Tables I. and II. show that particles large enough to meet the attenuation requirement are really too large to be considered Rayleigh scatterers or absorbers. Thus, although general conclusions reached in this section are correct, more precise calculations, particularly those on requirements for the 0.9- $\mu\text{m}$  system, must be done via Mie theory.

## 3. LARGE PARTICLES

Before examining the results of Mie calculations, let us consider particles large enough to warrant geometric approximation. For such particles the efficiency factor  $Q$  (optical cross section/geometric cross section) is 2. From equation 2.

$$19) \quad r = \alpha_{\text{vis}}/\alpha_{\text{ir}} = Q_{\text{vis}}/Q_{\text{ir}} = 1$$

Furthermore, the contribution to  $Q$  consists equally of blockage of radiation falling directly on the particle and diffraction due to disturbance of the incident wave front; the deflection angle for the diffracted radiation is small and the diffracted radiation may appear to the observer to be undisturbed.<sup>5</sup> Hence the effective efficiency lies between 1 and 2, and is closer to 1 for the visible than for the infrared, since the size parameter  $\pi d/\lambda$  is larger for the smaller wave length, making the effect more pronounced; therefore the effective XCR  $r = Q_{\text{vis}}/Q_{\text{ir}}$  is less than 1. Clearly large particles are useless in this context.

**UNCLASSIFIED**

**UNCLASSIFIED**

D-1

## 4. MIE CALCULATIONS

In order to confirm the results of section 2, and investigate the optical properties necessary to meet the attenuation and XCR requirements in the case of the 0.9- $\mu\text{m}$  system, a series of calculations based on Mie theory<sup>6,7,8</sup> has been made. It is assumed that the smoke consists of spherical particles whose diameters are log-normally distributed, usually with  $\sigma_g = 1.4$ ; optical constants are specified which may be different in the infrared from those in the visible; and the extinction coefficients, averaged over the size distribution and averaged photopically over the visible spectrum, along with the resulting XCR's, have been calculated and plotted for mass median diameters from 0.005 to 1.0  $\mu\text{m}$ .

The mass concentration of a log-normally distributed aerosol whose number concentration is  $N$  is given by

$$20) \quad c = N \cdot \frac{\pi}{6} D_0^3 e^{-\frac{9}{2}(\ln \sigma_g)^2}$$

whence inequality 14., expressing the visible attenuation requirement, may be rewritten

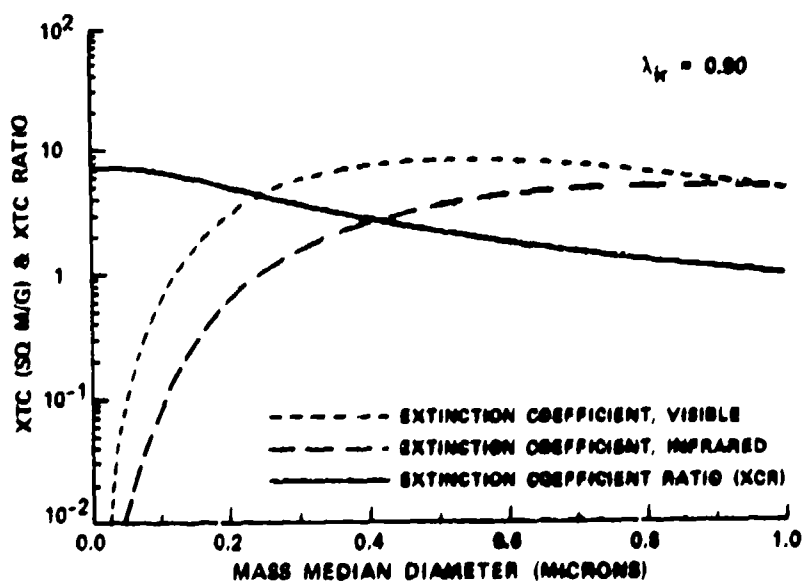
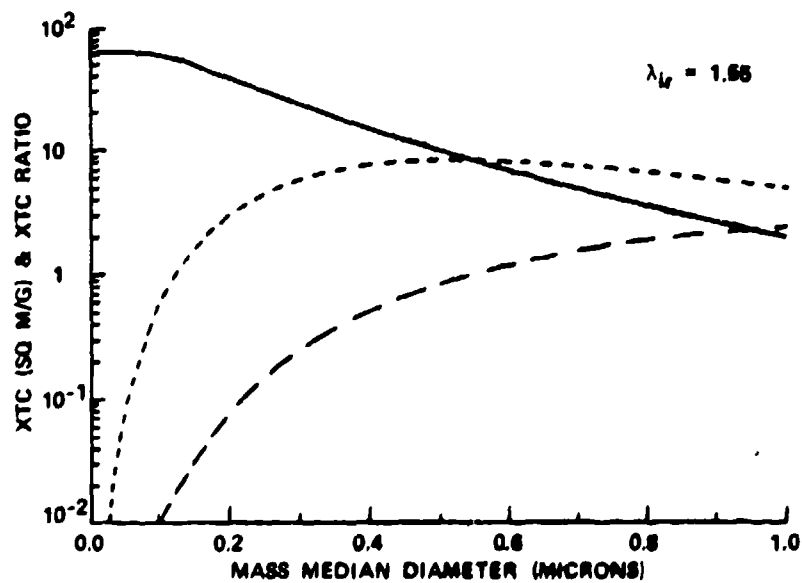
$$21) \quad a > 0.1316 \frac{6e^{-\frac{9}{2}(\ln \sigma_g)^2}}{\pi N D_0^3}$$

## 4.1 REFRACTIVE INDEX EQUAL IN VISIBLE AND INFRARED

Figure 4. displays the minimum value of the extinction coefficient meeting this requirement as a function of MMD for various values of  $\sigma_g$ . Figure 5. displays the extinction coefficients for the visible and infrared and the XCR vs MMD for aerosols with  $\sigma_g = 1.4$ , composed of non-absorbing material with a typical refractive index ( $n=1.5$ ) which is taken to be the same in the visible and near infrared. In this and subsequent plots the short-dashed line represents the visible extinction coefficient, the long-dashed line represents the infrared extinction coefficient, and the solid line represents the XCR. Comparison with the  $\sigma_g = 1.4$  curve in Figure 4. shows that smokes with MMD less than about 0.39  $\mu\text{m}$  do not meet the visible attenuation requirement. Smoke with MMD less than 0.5  $\mu\text{m}$  meet both the attenuation and XCR requirements for the 1.55- $\mu\text{m}$  system. No smoke with this refractive index meets the XCR requirement for the

**UNCLASSIFIED**

UNCLASSIFIED

FIGURE 5. EXTINCTION COEFFICIENT & XCR VS MMD FOR  $n_V = n_{VH} = 1.5$ 

UNCLASSIFIED

0.9- $\mu\text{m}$  system.

## UNCLASSIFIED

Figure 6. displays the XCR and the visible extinction for non-absorbers with refractive indices of 1.2, 1.33, 2.0, 3.0, and 5.0. Note that the zero-diameter limit of the XCR is the same for all values of  $n$  for a given infrared wave length, as required by equations 10 and 11. The actual values differ from those in equation 11, because here the integration was photopic. Comparison with Figure 4. again discloses the minimum MMD for which the attenuation criterion is met, and the XCR curves in Figure. 6. show the maximum MMD for which the XCR is greater than 10. The XCR requirement is not met for the 0.9- $\mu\text{m}$  system for any MMD for aerosol materials whose refractive index is less than 3, the two requirements are not met simultaneously for any refractive index for this system. The two requirements are met simultaneously for the 1.55- $\mu\text{m}$  system for a rather narrow range of MMD's (marked with an asterisk) which varies with the refractive index and which disappears for  $n>3$ . These results are displayed in Table III.

TABLE III. MIE RESULTS WHEN  $\text{RI}_{\text{ir}} = \text{RI}_{\text{vis}}$

$n$	0.9- $\mu\text{m}$ system		1.55- $\mu\text{m}$ system	
	$D_{\text{min}}$	$D_{\text{max}}$	$D_{\text{min}}$	$D_{\text{max}}$
1.2	0.59 $\mu\text{m}$	--	*0.59 $\mu\text{m}$	0.72 $\mu\text{m}$
1.33	0.46	--	*0.46	0.59
1.5	0.39	--	*0.39	0.50
2.0	0.30	--	*0.30	0.37
3.0	0.27	0.11	0.27	0.27
4.0	0.30	0.10	0.30	0.20
5.0	0.30	0.10	0.30	0.18

Figures 7. and 8. display the visible extinction and the XCR for absorbing particles for which  $\text{mir} = \text{mvis}$ ,  $n = 1.5$  and 2.0 respectively, and  $k$  takes on values from 0 (non-absorber) to 1 (very strong absorber). It is seen that for small  $k$  the zero-diameter limit of the XCR drops from the Rayleigh scattering ratio  $\lambda_{\text{vis}}^4 / \lambda_{\text{ir}}^4$  to the Rayleigh absorption ratio  $\lambda_{\text{ir}} / \lambda_{\text{vis}}$ , while the rest of the XCR curve is almost the same as for the non-absorber. As  $k$  increases the zero-diameter XCR limit does not change, but more and more of the XCR curve drops below the  $k=0$  curve. Very strongly absorbing aerosols do not meet the XCR requirement even for the 1.55- $\mu\text{m}$  system.

## UNCLASSIFIED

UNCLASSIFIED

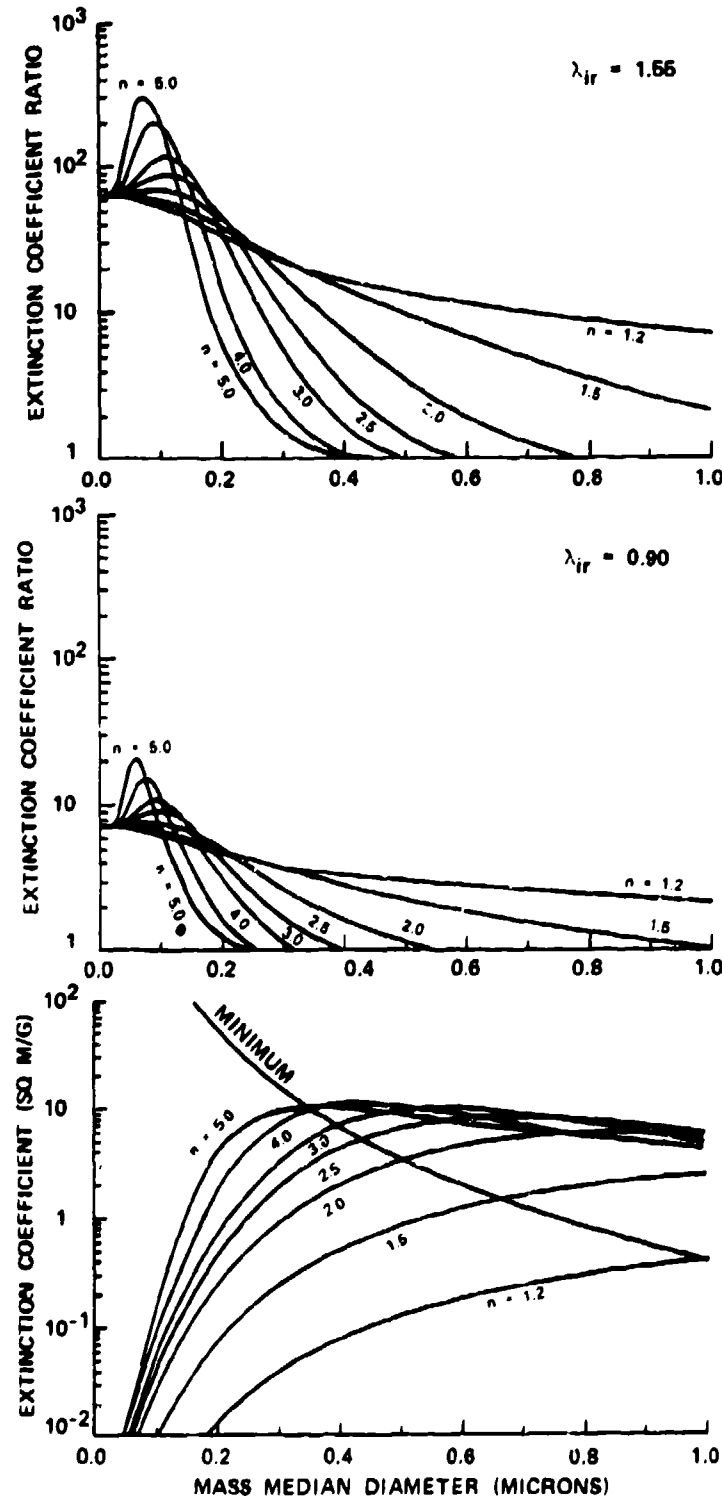
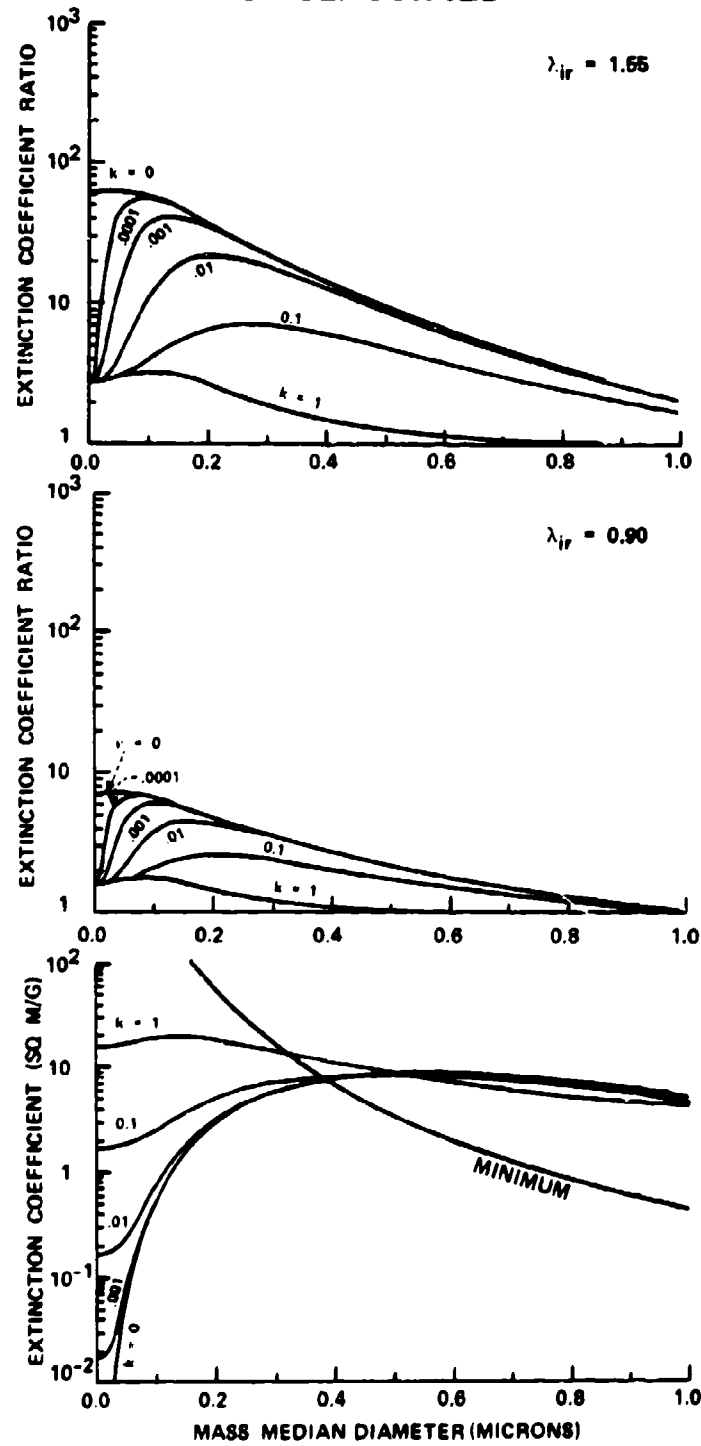


FIGURE 6. EXTINCTION COEFFICIENT & XCR VS MMD FOR NON-ABSORBERS  
FOR VARIOUS VALUES OF  $n$  ( $n_{ir} = n_{vis}$ )

UNCLASSIFIED

UNCLASSIFIED

FIGURE 7. EXTINCTION COEFFICIENT & XCR VS MMD FOR VARIOUS VALUES OF  $k$ ; $n = 1.6, m_{ir} = m_{vis}$ 

UNCLASSIFIED

UNCLASSIFIED

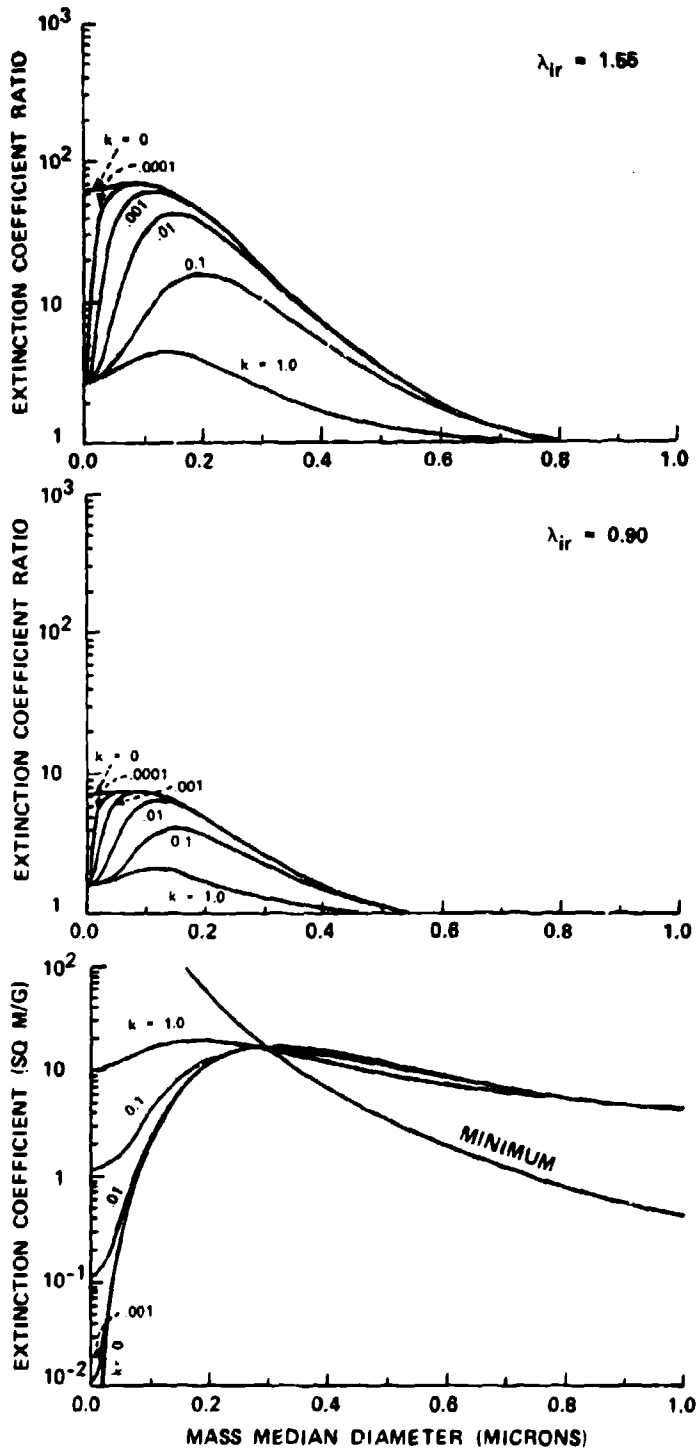


FIGURE 8. EXTINCTION COEFFICIENT & XCR VS MMD FOR VARIOUS VALUES OF K  
 $n_{ir} = n_{vis} = 2.0$

UNCLASSIFIED

**UNCLASSIFIED**

D-1

**4.2 SCATTERERS WITH UNEQUAL REFRACTIVE INDICES**

The XCR increases when  $n_{vis}$  becomes larger than  $n_{ir}$ . Figure 9. shows for a non-absorbing smoke how the XCR increases with  $n_{vis}$  when  $n_{ir} = 1.5$ , while at the same time the particulate diameter corresponding to the minimum extinction coefficient meeting the visible attenuation requirement decreases, so that the usable MMD interval for the 1.55- $\mu\text{m}$  system becomes larger, and when  $n_{vis} = 2.0$  a small usable MMD interval appears for the 0.9- $\mu\text{m}$  system. Figures 10. and 11. show the result of decreasing  $n_{ir}$  to 1.33 and 1.2 respectively when  $n_{vis} = 1.5$ . When  $n_{ir} = 1.33$ , both requirements are never simultaneously met for the 0.9- $\mu\text{m}$  system; when  $n_{ir} = 1.2$ , a usable MMD interval appears. The effect of enhancement of the XCR by increasing  $n_{vis}$  is shown shown in Table IV. (Note that where  $D_{min} > D_{max}$ , there is no usable MMD interval.)

TABLE IV. MIE RESULTS WHEN  $RI_{vis} > RI_{ir}$ 

$n_{vis}$	$n_{ir}$	0.9- $\mu\text{m}$ system		1.55- $\mu\text{m}$ system	
		$D_{min}$	$D_{max}$	$D_{min}$	$D_{max}$
1.5	1.5	0.39 $\mu\text{m}$	--	*0.39 $\mu\text{m}$	0.50 $\mu\text{m}$
1.6	1.5	0.36	--	*0.36	0.54
1.7	1.5	0.34	0.19	*0.34	0.55
1.8	1.5	0.32	0.25	*0.32	0.56
1.9	1.5	0.31	0.29	*0.31	0.55
2.0	1.5	*0.30	0.31	*0.30	0.55
2.0	2.0	0.30	--	*0.30	0.37
2.0	1.5	*0.30	0.31	*0.30	0.55
2.0	1.33	*0.30	0.44	*0.30	0.70
2.0	1.2	*0.30	0.63	*0.30	>1.0
1.5	1.33	0.39	0.24	*0.39	0.74
1.5	1.2	*0.39	0.63	*0.39	0.71
1.33	1.2	*0.46	0.33	*0.46	>1.0

**4.3 EFFECT OF ABSORPTION IN THE VISIBLE**

Another possible way to enhance the XCR is to make the aerosol material absorbing in the visible but not in the infrared, perhaps by adding a dye. Figure 12. shows the result of introducing moderate absorption in the visible when  $r = 1.33$ ; here  $k = .01$ , corresponding to an absorption coefficient of about 2300/cm. When the MMD  $> 0.2 \mu\text{m}$ , the curves are nearly the same as for the corresponding non-absorber. For smaller particles the absorption comes into play; the visible extinction coefficient attains the Rayleigh absorption limit at MMD = 0, causing the XCR curve to become

**UNCLASSIFIED**

841

UNCLASSIFIED

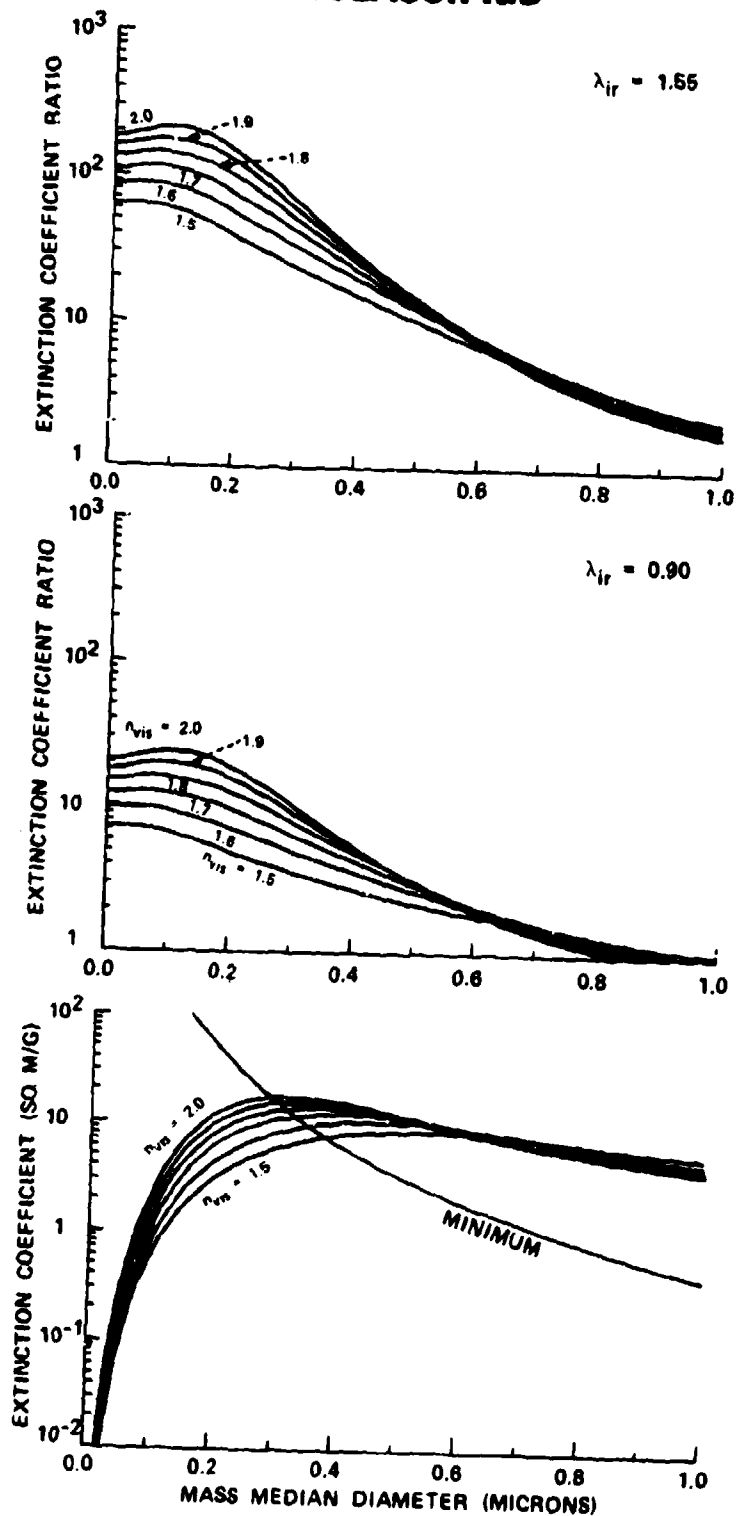


FIGURE 9. IMPROVEMENT OF XCR FOR NON-ABSORBERS BY MAKING  $n_{vis} > n_{ir}$ ;  $n_{ir} = 1.5$

UNCLASSIFIED

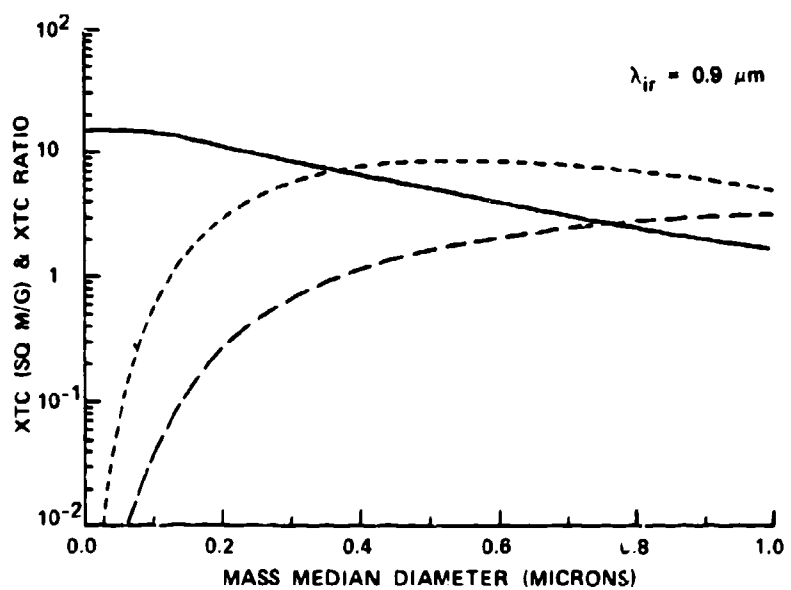
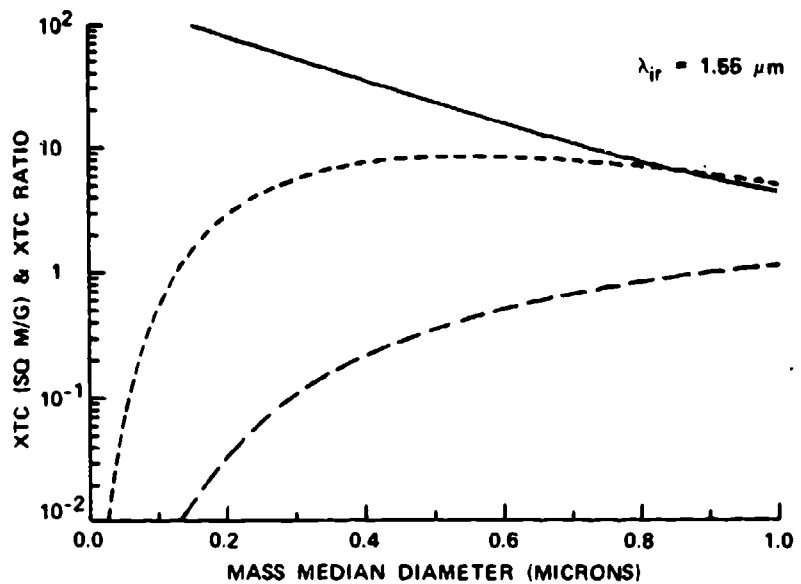
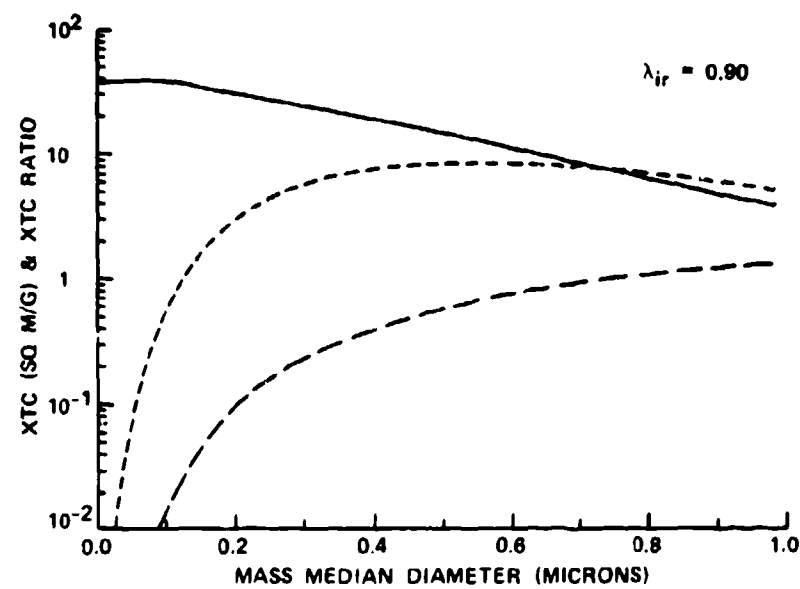
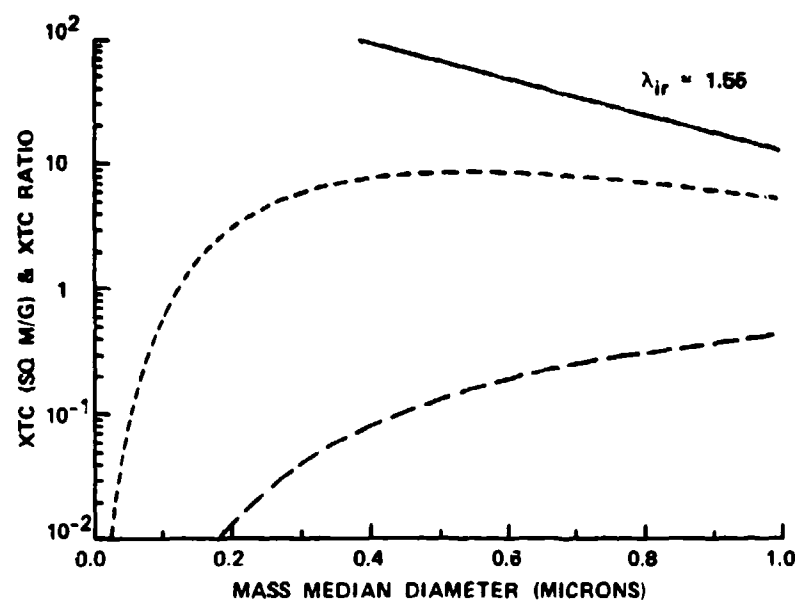
**UNCLASSIFIED**

FIGURE 10. XCR FOR  $n_{vis} > n_{ir}$ ;  $n_{vis} = 1.5$ ,  $n_{ir} = 1.33$

**UNCLASSIFIED**

UNCLASSIFIED

FIGURE 11. XCR FOR  $n_{vis} > n_{ir}$ ;  $n_{vis}=1.5$ ,  $n_{ir}=1.2$ 

UNCLASSIFIED

**UNCLASSIFIED**

D-1

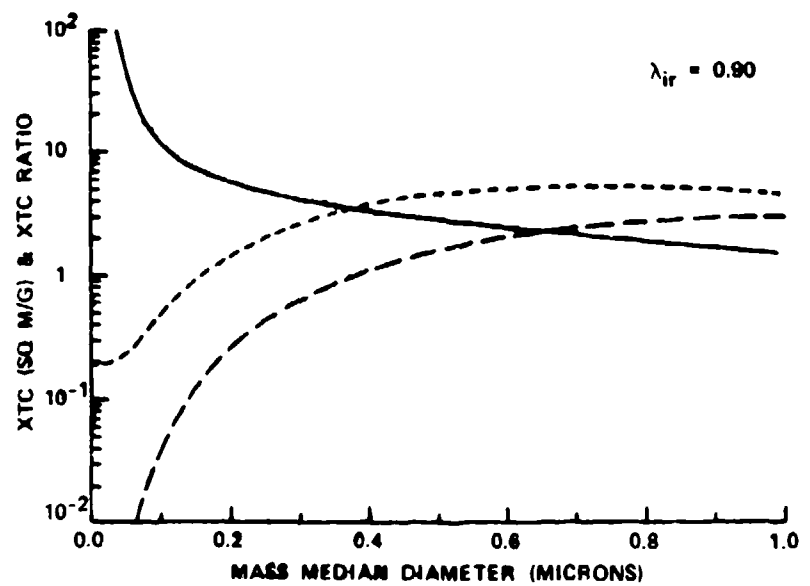
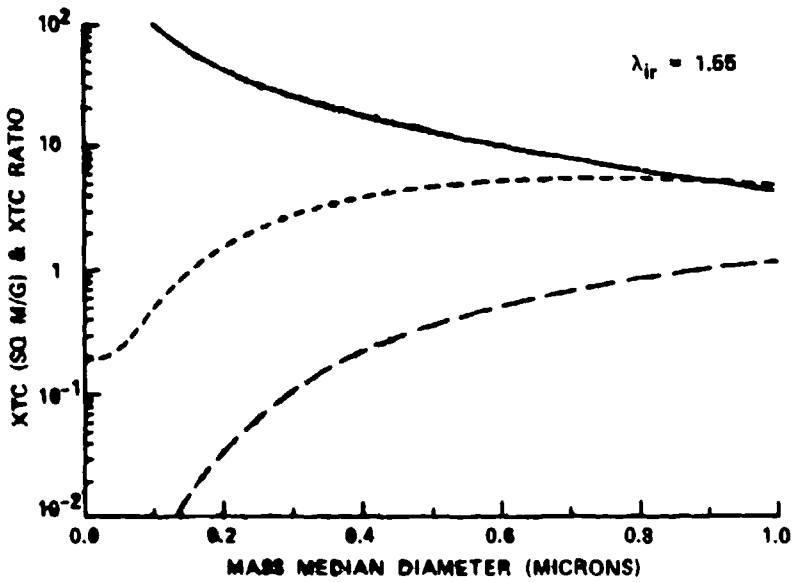


FIGURE 12. XCR ENHANCED BY ABSORPTION IN THE VISIBLE:  
 $m_{vis} = (1.33, .01)$ ,  $m_{ir} = (1.33, 0)$

**UNCLASSIFIED**

## UNCLASSIFIED

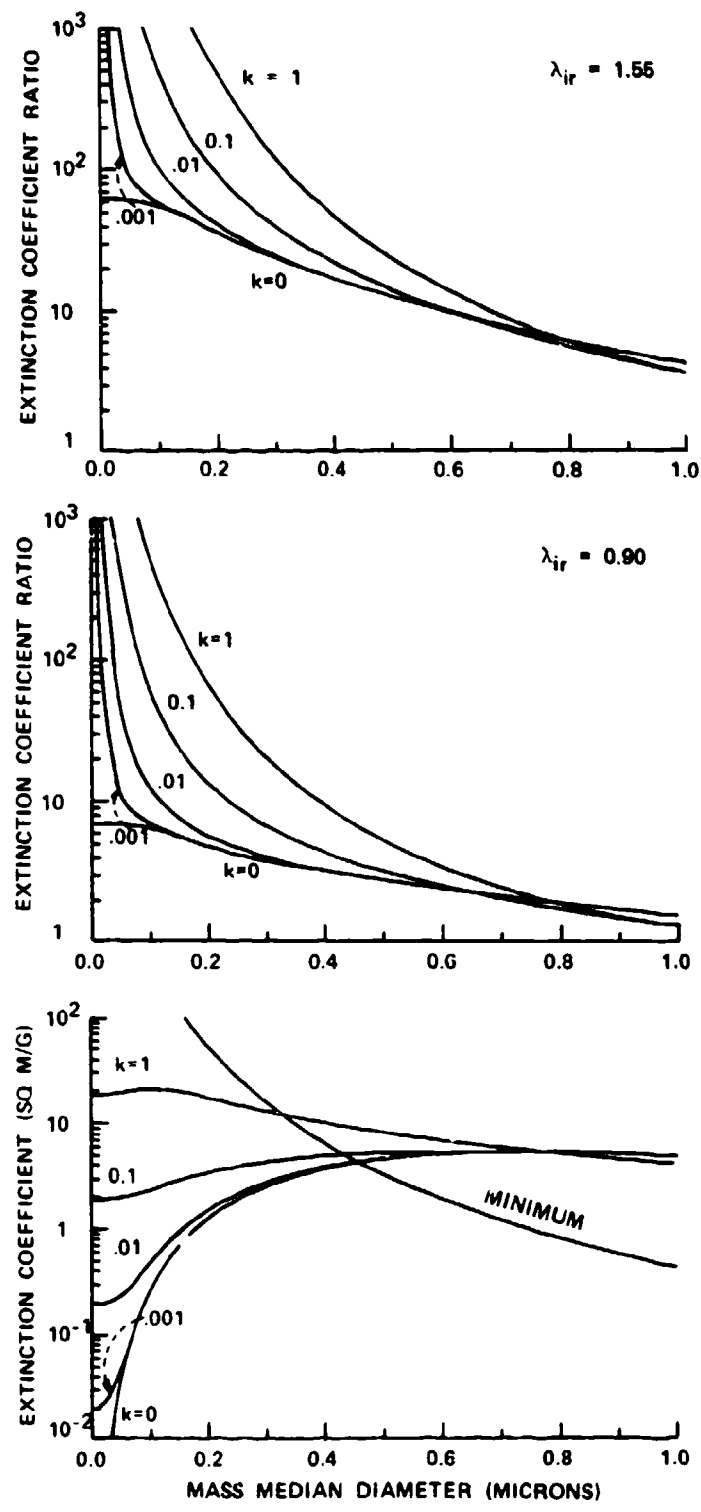
unlimitedly large, since the infrared extinction is due to scattering and goes to zero as the MMD goes to zero. This effect takes place only when the aerosol particles are too small to meet the visible attenuation requirement; a more strongly absorbing material must be used to achieve a usable MMD interval. Figures 13. displays the XCR and visible extinction curves for various values of the of  $k_{vis}$  for  $n_{vis} = n_{ir} = 1.33$ . It can be seen that the effect of absorption on the XCR and the extinction coefficient does not become important for particles larger than 0.2  $\mu\text{m}$  until the absorption becomes very strong ( $k_{vis} = 0.1$  to 1.0). The usable MMD intervals broaden as  $k_{vis}$  increases, but for the 0.9- $\mu\text{m}$  system a usable interval appears only for  $k=1.0$ . These and similar results for  $n = 1.5$  and  $n = 2.0$  are summarized in Table V. Note that no usable MMD interval appears for the 9- $\mu\text{m}$  system for  $n = 1.5$  or 2.0.

TABLE V. MIE RESULTS FOR ABSORPTION IN THE VISIBLE ( $n_{vis}=n_{ir}$ )

n	$k_{vis}$	0.9- $\mu\text{m}$ system		1.55- $\mu\text{m}$ system	
		D <sub>min</sub>	D <sub>max</sub>	D <sub>min</sub>	D <sub>max</sub>
1.33	0.0	0.46 $\mu\text{m}$		*0.46 $\mu\text{m}$	0.59 $\mu\text{m}$
1.33	0.001	0.46	0.05	*0.46	0.59
1.33	0.01	0.46	0.11	*0.46	0.59
1.33	0.1	0.44	0.23	*0.44	0.60
1.33	1.0	0.32	0.39	*0.32	0.67
1.5	0.0	0.39	--	*0.39	0.50
1.5	0.001	0.39	0.04	*0.39	0.50
1.5	0.01	0.39	0.09	*0.39	0.49
1.5	0.1	0.38	0.18	*0.38	0.48
1.5	1.0	0.32	0.29	*0.32	0.51
2.0	0.0	0.30	--	*0.30	0.37
2.0	0.001	0.30	0.03	*0.30	0.37
2.0	0.01	0.30	0.06	*0.30	0.36
2.0	0.1	0.30	0.13	*0.30	0.35

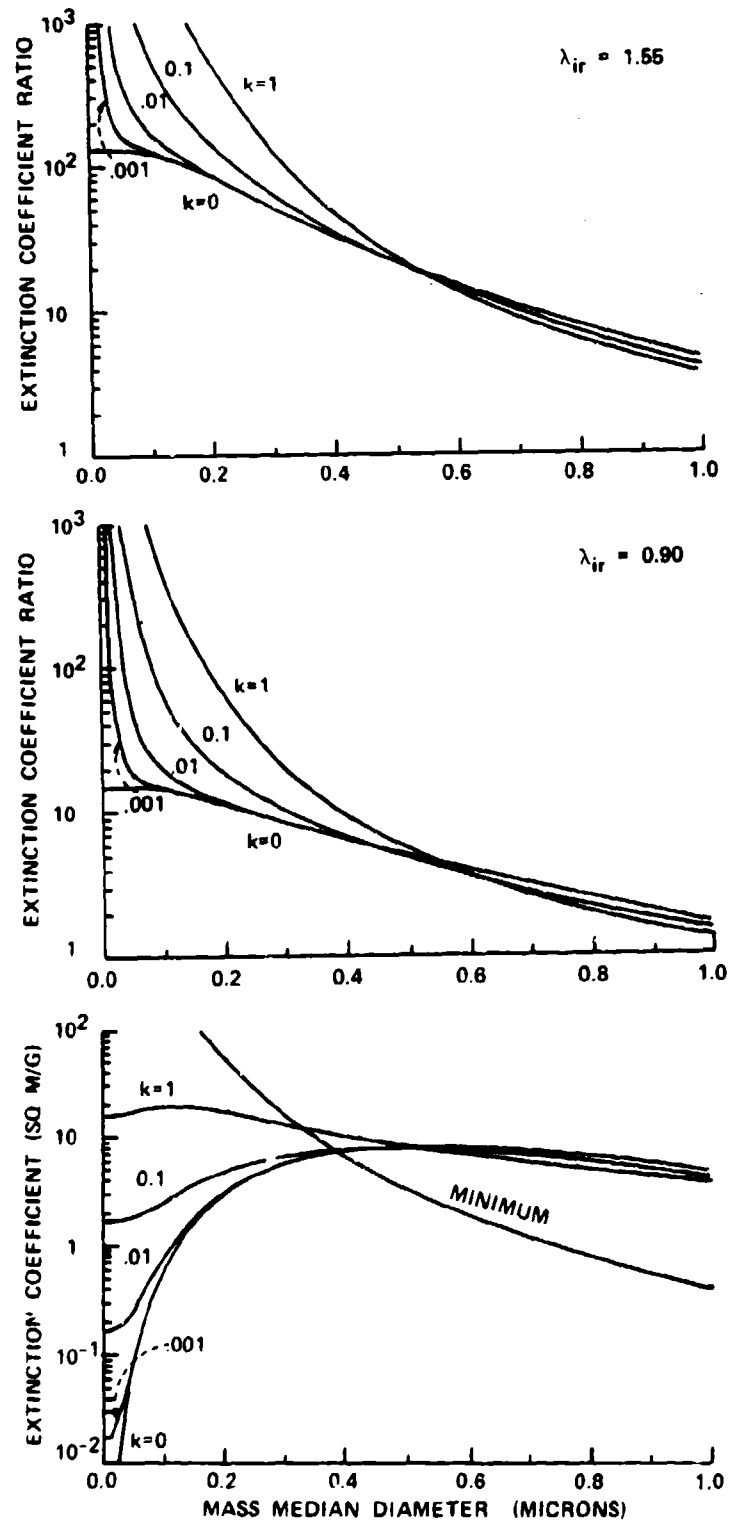
In Table IV. it was seen that for  $n_{vis}=1.5$  reducing  $n_{ir}$  to 1.33 did not produce a usable MMD interval. Figure 14. shows the effect of absorption in the visible in this situation. Again it is seen that unless  $k$  is very large, the absorption effect appears only for particles too small to meet the visible attenuation requirement. Table VI. summarizes the results depicted in Figure 14. and also for  $n_{vis}= 2.0$ ,  $n_{ir}=1.5$ . In the latter case the effect of very strong absorption is to destroy the small usable MMD interval present when  $k$  is small.

UNCLASSIFIED

FIGURE 13. XCR ENHANCED BY ABSORPTION IN VISIBLE;  $n_{ir}=n_{vis}=1.33$ 

UNCLASSIFIED

UNCLASSIFIED

FIGURE 14. XCR ENHANCED BY ABSORPTION IN VISIBLE;  $n_{vis} > n_{ir}$ ;  $n_{vis}=1.5$ ,  $n_{ir}=1.33$ 

UNCLASSIFIED

## UNCLASSIFIED

D-1

TABLE VI. MIE RESULTS FOR ABSORPTION IN THE VISIBLE ( $n_{vis} > n_{nir}$ )

$n_{vis}$	$n_{nir}$	0.9- $\mu\text{m}$ system			1.55- $\mu\text{m}$ system	
		$D_{min}$	$D_{max}$	$D_{min}$	$D_{max}$	
1.33	1.2	0.0	0.46 $\mu\text{m}$	0.33 $\mu\text{m}$	*0.46 $\mu\text{m}$	>1.0 $\mu\text{m}$
		0.001	0.46	0.34	*0.46	>1.0
		0.01	0.46	0.36	*0.46	>1.0
		0.1	*0.44	0.46	*0.44	>1.0
		1.0	*0.32	0.59	*0.32	0.99
1.5	1.33	0.0	0.39	0.24	*0.39	0.74
		0.001	0.39	0.24	*0.39	0.74
		0.01	0.39	0.25	*0.39	0.73
		0.1	0.38	0.31	*0.38	0.70
		1.0	*0.32	0.39	*0.32	0.68
2.0	1.5	0.0	*0.30	0.31	*0.30	0.55
		0.001	*0.30	0.31	*0.30	0.55
		0.01	*0.30	0.31	*0.30	0.55
		0.1	0.30	0.30	*0.30	0.54
		1.0	0.31	0.30	*0.31	0.51

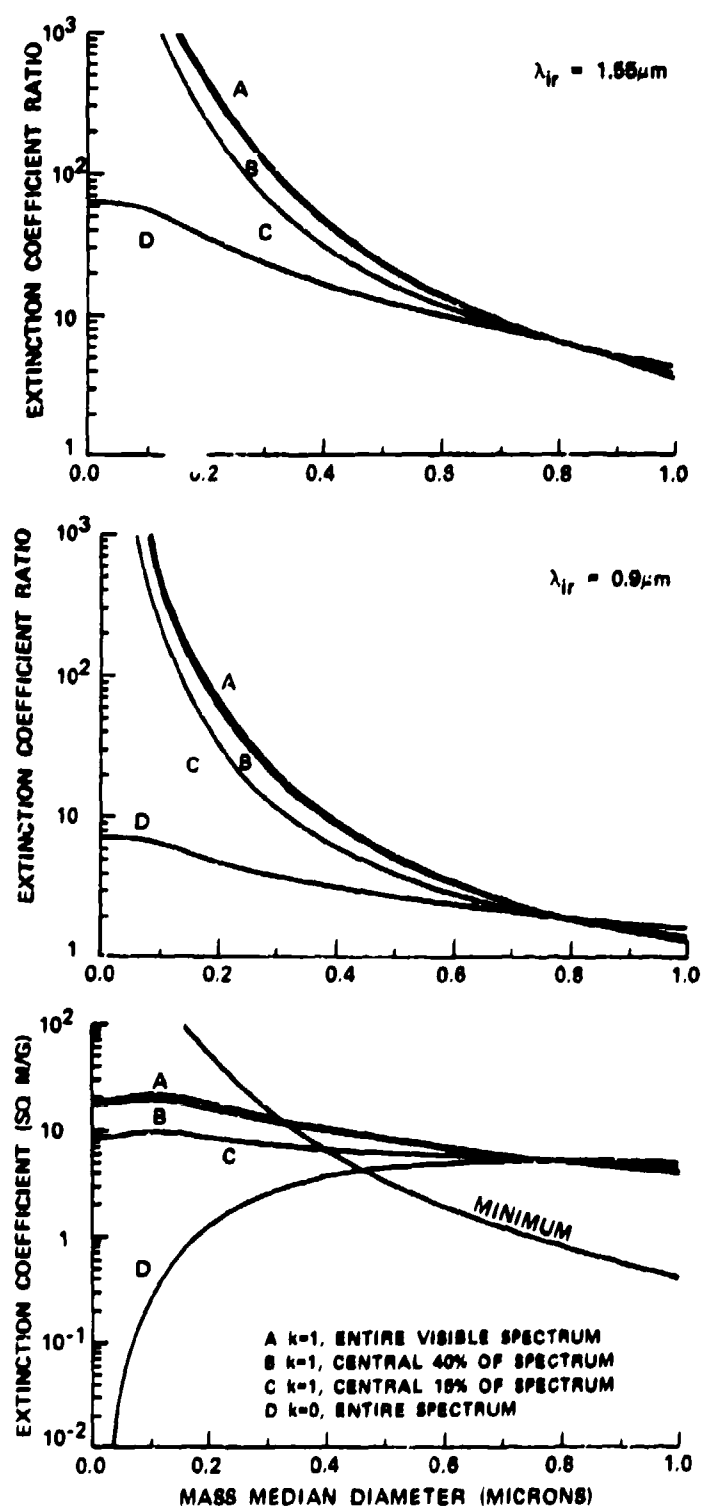
Consideration of the effect of absorption has shown that in order to be useful, the absorption must be very strong. So far only the effect of absorption over the whole visible spectrum has been considered. The effect of strong absorption over part of the visible spectrum is displayed in Figure 15. Here the central portion of the spectrum is assumed to be strongly absorbing; since the photopic response of the eye has been taken into consideration in integrating over the visible spectrum, the effect of absorption in the center of the spectrum is greater than at the red or violet end. Absorption over the central 40% of the spectrum (curve B) yields results that are almost the same as for absorption over the whole spectrum (curve A). Absorption over only the central 15% of the spectrum lowers the XCR and visible extinction curves enough that for the 0.9- $\mu\text{m}$  system the usable MMD interval is eliminated. The results of these and similar calculations for  $n = 1.33$ ,  $k_{vis} = 1$  are shown in Table VII.

TABLE VII. SPECTRAL ABSORPTION

$\lambda_{abs}$	0.9- $\mu\text{m}$ system			1.55- $\mu\text{m}$ system	
	$D_{min}$	$D_{max}$		$D_{min}$	$D_{max}$
----	0.46 $\mu\text{m}$	--		*0.46 $\mu\text{m}$	0.59 $\mu\text{m}$
.53-.58 $\mu\text{m}$	0.40	0.31		*0.53	0.64
.58-.63	0.42	0.28		*0.42	0.64
.58-.70	0.41	0.30		*0.41	0.65
.53-.68	*0.34	0.37		*0.34	0.67
.48-.63	*0.33	0.38		*0.33	0.67
.43-.58	0.37	0.34		*0.37	0.64
.40-.53	0.44	0.25		*0.44	0.61
.40-.70	*0.32	0.39		*0.32	0.67

UNCLASSIFIED

UNCLASSIFIED

FIGURE 16. XCR ENHANCED BY SPECTRAL ABSORPTION:  $n_{ir} = n_{vis} = 1.33$ ,  $k_{ir} = 0$ 

UNCLASSIFIED

**UNCLASSIFIED**

Note that absorption even over 40% of the spectrum does not produce a usable MMD interval for the 0.9- $\mu\text{m}$  system except when the absorption interval is in the central portion of the spectrum. For the 1.55- $\mu\text{m}$  system reducing the absorption interval to 40% of the spectrum shortens the usable MMD interval by varying degrees depending on which portion of the spectrum is absorbing, because of the nature of the photopic response curve.

It should be pointed out again that the result of integration over wave length depends on the CL product over which attenuation takes place. Integration of the form  $\int \alpha(\lambda)d\lambda$  used in section 2, or  $\int \alpha(\lambda)p(\lambda)d\lambda$  (where the integral is weighted photopically) used in this section, is accurate only when  $e^{aCL}$  is close to unity. Otherwise the correct integration yields smaller values for the integrated extinction coefficient because those wave lengths where the extinction is lowest are most strongly represented in the transmission spectrum. This means that when the extinction product  $aCL$  is not small, the wave-length-integrated values for spectral absorption given here for the visible are too large and the resulting XCR values are optimistic.

#### 4.4 VARIATION OF $\sigma_g$

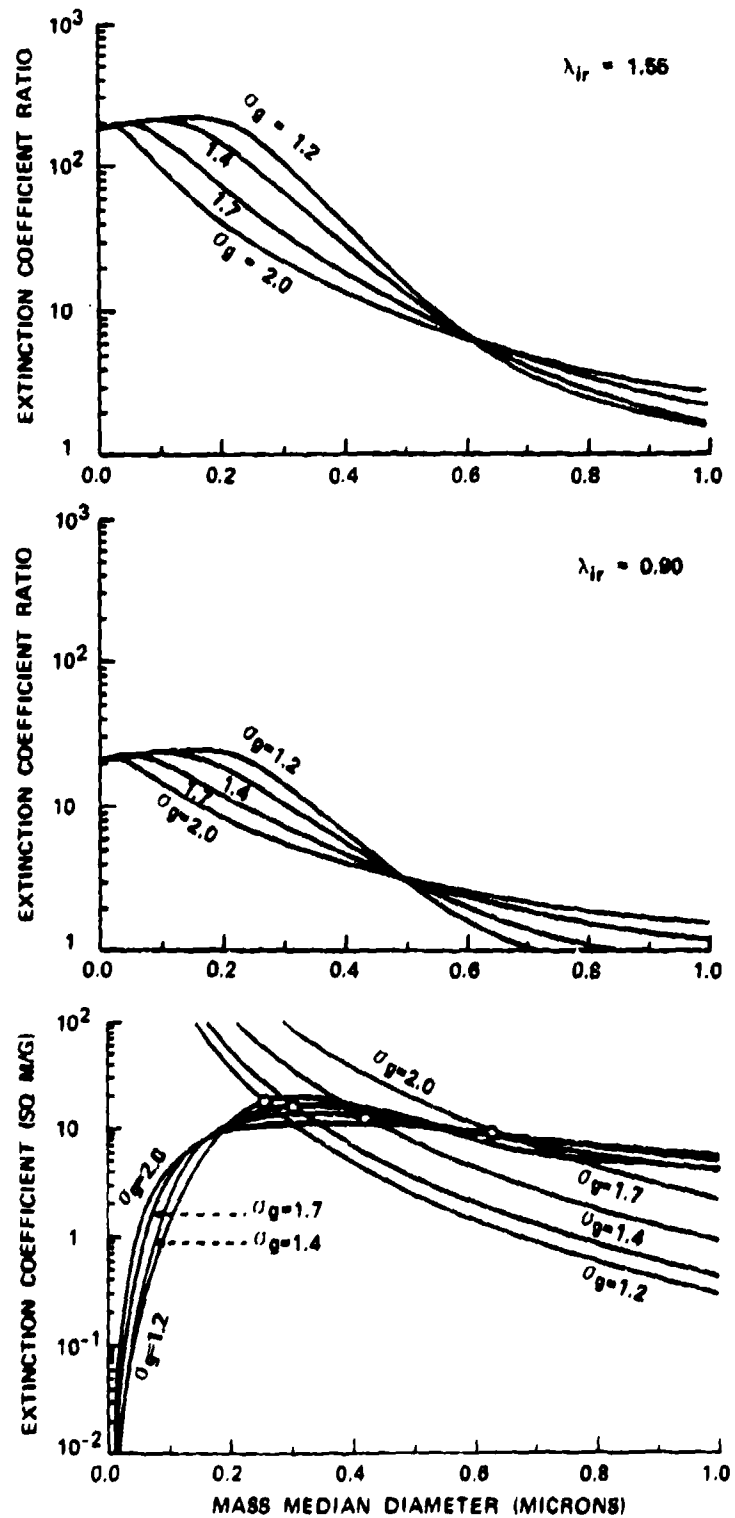
Calculations heretofore have been made using particle size distributions whose breadth is defined by  $\sigma_g = 1.4$ , because this is the "quasi-stable" value allegedly stable with respect to coagulation, and is consistent with the data obtained in experimental work done in the CSL Obscuration Sciences Section. The calculated values of the extinction coefficient and the XCR depend on the value of  $\sigma_g$ , as shown by Figure 16, and Table VIII., results being less satisfactory for broader distributions.

TABLE VIII. EFFECT OF VARIATION OF  $\sigma_g$

nvis	nir	$\sigma_g$	$\lambda_{IR} = 0.9 \mu\text{m}$		$\lambda_{IR} = 1.55 \mu\text{m}$	
			Dmin	Dmax	Dmin	Dmax
1.5	1.33	1.2	0.35 $\mu\text{m}$	0.28 $\mu\text{m}$	*0.35 $\mu\text{m}$	0.78 $\mu\text{m}$
		1.4	0.39	0.23	*0.39	0.74
		1.7	0.50	0.16	*0.50	0.63
		2.0	0.72	0.10	0.72	0.57
2.0	1.5	1.2	*0.26	0.35	*0.26	0.55
		1.4	*0.30	0.31	*0.30	0.55
		1.7	0.42	0.23	*0.42	0.52
		2.0	0.63	0.17	0.63	0.47

**UNCLASSIFIED**

UNCLASSIFIED

FIGURE 16. EFFECT OF DISTRIBUTION BREADTH;  $n_{vis}=2.0$ ,  $n_{IR}=1.5$ 

UNCLASSIFIED

# UNCLASSIFIED

D-1

## S. OTHER POSSIBILITIES

This study has considered only aerosols composed of spherical particles with "normal" values of the refractive index, i.e., having  $n > 1$ . An investigation might be made on the use of metals or other materials with unusual optical properties. Aerosol particles with shapes other than spherical might be considered. A study of Rayleigh sized rods and flakes (represented by prolate and oblate ellipsoids) could be relatively easily accomplished.

## 6. CONCLUSIONS

On the basis of these calculations certain conclusions can be drawn regarding the use of aerosols composed of spherical particles with ordinary indices of refraction ( $n > 1$ ) in the MILES system:

1. For materials whose complex index of refraction does not vary appreciably between the visible and the near infrared, a somewhat restricted range of MMD (which depends on the refractive index) can be found which will meet the requirements on both visible attenuation and the extinction coefficient ratio for the (proposed) 1.55- $\mu\text{m}$  system, but the 10:1 XCR cannot be obtained for the current 0.9- $\mu\text{m}$  system.

2. This unsatisfactory situation is exacerbated if the aerosol material is an absorber.

3. If the aerosol material is non-absorbing, the usable MMD range for the 1.55- $\mu\text{m}$  system is broadened and a usable range appears for the 0.9- $\mu\text{m}$  system if  $n_{\text{vis}}$  is sufficiently greater than  $n_{\text{irr}}$ .

4. If  $n_{\text{vis}}$  and  $n_{\text{irr}}$  are equal or not sufficiently different to produce a usable 10:1 XCR, this ratio may be achieved if the aerosol is made very strongly absorbing over all or most of the visible spectrum. A moderate absorber does not help.

5. Particles large enough to be considered geometric scatterers are unsatisfactory.

6. The XCR is adversely affected if the particle size distribution is broad.

7. Unusual refractive indices and non-spherical shapes should be considered.

8. The use of laser/detector wave lengths longer than 0.9  $\mu\text{m}$  for the MILES system should be considered.

# UNCLASSIFIED

853

**UNCLASSIFIED**

## REFERENCES

1. Van de Hulst, H.C., Light Scattering by Small Particles, John Wiley & Sons, 1957. p. 14.

2. Van de Hulst, H.C., Light Scattering by Small Particles, John Wiley & Sons, 1957, p. 270.

3. Stuebing, E. W., Deviations from Beer's Law which Sometimes Prevent Defining a Simple Overall Extinction Coefficient for a Smoke in Each Atmospheric Window. Proceedings of the Smoke/Obscurants Symposium II, DRCPM-SMK-T-004-78, Office of the Project Manager for Smoke/Obscurants, APU, MD (1978).

4. Friedlander, S.K., Smoke, Dust and Haze, John Wiley & Sons, 1975, pp. 179-80.

5. Van de Hulst, H.C., op cit, p 107,108.

6. Mie, G. Ann. Physik, 25, 377 (1908)

7. Van de Hulst, H.C., op cit, p114-30

8. Dave, J V. Subroutines for Computing the Parameters of Electromagnetic Radiation Scattered by a Sphere, Report No. 320-3237, IBM Scientific Center, Palo Alto, California, May, 1968

# UNCLASSIFIED

D-2

## THE EFFECT OF SMOKE IN SMALL UNIT TACTICS

Bruce W. Fowler  
US Army Missile Command  
Advanced Systems Concepts Office  
Redstone Arsenal, AL  
and

CPT James Price  
US Army Missile and Munitions Center and School  
Directorate for Combat Developments  
Redstone Arsenal, AL

### ABSTRACT

The effect of smoke in the execution of small unit tactics is examined. Use is made of the Small Unit Tactics Training Simulation (SUTTS) and the Line-Of-Sight Blockage (LOSBl model to examine the impact of smoke on the execution of small unit tactics. A series of company level tactical scenarios, executed both with and without smoke, are described. Outcome of these scenarios, carried out as man-in-the-loop exercises using the SUTTS and LOSB models, are presented. Insights into the tactical and doctrinal use of smoke gained from the investigation are discussed.

### 1. INTRODUCTION

The effect of smoke on small unit tactics is investigated. A combination of two models, the Small Unit Tactics Training Simulation, described in Section 2, and the Line-Of-Sight Blockage Model, described in Section 3, were combined. Company sized attacks, both with and without smoke, were simulated. The conduct of the experiment is described in Section 4. Preliminary results based on limited data are presented in Section 5.

### 2. SUTTS MODEL

The Small Unit Tactics Training Simulation (SUTTS) is a micro-computer based conflict simulation designed for use in training company and platoon level tactics. This is a one-sided simulation - the enemy force is "played" by the program itself. SUTTS is designed to allow players to exercise simulated command down to platoon level.

SUTTS incorporates an analytical terrain model. Indeed, that is one of the chief advantages of SUTTS - that it may be easily modified to incorporate terrain of an individual nature for each unit to be trained. In essence, the simulation can use any local terrain to enhance any pre-field training. The terrain used in this simulation is taken from a tank training area in Germany.

One of the advantages of the analytical terrain model is the ease of performing line-of-sight calculations. With an analytical terrain model, line-of-sight blockage determinations can be performed in an analytical manner. This facilitates subsequent calculations for the smoke model.

# UNCLASSIFIED

# UNCLASSIFIED

D-2

Movement and firing is conducted by the personnel being trained. They determine where (or at least in what direction) they will move their units. If a target is "seen," a Monte Carlo scheme is used to determine who shoots first. The current version of the model does not incorporate either search, nor recognition. That improvement is planned, however.

The outcome of engagements is determined by Monte Carlo calculation. This calculation incorporates a probability of hit (versus range) and a probability of kill (versus target type). Elaborate factors such as actual target size, presentation, and armor thickness do not enter into the model. Indirect fires also have a dispersion associated with them.

The enemy forces are largely predetermined since they must be controlled by the simulation in response to the actions of the players. This predetermination would seem to provide the players with an advantage in the offense - they could try to out wait a preprogrammed (at a specific time) withdrawing enemy - except for the requirement to the players to act as rapidly as possible. While this defect cannot be corrected in the computer operating memory (48K) available to the version to be fielded, an improved, more responsive enemy will be incorporated in this test bed version (480K).

During normal training execution, the trainees/players are prebriefed, allowed to formulate overall plans, and separated to use the simulation. Usually, each player commands a platoon sized unit and is allowed to communicate with the other players via a telephone for a limited time. This procedure was altered for this exercise.

A complete description of SUTTS is given in Reference 1.

## 3. LOSB MODEL

The Line-Of-Sight Blockage model is a parametric obscuration model. The model represents the effective blockage area of a single munition obscurant as a function of time by parameterizing time direction relative to line-of-sight (i.e., head/tail, quartering, or crossing), spectral band (visible, near, mid, or far IR), meteorology (neutral, lapse, or inversion), and wind speed (5, 10, or 15 knots).

# UNCLASSIFIED

# UNCLASSIFIED

D-2

The effective blockage area, because of the nature of the preparameterization model can be, represented by a half ellipse. The model represents the semi-axes of the ellipse as time dependent functions with parametric coefficients determined by linear regression of calculations performed using the preparameterization (general) model. A full description of the LOSB Model may be found in Reference 2, and references therein.

The model works in a simple manner. The type impact point, and impact time of each munition is maintained. The cloud centroid/center of the ellipse travels downwind after impact. The pertinent set of semi-axis parameters is determined by the angle between line of sight and wind direction, munition type, meteorology, and wind speed. The semi-axis may then be calculated. The half ellipse is then aligned perpendicularly to the line-of-sight ground trace. If the three-dimensional line-of-sight pierces the half ellipse, the line-of-sight is blocked.

## 4. EXPERIMENTAL DESCRIPTION

The LOSB Model was incorporated into the SUTTS Model. This largely amounted to a simple modification to the line-of-sight calculation. A relatively brute force approach was initially taken. Munitions were ignored only if they were behind the observer or beyond the target. This results in extensive unnecessary calculations and this situation is being alleviated. Munitions were dropped from the queue only once their semi-axis became negative. This situation is also being addressed.

One deviation in the normal use of the model is the role of the player. In this case, one player commands an entire company sized unit - tanks and ATGMs. After being briefed, the player develops three battle plans of attack, one without smoke, one with limited smoke, and one with unlimited smoke. To date, only 4.2" mortar delivered WP smoke. The player is then allowed to play out each plan (in the opposite order to that given above), up to three times. If a plan is replayed, the results are averaged to account for learning. The defending force is randomly varied each time.

## 5. PRELIMINARY RESULTS

Because of the amount of time required to carry out the play of a plan, the difficulty in finding "qualified" players, and the limited response of the foe, extensive results are not yet available.

# UNCLASSIFIED

# **UNCLASSIFIED**

D-2

Some limited results are available in the form of general comments.

A few problems in the model have surfaced. Several of these have been identified, including policing of the munitions queue, and nonresponsiveness of the foe. Additionally, there is no good way to indicate to the player when he has developed a continuous screen. This presents a real problem only when the player has limited smoke available. It may be noted that this is a real world as well as a simulation problem. A typical player response in this situation seems to be conservatism with resultant under-utilization of smoke assets.

Some differences in losses are seen when unlimited smoke is available. Inordinately large numbers of munitions are used to assure maintenance of continuous screens. There also seems to be some tendency to advance brazenly behind the smoke - this increases vulnerability to unobscured enemy. Additionally, there is some uncertainty on the part of some players as to what actions to take once they have closed on the enemy behind the smoke.

It is emphasized that these results are extremely preliminary and represent a small data base. Further, trials and improvements to the model are planned.

## **REFERENCES**

1. Price, James D., An Investigation into Development of a Military Small Unit Tactical Training Simulation, University of Alabama Master's Thesis, 1980.
2. Fowler, Bruce W., A Parametric Model For the Effect of White Phosphorus Smoke On Target Detection II; Multiband Line-Of-Sight Blockage Model, MICOM TR 0-80-4, 6 June 1980.

# **UNCLASSIFIED**

SMOKE EMPLOYMENT: AN OPERATIONAL CONCEPT

Dr. John W. Scully and MAJ Peter B. Harrington  
US Army Chemical School  
Fort McClellan, Alabama 36205

#### ABSTRACT

The Commander, US Army Training and Doctrine Command has recently approved and published the Army Operational Concept for Employment of Smoke. This concept provides guidance to Army activities involved in development of smoke materiel, doctrine and organizations. Concept purpose and objectives are presented along with specifics regarding smoke screen types and operations. Planned TRADOC efforts dealing with implementation of the Concept, such as, generation of materiel requirements documents, revised smoke unit force structuring, and supporting operational testing are discussed.

#### 1. INTRODUCTION

In recent years the Department of the Army has placed increased emphasis on the impact of the integrated battlefield on the effectiveness of combat operations. Many factors must be considered when describing the composition of this battlefield one of which is the appearance of man-made smoke, whether generated by friendly or threat forces, and how this smoke interacts with troop movements and the sophisticated electro-optical devices being fielded by both sides. When properly employed, smoke will significantly influence the effectiveness of tactical operations to include target acquisition, target designation, and fire control capabilities of many electro-optical devices.

The United States Army Training and Doctrine Command (TRADOC) recognizes the impact of smoke on the modern battlefield and has been actively involved in establishing a comprehensive smoke program which addresses combat developments, doctrine and training. Individual schools within TRADOC have the responsibility for developing doctrine, training programs and materiel requirements within their assigned areas of proponency. Overall integration of the smoke program within TRADOC is the responsibility of the TRADOC System Manager for Smoke/Obscurants who maintains close liaison with the materiel developer, the Project Manager for Smoke/Obscurants.

To provide the necessary direction for the smoke program TRADOC developed an operational concept for the employment of smoke and for smoke countermeasures, hereinafter referred to as the Smoke Concept.<sup>1</sup> In September 1980, TRADOC approved the Smoke Concept for use by combat developers, training developers, and trainers as a guide in meeting their program responsibilities. The purpose of this paper is twofold; first, to provide an overview of the salient features of the Smoke Concept, and, second, to address specific efforts presently being conducted by TRADOC which will contribute to the implementation of this concept.

## 2. SMOKE CONCEPT OVERVIEW

Reference to weapons utilizing electro-optical acquisition and guidance systems sets the tone of the Smoke Concept. These systems include devices using thermal imaging technology in the far infrared region of the electro-magnetic spectrum. Smoke, as used throughout the Smoke Concept, should be thought of as any material which may be disseminated for the purpose of providing screening capabilities against visible, infrared and millimeter wave regions. Not only must US forces be prepared to properly employ smoke under various battle conditions, but they must also be prepared to fight and operate in an environment characterized by low visibility. Threat forces possess a vast arsenal of smoke devices and munitions and are continually expanding their smoke employment capacity by developing new and improved smoke material and devices.<sup>2</sup> Threat doctrine emphasizes extensive troop training in smoke environments and extensive tactical use of smoke whenever it will provide an operational advantage.

## 3. EMPLOYMENT OF SMOKE

The proper use of smoke on the battlefield is a combat multiplier which increases the effectiveness of US operations by reducing the vulnerability of US forces. Proper application of smoke starts with careful planning at all levels of command in order to integrate smoke into combat operations. A complete plan must always include close coordination among all units involved in a smoke mission. Smoke, because of its susceptibility to even slight changes in meteorological conditions, has the potential of adversely affecting operations being conducted by adjacent friendly units. It is the responsibility of higher level command to conduct overall mission coordination to prevent such interference from occurring.

Smoke planning must be integrated into the overall preparations conducted prior to a combat mission. Tradeoffs must continuously be made between the amount of degradation to be expected in the threat capabilities versus the potential for adverse effects on friendly battlefield operations. The use of other combat multipliers, such as electronic warfare and conventional or chemical munitions, in conjunction with smoke employment, must also be considered in the planning process since such a combination will usually enhance the degrading effects of smoke. The planning and employment of smoke is not limited to hours of daylight but can also be conducted when operating during periods of darkness or limited visibility.

Whether used in an offensive or defensive role, smoke operations, when planned and executed properly, have specific objectives. These objectives are:

- (a) Deny the enemy information.
- (b) Reduce effectiveness of enemy target acquisition means.
- (c) Restrict nap of the earth and contour approaches for aircraft.
- (d) Disrupt enemy movement, operations and command control.
- (e) Create conditions to surprise the enemy.
- (f) Deceive the enemy.
- (g) Attenuate thermal effects of nuclear weapons.

#### 4. SMOKE CATEGORIES AND APPLICATIONS

4.1 SMOKE EMPLOYMENT CATEGORIES. Smoke operations are divided into two general categories, hasty and deliberate. Hasty smoke is used when minimal operational planning time is available and is usually employed when enemy actions pose an immediate combat threat necessitating quick response on the part of the unit commander. Normally the tactical situation dictates that hasty smoke operations be of short duration and cover a small area as would be appropriate to combat situations involving battalion and lower. Deliberate smoke involves detailed planning and preparation and is planned at brigade or higher level. Deliberate smoke is usually employed over a larger area and for relatively longer durations of time than is hasty smoke.

4.2 SMOKE APPLICATIONS. There are four general applications for smoke on the battlefield; obscuration, screening, deception and identification/signaling. Obscuration smoke is applied on or directly in front of the enemy to prevent enemy observation of friendly maneuvers, to degrade the effectiveness of enemy electro-optical weapon systems such as anti-tank guided missiles (ATGM), and adversely to affect the movement of advancing units by causing confusion and by forcing the enemy to deviate from his original operational plan. Smoke applications designed to place smoke on friendly positions or between friendly and enemy positions are termed screening smokes. Under these conditions friendly troops may assemble, maneuver, and deploy in relative safety while enemy observations posts and target acquisition systems are degraded by the screening effects. Other uses of screening smoke involve protection of combat support units conducting breaching or recovery operations and protection of combat service support activities and areas such as supply routes and maintenance facilities.

Deception smoke is used to deceive and confuse the enemy. Normally one or more deceptive smoke screens are used in conjunction with an obscuration or screening smoke to deceive the enemy of the friendly forces intentions.

Dummy screens are included in operational plans and orders to minimize adverse effects on friendly operations. Identification/signaling smoke is used for marking of specific battlefield and supply areas and for prearranged battlefield communications.

## 5. TACTICAL OPERATIONS

Depending on the combat situation and type of operation being considered, i.e., offensive, defensive or rear area, there are general smoke employment techniques which would be utilized by the field commander to provide the necessary smoke coverage and protection. Smoke hardware includes such diversified equipment as artillery and mortar rounds, smoke grenade launchers, smoke pots, and mechanical smoke generators. Each offers certain operational advantages with corresponding limitations depending on the conditions under which it is employed. The Smoke Concept sets forth the smoke employment functions and tasks to be conducted by field commanders. These generalized techniques are integral to the support of the overall battle plan and are addressed in the following sections.

**5.1 OFFENSIVE OPERATIONS.** In offensive operations, smoke employment should be fully integrated into the scheme of maneuver and fire support. For battalion operations, screening smoke is used prior to the attack to prevent enemy observation of troop movement and buildup. Dummy screens are utilized as a means of deceiving the enemy about the actual location of the main attack. As the attacking force advances, screening clouds can be generated along the axis of advance and continued until such time as an unobstructed view of the battle area is required for effective engagement of enemy forces. Concurrent with this screening smoke, obscuration smoke is placed on enemy observation posts to suppress their direct fires and on enemy weapon system sites to degrade the effectiveness of their target acquisition and fire control capabilities. Tactical situations will dictate screening of flank positions and the use of identification/signaling smoke. On board smoke grenade launchers and vehicle engine exhaust screening systems (VEESS) are utilized for self protection by armor vehicle commanders by providing smoke screens to reduce vehicle vulnerability against ATGM'S and directed fires, and to provide a curtain behind which the vehicle can maneuver.

Brigade level operations also utilize smoke in a similar manner as maneuver units but on a larger scale. Obscuration smoke can be used to isolate second echelons from forward engaging units. Division and corp units plan and coordinate smoke employment in their areas of operations which include allocating assets to subordinate units to include providing the necessary means to support the creation of deception screens.

5.2 DEFENSIVE OPERATIONS. Smoke is also used by commanders in the defense to gain an operational advantage over the enemy and to degrade the effectiveness of observation and target detection capabilities. Obscuration smoke placed on or in front of attacking units serves to disrupt the enemy's original battle plan, thereby changing his operational timing, decreasing the rate of advance, hindering visual communications, and requiring premature deployment of troops. Proper placement of smoke will allow a more effective servicing of enemy targets as vehicles emerge from the smoke cloud. Screening smoke is used to conceal defensive positions and maneuvers and is also utilized in supporting covering force actions. As in the offense all levels of command conduct smoke operations but usually brigade and above conduct smoke operations on a larger scale than do battalions. Brigades use smoke with scatterable mines to hinder movement of following echelons.

5.3 REAR AREA OPERATIONS. Rear area screening operations are required to support both offensive and defensive operations. The primary purpose of rear area smoke operations is to prevent enemy air surveillance of US forces and to degrade effectiveness of enemy air attacks. Rear area smoke operations have the potential to last days or weeks and are utilized to conceal staging and assembly areas and logistical installations.

#### 6. COUNTERMEASURES TO THREAT SMOKE OPERATIONS

The Warsaw Pact will employ smoke whenever the reduced visibility will provide them with an operational advantage. Countermeasures to threat smoke operations are limited. Friendly forces can move positions if the operational situation allows or they can utilize electronic devices that see through the obscuration. The simultaneous use of these two approaches are complimentary and increase the effectiveness of operations in a smoke environment.

Electronic devices such as thermal imagers can be used by armored vehicle drivers and commanders in an attacking mode to penetrate threat smoke screens thus preserving momentum required for a successful operation. At the same time thermal trackers and fire control systems will enable US forces to engage and attack targets of opportunity while immersed in threat smoke screens.

## 7. SMOKE CONCEPT IMPLEMENTATION

In recent years much emphasis has been placed on updating and expanding the Army smoke program because of its importance as a combat multiplier on the battlefield. This emphasis is reflected in the significant developmental smoke programs being conducted by the material developers and the extensive efforts underway throughout TRADOC to update the Army's smoke training, and combat development base posture. In particular TRADOC programs are being pursued which address smoke doctrine and tactics, training literature, force structuring, and material requirements.

The importance that the Army places on implementing smoke related programs is strongly reinforced in the recommendations resulting from the Chemical Systems Program Review (SPR).<sup>3</sup> These recommendations are consistent with the tenets of the Smoke Concept and support the ongoing efforts to improve and expand Army Smoke employment capabilities. The purpose of this section is to highlight those efforts which are designed for implementation of the Smoke Concept. These include the conduct of a Mechanized Smoke Force Development Test and Evaluation (FDTE), analysis and design of smoke units in the Army 86 studies, and material systems development to support operational deficiencies.

7.1 MECHANIZED SMOKE FDTE. The idea that proper emplacement of smoke on the battlefield is a combat multiplier is supported by a wealth of laboratory data which clearly illustrates the effectiveness of inventory smoke materials and devices in degrading the transmission of visible and near infrared radiation and of developmental smoke materials which promise a potential for defeating threat weapons possessing far infrared operational capabilities. Some field test data also exists which points out the performance degradation that can be expected of the electro-optical weaponry operating in battlefield obscuration. What is not clearly understood, however, is to what extent smoke will adversely affect these systems in operational terms, i.e., the reduction of the number of friendly casualties and the increase in survivability of combat and combat support equipment through the proper use of smoke employment has not been quantified. This kind of quantifiable information concerning the measures of effectiveness (MOC) of casualties and equipment in specific smoke environments is vital to the combat developments process.

The TRADOC community is sponsoring a program to establish MOE as they apply to scenarios involving smoke operations. In conjunction with an FDTE presently being developed to evaluate the concepts and organization of a mechanized smoke unit, the user community will address the operational advantages to be gained in terms of increases in the survivability of US resources. The FDTE is a three phase test with phase one scheduled to commence in the first quarter of Fiscal Year 1983. The first phase is more concerned with the technical aspects of mechanized smoke than the operational aspects. The major effort will be directed toward optimizing the mounting configuration of the mechanical smoke generators on armored vehicles and in determining the extent of the resulting smoke screens under various meteorological conditions. This phase is necessary before the test designers can continue with meaningful mechanized scenarios which depend in part on the technical and operational characteristic of the mechanized smoke unit.

The current motorized smoke generator unit will be utilized during phase two to establish an operational baseline against which the capabilities of the proposed mechanized smoke units can be evaluated. Determination will be made of the operational aspects of the motorized smoke unit such as mobility, smoke employment response times, vulnerability to enemy fire, and, most importantly, extent of increased survivability to resources of supported units, i.e., measures of effectiveness (MOE). Once this is accomplished, phase three will commence with the mechanized smoke unit being substituted into selected scenarios in place of the motorized unit. The military worth of mechanized versus motorized can then be effectively evaluated in light of the operational baseline established in phase two. The measures of effectiveness established in phase two and phase three will be used to evaluate the effectiveness of smoke in terms of force ratios/force multipliers.

**7.2 SMOKE FORCE STRUCTURE.** The Army 86 studies is a series of studies directed by DA and conducted by TRADOC. The purpose was to develop an effective fighting force to meet the increasingly sophisticated threat during the next decade. Units were designed to integrate the numerous new and advanced material systems that will be introduced in this time period. As part of this study effort and based on the emerging smoke concepts, smoke generator units were evaluated as part of this force development exercise. Mechanical smoke generator units are normally used to provide smoke support when there is a requirement for large area or long duration coverage or when the smoke is required near or within friendly areas of operations. As a result of the Army 86 studies, smoke generator elements will be found at every major tactical echelon from the division to the theater Army.

For the first time divisions will have an organic, large area smoke capability consisting of a platoon with 12 smoke generators within the divisional NBC company. This smoke unit provides a capability that is immediately responsive to the needs of the division commander while providing divisions with a capability to train in a smoke environment and to train maneuver elements to effectively integrate smoke into their operations. For heavy divisions (armor/mechanized infantry) the smoke generators will be mounted on a mechanized vehicle and will provide the smoke platoon with the armor protection and mobility necessary to operate with maneuver elements in the main battle area (MBA). Smoke missions in the MBA will be numerous, but relatively short in duration (15-45 minutes). A significant portion of these missions will be conducted while moving in order to support the scheme of maneuver and to reduce vulnerability to enemy fires. In light divisions (infantry, airborne, air assault) the smoke generators will be mounted on an armored, wheeled vehicle; however, the concept of operations will be similar to the smoke platoon in the heavy divisions.

The majority of large area smoke assets will be found at corps. Within the corps structure will be units designed to support operations in the division MBA as well as units designed to support the divisional and corps rear areas. The basic operating element for these smoke units will be the company. Although several smoke companies may be placed under a small battalion headquarters for administrative and logistical support, these companies will normally be operating relatively autonomously, therefore dictating a relatively light battalion structure and a heavier support (maintenance, supply, etc) structure within each company. For supporting heavy division operations in the MBA, mechanized smoke companies will be utilized. These units will be assigned to the corps and attached to divisions based on the tactical situation and priority for support. They will normally receive operational control of the divisional smoke platoon in order to coordinate smoke operations. Light divisions and rear areas will be supported by employing motorized smoke companies. Motorized units will be assigned at theater Army level to support units operating in the communications zone (COMMZ).

The new smoke force structure developed in the Army 86 studies provides a logical integration of smoke assets from the division to the COMMZ. The divisional smoke platoon provides the division commander with large area smoke assets that are immediately responsive to his needs. The majority of the smoke assets are assigned to corps where their employment can be tailored to meet the operational requirements of the divisions as well as the corps rear areas. Additional smoke assets are assigned to the theater army to support logistical activities operating in the COMMZ.

7.3 SMOKE MATERIEL REQUIREMENTS. This paper emphasized earlier the importance of smoke materials which not only degrade visual observations but also those materials which effectively block other militarily significant areas of the electromagnetic spectrum. More and more weaponry is being fielded whose operational capabilities depend on sophisticated devices which transmit or receive electromagnetic radiation of various wavelengths. A material capable of effectively attenuating the intensity of the appropriate wavelengths will have the effect of neutralizing the intended purpose of these devices, thus reinforcing the idea of a combat multiplier.

The highest priority of the smoke technology program is the need for a capability to effectively screen wavelengths beyond the visible, specifically in the far infrared region. The ideal solution would be the development of a full spectrum screening material which would be capable of attenuating radiation from the visible through the far infrared and beyond. However near term solutions to the operational deficiencies are constrained by the existing state-of-the-art-technology to narrow band extinction approaches, while basic and exploratory research continue to explore broadband screening concepts. Through the research and development technology base, a limited number of screening materials have been identified which have proven technically feasible for screening far infrared radiation. Thus the Chemical School, which has been assigned proponent responsibility for large area smoke systems<sup>4</sup>, has identified a material need<sup>5</sup> to overcome operational deficiencies associated with the current large area screening device, the M3A3 mechanical smoke generator. This device uses fog oil as the smoke material, which is an effective screen against visible and near infrared radiation; however, its operational concept of utilizing the hot exhaust gases of a pulse jet engine to vaporize the fog oil is incompatible with the dissemination techniques required for the infrared screening materials. In addition to being able to provide large area screening out through the far infrared, there is a requirement for the new system to be capable of being installed and operated from an armored vehicle while moving in order to effectively support highly mobile maneuver battalions. Technical and developmental details describing the overall operation of this approach are provided in Smoke Symposium Paper C-20<sup>6</sup>. When fielded, this item will provide the Army with a capability it does not now possess, i.e., an ability to place large area infrared smoke screens over potential targets to effectively degrade advanced sensors used by threat forces to engage the target with air and artillery strike capabilities.

## 8. CONCLUSION

As the Smoke Concept plainly states, full implementation of all of the ideas contained in the concept is not possible at this time; however, significant inroads have been made. It is beyond the scope and intent of this paper to address all of the efforts associated with the extensive smoke programs involving other TRADOC schools, centers and test activities. The discussion in the previous section is meant only to give a feel for the type of smoke programs being conducted within TRADOC which directly impact on implementation of the Smoke Concept. In conclusion, it can be stated that TRADOC proponents are actively pursuing programs which will significantly contribute to the implementation of the Smoke Concept and the trend is evident, although much work has been done toward meeting this objective, there is still much to accomplish in order to effect full implementation.

## NOTES

1. TRADOC Pamphlet 525-3, 26 Sep 1980. US Army Operational Concept, EMPLOYMENT OF SMOKE, Headquarters United States Army Training and Doctrine Command, Ft. Monroe, Virginia.
2. WOOLDRIDGE, ROBERT H., USE OF SMOKE IN SOVIET TACTICS (U), United States Army Intelligence and Security Command, 1978, Secret Noform.
3. Chemical Systems Program Review, May 1980, Ft McClellan, Alabama.
4. Letter, 13 March 1978, ASSIGNMENT OF SMOKE PROPOSER RESPONSIBILITY, Headquarters, Combined Arms Center and Fort Leavenworth, Fort Leavenworth, Kansas.
5. LETTER OF AGREEMENT, 29 Jun 1979, MANPORTABLE SMOKE/OBSCURANT GENERATOR SYSTEM, USATRADOC ACN 23137, Headquarters United States Army Training and Doctrine Command, Fort Monrie, Virginia.
6. ROUSE, WILLIAM G., 1981, XM49 MECHANICAL SMOKE GENERATOR, Proceedings of the Smoke/Obscurants Symposium V.

# UNCLASSIFIED

## THE JTCG/ME SAWG CONCEPTS STUDY

Charles K. Arpke  
Oklahoma State University Engineering Research Field Office  
Eglin AF Base, Florida 32542

and

Bruce W. Fowler  
United States Army Missile Command  
Redstone Arsenal, Alabama 35898

### ABSTRACT

During the past year the Smoke and Aerosol Working Group of the JTCG/ME supported a concepts definition study on obscuration. This effort, carried out by a study group comprised of SAWG members, examined the state of the art in obscuration devices and in the materials, tactics, and doctrine of obscuration use. The examination keyed on land, sea, and air use of obscuration rather than on strict single-service avenues. The preliminary results of this study are presented. These results include analyses of "available" munitions and tactical uses of obscuration. A cross-correlation of these analyses is presented, and the results of a deficiency analysis of the cross-correlation are discussed. These results are divided into three areas: munitions and tactical uses that match; munitions without uses; and uses without supporting munitions.

### 1. INTRODUCTION

This paper summarizes the report prepared by the concepts study group of the Smoke and Aerosol Working Group of the JTCG/ME.

The complete report is being published as a JTCG/ME special report, 61 JTCG/ME-80-5, *Obscuration Concepts: Materials, Tactics, and Doctrine*.

Readers desiring the complete text of the report can obtain it through publications channels.

The purpose of this study was to examine the use of smoke/obscuration within the framework of armed combat. The study group excluded as a matter of their concern the obscuring effect of the modern "dirty" battlefield where smoke from munitions or targets, or dust raised by either moving vehicles or exploding munitions, contributes to the overall effect. Members of the study group, representing all of the services, engaged in an open-forum discussion to develop the matters presented. Parallel approaches were used to develop the ideas. First, hardware systems were considered. These were categorized as either available (now or within two years), or future systems. The alternate approach considered tactical application of obscuration for land, sea, or air use, for self-protection, offensive/defensive purposes, or for deception. From the hardware and use analyses, a cross-correlation analysis identified obscuration systems with tactical uses. This latter analysis further permitted identification of systems without uses, or of other deficiencies. Deficiencies identify either inventory obscuration systems that the military user does not want or need or developmental systems that the user has no need for and that are therefore being developed either without requirement or to a false requirement. Finally, tactical uses of obscuration without a system to support them are identified; in this case there is, at least conceptionally, a military use for obscuration systems that neither exist nor are being developed.

# UNCLASSIFIED

**UNCLASSIFIED****2. OBSCURATION CONSIDERATIONS**

A listing of the obscuration systems and devices is given below without discussion. For full details, refer to the final JTCG/ME report.

Most of these systems can be used for land, sea, or air applications. (An asterisk indicates development required.)

Smoke grenades	Smoke rounds (WP and HC)
Smoke pots	2.75-inch WPW rocket
Fog oil generators	MS2 helicopter system
40-mm grenade launcher	Rifleman's Assault Weapon*
XM183/XM184 BIS*	Vehicular dust
Insect sprayers/foggers	Man-portable generator*
Instant smoke*	Foam smoke*
Wedge rounds*	Chaff
Outlaw Indian*	Salty Dog*
Jet engine smoke generator*	Seeded smoke*
CBU-88	Stack smoke (USN)
Exhaust smoke	Water sprays
Flares (anti-IR)	

A number of technical objectives were noted as desirable elements for service consideration. For example, it is desirable to extend the effectiveness of obscuration items but still leave a window through which friendly sensors may operate; likewise, it would be desirable to have a smoke that would allow friendlies to look out but that would prevent the enemy from looking in. A further need is to shift technology emphasis away from the near IR band and to develop active IR- or millimeter-band sensors. The group consensus was that obscurants need to be developed to provide firing-signature "meaks" so as to afford tanks and ATGMs longer stay-in-place times and increase their firing capability. Techniques for suppression or abatement of dust in regions with dry soil are needed to reduce firing signatures, while in the area of training there is need to train in smokes, and to be able to characterize the degree of obscuration at selected times and places during exercises. Such instrumentation should supplement the MILES system of the Army.

In the alternate approach, uses and tactics were emphasized. Several definitions were used to assure agreement on terms. First, self-protection obscuration was defined as an obscurant transported or maintained by an operational element for its own protection from the enemy, from either being taken under fire or from observation. An example is the smoke grenade system on armored vehicles. An offensive/defensive obscurant was defined as an obscurant emplaced and maintained by one operational element to protect another operational element from enemy fire or observation. Obscurant devices and agents were categorized as essentially either blanket (close-in) or projected (away-from-the-element) obscurants.

**UNCLASSIFIED**

## UNCLASSIFIED

Smoke generators, smoke grenades, smoke pots, and exhaust systems are termed blanket obscurants, essentially because there is no inherent method to project them to a distance. By the same token, mortar and gun rounds (the projected systems) have drawbacks in that they either have near-in dead zones or large delivery inaccuracies.

Considerations of the tactical uses of obscuration fall in the following categories: *on us, on them, In-between, riverine (and amphibious) operations, deception, and rear area*. From this listing, it is apparent that the location of the obscurant cloud in offensive or defensive operations was emphasized. Various combinations of factors that influence the field user of smoke and other obscurants were analyzed and are discussed in some detail in the final report.

### 3. NEEDS AND DEFICIENCIES

The cross-correlation analysis resulted in identification of a number of needs and deficiencies. The list presented here does not indicate precedence or priority, or urgency of needs, or corrective action.

There is a need for a safe training smoke, and for devices that affect the operational efficiency of sensors, sights, range finders and personnel in a degraded environment. Techniques are needed that would permit evaluation of cloud effectiveness during training, and there is a need for a standard target to test obscurant effectiveness in the far IR. Remote, preferably automatic and mobile, meteorology stations to provide support and planning data are needed. Future threat sensors, operating in the mid IR and beyond, may not be obscured by present smokes, so there is an urgent need to assess obscuration methods against such sensors. A combination of increased payload, improved agents, and more accurate emplacement would improve area coverage of smoke munitions and solve some of the basic load/resupply problems noted by the study group.

Specific comments are made in the final report on the following considerations.

Vehicle dust	M52 helicopter system
Chaff	RAW
2.75-inch WPW rocket	CBU-88
USAF support of ground operations	Corner reflector use
Smoke in MOUT operations	Large area smoke use
Salty Dog use in training	Stack smoke
Water spray use	Flares

The reader is referred to the final report for detailed discussion of these elements.

Unaddressed needs were identified in a number of areas. Canopy smoke *on us*, where a ceiling of smoke over the battlefield would prevent or degrade aerial observation while not impeding observation ground to ground, was considered for a contemporary environment of combat in which friendly air superiority cannot be assured. Such obscuration is promising tactically in terms of augmenting existing air defense systems in protecting ground troops from air attack. There are no obscuration systems either in inventory or development that will consistently and regularly provide this type of obscuration.

## UNCLASSIFIED

**UNCLASSIFIED**

*Smoke on them exposed two unaddressed needs: to develop obscuration/weapon systems that will allow easy tactical intermixing of smoke and either mines, ICM, or other munitions to screen, delay, and destroy advancing forces. The other need is to develop obscurants that enemy sensors cannot see through, but that our sensors can operate through.*

The study group identified a need for an obscurant or smoke that can be dissipated readily; no such smoke is either in the inventory or under development. In like terms, there exists a need for rapid-deployment smoke. This is particularly applicable to deception smoke because of the sensitivity of such an operation and the need to ensure that the subterfuge is not detected by the enemy. In rear area considerations, there was identified a need for canopy smoke to permit unimpeded operations free of aerial observation; coupled to this was the need for persistent smoke to provide essentially continuous protection.

In sea uses of obscuration, there was identified a need for close-in smoke screening for self-protection. There is a need for tube-delivered smoke and large-area coverage for amphibious operations, reflecting the desire to obscure beaches while forces are approaching the beach. The Navy has little capability to deliver smoke from naval guns, and little consideration seems to have been given to the need to emplace large-area screens over the beach area.

Airbase defense and air-delivered smoke were the major needs identified in air use of smoke. The impact of obscurants on the SHORAD system has not been fully addressed. Manpower limitations and the short early warning time appear to call for an automated system if smoke is to be used in airbase defense.

**4. SUMMARY**

The brief and synoptic presentation given in this paper will, we hope, generate interest in the complete final report. The final report is designed to stimulate exchange of information, requirements, and capabilities in obscurants applications and needs between developers and users in all the services.

**UNCLASSIFIED**

# UNCLASSIFIED

D-6

## DEVELOPMENT OF THE BATTLEFIELD ENVIRONMENT OBSCURATION HANDBOOK (U)

Robert E. Turner  
Science Applications, Inc.  
15 Research Drive  
Ann Arbor, MI 48103

### ABSTRACT (U)

(U) Obscurant material in the battlefield environment can have a deleterious effect on the performance of electro-optical sensors. The natural weather environment consists of haze, fog, rain, snow, and similar atmospheric particulates which can cause a loss of contrast in a military scene. In addition, the battlefield induced contaminants such as dust, smoke, and foreign gases can degrade the atmospheric medium between a target and sensor.

This paper describes the recent development of a Battlefield Environment Obscuration Handbook\*, a document which contains a detailed compilation of laboratory data, field data, mathematical models, studies, and other information pertaining to the natural and anthropogenic sources of obscurants which can be found in the modern battlefield. In the preparation of this handbook, we reviewed over one hundred reports and documents, extracted the relevant material, and synthesized the information into an organized compilation of models and data for use by groups and individuals who are interested in how battlefield obscurants affect electro-optical systems.

Here we describe how one can use the Handbook, what data and models exist, what the limitations of the Handbook are and suggestions for updated versions.

### 1. INTRODUCTION (U)

(U) As any user of scientific and engineering data and models knows there has been an "information explosion" in the last twenty years and this trend will undoubtedly continue. It is often quite difficult for scientists and engineers to find the information they are looking for and this is particularly true in interdisciplinary areas of research. Likewise, in the military community there has been a large amount of work done in recent years on obscurant materials in the battlefield environment. Unfortunately, much of the information exists in the form of government reports, contractor reports, conference proceedings, and technical papers published in journals which are sometimes unfamiliar to the user. In 1980 Science Applications, Inc. undertook the project of creating a handbook which would contain under one cover information on data, models, tests, and studies which relate to battlefield obscurants. This report, entitled Battlefield Environment Obscuration Handbook is the result of our survey and synthesis of approximately 250 technical reports and papers on various aspects of obscurants as of May, 1980. The Handbook format is of a form for inclusion of additional information as it becomes available.

### 2. CONTENTS OF THE HANDBOOK (U)

(U) The contents of the 529 page Handbook (431 page unclassified volume and 98 page classified volume) are illustrated in Table 1.

\*Mr. Luis Dominguez, U.S. Army TRASANA, WSMR, NM, provided the support for this project. Mr. Sidney Gerard, U.S. AMSAA was the contracting officer.

# UNCLASSIFIED

**UNCLASSIFIED**

TABLE 1. HANDBOOK TABLE OF CONTENTS (U)

<u>SECTION</u>		
1	USE OF THE HANDBOOK. . . . .	1-1
	1.1 Criteria for Segregation of the Data and Models . . . . .	1-1
	1.2 General Use of the Data and Models. . . . .	1-3
	1.3 Typical Examples of how Data and Models are Used. . . . .	1-4
2	RELATIONSHIPS BETWEEN BATTLEFIELD ENVIRONMENTAL CONDITIONS AND SIGNIFICANT PARAMETERS . . . . .	2-1
	2.1 Mass and Volume Attenuation Coefficients. . . . .	2-1
	2.2 Sky and Path Radiance . . . . .	2-4
	2.3 Aerosol and Gas Types . . . . .	2-11
	2.4 Aerosol and Gas Content . . . . .	2-12
	2.5 Contrast. . . . .	2-19
	2.6 Dispersion of Gases and Particulates. . . . .	2-24
	2.7 Surface Conditions. . . . .	2-31
	2.8 Optical Weather . . . . .	2-34
	2.9 Summary . . . . .	2-38
3	NATURAL ENVIRONMENTS . . . . .	3-1
	3.0 Introduction. . . . .	3-1
	3.1 Data Types, Sources, and Formats. . . . .	3-1
	3.1.1 Weather Data . . . . .	3-2
	3.1.2 Data for Particular Regions. . . . .	3-5
	3.2 Central European Region (Cold, Wet): The Climate and Topography of Germany . .	3-6
	3.2.1 Climatological Data. . . . .	3-6
	3.2.2 Terrain Characteristics. . . . .	3-14
	3.2.2.1 Topographic Description . . . . .	3-14
	3.2.2.2 Typical Albedo. . . . .	3-14
	3.2.3 Civilian Activities. . . . .	3-14
	3.2.3.1 Industrial Activities . . . . .	3-14
	3.2.3.2 Agricultural Activities . . . . .	3-15
	3.2.3.3 Population Density. . . . .	3-16
	3.3 Desert Region (Hot, Dry): The Climate of Syria . . . . .	3-17
	3.3.1 Climatological Data. . . . .	3-17
	3.3.2 Terrain Characteristics. . . . .	3-17
	3.3.3 Civilian Activities. . . . .	3-22
	3.3.3.1 Industrial Activity . . . . .	3-22
	3.3.3.2 Agricultural Activity . . . . .	3-22
	3.3.3.3 Population Density. . . . .	3-22
	3.4 Tropical Region (Hot, Wet): The Climate of Central and Northern South America	3-24

**UNCLASSIFIED**

# UNCLASSIFIED

D-6

TABLE 1. (CONTINUED) (U)

SECTION

3.5 Cold Regions (Cold, Dry): The Tanana River Basin of Central Alaska (Fairbanks, Alaska) . . . . .	3-29
4 INTENTIONALLY INDUCED BATTLEFIELD ENVIRONMENTAL CONDITIONS. . . . .	4-1
4.1 Smokes . . . . .	4-1
4.1.1 Phosphorous Smoke . . . . .	4-1
4.1.1.1 Bulk WP. . . . .	4-1
4.1.1.1.1 Munition Characteristics. . . . .	4-2
4.1.1.1.2 Yield Factor. . . . .	4-2
4.1.1.1.3 Environmental Effects . . . . .	4-4
4.1.1.1.4 Attenuation Coefficients. . . . .	4-19
4.1.1.1.5 Scattering Parameters . . . . .	4-25
4.1.1.1.6 Dispersion Parameters . . . . .	4-27
4.1.1.2 Wick WP/Wedges . . . . .	4-28
4.1.1.2.1 Munition Characteristics. . . . .	4-29
4.1.1.2.2 Yield Factor. . . . .	4-31
4.1.1.2.3 Environmental Effects . . . . .	4-32
4.1.1.2.4 Attenuation Coefficients. . . . .	4-39
4.1.1.2.5 Scattering Parameters . . . . .	4-46
4.1.1.2.6 Dispersion Parameters . . . . .	4-48
4.1.2 HC Smoke. . . . .	4-49
4.1.2.1 Bulk HC. . . . .	4-49
4.1.2.1.1 Munition Characteristics. . . . .	4-49
4.1.2.1.2 Yield Factor. . . . .	4-51
4.1.2.1.3 Environmental Effects . . . . .	4-52
4.1.2.1.4 Attenuation Coefficients. . . . .	4-53
4.1.2.1.5 Scattering Parameters . . . . .	4-59
4.1.2.1.6 Dispersion Parameters . . . . .	4-62
4.1.3 Diesel/Fog Oil Smoke. . . . .	4-63
4.1.3.1 . . . . .	4063
4.1.3.1.1 Munition Characteristics. . . . .	4-63
4.1.3.1.2 Yield Factor. . . . .	4-67
4.1.3.1.3 Environmental Effects . . . . .	4-68
4.1.3.1.4 Attenuation Coefficients. . . . .	4-69
4.1.3.1.5 Scattering Parameters . . . . .	4-79
4.1.3.1.6 Dispersion Parameters . . . . .	4-80
4.1.3.1.7 Other Par. . . . .	4-81
4.1.4 Developmental Smokes. . . . .	4-85
4.1.4.1 Deployment Characteristics. . . . .	4-85

# UNCLASSIFIED

## UNCLASSIFIED

TABLE 1. (CONTINUED) (U)

<u>SECTION</u>		
	4.1.4.1.1 Yield Factor . . . . .	4-85
	4.1.4.1.2 Dispersion . . . . .	4-86
4.1.4.2	E-O Characteristics . . . . .	4-87
4.1.4.2	E-O Characteristics . . . . .	4-1C*
	4.1.4.2.1 Attenuation Coefficients . . . . .	4-1C*
	4.1.4.2.2 Scattering Parameters . . . . .	4-4C*
	4.1.4.2.3 Environmental Effects . . . . .	4-4C*
	4.1.4.2.4 Other Parameters . . . . .	4-4C*
4.1.5	Threat Smokes . . . . .	4-88
	4.1.5.1 Munition Characteristics . . . . .	4-88
	4.1.5.2 Yield Factor . . . . .	4-89
	4.1.5.3 Environmental Effects . . . . .	4-90
	4.1.5.4 Attenuation Coefficients . . . . .	4-7C*
	4.1.5.5 Scattering Parameters . . . . .	4-7C*
	4.1.5.6 Dispersion Parameters . . . . .	4-7C*
	4.1.5.7 Other Parameters . . . . .	4-7C*
5	UNINTENTIONALLY INDUCED BATTLEFIELD ENVIRONMENTAL CONDITIONS . . . . .	5-1
5.1	Munition Explosion Conditions . . . . .	5-1
	5.1.1 Dust From Explosions . . . . .	5-1
	5.1.1.1 Yield Factor . . . . .	5-1
	5.1.1.2 Environmental Effects (Hygroscopicity, etc.) . . . . .	5-7
	5.1.1.3 Attenuation Coefficients . . . . .	5-9
	5.1.1.4 Scattering Parameters . . . . .	5-17
	5.1.1.5 Dispersion Parameters . . . . .	5-17
	5.1.2 Gaseous/Heat Emission from Explosives . . . . .	5-17
	5.1.2.1 Yield Factors . . . . .	5-18
	5.1.2.1.1 Heat Emissions from Exploding Munitions . . . . .	5-1C*
	5.1.2.2 Attenuation Coefficients . . . . .	5-24
	5.1.3 Dirt and Debris . . . . .	5-29
	5.1.3.1 Free-Falling Objects . . . . .	5-29
	5.1.3.2 Smoke from Explosives . . . . .	5-34
5.2	Vehicle-Induced Conditions . . . . .	5-42
	5.2.1 Dust from Vehicle Traffic . . . . .	5-42
	5.2.1.1 Yield Factors . . . . .	5-42
	5.2.1.2 Attenuation Coefficients . . . . .	5-46
	5.2.1.3 Scattering Parameters . . . . .	5-48
	5.2.1.4 Dispersion Parameters . . . . .	5-49
	5.2.1.5 Other Parameters . . . . .	5-50
	5.2.1.5.1 Particulate Size Distribution . . . . .	5-51
	5.2.1.5.2 Complex Indices of Refraction . . . . .	5-55

\*\*"C" designates Classified Sections

**UNCLASSIFIED**

D-6

TABLE 1. (CONTINUED) (U)

<u>SECTION</u>	5.2.2 Gaseous and Particulate Exhaust Emission . . . . .	5-58
	5.2.2.1 Yield Factor. . . . .	5-58
	5.2.2.2 Attenuation Coefficients. . . . .	5-63
	5.2.2.3 Scattering Parameters . . . . .	5-66
	5.2.2.4 Dispersion Parameters . . . . .	5-67
	5.2.2.5 Other Parameters. . . . .	5-68
5.3	Battlefield Fires . . . . .	5-72
	5.3.1 Fuel Fires . . . . .	5-72
	5.3.1.1 Yield Factors . . . . .	5-72
	5.3.1.2 Attenuation Coefficients. . . . .	5-73
	5.3.1.3 Scattering Parameters . . . . .	5-73
	5.3.1.4 Turbulence. . . . .	5-74
	5.3.2 Vehicle Fires. . . . .	5-76
	5.3.2.1 Burning Land Vehicles . . . . .	5-76
	5.3.2.2 Crashed Airplanes . . . . .	5-88
5.4	Launcher Induced Conditions . . . . .	5-89
5.4	Launcher Induced Conditions . . . . .	5-2C*
	5.4.1 Muzzle Emission. . . . .	5-2C*
	5.4.1.1 Gases . . . . .	5-2C*
	5.4.1.2 Gunflash. . . . .	5-2C*
	5.4.1.3 Smoke . . . . .	5-5C*
	5.4.2 Other Effects. . . . .	5-8C*
	5.4.2.1 Heating . . . . .	5-8C*
	5.4.2.2 Dust. . . . .	5-8C*
	5.4.3 Tests Involving Prototype Artillery Detection Systems. . . . .	5-8C*
	5.4.3.1 Hot Gun Barrel Locating System. . . . .	5-8C*
	5.4.3.2 Flash Detection System. . . . .	5-10C*
	5.4.3.3 Projectile Detection System . . . . .	5-10C*
6	MODELS . . . . .	6-1
6.1	Natural Battlefield Environmental Models. . . . .	6-1
	6.1.1 Line of Sight Obscuration Models . . . . .	6-1
	6.1.1.1 Aerosol Extinction Models . . . . .	6-1
	6.1.1.1.1 Lockheed Model . . . . .	6-2
	6.1.1.1.2 Laops Model. . . . .	6-6
	6.1.1.1.3 AFGL Model . . . . .	6-11
	6.1.1.1.4 SAI Water-Haze Model . . . . .	6-13

\*\*"C" designates Classified Sections

**UNCLASSIFIED**

**UNCLASSIFIED**

TABLE 1. (CONTINUED) (U)

<u>SECTION</u>		
	6.1.1.1.5 RAND Model . . . . .	6-17
	6.1.1.1.6 SAI (Aerosol Growth) Attenuation Model . . . . .	6-19
6.1.1.2	Fog Extinction Models . . . . .	6-24
	6.1.1.2.1 SAI Water-Haze Model . . . . .	6-24
	6.1.1.2.2 IDA Model. . . . .	6-25
	6.1.1.2.3 ASL Model. . . . .	6-27
	6.1.1.2.4 G/AP Aerosol Model . . . . .	6-28
6.1.1.3	Precipitation Extinction Models . . . . .	6-31
	6.1.1.3.1 Chu-Hogg Model . . . . .	6-31
	6.1.1.3.2 Polyakova Model. . . . .	6-34
	6.1.1.3.3 Selzer Model . . . . .	6-35
	6.1.1.3.4 G/AP Snow Model. . . . .	6-38
6.1.1.4	Molecular Extinction Models . . . . .	6-43
	6.1.1.4.1 LOWTRAN IV Band Model. . . . .	6-48
	6.1.1.4.2 ATLES Band Model . . . . .	6-48
	6.1.1.4.3 LASER Monochromatic Absorption Calculations. . . .	6-50
	6.1.1.4.4 Polynomial Fits to Laser Absorption Coefficients .	6-50
	6.1.1.4.5 FASCODE Algorithm. . . . .	6-51
6.1.1.5	Terrain Blockage Models . . . . .	6-52
	6.1.1.5.1 Foliage and Structure. . . . .	6-52
6.1.1.6	Smoke Extinction Models . . . . .	6-55
	6.1.1.6.1 GRC Smoke Model. . . . .	6-55
	6.1.1.6.2 AMSAA Transport and Diffusion Model. . . . .	6-57
6.1.1.7	Dust Extinction Models. . . . .	6-59
	6.1.1.7.1 GE-TEMPO Dust Model. . . . .	6-59
	6.1.1.7.2 DIRTRAN. . . . .	6-61
	6.1.1.7.3 SAI Dust Model . . . . .	6-62
6.1.2	Background Models. . . . .	6-64
	6.1.2.1 Terrain Radiation Models. . . . .	6-64
	6.1.2.1.1 RADTAU-2 . . . . .	6-64
	6.1.2.2 Sky Radiation Models. . . . .	6-67
	6.1.2.2.1 RADTAU-2 . . . . .	6-67
	6.1.2.3 Cloud Radiation Models. . . . .	6-68
	6.1.2.3.1 CLORAD . . . . .	6-68
	6.1.2.3.2 Monte Carlo Model. . . . .	6-69
	6.1.2.4 Other Background Radiation Models . . . . .	6-70
6.1.3	Illumination Source Models . . . . .	6-71
	6.1.3.1 Sun Illumination Models . . . . .	6-71
	6.1.3.1.1 Turner Solar Model . . . . .	6-71
	6.1.3.2 Moon Illumination Models. . . . .	6-75

**UNCLASSIFIED**

# UNCLASSIFIED

D-6

TABLE 1. (CONTINUED) (U)

<u>SECTION</u>		
	6.1.3.2.1 Brown's Model . . . . .	6-75
	6.1.3.2.2 Nighttime Model . . . . .	6-77
	6.1.3.2.3 Turner-Lunar Model . . . . .	6-80
	6.1.3.3 Artificial Source Illumination Models . . . . .	6-85
	6.1.3.3.1 Multiple Flare Model . . . . .	6-85
	6.1.3.4 Combat Illumination Models . . . . .	6-88
	6.1.3.4.1 COIL . . . . .	6-88
6.2 Sensor Models . . . . .		6-90
6.2.1 NVL Static Performance Thermal Model . . . . .		6-90
6.2.1.1 NVL Performance Model: Minimum Resolvable Temperature . . . . .		6-90
6.2.1.2 NVL Performance Model: Minimum Detectable Temperature . . . . .		6-92
6.2.1.3 NVL Performance Model: Modulation Transfer Function . . . . .		6-93
6.2.1.4 NVL Performance Model: Noise Equivalent Temperature . . . . .		6-95
6.2.1.5 NVL Target Submodel . . . . .		6-97
6.2.1.6 NVL Background Submodel . . . . .		6-97
6.2.1.7 NVL Atmospheric Submodel . . . . .		6-97
6.2.2 MAREAM Photographic Model . . . . .		6-98
6.2.2.1 MARSAM Atmospheric Submodel . . . . .		6-98
6.2.2.2 MARSAM Exposure Submodel . . . . .		6-100
6.2.2.3 MARSAM Decision Submodel . . . . .		6-100
6.2.2.4 MARSAM Display Submodel . . . . .		6-100
6.2.3 Realistic European Battlefield Target Acquisition Model (REBTAM) . . .		6-101
6.2.3.1 The REBTAM Target Signature Submodel . . . . .		6-101
6.2.3.2 REBTAM Atmospheric Propagation Submodel . . . . .		6-101
6.2.3.3 REBTAM Terrain Submodel . . . . .		6-102
6.2.3.4 REBTAM Sensor Model . . . . .		6-102
6.2.4 System Assessment Model . . . . .		6-103
6.2.5 Additional Sensor Models . . . . .		6-104
6.3 Combat Models . . . . .		6-105
6.3.1 Carmonette Model . . . . .		6-106
6.3.1.1 Carmonette Search Submodel . . . . .		6-109
7 TESTS AND STUDIES . . . . .		7-1
7.0 Introduction . . . . .		7-1
7.1 Tests . . . . .		7-1
7.1.1 Tests that Involve Battlefield Environment Only . . . . .		7-1
7.1.1.1 Optical Properties of Atmospheric Quantities in Europe (OPAQUE) Tests . . . . .		7-1
7.1.1.2 Dusty Infrared Transmission (DIRT) . . . . .		7-1
7.1.1.2.1 DIRT-I, October 1978 . . . . .		7-2
7.1.1.2.2 DIRT-II, July 1979 . . . . .		7-10

UNCLASSIFIED

**UNCLASSIFIED**

TABLE 1. (CONTINUED) (U)

<u>SECTION</u>		
	7.1.1.2.3 DIRT-III, April 1980. . . . .	7-11
	7.1.1.3 MIRADCOM Near-Millimeter Wave Transmission Measurements. . . . .	7-12
	7.1.1.4 NRLS km Path and Fourier Transform Spectrometer Measurements . . .	7-12
	7.1.1.5 Optical Signatures Program (OSP) . . . . .	7-13
	7.1.1.6 Dust/Debris Test at Ft. Sill, May 1978 . . . . .	7-15
	7.1.1.7 A.P. Hill Tests. . . . .	7-17
7.1.2	Tests Including Sensor Performance in a Battlefield Environment . . . . .	7-19
	7.1.2.1 Smoke Week Tests . . . . .	7-19
	7.1.2.1.1 Smoke Week I, November 1977 . . . . .	7-19
8	DESCRIPTION OF BASIC CHARACTERISTICS OF U.S. ARMY E-O SYSTEMS . . . . .	8-1C*
8.1	Passive Imaging Systems. . . . .	8-1C*
	8.1.1 Thermal Night Sights. . . . .	8-1C*
	8.1.1.1 Tank Thermal Sight . . . . .	8-1C*
	8.1.1.2 DRAGON Night Sight . . . . .	8-1C*
	8.1.1.3 TOW Night Sight. . . . .	8-2C*
	8.1.1.4 RPV FLIR Sensors . . . . .	8-2C*
	8.1.1.5 AGA Thermovision . . . . .	8-4C*
	8.2 Active Night Sights. . . . .	8-5C*
	8.3 Anti-Tank Missile E-O Links. . . . .	8-6C*
	8.3.1 Command to Line-of-Sight Links. . . . .	8-6C*
	8.3.1.1 The DRAGON Weapon System . . . . .	8-6C*
	8.3.1.2 Tube-Launched Optically-Tracked Wire-Guided (TOW) Missile System . . . . .	8-7C*
	8.3.2 Laser Designator Links. . . . .	8-8C*
	8.3.2.1 Laser Designator Systems: LTD, GLLD, and MULE . . . . .	8-8C*
	8.3.2.2 The COPPERHEAD System. . . . .	8-14C*
	8.3.3 Beam Rider Systems. . . . .	8-14C*
	8.4 Laser Rangefinders . . . . .	8-17C*
	8.4.1 Laser Rangefinders (1.06 $\mu$ m). . . . .	8-17C*
	8.4.1.1 Transmitter Module . . . . .	8-17C*
	8.4.1.2 Receiver Module. . . . .	8-18C*
	8.4.1.3 Power Supply Module. . . . .	8-18C*
	8.4.1.4 PPN Voltage Output . . . . .	8-19C*
	8.4.1.5 LRS Counter Display Module . . . . .	8-19C*
	8.4.1.6 AN/PVS-6 Counter/Display Module. . . . .	8-21C*
	8.4.2 Laser Rangefinders (2.06 $\mu$ m). . . . .	8-25C*
	8.5 Imaging IR Seekers . . . . .	8-27C*

\*"C" designates Classified Sections

**UNCLASSIFIED**

**UNCLASSIFIED**

D-6

TABLE 1. (CONTINUED) (U)

<u>SECTION</u>		
	8.5.2 Infrared Reticle Seeker . . . . .	8-29C*
9	PERFORMANCE DATA ON SYSTEMS IN BATTLEFIELD ENVIRONMENT CONDITIONS . . . . .	9-1C*
9.1	Passive Imaging Systems . . . . .	9-1C*
9.1.1	Thermal Night Sights . . . . .	9-1C*
9.1.1.1	Tank Thermal Sight. . . . .	9-1C*
9.1.1.2	DRAGON Night Sight. . . . .	9-2C*
9.1.1.3	TOW Night Sight . . . . .	9-2C*
9.1.1.4	RPV FLIR Sensor Performance . . . . .	9-6C*
9.1.1.5	AGA Thermovision. . . . .	9-8C*
9.2	Active Night Sights . . . . .	9-9C*
9.3	Anti-Tank Missile E-O Links . . . . .	9-9C*
9.3.1	Command to Line-of-Sight Links . . . . .	9-9C*
9.3.1.1	DRAGON Weapon System. . . . .	9-9C*
9.3.1.2	TOW Missile System Performance Data . . . . .	9-9C*
9.3.2	Laser Designator Performance . . . . .	9-13C*
9.3.2.1	Designator-to-Target Link . . . . .	9-13C*
9.3.2.1.1	Laser Designator Link Performance, Deliberate Activity . . . . .	9-13C*
9.3.2.1.2	Laser Designator Link Performance, Inadvertent Activity . . . . .	9-14C*
9.3.2.2	COPPERHEAD System Performance . . . . .	9-19C*
9.3.3	Beam Rider System Performance. . . . .	9-21C*
9.4	Laser Rangefinder Test Results. . . . .	9-25C*
9.4.1	Laser Rangefinder Test Results (1.06 $\mu\text{m}$ ) . . . . .	9-25C*
9.4.1.1	Comparison of Cavity Performance. . . . .	9-25C*
9.4.1.2	Concept Evaluation Test Results of AN/PVQ-3 (4) V . . . . .	9-26C*
9.4.2	Laser Rangefinder Performance (2.06 $\mu\text{m}$ ). . . . .	9-28C*
9.5	Infrared Imaging Seeker Results . . . . .	9-30C*
9.5.1	Infrared Imaging Seeker Results. . . . .	9-30C*
9.5.2	Infrared Reticle Seeker Test Results . . . . .	9-31C*
9.5.2.1	AN/DAW-1 Seeker Tower Test Results. . . . .	9-32C*

\*\*"C" designates Classified Sections

**UNCLASSIFIED**

# UNCLASSIFIED

D-6

## 3. USE OF THE HANDBOOK (U)

(U) In the modern battlefield environment there are many effects which can limit the capability of an observer to detect and/or recognize enemy forces. First, there is the presence of terrain, vegetation, or solid man-made objects which lie within the line of sight; and second, there is the presence of natural and/or anthropogenic material such as gases and particulates in the atmosphere. In fact, the definition of line of sight which we shall use in this Handbook is the following: "A point is said to be within the line of sight of a sensor (or equivalently, a sensor is said to have a line of sight to a point), if and only if, the energy to which the sensor reacts can travel from the point to the sensor unobstructed by terrain, vegetation, or solid man-made objects." In strict terms this definition would exclude anthropogenic smoke because it includes solid man-made particles. In this sense the line-of-sight definition is somewhat arbitrary, but we shall interpret it to refer to solid man-made objects which, if projected into the atmosphere, do not reach their terminal speed. Therefore, we shall consider as battlefield obscurants, natural and anthropogenic gases and particulates semi-permanently suspended in the atmosphere between a target and sensor.

The Handbook consists of models and data which are primarily of use to investigators of the response of electro-optical systems in the course of battlefield activity. A structured way of presenting this large and growing body of knowledge is the segregate the various models and data according to the origin and means of production of the obscuring material and the systems involved. In the Handbook we have therefore organized the data and models in the following way:

Section 3. Natural Battlefield Environmental Conditions for Specific Geographic Locations. This section contains general information which is necessary to characterize electro-optical system degradation for four geographic regions. One is the Central European region (Germany) which is representative of a cold, wet climate; another is a desert region (Syria) which is characteristic of a hot, dry region; the third is the climate of central and northern South America which is representative of a hot, wet region; and the fourth category is a cold region (Fairbanks, Alaska) which represents a cold, dry area.

Section 4. Intentionally Induced Battlefield Environmental Conditions. This section contains information on battlefield environmental conditions which may be intentionally induced to impair the performance of electro-optical or visual systems. Here we specify various kinds of smoke, their methods of production, attenuation coefficients, scattering parameters, dispersion parameters, and other basic properties which are of use in the analysis of electro-optical sensors and systems.

Section 5. Unintentionally Induced Battlefield Environmental Conditions. This section includes battlefield environmental conditions which can degrade electro-optical or visual system performance as a by-product of their primary functions. These effects are the result of munition explosions, gaseous and heat emission from explosives, dust from vehicles, battlefield fires, and launcher-induced conditions. Because of the uncertainty in the environment many of these characteristics are empirical in nature rather than

# UNCLASSIFIED

# UNCLASSIFIED

D-6

being more deterministic as in the case of smoke.

Section 6. Models. This section includes models which deal with sources of environmental degradation only. These include the models of natural and induced extinction. Many mathematical models have been produced over the last four years which are used to describe the extinction of radiation along a line of sight as a function of meteorological and other atmospheric parameters. Also, there are models which describe the radiation field in the atmosphere in terms of particular sources such as the Sun, the moon, and artificial sources as flares.

Section 7. Tests and Studies. This section includes tests, which are defined as those projects or activities which involve field measurements, whether they are for the battlefield environment only, sensor, or combat level. Studies are those projects which are more analytical in nature or are paper simulations rather than field measurements. The latter includes laboratory data because those data must be extrapolated or modeled to be applied to realistic field conditions. We include here the descriptions of DIRT-I, DIRT-II, DIRT-III, the Optical Signatures Program, Ft. Sill tests, A.P. Hill tests and some of the Smoke week tests.

Section 8. Description of Basic Characteristics of U.S. Army Electro-Optical Systems (Classified Section). This section includes the basic electro-optical (E-O) characteristics of the various Army E-O systems. A description is given of the type of sensor and sensor-system and how it is used.

Section 9. Performance Data of Sensor (Systems) in Battlefield Environment Conditions (Classified Section). This section summarizes the available performance data on specific sensor (system) performance in the battlefield environment. In this section we describe the actual data which have been obtained for the performance of specific sensors and sensor systems such as TOW night sights, Copperhead, and other systems for the realistic battlefield environment.

(U) Depending upon which test, model, or system one is interested in, there is a section of the Handbook which is applicable. The user of the Handbook may be concerned with the performance of a particular E-O sensor at a specific location under well-defined meteorological conditions. The user should be able to specify what his performance criteria are (i.e. contrast loss, transmission loss, etc.) or if necessary he can learn what specific criteria have been used by the E-O community by referring to the definition of relationships between battlefield environmental conditions and their significant parameters in Section 2 of the Handbook. In addition, the user can refer to the models and data given in Sections 8 and 9 to learn which performance criteria have been used for current E-O sensors and systems. It should be noted that the Handbook can be used in a variety of ways. For example, it is applicable not only for the analysis of specific sensors and systems, but also for more theoretical or analytical studies of the effects of the atmosphere on electromagnetic radiation

# UNCLASSIFIED

885

# UNCLASSIFIED

D-6

in a military environment. Thus, one can take parts of one section and use them with formulas, equations, charts, tables, or graphs from another section to perform whatever analysis one is interested in. Also, the looseleaf binding of the Handbook and the positioning of the sections allows one to update the Handbook in a convenient manner by merely inserting new sections or subsections.

## 4. RELATIONSHIPS AMONG VARIOUS BATTLEFIELD ENVIRONMENTAL PARAMETERS (U)

(U) Although gases and particulates contribute to the obscurant materials in the battlefield environment, the dominant obscurant is usually the semi-permanent suspension of particulates called an aerosol. This definition includes haze, smoke, dust, fog, and other combinations of low visibility conditions. These conditions will cause electromagnetic radiation to be scattered, absorbed, and emitted by the particles and gases of the medium. The attenuation of radiation along some path is given in terms of the spectral transmittance  $T(\lambda, s)$  for wavelength  $\lambda$ , i.e.

$$T(\lambda, s) = \exp \left[ - \int_0^s \kappa(\lambda, s') ds' \right] \quad (1)$$

where  $\kappa(\lambda, s)$  is the volume extinction (scattering plus absorption) coefficient at point  $s$  in the medium. The extinction coefficient which represents the total cross section per unit volume has units in reciprocal length, usually  $\text{km}^{-1}$ .

(U) The loss of radiation by scattering and absorption is important for transmittance but the gain of radiation by scattering and emission is important for contrast studies. The gain in radiation contributes to a quantity called the path radiance,  $L_p(\lambda, s)$  so that the complete expression for the radiance at a sensor is given by

$$L_{EO}(\lambda, s) = L_t(\lambda, 0)T(\lambda, s) + L_p(\lambda, s) \quad (2)$$

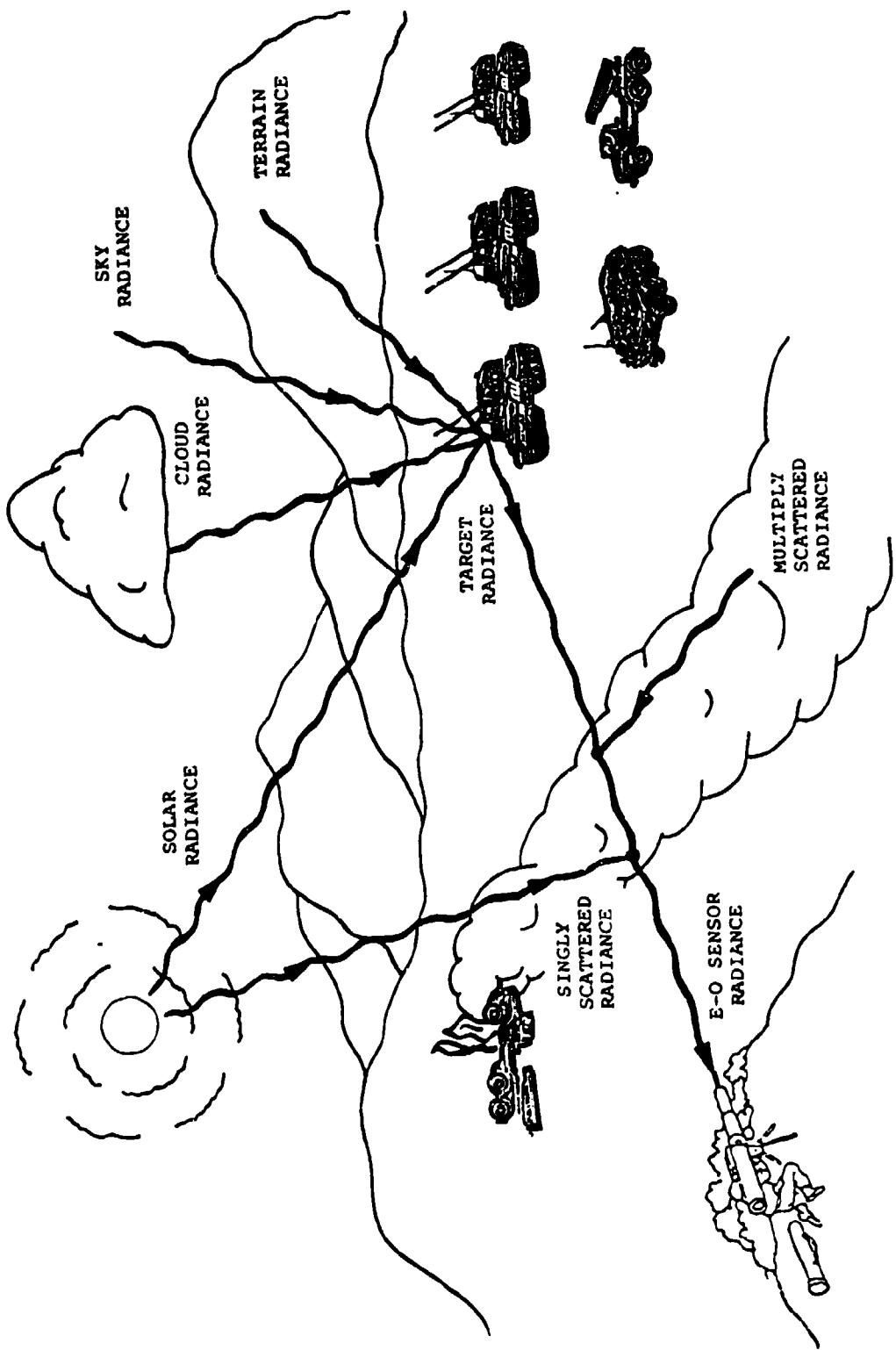
where  $L_t(\lambda, 0)$  is the target radiance. The radiometric quantities which contribute to the radiance at the electro-optical sensor are illustrated in Figure 1 for a typical battlefield scene. Radiation components from the sun (or moon), clouds, the sky, and the terrain all contribute to the illumination or temperature of the target. The target radiance is then attenuated by scattering and absorption processes and an additional path radiance is added to the attenuated component. The path radiance arises from the scattering and emission of radiation by the gaseous and aerosol components of the medium along the path which connects the target and sensor. The Handbook lists the various models which have been developed to account for the path radiance and transmittance by smoke, dust, and fog. It should be noted that the transmittance and path radiance are not necessarily constant with respect to time or space. For many electro-optical systems there can occur large variations in the transmittance and path radiance throughout the scene. This gives rise to variations which are of considerable importance in the analysis of the performance of these sensors in a military environment.

(U) Related to the quantities in Equation 1 and 2 are other, more basic parameters which are used in models and in data analysis. Table 2 is a list of the quantities with a simplified formulation.

# UNCLASSIFIED

**UNCLASSIFIED**

D-6



**UNCLASSIFIED**

Figure 1. RADIATION COMPONENTS FOR A PASSIVE MILITARY ELECTRO-OPTICAL SENSOR

# UNCLASSIFIED

D-6

TABLE 2. RELATIONSHIPS AMONG PARAMETERS (U)

1. Transmittance	$T(\lambda, s) = \exp [-\kappa(\lambda)s]$
2. Mass Content	$X(s) = \int_0^s \rho(s')ds'$
3. Extinction coefficient	$\kappa(\lambda, s) = N(s)\sigma_t(\lambda, s)$
4. Absorption coefficient	$\alpha(\lambda, s) = N(s)\sigma_a(\lambda, s)$
5. Scattering coefficient	$\beta(\lambda, s) = N(s)\sigma_s(\lambda, s)$
6. Spectral radiance at sensor	$L = L_t T + L_p$
7. Target radiance	$L_t = \frac{\rho}{\pi} E(\text{irradiance})$
8. Path radiance (scattering)	$L_p$ (complicated function of angles and medium parameters)
9. Path radiance (emission)	$L_p \approx (1 - T)B$
10. Particle size distribution	$\Psi(r) = ar^C \exp[-br^Y]$
11. Rayleigh cross section	$\sigma_R(\lambda) \propto \frac{1}{\lambda^4}$
12. Rayleigh phase function	$p(\chi) = \frac{3}{4}(1 + \cos^2 \chi)$
13. Aerosol phase function	(strongly peaked in forward direction)
14. Mass extinction coefficient	$\kappa_m(\lambda, s) = \frac{\kappa(\lambda, s)}{\rho(s)}$
15. Mass absorption coefficient	$\alpha_m(\lambda, s) = \frac{\alpha(\lambda, s)}{\rho(s)}$
16. Mass scattering coefficient	$\beta_m(\lambda, s) = \frac{\beta(\lambda, s)}{\rho(s)}$
17. Single-scattering albedo	$\omega_0(\lambda, s) = \frac{\beta(\lambda, s)}{\kappa(\lambda, s)}$
18. Contrast	$C(s) = \frac{L_t(s) - L_b(s)}{L_b(s)}$
19. Contrast transmittance	$T_c(s) = C(s)/C(0)$

# UNCLASSIFIED

**UNCLASSIFIED**

D-6

TABLE 2. (CONTINUED) (U)

20. Visual range	$V = \frac{3.912}{\kappa}$
21. Particle concentration (diffusion) (point source)	$C = C_0 \exp \left[ -\frac{1}{2} \left( \frac{x^2}{\sigma_1^2} + \frac{y^2}{\sigma_2^2} + \frac{z^2}{\sigma_3^2} \right) \right]$
22. Particle concentration (diffusion) (line source)	$C = C_0 \exp \left[ -\frac{1}{2} \left( \frac{x}{\sigma_3} \right)^2 \right]$
23. Reflected radiance	$L_r = \int \cos\theta d\Omega L_i d\Omega$
24. Exitance	$M = \int L_r \cos\theta d\Omega$
25. Irradiance	$E = \int L_i \cos\theta' d\Omega'$
26. Surface albedo	$\bar{\rho}(\lambda) = \frac{M(\lambda)}{E(\lambda)}$
27. Directional emissivity	$\epsilon(\lambda, \Omega) = \frac{L(\lambda, \Omega)}{B(\lambda)}$
28. Total emissivity	$\epsilon(T_e) = \frac{\pi \int \epsilon(\lambda, T_e) B(\lambda, T_e) d\lambda}{\sigma T_e^4}$
29. Flux (precipitation)	$\phi = \int_0^\infty n(r) u(z) dr$
30. Extinction (precipitation)	$\kappa = AR^C$

**UNCLASSIFIED**

# **UNCLASSIFIED**

D-6

## 5. CONCLUSIONS (U)

(U) The Battlefield Environment Obscuration Handbook represents an attempt to consolidate the relevant information on the various obscurants which are found in the modern military environments. New laboratory investigations and field tests are being conducted and new mathematical models are continually being developed which address the problems associated with battlefield obscurants. As a result, the Handbook will have to be updated periodically so as to include the latest information and perhaps to delete old or out of date material. With the rapid progress being made in this area I would suggest that the Handbook be updated annually. It would then become a valuable resource for the many investigators involved in the analysis of sensors, systems, models, and data for military environments.

## REFERENCES (U)

Turner, R.E., P.G. Eitner, C.D. Leonard, D.G.S. Snyder, Battlefield Environment Obscuration Handbook, Final Report, SAI 80-009-AA, Science Applications, Inc. December, 1980.

# **UNCLASSIFIED**

# UNCLASSIFIED

D-7

## OBSCURANTS AS A COUNTERMEASURE TO MODERN WEAPON SYSTEMS

LTC John F. Bulger  
Assistant Project Manager  
Smoke/Obscurants  
Aberdeen Proving Ground, MD

### DISCLAIMER

The conclusions expressed in this paper are the author's and do not necessarily reflect the views of the Project Manager for Smoke and Obscurants or the Department of the Army. This paper is unclassified; however, it has not been cleared for release to the public.

### A. FACT

The question of US Army ability effectively to use obscurants as a countermeasure to modern weapon systems is examined in three aspects: first, mechanisms by which presently fielded and future weapon systems are affected by obscurants; second, availability of obscurant resources in the field; third, doctrinal and training considerations. The paper concludes that, technically and tactically, obscurants will play an important role in future conflicts. The US Army has, with some well known shortfalls, the assets required for employment in combat. Doctrine for employment of obscurants must be updated. In addition, the Army must train more routinely in an obscured environment as well as in planning and executing smoke missions.

Modern technology has changed the face of battle. Our electronic age has fostered weapon systems of unparalleled accuracy, range and killing power. Modern electro-optical (EO) weapon systems which use various regions of the electro-magnetic spectrum for target acquisition and automatic or semi-automatic guidance have made the elusive dream of the first round hit come true.

Throughout history, every sensational advance in warfare has fostered effective countermeasures. There are also effective countermeasures to modern EO weapon systems. Interrupting the line-of-sight of the gunner, or the path of the laser beam at the system is responding to, can defeat the weapon system. This can be done in a number of ways. These include clever use of terrain, use of suppressing fires, and the use of obscurants such as military smokes.

Does the U.S. Army have the ability to effectively use obscurants as a countermeasure to modern weapon systems? To answer this question, we must examine at least three factors. First, technical feasibility. How do obscurants interact with present and future weapon systems? Does our present technology promise high probability of success in degrading modern weapon systems through the use of obscurants? Second, given technical feasibility, does the Army have the resources to successfully employ obscurants in battle? Last, doctrine, tactics, and training considerations.

# UNCLASSIFIED

**UNCLASSIFIED**

To this end, the questions are, does U.S. Army doctrine adequately address employment of smoke in combat, and is training in the use of this resource at a sufficient level to assure success?

Following answers to these fundamental questions, and presentation of conclusions, I will suggest some recommendations for future action.

Force structure issues will not be examined for several reasons. First, they may be classified. Second, they are the subject of study by the Army as of this writing. Third, the questions can be considered within the constraint of applications of present and currently planned force structure.

How do obscurants interact with present and future weapon systems? An understanding of how these systems work is a prerequisite to understanding how obscurants affect them. I will briefly describe examples of several types of systems, then describe how smoke and obscurants can defeat them or degrade their performance.

There are a number of technologies available to weapon designers for the design of "smart" weapon systems; that is, our modern electro-optical (EO) weapon systems, such as antitank guided missiles and laser guided munitions. For purposes of this paper, I will limit discussion to weapon systems operating in the visual and near infrared (IR) regions of the spectrum because weapon systems which operate in those regions are described in the open literature. This limitation is entirely appropriate even if one considers the potential for use of other regions of the spectrum in weapon design since the eyeball is the most common sensor on the battlefield. Further, there are a great number of EO systems working in the visual or near IR region in the field today. These systems will be in use for many years to come. It is important to note, however, that this constraint generally limits addressing the Warsaw Pact threat to that presented through the mid-80 timeframe. The picture changes rapidly after that period.

TOW (Tube-launched, optically tracked, wire guided missile) is a well known example of an anti-tank guided missile (ATGM) using a command to line-of-sight guidance system. It has many analogs in both the free world and Warsaw Pact arsenals. The gunner employing TOW visually acquires his target, lays the weapon system sight on the target, and releases the missile. The missile has a flare in the rear of it which is sensed by the weapons guidance system (located with the gunner). The gunner maintains his sights on the target as the missile flies toward it. The

**UNCLASSIFIED**

# UNCLASSIFIED

D-7

guidance system is able to compute the relative location of the missile and the target using information received from tracking the flare and from the orientation of the sights. The guidance commands are sent to the missile over a fine wire laid behind the missile. These commands are sent automatically without the intervention of the gunner.

Any countermeasure which denies line-of-sight from the gunner to the target or the missile will degrade or defeat the system. Figure 1, (14: 2-3) shows how obscurants can defeat command to line-of-sight ATGM's.

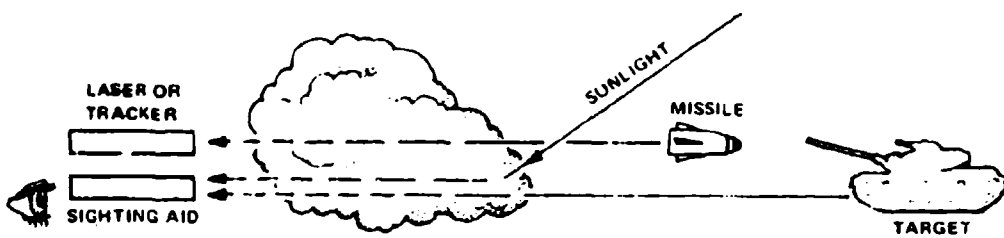


FIGURE 1. EFFECTS OF SMOKE ON COMMAND TO LINE-OF-SIGHT ATGM'S

Several defeat mechanisms are illustrated in Figure 1:

- \*First, the smoke cloud may block the gunner's image of the target.
- \*Second, the cloud may scatter ambient light so that no coherent image can be distinguished through the cloud. In either case, the gunner can no longer track the target.
- \*Third, the cloud may attenuate light from the tracking flare to the point that the missile tracker in the guidance system can no longer track the missile.

Smoke can also effectively defeat or severely degrade laser guidance systems. With laser guided systems, the target is normally designated with a laser spot from a laser designator operated by the gunner or an observer. A seeker in the nose of the missile senses the laser spot and guides the missile to the target. This technology has been implemented in bombs, missiles, and

# UNCLASSIFIED

**UNCLASSIFIED**

artillery projectiles.

Smoke affects these systems in two ways. (Figure 2) (14: 2-5):

\*First, smoke can attenuate either the primary or reflected laser energy to a level which the seeker cannot detect.

\*Second, the obscurant cloud may reflect the laser spot and appear to the seeker to be the target. The missile is then guided to the leading edge of the cloud rather than the target.

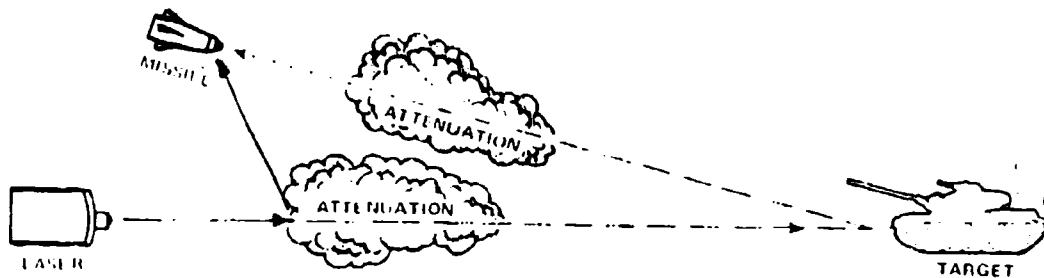


**FIGURE 2. EFFECTS OF SMOKE ON LASER GUIDANCE SYSTEMS**

Directed energy weapon systems are an emerging threat on the modern battlefield. "Star Wars" technology may be employed in the near future in both anti-materiel and anti-personnel laser weapons. The fact that these systems depend on coherent energy for damage-producing effects can be countered by smoke. Smoke scatters this coherent energy and may, therefore, greatly reduce the effectiveness of laser weapons. The concepts have yet to be tested, however, obscurants show promise for degrading this modern threat.

Thus, smoke can severely degrade the effectiveness of these modern systems. No new technology is required to execute the mechanisms described. Some authors believe that smoke is more effective than high explosives or other suppressive fires in limiting the effectiveness of these systems. A few hundred dollars worth of unsophisticated munitions can prevent a sophisticated missile worth thousands of dollars from hitting its target!

Given acceptance of the capability of smoke to defeat sophisticated electro-optical weapon systems, let's not forget that smoke has a much broader effect. I mentioned earlier that the eyeball is the most common sensor on the battlefield. Accomplishing any task which requires visual contact with your surroundings is affected by smoke. Land navigation using terrain features is

**UNCLASSIFIED**

# UNCLASSIFIED

D-7

impossible in a smoke cloud. Use of optical sights, binoculars and image intensifiers may be impossible. More subtly, the isolation created by the inability to see your surroundings may cause uncertainty and even panic which can alter the course of a battle.

How do these weapon system-defeating smoke clouds appear on the battlefield? The capability to employ smokes as combat tools is well-established in most modern armies. Table 1 provides employment and area coverage data for selected systems now in the field with the U.S. Army.

Meteorological conditions always require careful consideration. Smoke effects may be enhanced or degraded by the weather. The conditions used to construct Table 1 have been carefully selected neither to enhance nor degrade the effects of the obscurant. The table reflects a "middle of the road" view. Under more favorable conditions, less ammunition may be required for the same effect. There are also conditions, such as during high winds, when smoke employment may not be feasible.

Table 1 demonstrates that the U.S. Army has substantial resources available today for effective smoke employment. A number of programs are underway which will substantially enhance these capabilities. Among these are:

\*The XM825 Improved Smoke Screening Projectile. This system will improve present area coverage and duration capabilities of the 155mm artillery system to provide screening forward of the FEBA (forward edge of the battle area). The logistic burden of providing that support will also be substantially reduced.

\*The XM819 Improved 81mm Mortar Smoke Screening Cartridge. This round will enhance the present smoke screening capability of the 81mm mortar many fold.

\*The XM49 Smoke Generator. The screen described in Table 1 for M3A3 Smoke Generator will be capable of being established using XM49 generators with one-third fewer generators and half the manpower. In addition, the system will be capable of operating from a moving vehicle. It will also be capable of disseminating a number of different smoke agents, to include agents which obscure the far IR region of the spectrum.

\*The M259 2.75 Inch Smoke Rocket. This round is now being fielded. It will provide excellent capability for air to ground smoke employment. For example, one ripple of 19 rockets can produce a screen several kilometers in length. The screen will last for more than five minutes.

The conclusion must be that we have the means, at least from the standpoint of hardware capability, to counter modern weapon systems with smoke. Present and planned U.S. Army procurements will comfortably satisfy most projected requirements based on present demand.

# UNCLASSIFIED

UNCLASSIFIED

TABLE 1. CHARACTERISTICS OF SELECTED SMOKE SYSTEMS

<u>SYSTEM/ AMMUNITION</u>	<u>PURPOSE</u>	<u>EXPENDITURE</u>	<u>TYPICAL COVERAGE</u>	<u>TIME TO ESTABLISH</u>	<u>TYPICAL DURATION</u>	<u>RE- MARKS</u>	<u>REFER- ENCE</u>
M239 Grenade Launcher with L-8 Red Phosphorus Grenade	Rapid screening of armored vehicles	12 grenades	Screen 13 meters High, 38 meters wide, in front of vehicle	Two seconds	Three minutes	1, 2	(11:25)
107mm Mortar with M378A1 White Phosphorus Cartridge	Marking and obscuring	Four rounds	Cloud approximately 200m long	Thirty seconds	Cloud moves 1 off target after ninety seconds		(13:2-23)
81mm Mortar with M375 White Phosphorus Cartridge	Marking and obscuring	Three rounds	Cloud approximately 80m long	Thirty seconds	Cloud moves 1 off target after thirty seconds		(13:2-23)
155mm Howitzer with M116 HC Smoke Projectile	Screening and obscuring	Six rounds	Cloud approximately 600m long	Ninety seconds	Four minutes	1	(13:2-23)
M3A3 Smoke Generator	Screening	24 generators (one platoon)	Cloud 2km wide, 3km long	Twenty minutes	Indefinite	3	(8:21)
M5 Smoke Pot	Screening	Five pots	Screen approximately 1.5km long	Three minutes	Fifteen minutes	1	(8:21)

Remarks:

1. Meteorological conditions chosen are wind direction parallel to the forward edge of the battle area (FFBA), windspeed of five knots, and neutral conditions of atmospheric stability.
2. Does not include downwind travel of cloud.
3. Conditions are the same as #1. Wind direction is not critical because the platoon can normally move to adjust to wind direction.

UNCLASSIFIED

## UNCLASSIFIED

D-7

However, there are a number of points that could limit ability to employ the capability. First, smoke pots are in short supply. Second, and perhaps of more importance, demands for smoke ammunition have been low over the past twenty years. The succeeding paragraphs point out that U.S. Army use of smoke in training and planned use in combat is quite low. Increased use of smoke may drive requirements for increased production of standard smoke materiel.

Now let's examine some tactical considerations. Can this capability be integrated into plans of fire and maneuver to provide an effective tactical tool? The Soviets think so. In fact, the easiest way to answer this question is to borrow a few pages from the Soviet book (4:192):

"Now when the effectiveness of all types of weapons is significantly growing, screening with smoke plays an even more important role in safeguarding combat operation of troops. It makes observation, aimed fire and control of podrazdeleniye (units) difficult and does not permit the use of infrared, television, laser and other equipment."

Donnelley's recent article in the International Defense Review (3, 1099), provides considerable insight into how the Soviets intend to integrate the capability of smoke into offensive operations. The Soviets are concerned with what is considered to be an awesome anti-tank defense capability within NATO. According to Donnelley, ". . . . smoke is seen as the best way of reducing the effectiveness of NATO long range anti-tank weapons." (4:1105). The Soviets consider that the employment of smoke screens between advancing formations and threat weapons will reduce the effectiveness of those weapons by five times (4:195). Employment of smoke on defending positions in a blinding role will reduce the effectiveness of those weapons by approximately ten times. (4:195).

Open literature indicates that the Soviets not only accept these principles, but have the doctrine, and practice it in training, to support successful application in combat. Emphasis in training is extremely important. The Soviets recognize that smoke may hinder operations if it is not used in a coordinated combined arms role by soldiers who are familiar with its effects. Accordingly, planning and execution of smoke operations are routinely practiced in training exercises.

Integration of smoke into tactical operations is not a new concept for the U.S. Army. The annals of World War II and Korea contain numerous accounts of smoke operations. The Army has, however, been dangerously slow in using this experience to accommodate the modern "smart" weapons threat. We must also remember that smoke can be likened to a two-pointed spear. We must not only employ smoke to enhance survivability against threat electro-optical weapon systems, but we must also be prepared to cope with hostile employment of smoke agents on our forces.

## UNCLASSIFIED

**UNCLASSIFIED**

The problem faced by the Army is not so much one of failure to recognize the threat, but of one to rise to it completely. Former Vice Chief of Staff General W.T. Kerwin, Jr. highlighted the need in 1977 with this often quoted charge (18): "The Army's objective must be to man, equip, and train an Army which routinely thinks in terms of realistic battlefield environmental conditions, and can operate successfully when subjected to them." General Kerwin includes smoke and other limited visibility conditions in his reference to the realistic battlefield. This guidance has been responded to in a number of ways, some of which will be discussed below. However, one of the problems of our implementation tends to be that it is limited to occasional excursions into those conditions.

We must prepare to cope with the conditions of modern battle through day-to-day training and practice under those conditions. Occasional exposure to the realm of the obscured battlefield will not be adequate preparation for our next war. We will not succeed in that war unless we are capable of employing our combat resources in a means which will recap the synergistic effect of coordinated employment of combat assets.

The Chemical Systems Program Review (SPR) hosted by the Vice Chief of Staff of the Army at Ft. McClellan, AL in May 1980, pointed out our principal shortfalls in capability to employ smoke, as well as our ability to fight under conditions created by hostile employment of smoke. These shortfalls include insufficient doctrine and infrequent training (16). Doctrine in smoke employment has not kept pace with improvements in materiel and changes in tactical doctrine over the past twenty years. There are two facets to the training issue. The first is training under obscured conditions. This will prepare our forces to cope with hostile smoke employment as well as the undesirable effects of U.S. Army smoke employment. The second is training in employment of obscurants as a countermeasure to high technology weapon systems.

The adoption of recommendations resulting from the SPR will substantially enhance U.S. combat capabilities. SPR recommendations are already driving Army actions to that end. A concept for the employment of smoke (TRADOC Pamphlet 525-3), was published in September of this year. This concept will be used as a foundation for review and update of doctrinal literature applied in all Army mission areas. It serves as a keystone for integration of smoke as a combat multiplier in tactical planning at all levels of command. The ideas expressed in that concept, when fully adopted, will enhance the survivability of our forces for years to come.

That is not to say that the Army's tacticians and planners have completely ignored the capabilities of smoke, particularly since the mid-seventies. The number of commanders who will

**UNCLASSIFIED**

## UNCLASSIFIED

D-7

reject provisions for use of smoke in tactical plans because it will "screw things up" is fast declining. Few officers in today's Army will deny that we have a need for responsive and effective smoke employment in the field. However, too few officers routinely consider employment of smoke in formulating tactical plans.

Training in smoke employment and under obscured conditions remains inadequate. Scarce resources contribute to this lack of training. Suitable smoke producing ammunition is either scarce or inconvenient to use. Smoke pots are expensive and not readily available for training. They produce smoke too long for realistic simulation of artillery or mortar delivered smoke. Smoke generators, and trained personnel to operate them, are also scarce. They are also impossible to integrate into training scenarios to simulate realistically employment of artillery or mortar delivered smoke. There are some areas, notably Europe, where smoke employment for training must be severely limited due to training area limitations. This is not a severe limitation, however, in the United States.

In summary, our ability to integrate employment of smoke into future battles is marginal, but improving. Training is limited. Doctrine is insufficient. Corrections to these problems are, however, pending or in progress.

Can the U.S. Army use obscurants as a countermeasure to modern weapon systems? Let me first summarize the conclusions from each of the subtopics I have discussed:

First, from a technical point of view, smoke is an effective countermeasure. Current military smokes can severely degrade the performance of weapon systems which operate in the visual or near IR regions of the spectrum. This capability will hold well into the future.

Second, we have the hardware required to employ smoke in battle. Materiel presently under development will substantially improve that capability. However, if we begin to use smoke to the extent justified by its potential as a countermeasure to modern weapon systems, shortages in materiel may severely limit our opportunities to employ smoke.

The overall indication is a qualified yes. Yes, we can, (and should) use obscurants as a countermeasure to modern weapon systems. The "yes", while perhaps somewhat surprising in light of conclusions relative to training and doctrine, is based on several factors not previously discussed. First, there is nothing startlingly new in the recently published smoke concept. Second, historically, the American soldier has always shown remarkable ingenuity and initiative in applying the resources available to him. Integration of the smoke concept into tactical doctrine

## UNCLASSIFIED

# UNCLASSIFIED

D-7

is an important task facing the Army. However, the soldier in the field will not wait for the books to be published before he applies the concept if it is useful to him.

The issue of training in smoke is one which must get high priority. If our soldiers are to be prepared to cope with fighting in an obscured environment, they must experience the effects of smoke on their primary weapon systems, their ability to maneuver, and their own psychological responses. Their leaders need experience in integrating smoke into tactical plans. They need to be able to make firsthand assessments of the benefits and burdens of smoke employment and have an opportunity to adjust their tactics accordingly.

If the Army is to improve its capabilities in this area, several actions need to be pursued:

First, complete integration of the smoke concept into "how to fight" manuals and other training literature.

Second, adopt training devices which make smoke employment during training more realistic and efficient.

Third, train routinely (and frequently) in the employment of smoke and in operations in an obscured environment. Two aspects of training need to be emphasized:

\*Individual and new unit training, including training gunners and crews in operation of primary weapon systems under obscured conditions. Training of officers and NCO's in smoke employment also needs to be emphasized.

\*Unit training, particularly at the battalion level and below. Such training should emphasize integration of smoke employment into tactical plans, and maneuvers under obscured conditions.

Considerations should be given to adding performance of critical functions under obscured conditions as mandatory tasks in Army Training and Evaluation Programs (ARTEP).

Fourth, assess quantities of smoke immediately available for contingencies in light of potential increased requirements and adjust procurement plans accordingly.

Our consideration of the realistic battlefield must be on a continuous basis, not through occasional excursions into that realm. Employment of smoke and fighting in an obscured environment

# UNCLASSIFIED

**UNCLASSIFIED**

D-7

is a significant part of the realistic battlefield. I believe we have a long way to go if we are to be prepared to cope with obscured conditions and use obscurants to their full potential.

**UNCLASSIFIED**

901

# UNCLASSIFIED

D-7

## BIBLIOGRAPHY

### Periodicals

1. Abrantgev, MG B., "Use of Smoke in the Offensive," Military Herald (December 1976). Pp. 191-200.
2. Afansov, MG I., "Under Cover of a Smoke Screen," Military Herald (August 1972). Pp. 89-94.
3. Donnelley, C.N., "Soviet Tactics for Overcoming NAO Anti-Tank Defenses," International Defense Review (July 1979). Pp. 1099-1106.
4. Grabovoy, COL I., "Under Smoke Screen Conditions," Military Herald (October 1975). Pp. 192-198.
5. Kamenko, COL P., "Employment of Smoke in Combat," Military Herald (January 1966). Pp. 66-68.
6. Shelton, COL Henry R., "Smoke as a Weapon" Army Magazine (August 1977). Pp. 33-35.
7. Yezhov, COL N., "Duel With the Anti-tank Guided Missile," Military Herard (March 1974). Pp151-155.

### DOD Publications

8. Department of the Army, Chemical Smoke Generator Units and Smoke Operations, (FM3-50), Washington: U.S. Government Printing Office, April 1967. 80 pp.
9. Department of the Army, Small Unit Smoke Operations, (Training Circular 3-50-2). Washington: U.S. Government Printing Office, December 1978.
10. Department of the Army, Smoke. (Special Text 7-999S). Fort Benning, Georgia: U.S. Army Infantry School, June 1979. 32 pp.
11. Department of the Army, Tank Self Screening Smoke (Training Circular 17-15-9). Washington: U.S. Government Frinting Office, January 1978. 35 pp.
12. Department of the Army, U.S. Army Operational Concept, Employment of Smoke, (Pamphlet 525-3). Fort Monroe, Virginia: U.S. Army Training and Doctrine Command, September 1980. 10 pp.
13. Department of Defense, Joint Technical Coordinating Group for Munitions Effectiveness, Obscurant Effectiveness Manual, (FM 101-61-8). Washington: U.S. Government Printing Office, February 1980. 174 pp.
14. Department of Defense, Joint Technical Coordinating Group for Munitions Effectiveness, Smoke, an Obscuration Primer, (61 JTCG/ME-77-13). Washington, U.S. Government Printing Office, January 1978. 35 pp.

### Other Sources

15. Browning, Robert A., Soviet Capability to Employ Smoke to Limit the Effectiveness of U.S. Anti-Tank Guided Missiles, (Thesis). Fort Leavenworth, Kansas: U.S. Army Command and General Staff College, July 1978.
16. Crawford, Charles N., Briefing to the Chemical Systems Program Review Fort McClellan, Alabama, 28 May 1980.
17. Eure, COL Samuel L., Briefing to the Chemical Systems Program Review, Fort McClellan, Alabama, 28 May 1980.
18. Headquarters, Department of the Army Messae, file symbol DAMO-RQS, subject: The Use of Realistic Battlefield Environmental Conditions Throughout the Army. Washington DC: 22 December 1977.
19. Headquarters, U.S. Army Training and Doctrine Command Message, file symbol ATDO-ZA, subject:

# UNCLASSIFIED

**UNCLASSIFIED**

D-7

Integrated Operations, Fort Monroe, VA, 9 July 1980.

20. Shurtz, LTC Gerald P. et. al., A Dynamic Analysis of the Medium Tank Battalion Conducting Hasty Offensive Operations. Newport, Rhode Island: The United States Naval War College Center for Advanced Research, June 1978. 52 pp. plus annexes.

**UNCLASSIFIED**

903